



**Évaluation du comportement cinétique et du risque
associé aux glissements de terrain rocheux actifs à
l'aide de mesures de surveillance
Le cas du glissement de Gascons, Gaspésie, Canada**

Thèse

Catherine Cloutier

**Doctorat interuniversitaire en sciences de la Terre
Philosophiae Doctor (Ph.D.)**

Québec, Canada
© Catherine Cloutier, 2014

Résumé

Un glissement de terrain actif menace l'intégrité de l'unique chemin de fer qui relie la ville de Gaspé au reste du Québec. Il est impératif de comprendre les mécanismes qui contrôlent cette instabilité afin d'augmenter la sécurité de ce tronçon de la voie ferrée. Un système d'instrumentation du massif fût mis en place en 2009 pour caractériser le glissement, décrire son comportement cinétique, proposer des scénarios de rupture et évaluer le risque. Cette thèse de doctorat rassemble trois articles portant sur ces aspects. Ce document se veut aussi un moyen de partager les connaissances acquises sur l'instrumentation d'un massif rocheux, ainsi que la contribution de ces instruments à un système de prédiction d'un événement potentiellement dangereux.

Le glissement de Gascons est une rupture dièdre asymétrique de 410 000 m³. Il glisse sur le litage de la formation sédimentaire de l'Anse-à-Pierre-Loiselle, une unité de transition composée majoritairement de calcilutite à nodules. Le glissement est divisé en blocs par l'étude des linéaments et des fractures. De plus, des surfaces de rupture intermédiaires sont reconnues. Le suivi *in-situ* couplé au suivi satellitaire mesure des déplacements variant de 6 à 111 mm/an selon les secteurs. L'interaction entre le glissement et les facteurs environnementaux, comme la présence d'eau, est complexe, mais bien présente. La nappe phréatique se situe généralement tout juste sous la surface de rupture dans la majorité du glissement, mais les précipitations et la fonte des neiges augmentent les pressions d'eau et le niveau équivalent de l'eau sous-terrainne augmente au-dessus de la surface de rupture dans le secteur amont du glissement.

Une analyse quantitative du risque est effectuée en adaptant la méthodologie proposée par Fell *et al.* (2005). Des scénarios de ruptures sont déterminés et l'effet domino d'une rupture partielle est étudiée avec un arbre d'évènements qui permet d'associer des probabilités relatives. La probabilité spatio-temporelle minimale sans prédiction est définie afin de caractériser le risque associé à un glissement actif sans prédire la rupture.

Enfin, cette recherche contribue à améliorer la compréhension théorique des mécanismes associés au domaine de la post-rupture, par exemple le rôle de l'eau dans la progression d'une instabilité active.

Abstract

An active rockslide threatens the integrity of the single railway connecting the town of Gaspé to the rest of Quebec. A better understanding of the mechanisms controlling this instability is needed to increase the safety of this section of the track. An instrumentation system was set up in 2009 to characterize the rockslide, describe its kinematic behaviour, propose failure scenarios and assess the risk. This thesis presents three papers covering these aspects. This document is also meant to share knowledge on the instrumentation of a very slow rockslide, and the contribution of these instruments to an early warning system of a potentially dangerous event.

The Gascons slide is a 410 000 m³ asymmetrical wedge failure. It slides on the bedding of the sedimentary Formation of Anse-à-Pierre Loiselle, which is a transition unit mostly made up of nodulous calcilutite. The slide is divided into blocks by the study of lineaments and fractures and intermediate sliding surfaces are identified. In-situ monitoring, coupled with satellite monitoring, shows displacements varying from 6 to 111 mm/yr across different sectors. The slide is sensitive to environmental forces, such as groundwater level variations, but the interactions are complex. The water table is generally right below the sliding surface, but rainfall and snowmelt increase groundwater pressure, and the equivalent water level is then above the sliding surface in the uphill part of the slide.

A quantitative risk analysis is carried out by adapting a methodology proposed by Fell *et al.* (2005). Failure scenarios are determined and the domino effect of a partial collapse event is evaluated by constructing an event tree, which enables the determination of relative probabilities. The concept of minimum temporal spatial probability without forecasting is defined to characterize the minimal risk associated with an active slide without predicting the rupture.

Finally, this work contributes to improving the theoretical understanding of the mechanisms associated with the post-failure stage, for example the role of water in the progression of an active instability.

Table des matières

Résumé.....	iii
Abstract.....	v
Table des matières.....	vii
Liste des tableaux.....	xi
Liste des figures.....	xiii
Liste des symboles et des abréviations.....	xix
Remerciements.....	xxi
Avant-propos.....	xxiii
1 Introduction.....	1
2 The Anatomy of an Active Slide: the Gascons Rockslide, Québec, Canada.....	5
2.1 Résumé.....	5
2.2 Abstract.....	5
2.3 Introduction.....	6
2.4 Data and Methods.....	7
2.4.1 Historical Background Compilation.....	7
2.4.2 Digital Elevation Models.....	7
2.4.3 Monitoring System.....	8
2.4.4 Discontinuities and Lineaments Characterization.....	9
2.4.5 Kinematic Analysis.....	11
2.4.6 Characterization of the Rockslide's Geometry.....	11
2.4.7 Limit Equilibrium Analysis.....	12
2.5 Geomorphology.....	12
2.5.1 Observations.....	12
2.5.2 Interpretations.....	13
2.6 Geology.....	15
2.7 Structural Geology.....	17
2.7.1 Discontinuity Evaluation.....	17
2.7.2 Comparison with the morphological analysis.....	19
2.8 Kinematic Analysis.....	22
2.9 Failure Mechanism and Shape of the Rockslide.....	23
2.10 Hydrogeological Model of the Slide.....	24
2.10.1 Surface Observations.....	24

2.10.2	Climate Records.....	24
2.10.3	Piezometer Records.....	24
2.10.4	Hydrogeological Model.....	26
2.11	Failure Analysis.....	27
2.12	Post-failure Characterization.....	28
2.12.1	Overall Displacements	28
2.12.2	Petit-massif	28
2.12.3	East-Centre and Block-E.....	29
2.13	Conceptual Model of the Slide	30
2.13.1	A Complex Wedge Failure	30
2.13.2	Uncertainties Related to the Shape of the Sliding Surface.....	31
2.13.3	Comparison with the Ancient Slide's Shape.....	31
2.14	Discussions.....	32
2.15	Conclusions	33
3	Understanding the Kinematic Behaviour of the Active Gascons Rockslide from In-situ and Satellite Observation Data.....	53
3.1	Résumé.....	53
3.2	Abstract.....	54
3.3	Introduction	54
3.4	A Review of Displacement Analyses of Cases Similar to the Gascons Slide.....	56
3.5	Description of the Gascons Rockslide	58
3.6	Methodology: Presentation and Analysis of Monitoring Data.....	60
3.6.1	Relative Surface Displacements.....	61
3.6.2	Absolute Displacements	65
3.6.3	Horizontal SAA	71
3.6.4	Weather and Pore Water Monitoring	72
3.7	Kinematic Analysis and Interpretation.....	73
3.7.1	Overall Behaviour	73
3.7.2	Petit-massif.....	74
3.7.3	Block-E	75
3.8	Time Variations and Climatic Factors	76
3.8.1	Climatic Effects on Displacement Rates	76
3.8.2	Seasonal Patterns	78
3.9	Kinematic Evolution of the Gascons Slide	80

3.9.1	Estimating the Age of the Rockslide.....	80
3.9.2	Kinematic Behaviour Prior to Rapid Failure: the 1998 Event.....	81
3.9.3	Evolution of the Rockslide	82
3.10	Discussion	82
3.10.1	Comparisons to Cases Similar to the Gascons Slide.....	82
3.10.2	Evolution of the Rockslide.....	84
3.10.3	Lessons Learned	84
3.11	Conclusions and Recommendations	86
3.11.1	Summary.....	86
3.11.2	Recommendations	87
4	Risk Analysis of an Active Rockslide: the Gascons Rockslide, Québec, Canada	107
4.1	Résumé	107
4.2	Abstract.....	107
4.3	Introduction.....	108
4.4	Current State of the Gascons Rockslide.....	109
4.4.1	General Settings.....	109
4.4.2	Monitoring System.....	110
4.4.3	Rockslide Displacements and Morphology.....	110
4.4.4	Damage Related to the Current State of the Rockslide.....	112
4.4.5	The 1998 Collapse Event.....	112
4.5	General Concepts of Risk Assessment	113
4.5.1	Definitions.....	113
4.5.2	Determination of Risk Equation Parameters.....	116
4.5.3	Risk Acceptability	118
4.6	Methodology of the Gascons Rockslide Risk Analysis	120
4.6.1	Adaptation of the Methodology Proposed by Fell <i>et al.</i> (2005).....	120
4.6.2	Hazard Analysis	121
4.6.3	Consequence Analysis.....	122
4.6.4	Evaluation of Failure Scenarios by Event Tree	124
4.6.5	Risk Mitigation and Warning Criteria Definition	125
4.7	Hazard Evaluation	126
4.7.1	Probability of Occurrence of a Collapse Event ($P_{(L)}$).....	126
4.7.2	Description of Collapse Event Scenarios	127

4.7.3	Event Tree Analysis and Evaluation of the Domino Effect.....	129
4.8	Evaluation of the Consequences: $P_{(S,T)}$, $P_{(T,L)}$, and $V_{E,T}$	130
4.9	Risk Analysis Results.....	131
4.10	Warning System and Warning Criteria Determination.....	132
4.10.1	The Idea behind a Warning System.....	132
4.10.2	Approach of the WEB-based Warning System.....	133
4.10.3	Threshold Values.....	134
4.10.4	Limitations of the Warning System.....	136
4.11	Discussion on the Risk Analysis Uncertainties.....	138
4.12	Concluding Remarks and Recommendations.....	139
	Conclusions (English version).....	153
	Conclusions (version française).....	157
	Références.....	163
	Annexes.....	171
	Annexe A. Mise en place et validation du système de surveillance de Gascons.....	172
	Annexe B. Caractérisation des instabilités côtières dans le secteur de Port-Daniel-Gascons, Gaspésie, Québec.....	191
	Annexe C. Analysis of one year of monitoring data for the active Gascons rockslide, Gaspé Peninsula, Québec 201.....	201
	Annexe D. Kinematic considerations of the Gascons rockslide, Québec (Gaspésie).....	210
	Annexe E. Preliminary numerical modelling with the distinct element code 3DEC.....	217
	Annexe F Données brutes des instruments à lectures manuelles.....	235
	Annexe G : Logs des trois forages échantillonnés.....	263

Liste des tableaux

Table 2-1 Qualitative descriptors for spacing and persistence values (ISRM 1978)	10
Table 2-2 Discontinuity sets orientations presented in stereographic projections of Figure 2-10. Refer to the stereographic plots in Figure 2-10 to observe the variability of the different discontinuity sets. The sectors 1 to 4 are identified in Figure 2-1 by the red rectangles.	20
Table 2-3 Spacing and persistence evaluation of discontinuity sets A, C, and D using the TLS point clouds. SD stands for standard deviation.	21
Table 3-1 The table presents information relative to the extensometer network.	64
Table 3-2 This table present the information relative to the 13 crackmeters. The yearly and total displacements are indicated. The average rate is obtained by a linear regression performed on the complete data set. The fissure's initial width was measured with a measuring tape.	65
Table 3-3 Information relative to the targets surveyed with the total station.....	70
Table 3-4 Average displacement rates from 2010 to 2012 obtained from the PTA-InSAR analysis that was performed by the team of the Canadian Centre for Mapping and Earth Observation (ESS-CCMEO, Natural Ressources Canada) (Couture <i>et al.</i> 2010, Couture <i>et al.</i> 2011). Only markers on which a 3D analysis could be performed are presented.....	71
Table 3-5 Computed times to close fissures assuming that the displacement rates are constant through time. The underlined instrument names indicate the ones measuring cracks at the surrounding of the rockslide.....	81
Table 4-1 Summary of Hong Kong vulnerability ranges for death from landslide and recommended values to use in risk analyses (from Finlay <i>et al.</i> 1996, cited by Dai <i>et al.</i> 2002).....	117
Table 4-2 Probability values associated to qualitative terms describing the occurrence potential of a dangerous event after Lacasse (2008).....	122
Table 4-3 Time needed to cumulate an extra meter of displacement, if the displacement rates stay constant in time. For more information about the displacement rates, read Chapter three of this thesis.	127
Table 4-4 Parameter values used to calculate the <i>minimum $P_{(S,T)}$ without forecasting</i>	131

Liste des figures

Figure 1-1 Les différents stades des mouvements de terrain tel qu'illustré par Leroueil <i>et al.</i> (1996). Le glissement de Gascons se situe dans le domaine de la post-rupture et est actif. Il correspond au cas identifié <i>active slide</i> dans la figure.	4
Figure 2-1 (p 35) Geological map modified from Bourque and Lachambre (1980) presented on the DEM and the 2004 aerial photograph, and the shallowest part of the bathymetric survey revealing a rocky sea floor and the fold indicated with a white dotted line. On the DEM, the white dashed line indicates the contours of the active slide and the white dotted line the adjacent ancient slide. White arrows indicate the sliding direction of planar slides. The yellow arrow is the slide that can be dated from aerial photographs. The red rectangles indicate the location of data shown in the stereonet of Figure 2-10. Insert: Geographic location of the Gaspé Peninsula in Québec, Canada (© Natural Resources Canada. All rights reserved).....	36
Figure 2-2 Monitoring system of the Gascons rockslide shown on the DEM created from ALS data. Insert: Details of the Petit-massif sector, where the 13 crackmeters and Site 1 are located. Sensors installed in boreholes are detailed in the table in the figure.	36
Figure 2-3 Evolution of the Gascons rockslide as seen on aerial photographs of 1934 (top) and 2004 (bottom).	37
Figure 2-4 Block representation of the rockslide. The letters BA to BH refers to the rosettes on the right, that are presenting the lineaments mapped inside the Gascons rockslide by Lord <i>et al.</i> (2010) and Lord (2011)...	38
Figure 2-5 Reconstruction of the ancient slide topography prior to failure using A) SLBL algorithm and B) plane fitting. C) Sliding surfaces of the active and the ancient slides created using planes.....	39
Figure 2-6 A) Cliff as viewed from the Chaleurs Bay showing the limits of the geological formations. The blue line indicates a zone that is always wet indicating the water table position. B) Photo of the fold taken from the beach.	40
Figure 2-7 Rock specimens with slickensided surfaces. A) Photography taken in fracture A (Figure 2-2) showing limestone beds with slickenlines alternated with weathered mudstones. B) Fracture covered with calcite and iron oxide observed in the borehole core of Site 1 (Figure 2-2) and photographed with a binocular. C) Binocular photography of a fracture in the APL Formation taken from Site 1. D, E) Pictures of the APL Formation in the core of Site 1. Figure 2-8 shows SEM images of a sample coming from the unit shown in D.41	
Figure 2-8 SEM images from a longitudinal cut in the shale sample shown in Figure 2-7D taken at 21.8 m a.s.l. in the core of Site 1 in the APL Formation. The positions of images B,C, and D are shown in A.....	42
Figure 2-9 Cross-sections illustrating the hydrogeological model. Their location is indicated on the top map. SAA3 and SAA2 displacement profiles are indicated on cross-sections AA' and BB' respectively.....	43
Figure 2-10 Four stereographic projections (lower hemisphere, equal angle, with Fisher representation) showing structural data collected in three sectors identified by red rectangles in Figure 2-1. Measurements of stereographic projection 1 were realised in the active rockslide with a compass. Data from stations 2 and 3 are obtained from the study of TLS point clouds with <i>Coltop 3D</i>	44
Figure 2-11 This Figure shows three representations of the Petit-massif and presents the discontinuities identified in the Petit-massif based on the TLS point cloud and DEM. A) Color representation in <i>Coltop 3D</i> . The	

colors are associated to point normals as shown on the stereonet in B. C) Same area view in Polyworks D) Photograph on the same area with some discontinuities identified.44

Figure 2-12 Kinematic tests using both the active slide and the Pointe-au-Maquereau slopes. Great circles in blue correspond to the slope faces. The instability zones are presented in yellow.45

Figure 2-13 A) The sliding surface is constructed with planes and shown on an oblique view of the DEM. The dip and dip direction of planes are indicated. The East-Centre and the Petit-massif are identified. B) Interpretation of the sliding surface of the East-Centre, approximated by planes. C) Block-E is marked out on the DEM.46

Figure 2-14 Displacements measured at Gascons. A) Inclinometer (black) and SAA3 (orange) at Site 1 from May 2010 to May 2013. B) SAA2 data from January 2010 to October 2011 at Site 2.47

Figure 2-15 Hydraulic head of the nine piezometers installed in the three boreholes, for the time span between October 2011 and March 2012. The altitudes of the sensors are indicated on the Y-axis. Below, temperatures and daily precipitations are presented.48

Figure 2-16 Hydraulic head of the three piezometers installed at Site 2 and their installation elevations. Rock Quality designation (green) and recuperation data of the core (orange) are indicated in % on the right. Below, temperatures and daily precipitations are graphed. The vertical lines indicate the start of yearly snow melt.49

Figure 2-17 Limit equilibrium sensitivity analyses results. Above the Factor of Safety is computed for changing friction angle for four different water pressures. Below: The factor of safety is computed for changing fissures water percent filled.50

Figure 2-18 A) Displacement-time plots from SAA2, inclinometer, crackmeter F11, and extensometers (G and EX34-35). Instruments locations are indicated in Figure 2-2. B) Displacement-time plots of four crackmeters.51

Figure 3-1 The location of the Gascons rockslide is indicated in the right corner insert (© Natural Resources Canada. All rights reserved.) The rockslide (dashed lines), the railroad (white line) and major geological features (black lines) are marked on the elevation model hill shade. Arrows indicate planar slides on the Pointe-au-Maquereau. The ancient wedge slide is surrounded by a dotted line.89

3-2 Idealized creep behaviour where the three phases are identified (taken from Crosta and Agliardi, 2003)..89

Figure 3-3 **A-A'**: Cross-section through the Petit-massif sector with the inclinometer displacement profile, location of crackmeter F11, and piezometers at Site 1. **B-B'**: Cross-section passing through Site 2, East-Centre and Block-E. The dashed blue line represents schematically the maximum water level measured by P5 and the blue polygon the lower water level measured by piezometers at Site 2.90

Figure 3-4 A) Oblique view of the elevation model and in green the sliding surface of the rockslide. Key sectors are identified: Petit-massif, Block-E and East-Centre B) Stereographic representation of the discontinuity sets. The planes forming the wedge sliding surface are indicated in bold. The red arrow represents the intersection line of the discontinuity pair forming the wedge.91

Figure 3-5 View towards the east showing deformation of the railroad with a clear departure from a straight line at the eastern limit of the rockslide. The horizontal displacement from the initial alignment is estimated to be about 1 m from the observation of aerial photographs and DEM.91

Figure 3-6 Horizontal displacement rates are represented by vectors and vertical displacement rates by circles. The negative values are for downward displacements. The points inside the white dashed rectangle are

located on the retaining walls, thus they are measuring displacement caused by the slide and also linked to the retaining walls deformation. Only the ones useful for this paper are presented. Time spans of the data set on which the displacement rates are computed vary between instruments, refer to the different tables of this chapter for more information. The block representation of the slide is presented on top of the hill shade of the elevation model. 92

Figure 3-7 Monitoring system of the Gascons rockslide shown on DEM. Fissures A to G are indicated. Insert: Details of the Petit-massif sector, where the 13 crackmeters and Site 1 are. The sensors installed in boreholes are detailed in the table. 93

Figure 3-8 Location of the total station targets and of the permanent reflectors for PTA-InSAR analyses. 94

Figure 3-9 Displacement-time curves of different instruments. The time is relative to the beginning of the measurement for each station. This allow to plot on the same graphic the 1993-94 data with more recent ones. 94

Figure 3-10 Crackmeters displacement curves. F11 curve uses the y-axis to the right, the other are plot using the left y-axis. The inset in the left top corner traces F11 and F6 using the same y-axis to show how displacements of F11 are more important than other crackmeters. 95

Figure 3-11 Maximum displacement rates measured on a period longer than 10 days for the crackmeters installed on pre-existing fractures. The rates are calculated by a linear regression. The coefficient of determination (R^2) and the time period on which they are calculated are indicated. 96

Figure 3-12 Site 1 in depth displacements profiles. Left: Inclinometer data in black and one SAA3 profile in orange. The x-axis is towards 183° , the y-axis towards 093° . Right: SAA3 profiles starting in December 2009. The SAA3 data are rotated to fit with the inclinometer's axis orientation. The ground surface is 63 m above sea level. 97

Figure 3-13 X and Y components of displacements of inclinometer (dashed lines) and SAA3 (hard lines). SAA3 curves are created using only the records that were taken simultaneously to the inclinometer surveys, in order to compare both instruments. An example of SAA3 records taken every 6 hour is presented in grey ($z=3.5$ m). 98

Figure 3-14 (on the next page) Vertical SAA3 displacement-time curves at depths of $z=1$ m and $z=33$ m. Their displacement rates computed as linear regressions over a period of 20 days are presented (black curve for $z=1$ m and blue for $z=33$ m). Cumulated and daily rainfalls are presented. Piezometer head measured by P5 (Site 2) and P3 (Site 1) are also plotted 98

Figure 3-15 A) Displacement profiles of SAA2, located at Site 2 (Figure 3-7) between November 2009 and October 2011. B) X and Y displacement components of SAA2, showing an apparent rotation of the displacement direction. 100

Figure 3-16 In black are displacement versus time curves of SAA2 at three different depths: 1, 12, and 27.4 m (elevation of 98.25, 87.25, and 71.85 m). In red is the piezometer equivalent elevation of water level measured at a depth of 36.6 m (elevation of 62.65m), which is under the sliding surface. In blue are the displacement rates measured on a 20 day period. The bar chart presents the daily precipitations. The pale blue line is the cumulated precipitation. 101

Figure 3-17 The top graphic presents monthly settlement profiles measured by the two horizontal SAA from September 2011 to June 2013. The two chains are joined together, by imposing the displacement of the last

segment (east side) of SAA4 to the first (west side) segment of SAA1. Both graphics at the bottom present SAA1 profiles for shorter time intervals. 102

Figure 3-18 Monthly precipitations measured with the weather station on site. 103

Figure 3-19 Temperatures and precipitations measured by the weather station at Gascons. The shaded areas are the estimated snow melt periods. 104

Figure 3-20 Tentative modeling of creep phase II and III for the 1998 slide event. The dashed blue line is an interpolation considering a constant displacement rate, while the black curves present different hypotheses concerning the accelerating phase of the creep model. The curves in grey present displacement measured between 2009 and 2013 and they show no signs of acceleration. 105

Figure 4-1 The Gascons rockslide’s location in the Gaspé Peninsula is indicated in the inset (© Natural Resources Canada. All rights reserved.). The elevation model of the rockslide and its surroundings is showing the railroad, the road, past rockslides (black arrows) and geological features (angular unconformity and Port-Daniel River fault). 141

Figure 4-2 A) Oblique view of the elevation model of the Gascons rockslide. The main sliding surface appears in green and the rockslide different sectors are identified. B) Stereographic representation of the discontinuity sets. The failure surface is a wedge formed by the bedding planes (S0) and discontinuity set D. The lateral surface has a stepped morphology and is formed by the intersections of sets A and D. 141

Figure 4-3 Instrumentation map, displacement vectors and block representation of the rockslide presented over the hill shade of the elevation model. The inset presents a zoom of the Petit-massif sector. 142

Figure 4-4 Photography taken in 2009 before the installation of the monitoring system looking towards the west and the Petit-massif sector. 143

Figure 4-5 Cross-sections AA’ and BB’ locations are indicated in the top corner image. Cross-sections show the sliding surfaces, vertical profiles of displacements, piezometers locations and the water level. **AA’** shows the Petit-massif, while **BB’** shows East-Centre and Block-E sectors. 144

Figure 4-6 Displacement measurements: Blue curves are measurements taken in 1993-1994 and the other ones between 2009 and 2012. All reading sequences are starting at a time value of 0. 145

Figure 4-7 Examples of damage caused by the accumulation of displacements on the infrastructures and of the 1998 collapse event. A) Undermining of the railway ballast in an underlying fissure in February 2011. B) Deformation of the retaining wall and of the railway. C) Deformation in the retaining wall built in 1998 D) Newspaper cut showing the damaged railroad after the 1998 slide event (Le Soleil, 1998). 146

Figure 4-8 Flow chart of landslide risk management as proposed by Fell *et al.* (2005). 147

Figure 4-9 A) Example of a cumulative frequency curve in a risk analysis of a road threaten per landslides presented by Wong (1997) and B) Societal risk tolerability criteria in Hong Kong presented in Ho and Ko (2009). 148

Figure 4-10 Event tree analysis to evaluate the domino effect. Every event is described in section 4.7.2. The sum of the joint probabilities (in red) leading to a major collapse are indicated in black for each of the five initial events. 149

Figure 4-11 The grey zone presents the range of risk values computed in this study. The estimated residual risk, the risk considering that 1% of the time the train will not be able to stop if a danger occurs and the risk computed with a return period of 70 years are plotted for an arbitrary number of fatalities (N) of 20..... 150

Figure 4-12 Proposed velocity based warning criteria found in the literature. The green stars show the criteria that were defined prior to brutal failure. In the vast majority of cases, the authors proposed intervals associated with different alert levels. The author associated colors to the values, even though some authors have not. Green and blue colors are used to represent situations considered normal, yellow is use for an increase activity, orange is a preoccupying situation and must be evaluated by an expert while red is the superior alert level associated with immediate actions. The red warning criteria were generally presented as “more than”. In the figure, the maximum values have been limited to facilitate presentation..... 151

Liste des symboles et des abréviations

abréviation	définition française	English definition
a.l.s	au-dessus du niveau de la mer	above sea level
ALARP		As low as reasonably practicable
ALS	scanner laser aérien	airborne laser scan
APL	Anse-à-Pierre Loïsele	
Ave.	moyenne	average
BP	avant le présent	before present
jr / d	jour	day
<i>d</i>	délai	delay
DEM	modèle numérique d'élévation	digital elevation model
dir.	direction	direction
dis.	déplacement	displacement
E	élément à risque	element at risk
f_p	fréquence annuelle de passage du train	yearly train frequency
H.	horizontal	horizontal
K	constante de Fisher	Fisher's constant
LaVinf	La Vieille Inférieure	
$P_{(L)}$	probabilité d'occurrence d'un glissement	occurrence probability of a landslide
$P_{(LOL)}$	probabilité de perte de vie humaine	probability of loss of life
$P_{(S:T)}$	probabilité spatio-temporelle	temporal spatial probability
$P_{(T:L)}$	probabilité que le glissement atteigne l'élément à risque	probability of the landslide reaching the element at risk
P_s	probabilité d'occurrence relative d'un scénario	relative occurrence probability of a scenario
R	risque	risk
R^2	coefficient de détermination	coefficient of determination
RQD		Rock Quality Designation
SAA		Shape Accelerometre Array
SD	écart-type	standard deviation
SEM	microscopie à balayage électronique	Scanning Electron Microscopy
SLBL	niveau de base local de la pente	slope local base level
TLS	scanner laser terrestre	terrestrial laser scan
t_p	durée de la traversée du glissement	time to cross the landslide
t_v	temps d'arrêt du train	time to stop the train
$V_{(D:T)}$	vulnérabilité d'une personne si atteinte par un glissement	vulnerability of a person if touched by a landslide
$V_{(prop:S)}$	vulnérabilité de l'élément à risque au glissement	Vulnerability of the element at risk to the landslide
V.	vertical	vertical
yr		year

Remerciements

Plusieurs personnes ont épaulé l'auteure lors de ses travaux de recherche. Je souligne donc ici les contributions de ces personnes.

Je remercie d'abord grandement le professeur Jacques Locat, mon superviseur de thèse et mentor, pour les nombreux encouragements et conseils, mais aussi pour sa capacité à créer et saisir toutes sortes d'opportunités qui ont transformé ce doctorat en une expérience mémorable!

Merci à Réjean Couture qui a agi en tant que co-superviseur. Ce fût très agréable de discuter et de travailler avec une personne si généreuse et inspirante.

Merci aux examinateurs de la thèse pour les commentaires constructifs: Corey Froese (externe), Martin Grenon (interne) et Michel Jaboyedoff (interne).

J'ai eu la chance d'effectuer deux stages très formateurs. Merci au professeur Michel Jaboyedoff de l'Université de Lausanne pour son généreux accueil et les discussions qui ont fait avancer ma recherche. Merci au professeur Douglas Stead, de l'Université Simon Fraser (SFU) qui m'a accueilli et permis d'utiliser les outils de son laboratoire. Je me dois de souligner l'accueil et le support offerts par les étudiants-chercheurs et chercheurs rencontrés dans ces stages. Un merci particulier à Clément, Andrea P., Dario et Marc-Henri de Lausanne, ainsi qu'à Andrea W., Fuqiang, Mirko et Mohsen de SFU et tous les autres!

De retour à l'Université Laval, un énorme merci à mes collègues du 5^e! Tout d'abord, merci à Pierre-Étienne Lord, dont la débrouillardise nous a sorti de situations impossibles sur le terrain. Un merci particulier à Dominique Turmel que j'ai souvent dérangé au cours de cette dernière année. Enfin merci à mes collègues: professeure A. Locat, Geneviève, Andrée-Anne, et Sarah, ainsi qu'aux nombreux stagiaires et professionnels qui se sont salis à Gascons : Luc Boisvert, Marie-Pierre, Mélanie, Florence, Agathe, François, Nicolas et Andrea Pedrazzini. Je remercie Pierre Therrien pour tout le développement et le support au niveau des composantes informatiques du système de surveillance et pour les travaux de terrain.

Beaucoup de gens ont rendu le projet Gascons réalisable. Merci à Chantal Jacob, Pierre Dorval, André Drolet, François Bossé (MTQ), Daniel Hébert (TC), François Charbonneau, Vern Singhroy et Christian Prévost (SST-CCCOT, Ressources Naturelles Canada), Olivier Demers (CRE-GIM), Stephan Gravel (B-Ver), Marcel Parisé et les employés du chemin de fer Baie des Chaleurs, ainsi qu'à Marcel Langlois (U.Laval).

Merci à la compagnie Measurand, son président Lee Danisch et ses employés Christiane Lévesque, Martin et Terry pour leurs travaux à Gascons, les dépannages et les nombreuses discussions.

Enfin, merci à Joël, à mes parents Andrée et Roger et à mon frère Louis pour leur support et leur compréhension.

Le Ministère des transports du Québec, le Ministère québécois de l'éducation du loisir et du sport et Transport Canada ont financé le projet. Le Fonds québécois de la recherche sur la nature et les technologies a aussi accordé une bourse d'études à l'auteure.

Bonne lecture!

Avant-propos

Cette thèse de doctorat a été réalisée dans le cadre d'un projet de recherche mené par le Laboratoire d'études sur les risques naturels (LERN) de l'Université Laval, chapeauté par le Ministère des transports du Québec (MTQ) et Transports Canada (TC).

Les chapitres 2, 3 et 4 sont écrits sous forme d'article en langue anglaise, car l'auteure a l'intention de les soumettre pour publication. Ils ont entièrement été écrits par Catherine Cloutier. Lors de la soumission, des co-auteurs seront ajoutés.

Trois articles publiés dans les comptes rendus de conférences sont présentés en annexes. L'auteure de la thèse a entièrement écrit ces articles, en tenant compte des commentaires et opinions des co-auteurs.

1 Introduction

En Gaspésie, au Québec, un tronçon de l'unique chemin de fer reliant Matapédia à Gaspé est menacé par un glissement rocheux actif et qualifié de très lent (Cruden et Varnes 1996). La voie ferrée traverse le glissement de Gascons sur une portion de 200 m. Elle fût acquise en 2007 par le gouvernement du Québec pour assurer le maintien d'un service ferroviaire sécuritaire dans la région, puisque le chemin de fer y revêt une importance particulière pour son développement socio-économique.

Lorsqu'un glissement actif est reconnu, il est possible de suivre ses déplacements pour documenter son comportement post-rupture (tel que défini par Leroueil *et al.* (1996) et illustré à la figure 1-1) et pour prédire son évolution. Des exemples de suivis de glissements rocheux jusqu'à la rupture sont décrits dans la littérature (Cruden et Masoumzadeh 1987; Gigli *et al.* 2011; Mufundirwa *et al.* 2010; Rose et Hungr 2007; Froude 2011; Oppikofer *et al.* 2008; Helmstetter *et al.* 2004; Zvelebil et Moser 2001). Toutes ces études montrent une accélération non-linéaire des déplacements précédant une rupture rapide. L'accélération des déplacements est donc un signe précurseur des ruptures rapides.

C'est donc pour tenter de prédire les mouvements rapides, tels que définis par Cruden et Varnes (1996), et donc plus risqués (Glastonbury et Fell 2008), du glissement de Gascons que le Laboratoire d'études sur les risques naturels (LERN) de l'Université Laval a mis en place un système d'instrumentation in-situ en 2009. Simultanément, un système de suivi satellitaire a été mis en place par Ressources Naturelles Canada (SST-CCCOT).

Les diverses contributions originales attendues des résultats de la recherche découlent de l'atteinte des principaux objectifs décrits ici. Le premier objectif est lié à la caractérisation du glissement de Gascons, c'est-à-dire de développer des modèles géo-mécanique et hydrogéologique, en plus de décrire le comportement cinétique du glissement. Le second objectif est d'intégrer des outils de surveillance terrestre et satellitaire dans une analyse cinétique visant à cerner les zones critiques du glissement pour le chemin de fer et de proposer des scénarios d'évolution du glissement. Le troisième objectif est de déterminer l'aléa posé par un glissement actif pour la voie ferrée et de développer une méthodologie permettant d'évaluer le risque lié à la présence de la voie ferrée dans le glissement actif de Gascons. Enfin, le dernier objectif est de discuter de la pertinence des divers instruments utilisés initialement comme outils de surveillance et d'analyse en un ensemble intégré pour la détermination de critères d'alerte et d'étudier la capacité d'un système d'alerte comme outil de réduction du risque.

Afin de réaliser ce projet, une série d'instruments a été mise en place à l'automne 2009 et à l'été 2010. Il s'agit d'appareils à lectures manuelles (extensomètres, inclinomètre et cibles pour station totale), d'appareils avec

système d'acquisition (fissuromètres, piézomètres, clinomètre, chaînes de capteurs shape-accelerometre-array (SAA) et station météo) (Cloutier *et al.* 2010; Locat *et al.* 2010), et d'un suivi par satellite radar (PTA-InSAR) sur des réflecteurs permanents (Couture *et al.* 2010).

L'auteure de cette thèse a réalisé un passage accéléré au doctorat. Au cours de sa maîtrise, elle a réalisé la conception et la mise en place du système de surveillance en collaboration avec Jacques Locat et Pierre-Étienne Lord, qui a réalisé sa maîtrise dans le cadre du projet Gascons sur la cartographie des blocs du glissement (Lord 2011). Pierre Therrien a développé la partie informatique du système d'acquisition.

L'auteure a planifié et dirigé treize visites de terrain qui ont permis d'effectuer des mesures de déplacements, de cartographier le glissement, de documenter son évolution, d'étudier sa géologie et sa structure et de réaliser des scans lasers. Enfin, ces travaux ont aussi permis d'installer, d'améliorer et d'entretenir le système d'instrumentation.

En se basant sur les informations acquises, les caractéristiques morphologiques, géo-mécaniques et hydrogéologiques sont évaluées. Ensuite, l'analyse des déplacements est effectuée en comparant et en combinant l'information provenant des divers instruments. Enfin, des approches existantes dans la littérature ont été adaptées afin de déterminer le risque associé au glissement, avec une emphase sur l'évaluation de l'aléa.

Cette thèse est composée de trois chapitres de développement écrits sous forme d'articles en anglais et précédés d'un résumé en français. Ces articles n'ont pas encore été soumis pour publication au moment d'écrire ces lignes, mais ont été rédigés entièrement par l'auteure de cette thèse.

Le chapitre deux caractérise le glissement de Gascons en termes de la géologie, de la structure, du mécanisme de rupture, des déplacements et de l'hydrogéologie. Le troisième chapitre analyse les données acquises du système de surveillance afin de décrire les déplacements du glissement de terrain de Gascons. Une section est dédiée à la description des données. Enfin, le quatrième chapitre présente l'évaluation du risque pour le train et ses passagers lié au glissement de Gascons. Ce chapitre propose brièvement un modèle de système d'alerte et l'effet sur le risque y est discuté.

La thèse se termine avec le chapitre 5, où les principales conclusions sont présentées. De plus, des recommandations sont émises selon les conclusions de cette recherche pour des travaux futurs, mais aussi pour l'opération du chemin de fer et la poursuite du suivi avec le système de surveillance.

Les annexes de cette thèse présentent une partie d'un rapport interne réalisé dans la progression du projet de recherche ainsi que certaines données brutes afin de les rendre accessibles aux collaborateurs du projet qui

continueront la surveillance du glissement. Une étude préliminaire réalisée avec le logiciel 3DEC de Itasca est aussi annexée.

De plus, trois articles présentés dans des conférences sont annexés. Il s'agit des articles suivants qui ont été entièrement rédigés par l'auteure de cette thèse en considérant les opinions et les corrections proposées par les co-auteurs :

Annexe B : Cloutier, C., Locat, J., Lord, P.-É., et Couture, R., 2010. Caractérisation des instabilités côtières dans le secteur de Port-Daniel-Gascons, Gaspésie, Québec. Comptes rendus de la 63^e Conférence canadienne de géotechnique, Calgary, pp. : 71-79.

Annexe C : Cloutier, C., Locat, J., Couture, R. et Lord, P.-E., 2011. Analysis of one year of monitoring data for the active Gascons rockslide, Gaspé Peninsula, Québec. 5th Canadian Conference on Geotechnique and Natural Hazards, Kelowna, BC, Canada, 8p.

Annexe D : Cloutier, C., Locat, J., Lord, P.-É., Couture, R., et Jaboyedoff, M., 2012. Kinematic considerations of the Gascons rockslide, Québec (Gaspésie), Canada, 11th International Symposium on Landslides and 2nd North American Symposium on Landslides, Eds.: E. Eberhardt, C. Froese, A. K. Turner, S. Leroueil, Taylor and Francis Group, London, Banff, 2012, vol. 2, pp. 1264-1270.

L'étude détaillée du comportement cinétique du glissement de Gascons à partir de données de surveillance permettra d'améliorer les connaissances dans le domaine de la post-rupture, pour un glissement qui se déplace très lentement. Les systèmes d'instrumentation sont peu répandus, car ils sont coûteux à installer et à entretenir. Le Mont St-Pierre est le seul autre glissement actif rocheux instrumenté dans l'est du Québec, mais l'instrumentation du ministère des Transports y est manuelle et il s'agit d'un bloc monolithique. On trouve quelques équivalents au Canada, dont le système de surveillance de Turtle Mountain (*glissement de Frank*) géré par la Commission géologique de l'Alberta, et celui du glissement de Downie suivi par BC Hydro (Kalenchuck, 2010).

Le projet Gascons est rendu possible grâce à la participation financière du Ministère des transports du Québec, du Ministère de l'éducation, du loisir et du sport, ainsi que de Transports Canada. De plus, l'Agence spatiale canadienne fournit le soutien financier au Centre canadien de télédétection et à la Commission géologique du Canada afin qu'ils participent à l'intégration d'applications satellitaires pour la surveillance du site.

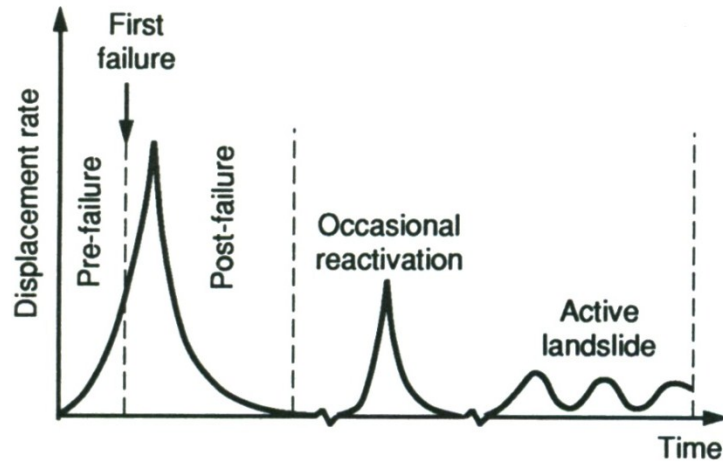


Figure 1-1 Les différents stades des mouvements de terrain tel qu'illustré par Leroueil *et al.* (1996). Le glissement de Gascons se situe dans le domaine de la post-rupture et est actif. Il correspond au cas identifié *active slide* dans la figure.

Chapter 2

The Anatomy of an Active Slide: the Gascons Rockslide, Québec, Canada

2.1 Résumé

Ce chapitre présente la caractérisation du glissement côtier de Gascons à partir de données provenant du système de surveillance, de carottes de forages et de travaux de terrain. Cette étude vise à comprendre les mécanismes de rupture associés au glissement et à décrire son comportement en post-rupture, *i.e.* sa situation actuelle. Le glissement se produit dans des roches sédimentaires de l'unité de transition de l'Anse-à-Pierre-Loiselle constituées d'une alternance de lits centimétriques de calcilutite à nodules, de grès et de calcaire. Le mécanisme de rupture est associé à un dièdre asymétrique de 410 000 m³ qui glisse sur les lits sédimentaires. La surface de rupture voit le jour dans la pente à l'ouest, au niveau de la plage et son élévation augmente vers l'est. La présence d'une faille et d'un pli aplanit la surface de rupture dans le coin inférieur du dièdre, agissant comme une butée. Cinq familles de discontinuités sont reconnues à partir de levés structuraux réalisés sur le terrain et d'une étude réalisée avec le logiciel Coltop 3D sur des nuages de points obtenus de scans laser terrestres. Le comportement post-rupture du glissement se traduit par un mouvement continu avec des vitesses variant de 6 à 111 mm/an et par un désenchevêtrement de la masse en blocs. D'ailleurs, deux secteurs avec des déplacements différents sont reconnus : le Petit-massif et le Centre-Est. Le modèle conceptuel hydrogéologique présente deux niveaux de nappe phréatique, (1) le premier se situe sous la surface de rupture et correspond au niveau le plus bas mesuré et (2) le deuxième est au-dessus de la surface de rupture dans la partie amont du glissement et correspond au niveau atteint lors de la fonte des neiges ou de fortes précipitations. Le modèle permet de conclure que le glissement est très drainant et que l'écoulement se fait vers la mer. Cette caractérisation du glissement met en place les éléments nécessaires à l'analyse détaillée des mesures de déplacements.

2.2 Abstract

This chapter presents the characterization of the coastal Gascons rockslide, based on data from the monitoring system, borehole cores, and field work. This study aims at understanding the failure mechanisms and at describing the post-failure behaviour of the rockslide, *i.e.* its current situation. The slide is taking place in the sedimentary rocks of the Anse-à-Pierre-Loiselle Formation, which is made up of centimetric beds of nodulous calcilutite alternating with sandstones and limestone. The failure mechanism is an asymmetrical wedge failure of 410 000 m³, which is sliding on the bedding. The sliding surface daylights at the beach level

west of the slope and its elevation increases towards the east. The presence of a fault and a fold contribute to flatten the sliding surface near the lower wedge corner, resulting in a sort of buttress. Five discontinuity sets are identified from structural data obtained from field work and extracted from terrestrial laser scanner point clouds with the software Coltop 3D. The post-failure stage of the rockslide is characterized by continuous movement with velocities ranging from 6 to 111 mm/yr and by the individualisation of the mass in blocks. Two specific sectors are identified because they have different displacement rates: le Petit-massif and the East-Centre. The conceptual hydrogeological model presents two water levels, (1) the first is below the sliding surface and corresponds to the lowest measured level and (2) the second level is above the sliding surface in the uphill part of the rockslide and corresponds to the highest level attained during precipitation events and snowmelt. The sliding mass is very well drained and the flow is toward the sea. Characterizations of the rockslide's sliding surface and of the hydrogeology are required to accomplish the kinematic analysis presented in Chapter 3.

2.3 Introduction

Along the coast of the Gaspé Peninsula, in Québec, Canada (Figure 2-1) the only railroad that reaches the town of Gaspé runs directly across an active rockslide over a distance of 200 m. The Gascons rockslide is an active very slow rock slide (Cruden and Varnes 1996) which is in its post-failure stage (Leroueil *et al.* 1996). It was first identified in 1988 by the Ministère de la sécurité publique du Québec (Civil Protection Department). The first geotechnical investigation carried out in 1994, revealed an important network of opened cracks (Figure 2-2) and significant displacements of up to 13 mm/month (Locat and Couture 1995a; b). The evolution of the rockslide is a threat for the railway.

In geotechnical practice, forecasting catastrophic failure remains a major challenge particularly for active rockslides. An active slide has a factor of safety of 1 or less and has already developed its full sliding surface. Conventional tools are not suitable to evaluate the stability in the post-failure stage. For example, a stability assessment by the computation of a factor of safety does not consider the displacements and the long term evolution of the mass mechanical proprieties (Crosta and Agliardi 2002; Faillettaz *et al.* 2010). Therefore, the stability of an active slide must be evaluated by measuring its displacement and by analysing its geometry.

In order to contribute to the safe operation of the railroad, the Gascons project was initiated in 2009. A monitoring system was put in place to understand the various types of movement in an attempt to develop both warning criteria and risk assessment scenarios to be considered as part of a risk management of the Gascons site (Locat *et al.* 2010). Because the slide is undergoing post-failure displacements, various in situ instruments were put in place not to evaluate the factor of safety of the slope, but to understand what affects

the slide's displacements and to understand the influence of the various contributing factors such as coastal erosion and pore pressure variations.

The objectives of the research presented in this chapter are to characterize the geological and structural features, failure mechanism, geometry, hydrogeology, and the activity state of the Gascons rockslide. This information is then used to create an hydrogeological model of the instability. The input data used in the analysis were generated by field work, remote sensing, in situ monitoring, and desktop analysis.

After the presentation of data and methods, the geomorphology and the geology of the slide and its surrounding are described. Then, the structural analysis is presented and followed by the failure mechanism investigation, which is done by carrying out a kinematic analysis. It leads to the description of the sliding surface shape and to the computation of the volume of the instability. With the instability characterized, a conceptual hydrogeological model is presented. Next, the initial failure is investigated with a limit equilibrium analysis and then the post-failure is characterized by its displacement and the rockslide separation into different sectors. The paper ends with a discussion about the slide's general model.

2.4 Data and Methods

The approach used to interpret the geometry and the kinematic behaviour of the rockslide includes studies of historic data, field work, interpretation of monitoring data, remote sensing techniques and office work. Fourteen field visits were realised between June 2009 and May 2013 to collect the data and install the monitoring system.

2.4.1 Historical Background Compilation

All the information available on the Gascons rockslide prior to this project is presented in the report LERN-GASCONS-09-02 (Cloutier *et al.* 2009). This compilation includes work by Locat and Couture (1993 to 1995) and technical reports written by a consultant firm (Journeaux *et al.* 2000; 2003a; b). Aerial photographs of the sector are available through the Quebec government from 1934 to 2011.

2.4.2 Digital Elevation Models

The digital terrain models (DEM) were constructed using airborne laser scan (ALS) obtained in fall 2009 and terrestrial laser scans (TLS) carried out during the summers of 2010, 2011, and 2012. A digital terrain model from an ALS realised in 2008 was available, but its resolution was too low to allow fracture mapping. It has an average point density on the ground of 0.025 point/m² in forested area and 0.5 point/m² in bare area (Lord 2011; Lord *et al.* 2010).

The 2009 airborne survey was conducted at a flight elevation of 500 m, at a frequency of 100 Hz with the scanner Gemini 167 from Optech. The point density on the ground is of 3.8 points/m² in forested areas and of 17 points/m² in bare areas (Lord *et al.* 2010), so 152 and 34 times more dense than the 2008 scan.

The terrestrial scans were undertaken using the Optech IIRIS scanner (Optech 2006). Shadow areas, where no points are generated, are created behind obstacles that are not crossed by the laser (Jaboyedoff *et al.* 2012; Lato *et al.* 2012). In order to limit this phenomenon, called occlusion (Lato *et al.* 2010), scans are taken from many viewpoints. Terrestrial lidar enables point acquisition on vertical and overhanging faces. The TLS point clouds were used to fill gaps in the DEM created from the airborne survey. In Gascons, the TLS scans were useful to get a proper DEM in the cliff area.

At each one of the three TLS campaigns, 15 to 50 scans were taken in order to cover properly the cliff area. The scans were visualized and aligned with Polyworks (Innovmetric 2011) and then aligned with the ALS DEM for georeferencing. Vegetation was removed manually and also automatically from the scans using CANUPO (Brodu and Lague 2012) in conjunction with CloudCompare (Girardeau-Montaut 2012).

In the marine environment, the DEM is obtained from a multi-beam bathymetric survey for water depths of five to about 70 meters, which corresponds to a distance of 3 km from the coast. The survey was carried out by a local company, CIDCO (Rondeau 2010) using the RESON Seabat 7125 SV and the inertial station APPLANIX POS MV 320.

2.4.3 Monitoring System

The monitoring enables one to follow surface and in depth displacements (magnitude and direction), pore water pressures, tilting of the retaining wall, settlement of the railway ballast, and some weather conditions. The system is composed of sensors connected to an automatic acquisition system and of manually made measurements. A complete description of the system's design is available in Appendix A.

Surface displacements are measured by an extensometer network, which consists of 44 rods of 45.7 cm anchored in rock and in soil over fissures. The rods were installed perpendicular to the fissures' orientation. The distance between pairs of rods was measured manually with sub-millimetric precision. The data set is composed of measurements taken during the fourteen field visits realized between June 2009 and May 2013. Surface displacements are also followed by thirteen crackmeters (Geokon model 4420), read automatically every five minutes. They are installed along the railroad and in the cliff area (Figure 2-2). Total station surveys were carried out to follow markers on the H-Beam retaining wall. Displacement data interpreted from Point Target Analysis technique of Interferometric Aperture Radar (PTA-InSAR, Ferretti *et al.* 2001) are also

available from the Canada Centre for Remote Sensing in collaboration with the Geological Survey of Canada (Couture *et al.* 2010; Couture *et al.* 2011).

Displacement profiles with depth are obtained from a 60 m deep traditional inclinometer casing and probe (DIS-500, RocTest Group), and from two shape accelerometers arrays (SAA) (Measurand, Danisch *et al.* 2010) of 52 and 48 m long at Sites 1 and 2 respectively (Figure 2-2). The SAA is a chain of 50 cm joint-linked rigid segments (Danisch *et al.* 2010). Each segment has accelerometers to measure inclination. It acts as an in-place inclinometer and data are collected four times a day. The inclinometer data set is a compilation of nine surveys between December 2009 and May 2013.

Nine vibrating wire piezometers (Geokon, model 4410) are installed in three boreholes. Their location is identified in Figure 2-2. There are three sensors per borehole and their position was determined as follow: (1) the deepest was installed in the bottom of the hole; (2) the top one was positioned two meters below the water level in order for it to remain saturated even if the water level fluctuates; (3) the third sensor was placed at equal distance between the two others. Time was allowed to try to obtain a stable water level before proceeding to the installation. In average, the installation took place 24h after the end of drilling. The piezometers measure water pressure and are installed in a fully grouted borehole (McKenna 1995; Mikkelsen and Green 2003). In each borehole, the shallowest piezometer has a range of 350 kPa, while the two deeper have a range of 700 kPa, which is equivalent to water columns of 35 and 70 m. Sensor's sensitivity is 1 cm for the 350 kPa range and 2 cm for the 700 kPa range. The reading interval of six hours is short enough to detect the pressure changes caused by precipitation and snow melt.

A weather station that consists of a thermometer, a barometer, a relative humidity sensor, a wind speed sensor, and a precipitation gauge (water and rain) is located on the "guérite" (Figure 2-2).

Cores of three of the six diamond-drilled boreholes were kept to study the stratigraphy. They reach a depth of 48, 51, and 53 m.

2.4.4 Discontinuities and Lineaments Characterization

The interpretation of the geometry and of the failure mechanism of the Gascons slide is made by combining the historical, rock structure, and monitoring data.

The structural analysis was first carried out using field compass and then completed with the TLS point clouds analysis in the software Coltop 3D (Jaboyedoff *et al.* 2009; Terr@num 2011). The extraction of georeferenced points' orientation in Coltop 3D is based on the calculation of the normal vector and its visualisation in the form of a unique colour coded representation. The color shaded elevation model helps to recognize long persistent

discontinuities. This remote technique makes it possible to get information in sectors that would be otherwise hazardous to physically reach in order to take compass readings. It has been applied successfully in previous studies (Brideau *et al.* 2012; Derron *et al.* 2005; Jaboyedoff *et al.* 2009; Jaboyedoff *et al.* 2012; Oppikofer *et al.* 2011; Pedrazzini 2012).

Spacing and persistence of large scale features are evaluated using the DEM created from TLS. The approach used is inspired by work previously done by Sturzenegger and Stead (2009) and Lato *et al.* (2012). The spacing is evaluated in Polyworks. A line is traced perpendicularly to the joint set evaluated and the spacing between the discontinuities is measured along that line. Visualization of the point cloud in Coltop 3D helped to identify the discontinuities.

Persistence is evaluated by fitting circular planes to the discontinuities. The persistence is represented by the diameter of the circular plane termed the equivalent trace length (Sturzenegger and Stead 2009). A window approach is used to characterize the discontinuities. The technique is applied only on large scale features, *i.e.* with traces larger than 30 cm. This causes a truncation bias, as smaller discontinuities are not taken into account for persistence and spacing evaluation. The values are then compared with the classification proposed by ISRM (1978) and described in Table 2-1.

Table 2-1 Qualitative descriptors for spacing and persistence values (ISRM 1978)

Spacing Description	Spacing	Persistence Description	Persistence
Extremely close spacing	< 20 mm	Very low persistence	< 1 m
Very close spacing	20-60 mm	Low persistence	1-3 m
Close spacing	60-200 mm	Medium persistence	3-10 m
Moderate spacing	200-600 mm	High persistence	10-20 m
Wide spacing	600-2000 mm	Very high persistence	> 20 m
Very wide spacing	2000-6000 mm		
Extremely wide spacing	> 6000 mm		

In order to assess and characterize the rockslide in terms of blocks, Lord (Lord 2011; Lord *et al.* 2010) proposed to define a block according to the following three simple rules: (1) a block is limited by cracks, lineaments and depressions, (2) all the fissures reach the sliding surface, and (3) a fracture stops when it intercepts another one. Such a representation is useful to interpret the displacement measurements.

2.4.5 Kinematic Analysis

The discontinuity sets are used to conduct a classical kinematic analysis (Hoek and Bray 1981; Norrish and Wyllie 1996) to determine the feasibility of planar, wedge, and toppling failure mechanisms, using stereographic techniques with Dips (Rocscience 2005). This stability test takes into account the discontinuities and slope orientations as well as the friction angle on the discontinuity surfaces.

For planar failure to be feasible, the following conditions must be respected:

1. the dip direction of the discontinuity must be within 20° of the dip direction of the slope face;
2. the discontinuity must daylight in the slope face;
3. the dip of the planar discontinuity must be greater than the angle of friction of the surface.

These conditions consider that lateral release surfaces that defines the potential failure mass exist and do not contribute to the stability of the mass.

The criteria for wedge failure are described hereunder.

1. The plunge of the line of intersection of the discontinuity sets must be less than the dip of the slope face in order to daylight in the slope.
2. The trend of the line of intersection between the two discontinuities forming the wedge must approximate the dip direction of the slope face.
3. The plunge of the line of intersection must be greater than the friction angle of the surface.

Three conditions are considered in kinematic tests for toppling failures.

1. The strike of the layers must be within 30° of the strike of the slope face.
2. The dip of the layers must be into the slope face.
3. The normal to the discontinuity plane must have a plunge less than the inclination of the slope face minus the friction angle of the surface.

2.4.6 Characterization of the Rockslide's Geometry

ImSurvey (Innovmetric 2011) and ArcGIS (ESRI Inc 2009) were used to construct the sliding surface and calculate the volume of the slide. The interpretation of the sliding surface is based on: fracture mapping, core sampling data, observations of the adjacent ancient slide, and on three profiles of displacement with depth obtained from the traditional inclinometer system and from the two SAA.

A similar exercise was conducted on the ancient scar located to the east (Figure 2-1). The pre-failure topography and the sliding surface were constructed in order to evaluate the volume of the slide. The pre-failure topography was estimated using two approaches: (1) adjusting planes to the actual topography and (2) using the Sloping Local Base Level (SLBL) technique using Conefall 1.0 software (Jaboyedoff 2002; Jaboyedoff *et al.* 2009). The SLBL technique proceeds by iterations to determine a surface above which the land is erodible. This surface can be used to estimate the sliding surface position. Two input parameters are

necessary: a DEM and a polygon (or points) to mark the limits of the erodible zone. The same algorithm can be used to construct the pre-failure surface by inverting the DEM and setting the limit of the slide as fixed points (non-erodible). The result is then reversed, by applying a multiplication of -1, to obtain a new DEM where the slide scar is filled by a smooth surface (Pedrazzini 2012).

2.4.7 Limit Equilibrium Analysis

A limit equilibrium analysis for the translational slip of a tetrahedral wedge was done using the software Swedge from Rocscience (2003). This analysis is used to test the geometric hypothesis of the slide, to back calculate the friction angle required to obtain a factor of safety equal to 1, and to observe the role of water on the instability.

Swedge code (Rocscience, 2003) applies the laws of static to evaluate the factor of safety of a wedge formed by two planar discontinuities and an optional tension crack. It returns a factor of safety and information about the wedge generated, as its volume, orientation of line of intersection, etc.

The method called *gravitational pressure* in Swedge (Rocscience, 2003) is used to apply water pressures on the wedge faces. The water table is assumed parallel to the upper slope face. In the case of a wedge with no tension crack, the maximum water pressure is applied in the middle of the line of intersection and the water pressure decreases down to zero at the ends of the intersection line. In the case with a tension crack, the maximum water pressure is at the base of the tension crack. It decreases to zero where the line of intersection daylight in the slope face and going upward in the tension crack.

2.5 Geomorphology

2.5.1 Observations

The study of the geomorphology by the observation of elevation models and aerial photographs enables to recognize an active slide and scars of past translational slides, all located in between two geological features. The sector of interest (Figure 2-1) is bounded by the Port-Daniel River fault to the west and by the angular unconformity to the east, separating Silurian-Devonian sedimentary rock from Cambrian meta-sedimentary rock.

The Pierre-Loiselle cove is located at the border between the Chaleurs Bay and the St.Lawrence Gulf. This marine erosive shelf has a slope of 3° at water depth between 5 and 17 m. It is then of 1° until the end of the sector covered by multi-beam bathymetric survey which extends to a depth of 70 m. The shallowest part of the survey shows a rocky sea floor, visible up to a distance of about 300 m from the coast. In deeper water, the seafloor is covered with sediments.

The coastal Gascons rockslide is characterized on the elevation model by opened fractures and linear depressions. At the surface, fractures reach widths up to 12 m and depths from 2 to 12 m. Fractures are filled with debris of all kinds: rock, soil, trees, and sometimes garbage such as old tires.

The railroad crosses the active slide at an elevation of 63 m (Figure 2-1) over a length of 200 m. A track section of 65 m is supported by two retaining walls. One retaining wall is as old as the railroad construction (1907-1912), while the second was constructed in 1998. The second retaining wall was built after a rockfall which damaged the railroad. At that time, the failed rock mass and the railroad were located approximately at the same elevation (63 m above sea level (a.s.l.)); as a result, the granular material supporting the tracks followed the block down the cliff as well as part of the retaining wall.

To the north, the railroad follows a rock slope of 5 to 16 m high, with an average slope of 45°. Above this slope, the slide's ground surface is characterized by a forested 16° slope. In the western part of the slide, directly under the railroad, the rock surface appears to be lower than directly north and south of the railroad. This was observed during an excavation in the railway ballast (Cloutier, 2011a). The excavation size was limited to a hole of about 4 m diameter at surface. This could indicate that the railroad was constructed in a pre-existing depression or graben. At the time of the railroad construction, it could have appeared advantageous because it would mean less blasting.

Figure 2-3 presents aerial photographs taken in 1934 and 2004. On the 1934 photograph, the slide area is bare of vegetation and the large fissures visible today are not visible (Figure 2-3). On subsequent aerial photographs, the forest starts to take over the sector as agricultural activity stops.

An important scar was identified on the ALS DEM directly east of the active rockslide. This ancient slide was unnoticed by previous studies that were based on aerial photographs and field work. This ancient slide occurred before the construction of the railroad. The railroad's ballast fills part of the depression left by the slide and is kept in place by a retaining wall that shows no sign of anomalous deformation. Moreover, inside this ancient slide, seven scars of smaller translational slides are counted and some are indicated with arrows in Figure 2-1. All scars have a similar geometry with most of them having no left lateral releasing surface. Time series of aerial photographs enable to date one of the smaller slides in the period between 1948 and 1963. Other slides happened before the 1934, as they are identified on the first available aerial photograph.

2.5.2 Interpretations

No fractures are visible in the upper part of the slope on the 1934 aerial photograph and people living nearby recall that when they were kids (1950-1960's) the fractures were either nonexistent or small enough to walk over them (pers. comm.). The Gascons rockslide has probably been active for about a hundred years, at least

in its current shape. Smaller instabilities were certainly occurring long before in the cliff. Furthermore, the observation that the railroad might have been constructed in a pre-existing trench could indicate that the slide was already active in 1912.

The morphological elements inside the active rockslide were mapped and used to separate the rockslide into distinct blocks following the methodology presented in section 2.4. A first model was presented in the Master thesis of Pierre-Etienne Lord (2011) and a modified version is presented in Figure 2-4. This model assumes that the surface fissures project onto the sliding surface underneath. Lord (2011) divided the rockslide into eight sectors, BA to BH and presented their features orientations in rosette plots (Figure 2-4). Sector BA on Figure 2-4 has been named the Petit-massif by Locat and Couture (1995). This sector is divided into smaller blocks than the rest of the slide, which are a concern for the railroad stability: the fall of one block can partly destabilize the railroad foundation, as it happened in 1998.

Both the ancient and the actual slides have similar morphological features. This is suggesting a structural control of the rockslide geometry. The ancient slide's geometry is studied in order to compute its volume and determine its failure mechanism. To do so, the ancient slide's sliding surface is constructed by fitting planes to the morphological elements. As shown in Figure 2-5C, it has a wedge shape. Then, in order to estimate the volume, two different pre-failure topographies are created; one is constructed with planes while the second is created by the slope base level technique, shown on Figures 2-5A and B respectively. The computed volume between the topography created with planes and the sliding surface is 350 000 m³, while it is of 224 000 m³ for the SLBL surface. The average volume is 287 000 m³.

When the computation is done using the constructed sliding surface, it removes the railroad ballast and the debris that did not evacuate from the scar. This constructed sliding surface removes a volume of 126 000 m³, calculated by the subtraction of the sliding surface from the DEM.

This volume estimation is subjected to many sources of uncertainties: the sliding surface shape, the amount of debris remaining in the scar and most importantly the terrain's pre-failure topography.

The smaller scars identified inside the main scar have volumes between 1000 and 20 000 m³ and are associated with planar sliding. The actual slope inclination that represents their sliding surface is between 20 and 45°, with an average around 35°.

With the existing data, it is difficult to date the ancient rockslide, but it could have been triggered after the last deglaciation. After reaching the maximum relative sea level (Syvitski 1992) 10 000 years ago, which was about 100 m above modern sea level, the relative sea level dropped rapidly to a minimum level 90 m below modern

sea level. The low relative sea level is estimated to have occurred 9000 years BP (Syvitski 1992). This situation in the Chaleurs Bay is unlike the one of the St-Lawrence estuary. Sea level changes were due to the isostatically-controlled rebound. The scar is totally forested except where smaller slides have occurred. The ancient slide thus occurred well before the construction of the railroad and is now inactive.

2.6 Geology

The cliff of the Pierre-Loiselle bay is cut into Silurian to Devonian sedimentary rocks lying as an angular unconformity on the Cambrian Maquereau group (Bourque and Lachambre 1980). The active rockslide is mostly taking place in the Anse-à-Pierre-Loiselle Formation (APL) described by Bourque and Lachambre (1980) as a transition unit between the sandstones of Anse Cascon Formation and the limestones of La Vieille inférieure Formation (La Vinf). The three formations are part of the Chaleurs Bay synclinorium. Strata are dipping 22° with a dip direction of 193° (Figure 2-1). Next to the fault, the bedding planes are curving upwards, forming a syncline fold that is shown in Figure 2-6 and in the bathymetric survey of Figure 2-1.

The Cascon Formation is seen at the bottom of the cliff and inside the old scar. Its 10-50 cm thick sandstone beds are interbedded with thinner mudstone beds. Few conglomeratic-sandstones beds were noted. The APL Formation overlays the Cascon Formation and is 60 m thick in the sector of the active rockslide. The APL bottom part is similar to the Cascon Formation, with mudstones and sandstones alternating in beds of 3 to 20 cm. As we move upwards in the formation, the mudstones are becoming more abundant, as well as their content of calcilutite and calcarenite nodules. A sandy-conglomeratic unit marks the middle of the APL Formation, made of quartz, feldspars, and chert with a calcareous matrix. From observation of borehole cores, this conglomeratic unit is not homogenous over the rockslide, reaching a thickness of 8 m at Site 2, while it is of 6 m at Site 1. It laterally varies from a conglomerate with a fine calcareous matrix to coarse calcareous sandstone containing conglomeratic grains. In the cliff, this coarser unit is mostly covered by debris (Figure 2-6). The APL Formation upper part is essentially composed of centimetric nodular mudstones with some calcilutite beds. Many fossils, including colonial corals and stromatoporoids, can be observed. The mudstones are mainly arenaceous. The transition between APL and La Vieille inférieure Formation is marked by a coral biolithite layer of about 90 cm thick.

The La Vinf Formation is not widely spread in the instability sector, but is nonetheless present in the upper part of the cliff and forms the Petit-massif. It is described as a more or less nodular limestone unit of 5 to 10 cm thick, interbedded with calcareous mudstones. This formation contains also a large amount of fossils.

Because the APL Formation is a transition unit, the contacts between the neighbouring formations are not clearly defined and their position is subjected to interpretation. Throughout the formations, calcite veins are

observed and fracture surfaces are often covered with calcite (Figure 2-7B). In the field, long crusts of calcite are present on the lateral surface of the 1998 event. In borehole cores, some of the fractures are covered with an orange weathering coating, associated with iron oxide (Figure 2-7B) which results from the presence of calcite and pyrite.

Slikensided surfaces are observed in the field and in the core at different scales (Figure 2-7A, B and C). Figure 2-7C shows a photograph of a slikensided surface in a mudstone unit taken with a binocular. These surfaces represent shearing surfaces, either created by the Port-Daniel-River fault action or by the rockslide's movement.

All units above the conglomeratic one react to hydrochloric acid but a 3 to 10 centimeters thick shale bed located inside this coarser unit and observed in three cores. This shale bed is highly fissile (Figure 2-7D) and is located at an elevation of 21.8 m at Site 1. At Site 2, the same unit is at an elevation of 74.0 m. Such a rock can offer shearing strength near or at residual value.

The structure of this shale bed was observed with Scanning Electron Microscopy (SEM) (Figure 2-8). The sample preparation consisted in gently breaking the rock apart, by hand, to the desired dimension to obtain longitudinal and transversal surfaces. The rock was breaking in steps following orthogonal surfaces, as it can be observed on Figures 2-8A, B, and D that show both longitudinal and transversal faces. The grains are aligned and stacked in layers. Figure 2-8C shows slikenlines from this sample that are much smaller than the ones presented in Figures 2-7A and C.

At the bottom of the cliff, in the transition between the APL and the Cascon Formation, a soil-like layer was observed. This two centimetres thick layer is more eroded than others and is composed of silty to sandy size particles.

In the core of Site 3 (Figure 2-2) a crushed zone is related to the presence of the Port-Daniel-River fault, while in the core of Site 1 the presence of a fractured zone just below the conglomeratic unit is associated to the fold. This fractured zone is indicated in Figure 2-7. The core logs are presented in Appendix G.

Laboratory direct shear tests were conducted in 1995 on eight samples taken in the Petit-massif area, either in the APL or in the LaVinf Formations and reported in Roberge (1995). Two shear tests were conducted on saw surfaces and six on polished surfaces. The computed friction angle is 38° on the sawed discontinuities and 27° on the polished ones. There is no description of the samples in the shear test report. Because the rock lithology is not homogeneous in the rockslide, it is hard to associate these values to a particular lithology. The samples were probably taken near the transition from the APL to the LaVinf Formation. The values obtained

are typical of limestone and for this reason, the author believe that LaVinf Formation was the one sampled. Slikenlines, polished surfaces, brittle shale, and soil-like layers are all indices that a lower friction angle than the one measured in these tests should be considered in the stability analysis of the APL Formation. These tests were thus not realized on the material forming the main sliding surface. No mechanical tests were conducted in this study, because as the slide is active, the mobilized friction angle can be evaluated from limit equilibrium stability analysis assuming a factor of safety of 1.

The stratigraphy of the slide is illustrated by two cross-sections in Figure 2-9. The top one illustrates the western side of the slide and the Petit-massif, while the bottom cross-section is located in the middle of the slide. Both cross-sections are not parallel to the bedding dip direction, which is 193° , resulting into an apparent dip of less than 22° and towards the bottom of the slope. Near the bottom of cross-section AA', the beddings are dipping less steeply. In fact, as shown in Figure 2-6, they are folded next to the fault. The surface of rupture indicated by a red dashed line is parallel to the bedding. Its dip is lower in the syncline part of the slope to follow the bedding. The Port-Daniel-River fault and the syncline increase the stability of the rockslide to a point where the wedge sliding is not possible anymore due to the change in the dip of S0.

The geological units' representation on the cross-sections stops at the same depth than the borehole investigation ended. The Cascon Formation (sandstones alternated with mudstones) that is under the APL Formation in the stratification is not illustrated.

The conglomeratic unit marking the middle of the APL Formation is presented as a regular layer. However, the borehole core logging showed that the layer is not homogeneous in term of grain size and thickness. The sliding surface is associated with this conglomeratic unit, as it includes a very fissile and smooth mudstone layer shown in Figures 2-7D and 2-8.

2.7 Structural Geology

2.7.1 Discontinuity Evaluation

Four stereographic representations of the structural data taken with a compass (stereonet 1 and 4) and from TLS point clouds (stereonet 2 and 3) are presented in Figure 2-10. The three sectors, where the data of stereonet 2, 3, and 4 were taken, are indicated in Figure 2-1 by red rectangles. The data forming stereonet 1 were taken in different places inside the active rockslide.

The bedding dip and dip direction is $22/193^\circ$ and is mostly homogeneous throughout the APL and LaVinf Formations, except next the Port-Daniel River fault where it curves upward (Figure 2-6). In the western part of the Cascon Formation the beds are also dipping at a 22° angle, as shown on stereographic projections 1 and

3 of Figure 2-10. In the eastern sector, near the angular unconformity (Figure 2-1, station 4), the beds dip at a higher angle and the average set orientation is 32/200°.

Bedding surfaces are difficult to sample in Coltop 3D, because the bedding appears mostly as traces and not as surfaces in the point cloud. The lack of bedding surfaces scanned with the TLS is due to the slope face being nearly perpendicular to the bedding surfaces. Consequently, the measurement of S0 cannot be accomplished over the entire study domain. Bedding surfaces can be sampled on the TLS DEM at the bottom of the cliff at station 3 (Figures 2-1 and 2-10). The visualisation of terrestrial laser scanner data in Coltop 3D shows that in the cliff, the debris accumulate following the dip direction of the bedding, but as debris cumulates the dip increases to reach an average of 40°.

Five discontinuity sets were identified in the field and with Coltop 3D software in addition to the bedding and are presented in Table 2-2. The persistence and spacing of the large features were estimated using the DEM created with the TLS point clouds. Figure 2-11 presents the Petit-massif as it is visualized into Polyworks and into Coltop 3D, in addition to a photograph of the Petit-massif on which some fractures are associated with sets A, C, and D. The evaluation was carried out for two windows, chosen in order to take into account the different geological units. Moreover, sectors with a varying slope orientation were chosen to be able to identify all the discontinuity sets. One is the Petit-massif view from the beach (La Vinf and APL Fm.) and the other is at the bottom of the cliff in the Cascon Formation. It was not possible to find a window located totally in the APL Formation, as this formation is hidden by debris in the cliff. The study of spacing and persistence was thus carried out only for two sectors resulting into a limited number of measurements. The information extracted from this methodology is presented in Table 2-3.

Sets A and B are orthogonal with the bedding. The near vertical set A is separated in two sets, A1 and A2, with dip direction 180° apart. The discontinuity set A is identified at two scales in the rock mass: (1) into single beds and (2) crossing multiple beds. The larger scale features are classified by the ISRM (1978) as having a wide to very wide spacing with a medium to high persistence. This discontinuity set is measured all over the study area. In fact, many of the large fractures that can be seen on the DEM are associated with this discontinuity set (fissures B, G, and I identified in Figure 2-2). Release surfaces of the 1998 event are formed by discontinuity set A2.

Set B has an average orientation of 79/037°. Contrary to the field analysis, it was not identified as a major discontinuity set by the Coltop analysis. It is absent from the stereographic projections 2 and 3 of Figure 2-10. The B discontinuity set is limited to joints with spacing average of 15 cm and persistence that is limited to one or a few beds and this is the reason why it is not identified in Coltop 3D.

Discontinuity set D, that is strongly dipping, is separated in D1 and D2 to differentiate the two dip directions (84 and 256°). It is forming the lateral surface of the ancient slide and release surfaces of the 1998 event. The DEM analysis of spacing and persistence classifies the discontinuity set as being wide to very wide with a medium persistence.

The discontinuity set named C is dipping inside the slope and has been observed in every sector of the TLS point clouds. Contrary to discontinuity set B that was clearly defined in the manual field measurements but not in Coltop 3D, set C was at first not considered as a major discontinuity sets by the field measurements. It was first recognized as distinct from B with the study of lineaments in ArcGIS and then undoubtedly certified by the Coltop 3D analysis. The discontinuity set has a wide spacing and a medium persistence.

The last discontinuity set, named F, is less frequent but observed in the bottom of the cliff and at station 3 (Figure 2-1). It has the same dip direction than S0, but dips at 64°.

2.7.2 Comparison with the morphological analysis

The lineaments presented in Figure 2-4 are compared with the discontinuity sets in order to find if the blocks geometry is influenced by the rock structure. First of all, discontinuity set A prevails in most rosettes and is thus a dominant structural feature forming the blocks. Secondly, discontinuity set C is also present in every rosette, but represents rarely the main orientation of a sector. Discontinuity set D is identified in rosettes BB, BC, BF, and BH. The influence of set B is also noted in rosettes BA, BC, BE and BF, which is surprising as this set is considered to have a limited persistence.

The rosettes in Figure 2-4 are also indicating preferential orientations with trends between sets A and C and in between sets A and D. These orientations are associated to lineaments created by the combination of two discontinuity sets in a step-like geometry resulting into persistent lineaments.

Preferential orientations identified from the block representation correspond to those obtained from the structural analysis. Because the block representation is not based on structure data, but exclusively on morphological features, it indicates that the block geometry is closely linked to the rock mass structure. The structural analysis will be used to assess the geometry and failure mechanism of the active and past rockslides.

Table 2-2 Discontinuity sets orientations presented in stereographic projections of Figure 2-10. Refer to the stereographic plots in Figure 2-10 to observe the variability of the different discontinuity sets. The sectors 1 to 4 are identified in Figure 2-1 by the red rectangles.

Stereo Fig. 2-9	1		2		3		4		Synthesis				
Type	Compass		Coltop		Coltop		Compass		Both techniques				
Sector	Active rockslide		Petit-massif		Cascon west		Cascon east		Active rockslide				
	dip	dip dir ¹	dip	dip dir	dip	dip dir	dip	dip dir	dip	dip dir	# points	K ²	Variability limit 1 SD ³ (68%) (°)
A1	78	122	72	126	78	127	88	125	79	125	60	66	11
A2	78	298	74	299	84	307			79	301	107	66	11
B	79	37					85	208	79	37	61	55	12
C	80	0	73	359	69	5	67	358	72	1	99	39	14
D1	86	90	73	78	83	80	81	88	81	84	100	37	14
D2			69	257	84	255			77	256	44	28	14
F							64	192	64	192			
S0	22	193			26	197	32	201	22	193	98	165	7

¹dip dir: Dip direction

²K: Fisher's constant (Dips, Rocscience 2005)

³SD: Standard deviation

Table 2-3 Spacing and persistence evaluation of discontinuity sets A, C, and D using the TLS point clouds. SD stands for standard deviation.

Scan line and length (m)	Nb of dis.	Spacing (cm)	Persistence (cm)	Average/SD	
Discontinuity set A (A1 and A2)					
Slope North of the railroad	8	198	768	Spacing (cm)	
		126	828	Average	342
		109	618	SD	270
		372	548	ISRM: wide to very wide	
		170	2200	Persistence (cm)	
		618	110	Average	925
		800	280	SD	778
			2046	ISRM: Medium to high	
Station 3 (63m)	12	163	73		
		409	143		
		462	541	Spacing (cm)	
		174	151	Average	496
		259	80	SD	380
		236	36	ISRM: Very wide	
		861	266	Persistence (cm)	
		251	304	Average	263
		371	107	SD	258
		1331	232	ISRM: Low to medium	
		938	957		
	260				
Discontinuity set C					
Petit-massif	6	180	108	Spacing (cm)	
		511	357	Average	676
		923	325	SD	357
		671	356	ISRM: Very to extremely wide	
		1094	342	Persistence (cm)	
			707	Average	366
				SD	193
		ISRM: Low to medium			
Station 3 (36m)	7	105	300	Spacing (cm)	
		167	134	Average	394
		133	290	SD	403
		231	60	ISRM: Very wide	
		1129	42	Persistence (cm)	
		598	68	Average	136
			56	ET	113
		ISRM: Low			
Discontinuity set D					
Station 3 (25m)	7	791	463	Spacing (cm)	
		413	412	Average	383
		278	1019	SD	232
		457	152	ISRM: Very wide	
		183	178	Persistence (cm)	
		173	154	Average	357
			121	SD	322
		ISRM: Low to high			

2.8 Kinematic Analysis

Stereonet can be evaluated for possible kinematic instabilities. Figure 2-12 illustrates the potential for planar, wedge, and toppling failure mechanisms. The three stereographic projections in the top of Figure 2-12 were realised using a slope face of $45/155^\circ$ to represent the geometry of the active slide. The bottom ones were realised with a slope of $33/192^\circ$ to represent the east part of the cove, named the Pointe-au-Maquereau. The three failure mechanisms were tested using friction angles of 20° , 25° , and 30° , to represent the different rock types forming the cliff.

The only discontinuity set that has a potential for creating planar failures is the bedding (S0 set). In the active slide, the planar failures are not possible as the dip direction of S0 and of the slope face are 38° apart. The threshold is fixed to a maximum difference of 20° . At Pointe-au-Maquereau, the slope face orientation favours planar failures as the dip direction of S0 and of the slope face are the same.

In the active slide, the pairs S0-D1 and S0-D2 could lead to wedge failures, if the friction angle is below 21° . The wedge intersection line formed by S0 and D1 is plunging at 21° towards 169° . There are other discontinuity intersections falling in the yellow shaded zone of Figure 2-12, but as the trend is more than 30° apart from the slope face's dip direction they are not kinematically possible. For the Pointe-au-Maquereau, wedges formed with S0-A1, S0-A2, S0-D1, and S0-D2 would be possible if the friction angle is less than 20° .

The toppling failure evaluation presented in Figure 2-12 uses the most permissive criteria, *i.e.* a friction angle of 20° and an acceptable strike difference of 30° between the slope face and the discontinuity. Even with these permissive criteria, the toppling seems to be only marginally possible as little discontinuity poles falls into the shaded area. Part of the discontinuity poles related to sets A2 and C could lead to toppling failures in the active slide. Toppling on set A2 could be favoured if the strike of the slope is reduced. Toppling failures are not considered possible in the Pointe-au-Maquereau, as only a small portion of set B, which is not persistent, falls into the shaded zone. For toppling failure to develop, persistent joints are necessary in order to form rock columns.

The kinematic analysis, performed with stereographic projection techniques, shows that planar, wedge and toppling failures are possible to a certain extent in the sector bonded by the angular unconformity and the Port-Daniel-River fault. In fact, planar failures have occurred in the Cascon Formation and are shown by white arrows in Figure 2-1. On Pointe-au-Maquereau, the dip direction of the slope is similar to the one of the bedding and the dip of the bedding planes increases near the unconformity to reach an average value of 32° , two factors creating a slope prone to planar failures. The situation is different for the active slide, where the dominant failure mechanism is associated to wedge failure sliding along S0.

2.9 Failure Mechanism and Shape of the Rockslide

There are two scales of instabilities in the Gascons rockslide. The first one takes place in the cliff, where smaller rockslides can evolve into rockfalls. Their failure mechanisms are associated to planar, wedge, and toppling failures. Planar slides are possible where locally the direction of the slope is approaching the dip direction of the bedding. This is possible when the slope face is created by discontinuity set C. Toppling failures were observed during the first geotechnical investigation in 1993 and reported in Locat and Couture (1995). The stereographic analysis shows that toppling failures are possible along discontinuity sets A and C forming the tension cracks and S0 as the basal surface.

The second scale of instability is the one related to the main sliding body, which is outlined by a white dashed line in Figure 2-1 and associated to a wedge failure.

A tri-dimensional sliding surface was generated based on the various sources of information: geology (discontinuity sets and borehole core logging), geomorphology (mapping of fractures and lineaments) and displacement records. It is presented in Figure 2-13A. The volume computed from this geometry (Figures 2-5C and 2-13A) is 410 000 m³.

Three displacement profiles with depth confirmed the position and shape of the sliding surface that was assumed from the morphological and geological characterization presented previously (Figures 2-14A and B). An SAA (SAA3) and a traditional inclinometer are positioned side by side in the Petit-massif sector (Site 1, Figure 2-2) and one SAA (SAA2) is in the upper part of the active rockslide, at Site 2 (Figure 2-2). SAA2 (Figure 2-14B) shows a clear sliding surface at an elevation of 77.3 m. At Site 1, the deepest significant displacements are observed at an elevation of 21.9 m in the inclinometer and at 21.4 m in SAA3 (Figure 2-14A). The presence of intermediate sliding surfaces will be discussed with the post-failure characterization in section 2-12.

The resulting shape is similar to the ancient slide geometry. The ancient and active slides rupture surfaces are both shown in Figure 2-5C.

In average, this 3D sliding surface corresponds well to all sources of information, but some differences are noted. For example, at Site 2, the constructed sliding surface elevation is 3.1 m lower than the shearing plane observed in the displacement profiles of SAA2. In the Petit-massif sector, the constructed sliding surface is 2.4 m higher than the shearing surfaces observed with the inclinometer and SAA3. However, this 5.5 m difference reflects a normal uncertainty. In fact, a change in inclination of 1° of the bedding plane changes the height by 4.6 m at a distance of 200 m. Moreover, the bedding might have a certain waviness that is not accounted for as it is represented by a plane.

2.10 Hydrogeological Model of the Slide

2.10.1 Surface Observations

In the active rockslide, all the surface water is drained into the fractures. Surface flow and water accumulations were never observed in the slide. For example, while drilling the SAA borehole at Site 1, the water coming from the drill rig was all drained by a 30 cm wide fracture.

West of the rockslide a small stream flows during fall and spring and dries in summer. It ends in the cliff near the Port-Daniel-River fault (Figure 2-1), where it reaches the sea. A creek is following the trace of the angular unconformity and ends in a waterfall in the Chaleurs Bay (Figure 2-1).

At the bottom of the cliff in the active slide, some springs are observed and indicate the water table position. There is a zone of 10 to 15 m wide at an elevation of 10 m that appears humid and identified in Figure 2-6. This zone is considered continuous in time as it was observed at every visit and described by Locat and Couture (1995). It is aligned with the retaining walls that are located higher in the cliff. It follows the bedding orientation and it is near the estimated sliding surface's trace. Two springs, producing about 12 L/min (measured in August 2011), are present at the bottom of the cliff in the folded strata.

The tidal range yearly average is 1.3 m and high tides reach 2 m (Fisheries and Oceans Canada, 2012). South-east winds, associated with storm wind, can create waves which could erode the cliff.

2.10.2 Climate Records

A weather station has been installed at Gascons and consists of a rain and snow gage, an air temperature and relative humidity sensor, a barometric pressure sensor, and a wind speed sensor. Moreover, the two closest federal weather stations are the ones of Cap-d'Espoir, located about 45 km north-east and of New-Carlisle station located 35 km south-west. The Gaspé region is characterized by cold winters and warm summers. The average yearly precipitation computed for the years between 1971 and 2009 is 1295.9 mm, of which 931 mm are water precipitations. Air temperature and precipitation recorded with the Gascons weather station are presented in Figures 2-15 and 2-16.

2.10.3 Piezometer Records

A good temporal resolution is achieved with the nine vibrating-wire piezometers read four-time a day and it allows the observation of variations that would go unnoticed with traditional manual piezometers. Hydraulic head against time plots are presented in Figure 2-15 for the period from October 2011 to March 2012. The piezometers elevations are indicated on the y-axis of Figure 2-15. For every piezometer, hydraulic head is highest in fall and lowest in summer. However, water pressure behaviour differs from site to site.

Site 1 is located just south of the rails between the blocks delimited by fissures B and C (Figure 2-2). The piezometers are installed at 13.39, 15.39 and 17.39 m a.s.l., so they are under the sliding surface as is shown in cross-section AA' of Figure 2-9. Seasonal variations are marginal and precipitation events do not influence the water level (Figure 2-15), except for one event in 2011. Therefore, the water level is constant and there is no vertical flow. The proximity to the cliff and the opened fissures surrounding the area are signs of high drainage capacities. Moreover, while drilling the SAA3 borehole, next to the piezometer borehole, a cavity of 1.8 m was intercepted at an elevation of 39.4 m showing that the fracture network is also present at depth.

Site 3 is believed to be in stable ground and is located directly north of the rails and west of fracture A (Figure 2-2). Piezometers 9, 8 and 7 are installed at elevations of 13.58, 17.08 and 20.58 m. P8 and P9 are located approximately at the same elevations than P1 and P3, the difference in ground elevation between Sites 1 and 3 is about 30 cm, and the two boreholes are separated by only 30 meters horizontally. Despite their proximity the water levels and related behaviours are different as shown by the plots in Figure 2-15. Water pressures are higher at Site 3 than at Site 1 and react to external factors as snow melt and precipitations.

Year round, P7, P8, and P9 measure fast rises of water pressures followed by slower decreases. The amplitude of the variations is bigger for the shallowest piezometer (P7) than for the two deeper ones, P8 and P9. The higher hydraulic head is measured, most of the year, by the deepest piezometer in the borehole, P9, which indicates the presence of an ascendant flow component.

Site 2 is located in the upper part of the slide. Piezometers P4, P5 and P6 are installed at elevations of 76.05, 62.65 and 48.35 m. Data from these piezometers, along with daily precipitations and temperature records are presented in Figures 2-15 and 2-16. P5 and P6, which are below the sliding surface, are measuring variations of pressures linked with external factors. P4, located just below the sliding surface, does not react to precipitation and snow melt. Small variations measured by this sensor are related to atmospheric pressure changes. The variations due to the atmospheric pressure changes are recorded by every piezometer.

Piezometer 5 is showing the most important variations. Both snow melt and precipitation events can cause a rise up to 9 m within a week period. The increase is always faster than the decrease. In 2010, the fastest rate of increase was 1.90 m/d and the slowest was 0.36 m/d, with an average and a standard variation of 1.15 and 0.47 m/d. Rates of decrease have an average and a standard variation of -0.28 and 0.11 m/d. For example, from March 31 to April 6 2010, the pressure head changed from 13.74 to 22.02 m (Figure 2-16). The pressure head came back to 13.74 m on June 28, 2010.

P5 and P6 records are similar. The variations are simultaneous, but P6's variations are 60% smaller than those of P5. Variations measured at Site 3 (P7, P8, and P9) are occurring also at the same time. This

synchronism supports the hypothesis that the changes are caused by precipitation and snow melt events. However, some differences can be noted: (1) snow melt is measured first at Site 3 and (2) the pressure is decreasing faster at Site 3 than at Site 2.

Vertical component of water flow at Site 2 is descendant, as the hydraulic head decreases from P4 (higher) to P6 (lower). But, when pore water pressure rises, the hydraulic head measured by sensor P5 exceeds the one measured by P4 as this one is not influenced by water inputs. This might mean that the water flow reverses at some period of the year or, more likely, that the two are not linked, but hydraulically separated. These fast and important increases of pore water pressure are likely linked to fractures filling with water. As the piezometer P4 is near the sliding mass, the pressure at this level can evacuate quickly in the well-drained mass.

The piezometers measuring variations all appear to have a maximum level that is not exceeded, as shown in Figure 2-16 for P5.

All pressure rises are preceded by an important precipitation event or by the snow melt. The magnitude of the rise caused by the precipitation differs depending on the previous precipitations and also on the hydraulic head present before the precipitation event.

2.10.4 Hydrogeological Model

The hydrogeological model is schematized on the cross-sections of Figure 2-9. In a fractured rock mass, as the one at Gascons, water flows essentially through the fracture network that has a higher permeability than the intact rock mass (Hoek and Bray 1981). In fact, every borehole drilled at Gascons crossed opened fractures.

In the model, two water levels are considered. The first, represented by the blue polygon, corresponds to the water level determined by P4, the three piezometers of Site 1 (P1, P2 and P3), and by the elevation of water sources observed in the cliff. Most of the rockslide is dry as the water level drops as it enters the moving mass. On cross-section BB', it corresponds to where it goes through the back tension crack.

The second water level is represented by the dashed blue line. It corresponds to the hydraulic head highest levels as measured by P5 and P7. Water pressure increases after rainfalls and snow melts. These pressure rises are measured by piezometers P5, P6, P7, P8, and P9. They are not measured by piezometers P1, P2, P3, and P4.

The rock mass outside the slide is less fractured and consequently has a lower storage capacity. Therefore, the water pressure will increase faster outside the sliding mass than inside. Inside the moving mass, the wide

fractures increase the storage capacity limiting the possibility for pore pressures to build up and enabling a fast drainage of the water.

The flow direction is indicated by blue arrows in the schematized model of Figure 2-9. Inside the rock mass, the water follows the fracture network by gravity. The piezometers records show that (1) the vertical component of the flow is downward in the upper part of the hill, (2) there is no vertical component in the bottom near the cliff, and (3) at Site 3 an upward component is measured.

Many findings are related to the study of the piezometer data and to their high temporal resolution. The important difference measured between Sites 1 and 3 that are only 30 m apart, shows that the hydraulic properties of the rock mass vary rapidly between the two drilling sites. Site 1 is surrounded by opened fractures, so it is well-drained, while Site 3 is outside of the sliding mass and in a better rock quality as seen from the borehole Rock Quality Designation measurements. The water level represented by the dashed blue line represents the maximum water pressure that could have affected the moving mass during the observation period and should be used when considering the effect of water in stability analyses.

2.11 Failure Analysis

The limit equilibrium analysis is performed using a deterministic method as the shape of the failure surface is known. The slope topography is estimated by two surfaces, one to represent the steeper rock cliff ($45/155^\circ$) and another to represent the forested sector ($16/155^\circ$). The bedding and discontinuity D are imposed as joints 1 and 2 respectively. A tension crack that has the orientation of set A1 is imposed. The resulting wedge has a volume of $370\,260\text{ m}^3$, which is about $40\,000\text{ m}^3$ (10%) less than the computed volume of the active slide. The intersection line plunges at 21.8° , with a trend of 173.3° .

Dry and considering water pressures limit equilibrium computations were realised, using a Mohr-Coulomb strength model with zero cohesion. The friction angle required to obtain limit equilibrium ($F=1$), in dry conditions, is about 20° on both joints forming the wedge, as illustrated in Figure 2-17. In the software Swedge (Rocscience, 2003), the option *% filled fissure* is used to apply water pressures. The influence on the factor of safety is illustrated in the plots presented in Figure 2-17. The effect of filling 30% of the fracture is minor on the safety factor. The required friction angle is 19.8° for equilibrium. With fissures filled at 55% the required friction angle for stability increases to 21° .

The bottom graphic in Figure 2-17 shows the effect of the *water percent filled* parameter on the factor of safety which is not linear, but cubic. The friction angle was kept constant at 20° . The representative values for the percentage of filled fissure evaluated from the water levels measured with the piezometers is ranging from 30

to 55%, which corresponds to factor of safety of 1 and 0.95 in Figure 2-17. In this analysis, increasing water pressures lower the safety factor by a maximum of around 5%.

2.12 Post-failure Characterization

2.12.1 Overall Displacements

Although details about the displacement analysis of the various parts of the slide are described in Chapter 3, the following is presented in order to provide a basis for describing how to classify the slide in terms of overall movement according to the classification proposed by Cruden and Varnes (1996). Then, two specific sectors are described: the Petit-massif and East-Centre.

Figures 2-18A and B show displacement-time plots of different instruments in the rockslide identified in Figure 2-2. Figure 2-18A shows that the displacement rates are not homogeneous throughout the landslide. In general, the eastern side of the slide moves faster than the Petit-massif. In fact, at Site 1, the inclinometer (Figures 2-14A and 2-18A) measures an average velocity of 14 mm/yr at surface; while at Site 2, SAA2 (Figure 2-14B and 2-18A) measures an average rate of 55 mm/yr at surface. In Cruden and Varne's classification the Gascons rockslide has a very slow velocity (Cruden and Varnes 1996).

Repeating patterns associated with periods of faster or slower displacement rates are observed by instruments with a high reading frequency. Such patterns can be noticed on the four crackmeters displacement plots of Figure 2-18B. These sensors are read automatically every five minutes. It can be noted that the faster and slower periods in the plots do not happen at the same time. This means that it does not represent a general acceleration of the whole rockslide.

The direction of movement of a wedge failure can be evaluated from stereographic analysis, as the one presented in Figure 2-12. The trend of the intersection line of the two joint sets forming the wedge indicates the movement direction. The intersection line of discontinuity sets D1 and S0 is plunging at 21° with a trend of 169° (Figure 2-12). The western limit of the geometric surface presented in Figure 2-13A is delimited by planes of two orientations (57/101° and 73/097°) that are about 10° off from the average orientation of set D1. The trend and plunge of the resulting intersection lines are 176/21° and 179/22°. Thus, the monitoring system should indicate a main direction of movement SSE, which is the case and will be presented in detail in Chapter 3.

2.12.2 Petit-massif

The complexity of the block representation presented in Figure 2-4 increases in the Petit-massif sector, where the sliding mass thickness is the largest. In this sector, the displacement profiles with depth obtained from

SAA3 and the inclinometer indicate the presence of multiple shearing surfaces. When interpreting the block model, the fractures are considered to reach the deepest sliding surface. In the Petit-massif, the vertical fractures cannot be continuous to the deepest sliding plane, as movement on higher ones truncates them. The intermediate sliding surfaces are integrated in the displacement analysis which is presented in Chapter 3.

In fact, in addition to the deepest failure surface located at an elevation of 21.6 m, two other shearing zones are identified in the displacement profiles of Figure 2-14A at elevations of 40.4 and 51.4 m. They are shown on cross-section AA' (Figure 2-9). The volume of the Petit-massif above the shallowest sliding surface is evaluated to 13 300 m³.

The 1998 event is a good example of a rockslide that did not mobilized on the main sliding surface. The 1998 sliding surface is shown in Figure 2-9.

While boring in the Petit-massif area, many fractures were intercepted, with the largest one corresponding to a cavity of 1.8 m located at an elevation of 39.4 m. Due to the terrain conditions it was difficult to correctly grout the inclinometer casing and the SAA in order to assure their cohesion to the rock mass. Therefore, the interpretation of the data must take into account possible casing deformation induced by the lack of support. This could explain the two bumps in the displacement profiles of the inclinometer at elevation of 31 an 38.5 m.

The direction of displacement changes with depth and the direction of the two higher sliding surfaces are diverging from the direction predicted by the wedge failure. At these elevations, the direction of displacement is of 144°, towards the average slope dip direction. Movement on the lower sliding surface is towards an average direction of 177°, corresponding to the one predicted from the kinematic analysis.

2.12.3 East-Centre and Block-E

The lineaments and fractures analysis led to the identification of a slide inside the main slide that is indicated in Figure 2-13A by a white dashed line and by the blue surface in Figure 2-13B. This sector is named the East-Centre. Its geometry is similar to the main active slide, but even more to the ancient slide. The volume computed using the blue sliding surface of Figure 2-13B is 75 600 m³. The sliding surface is hanging in the slope as can be observed in cross-section BB' (Figure 2-9) and in Figure 2-13B and is not influenced by the syncline. For these reasons, the East-Centre could turn into a fast rockslide.

The study of the block geometry showed that Block-E (Figure 2-13C), which is inside of the East-Centre sector, shows more deformation than other blocks. To create the sliding surface, the back wall is assumed to extend to the sedimentary layer daylighting east of Block-E, giving the sliding surface shown in cross-section

BB' (Figure 2-9). Its sliding surface is believed to extend under the retaining walls. The volume of this geometry is 23 400 m³.

The morphological expression of the back scarps of East-Centre and Block-E is different from the one of the main slide. The active slide is characterized by some tension cracks clearly visible in the DEM and in the field. No such tension cracks are seen at the back of East-Centre and Block-E. They are rather characterized by a steep slope.

2.13 Conceptual Model of the Slide

2.13.1 A Complex Wedge Failure

The displacement monitoring indicates clearly that the slide is active and moving very slowly. The slide is associated to a wedge failure mechanism, but some observations indicate that the mass is not moving as a monolithic wedge failure.

Firstly, the syncline appears to locally increase the stability by flattening the bedding. In fact, displacements recorded on the deepest sliding surface in the inclinometer and SAA3 are less than everywhere else in the rockslide. For example, as shown in Figure 2-14, more displacements are measured at Site 2 on the same sliding surface. This sliding surface is the one presented in Figures 2-13A, 2-5C, and 2-9. If the rockslide was moving as a monolithic wedge, the displacement measured at Sites 1 and 2 would be the same. The large fractures are an indication that the rock mass is separated in blocks and that a block can move without involving other blocks.

Secondly, the cross-sections presented in Figure 2-9 present different levels of sliding surfaces, again illustrating the complexity of the slide.

Thirdly, if the direction of displacement was strictly towards SSE as predicted by the kinematic analysis, the western boundaries would be characterized by shearing surfaces, but they are in fact opened tension cracks. An example is Fracture F, a 3 m wide fracture, identified in Figure 2-2. Consequently, displacements must have an east component to explain the opening of the lateral fractures, which is observed on the upper sliding surface in the inclinometer records that have a mean direction of 144°.

To conclude the discussion on the wedge failure mechanism, the form of the blocks might indicate that a certain rotation is induced. It would be induced by the asymmetrical shape of the wedge and by the syncline acting as a buttress.

2.13.2 Uncertainties Related to the Shape of the Sliding Surface

The geometry of the slide is well characterized based on different types of information (displacement, geology, and geomorphology). However, some uncertainties remain and the detailed analysis raised a few questions presented hereunder.

The exact shape of the lateral surface in the cliff vicinity is still unknown. The surface is represented by a plane with dip and dip direction of 73/097° (Figure 2-13A), which is in between D and A sets. This plane was created by matching features in the cliff and opened fractures on the flat ground south of the rail. Moreover, the plane had to be steep enough to intercept SAA3 and inclinometer boreholes at the elevation of the measured sliding surface. The dip direction of the plane is 20° off the ancient scar lateral surface which is 77/076°.

The main lineaments and fractures in the rockslide are represented by dashed lines on both cross-sections of Figure 2-9 and most of them are projected on the sliding surface. East-Centre and Block-E back fractures do not project unto the sliding surface as an intermediate one is assumed. The sliding surfaces of East-Centre and Block-E are only interpreted from geomorphology. Displacement profiles obtained from borehole instrumentation would allow to confirm or infirm this theory. It would also give information on the failure mechanism of Block-E. In fact, the morphology of Block-E is different from the one of the main slide and of East-Centre, which could indicate that the failure mechanism is not exactly a wedge slide.

In cross-section AA', (Figure 2-9) the intermediate sliding surfaces identified in the Petit-massif sector are not continued north of the railway trench. In fact, as there is a fracture along the railroad, the rules used to create the block model assume that a fracture ends when it intercepts another one. This hypothesis seems right for vertical fissures, however its application to sliding surfaces that are following fully persistent bedding surfaces appears less appropriate. However, there was no information to corroborate the continuity of these intermediate sliding surfaces north of the railway trench. In fact, displacement measurements indicate that the blocks forming the Petit-massif are getting away from the slope face north of the railroad.

2.13.3 Comparison with the Ancient Slide's Shape

The active slide and the ancient slide have similar geometries, but the planes orientations of the reconstructed failure surfaces are not exactly the same. The S0 plane is the same, but in the case of the ancient scar, it must be joined to a steeper plane to fit the geomorphological features. The presence of the unconformity and the steeper dip of S0 in this sector (Figure 2-10, stereonet 4) can explain this difference. The back releasing surface is approximated by one plane only, corresponding to the discontinuity set A and the lateral surface by the discontinuity set D. On the TLS point cloud visualized with Coltop 3D we can see that the lateral surface of the active slide is formed by sets A and D that give a stepped shape to the lateral western limit.

2.14 Discussions

Oppikofer *et al.* (2011) observed a stepped sliding surface of a rockslide located near the Aknes rockslide, in Norway, and proposed a similar model to represent the Aknes sliding surface. Such step-path geometries would involve both failure on pre-existing discontinuities and failure of intact rock bridges (Sturzenegger and Stead 2012). Such geometry is excluded at Gascons. The information available indicates that the main wedge is sliding on a continuous level of S0. The step-path characteristic is observed on the lateral surface, which is composed of A and D alternating discontinuity sets. On cross-sections, the vertical fractures inside the slide are drawn as persistent fractures reaching the sliding surface, but it is not excluded that their true shape might be stepped.

The characterization of the rockslide presented in this thesis focuses on its post-failure behaviour. How did the failure evolve towards its current state has not been directly studied. One could ask if the blasting required for the railroad construction was a trigger. The proposed failure sequence is that the failure of the main wedge first developed, triggered by the active erosion, by water pressures, and of course due to the favorable geology and structure. Then, the rockslide broke into the different blocks to accommodate more displacements. The blasting could have a role in the destabilization of block-E and the creation of other intermediate sliding surfaces identified in the Petit-massif, but it is difficult to imagine how the railroad construction could have triggered a sliding surface located 40 m deeper. However, no computation was realised to try to characterize the influence of the blasting on the rock fracturing. Moreover, no information is available about the blasting done during the railroad construction that took place from 1907 to 1912.

In the current state of the rockslide, which is very well drained, the pore water pressures have a limited influence on the factor of safety estimated to 5%. However, the water pressure impact on the factor of safety increases when the percent of fissure filled is over 55% (Figure 2-17) in the analysis carried out in Swedge (Rocscience 2003). Before the rockslide separated into different blocks, pore water pressure could certainly build up and increase the driving forces. Thereby, even though the current effect of pore water pressure is limited, it probably played a role in the initial failure.

No pore water pressure is measured inside the moving mass, but the piezometers below the sliding surface measure a pressure head with an elevation above the failure surface. For post-failure stability calculation, water pressure could be applied below the sliding surface to create an uplifting force. The tension cracks can be partly filled with water, but never totally as water inside the fractures that are about 10 m deep has never been observed.

The proposed model is that the slide is active all the time, even if the pore water pressures are low. Higher pressures might contribute to accelerate the sliding rates but are not necessary to drive the rockslide in post-failure.

Groundwater was characterized by piezometers with automatic acquisition. Rises of up to 9 m are measured by piezometers located below the sliding surface. Important water table fluctuations are also measured in other rockslide, such as at Aknes where they reach 5 m (Ganerod *et al.* 2008) and at La Clapière where they reach 6 m (Binet *et al.* 2007). At La Clapière, the rises are always faster than the decrease of the pore water pressures, as it is the case at Gascons.

If the piezometers would have been installed at higher altitude, *i.e.* not below the sliding surface, the description made of the hydrogeological model would have been completely different. In fact, large rises of water pressures are only measured by sensors that are below (Site 2) and outside (Site 3) of the sliding mass. This emphasize the importance of a carefully planned instrumentation program and brings knowledge on pore water pressure in and around of an active rockslide under the influence of seasonal variations. The extent and shape of the hydraulic head variations have been detailed. Rises are fast and sharp, while decreases of pressure are slower. Knowledge on pore water pressures is important in developing risk mitigation strategies.

The comparison of the morphological analysis of blocks with the structural geology showed that the blocks are defined by the discontinuity sets, thus the mechanism imply mostly failure along pre-existing discontinuities. Eberhardt *et al.* (2004) explain that for a failure occurring along pre-existent structure, the internal deformation required to cause failure will be very small. This appears to be the case at Gascons, where the internal deformation has only been characterized by tension cracks, lineaments and slope breaks.

2.15 Conclusions

A detailed characterization of the geometry, geological features, hydrogeology and state of activity of the Gascons rockslide was proposed in this chapter based on records from the monitoring system installed in 2009, field work, borehole cores, and desktop analyses. The main conclusions about the rockslide are briefly stated below:

1. The failure mechanism is related to wedge failure, but the instability does not exactly act as a monolithic wedge. It is separated into regions moving at different rates.
2. The shape of the sliding surface and of the unstable mass is known with a good level of confidence and a 3D model of the surface was created with the software Polyworks. Displacement profiles with depth have been studied to assess the sliding surface position.

3. The wedge is formed by the bedding and discontinuity set D. The tension cracks are related to the discontinuity set A.
4. The volume is estimated at 410 000 m³.
5. Displacement rates are varying across the rockslide. In general, the East-Centre is moving faster than the Petit-massif sector which the deepest sliding surface appears to be constrained by the fold. The measured yearly displacement rates range from 14 to 110 mm/yr, so that the Gascons slide is classified as a very slow landslide.
6. A unique set of piezometric data has been able to demonstrate that pore water pressures vary quickly in space and in time. During the snowmelt period, a piezometer can measure a rise in pressure equivalent to 9 m of water over a week, while a piezometer situated in the same borehole but 15 m higher will measure a constant water pressure. Most of the sliding mass is above the piezometric surface.
7. The good temporal resolution of piezometer data read every six hours allows the characterization of rises and decreases of water pressures. The diminution in water pressures is always slower than the rise.

Moreover, through this study new information and data were acquired on the area:

1. A high resolution DEM of the rockslide was created from airborne and terrestrial laser scanner data.
2. The geological map proposed by Bourque and Lachambre (1980) has been georeferenced and slightly modified to adjust to the morphology seen on the DEM and to correspond to new field information. Bathymetric survey permits to extend the geological map and the trace of the Port-Daniel-River fault underwater.
3. The structural analysis done in the field was completed by an analysis performed in Coltop 3D to visualise and extract the orientations of surfaces of the georeferenced point clouds. Field surveys and Coltop 3D analyses proved to be very complementary.
4. An extensive monitoring system was put in place to follow the displacement of the instability. Four shape accel arrays (SAA) of the company Measurand are installed. It was the first installation of vertical SAAs in a rockslide and it proved to be successful to detect sliding surfaces with results similar to those of conventional inclinometer.

Finally, the Gascons rockslide is a concern for the authorities in charge of the railroad that is running across the instability. This study improves the understanding of the phenomenon responsible of deformation and settlement in the railroad and should provide a baseline to interpret the near real-time data that have been collected since 2009, and to predict the evolution of the instability.

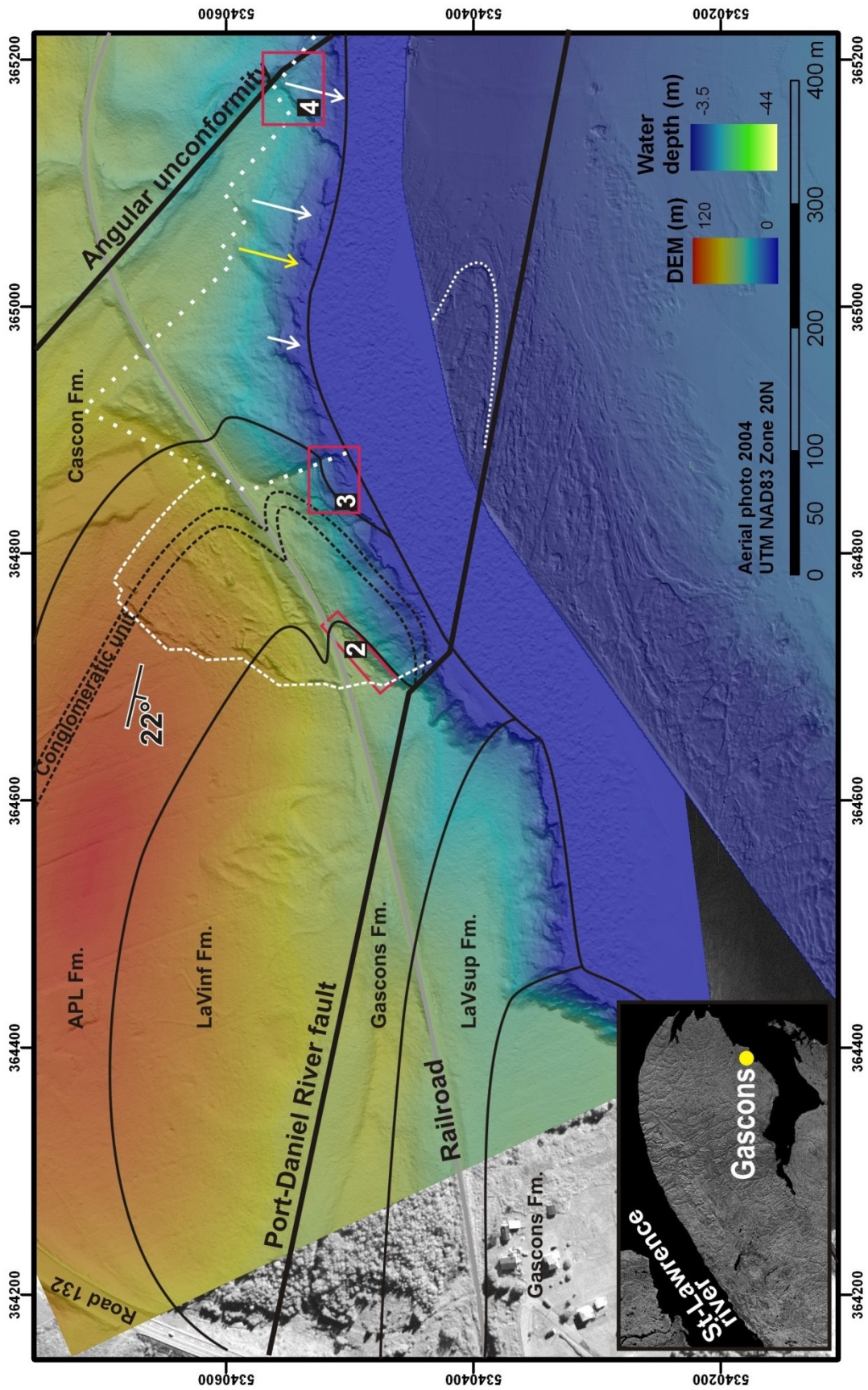


Figure 2-1 (p 35) Geological map modified from Bourque and Lachambre (1980) presented on the DEM and the 2004 aerial photograph, and the shallowest part of the bathymetric survey revealing a rocky sea floor and the fold indicated with a white dotted line. On the DEM, the white dashed line indicates the contours of the active slide and the white dotted line the adjacent ancient slide. White arrows indicate the sliding direction of planar slides. The yellow arrow is the slide that can be dated from aerial photographs. The red rectangles indicate the location of data shown in the stereonets of Figure 2-10. Insert: Geographic location of the Gaspé Peninsula in Québec, Canada (© Natural Resources Canada. All rights reserved).

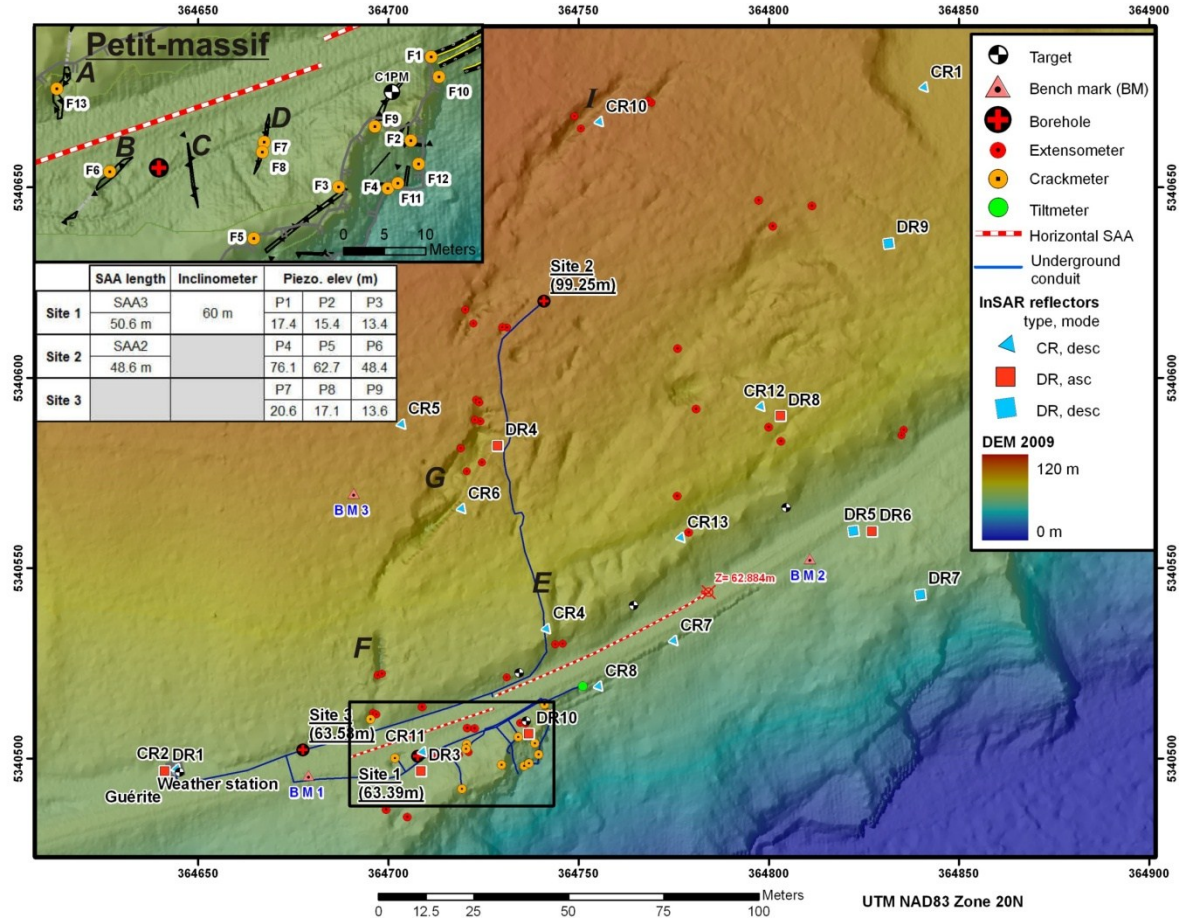


Figure 2-2 Monitoring system of the Gascons rockslide shown on the DEM created from ALS data. Insert: Details of the Petit-massif sector, where the 13 crackmeters and Site 1 are located. Sensors installed in boreholes are detailed in the table in the figure.

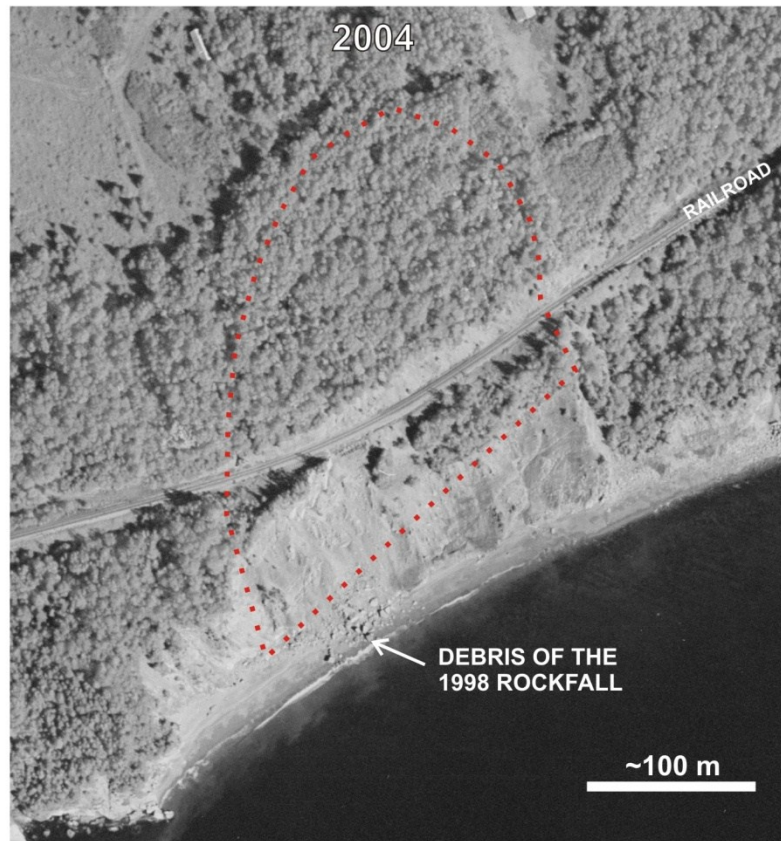
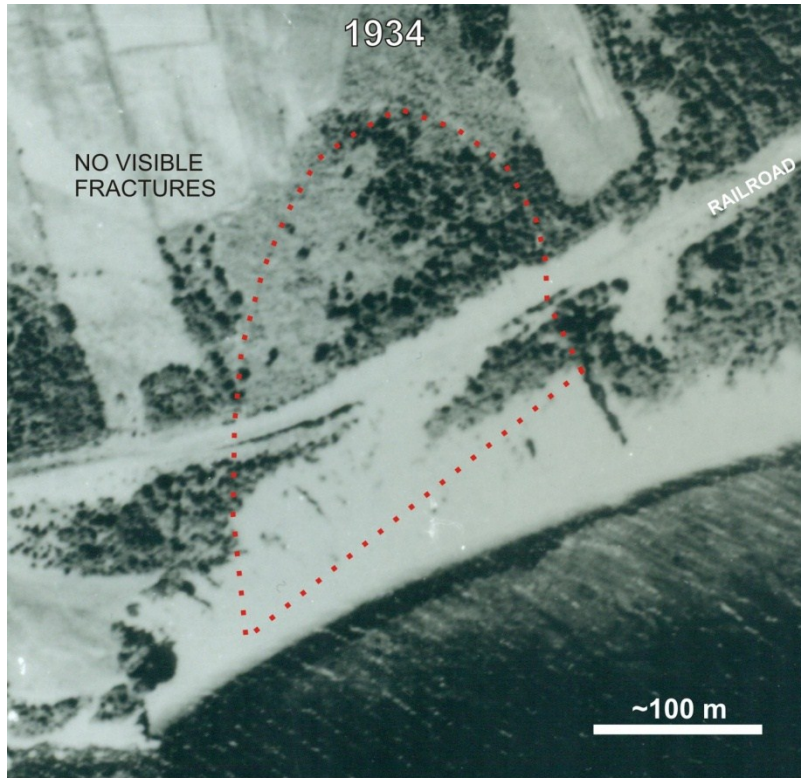


Figure 2-3 Evolution of the Gascons rockslide as seen on aerial photographs of 1934 (top) and 2004 (bottom).

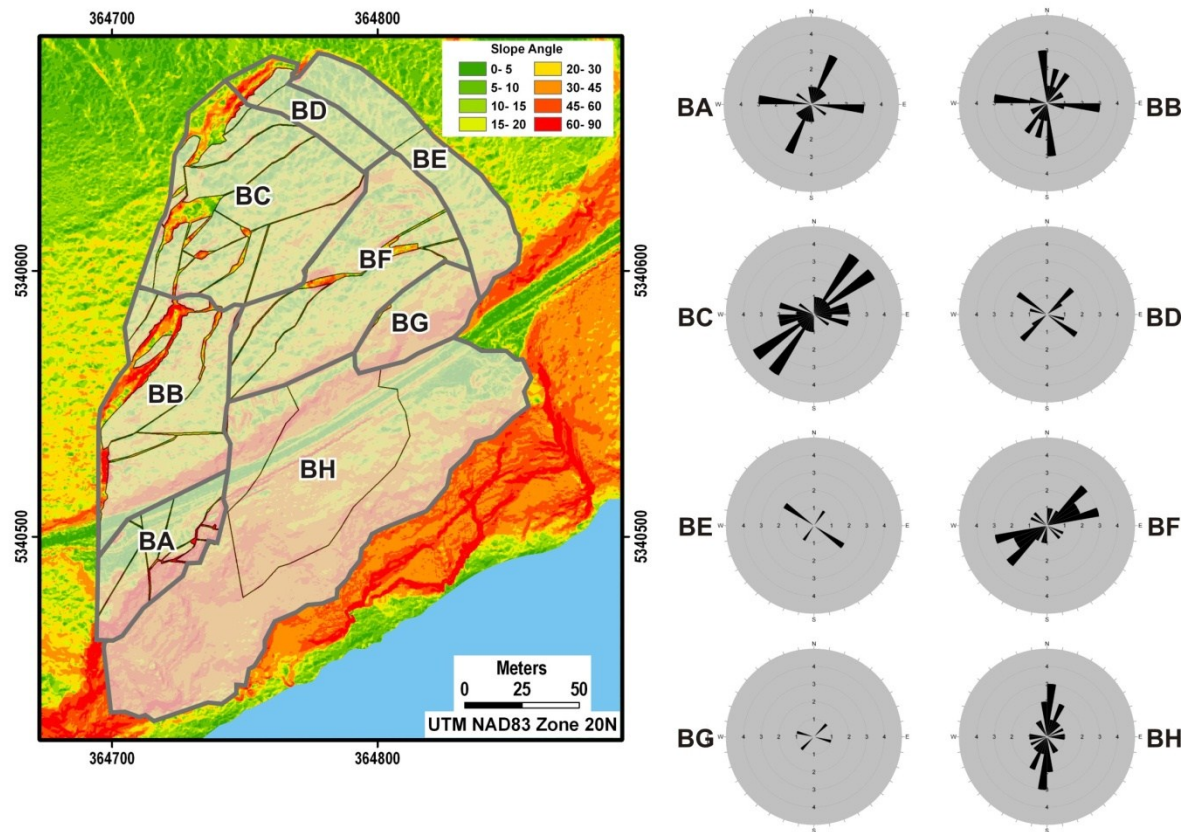


Figure 2-4 Block representation of the rockslide. The letters BA to BH refers to the rosettes on the right, that are presenting the lineaments mapped inside the Gascons rockslide by Lord *et al.* (2010) and Lord (2011).

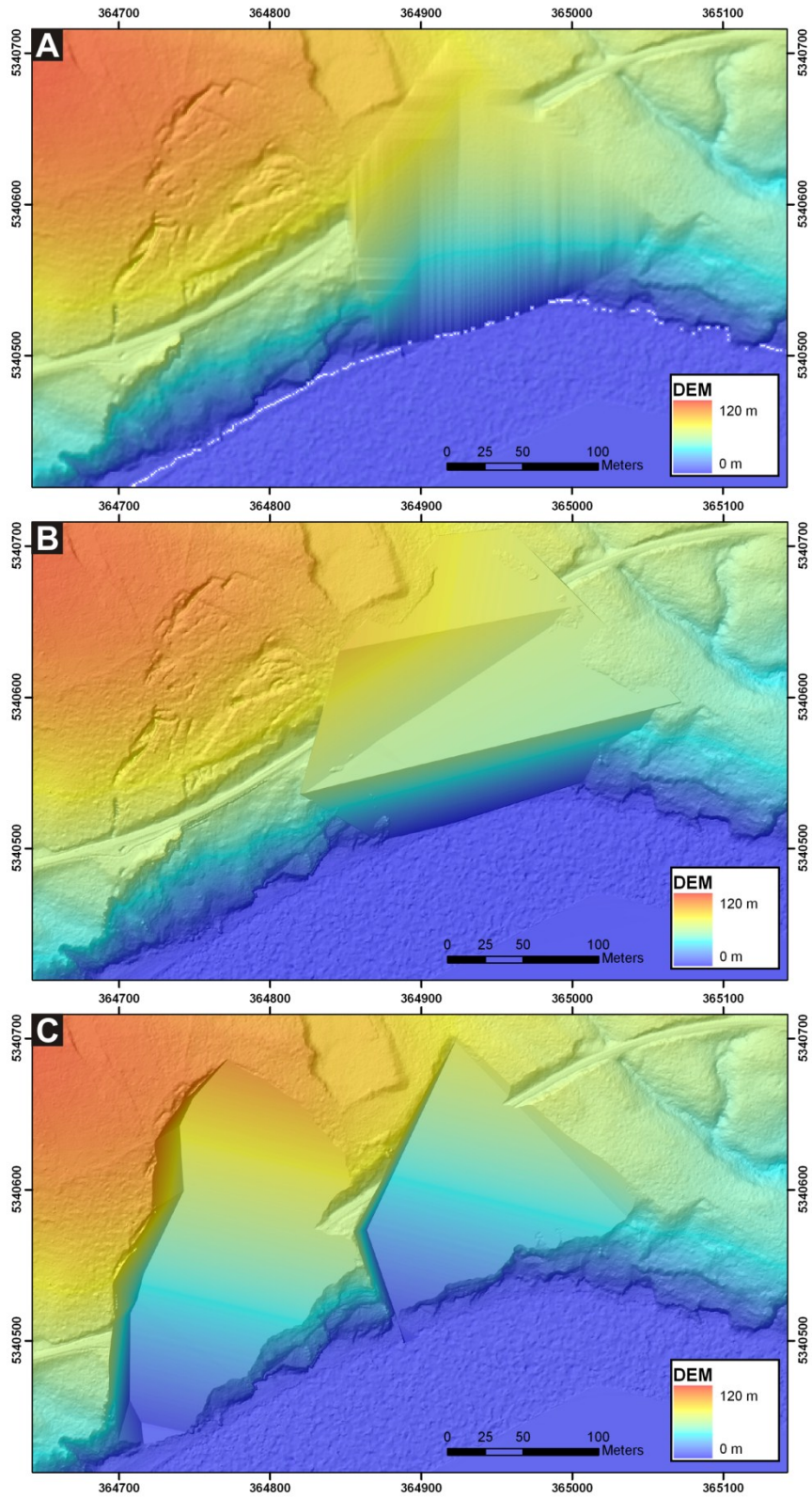


Figure 2-5 Reconstruction of the ancient slide topography prior to failure using A) SLBL algorithm and B) plane fitting. C) Sliding surfaces of the active and the ancient slides created using planes.



Figure 2-6 A) Cliff as viewed from the Chaleurs Bay showing the limits of the geological formations. The blue line indicates a zone that is always wet indicating the water table position. B) Photo of the fold taken from the beach.

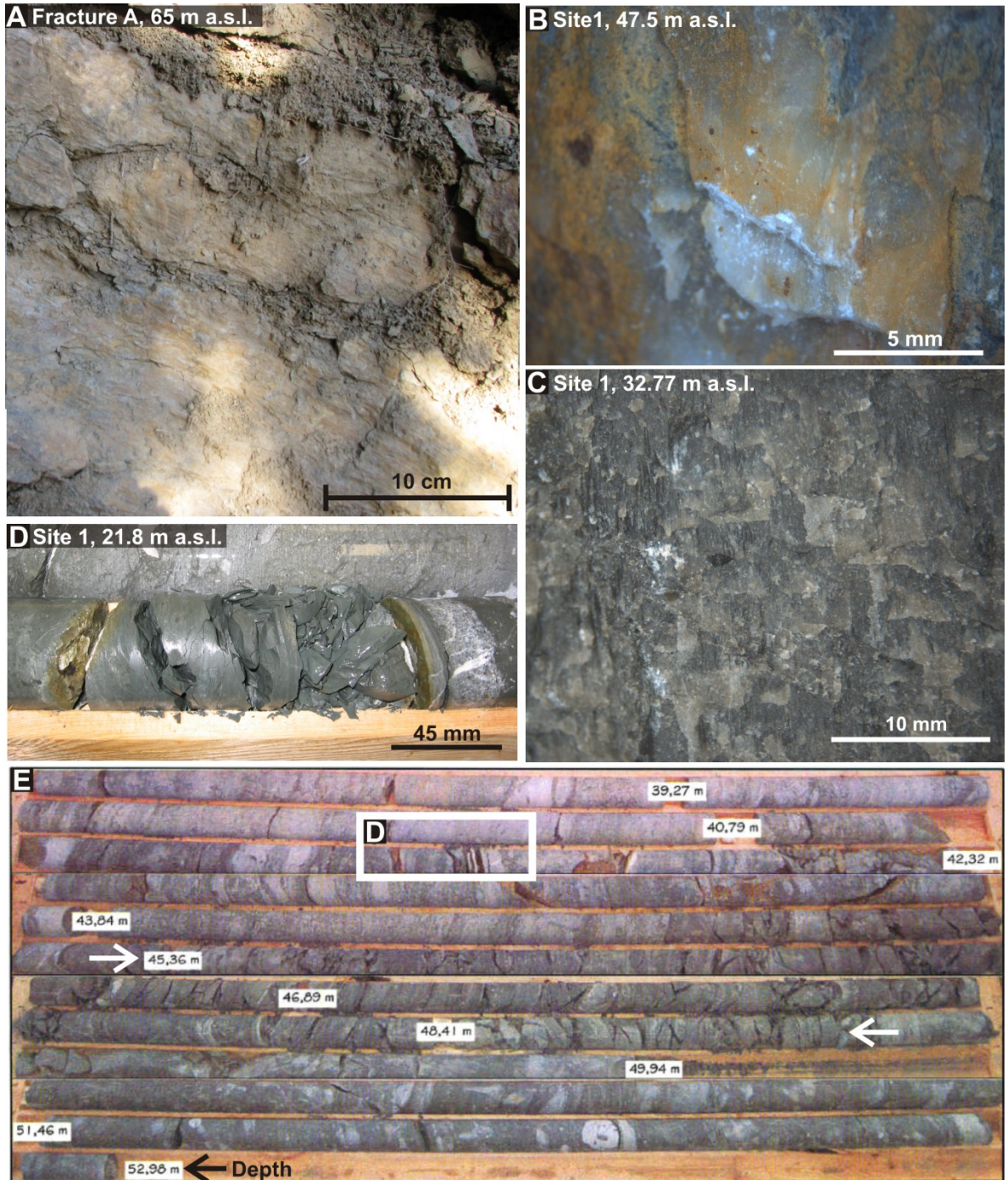


Figure 2-7 Rock specimens with slickensided surfaces. A) Photography taken in fracture A (Figure 2-2) showing limestone beds with slickenlines alternated with weathered mudstones. B) Fracture covered with calcite and iron oxide observed in the borehole core of Site 1 (Figure 2-2) and photographed with a binocular. C) Binocular photography of a fracture in the APL Formation taken from Site 1. D, E) Pictures of the APL Formation in the core of Site 1. Figure 2-8 shows SEM images of a sample coming from the unit shown in D.

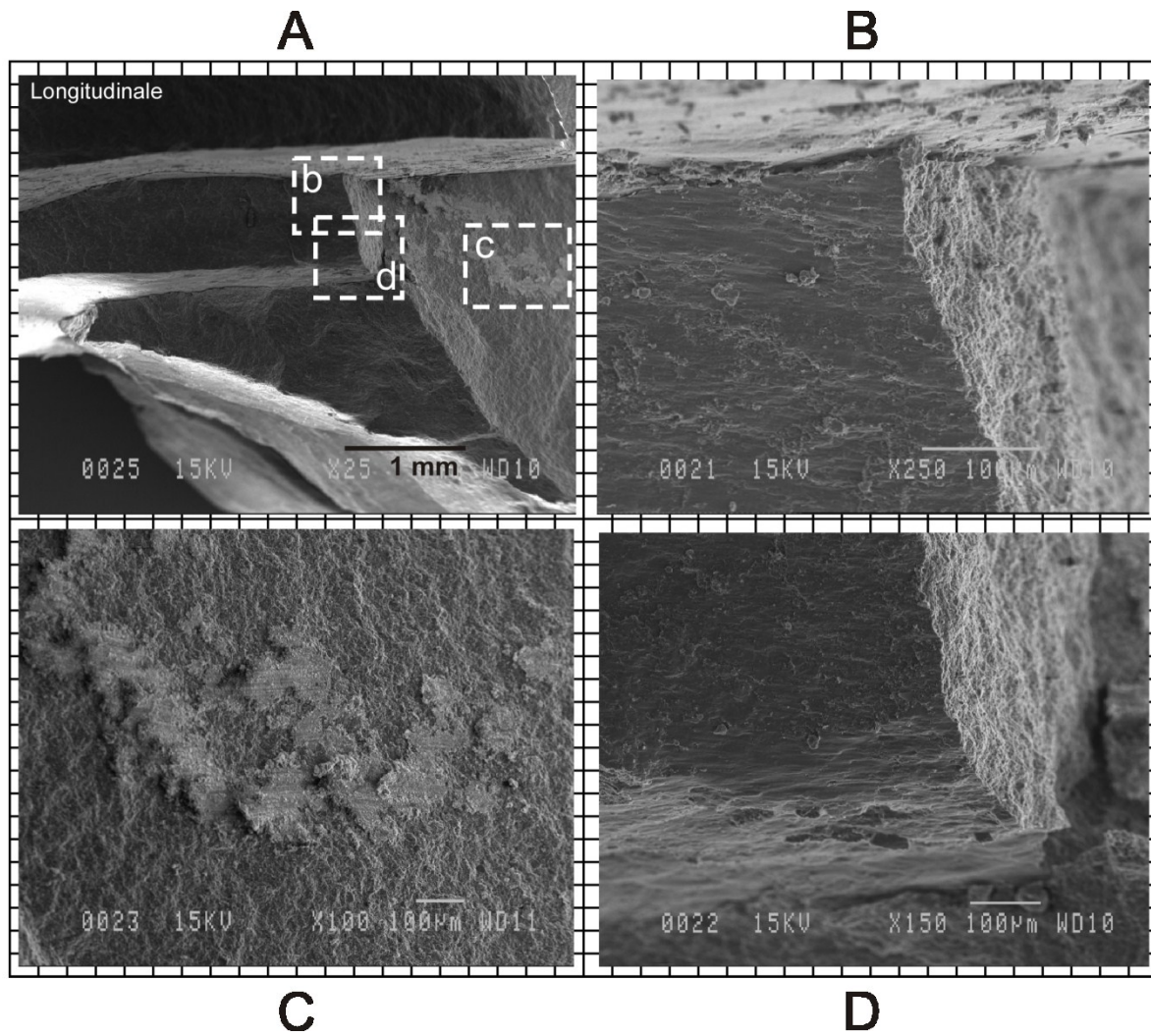


Figure 2-8 SEM images from a longitudinal cut in the shale sample shown in Figure 2-7D taken at 21.8 m a.s.l. in the core of Site 1 in the APL Formation. The positions of images B,C, and D are shown in A.

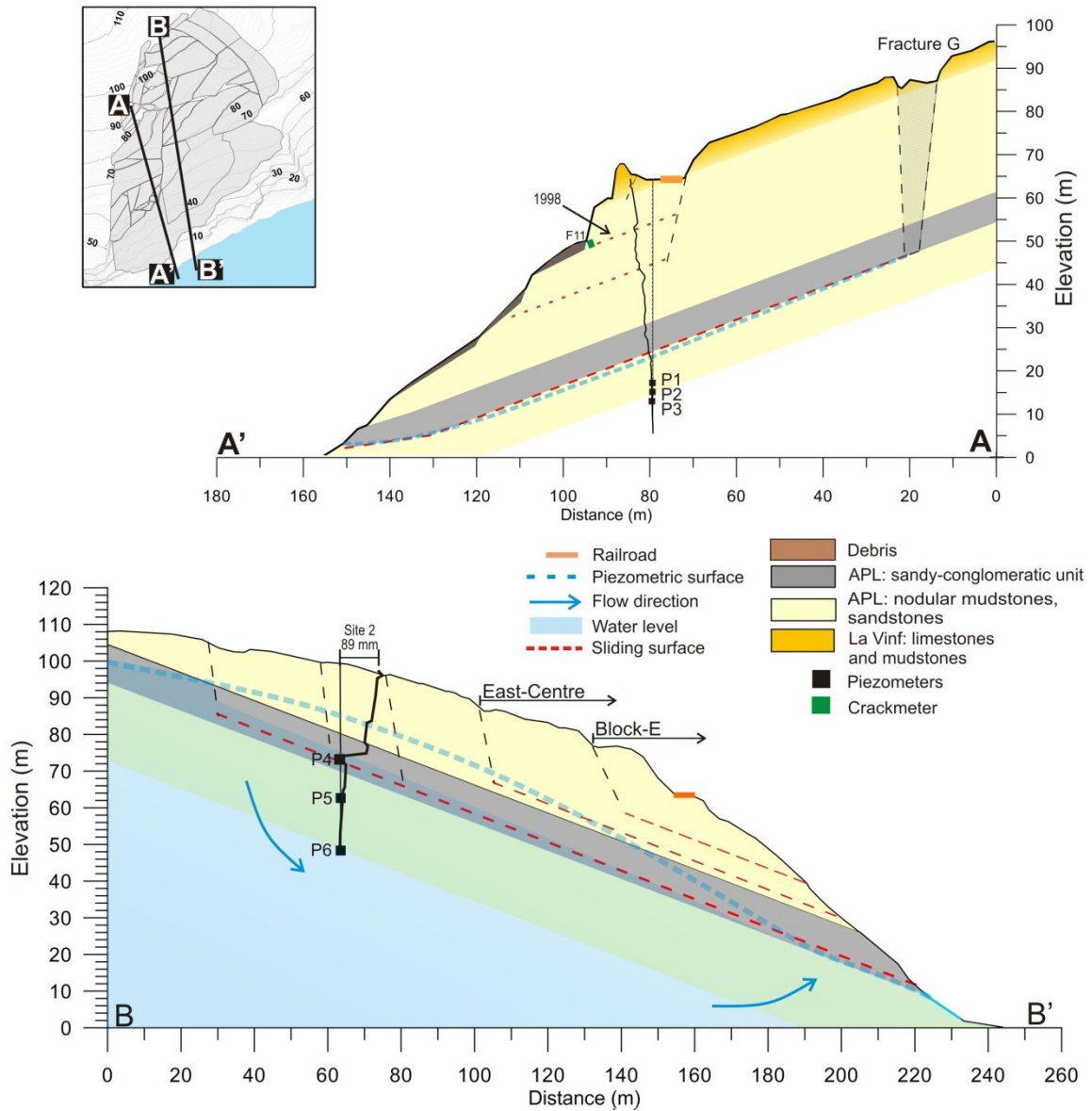


Figure 2-9 Cross-sections illustrating the hydrogeological model. Their location is indicated on the top map. SAA3 and SAA2 displacement profiles are indicated on cross-sections AA' and BB' respectively.

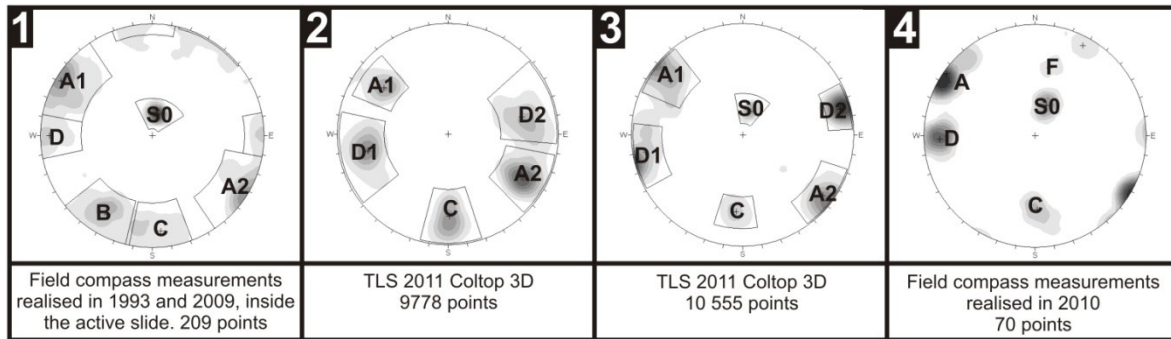


Figure 2-10 Four stereographic projections (lower hemisphere, equal angle, with Fisher representation) showing structural data collected in three sectors identified by red rectangles in Figure 2-1. Measurements of stereographic projection 1 were realised in the active rockslide with a compass. Data from stations 2 and 3 are obtained from the study of TLS point clouds with *Coltop 3D*.

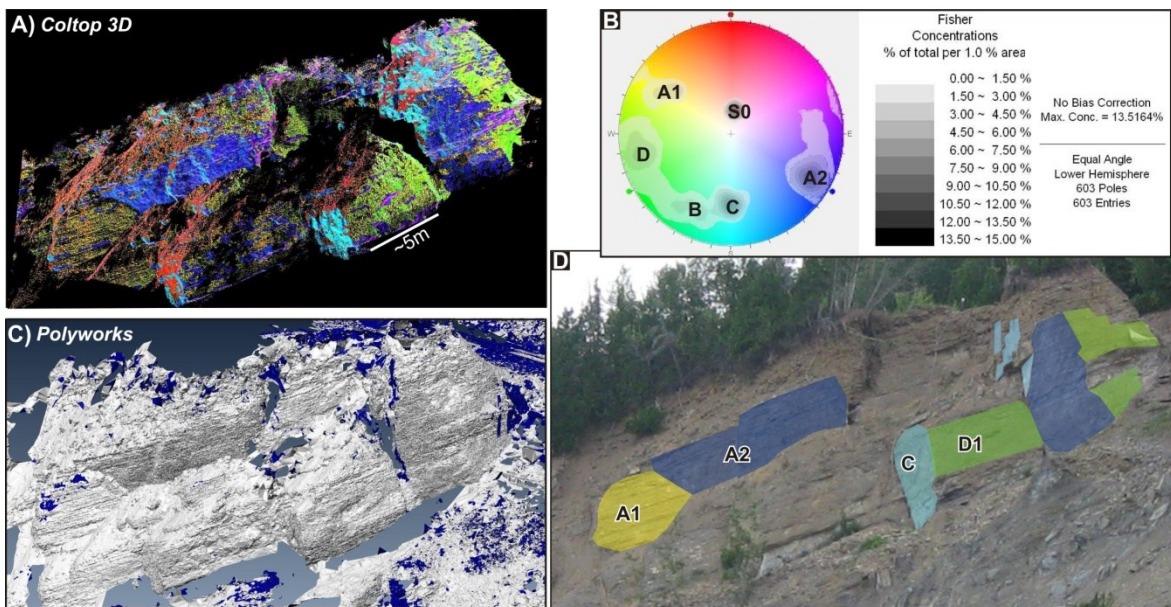


Figure 2-11 This Figure shows three representations of the Petit-massif and presents the discontinuities identified in the Petit-massif based on the TLS point cloud and DEM. A) Color representation in Coltop 3D. The colors are associated to point normals as shown on the stereonet in B. C) Same area view in Polyworks D) Photograph on the same area with some discontinuities identified.

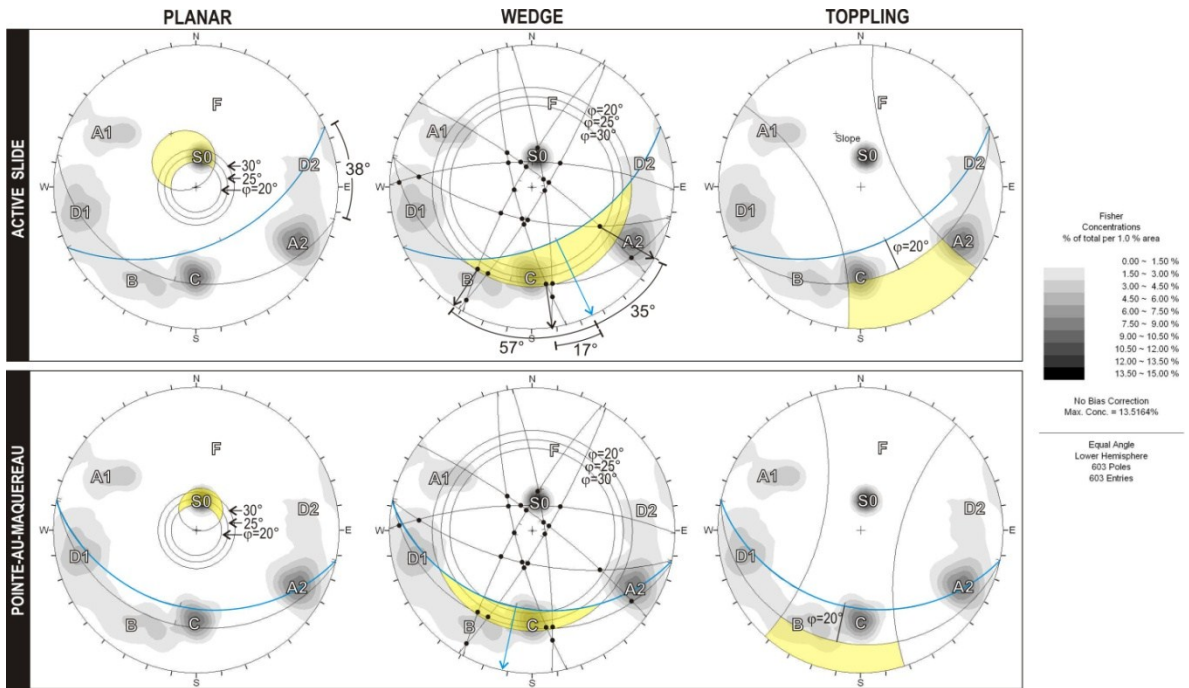


Figure 2-12 Kinematic tests using both the active slide and the Pointe-au-Maquereau slopes. Great circles in blue correspond to the slope faces. The instability zones are presented in yellow.

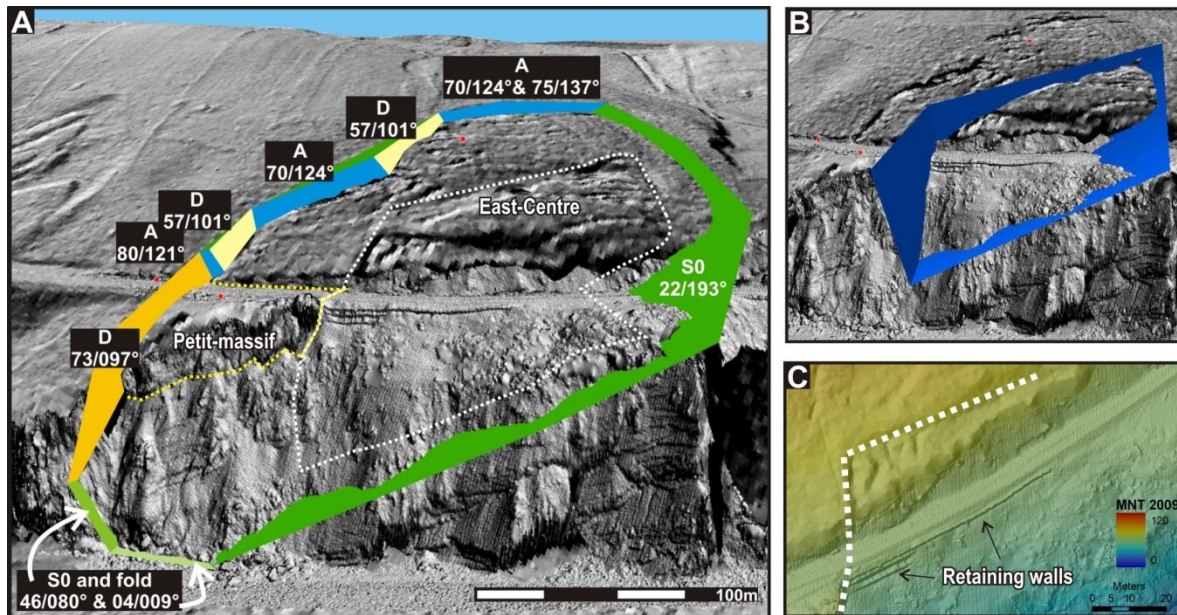


Figure 2-13 A) The sliding surface is constructed with planes and shown on an oblique view of the DEM. The dip and dip direction of planes are indicated. The East-Centre and the Petit-massif are identified. B) Interpretation of the sliding surface of the East-Centre, approximated by planes. C) Block-E is marked out on the DEM.

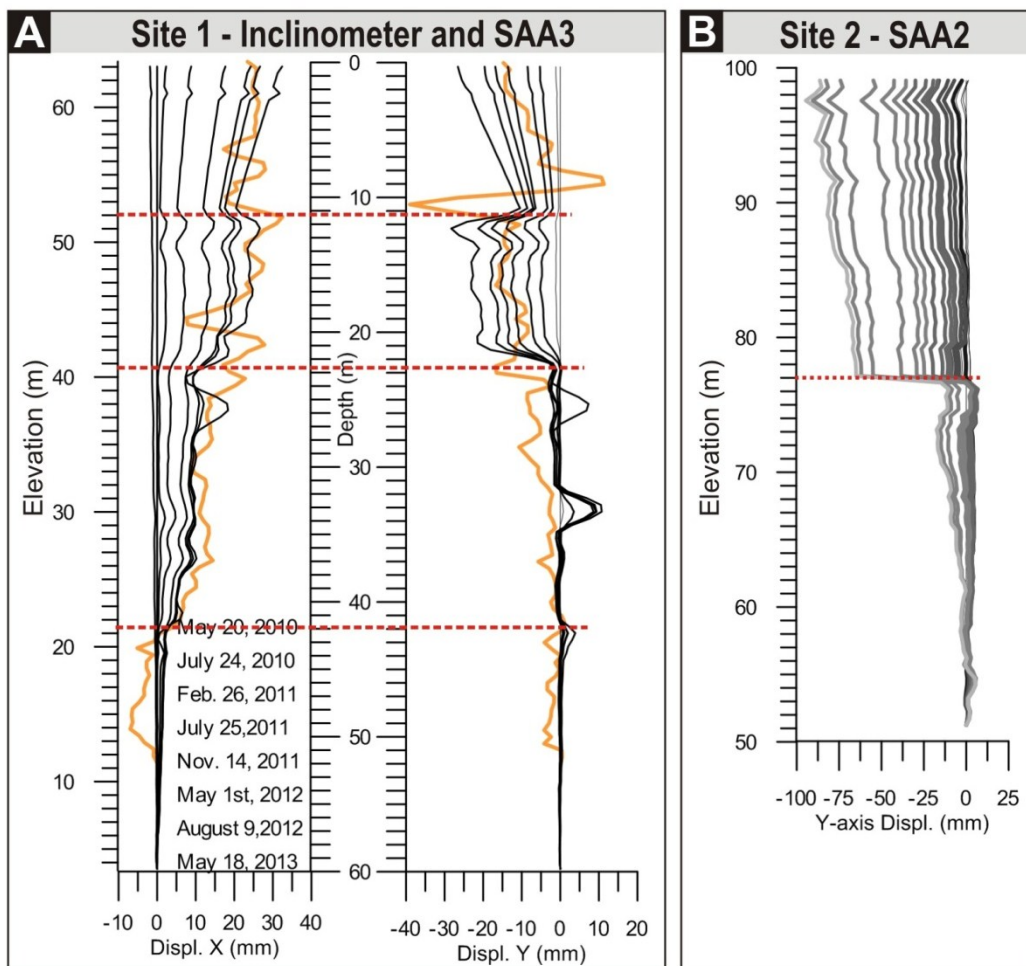


Figure 2-14 Displacements measured at Gascons. A) Inclinator (black) and SAA3 (orange) at Site 1 from May 2010 to May 2013. B) SAA2 data from January 2010 to October 2011 at Site 2.

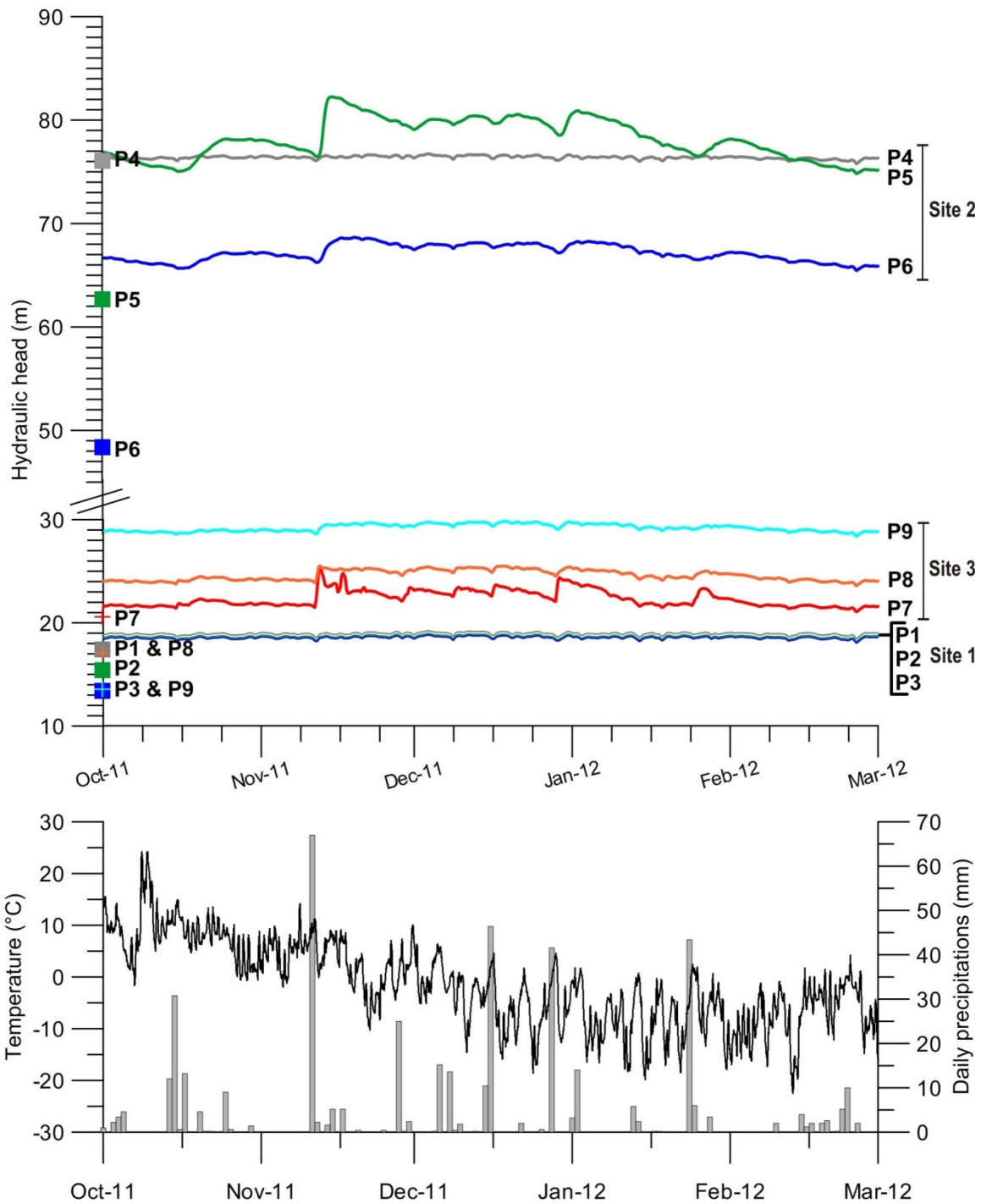


Figure 2-15 Hydraulic head of the nine piezometers installed in the three boreholes, for the time span between October 2011 and March 2012. The altitudes of the sensors are indicated on the Y-axis. Below, temperatures and daily precipitations are presented.

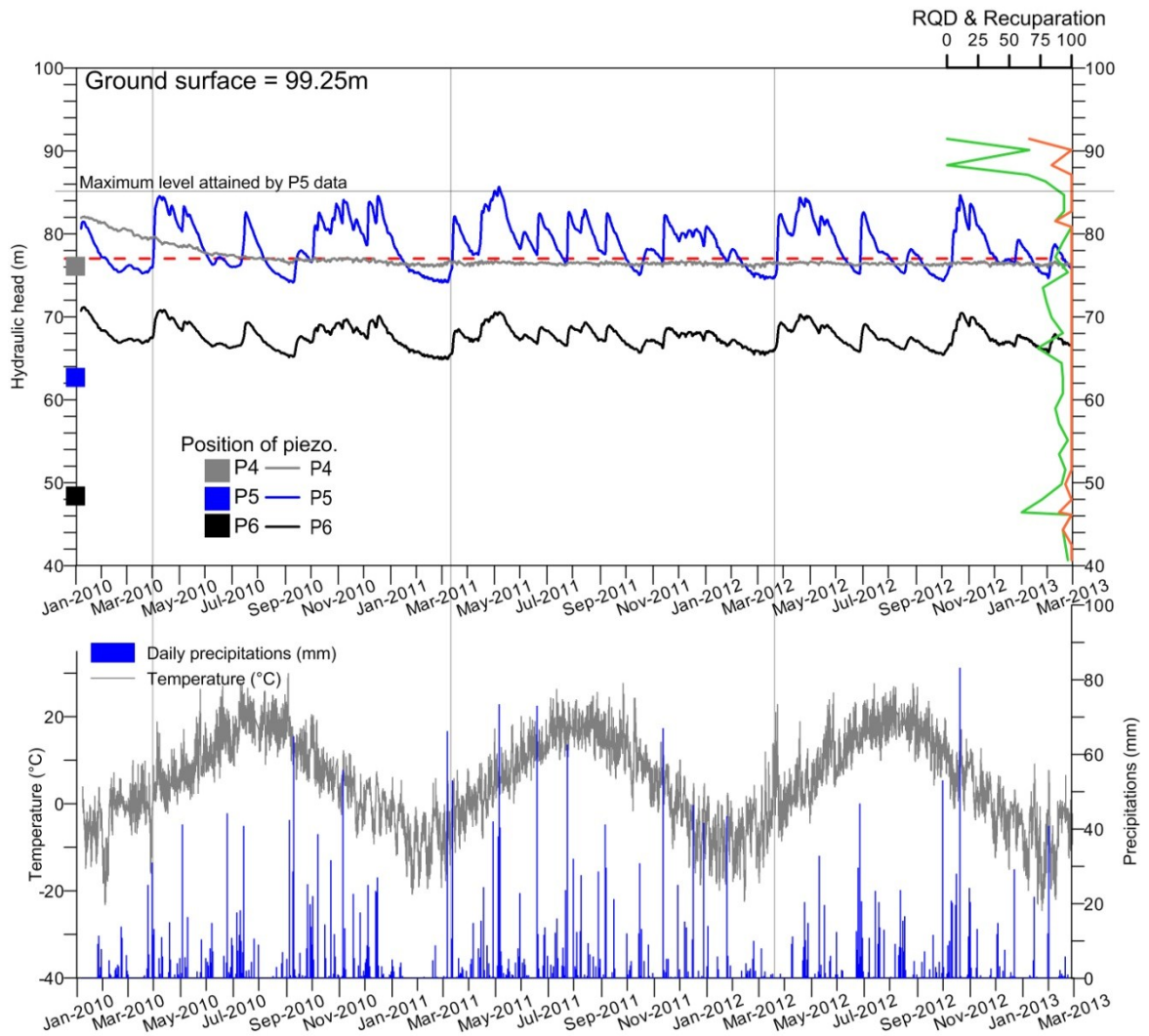


Figure 2-16 Hydraulic head of the three piezometers installed at Site 2 and their installation elevations. Rock Quality designation (green) and recuperation data of the core (orange) are indicated in % on the right. Below, temperatures and daily precipitations are graphed. The vertical lines indicate the start of yearly snow melt.

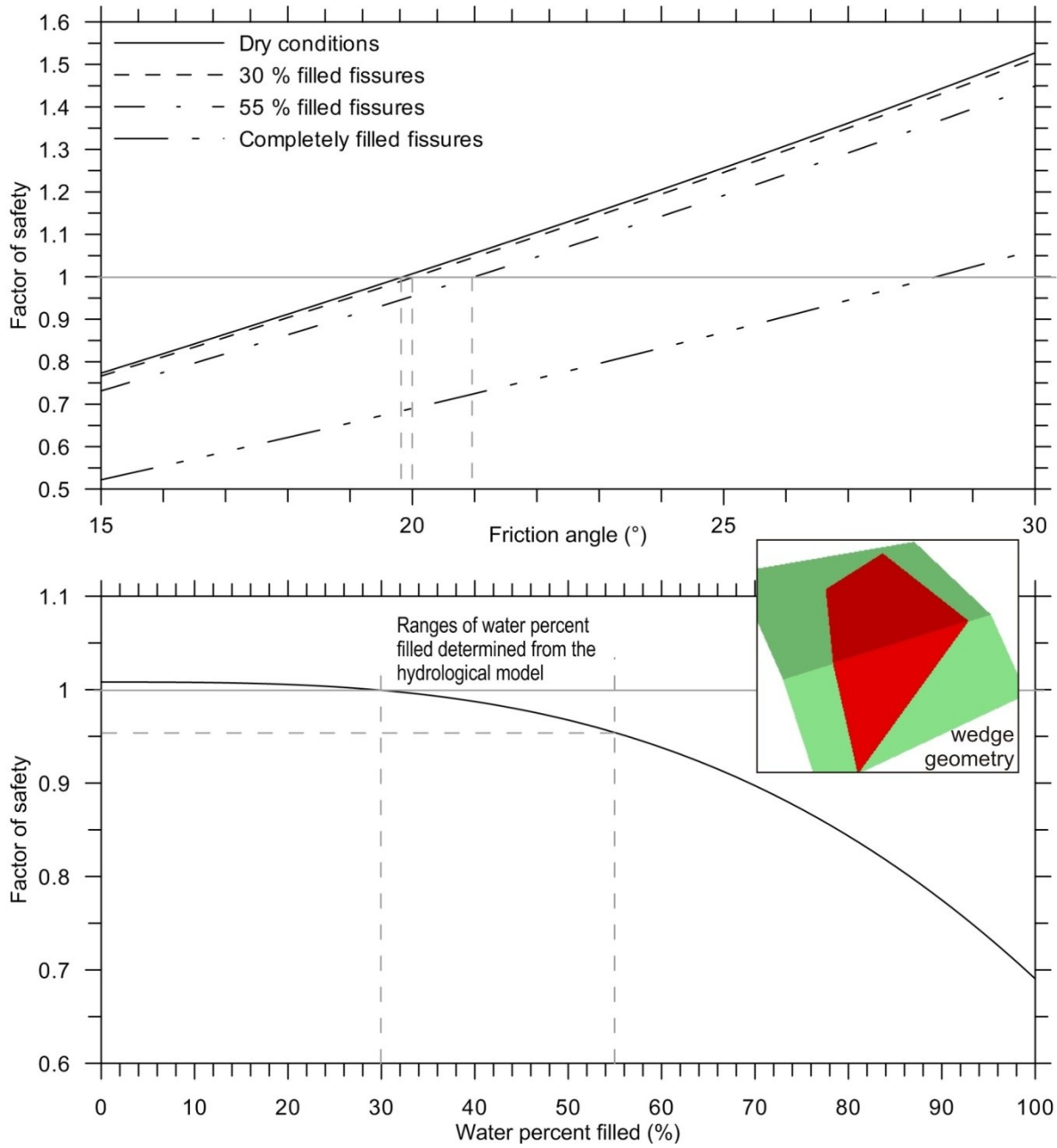


Figure 2-17 Limit equilibrium sensitivity analyses results. Above the Factor of Safety is computed for changing friction angle for four different water pressures. Below: The factor of safety is computed for changing fissures water percent filled.

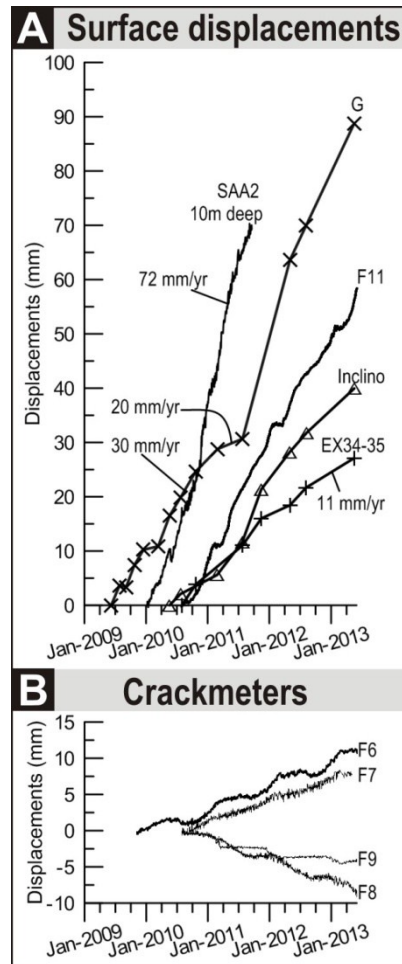


Figure 2-18 A) Displacement-time plots from SAA2, inclinometer, crackmeter F11, and extensometers (G and EX34-35). Instruments locations are indicated in Figure 2-2. B) Displacement-time plots of four crackmeters.

Chapter 3

Understanding the Kinematic Behaviour of the Active Gascons Rockslide from In-situ and Satellite Observation Data

3.1 Résumé

La surveillance du glissement côtier de Gascons, un dièdre asymétrique impliquant un volume de 410 000 m³, a débuté en 2009. Dans ce chapitre sont présentées, analysées et combinées les données provenant des outils de surveillance terrestre et satellitaire dans une analyse cinétique qui permet de cerner les zones critiques du glissement pour le chemin de fer et de proposer des scénarios d'évolution du glissement. Les données disponibles pour réaliser l'étude sont: (1) des déplacements relatifs, mesurés par treize fissuromètres et manuellement avec un ruban extensométrique, (2) des déplacements absolus, obtenus d'un inclinomètre et de deux SAA verticaux en forages, de levés à la station totale et d'un suivi PTA-InSAR à partir de données satellitaires, (3) le tassement du ballast de la voie ferrée suivi avec deux SAA horizontaux, (4) les pressions interstitielles de neuf piézomètres et (5) les conditions météorologiques. Les taux de déplacement varient spatialement, ce qui permet d'identifier des secteurs dans le glissement, qui concordent bien avec ceux déterminés de l'étude de la morphologie. De ces secteurs, ceux du Centre-Est et du Bloc-E se déplacent plus rapidement que les autres secteurs. De plus, les déplacements verticaux du Bloc-E sont plus importants que ceux mesurés dans le restant du glissement. Conséquemment, le Bloc-E est identifié comme un secteur critique pour la voie ferrée. Les résultats obtenus indiquent une composante des déplacements vers l'est, qui peut être expliquée par la rotation du dièdre, causée en partie par la butée créée par la faille et le plissement des strates sédimentaires dans le coin inférieur du dièdre. La variation temporelle des taux de déplacement prend diverses formes. Il a été possible de démontrer que l'eau souterraine influence les déplacements dans le haut du glissement, à proximité du Site 2. Dans le secteur du Petit-massif, certaines accélérations et décélérations sont associées avec des événements tels que de fortes pluies ou la fonte des neiges, mais cela ne se répète pas pour chaque événement. Ainsi, le rôle de l'eau et des autres facteurs environnementaux sur les déplacements est complexe et varie spatialement dans le glissement. Ces connaissances permettent de déterminer des scénarios d'évolution du glissement qui seront utilisés dans l'analyse du risque présentée au chapitre 4.

3.2 Abstract

The monitoring of the coastal Gascons rockslide, which involves a volume of 410 000 m³, started in 2009. This chapter presents, analyzes, and combines the in-situ instrumentation and the satellite-based monitoring to interpret the kinematic behaviour of the slide. This interpretation leads to the identification of critical zones for the railroad security and the development of possible scenarios. The available data are (1) relative displacements, measured by thirteen crackmeters and manually with an extensometer tape, (2) absolute displacements, obtained from inclinometer and vertical SAA in boreholes, total station surveys, and satellite-based PTA-InSAR, (3) the settlement of the railway ballast monitored by two horizontal SAA, (4) groundwater pressures from nine vibrating wire piezometers, and (5) weather conditions. The spatial variation of the displacement rates allows the identification of sectors which correlates well with those determined from the morphological analysis. The East-Centre and Block-E are the sectors with the fastest velocities. Moreover, the vertical downward displacements of Block-E are faster than the one of the rest of the slide. Block-E is identified to be a critical sector for the railroad. The analysis shows that some displacements occur towards the east, which can be explained by the rotation around a vertical axis of the wedge, partly caused by the buttress created by the folding of the sedimentary beds in the lower wedge corner. The temporal variations are taking different forms. The study shows that groundwater is acting on the displacement rates, uphill, near Site 2. In the Petit-massif sector, some periods of acceleration can be linked to snow melt and heavy precipitation events; however the pattern is not repeated at every event. Thereby the role of water and other environmental factors on displacements is complex and varying spatially in the rockslide. The rockslide kinematic behaviour enables to develop evolution scenarios of the rockslide, which will be useful for the risk analysis presented in Chapter 4.

3.3 Introduction

Slow landslides and humans do co-exist and this is why understanding their behavior is so crucial. As long as the movement remains slow the consequences to human life are very low and infrastructure built on or near the landslide can stay functional with proper maintenance. It is the case of multiple roads, railroads, dams, and in some cases villages (Barla *et al.* 2010; Corominas *et al.* 2005; Corsini *et al.* 2005; Cotecchia 2006; Picarelli 2007; Strozzi *et al.* 2005; Yueping *et al.* 2010). However, the potential acceleration of slow landslides is still a threat to human life if an unpredicted acceleration of the sliding mass takes place. When stabilisation of the landslide or protection works are not feasible, monitoring systems can be installed to avoid or lower potential loss of human lives. In addition to understanding the landslide mechanics, a monitoring system may also have the objective to observe precursory signs of an acceleration phase in order to predict the failure and minimize its impact. To do so, it is essential to first understand the geometry (volume), displacement rates and

directions, and to examine the role of various environmental factors on the instability. The installation of a monitoring system is just a first step to achieve in order to forecast a failure.

To characterize the displacements of a rockslide, sufficient spatial and temporal resolution can be achieved by combining different monitoring techniques. Large landslide studies based on data sets acquired from such monitoring systems revealed the complex nature of a rockslide's geometry and displacement patterns. Many slides have multiple sliding surfaces, others are separated into sectors with different displacement rates, while others are controlled by many mechanisms (Aknes (Grøneng *et al.* 2011; Grøneng *et al.* 2010), Ruinon (Crosta and Agliardi 2002; Crosta and Agliardi 2003; Strozzi *et al.* 2005), Downie (Kalenchuk 2010), and many others (Barla *et al.* 2010; El Bedoui *et al.* 2009; Froese *et al.* 2009; Gigli *et al.* 2011; Helmstetter and Garambois 2010; Zangerl *et al.* 2010)). Their complexity and the difficulty to have a complete picture of their behaviour explain partly why the mechanisms and process through which rockslides occur are still misunderstood (Eberhardt 2008; Glastonbury and Fell 2008; Petley *et al.* 2005; Stead *et al.* 2006).

In 1998, a small rockslide damaged a portion of the only railroad that reaches the town of Gaspé, in Québec, Canada (Figure 3-1). In this sector, the railroad is following a 63 m high cliff overlooking the Chaleur Bay. A derailment could cause the train to fall down into the bay. The failed mass was part of a known larger rockslide of 410 000 m³, the Gascons rockslide which is still active today. In 2009, following the acquisition of the railroad by the Provincial government, the monitoring of the slide started (Locat *et al.* 2010). The monitoring is carried out in collaboration with the Earth Science Sector (ESS-CCMEO) of Natural Resources Canada (Couture *et al.* 2010), who has expertise in monitoring the slope movements remotely using SAR satellite images.

This paper examines the surface and sub-surface displacement measurements monitored over a three year period to describe the general kinematic behaviour of the Gascons rockslide, its seasonal patterns and mechanisms. At first a review of displacements monitored in other rockslides is presented. Then, the Gascons rockslide is presented, followed by the description of the monitoring data available to conduct this study. Then, their interpretation allows the characterization of the rockslide's kinematic behaviour, the identification of cyclic patterns, and the description of external factors influencing the displacement rates. Finally, a discussion including comparison with other studies, conclusions, and recommendations are made.

3.4 A Review of Displacement Analyses of Cases Similar to the Gascons Slide

In the literature, examples of extensive monitoring system such as the one installed at Gascons are often related to deep seated rockslides involving the entire side of a mountain (Blikra 2008; Crosta and Agliardi 2003; Froese and Moreno 2011; Kalenchuk *et al.* 2009; Sornette *et al.* 2004).

The rockslide of Aknes, in Norway is monitored by multiple types of instrumentation (Blikra 2008; Ganerød *et al.* 2008) and periodic variations in displacement rates are observed. Nordvik and Nyrnes (2009) conducted a statistical analysis on the displacement records of the rockslide and found that the displacement measured from the extensometers on the back tension crack were strongly correlated with the ground water level variations. Groundwater maximum levels are reached in spring due to snow melt and in autumn due to high precipitations. However, no such correlations were found with the GPS data (Nordvik and Nyrnes, 2009).

Another study of the Aknes rockslide is presented in Groneng *et al.* (2011). They identified manually twelve events of increase or reduction of movements recorded simultaneously by many instruments with time spans ranging from 5 to 13 days. Four events are found in spring, three in fall, three in winter, and two in summer. They found that snow melting periods caused the largest annual deformation and linked the increased displacements to the combination of melting water and fluctuation of temperature around 0°C. In summer and early fall, no significant acceleration phases are recorded in the tension crack. Moreover, reductions of the distance are also recorded in many events and are linked to decreasing temperature. The physical explanation that links the decreasing temperature with the reduction of distance is not well defined.

Even though cyclic variations are recognized, establishing a link with external factors is often not obvious. It is the case of the Ruinon rockslide, in Italy, that is presented in a number of papers (Agliardi *et al.* 2013; Crosta and Agliardi 2002). Agliardi *et al.* (2013) suggested that the effect of precipitation varies within the rockslide sectors.

Concerning the Randa rockslide in Switzerland, Willenberg *et al.* (2008a) stated that establishing a relation between ground water and displacements is complicated by the presence of perched groundwater table. The Mannen rockslide in Norway has been recently instrumented (Blikra and Kristensen 2013; Kristensen and Blikra 2013) and the data acquired in a 15-month period in one borehole indicate that the groundwater table is located under the sliding surface. Despite that, increasing displacement rates were observed during snow melt. This increase is related to the effect of water seeping into fractures and reducing the shear strength of the rupture surface (Blikra and Kristensen 2013).

Gischig *et al.* (2010) proposed that the temperature changes are responsible for the seasonal pattern observed in Randa rockslide, in Switzerland. The displacement rates increase when the temperature drops below zero in fall and decrease after snow melt in spring. Their explanation is that the thermo-elastic strains significantly influence the seasonal pattern, while groundwater and precipitations are not correlated to the displacement rates. Similar hypotheses are proposed for the Checkerboard Creek slide by Watson *et al.* (2004).

In Norway, the Nordnes rockslide's seasonal pattern is not characterized by acceleration with snowmelt (Nordvik *et al.* 2010). In fact, the largest displacement rates occur in fall and early winter with a stagnation or retreat in spring and summer, which is similar to what is observed in Randa. The presence of permafrost and ice are supposed to be key factors influencing the movements of the Nordnes rockslide (Nordvik *et al.* 2010).

In the statistical relations established by Nordvik *et al.* (2010) for the Nordnes rockslide, the observed distance on crackmeters is expected to decrease with the increasing air temperature. They proposed that the thermal expansion of the rock faces, on each side of the crack, causes compression of the crackmeters. However, the temperature fluctuations alone do not permit to explain the total seasonal fluctuation. In Randa, the fluctuations of the crackmeters installed at surface are also related to shallow thermo-elastic strains of the rock (Willenberg *et al.* 2008a).

Seasonal variations in rockslide appear to be the result of complex interactions of groundwater level, precipitation, thermo-elastic strains, and geological and geometric structures. In most cases, the relations are not straightforward. Even though the correlations are sometimes hard to establish between seasonal variations and the water influence (precipitation and groundwater level), water is often a driving factor in rockslides. Water drainage was used successfully to stabilize rockslides, such as the Downie slide (Kalenchuk 2010) and the Campo Vallemaggia landslide (Eberhardt *et al.* 2007) among others.

A known technique for time to failure prediction is the inverse velocity technique (Fukuzono 1985; Saito 1969; Voight 1988; 1989) that was applied to rock slope failures (Crosta and Agliardi 2002; Crosta and Agliardi 2003; Mufundirwa *et al.* 2010; Rose and Hungr 2007). The method is based on the slope creep theory: a time dependent material failure relationship. The material goes through three creep phases illustrated in Figure 3-2 by a strain versus time curve. The primary phase is strain hardening, the secondary shows steady state rate of displacement, and the tertiary is an accelerating phase leading to failure. Not all the natural slopes failures go through these three phases. However, the accelerating phase has been observed in many types of slides (volume and material) and many are reported in Froude (2011).

3.5 Description of the Gascons Rockslide

The Gascons rockslide is a wedge failure of 410 000 m³. The wedge slides on the bedding planes of the Anse-à-Pierre-Loiselle Formation (APL) that are dipping 22° SSW. The APL Formation is a transition unit between Anse Cascons Formation (sandstones) and La Vieille inférieur (limestones). The APL is composed at the bottom by sandstones alternating with centimetric fossiliferous mudstones layers. Going upward, the percentage of limestone concretions is increasing (Bourque and Lachambre 1980) while the sandstones are disappearing. A conglomeratic unit is marking the middle of APL Formation and is shown on cross-sections in Figure 3-3.

The rock mass is characterized by four main discontinuity sets in addition to the bedding. Structural data are obtained from field compass measurement and extracted from terrestrial laser scans with *Coltop 3D* software (Jaboyedoff *et al.* 2009, and Chapter 2 of this thesis). The geometry of the sliding surface was interpreted from structural, morphological, and in depth displacement data. It is represented by a green surface in Figure 3-4A and the discontinuity sets forming the wedge are shown in bold on the stereographic projection of Figure 3-4B. The lateral and back release surfaces are formed by the combination of sets A and D shown on the stereographic projection. The eastern lateral extent of the rockslide is also identified in the field by deformation in the railroad that is shown in Figure 3-5.

The Gascons rockslide is constrained between two geological features (Figure 3-1), the Port-Daniel-River fault (west) and an angular unconformity (east) separating Cambrian metasedimentary rocks from the Silurian sedimentary rocks in which the instability takes place. Near the fault, the beds are curving upward. The geometry of the surface of rupture is influenced by this syncline. In fact the sliding surface showed in Figure 3-4A uses two planes in the bottom corner of the wedge in order to match the folded beds.

Large cracks are observed all over the rockslide and are seen on the elevation model of Figures 3-1 and 3-4. Lineaments, depressions, and opened fractures were mapped in the field and the resulting cartography was used to create a model where the slide is divided into blocks and is shown on Figure 3-6. The rules followed to create the blocks were that: (1) a block is delimited by cracks, lineaments, or depressions; (2) all fissures are reaching the sliding surface, and (3) a fracture stops when it intercepts another fracture (Cloutier *et al.* 2012; Lord 2011). Therefore, the model presented here is a pseudo-three-dimensional block model which assumes that the surface fissures project onto the sliding plane underneath. Considering that the shape of the slide is a wedge and that the thickness of the sliding material is thinning from west to east, a three-dimensional understanding is necessary to analyze the displacement data.

Two specific sectors are identified in the rockslide: the Petit-massif and the East-Centre. The Petit-massif is composed of the blocks south of the railway trench and west of the retaining walls (Figure 3-4A). Three levels of sliding surface were identified in the inclinometer of Site 1 (identified in Figure 3-7) and are drawn in cross-section AA' of Figure 3-3.

In July 1998, the eastern part of the Petit-massif slid down. Its sliding surface is indicated on cross-section AA'. This rock mass was acting as a retaining wall for the railway ballast. Consequently, when it slid, part of the ballast followed it leaving the tracks without support. As part of the repair work, the remaining retaining wall was extended to the west to fill the gap left by the slide.

The East-Centre was first identified by the observation of the elevation model. It appears to be partly individualised from the main sliding mass and its volume is estimated to 75 600 m³. Its sliding surface daylights in the slope face as can be observed in cross-section BB' (Figure 3-3) and in Figure 3-4A, and is not influenced by the syncline. The morphological expression of the East-Centre's back scarp is different from the one of the main slide. The active slide is characterized by tension cracks clearly visible in the DEM and in the field, while no such tension cracks are seen at the back of East-Centre. It is rather delineated by a steep slope.

The sliding mass is well drained due to its highly fractured nature. The water flows towards the bay, and water sources and water seepage are observed on the beach. The pore water pressures are monitored by vibrating wire piezometers in three boreholes. The water level is indicated on the cross-sections of Figure 3-3. The water table is just under the sliding surface, but the piezometric level measured at Site 2 (identified in Figure 3-7) can increase up to 8 m above the sliding surface following the snow melt and precipitation events and is presented by the dashed blue line in cross-section BB' (Figure 3-3). Water level fluctuations are discussed later in this paper.

Smaller rockslides could take place in the cliff area, within the Gascons rockslide. Their sliding mechanisms are associated to toppling and planar failures. In fact, in some sector the cliff orientation is proper to develop planar failure of modest volumes. Toppling could marginally form with discontinuity sets A and C.

On the Pointe-au-Maquereau, the coast line is perpendicular to the dip direction of the bedding creating translational slides that are marked by black arrows in Figure 3-1. Erosion of the toe of the slope is the key factor leading to the instabilities. An ancient wedge slide has been identified on the elevation model and surrounded by a dotted line in Figure 3-1. It is similar in shape to the active Gascons rockslide. The evaluation of the ancient slide's volume gives an average value of 287 000 m³. This volume estimation is subjected to many sources of uncertainties: the sliding surface shape, the amount of debris remaining in the scar and most importantly the terrain's pre-failure topography (for more information see the chapter 2 of this thesis).

3.6 Methodology: Presentation and Analysis of Monitoring Data

In order to study the kinematics of the Gascons slide, one must develop a comprehensive analysis of the observed displacements and this can only be done by a relevant monitoring methodology providing displacement and pore pressure data. To that effect, this section will present and analyze the various instruments installed at Gascons to enable monitoring surface and in depth displacements, pore water pressures, tilting of the retaining wall, settlement of the railway ballast, and weather. This involves a monitoring system which is composed of sensors connected to an automatic acquisition system and of manually made measurements. A complete description of the system design is available in Appendix A and instrumentation locations are presented in Figures 3-6 and 3-7.

The investigation of the rockslide started in June 2009. The monitoring system was installed in fall 2009 and completed in summer 2010. Since then, some sensors have been added or modified as we felt that some modifications were necessary to improve the monitoring. The data presented in this paper start at the earliest in June 2009 and end in June 2013. However, most data sets start in November 2009. The system is still acquiring data, except for a few instruments that have stop working, as crackmeter F7 in May 2013 (replaced in November 2013) and vertical SAA2 in October 2011.

In this section, the data are grouped based on the type of information they acquire. The first category, the relative surface displacements, is composed of the crackmeter and extensometer networks that are measuring the distance between two points inside the slide. They give information about a fissure opening or closing in one direction. Alone, they do not reflect the total displacement of the mass, but the differential displacements inside the sliding mass. They are presented in section 3.6.1.

The second category, called the absolute displacements, is related to instruments measuring the displacements compared to a point outside of the rockslide. This category, presented in section 3.6.2, includes the inclinometer, the vertical SAA, the total station, and the PTA-InSAR.

The third category (section 3.6.3) is made up of instruments following the infrastructure, namely a tiltmeter installed on a retaining wall and two horizontal SAA buried in the ballast. Finally, water pressures and weather information are presented in section 3.6.4.

The displacements are presented in various forms depending on the type of measurement, such as total displacement, rates of displacement, displacement versus time plots, and others. To ease the interpretation and the coupling of various data sets, a displacement rate in mm/yr is computed for every data set. These displacement rates are obtained from sets of different duration, which is always specified. Moreover, various methods are used to estimate the rates. For example, the equivalent displacement rate computed for the

extensometers is obtained by dividing the total displacement (mm) by the time span (days) and multiplied by 365 to have the mm/yr unity. Other examples are the average and maximum rates that are given by the slope of a linear regression processed on the data.

3.6.1 Relative Surface Displacements

Distances measured between two points inside the slide are the most common type of measurements taken on site; they are the crackmeter and extensometer networks. Relative surface displacements are the changes in distance between the two points. Two facts must be kept in mind when interpreting these displacements: (1) the computed displacement depends on the measurement's trend, and (2) as both points might be inside the slide, the computed displacement does not represent the total displacement of the slide, but rather the opening or closing of fissures. Most of the crackmeters and rods were installed perpendicular to the fissures, as this orientation was assumed to be the main direction of movement. For each relative displacement monitoring point, trend of measurements, acquisition period, and width of the fissure at the time of installation are presented in Table 3-1 for extensometers and Table 3-2 for crackmeters.

The extensometer network consists in 44 rods, 45.7 cm long anchored in rock and in soil. Their locations are indicated in Figure 3-7. The distance between pairs of rods is measured manually with a sub-millimetric precision tape, called the extensometer (model Convex Ealey). The measurements were done every field visit, but some rods are not accessible in winter. The measurements are presented in Appendix F in tables and graphics. Consequently, the data sets are composed of 4 to 13 readings. Displacement-time curves obtained from extensometers are shown in Figure 3-9. When doing a measurement the distance between two points is taken three to six times. The half-difference between the highest and lowest values are used to quantify the uncertainty. Errors on the measurements increase with the length of the measurement and are related to the solidity of the anchor and the wind. Moreover, the value is influenced by the operator. The uncertainty magnitude varies between 0.03 and 0.24 mm and the average error for each pair is presented in Table 3-1.

Surface displacements are also monitored by thirteen vibrating wire crackmeters (Geokon model 4420), linked to the acquisition system by electric cable and read automatically every five minutes. They are installed along the railroad and in the cliff area and named F1 to F13 (Figure 3-7). They are anchored in the rock with epoxy-injected anchors and covered by a protective hood. Eleven crackmeters are installed on pre-existing opened fractures (F2-F9, F11, and F13), opened by an average value of 220 mm (Table 3-2). Of these eleven sensors, two (F7 and F8) are installed on the same fracture at a 90° angle in order to measure different components of displacements. F10 and F12 are installed parallel to the bedding surfaces to detect displacements on possible sliding surface. F1-new is installed between the retaining wall and the rock face. All crackmeters were installed at 50% of their ranges which are of 100, 150, or 300 mm to accommodate opening and/or closing of fractures.

All crackmeters are measuring significant displacements, except for the shearing crackmeters F10 and F12. This analysis will focus on the ten sensors that are installed on pre-existing opened fractures.

The data are converted to engineering units and corrected for temperature using a linear correction proposed by the manufacturer. The whole process is automated. The vibrating wires sensors have 0.1% accuracy and 0.025% resolution when stretch at full range, which corresponds for the 300 mm range sensors to 0.3 and 0.075 mm respectively.

However, the evaluated uncertainty is more important. The data are characterized by daily variations and their amplitude is differing in between sensors and from day to day. These variations that range from 0.08 to 1.91 mm are important compared to the average crackmeter's displacement rate evaluated to 0.012 mm/d (4.4 mm/yr). F11 is the crackmeter with the less noisy signal; it is also the one with higher displacement rates. It appears that the daily variations are decreasing in periods with faster rates. The noise is related to the effects of temperature on the system, including the rock, the anchors, and the crackmeter.

These variations are observed after the application of the temperature correction proposed by the manufacturer. Temperature corrections proposed by the manufacturer tend to sometime increase the thermal effect, meaning that some phenomenon is acting in an opposite direction to the sensor variation caused by temperature changes.

When observing the data only on a short period, these variations are hiding the general trend. Moreover, these variations have important effects on the calculation of the first and second order derivatives used to characterize the rates and acceleration of the displacements, which can be used to issue warnings. The data must be filtered and/or average.

The crackmeters data plotted in Figure 3-10 are daily averages, calculated from the 288 measurements recorded over a 24-hour period. The circle in Figure 3-10 illustrates the daily variations by plotting on top of each other the 5-minute data and the daily average. The uncertainty is characterized as the half-amplitude of the 5-minute data and is presented in Table 3- 2.

F2 to F6 were installed in November 2009, F7 to F12 in August 2010, and F1-new and F13 in August 2012. The data presented here end in May 31st 2013. Total and yearly displacements for every crackmeters are presented in Table 3-2. If a crackmeter opens and then closes of the same amount, this is equivalent to zero displacement. Four crackmeters are measuring a decreasing distance between their anchors, even though they were all installed on pre-existing cracks.

The maximum total displacement is measured by F11. The upper inset in Figure 3-10 shows F11 and F6 on the same vertical axis, in order to show how important the displacements measured by F11 are compared to other crackmeters. The two fractures that were the largest at the moment of installation are also the ones with the fastest rates of displacement (F11 and F13).

The average displacement rates over the whole period of acquisition, simply evaluated by doing a linear regression over the data is specified in Table 3-2, along with the associated determination coefficient (R^2) of each regression. Linear regressions have also been performed on yearly data, but poor representative values were obtained for most sensors due to non-linear variation patterns that are repeating yearly. The average rate of displacement of every crackmeters is 4.4 mm/yr.

Figure 3-11 presents the maximum rate of displacement per year for every crackmeters. They were evaluated by first choosing visually the faster periods that were judged to be part of the general displacement trend measured by the sensor. Secondly, the rates are evaluated with a linear regression. The rates had to last at least 10 days to be considered valid. The results are presented in Figure 3-11. The average maximum rate of displacement of the ten crackmeters is 13.1 mm/yr and it lowers to 8.4 mm/yr when excluding F11 from the calculation.

Table 3-1 The table presents information relative to the extensometer network.

Pair	Trend	Plunge	Initial opening	Start date	End date	Total disp.	uncertainty	Eq. Rate
	(°)	(°)	mm			mm	± mm	mm/yr
EX1-2	104	0	100	08/06/2009	17/05/2013	15.4	0.05	3.9
EX3-4	71	0	200	08/06/2009	17/05/2013	-9.4	0.04	-3.0
EX5-6	275	27	170	08/06/2009	17/05/2013	-9.7	0.03	-2.5
EX5-7	174	0	no opening	08/06/2009	17/05/2013	27.5	0.13	7.0
EX6-7	157	0	no opening	08/06/2009	17/05/2013	64.4	0.13	16.3
EX8-9	51	0	2000 (at surface)	08/06/2009	17/05/2013	-17.0	0.13	-4.3
EX10-11	233	N/D	100	08/06/2009	17/05/2013	8.9	0.05	2.3
EX12-13	105	26	550	08/06/2009	17/05/2013	21.9	0.03	5.6
EX14-15	124	25	6450	08/06/2009	17/05/2013	88.7	0.05	23.3
EX14-16	251	11	not a fissure	08/06/2009	17/05/2013	-46.8	0.06	-11.9
EX15-16	165	33	5586	08/06/2009	17/05/2013	127.1	0.05	32.2
EX17-18	299	3	1700	08/06/2009	17/05/2013	17.6	0.08	4.5
EX19-20	277	15	1100	08/06/2009	17/05/2013	26.9	0.10	6.8
EX21-22	295	4	850	08/06/2009	17/05/2013	-6.7	0.06	-1.7
EX23-24	146	20	4000	08/06/2009	17/05/2013	24.4	0.07	6.2
EX25-26	154	14	2300	08/06/2009	17/05/2013	48.1	0.16	12.2
EX27-28	111	25.5	1800	08/06/2009	26/07/2011	11.5	0.1	5.4
EX29-30	234	42	600	08/06/2009	03/05/2012	13.5	0.04	4.2
EX31-32	73	7	no opening	01/08/2010	17/05/2013	-14.0	0.1	-5.0
EX31-33	142	15	no opening	01/08/2010	17/05/2013	1.4	0.13	0.5
EX32-33	217	3	no opening	01/08/2010	17/05/2013	-1.2	0.09	-0.4
EX34-35	143	8	7500	01/08/2010	17/05/2013	27.1	0.13	9.7
EX36-37	148	19	1000	01/08/2010	17/05/2013	21.8	0.05	7.8
EX38-39	150	38	no opening	01/08/2010	17/05/2013	22.5	0.22	8.0
EX41-42	106	0	1300	01/08/2010	17/05/2013	-5.6	0.1	-2.0
EX43-44	95	0	200	01/08/2010	17/05/2013	-8.1	0.04	-2.9
EX7-2	219	12	multiple fractures	20/05/2010	17/05/2013	-19.3	0.12	-6.4
EX7-1	222	12	multiple fractures	20/05/2010	17/05/2013	-20.3	0.24	-6.8
40-1	169	10	multiple fractures	01/08/2010	17/05/2013	12.2	0.17	4.4
40-2	162	7	multiple fractures	01/08/2010	17/05/2013	20.5	0.22	7.3
40-3	143	6	multiple fractures	01/08/2010	17/05/2013	20.0	0.16	7.2
40-5	281	1	multiple fractures	01/08/2010	17/05/2013	26.5	0.14	9.5
40-6	278	1	multiple fractures	01/08/2010	17/05/2013	28.1	0.23	10.1
40-44	111	8	multiple fractures	01/08/2010	17/05/2013	24.8	0.15	8.9
43-5	263	9	multiple fractures	01/08/2010	17/05/2013	-5.4	0.13	-1.9
43-6	263	10	multiple fractures	01/08/2010	17/05/2013	-13.3	0.14	-4.8
43-7	215	8	multiple fractures	01/08/2010	17/05/2013	-17.5	0.17	-6.3
44-5	261	10	multiple fractures	01/08/2010	17/05/2013	5.6	0.07	2.0
44-6	264	11	multiple fractures	01/08/2010	17/05/2013	-3.8	0.15	-1.4
44-7	210	9	multiple fractures	01/08/2010	17/05/2013	-3.2	0.16	-1.1

Table 3-2 This table present the information relative to the 13 crackmeters. The yearly and total displacements are indicated. The average rate is obtained by a linear regression performed on the complete data set. The fissure's initial width was measured with a measuring tape.

F#	Trend (°)	Plunge (°)	fissure's initial width (mm)	Start date	End date	Yearly displacement (mm)					Average rate		
						±	2010	2011	2012	2013	total	mm/yr	R ²
F1 - new	200	21	200	09/08/2012	31/05/2013	0.5				2.2	1.9	4.7	0.74
F2	143	0	210	07/11/2009	31/05/2013	0.7	1.5	3.1	2.9	1.9	9.4	2.7	0.97
F3	180	29	250	07/11/2009	31/05/2013	0.4	-2	-1.1	-1.5	-0.5	-5	-1.5	0.95
F4	190	24	50	07/11/2009	31/05/2013	0.4	-2.3	-2.5	-2.6	-2.45	-11.2	-2.8	0.99
F5	107	22.5	300	07/11/2009	31/05/2013	0.6	1.7	2.4	1	-0.2	4.4	1.9	0.88
F6	146	0	300	07/11/2009	31/05/2013	0.3	2.5	3.7	3.3	1.3	11	3.2	0.97
F7	337	0	200	30/07/2012	03/05/2013	0.4	1.6	3	2.8	0.6	8.1	3.0	0.98
F8	245	0	200	30/07/2012	31/05/2013	0.4	-0.2	-2.8	-3	-2	-8.6	-2.9	0.97
F9	305	3	50	30/07/2012	31/05/2013	0.3	-0.4	-2.6	-0.7	0.4	-4.2	-1.5	0.89
F10	190	22.8	0	30/07/2012	31/05/2013	Shearing crackmeter							
F11	94	8	460	30/07/2012	31/05/2013	0.2	8	23.5	17.5	9	58	20.6	0.99
F12	190	22.8	0	30/07/2012	31/05/2013	Shearing crackmeter							
F13	293	12	550	09/08/2012	31/05/2013	0.3				3.17	4.1	4.1	0.80

3.6.2 Absolute Displacements

3.6.2.1 Site 1: Inclinator and Vertical SAA

At Site 1 (Figure 3-7), profiles of displacement with depth are obtained from a 60 m long traditional inclinometer casing and probe (DIS-500, RocTest Group) and from a shape accelerometer array (SAA) of 52 m long (Measurand). The SAA is a chain of 50 cm joint-linked rigid segments (Danisch *et al.* 2010). Each segment has accelerometers that enable calculating its inclination and the shape of the chain. It acts as an in-place inclinometer. It was the first installation of an SAA chain carried out in a rock mass. One of the objectives of this installation was to validate the application of SAA technology to monitor a rockslide by comparing the results with the ones of a traditional inclinometer system. Similar systems were installed in other rockslides outside of Canada, such as the DMS column that were installed, among others, at the La Saxe rockslide (Crosta *et al.* 2013).

The inclinometer data set is made of eight surveys conducted between May 2010 and May 2013 carried out with the biaxial DIS-500 probe in a 70 mm Geo-Lock casing. As the probe is biaxial, data can be acquired by lowering the probe twice in the same set of the casing grooves and rotating the probe by 180° between the two lowerings. To increase the accuracy of the surveys, the probe is lowered four times, so twice in both sets

of grooves. In fact, we realised that the B-axis of the probe was drifting with temperature in summer surveys. Thus, by carrying the survey in both pair of grooves it is possible to use only the measurements taken from the A-axis of the probe. In winter, both sensors gave good results.

The vertical SAA3 records extend from November 2009 to June 2013. Data are collected four times a day. Figure 3-12 presents displacement profiles with depth for both the inclinometer and SAA3. To make the comparison with the inclinometer, the SAA data are truncated to start in May 2010 in Figures 3-12 and 3-13.

SAA3 data are rotated to match the displacement direction of the inclinometer data. In fact, the installation method used in Gascons made it difficult to assess correctly the direction of the X and Y axes of the SAA sensors. The Gascons experience led the manufacturer to modify their installation methods and sensors to be able to know the direction of the sensors while they are in the borehole. Thus, the interpretation of the direction of both SAA (Sites 1 and 2) was an issue. The directions of displacement of the inclinometer and SAA3 are illustrated by plotting the X and Y components of displacements in Figure 3-13.

For both instruments, displacements are computed by assuming that the bottom sensor is in stable ground, thus under the sliding surface. The position of each 50 cm segment is based on the position of the sensors below. As a result, the errors are cumulating from the bottom to the top. The manufacturer evaluates the inclinometer's precision to be of 2 mm/25 m, which makes 4.8 mm for the top section of the Gascons 60 m long installation. On Figure 3-13, the 6-hour SAA data at a depth of 3.5 m are plotted in grey. The width of the grey zone in the plot illustrates the precision of the sensor which is evaluated to be around 3 mm.

The depth profiles of Figure 3-12 show significant displacements down to 43 m deep. Above 22 m deep, the displacement is increasing and changing direction. In fact, the lower part is moving towards the south (curves z 30.3 and 37.3 m in Figure 3-13) while above 22 m deep an eastern component is also observed. The average direction of displacement is 144° at depth of 1.3 and 13.3 m in Figure 3-13.

Average rate of displacement in the upper part of the inclinometer ($z=1.3$) are 14 mm/yr and in the lower part ($z=30.3$ m) 4 mm/yr. They are evaluated from a linear regression and the R^2 are respectively of 0.97 and 0.88. The maximum displacement measured is 40 mm with the inclinometer and 41 mm with SAA3 for the period between May 2010 and May 2013 which shows an excellent correlation. The displacement rate of the top meter of SAA3 is 14 mm/yr ($R^2 = 0.93$). Figure 3-14 presents two displacement-time curves of SAA3 at 1 and 33 m deep.

As can be seen on Figure 3-13, SAA3's higher frequency of data acquisition shows that the path taken by the SAA3 plot is not as straight as the one drawn from inclinometer data. SAA3 shows clearly some episodes of

movements towards the south and other towards the average direction of displacements of 144°. When plotting displacement from different time intervals, it is clear that the displacement occurring on the deepest failure surface, at 43 m deep, are affecting the whole mass and are towards the south. The rest of the time, only the upper 22 m are moving towards an average direction of 144°. It is important to note that SAA3 data were rotated in order to match the direction of displacement measured with the inclinometer.

Finally, the upper 11 m might indicate toppling towards south-east. In fact, the displacements are larger at the surface than they are at 11 m deep. This shows that the movement is complex. The whole mass undergoes episodic movements towards the south, to which adds an eastern component of movement in the upper 22 m that is more regular through time. It leads to an overall displacement direction in the upper part of 144° which is illustrated by a vector in Figure 3-6.

3.6.2.2 Site 2: SAA2

SAA2 is installed in the upper part of the slide at Site 2 (Figure 3-7) and is 48 m long. It has been acquiring data from November 2009 to July 2012, when it stopped working due to shearing. In October 2011, an electronic device that was probably damaged by lightning had to be change. It was not feasible to merge the data sets from before and after repair without doing major assumptions that decreased the usefulness of the data to help understand the kinematic behaviour of the rockslide. Therefore, only the data from November 2009 to October 2011 are presented.

Displacement profiles with depth are presented in Figure 3-15 and displacement versus time plots in Figure 3-16. A clear and sharp shearing surface is measured at a depth of 23 m. The mass above 23 m deep moves mostly as a whole, except for some events when the mass above 14 or above 6 m deep accelerates without involving the whole part above 23 m deep. The average displacement rate at 12 m deep measured on the whole acquisition period is 48 mm/yr with a R^2 of 0.96. The rate of displacement is higher between November 2010 and June 2011. For example, from February to April 2011 a rate of 77 mm/yr is computed. The rate then slows down to an average of 56 mm/yr until the end of the acquisition period. The total displacement measured by this sensor is 89 mm with a 5 mm precision.

The analysis of the direction of displacements measured by SAA2 is problematic. In fact, it was not possible to have information about the orientation of the instrument once it is in the borehole. But, during the repair done in October 2011, we saw the orientation of the sensor, which was not in the direction we thought it was. This new measured direction was partly solving the issues related to the direction.

The curves plotted in Figure 3-15B show a 90° rotation occurring from January to July 2011 and that is affecting the whole length of SAA2. Even the sensors under the sliding surface are affected. The directions are

stable before and after this period. Figure 3-15B was created using the direction measured in October 2011; the X-axis is pointing towards 098°.

At first, data indicate that the mass is sliding toward 160°. This direction corresponds to what is predicted from the geometry of the slide and measured with other instruments (see vectors in Figure 3-6 and chapter sections on PTA-InSAR and total station). Then, the direction reaches 229°. The dip direction of the bedding is 193°, thus, that direction would imply that the rock is moving upward or rotating on itself. However, as this rotation is observed also on segments situated under the 23 m deep shearing zone, this rotation is considered as an instrument problem. However, we believe that the total displacement computed during and after the rotation represents real displacements and it is considered in the kinematic behaviour interpretation.

In Figure 3-6, the vector corresponding to SAA2 represents a planar displacement rate of 48 mm/yr towards a direction of 160°.

Sensors from 23 to 32 m deep which are under the sliding surface are moving perpendicular to the part above the sliding surface and reach a total displacement of 35 mm, corresponding to 40% of the total displacement of the upper part. It is considered an artefact caused by dragging of this instrument by the upper part.

3.6.2.3 *Total Station Survey*

Total station surveys were carried out every field visit from 2010 to 2013 to follow a number of targets in the railroad sector, including marks on the retaining wall's H-beams. The position of the targets is indicated in Figure 3-8. As some targets are not accessible in winter, the data sets are composed of five or height measurements. The measurements are presented in Appendix F.

The surveys show a general trend of displacement towards the south with a varying E-W component. The average direction of the data set is S-E. The targets in the eastern part of the rockslide (BM2, SAA_E, and the retaining wall's H-beams) are moving more than the western targets located in the Petit-massif (C1PM, C2, Inclino, SAA_W). The total station surveys give information on the general trend of displacement and on differences between the sectors of the rockslide. However, these data are not used to compare the changes of rate and direction with time, because the surveys' precision is less than what was expected and the surveys are not frequent enough.

The errors are due to the following sources listed in order of importance: (1) surveys were carried out by four different operators that had little or no experience, (2) atmospheric conditions (snow, rain and hot air over the railroad) affecting the electronic distance measurements, and (3) the reference target is most likely not totally stable. The measurements are made in an E-W orientation; this component is thus measured by the electronic distance measurement, while the N-S component is calculated from the horizontal azimuth measurement that

has a better repeatability. For this reason, the precision of the N-S component of displacement is better than the one of the E-W component.

Displacements and displacement rates computed from total station surveys are presented in Table 3-3. The N-S displacement-times plots are showing regular displacements, while in the E-W axis the displacement-time curves are irregular. It results into a wide range of displacement directions computed from one survey to another. In Table 3-3, the average direction of the data set and the range of directions measured between two subsequent surveys are presented. Linear regression performed on the displacement-time curves of both the E-W and N-S directions are presented. The determination coefficient (R^2) is generally low for the E-W component and high for the N-S component. The average horizontal rate is given by the vector obtained from the combination of N-S and E-W displacement rates. Average horizontal displacement rates are used to trace the black vectors in Figure 3-6.

C1PM (Figure 3-8) movement has an average direction of 130° and a horizontal rate of 55 mm/yr and a vertical rate of -7 mm/yr. The target C2 (Figure 3-8) moves towards a direction of 110° to horizontal and vertical rates of 45 and -6 mm/yr respectively. C1PM and C2 are placed near the extensometer pair EX6-7. In order to compare the displacement measured between EX6-7 to the one measured with the total station, the change of distance between C1PM and C2 was computed. The result reveals good agreement between the two techniques. From total station survey, the distance between C1PM and C2 increased by 49 ± 15 mm, while the distance between EX6 and EX7 increased by 45 ± 0.13 mm. The distances were computed for the same time interval.

BM2, located at the eastern limit of the slide (Figure 3-8) has an average rate of displacement around 94 mm/yr towards 138° . This rate is similar to the highest displacement rate measured with the vertical SAA2.

HB8, the middle H-Beam of the retaining wall, moves in the horizontal plane at 99 mm/yr. For HB8, the average direction is 180° . As will be shown below (section 3.6.2.4), this value corresponds well with PTA-InSAR measurements.

The total station surveys were useful to quantify the internal deformation of the H-beam retaining wall. It was done by comparing the position of marks carved on H-beams with the position of other H-Beams. By doing so, it is possible to get rid of uncertainties related to errors 1 and 3 listed before. A total station survey of the retaining wall carried out in 1993 was used as well (Locat et Couture, 1995b). A relative downward displacement of the middle H-beam (HB8) relative to the western H-beams (HB14 and HB15) of 28 mm/yr (R^2 of 0.99) is computed. It is 13 mm/yr ($R^2 = 0.99$) relative to the eastern H-Beam (HB1). The displacement rates vary from one H-Beam to another as the retaining wall is subject to important differential displacements.

Table 3-3 Information relative to the targets surveyed with the total station.

Target	Date		Ave. dir.	Dir. range	total dis (± 15)	Ave. East rate	R ²	Ave. North rate	R ²	Ave. H. rate	Ave. V. rate	ratio V/H
	start	end	(°)	(°)	mm	mm/yr		mm/yr		mm/yr	mm/yr	%
Inclino	06/08/2010	20/05/2013	121	092-230	70	17	0.688	-17	0.833	24	-2	-8
C2	06/08/2010	20/05/2013	110	097-259	140	41	0.726	-19	0.935	45	-6	-13
C1PM	06/08/2010	20/05/2013	130	104-263	160	41	0.759	-37	0.985	55	-7	-13
SAAH_W	06/08/2010	20/05/2013	130	106-267	90	17	0.273	-21	0.976	27	-6	-22
SAAH_E	06/08/2010	20/05/2013	140	104-258	200	21	0.249	-65	0.970	69	-21	-30
BM2	06/08/2010	20/05/2013	138	128-253	274	48	0.661	-81	0.968	94	-10	-11
HB8	02/08/2011	20/05/2013	180	145-234	180	15	0.178	-98	0.990	99	-30	-30
HB1	02/08/2011	20/05/2013	185	135-257	140	7	0.030	-80	0.975	80	-14	-18
HB5	02/08/2011	20/05/2013	182	130-250	147	8	0.089	-82	0.996	83	-22	-27
HB12	02/08/2011	20/05/2013	180	130-250	148	15	0.148	-82	0.916	83	-10	-12
HB15	02/08/2011	20/05/2013	180	135-250	131	10	0.092	-74	0.99	74	-6	-8

3.6.2.4 PTA-InSAR

Permanent corner reflectors were installed in 2009 and in 2010 (Figure 3-8) to conduct Point Target Analysis technique of Interferometric Aperture Radar (PTA-InSAR) (Ferretti *et al.* 2001). Data are acquired and processed by the Canadian Centre for Mapping and Earth Observation of Natural Resources Canada (ESS-CCMEO)(Couture *et al.* 2010; Couture *et al.* 2011). These results are integrated in the displacement analysis. All the information presented in this section comes from the report presented by François Charbonneau (ESS-CCMEO) to the Laboratoire d'études sur les risques naturels (LERN).

The Gascons site is challenging for the use of satellite based displacement monitoring, because of the large forested area and the complexity of the displacements that have both vertical and horizontal components. This is why it was chosen to make InSAR on artificial targets that are the corner and wedge reflectors indicated in Figure 3-8.

In order to characterize both the horizontal and vertical components of displacement, it was decided to acquire data from different satellite geometries to be able to compute three-dimensional displacements. Thus, the analysis is based on data coming from three satellite geometries of RADARSAT-2: two incident angles in the descending mode (Spotlight 19 and 76) and one in the ascending mode (Spotlight 3).

It was possible to obtain three-dimensional displacement rates which are presented in Table 3-4, for reflectors CR3, CR8, CR11, CR12, and CR13. The precision of three-dimensional displacements is less in the N-S orientation, due to the satellite geometries that is not optimal. The displacement rates are presented in Figure 3-6.

Only the three-dimensional displacements are presented in this paper. However, the two-dimensional data were useful for the interpretation. They give the displacement in two directions: the vertical component and the horizontal displacement in the line of sight of the satellite.

Corner reflectors CR7 and CR8 are fixed on the retaining walls (Figure 3-8). CR7, CR8 and to a lesser extent CR13 have a strong downward displacement compared to other targets. The other reflectors move mostly in the horizontal plane.

Table 3-4 Average displacement rates from 2010 to 2012 obtained from the PTA-InSAR analysis that was performed by the team of the Canadian Centre for Mapping and Earth Observation (ESS-CCMEO, Natural Resources Canada) (Couture *et al.* 2010, Couture *et al.* 2011). Only markers on which a 3D analysis could be performed are presented.

	Vertical	H - Est	H - Nord	H. Rate	Ratio V/H*100	Average direction
	[mm/yr]	[mm/yr]	[mm/yr]	mm/yr	%	(°)
CR3 - DR10	-11	13	-72	73	-15	170
CR8	-18	18	-27	33	-56	147
CR11 - DR3	-3	11	-19	22	-12	151
CR12 - DR8	-20	38	-100	107	-18	159
CR13	-30	30	-107	111	-27	164

3.6.3 Horizontal SAA

Two SAA are installed horizontally to monitor the settlement of the railroad ballast. They are buried in the coarse aggregate material forming the ballast at either the south or north end of the ties. The instruments are placed inside a PVC conduit that is surrounded by a sand layer and wrapped in a geotextile. SAA1 was installed in November 2009 and is the one located in the eastern part of the rockslide, below Block-E and north of the railroad (Figure 3-8). It is 60 m long. The installation of SAA4, carried out in 2011, was motivated by two reasons: (1) to extend the horizontal SAA's coverage outside of the rockslide in order to have a stable point to measure absolute settlements and (2) to monitor a sector where a 2 m wide and 1 m deep hole formed under

the railroad due to ballast undermining into an underlying opened fissure. Pictures of this event are shown in the next chapter of this thesis (Chapter 4 Figure 4-7A). SAA4 is located south of the railroad. SAA4 extends beyond the western slide boundary and is 40 m long (Figure 3-8). Both horizontal SAAs are acquiring data every hour.

Because these instruments are installed in coarse granular material, their displacements do not reflect directly the movement of the rockslide. They can be partly “floating” over the rockslide; they are not anchored to the rock.

Figure 3-17 presents profiles of displacement over the length of the instruments. The top graphic presents monthly displacement profiles of SAA4 and 1 coupled together. The two bottom graphics show displacements of SAA1 on two specific time periods, February to May 2011 and December 2011 to February 2012. On the bottom graphics, the profiles are plotted every 5 days.

The following observations are made from the horizontal SAA:

- Settlement is greater in SAA1 than in SAA4, thereby it is greater inside Block-E.
- The settlement also increases toward the east, in the H-beam retaining wall. It corresponds with the observation made from total station surveys and PTA-InSAR analyses.
- The settlement in SAA4 is larger in the part over the fissure crossing the rails that caused the undermining observed in February 2011. This part is pointed out in Figure 3-17.
- Both SAA are subject to periods of swelling. In SAA1, period of swelling lasted from March to September 2011 and from April to September 2012.

3.6.4 Weather and Pore Water Monitoring

Nine vibrating wire piezometers (Geokon, model 4410) are installed in three boreholes at Sites 1, 2, and 3 located on Figure 3-7. Piezometric measurements are collected four times a day, since January 2010. A weather station that consists of a thermometer, a barometer, a relative humidity sensor, a wind speed sensor, and a precipitation gauge (rain and snow) is installed on the top of the “guérite” (Figure 3-7) and data are collected every half hour since November 2009.

Monthly precipitations are presented in Figure 3-18. Figure 3-19 presents the air temperature and the daily precipitations over the whole acquisition period. The snowmelt periods are indicated by shaded rectangles and are estimated from air temperature, piezometer, and field visit observations.

Piezometers P5 and P3 measurements are plotted in Figure 3-14. At Site 2 (P5), snow melt and precipitations events can create rises of up to 8 m of water level. Rises are always faster than the decrease of pressures. These variations in the pore water pressure monitored are believed to be related to water filling fractures.

3.7 Kinematic Analysis and Interpretation

3.7.1 Overall Behaviour

This section presents the characterization of the rockslide's displacement interpreted from data presented in the previous section. The average displacement rates are presented in Figure 3-6. The displacement rates in the horizontal plane are illustrated as vectors while the vertical displacement rates are represented by circles. No vertical displacement rates are computed for the crackmeters and extensometers that measure relative surface displacements. Therefore, the kinematic analysis will be mostly centered on PTA-InSAR, inclinometer, SAA, and total station data.

Horizontal displacement rates in the centre part of the slide are between 80 and 111 mm/yr (CR12, CR13, HB1, and HB8). In the Petit-massif sector, the inclinometer, SAA3, and CR11 average displacement rates are 14, 14, and 22 mm/yr respectively. In the upper part of the slide (Site 2), vertical SAA2 shows a clear sliding surface at 23 m deep (Figure 3-15A), which corresponds to the green surface in Figure 3-4A with an average displacement rates of 48 mm/yr at 12 m deep. It corresponds also to the deepest sliding surface identified at Site 1 at 43 m deep (Figure 3-12), where the average displacement rate is much lower and is 4 mm/yr. The rockslide does not move as a monolithic wedge.

The orientations of the displacement vectors presented in Figure 3-6 are ranging from 110 to 185° with an average value of 150°. The average direction of displacement is thus SE and has been computed from inclinometer, SAA, total station, and PTA-InSAR data. As the mass is sliding towards an average direction of 150° on bedding planes with dip and dip direction of 22°/193°, this would indicate that the mass is sliding on an apparent slope inclination of 17°.

The directions are more towards the east in the Petit-massif (SAA=140°, CR11=151°) and more towards the south in the centre part (HB8 = 180°, CR12= 164°, and CR12 = 159°). BM2 (Figure 3-8), which is surveyed with the total station has an average direction of 138°. However, the directions computed from total station surveys show lots of variation, as indicated by the range of measured directions in Table 3-3, thus the interpretation of the movement's direction from total station surveys must be done carefully.

The kinematic analysis shows that even though the sliding surface is assumed to be continuous and fully defined, displacement rates are faster at Site 2 than at Site 1. Moreover, the East-Centre sector is moving

faster, which is associated to two factors: (1) the East-Centre (Figure 3-4A) sliding surface is higher in the slope and thereby it is more kinematically free to move as its sliding surface daylight in the slope, and (2) the main wedge corner is constrained by the syncline (Figure 3-4A) and depends on the erosion of the slope.

The stereographic kinematic test presented in the stereonet of Figure 3-4B indicates that the wedge should be sliding towards 170° which is determined by the intersection line of the two planes forming the wedge. These different directions might be partly explained by the blocks having various shapes, resulting from the orientation of the discontinuity sets. For example, the interaction between blocks could induce the changing directions observed in SAA3 and shown in Figure 3-13.

The shapes of the blocks drawn in Figure 3-6 and the shape of Fissure G (identified in Figure 3-7) seem to indicate that the slide is rotating. This rotation could be induced by the buttress caused by the fold near the wedge lower corner and the Port-Daniel-River fault and by the wedge asymmetric shape. This rotation could explain that some displacements have a stronger eastern component.

The wedge failure mechanism which was interpreted from geometric and structural analyses is confirmed by the displacement data. The displacement analysis reveals the complex blocky geometry of the slide and that the displacement rates and directions vary over the slide area and through time. Two specific sectors are detailed hereunder: the Petit-massif and the Block-E.

3.7.2 Petit-massif

On the block representation of the slide in Figure 3-6, the size of blocks making up the Petit-massif is generally smaller than in other sectors. This can be partly due to an easier mapping of the fracture network as there is almost no vegetation and soil. Still, it is also the sign of the dislocation of the rock mass and the presence of persistent fractures.

The in-depth displacement profiles show that there are three shearing surfaces (Figure 3-12). The deepest surface measured at Site 1 is at 43 m and corresponds to the one shown in green in Figure 3-4A. Displacements measured on this level are affecting all the rock above and are in the south direction, towards 184° (Figure 3-13 $z = 37.3\text{m}$). They are not continuous in time (Figure 3-14 $z = 33\text{ m}$) and they happened in the period between October 2010 and May 2012. Displacements on the two upper sliding surfaces, located at 22 and 10 m deep, are in an average direction of 144° (Figures 3-12 and 3-13).

The displacements are smaller at a depth of 10 m and are increasing regularly going upward in the inclinometer profile of Figure 3-12. This pattern is associated with toppling of the upper part of the block on

which is installed the SAA and inclinometer. The direction of movement on the upper sliding surfaces is almost perpendicularly to the fractures delimiting this blocks, as shown in Figure 3-6.

The upper rupture surface was used to estimate the volume of the Petit-massif sector that is 13 300 m³.

Displacement rates measured with the extensometer pair EX12-13 and crackmeter F13 into the fissure forming the lateral surface are 5.6 and 9 mm/yr. Further east are the inclinometer and CR11 with displacement rates of 14 and 21.5 mm/yr. The most eastern block displacement rate is measured on the target C1PM (total station) and CR3 (PTA-InSAR) and is 59 mm/yr and 73 mm/yr, respectively. These records indicate that the displacements are slower near the lateral surface and the Port-Daniel river fault syncline and are increasing going east in the Petit-massif sector.

The slide of the block monitored by C1PM and CR3 (Figure 3-8) located SE in the Petit-massif could lead to an event similar to the 1998 one that damaged the railroad. The eastern part of the Petit-massif fell down the cliff bringing part of the railway foundation in its fall. Still today, the most precarious blocks are the one located in the eastern portion of the Petit-massif sector, as they are the ones with the highest displacement rates.

3.7.3 Block-E

The volume of Block-E, identified on Figure 3-4A, is estimated to 23 400 m³. The estimation was done by presuming a sliding surface formed by the continuity of the back scarp joining the sedimentary bed that matches the eastern limit of Block-E, as illustrated in cross-section BB' (Figure 3-3).

The height of Block-E's back scarp is increasing from west to east suggesting a higher deformation of the eastern part. This is correlated by the horizontal SAA buried in the railway ballast (Figure 3-17), where settlements (vertical displacements) increase from west to east in that sector. These differential vertical displacements are assumed to be causing the fractures that are opening on top of Block-E perpendicularly to the back wall and seen on the DEM.

The ratio of vertical over horizontal displacements measured in the Block-E sector are 55% for CR8, 27% for CR13, and 31% for HB8 (Table 3-3 and 3-4). Outside of Block-E, they are 18% for CR12, 13% for CR11 and 15% for CR3. Therefore, Block-E has higher vertical displacements (Figure 3-6) than the rest of the slide. In addition, the H-Beam retaining wall is undergoing differential movements; its middle is settling 20 mm/yr faster than the extremities.

The downward displacements measured with the total station on the eastern end of SAA1 and with PTA-InSAR on CR13 (Figure 3-8) correspond well with the downward displacement measured on the retaining walls. The displacement vectors presented in Figure 3-6A show that the retaining walls are deforming and

subject to the same displacements than the top of Block-E which supports the assumption that the sliding surface passes under the retaining walls

The proposed interpretation of Block-E's sliding surface does not explain that it moves faster in the downward direction than the rest of the slide, as it is also sliding on S0. More detailed analyses are needed to locate with certainty the sliding surface and its shape. Blasting done at the time of the construction of the railroad a hundred years ago could have increased the degree of fracturing of the rock mass, and so, it could have influenced the sliding mechanism. For example, in a closely and randomly jointed rockmass, the failure mechanism can be a rotational failure, instead of a translational failure as it is the case in regularly jointed rocks. In the case of a rotational failure, the discontinuities are only partly defining the sliding surface (Norrish and Wyllie 1996). However, as downward displacements are measured on the top of Block-E and on the retaining walls, a purely rotational slide is not possible.

As of now, the Petit-massif sector has been the one attracting most attention as it is in this sector that the only failure that damaged the railway was observed. Moreover, the large fractures that are seen from the railway are of concern. However, the faster displacements (vertical and horizontal) are measured in Block-E and its morphology shows a higher degree of deformation. Thereby it is identified as the most critical sector, albeit the Petit-massif sector is also a sensitive sector for the railway integrity. Block-E is considered critical for the integrity of the railway as its presumed sliding surface daylights in the cliff under both retaining walls. If one of the retaining walls collapses, the railway will be strongly damaged.

3.8 Time Variations and Climatic Factors

3.8.1 Climatic Effects on Displacement Rates

Displacement rates and directions are not constant through time; they vary seasonally and from year to year. The time span covered by the data sets is still short to enable a complete correlation between the patterns and the climatic factors, such as dry/wet year, early/late snow melt, etc. On the other hand, the seasonal variations and their cyclic behaviour are clear. Links with precipitation and water pressures are possible for certain sensors.

The displacement rate measured by SAA2 (Site 2, Figure 3-7) slows down when the water pressure is at its lowest at the end of winter and accelerates with the snow melt. The phenomenon was observed for both years monitored by SAA2 (2010 and 2011) and is illustrated in Figure 3-16, where the displacement rates computed as the slope of a linear regression on a 20 day period are plotted along with the adjacent piezometer data (P5), and daily and cumulated rainfalls. From these observations, it is assumed that, near SAA2, the blocks' movement are influenced by water pressures.

In fall 2010, there were important rainfalls and in December 2010, high tides joined with storm winds caused particularly important erosion in Gaspésie. The highest amount of monthly precipitation recorded with the Gascons monitoring system occurred in fall 2010 (Figure 3-18). At Site 2, the water pressures stayed high for the whole period, but did not exceed the values of other events (Figure 3-16). Actually, there is a maximum level that most of the high pressure periods reach but have never exceeded yet. An acceleration occurred at the same time in SAA2 (Figure 3-16). Thus, a constant high pressure can also induce acceleration.

This acceleration period stopped after the 2011 snow melt in May 2011. The rates stayed higher than in 2010, possibly because of numerous precipitation events in summer 2011 that prevented the water pressures to lower as much as in 2010.

Such a correlation is harder to establish with the vertical SAA3. In fact, the displacement rates show lots of variations which complicate the interpretations and link with climatic factors. These variations are partly due to the slower rates of displacement, recorded in the Petit-massif sector, that are closer to the instruments precision. The water table is below the sliding surfaces in that sector and the large opened fissures guarantee a fast and efficient drainage preventing high pressures to build up (Figure 3-3 AA'). Consequently, the Petit-massif sector is less influenced by water pressures and possibly more by the displacements of adjacent blocks. However, some acceleration events can be associated with precipitation and snow melt. For example, in 2012 acceleration occurred during snowmelt, but this was not the case in 2010, 2011, and 2013 (Figure 3-14). As for the rest of the slide, rates measured in SAA3 (Figure 3-14) are higher from fall 2010 to spring 2011, which corresponds to the fall with the highest amount of precipitation.

Also, the high tides of December 2010 might have contributed to make of fall 2010 and winter 2011 the most active period. An increase in the erosion rate should provoke displacement on the deepest sliding surface. However, no particular event was recorded by SAA3 at a depth of 33 m (shown in Figure 3-14), or deeper. This could indicate that this storm event did not erode the wedge corner.

In May 2011, a sudden rise of 1.8 m of pore water pressures was measured at Site 1 in the Petit-massif sector by the three piezometers from May 5th at 12h00 until May 6th at 18h00. Piezometer 3 records are plotted in Figure 3-14. The rise occurred during a three-day period of important rain. The precipitation gage measured 80 mm of rain. At Sites 2 and 3, water pressures were already high due to the recent snow melt and water precipitations of March and April. A small pressure rise was measured. However, at Sites 2 and 3, these high pressures were not considered abnormal. There were no signs on the displacements measured by crackmeters and SAA3 of that fast pressure rise measured at Site 1. A second rise, also of 1.8 m, was measured October 21st 2012 at midnight. The rise lasted only one measurement but was measured by the

three piezometers and also associated with strong precipitations. Again, no particular displacements were noticed on crackmeters and SAA3.

When drilling in the Petit-massif sector, a 4.7 mm opening of Fracture D identified in Figure 3-7 was measured. The displacement-time curve of EX3-4 is shown in Figure 3-9. This displacement was related to the water injected in the fractures by the drilling activity that must have increase the water pressure in the fractures. This displacement was measured with the extensometer tape after the drill got stuck at about 25 m deep. After this event, it was decided to move the drill rig and to drill Site 1 at a further distance from the cliff.

In the following days, the width of the fracture stayed constant indicating that the displacement stopped. This event is a sign that water pressures can play a role in the Petit-massif sector. However, this was no natural phenomenon and when the drilling stopped the movement stopped as well.

These events are confirming the limited, but complex, influence of pore water pressures on the Petit-massif stability, at least in the current state of the slide. Similar meteorological events do not lead to the same response, in terms of displacement. Moreover, the presence of three sliding surfaces adds complexity to the interpretation of displacements. In the future, filling of fractures or locking of fractures and drainage paths by cumulated displacements could lead to a situation where water pressures could build into a fissure and influence displacements as it is the case near SAA2.

The East-Centre lacks displacement data with high temporal resolution to correlate them with the water pressures. However, the water level is probably below its sliding surface and probably has a limited influence.

3.8.2 Seasonal Patterns

As can be seen from Figure 3-10, the crackmeters all have their own signature and repeating pattern from year to year. Crackmeters displacement curves are characterised by one faster period per year, with either slower or no movement, or a reversed trend for the rest of the year. Only F11 differs with two distinct acceleration periods. Groups of crackmeters with similar patterns (timing and length of faster periods) can be made. The first group is composed of F2, F6, and F7 (Figure 3-7). Their acceleration period is from November to March followed by either no opening or a light closing for the rest of the year. The active period of year 2011 was longer and extended until June. F5 can also be added to this group, even if in addition to this pattern there is a quick opening followed by a closing of the same magnitude in winter.

F3, F4, and F8 (Figure 3-7) are forming the second group. The activity period lasts from January to September. F3 and F4 have a faster period in February to March that F8 does not have. F9 can be added to this group, but the active period is shorter (January till March) and followed by a complete stop.

F11 cannot be paired with other sensors as it shows two different acceleration periods: fast movements from November to February, followed by a complete stop of displacements till the second fast period that extends from April to June. From June to October the displacement rate is slower than in the two fast periods but does not stop completely. F11 is the most seaward sensor and it monitors a block in the cliff (Figures 3-3 and 3-7) for which the displacements might be linked to the readjustment of the debris cone right at the bottom of the cliff. Consequently, the fall acceleration period could be a reaction to the high tides. Even if these high tides do not erode the rock cliff, they can provoke readjustment in the debris cone located at beach level, which is in line with F11 that is located higher in the slope.

Furthermore, F11 acceleration periods do not fit with the snow melt period. This can be explained by the fact that little snow accumulates in this steep sector which is facing south and the main water table is very low and certainly does not affect directly this block. However, the effect of the water pressure on blocks uphill, might affect this block indirectly by a kind of domino effect.

F3 and F5 both show an opening in January followed by a closing of the same amount in February. They are both monitoring the same block that is a large column at the top of the cliff. This pattern is not fully understood but could result from the effect of freeze-thaw and ice formation during this period.

Another way of grouping the crackmeters is by their orientation; the groups created this way are the same. F6 and F2 are separated by at least three open cracks and still show the same displacement patterns. As they are installed approximately in the same orientation, they are more sensitive to movements in a certain direction. Thus, this observation suggests that the seasonal variations observed by the crackmeters could be linked to changes in direction of movement. There are some indications that directions of movement are changing with time, for example from the total station surveys and inclinometer data. Another example is given by F7 and F8 which are monitoring the same fissure. They are installed perpendicular to each other and sharing a common anchor, but their active period is not simultaneous (Figure 3-10). This is indicating a change in the direction of displacement of the two blocks on which they are anchored.

Variations of the movement's direction are also seen in inclinometer, SAA3 (Figure 3-13), and PTA-InSAR. CR12, CR13, and total station surveys show a change in the average direction of displacements between 2011 and 2012; 2012 has a stronger southern component.

3.9 Kinematic Evolution of the Gascons Slide

3.9.1 Estimating the Age of the Rockslide

The age of the rockslide can be estimated by calculating the time needed to reach the current width of the fissures, assuming that the rate of displacement has been constant through time. To do so, a representative width is divided by the average displacement rate. First, fissure widths representative of the rockslide displacement must be estimated, because erosive phenomena, such as freeze-thaw cycles, tend to enlarge the fissure at surface. This is mostly observed in the large fissures surrounding the rockslide.

Cracks forming the surrounding of the rockslide are more appropriate for this analysis as they should have been opening only, rather than undergoing cycles of extension and compression. The age estimation is done only for fissures that are currently opening.

The results are presented in Table 3-5. The ages evaluated range from 22 to 224 years, with an average of 116 years. For the fractures that are surrounding the rockslide, which are A, F, G, and I (all identified in Figure 3-7), the ages computed are respectively 99, 144, 62, and 123 years.

The creep relationship presented in Figure 3-2 states that the first stage is characterized by a faster rate of displacement than the second stage, in which the Gascons rockslide might be. This would mean that the displacement rates were faster at the beginning of the rockslide and that this methodology is overestimating the rockslide's age. Thus, the ages computed probably represent maximum, at least for the upper part of the rockslide. In fact, instabilities of smaller volumes have probably been active for a longer time in the rock cliff and contributed to form the sharp edges at the bottom of the cliff. The average value of 116 years corresponds with the age estimated from aerial photographs and discussions with locals which is of around a hundred years.

Table 3-5 Computed times to close fissures assuming that the displacement rates are constant through time. The underlined instrument names indicate the ones measuring cracks at the surrounding of the rockslide.

Instruments	Equivalent yearly rate mm/yr	Width of fracture Mm	Time required to close the fracture yr
EX1-2	3.9	100	26
<u>EX12-13</u>	5.6	550	99
EX15-16	32.2	1500	47
EX17-18	4.5	1000	224
EX19-20	6.8	1100	161
EX23-24	6.2	1000	162
<u>EX25-26</u>	12.2	1500	123
<u>EX29-30</u>	4.2	600	144
EX34-35	9.7	2000	206
EX36-37	7.8	1000	128
F2	2.7	143	77
F5	1.9	107	155
F6	3.2	146	93
F7	3.0	337	66
F11	20.6	94	22
<u>F13</u>	4.1	293	134

3.9.2 Kinematic Behaviour Prior to Rapid Failure: the 1998 Event

The monitoring of the Gascons rockslide shows no sign of a general acceleration of displacements. Apart from the cyclic patterns of acceleration and deceleration, the average yearly displacement rates appear stable through the two to three years of monitoring. The displacement analysis presented here thus places the Gascons rockslide into the secondary creep phase, which is characterized by a constant deformation rate.

However, the 1998 collapse event can be used to study the behaviour prior to rapid failure of blocks forming the Gascons rockslide. Measurements taken in the year 1993-1994 on the fracture that delineated the 1998 sector are plotted in blue in Figure 3-9. The average displacement rate measured four years prior to the failure was 110 mm/yr. Displacement measured with the current monitoring system are also presented on the graphic. To enable plotting 1994 and 2009 measurements on the same time axis, the time axis represents days after the first acquisition in Figure 3-9. The current displacement rates are slower than the one measured in 1994, except for the absolute displacement measured in the East-Centre and Block-E sectors. Displacement rates measured from SAA2 (Site 2, Figure 3-7) are almost as rapid.

The final acceleration occurred on July 23rd, 1998. It is possible to stipulate on how the displacement rates evolved between the last measurement taken in 1994 and July 23rd, 1998 as shown in Figure 3-20. First, the displacement-time curve is extrapolated assuming a constant displacement rate (dashed blue line). In that

case, a displacement of 517 mm is reached prior to failure. Secondly, accelerating displacement curves such as the one predicted by the creep model (Figure 3-2) are assumed. The moment of the onset of the acceleration is unknown, thus different curves representing accelerating displacements are drawn in Figure 3-20. When assuming acceleration prior to failure, the total displacement reached at failure increases compared to the constant rate case. Such an analysis provides a way to evaluate displacement rates threshold values.

3.9.3 Evolution of the Rockslide

Although this will be discussed in the next chapter, it is considered that the rockslide will probably develop into a series of small sectors accelerating and sliding down the cliff to the beach. The acceleration of the whole rockslide in a catastrophic manner is considered very unlikely, due to the structural constraints in the lower wedge corner. Moreover, the cumulated displacement over the sliding surface indicates that the material properties have already degraded to or near to their residual state. Consequently, an acceleration of the mass would need a destabilizing factor, such as fast erosion or maybe an important amount of input water that would increase the pressures in the fractures. Even under such conditions, it is more likely that this will lead to the fast sliding of only part of the rockslide. Fast erosion is unlikely in the actual setting (rock cliff, beach, presence of ice in winter).

The evolution of the rockslide will probably imply the failure of Block-E that could evolve into a fast movement. The deformation of Block-E could also cause small collapses in the slope above the railroad. The volume could be enough to cover the rails and be a threat for the train, but such a situation is usually taken care by normal railroad maintenance. An event similar to the failure of a block in the Petit-massif in 1998 is likely to occur.

3.10 Discussion

3.10.1 Comparisons to Cases Similar to the Gascons Slide

As it has been demonstrated in this paper, even though the rockslide is of modest size its complexity appears to challenge the ones of bigger slides, with intermediate sliding surfaces and different kinematic sectors. Cyclic patterns observed in other extremely slow to slow rockslides are also observed at Gascons.

However, even though cyclic variations are recognized, establishing a link with external factors is not always obvious due to the complex behaviour of the rockslide. Similar observations are found in cases reported in the literature. The role of water appears to be important in most of the rockslide cases. It can be attributed to snow melting, precipitation, water table variation, and surface water runoff flowing through tension cracks. Even in rockslides where the water table is below the sliding surface as it is the case in Gascons, the water does influence the displacements. It is the case in the Mannen rockslide, in Norway, where the displacement rates

increases are related to the effect of water seeping into fractures and reducing the shear strength of the rupture surface (Blikra and Kristensen 2013).

At Gascons, the role of water is changing depending on the sectors of the rockslides, as this was observed in the Ruinon rockslide (Agliardi *et al.* 2013). Links with the groundwater level and snow melting were established at Site 2 in the upper part of the slide (Figure 3-8). At Site 1, some increases in displacement rates could be link with important precipitation events and snow melt, but similar water pressure variations lead to different behaviours. The movement provoked by drilling near the Petit-massif in 2009 shows that runoff water infiltrating in tension cracks can lead to short duration accelerations.

Concerning the study of the seasonal patterns from crackmeter records, the links with external factors are hard to establish as three different patterns are recognized in the 13 crackmeters. Because they do not have all the same patterns, a single destabilizing agent, such as snow melt, is not enough to explain the complexity. These three different seasonal patterns can be associated to patterns observed in other rockslides. For example, the pattern observed in Nordnes, Randa, and Checkerboard (Nordvik *et al.* 2010; Willenberg *et al.* 2008a; Watson *et al.* 2004) rockslides which is characterized by acceleration in the cold season is observed on crackmeters F6 and F2. The displacement rates increase when the temperature drops below zero in fall and decrease after snow melt in spring. This pattern is explained in Nordnes rockslide (Nordvik *et al.* 2010), by the presence of permafrost, which is obviously not the case at Gascons. A similar cyclic behaviour observed at Randa is related to the temperature changes (Gischig *et al.* 2010). This could explain partly the displacement observed at Gascons.

A second group, F3, F4, F8, and F9, acceleration periods starts in winter and last until the end of spring. It is unclear if snowmelt or temperature has a link with this behaviour. The last pattern, the one of F11, has two periods of accelerations: the first corresponds with the snow melt and the second with the increase precipitation and high tides occurring in late fall.

Crackmeter records in Gascons are showing daily fluctuations and also fluctuations over a week or two week periods (Figure 3-10). These fluctuations that are affecting the records corrected for temperature using the manufacturer equation are linked with temperature effects on the overall crackmeter system, including the rock and anchors.

Temperature effects on vibrating wire crackmeter records are also noted by Norvik *et al.* (2010) and Willenberg *et al.* (2008a). Our observations tend to corroborate with their findings, but for us the temperature impact is observed on shorter periods (day, week), while their observations are over a year period and reflects seasonal temperature changes.

The author suggests that the seasonal patterns observed in the crackmeters at Gascons might reflect changes in the direction of movement of the blocks forming the Petit-massif. This hypothesis is linked with the fact that crackmeters measuring displacements in the same orientations have similar cyclic variations. Why there is a cyclic variation in the displacement directions is not clear yet. Inclinator, PTA-InSAR, and SAA3 all show that the direction is varying in time, but no repeating patterns were observed. However, over a longer observation period, if the cyclic changes of direction exist, they should be identified with the instrumentation in place. Another reason that could explain that the cyclic changes in direction are not observed with SAA3 and PTA-InSAR is that the displacement variations are too small to be measured by these instruments. Finally, it could also indicate that the seasonal variations observed by the crackmeters are not due to cyclic direction changes. As of now, the variations in the direction of displacement are related to the interactions between blocks.

As in other cases, the seasonal variations observed in the Gascons rockslide appear to be the results of complex interactions of ground water level, precipitations, thermo-elastic strains and geological and geometric structures. The displacement analysis presented in this chapter uses two to three years of records thereby they might not reflect the long term displacement rates of the rockslide that has been active for about a hundred years.

3.10.2 Evolution of the Rockslide

In the case of relatively small structurally-controlled failures, the onset of acceleration might be caused by the effect of cumulated displacements on the geometry of the problem, rather than by reducing the shearing strength parameters of the rock. If we take, for example, a rigid block that is slowly sliding down a finite sliding plane, it will eventually reach the end of the sliding plane and simply topples or fall down the slope. This situation would imply a fast, almost instantaneous acceleration. This model is very simple, but might better represent the situation of the well-defined blocks at the top of the cliff in the Petit-massif, than the creep model presented in Figure 3-2. The possibility of such behaviour needs to be considered in the development of threshold values to predict the onset of a rapid collapse.

3.10.3 Lessons Learned

As the rockslide moves slowly, it took about a year before the data became meaningful. All the noise sources are significant compared to the signal coming from the displacements. This is particularly true for the surface instruments, such as the crackmeters, that are subjected to temperature variation. On a short period, the daily variations are completely hiding the general displacement trend of the crackmeters. The study of a very slow slide needs a certain observation time before the displacement patterns can be confirmed.

It is very probable that the next years will reveal new information about the rockslide as the data sets will span over a longer time period and will be more revealing of the overall behaviour of the rockslide.

Having a lot of data did not make the task of interpretation easier, as more data means that more complexity must be accounted for. Sufficient temporal and spatial resolutions are needed to conduct a proper kinematic analysis. In the Gascons rockslide monitoring system, this was achieved by coupling different kind of instrumentation. A good spatial coverage was essential to recognize the existence of faster displacement rates in the East-Centre and Block-E. A good temporal resolution made it possible to characterize the ground water level variations and the cyclic pattern of displacements.

At Gascons, the direction of displacement turned out to be the most difficult parameter to measure. For example, 3D displacements could only be computed for some targets with the PTA-InSAR method. On the other targets, only the displacements in the line of sight and in the vertical axis are known. Moreover, as a consequence of the satellite and site geometries, the NS component is less precise. Another issue presented in this paper is getting the real direction measured by the two vertical SAA. A third type of instruments providing direction of displacement is the total station surveys, but unfortunately inexperienced users increased the measurement errors. Consequently, the direction of displacement is the parameter with the most uncertainties.

Longer data sets might help to resolve the direction of displacement that appears to undergo variations. The possibility for rotation of sliding blocks around a vertical axis is discussed in Hungr and Amann (2011). They derived a method to consider this mechanism in limit equilibrium analysis. The geometry of the Gascons rockslide corresponds to the one described by Hungr and Amann (2011) as being prone to rotation: an asymmetric wedge, often due to structural controls, sliding on a weak surface and separated from the stable ground by an approximately vertical surface striking down-dip and referred as a constraint surface .

In fact, the hypothesis of a clockwise rotational component of displacement at Gascons was posed early in the analysis to explain the shapes of the fissures surrounding the slide (Lord 2011; Lord *et al.* 2010). Displacement data showed that the directions of displacement are sometime SE rather than SSE which is the direction from the line of intersection of the discontinuities forming the wedge. The rotation would be caused partly by the fault and fold having a buttressing effect.

The redundancy in instruments proved to be very useful. For example, the direction of SAA3 could be corrected and the total station data validated by the PTA-InSAR and with some pair of extensometers. Thus, the redundancy provided an improved confidence in data with higher uncertainties.

3.11 Conclusions and Recommendations

3.11.1 Summary

The surface and sub-surface displacements monitored over a three year period were examined to describe the overall kinematic behaviour of the Gascons rockslide, its seasonal patterns and failure mechanism. The analysis and interpretation of displacement data confirmed the interpretation of structural data that the kinematics of the overall slide is that of a wedge failure more or less in a southern direction. The size of the Gascons slide likely provided an opportunity to recognize the role of inter-block movements on the behaviour of fissures and local displacement trends.

The East-Centre's horizontal displacements are between 82 and 111 mm/yr. In the Petit-massif sector, the displacement rates are increasing from west to east, from 5.6 and 73 mm/yr. In fact, geometric analysis shows that two factors are contributing to increase the stability of the wedge corner: (1) the toe of the slide is at the beach level and erosion is needed to allow displacements and (2) the syncline formed next to the Port-Daniel-river fault is lowering the dip of the sliding surface. To accommodate more movements, the mass is sliding on three levels of sliding surface in the Petit-massif sector. Displacement over the deepest failure surface is towards the south, while the direction is towards an average of 144° in the upper part of the rock mass.

Block-E was identified as being the most critical for the railway stability. In this sector, the horizontal displacement rates are of 111 mm/yr and the vertical component of the displacement is more important than elsewhere in the slide.

As for other cases in the literature, movements of parts of the Gascons slide are influenced by precipitation and snow melt. Water pressures are acting on the stability of the rockslide in the upper part, near Site 2. Such a correlation does not apply to the Petit-massif sector, where the water level is below the sliding surface and the mass is very well drained due to its proximity with the sea and the presence of opened fractures. However, cyclic patterns in displacement rates are observed in the Petit-massif crackmeters records.

The Gascons slide activity would put it in the secondary creep phase, *i.e.* nearly constant velocity. Based on displacement data, the age of the Gascons slide would be of around 100 years but there is not enough data to correlate it to the construction of the railroad. The railroad construction does not easily explain how to generate a deep rupture surface at 40 m below the railroad.

The use of PTA-InSAR proved essential in providing information on 3D displacement rates.

The Gascons project provided the first opportunity to use SAA in a rockslide and the results proved that this technique is very useful for providing vertical and horizontal displacements. The experience gained in this project has already been used by the manufacturer to improve its technology.

This study helps to understand the evolution of the rockslide and the possible mechanisms which can lead, or not, to an accelerating phase of movements. It also provides a unique data set.

3.11.2 Recommendations

The analysis revealed that Block-E and East-Centre have faster rate of displacements than the rest of the slide. As no boreholes were drilled in East-Centre, the interpretation of the sliding surface is based on morphological evidence. Instruments in borehole such as a vertical SAA would give more information about the sliding surface and the displacement rates. At the moment, the East-Centre is monitored with extensometers and PTA-InSAR, both having low acquisition frequencies. A vertical SAA in Block-E would be useful to improve its characterization and to increase the railroad safety as this block is considered critical. However, drilling on Block-E will be very challenging, maybe not feasible. If only one vertical SAA is to be installed, we suggest installing it in the East-Centre. However, other technology, such as GPS might be adequate to monitor the displacement of Block-E.

The PTA-InSAR displacement analysis gives useful information about the rockslide. It is recommended to continue the analysis and integrate it to the monitoring system and maybe eventually to a warning system. An advantage of this method is that there is almost no maintenance required. However, before it can be used in a warning system, the data processing must be automated in order to generate results faster.

The manual reading of instruments represents an important part of the information acquired on the rockslide, such as the extensometers and the total station. These measurements should be continued on a regular basis as they give information on parts of the rockslide where there is little or no other monitoring, such as in the upper part of the rockslide and the retaining walls.

A number of interrogations remain on the rockslide and numerical modelling might be a way to find some solution to them. These questions are:

- Why are the directions of displacement changing through time?
- How will evolve the rockslide and which sector is the most critical for the landslide evolution?
- How does the water influence the displacement and could it alone generate a quick acceleration?
- Did the construction of the railroad contributed to the destabilization of the rockslide?

Some basic numerical modelling was carried out with Itasca 3DEC software and is presented in Appendix E. However, the above questions remain unanswered, but the work allowed studying the role of the erosion on the rockslide and that of the fault on locally modifying the dip of the sliding surface

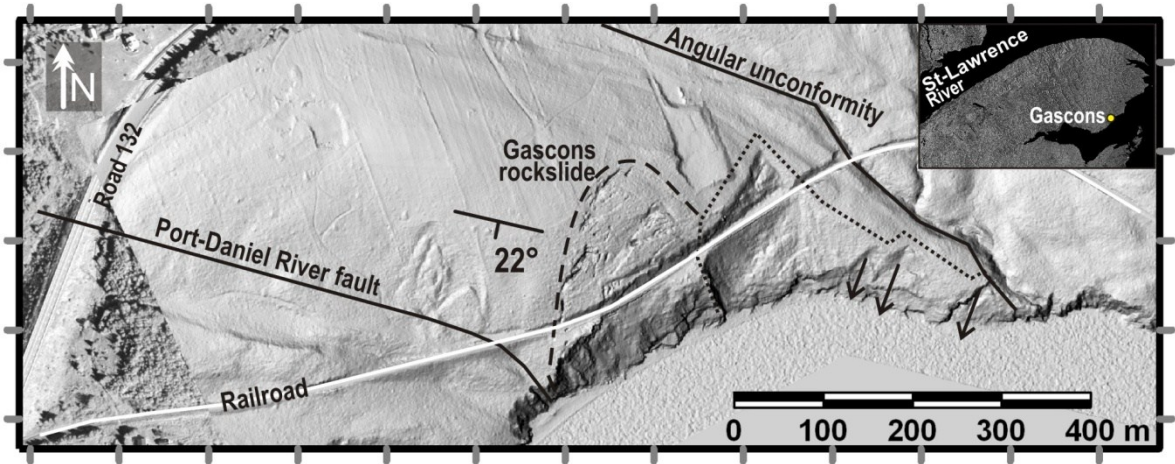
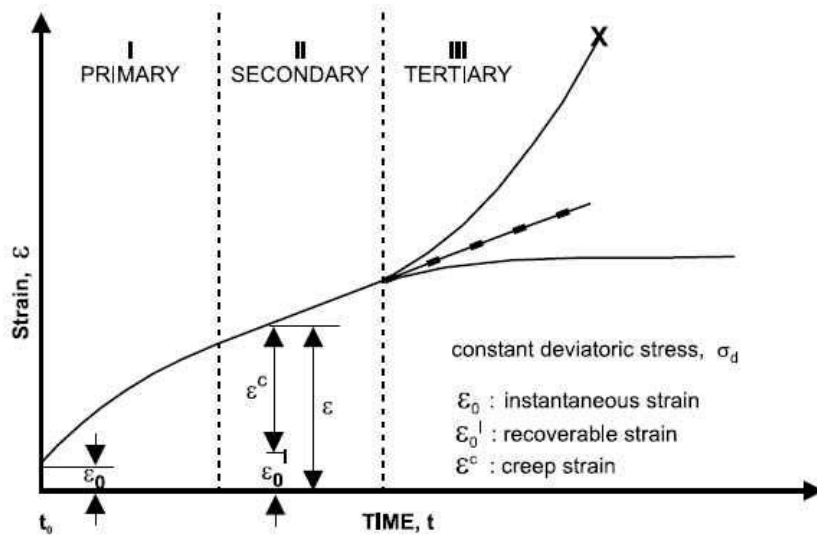


Figure 3-1 The location of the Gascons rockslide is indicated in the right corner insert (© Natural Resources Canada. All rights reserved.) The rockslide (dashed lines), the railroad (white line) and major geological features (black lines) are marked on the elevation model hill shade. Arrows indicate planar slides on the Pointe-au-Maquereau. The ancient wedge slide is surrounded by a dotted line.



3-2 Idealized creep behaviour where the three phases are identified (taken from Crosta and Agliardi, 2003).

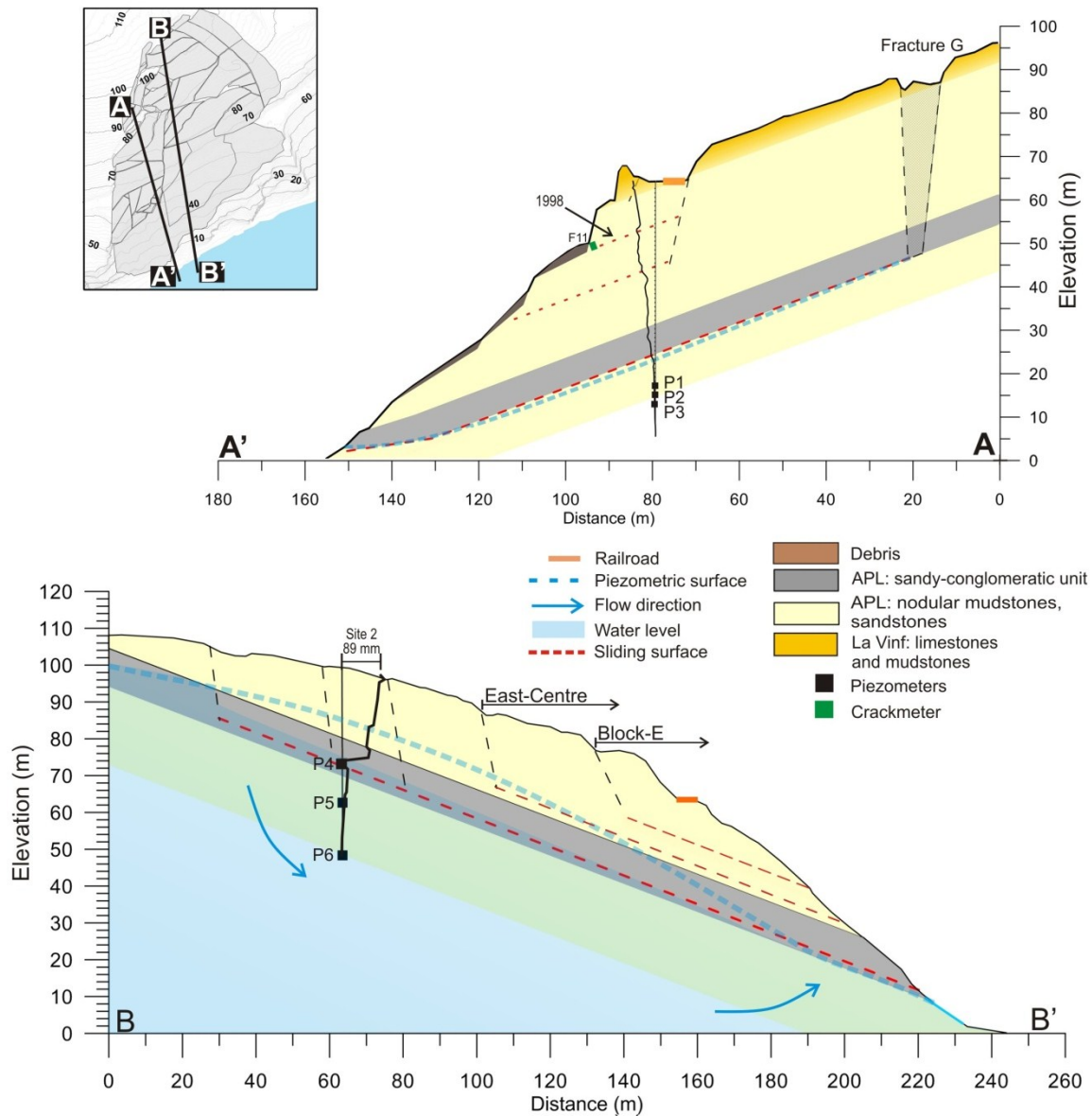


Figure 3-3 **A-A'**: Cross-section through the Petit-massif sector with the inclinometer displacement profile, location of crackmeter F11, and piezometers at Site 1. **B-B'**: Cross-section passing through Site 2, East-Centre and Block-E. The dashed blue line represents schematically the maximum water level measured by P5 and the blue polygon the lower water level measured by piezometers at Site 2.

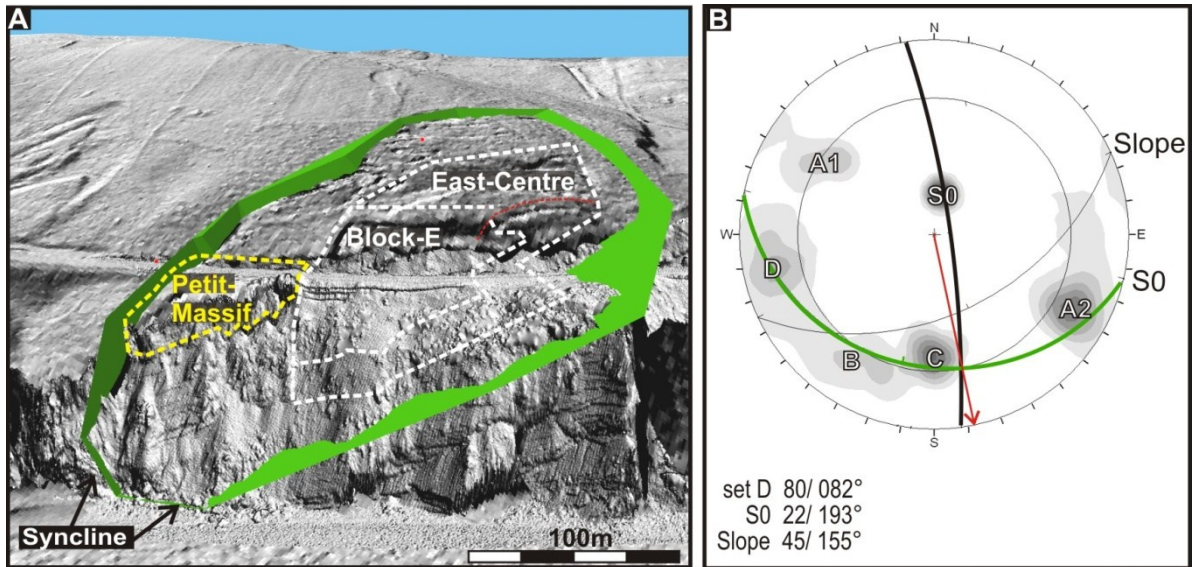


Figure 3-4 A) Oblique view of the elevation model and in green the sliding surface of the rockslide. Key sectors are identified: Petit-massif, Block-E and East-Centre B) Stereographic representation of the discontinuity sets. The planes forming the wedge sliding surface are indicated in bold. The red arrow represents the intersection line of the discontinuity pair forming the wedge.



Figure 3-5 View towards the east showing deformation of the railroad with a clear departure from a straight line at the eastern limit of the rockslide. The horizontal displacement from the initial alignment is estimated to be about 1 m from the observation of aerial photographs and DEM.

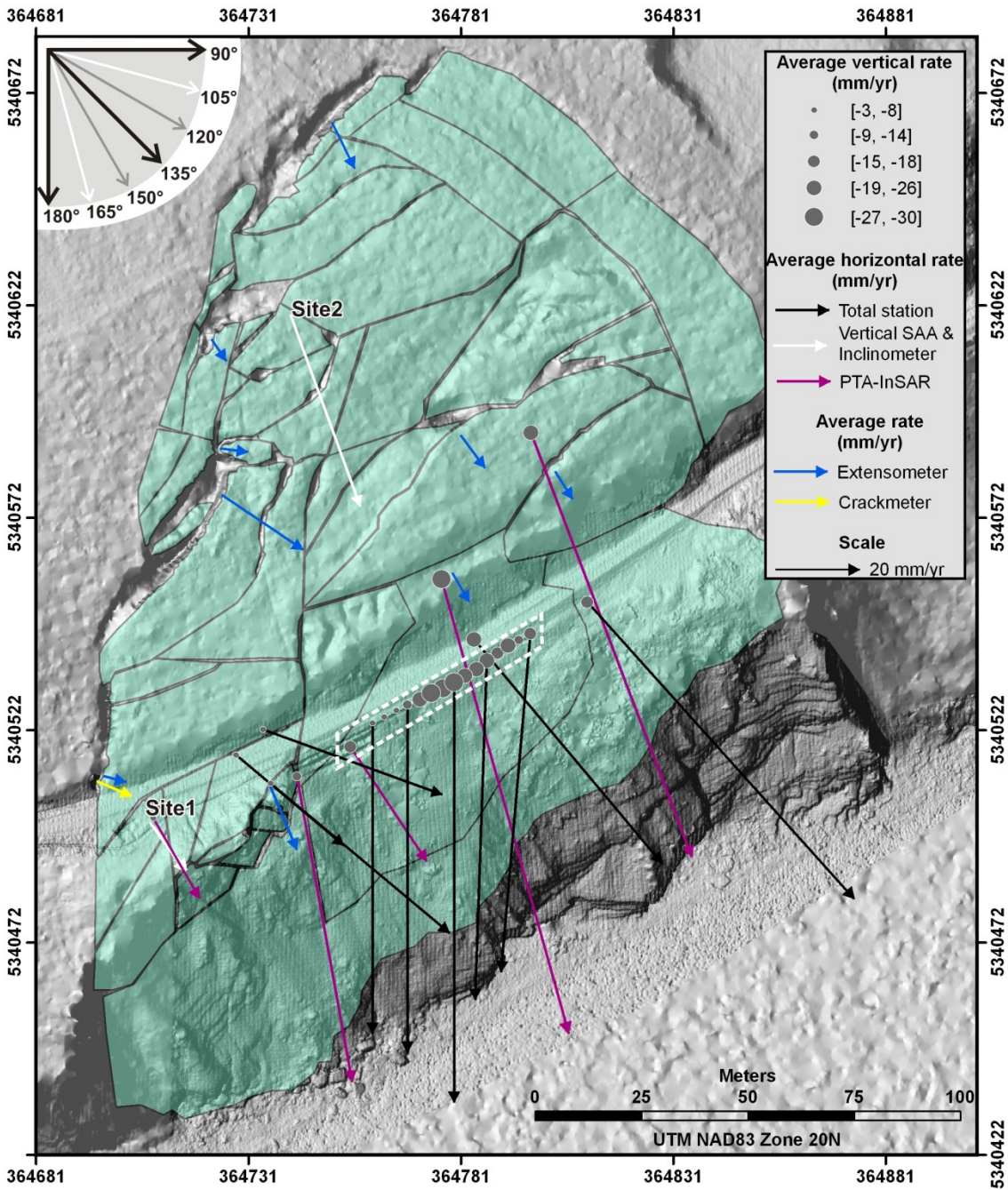


Figure 3-6 Horizontal displacement rates are represented by vectors and vertical displacement rates by circles. The negative values are for downward displacements. The points inside the white dashed rectangle are located on the retaining walls, thus they are measuring displacement caused by the slide and also linked to the retaining walls deformation. Only the ones useful for this paper are presented. Time spans of the data set on which the displacement rates are computed vary between instruments, refer to the different tables of this chapter for more information. The block representation of the slide is presented on top of the hill shade of the elevation model.

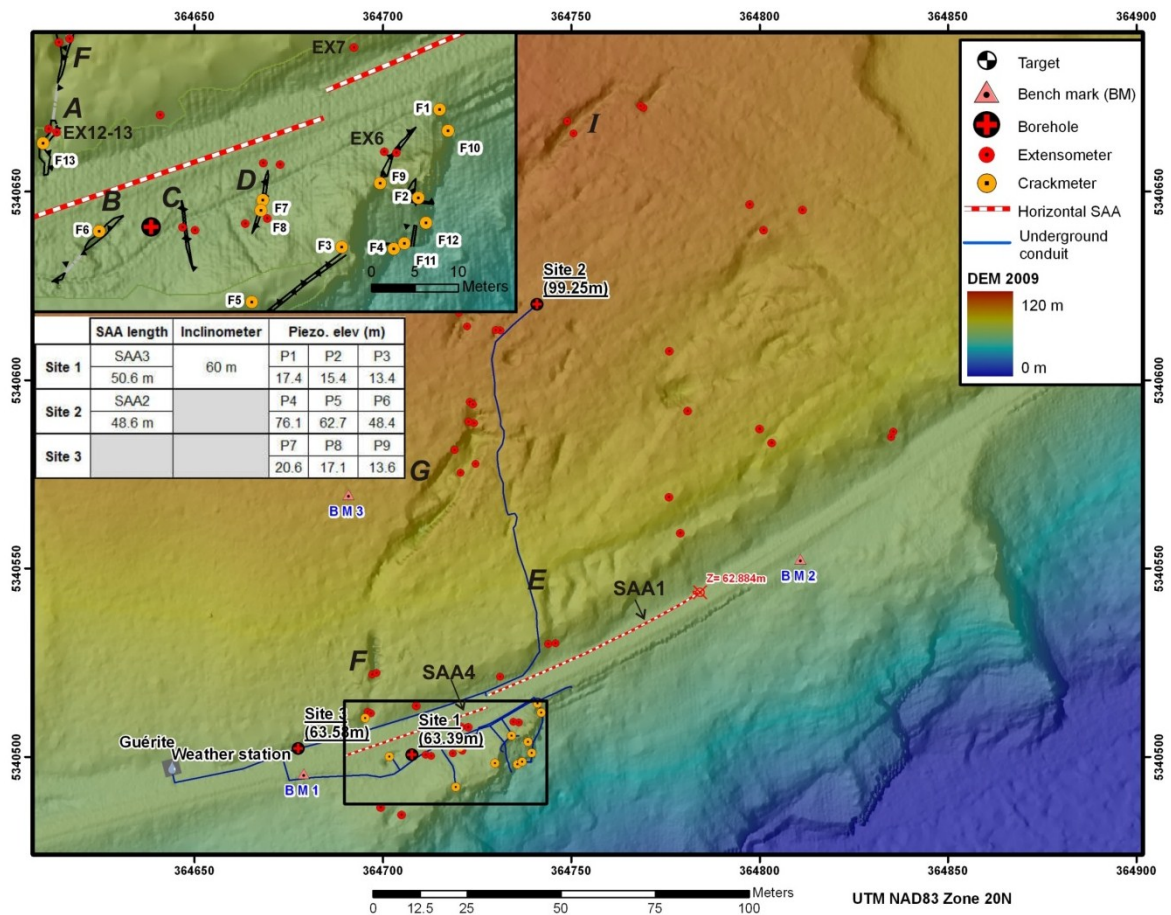


Figure 3-7 Monitoring system of the Gascons rockslide shown on DEM. Fissures A to G are indicated. Insert: Details of the Petit-massif sector, where the 13 crackmeters and Site 1 are. The sensors installed in boreholes are detailed in the table.

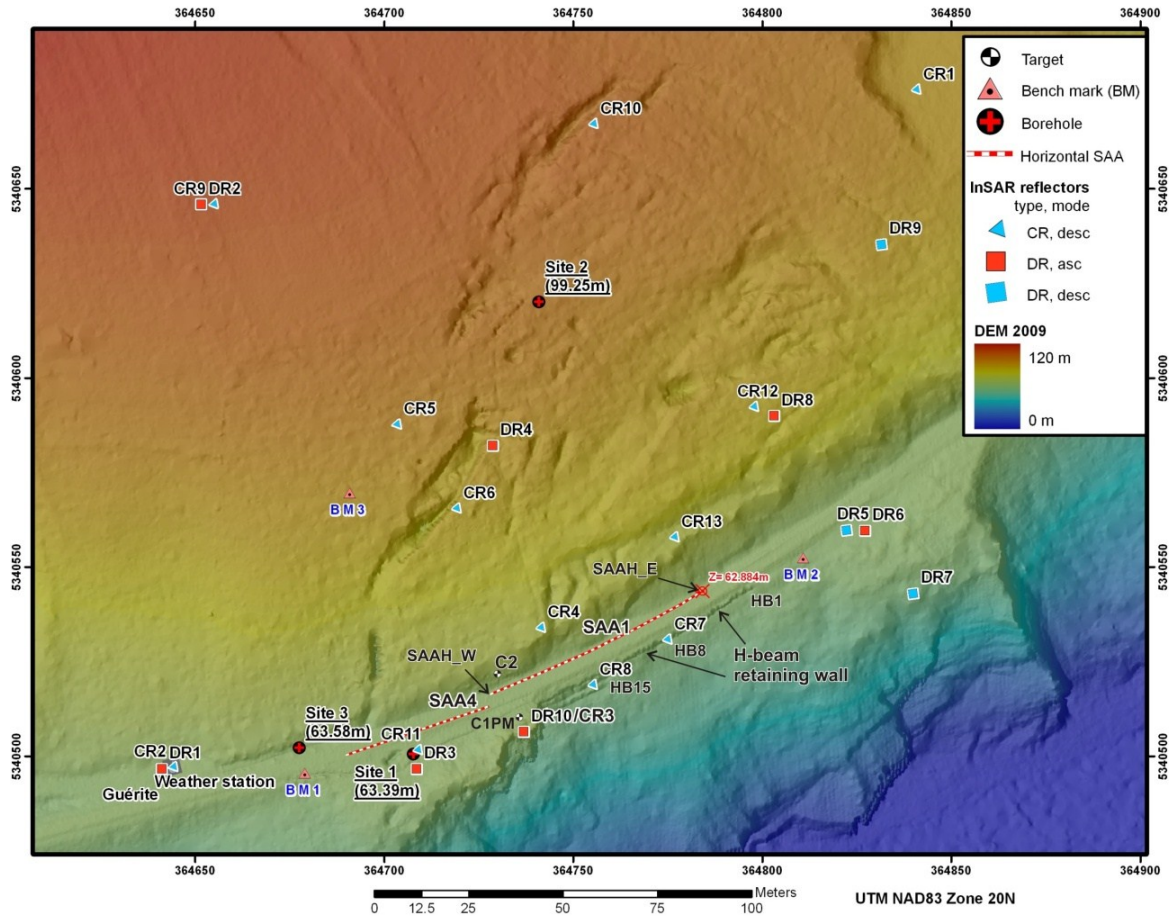


Figure 3-8 Location of the total station targets and of the permanent reflectors for PTA-InSAR analyses.

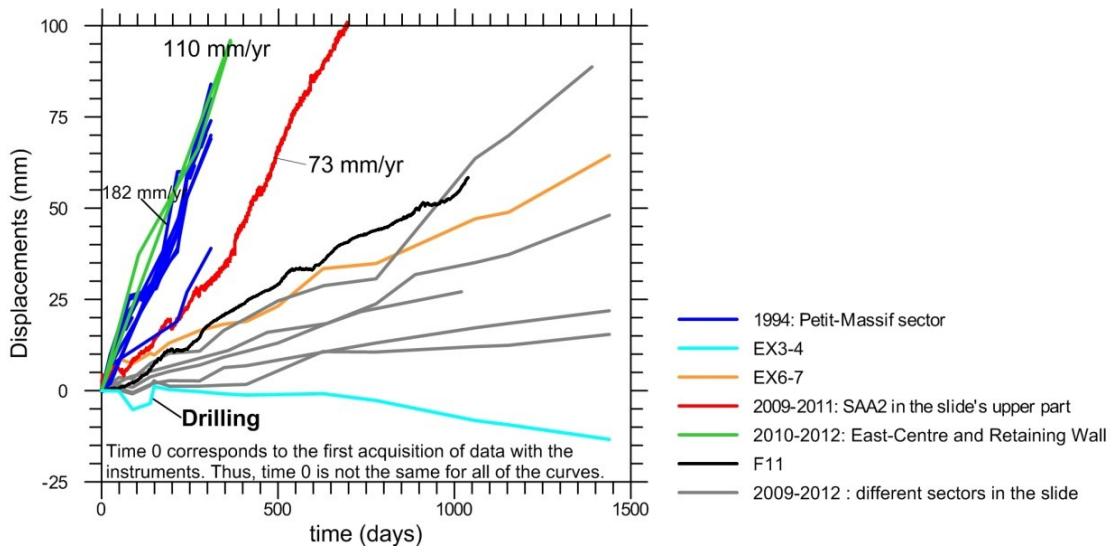


Figure 3-9 Displacement-time curves of different instruments. The time is relative to the beginning of the measurement for each station. This allow to plot on the same graphic the 1993-94 data with more recent ones.

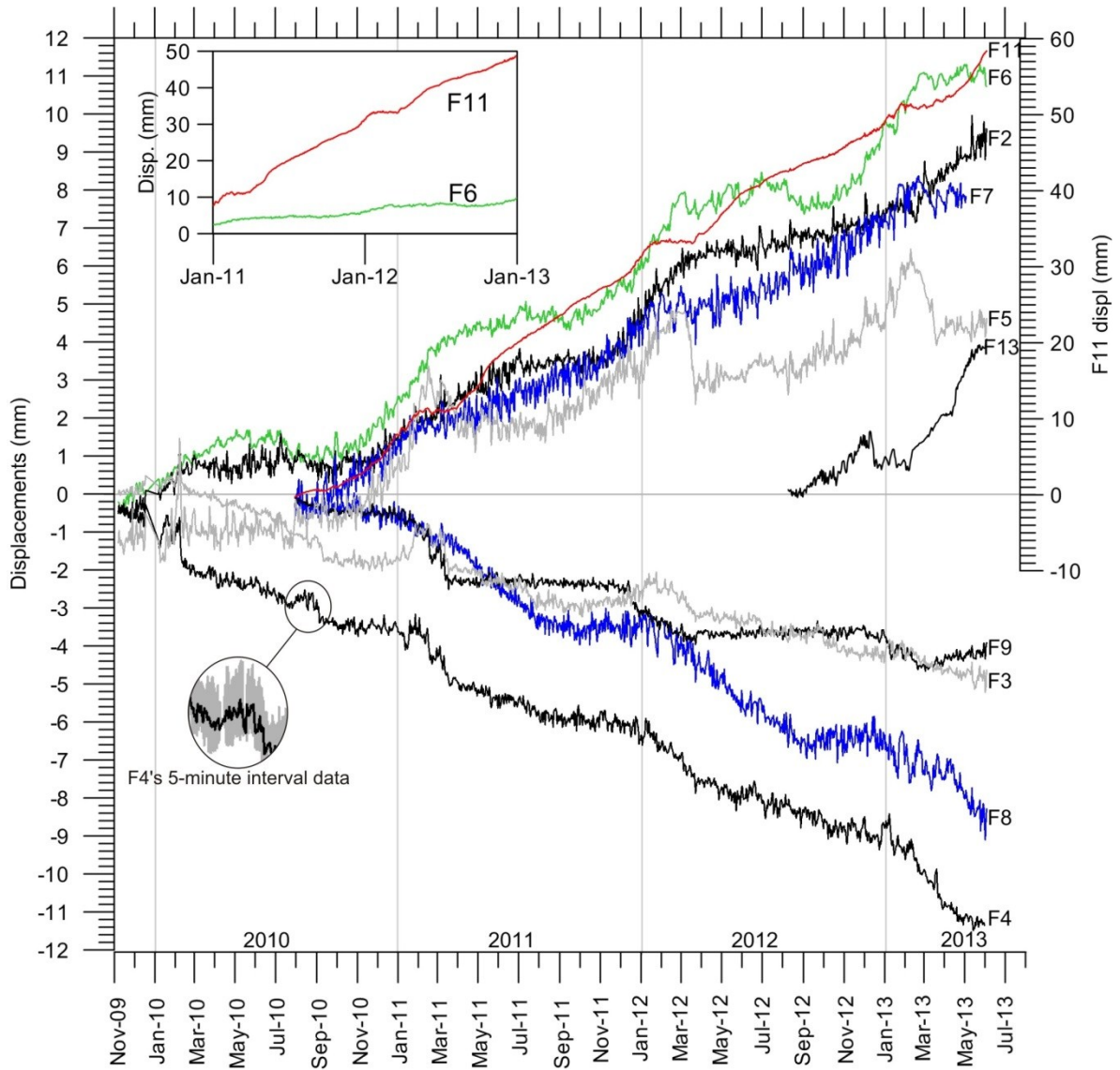


Figure 3-10 Crackmeters displacement curves. F11 curve uses the y-axis to the right, the other are plot using the left y-axis. The inset in the left top corner traces F11 and F6 using the same y-axis to show how displacements of F11 are more important than other crackmeters.

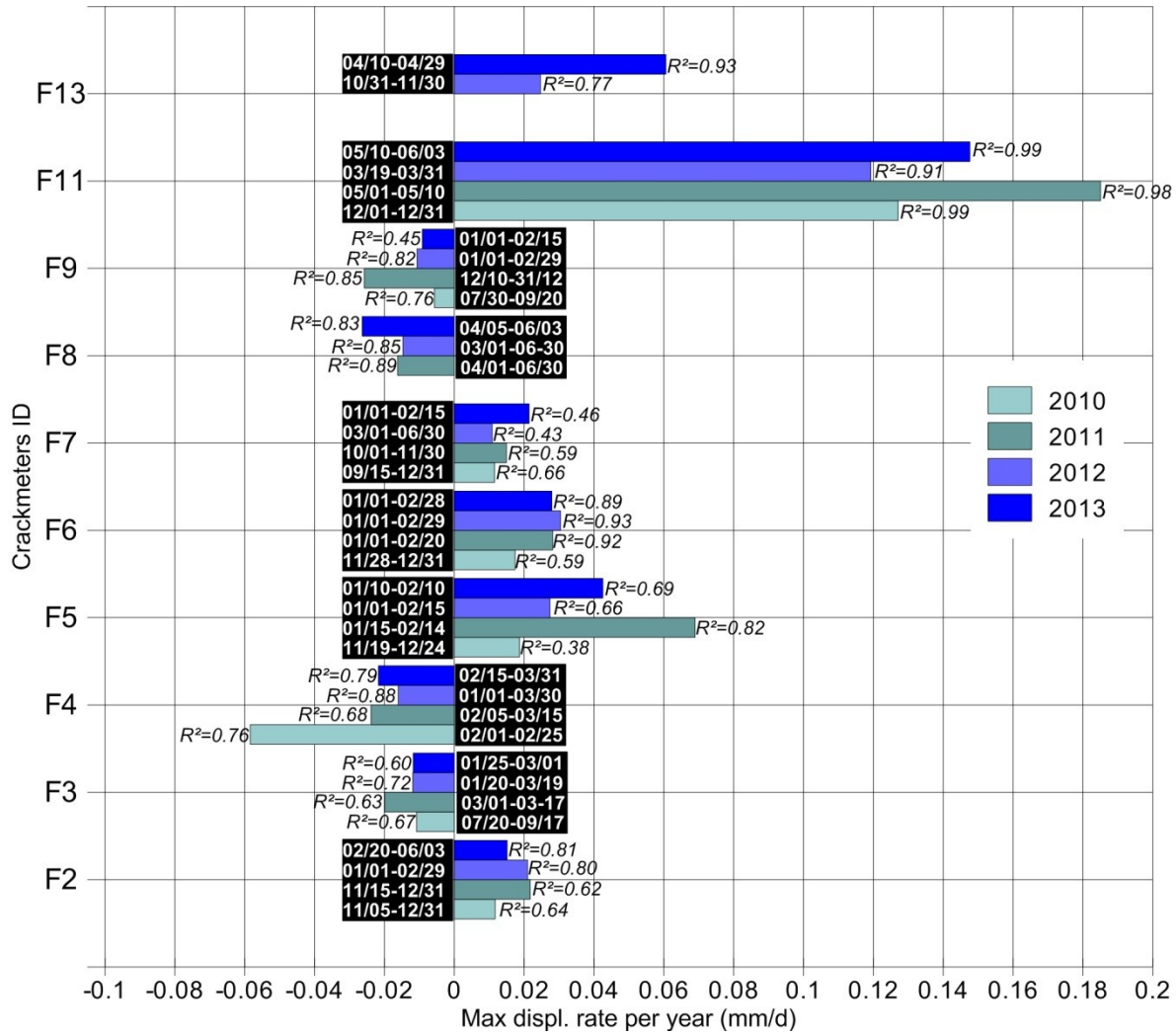


Figure 3-11 Maximum displacement rates measured on a period longer than 10 days for the crackmeters installed on pre-existing fractures. The rates are calculated by a linear regression. The coefficient of determination (R²) and the time period on which they are calculated are indicated.

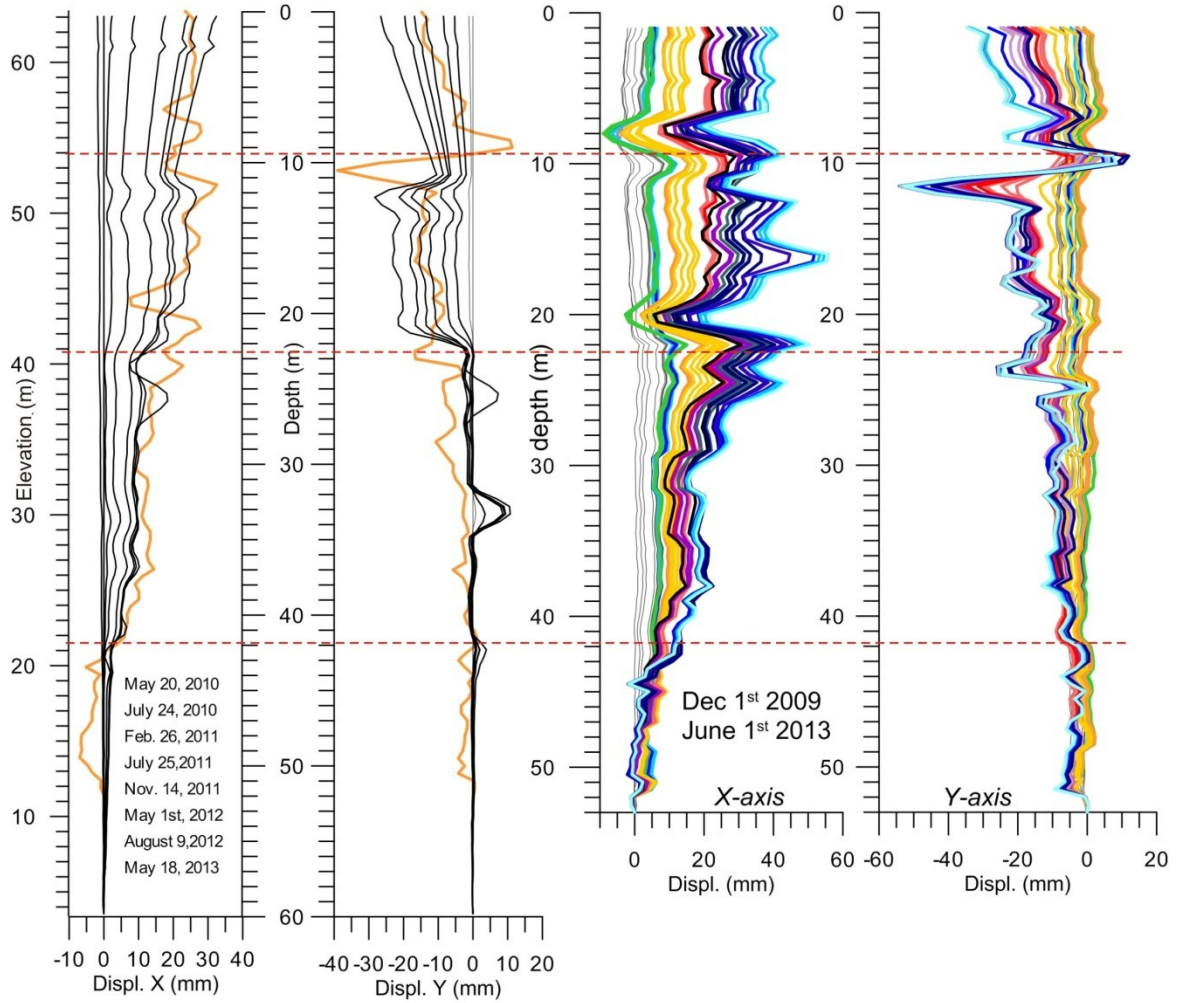


Figure 3-12 Site 1 in depth displacements profiles. Left: Inclinometer data in black and one SAA3 profile in orange. The x-axis is towards 183°, the y-axis towards 093°. Right: SAA3 profiles starting in December 2009. The SAA3 data are rotated to fit with the inclinometer's axis orientation. The ground surface is 63 m above sea level.

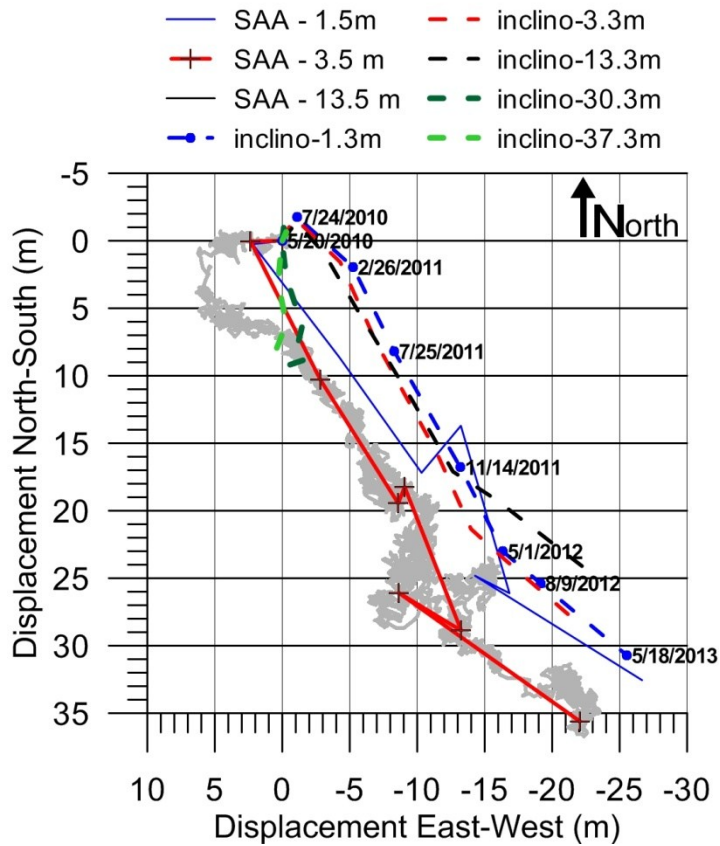
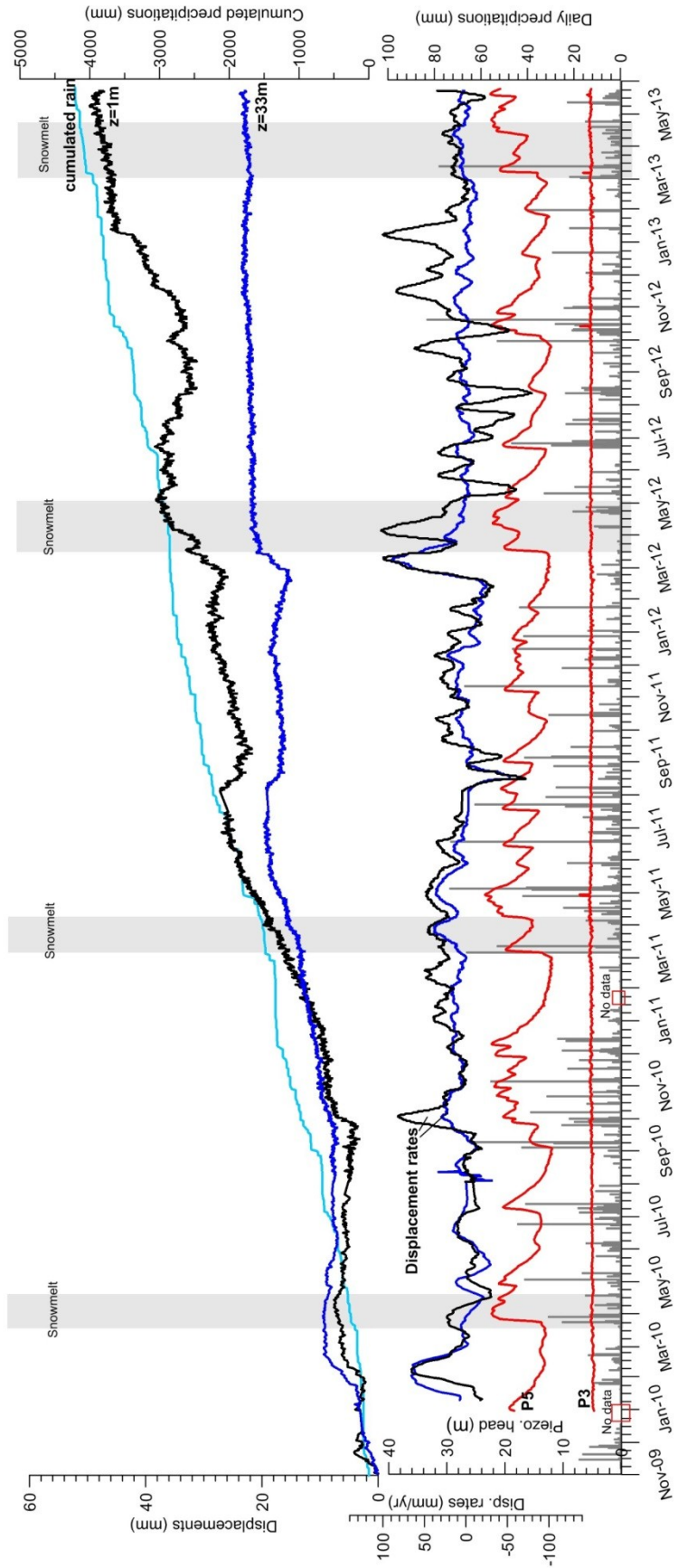


Figure 3-13 X and Y components of displacements of inclinometer (dashed lines) and SAA3 (hard lines). SAA3 curves are created using only the records that were taken simultaneously to the inclinometer surveys, in order to compare both instruments. An example of SAA3 records taken every 6 hour is presented in grey ($z=3.5$ m).

Figure 3-14 (on the next page) Vertical SAA3 displacement-time curves at depths of $z=1$ m and $z=33$ m. Their displacement rates computed as linear regressions over a period of 20 days are presented (black curve for $z=1$ m and blue for $z=33$ m). Cumulated and daily rainfalls are presented. Piezometer head measured by P5 (Site 2) and P3 (Site 1) are also plotted



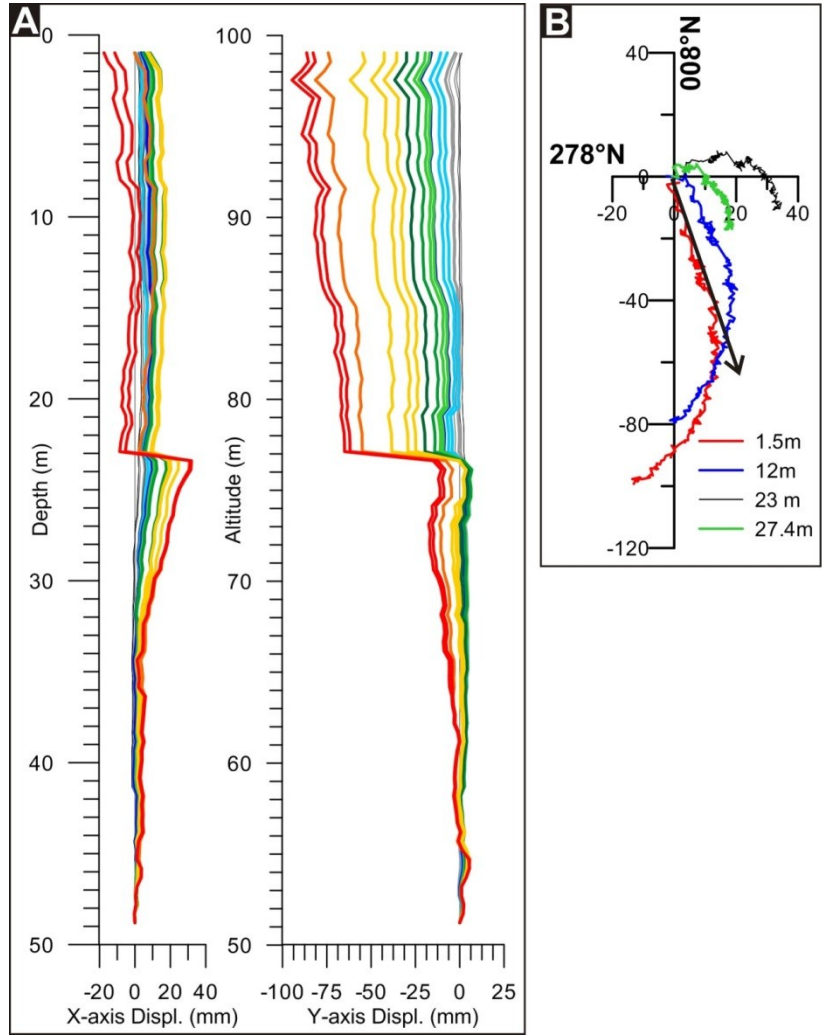


Figure 3-15 A) Displacement profiles of SAA2, located at Site 2 (Figure 3-7) between November 2009 and October 2011. B) X and Y displacement components of SAA2, showing an apparent rotation of the displacement direction.

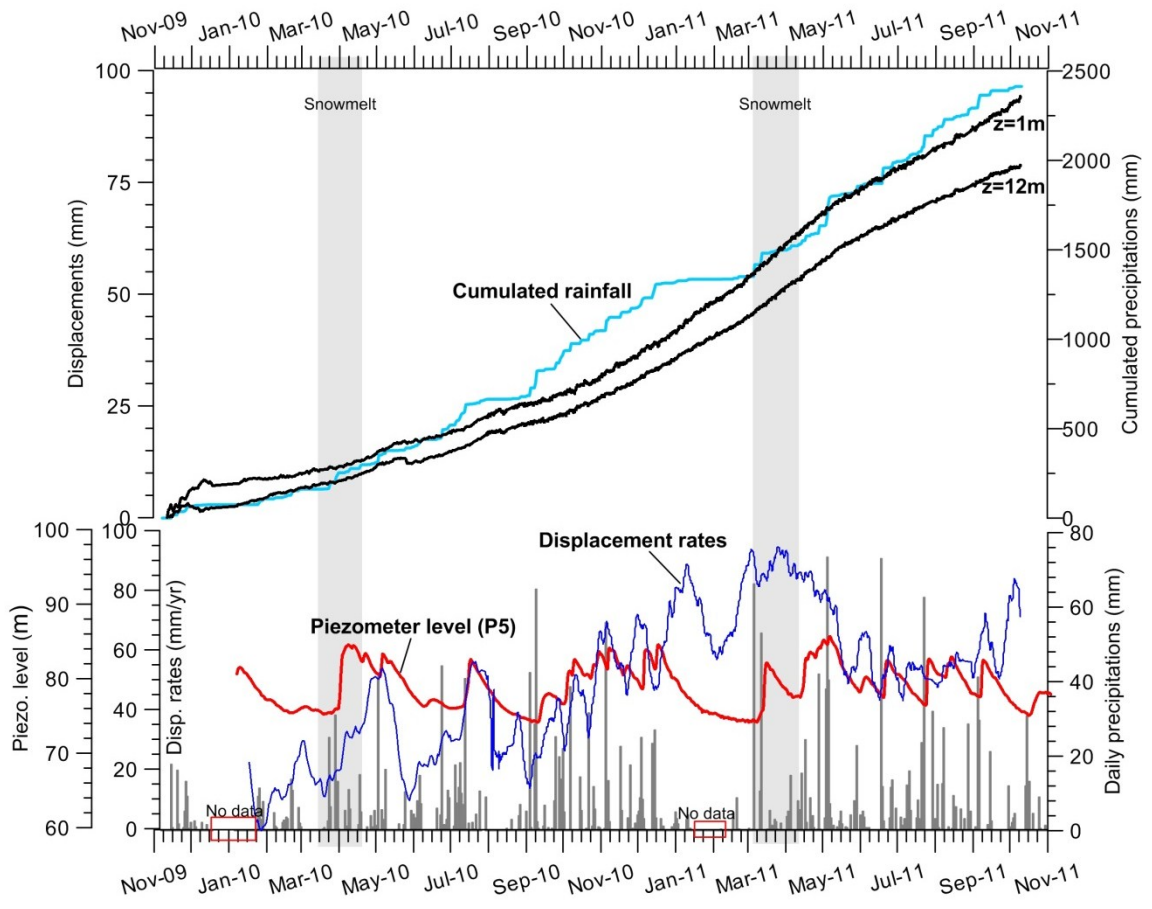


Figure 3-16 In black are displacement versus time curves of SAA2 at three different depths: 1, 12, and 27.4 m (elevation of 98.25, 87.25, and 71.85 m). In red is the piezometer equivalent elevation of water level measured at a depth of 36.6 m (elevation of 62.65m), which is under the sliding surface. In blue are the displacement rates measured on a 20 day period. The bar chart presents the daily precipitations. The pale blue line is the cumulated precipitation.

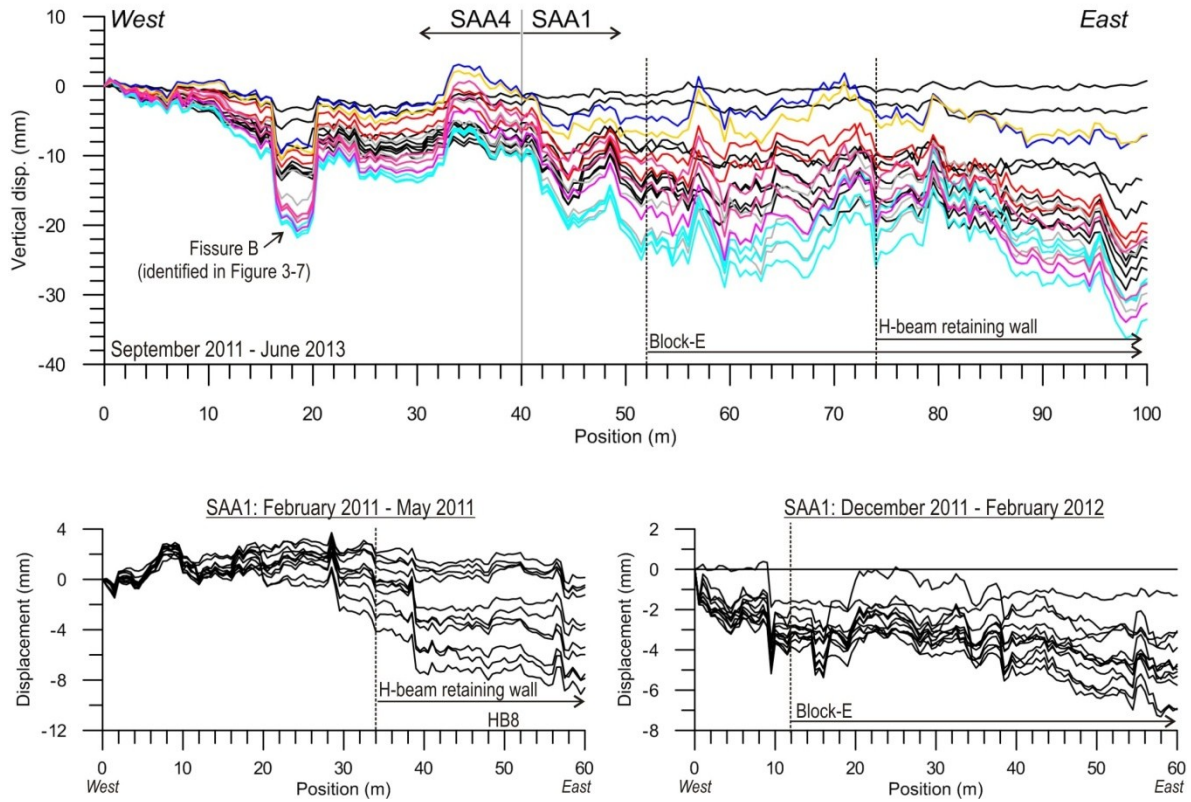


Figure 3-17 The top graphic presents monthly settlement profiles measured by the two horizontal SAA from September 2011 to June 2013. The two chains are joined together, by imposing the displacement of the last segment (east side) of SAA4 to the first (west side) segment of SAA1. Both graphics at the bottom present SAA1 profiles for shorter time intervals.

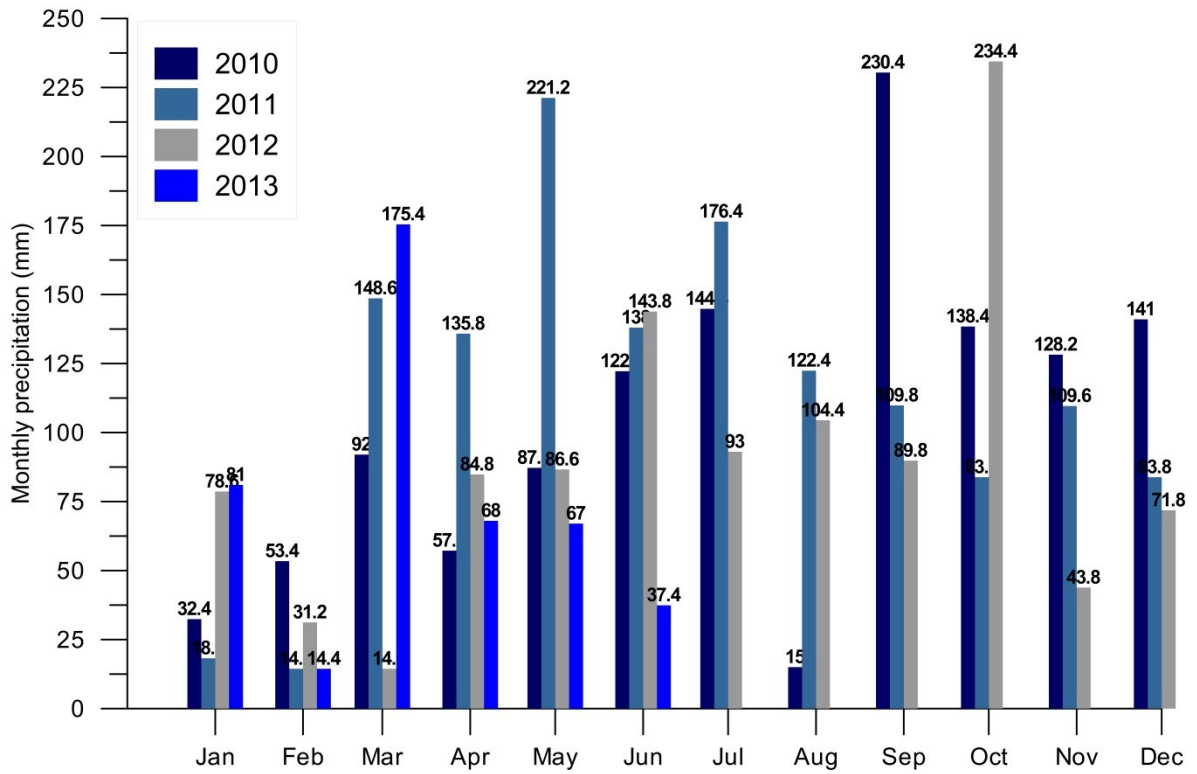


Figure 3-18 Monthly precipitations measured with the weather station on site.

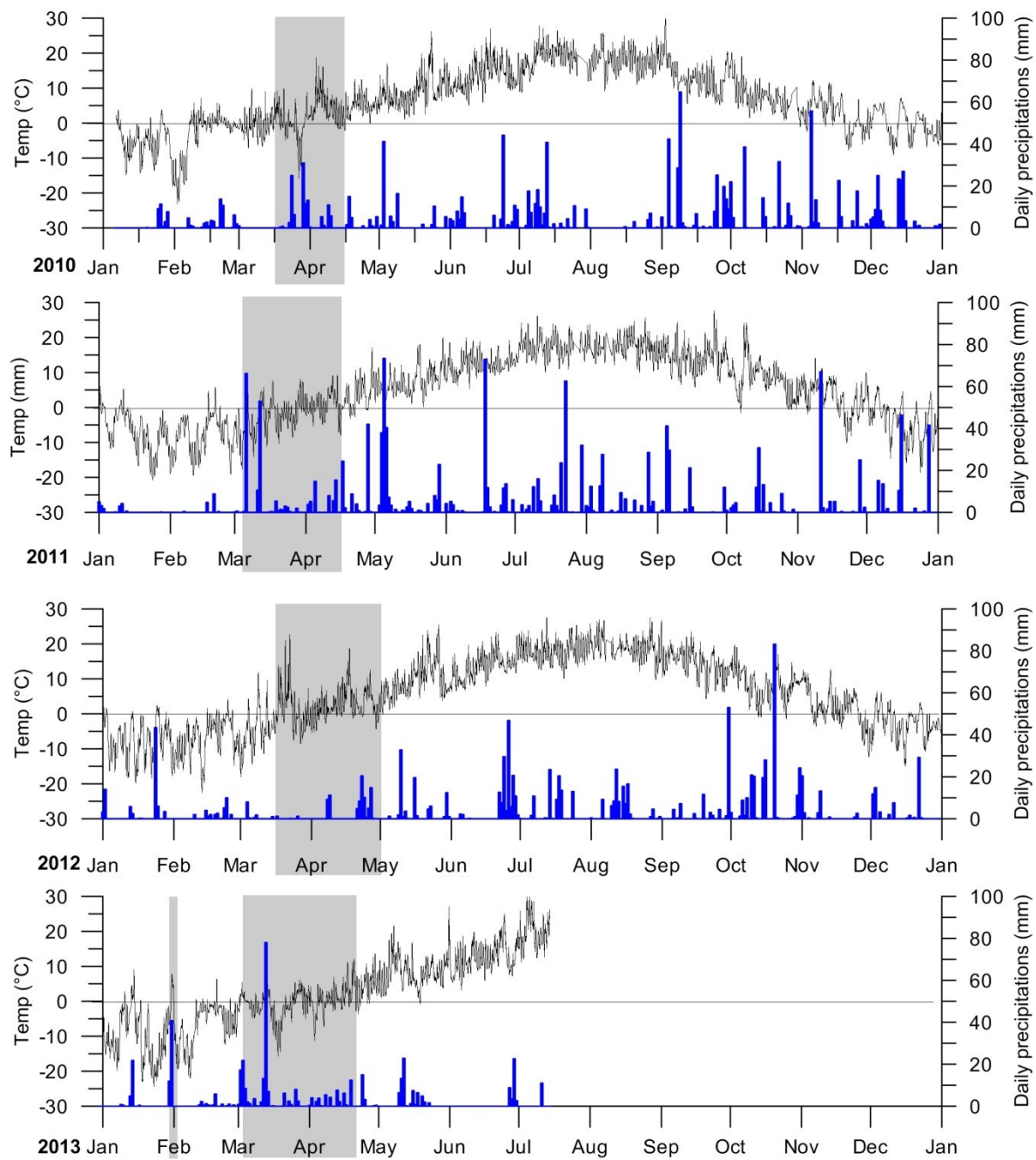


Figure 3-19 Temperatures and precipitations measured by the weather station at Gascons. The shaded areas are the estimated snow melt periods.

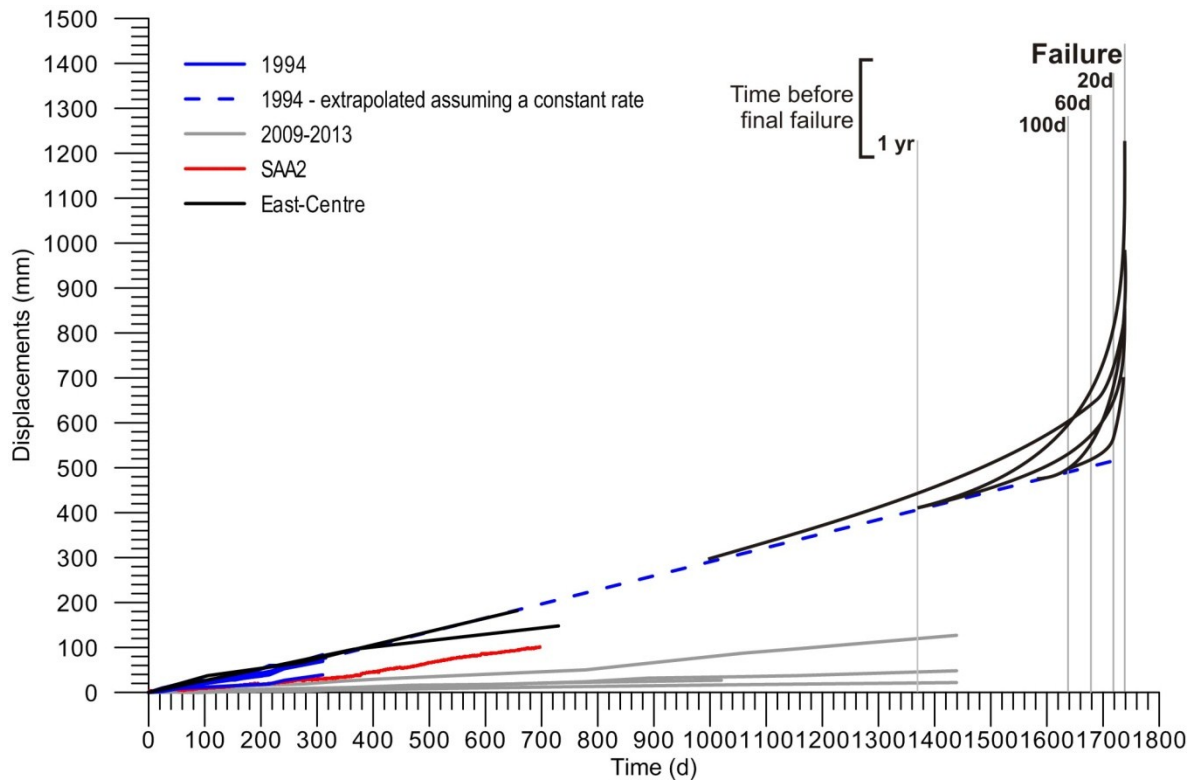


Figure 3-20 Tentative modeling of creep phase II and III for the 1998 slide event. The dashed blue line is an interpolation considering a constant displacement rate, while the black curves present different hypotheses concerning the accelerating phase of the creep model. The curves in grey present displacement measured between 2009 and 2013 and they show no signs of acceleration.

Chapter 4

Risk Analysis of an Active Rockslide: the Gascons Rockslide, Québec, Canada

4.1 Résumé

Le glissement de Gascons, un glissement côtier actif d'un volume de 410 000 m³, menace l'intégrité de la voie ferrée qui le traverse. Les conditions actuelles du glissement sont bien caractérisées grâce à l'installation en 2009 d'un système de surveillance qui permet de suivre les déplacements et les pressions interstitielles. La question est de savoir comment et quand évoluera l'instabilité. Une méthodologie est proposée afin d'évaluer le risque pour le train et ses passagers associé à un glissement très lent. L'approche adoptée est une modification de la méthodologie proposée par Fell *et al.* (2005). L'aléa est estimé par jugement en déterminant d'abord une période de retour basée sur les conditions actuelles du glissement, puis transformée en probabilité. Divers scénarios d'évolution de l'instabilité sont déterminés et décrits, puis l'effet d'une rupture partielle est évalué par une analyse par arbre d'évènement qui permet d'associer une probabilité relative à chaque scénario. Le scénario avec la probabilité la plus élevée est la rupture partielle ou complète du Bloc-E. Le concept de probabilité spatio-temporelle minimale sans prédiction est proposé pour représenter le cas où le train sera endommagé si, et seulement si, l'évènement dommageable se produit lorsque le train circule dans le glissement. Pour réduire le risque sous la valeur du cas sans prédiction, sans avoir recours à d'autres méthodes de mitigation que l'installation d'un système de surveillance, il est nécessaire de prédire l'évènement dommageable. Le concept de probabilité spatio-temporelle minimale sans prédiction permet d'évaluer l'efficacité d'un système de prédiction et d'alerte sur la diminution du risque. Dans cette optique, l'option d'utiliser un système d'alerte et sa conception sont discutées.

4.2 Abstract

The Gascons rockslide, an active coastal slide of 410 000 m³, is threatening the integrity of a railroad that is running through the slide. The current state of the rockslide is well defined due to the installation in 2009 of instruments to monitor displacements and groundwater pressures. The main concern is to predict if and when the rockslide will turn into a rapid slide. A methodology is presented in order to evaluate the risk for the train and its passengers associated to a very slow rockslide. It is an adaptation of the methodology proposed by Fell *et al.* (2005). The hazard is assessed by judgement by estimating a return period, based on the current knowledge of the rockslide, which is then transformed into a probability. Five evolution scenarios are proposed. The domino effect of a partial collapse is evaluated by using an event tree and a relative probability

is associated to each scenario to allow the evaluation of the most probable hazard. The scenario with the highest occurrence probability is the partial or total collapse of Block-E. The concept of the minimum temporal spatial probability without forecasting is proposed to represent the case that the train will be damaged if, and only if, the danger occurs while the train is circulating in the zone. To reduce the risk below the value computed using the minimum temporal spatial probability without forecasting, the occurrence of the danger must be predicted. The minimum temporal spatial probability without forecasting can be used to evaluate the efficacy of an early warning system to reduce the risk of the train circulating in the rockslide while the danger occurs. The design of a warning system is proposed and discussed from this perspective.

4.3 Introduction

In the Gaspé Peninsula in Québec, Canada, the only railroad that reaches the town of Gaspé is running directly across an active rockslide (Figure 4-1), involving a volume of 410 000 m³. The rockslide's rates of displacement are in the order of centimetres per year. Mass movements observed in this sector, located along a coastline formed in sedimentary rocks of Silurian age, are first caused by coastal erosion which locally triggers smaller planar failures that eventually transfer the instability to the upper part of the slope (Figure 4-1). The Gascons rockslide is failing more or less along the bedding plane but as wedge failure (Cloutier *et al.* 2010; Cloutier *et al.* 2012; Lord *et al.* 2010).

The railroad construction was completed in 1911 and little or no fissures are apparent north of the railroad on a 1934 aerial photograph (see Figure 2.3 in Chapter 2). First geotechnical studies in the early 1990's revealed an important fissure network and significant displacements of up to 110 mm/yr (0.5 mm/d). In July 1998, a moving rock compartment of approximately 1500 m³ fell down the cliff and damaged the railroad interrupting the traffic for several days. The failed rock mass and the railroad were approximately at the same elevation (60 m above sea level), and as a result, the granular material supporting the tracks followed the block down the cliff. A derailment in the rockslide sector could cause a train to fall 60 m into the Chaleurs Bay.

The railroad between Matapédia and Gaspé has been acquired in 2007 by local municipalities with the financial support from Provincial and Federal governments as part of an effort to support the socio-economic development of the Gaspé Peninsula. A monitoring system was put in place to understand the instability and to conduct risk assessment. The knowledge acquired from monitoring will be useful for the managers that will have to evaluate different mitigation avenues, one of which being the warning system.

According to the classification of Cruden and Varnes (1996), the Gascons slide is a very slow moving slide. The main challenge associated is to assess if and when a rapid acceleration could take place, as it likely did in 1998. In this context, the paper will address the development of a risk estimation strategy for the Gascons

slide. The methodology is based on the approach proposed by Fell *et al.* (2005) that has been used for rockfall associated risks (Bunce *et al.* 1997; Corominas *et al.* 2005). As decisions concerning risk acceptance must involve the owners and the public agencies, this study does not go through all the risk management process. A preliminary risk analysis of the Gascons rockslide is presented in Locat *et al.* (2013).

The paper starts with the presentation of the current state of the Gascons rockslide, followed by a short literature review that presents definitions and concepts that are applied in this study. Then, the methodology developed for the risk analysis of the Gascons rockslide is presented. Simple parameters are assumed for railroad performance. The dangers are characterized by defining evolutions scenarios and using an event tree analysis to take into account the possible domino effect related to partial failures. The development of the warning system and criteria is finally presented and discussed.

As of today, it was not possible to find a risk assessment approach that could be directly applied to slow moving rockslides, like the Gascons slide. Therefore, a novel approach for risk analysis is proposed here which introduces the concept of minimum spatial temporal probability without forecasting and its associated risk: the risk without forecasting. They are presented hereafter and employed to discuss the warning system's role for risk reduction. The idea behind this analysis is to determine parameter values in order to study their impact on the risk value, more than to try to find the real value representing the current situation in Gascons.

4.4 Current State of the Gascons Rockslide

4.4.1 General Settings

The Gascons rockslide is taking place in the Anse-à-Pierre-Loiselle Formation, a transition unit between the Cascon sandstone Formation and the La Vieille inférieure limestone Formation (Bourque and Lachambre 1980). Near the Port-Daniel-river fault, indicated in Figure 4-1, the beds are curving upward forming a tight syncline fold.

The interpretation of the sliding surface is illustrated in green in Figure 4-2A. This wedge type failure slides on the bedding planes dipping 22° towards a dip direction of 193° . The lateral and back releasing surfaces are formed by two discontinuity sets named A and D, represented on the stereographic projection of Figure 4-2B. The syncline influences the shape of the sliding surface as pointed out in Figure 4-2A. The volume of the instability is estimated to $410\,000\text{ m}^3$.

4.4.2 Monitoring System

The current situation of the rockslide is well documented due to the installation in 2009 of a monitoring system that enables monitoring surface and sub-surface displacements, water pressures, tilting of the retaining walls, settlement of the railway ballast, precipitation, and air temperature.

The displacements of the rockslide are followed automatically by 13 crackmeters situated in the Petit-massif sector (Figure 4-3) and by two vertical SAA chains. The SAA chains are jointed 50 cm rigid segments, comprising three accelerometers to detect inclination changes (Danisch *et al.* 2010). They act as in-place inclinometers. The railway foundation is monitored by two horizontal Shape Accel Arrays chains (SAA), totaling a length of 100 m (Figure 4-3, insert). The pore water pressures are monitored by vibrating wire piezometers in three boreholes. One tiltmeter is installed on a retaining wall (Figure 4-4). The instruments are wired to an automatic acquisition system and data are transferred four times a day to an external server.

Displacements are also monitored by point target analysis interferometric synthetic aperture radar (PTA-InSAR) (Couture *et al.* 2011; Ferretti *et al.* 2001) on a number of permanent reflectors. In Figure 4-3, the reflectors for which the displacements could be resolved in three-dimension are shown (see Chapter 3 of this thesis for more information).

Displacements are also monitored manually by total station surveys, by one traditional inclinometer and by measuring the distance between pairs of markers set on both sides of fissures, called the extensometer network.

4.4.3 Rockslide Displacements and Morphology

The sliding mass is well drained. The water flows toward the sea, and water sources and seepage are observed on the beach. The water table is situated just under the sliding surface, but the piezometric level measured at Site 2 (Figure 4-3) has increased by up to 8 metres above the sliding surface with the snowmelt and precipitation events (see Figure 2-16, in Chapter 2). The water levels are indicated on the cross-sections of Figure 4-5.

The rockslide is continuously moving, but the displacement rates and direction are varying in space and in time. For this reason, two sectors are identified and described hereunder: the East-Centre and the Petit-massif (Figure 4-2A and 4-4).

4.4.3.1 East-Centre and Block-E

The East-Centre has been recognised by the observation of the elevation model and appears to be partly individualised from the main sliding mass. The volume is estimated to 75 600 m³, assuming that the sliding

surface is following the bedding plane which is forming the lineament defining the eastern limit of the sector and shown in Figure 4-3 by a dashed yellow line. Its sliding surface is daylighting in the cliff (Figure 4-5 on cross-section BB').

Its shape is similar to the adjacent ancient wedge slide located on the east side of the active slide and identified in Figure 4-1. Contrarily to the main slide, there is no tension crack visible at the head of the East-Centre sector, but a slope break. The ground is very irregular, a sign that this part of the slide has been subjected to more deformation than the upper part.

Displacement rates measured from PTA-InSAR inside the East-Centre sector are faster than the one measured uphill at Site 2 (Figure 4-3). The East-Centre is moving at 107 mm/yr (point CR12 in Figure 4-3) while at Site 2 a rate of 48 mm/yr was measured with a vertical SAA. The displacement curves are shown in Figure 4-6, in red for Site 2 and in green for CR12. The East-Centre is individualizing from the uphill part of the slide.

Inside the East-Centre, Block-E is recognised to have different displacement rates and morphology (Figures 4-2A and 4-4). Block-E's volume is computed from the sliding surface morphology hypothesis shown in cross-section BB' in Figure 4-5 and is estimated at 23 400 m³. The morphology of the rupture surface was interpreted from morphological evidences only and some uncertainties remain concerning its shape.

Block-E's displacement rates are characterized by faster downward vertical movements (*i.e.* negative values in Figure 4-3), than what is observed for the rest of the slide. The vertical displacements represent 55% of the horizontal displacements for CR8, 27% for CR13 and 31% for HB8, while outside Block-E they represent 18% for CR12, 13% for CR11, and 15% for CR3 (Figure 4-3). As the retaining walls are part of Block-E, they are subjected to the same rates of displacement. Moreover, the retaining walls are subjected to differential settlements, observed from total station surveys and also from visual inspections. The middle H-Beam, called HB8, is settling 20 mm/yr compared to the eastern H-Beam, HB1.

4.4.3.2 *Petit-massif*

The other sector, the Petit-massif, is composed of the blocks south of the railway trench and west of the retaining walls (Figures 4-2A and 4-4). Analyses of the displacement profiles with depth obtained from a traditional inclinometer and a vertical SAA at Site 1 (Figure 4-3) are revealing three levels of shearing surfaces. Displacements on the deepest sliding surface are towards the south and are smaller than displacements on upper sliding surfaces that are towards an average direction of 145°. Two factors are limiting the displacements on the deepest sliding surface: the synclinal fold (Figure 4-2A) that is flattening the sliding

surface and the fact that the sliding surface is at the toe of the slope and erosion is needed to allow more displacements (Figure 4-5, cross-section AA').

In the Petit-massif, the displacement rates measured at the surface and subsurface are decreasing from east to west, reflecting those geometric constraints. The inclinometer and CR11 displacement rates are of 14 and 21.5 mm/yr respectively (Figure 4-3). The displacements measured by total station survey and PTA-InSAR on the most eastward block forming the Petit-massif showed on Figure 4-4 are of 55 mm/yr (C1PM) and 73 mm/yr (CR3) (Figure 4-3).

The water table is below the sliding surface in the Petit-massif sector and the large open fissures ensure a fast and efficient drainage preventing high pore pressures to build up. Thus, the Petit-massif sector is less influenced by water pressures than the upper part of the slide. In the future, the cumulative displacements of the blocks could lead to filling of fractures with less permeable materials creating a situation where water pressures could build into a fissure and influence displacements.

4.4.4 Damage Related to the Current State of the Rockslide

Damages related to the actual state of the slide are caused by the slow accumulation of displacements and are (1) events of undermining of the ballast (Figure 4-7A), (2) differential settlements and maybe failure of the retaining wall (Figure 4-7B and C), (3) modification of the railroad alignment (Figure 4-7B), and (4) differential settlements under the railroad. Two cases of undermining are documented, one in 2000 and the other in 2011 (Figure 4-7A). These events are not considered in the present risk analysis, as they can be controlled with regular maintenance. The risk analysis takes into account damages related to rapid slide events, like the 1998 partial collapse of the Petit-massif (Figure 4-7D), which is described in the next section.

4.4.5 The 1998 Collapse Event

Part of the Petit-massif, situated at the top of the cliff, slid down on July 23rd 1998 and is the only major slide reported at this site since the completion of the railroad in 1911. The rock fall brought part of the railroad ballast down to sea level 60 m below, leaving the rails suspended in the air on a distance of about 15 m (Figure 4-7D). The accounts of this event are poorly reported and the information is mostly taken from newspapers. According to this source, railroad workers had already noticed that ballast was collapsing under the railway since a week. They were adding ballast to maintain the railroad stability. After observing 30 cm of settling, they closed the railroad and the final event took place four hours later. They forecasted the collapse event. The railway remained closed to traffic for a week in order to build the western part of the retaining wall, which is seen in Figure 4-7C. The failed volume is estimated to 1500 m³.

This type of sliding activity is considered as a rapid and damaging slide event, *i.e.* it poses a risk to people or infrastructures. It can result from the linear accumulation of displacements to excessive values or from an acceleration of part or all of the sliding mass.

Locat and Couture (1995) had already indicated in 1994 that this part would fail sooner than later. They had observed more or less constant displacement of the order of about 110 mm/yr (0.3 to 0.4 mm/d). Measurements taken by Locat and Couture (1995) are compared with more recent measurements taken between 2009 and 2012 in Figure 4-6. It shows that actual velocities within the Petit-massif and in the upper part of the slide (see also data from SAA2) are less than what was measured on the block in 1994, but, that the actual velocities measured in the East-Centre are similar to the ones measured in 1994 in the Petit-massif sector. It is not known what the displacement rates of the East-Centre were in 1994. It should be noted that the displacements are measured with different methods and that a direct comparison must be done carefully. In 1994, the displacements were measured by following markers on both side of a fissure, thus indicating relative displacements of one block compared to the other. The results showing actual displacement rates as fast as the ones of 1994 (green curves in Figure 4-6) are the absolute displacement measured with total station and PTA-InSAR techniques. The relative displacement measurements taken in the East-Centre (some of the grey curves in Figure 4-6) are also less than the relative displacement measured in 1994. Even though the general velocity of the slide is less than the one measured in 1994 on the block involved in the 1998 failure, the constant movement of the slide will likely lead to similar events.

4.5 General Concepts of Risk Assessment

This section reviews the literature to present the general concepts of risk assessment and management that were useful to the development of the approach applied for the Gascons rockslide quantitative risk analysis. The methodology specific to this study is presented in section 4.6.

4.5.1 Definitions

Quantitative risk analysis (QRA) is used to evaluate the acceptability of large projects such as dam and residential development regarding the risk to human life. It is also used to evaluate the risk related to existing infrastructures. QRA involves the evaluation of the probability of failure and its adverse consequences to life, property, environment, and economy. In the literature, the generic formula of risk is written in a number of ways, always representing the *Hazard* multiplied by the *Consequences*. Only two examples are reported hereunder:

$$\text{Risk} = \text{Hazards} \times \text{Element at risk} \times \text{Vulnerability} \text{ (Glade and Anderson 2005)}$$

$$\text{Risk} = \text{Hazard} \times \text{Potential Worth of Loss} \text{ (Fell } et al. \text{ 2005).}$$

The risk assessment and management process can be divided in three steps: estimation, assessment, and mitigation. The risk management process is schematized in Figure 4-8, taken from Fell *et al.* (2005). The risk estimation includes the characterization of the danger, its probability of occurrence and the analysis of the consequences. It is the process that leads to the resolution of the equations mentioned above. Then, the estimated risk must be compared to tolerance criteria to evaluate if the risk is unacceptable, tolerable or acceptable. The risk assessment is done here in a risk-benefits analysis. The risk assessment outcome is then used to decide on a mitigation plan, in order to manage the risk. In the risk generic equations given previously, the terms are multiplied, which means that if one term is zero, the risk is zero. Thus, the management process can act on any term of the equation to lower the risk. The risk management plan can go from risk acceptance, to avoidance, or to various active or passive mitigation works. A general framework for risk management can be found in Canadian Standard CAN/CSA-Q850-97 (Canadian Standard Association (CSA) 1997) and in CAN/CSA-ISO 31000 Q31001-11 (Canadian Standard Association (CSA) 2011).

Fell *et al.* (2005) proposed a risk glossary and the terms used in this paper will be in accordance with these definitions, some of which are recalled hereunder:

Consequence: In relation to risk analysis, the outcome or result of a hazard being realised.

Danger (Threat): The natural phenomenon that could lead to damage, described in terms of its geometry, mechanical and other characteristics. The danger can be an existing one (such as a creeping slope) or a potential one (such as a rockfall). The characterisation of a danger or threat does not include any forecasting.

Element at risk: Population, buildings, and engineering works, infrastructure, environmental features and economic activities in the area affected by a hazard.

Frequency: A measure of likelihood expressed as the number of occurrences of an event in a given time or in a given number of trials (sees also likelihood and probability).

Hazard: Probability that a particular danger (threat) occurs within a given period of time.

Individual risk to life: The increment of risk imposed on a particular individual by the existence of a hazard. This increment of risk is an addition to the background risk to life, which the person would live with on a daily basis if the facility did not exist.

Likelihood: Conditional probability of an outcome given a set of data, assumptions and information. Also used as a qualitative description of probability and frequency.

Probability: A measure of the degree of certainty. This measure has a value between zero (impossibility) and 1.0 (certainty). It is an estimate of the likelihood of the magnitude of the uncertain quantity, or the likelihood of the occurrence of the uncertain future event. There are two main interpretations:

Statistical – frequency or fraction – The outcome of a repetitive experiment of some kind like flipping coins. It includes also the idea of population variability. Such a number is called an “objective” or relative frequentist probability because it exists in the real world and is in principle measurable by doing the experiment.

Subjective probability (degree of belief) – Quantified measure of belief, judgement, or confidence in the likelihood of an outcome, obtained by considering all available information honestly, fairly, and with a minimum of bias. Subjective probability is affected by the state of understanding of a process, judgement regarding an evaluation, or the quality and quantity of information. It may change over time as the state of knowledge changes.

Risk: Measure of the probability and severity of an adverse effect to life, health, property, or the environment. Quantitatively, Risk = Hazard X Potential Worth of Loss. This can be also expressed as “Probability of an adverse event times the consequences if the event occurs”.

Residual Risk (defined in CAN/CSA-Q850-97, 1997): the risk remaining after all risk control strategies have been applied.

Societal Risk: The risk of widespread or large scale detriment from the realisation of a defined risk, the implication being that the consequence would be on such scale as to provoke a socio/political response.

Tolerable risk: A risk within a range that society can live with so as to secure certain net benefits. It is a range of risk regarded as non-negligible and needing to be kept under review and reduced further if possible.

Vulnerability: The degree of loss to a given element or set of elements within the area affected by a hazard. It is expressed on a scale of 0 (no loss) to 1 (total loss). Also, a set of conditions and processes resulting from physical, social, economic and environmental factors, which increase the susceptibility of a community to the impact of hazards.

The annual risk for a property in the methodology proposed Fell *et al.* (2005) is calculated with the following equation:

$$R_{(prop)} = P_{(L)} \times P_{(T:L)} \times P_{(S:T)} \times V_{(prop:S)} \times E \quad [1]$$

It becomes the following equation for the probability that a particular person may lose his/her life (Fell *et al.* 2005):

$$P_{(LOL)} = P_{(L)} \times P_{(T:L)} \times P_{(S:T)} \times V_{(D:T)} \quad [2]$$

Where:

$R_{(prop)}$: is the annual loss of property value;

$P_{(L)}$: is the frequency of the landslide;

$P_{(T:L)}$: is the probability of the landslide reaching the element at risk;

$P_{(S:T)}$: (Temporal spatial probability) is the probability that the element at risk is in the area affected by the danger (threat) at the time of its occurrence;

$V_{(prop:S)}$: is the vulnerability of the element at risk to the landslide event;

E : is the element at risk (e.g. the value or net present value of the property);

$P_{(LOL)}$: is the annual probability that the person will be killed;

$V_{(D:T)}$: is the vulnerability of the person to the landslide event.

If the element at risk is exposed to multiple hazards (Fell *et al.* 2005) or if a hazard threatens more than one element at risk (Van Westen *et al.* 2006), then the risk is the sum of all the hazards times their consequences, as follow:

$$R_{(prop)} = \sum_1^N (P_{(L),N} \times P_{(T:L),N} \times P_{(S:T),N} \times V_{(prop:S),N} \times E_N) \quad [3]$$

4.5.2 Determination of Risk Equation Parameters

The first term in the risk equation is the hazard ($P_{(L)}$). It can be estimated based on historically determined frequency and magnitude of landslides (Fell *et al.* 2005). Another mean is to analyse the triggering agents of landslide, such as rainfall or earthquake, that have sometimes longer records than the landslides inventory (Glade and Anderson 2005).

The other terms are related to the consequences that could result if the danger occurs. One of them is the vulnerability. Very limited data exist on the vulnerability of human and infrastructures to landslide and even less with respect to specific types of landslides (Glade and Anderson 2005). In addition, they are hard to define quantitatively. The wide diversity of landslides types and processes, e.g. their velocities, are impacting on our ability to evaluate the vulnerability of elements at risk. Finlay *et al.* (1996) proposed quantitative values for the vulnerability of individuals exposed to landslides which are reported in Dai *et al.* (2002) and presented in Table 4-1. Leone *et al.* (1996) proposed an explicit framework for structuring the concept of vulnerability, in particular through the use of damage matrix. Vulnerability of certain types of infrastructure can be assessed by

comparing losses with the actual values of the elements affected and expressing it as a fraction between 0 and 1, based on past damages in relation with the magnitude of events, like it was done by Remondo *et al.* (2008). Li *et al.* (2010) proposed a model to estimate the vulnerability of persons and infrastructures. They defined the vulnerability as a function of the hazard's intensity, the exposed elements at risk, and the resistance ability of the elements to withstand a threat. Their method uses different correction factors to consider the characteristics of elements at risk. For example, the resistance factor for human life in open area is dependent on the age and the knowledge of the exposed persons.

In the definitions given above, the vulnerability is expressed as a non-dimensional value between 0 and 1, with 1 being a total loss. However, Remondo *et al.* (2008) proposed that the vulnerability could be above 1 in the case that repair costs are greater than the one of a new construction.

Table 4-1 Summary of Hong Kong vulnerability ranges for death from landslide and recommended values to use in risk analyses (from Finlay *et al.* 1996, cited by Dai *et al.* 2002).

Case	Vulnerability of person		Comments
	Range in data	Recommended value	
<i>Person in open space</i>			
1. If struck by a rockfall	0.1 - 0.7	0.5 ^a	May be injured but unlikely to cause death
2. If buried by debris	0.8 - 1.0	1.0	Death by asphyxia
3. If not buried	0.1 - 0.5	0.1	High chance of survival
<i>Person in a vehicle</i>			
1. If the vehicle is buried/crushed	0.9 - 1.0	1.0	Death is almost certain
2. If the vehicle is damaged only	0 - 0.3	0.3	Death is highly likely
<i>Person in a building</i>			
1. If the building collapses	0.9 - 1.0	1.0	Death is almost certain
2. If the building is inundated with debris and the person not buried	0.8 - 1.0	1.0	Death is highly likely
3. If the building is inundated with debris and the person not buried	0 - 0.5	0.2	High chance of survival
4. If the debris strikes the building only:	0 - 0.1	0.05	Virtually no danger ^a

^aBetter considered in more detail, i.e. the proximity of person to the part of the building affected by sliding

The two remaining parameters in Eq. [3] are the probability of the landslide reaching the element at risk ($P_{(T,L)}$) and the probability that the element at risk is in the area affected by the danger at the time of its occurrence ($P_{(S,T)}$). They are evaluated by formulas established depending on the case studied. For example, to evaluate these parameters, Bunce *et al.* (1997) considered the traffic and the length of vehicles.

Three ways to express the risk estimation are proposed in Fell *et al.* (2005) and reported hereunder:

- a) The annual risk (expected value) in which the probability of occurrence of the danger is multiplied by the consequences summed over all the hazards. This is expressed in monetary value as \$x damage per annum, or as potential loss of lives per annum.
- b) Frequency-consequence (f-N) pairs- for example for property, the annual probability of minor damage (\$x); medium damage (\$y) and major damage (\$z); and for risk to life, the annual probability of loss of 1 life, 5 lives, 100 lives, etc.
- c) Cumulative frequency – consequence plots (F-N plots), for example a plot of annual probability of N or more lives being lost. They are made by calculating the frequency per year of events with magnitudes that could cause the loss of 1 life, 5, 10, 100, 1000 lives etc. and summed, as presented in Wong (1997), and represented in Figures 4-9A and 4-9B with tolerability criteria for societal risk (Ho and Ko 2009; Geotechnical Engineering Office 1998).

Quantitative risk analysis is not always achievable; in such cases the risk is estimated by expert judgement and expressed in qualitative terms. The subjectivity related to qualitative description of risk can lead to various interpretations of the same results. Quantitative risk analysis overcomes this limitation if the data on which it is based have a limited uncertainty. The ultimate aim of risk estimation is the derivation of some reproducible standard measure of risk that can be compared and evaluated along with other similarly estimated risks.

4.5.3 Risk Acceptability

Song *et al.* (2007) defined acceptable and tolerable risks as:

Acceptable risk: A risk for which, for the purposes of life or work, we are prepared to accept as it is with no regard to its management. Society does not generally consider expenditure in further reducing such risks justifiable.

Tolerable risk: A risk that society is willing to live with so as to secure certain net benefits in the confidence that it is being properly controlled kept under review and further reduced as and when possible. In this zone the **ALARP (As Low As Reasonably Practicable)** principle should be applied.

Some common general principles about risk to loss of life tolerance criteria are mentioned in IUGS Working Group on Landslides (1997). They show that a multitude of factors will influence risk perception which can vary amongst members of the same community. These principles are (IUGS Working Group on Landslides, 1997):

- a) The incremental risk from a hazard to an individual should not be significant compared to other risks to which a person is exposed in everyday life.
- b) The incremental risk from a hazard should, wherever reasonably practicable, be reduced, i.e. the As Low As Reasonably Practicable (ALARP) principle should apply.

- c) If the possible loss of life from a landslide incident is high, the likelihood that the incident might actually occur should be low. This accounts for society's particular intolerance to incidents that cause many simultaneous casualties, and is embodied in societal tolerable risk criteria.
- d) Persons in society will tolerate higher risks than they regard as acceptable, when they are unable to control or reduce the risk because of financial or other limitations.
- e) Higher risks are likely to be tolerated for existing slopes than for planned projects, and for workers in industries with hazardous slopes, e.g. mines, than for society as a whole.
- f) Tolerable risks are higher for naturally occurring landslides than those from engineered slopes.
- g) Once a natural slope has been placed under monitoring, or risk mitigation measures have been carried out, the tolerable risks approach those of engineered slopes.
- h) Tolerable risks may vary from country to country, and within a country, depending on historic exposure to landslide hazard, the system of ownership, the control of slopes and natural landslides hazards.

Guidelines for risk acceptability related to landslide hazards are limited. In Hong Kong, risk criteria for individual risk is presented in Ho and Ko (2009) and is 10^{-5} for new developments and 10^{-4} for existing developments. The criteria are applied to the most vulnerable person at risk.

Societal risk criteria are presented on F-N diagrams, as the example from Hong Kong presented in Figure 4-9B taken in Ho and Ko (2009). The tolerable frequency of loss of life is lower for events with higher consequences (here the number of fatalities). It takes into account the aversion that society has against events causing a high number of fatalities. In Figure 4-9B, there is no acceptable zone, but only the tolerable and unacceptable zones. The presentation of results on F-N plots enables comparing the risk associated to other dangers to that of tolerance criteria.

The y-axis of the F-N diagram is either named *Probability of failure per year*, *Frequency of N or more fatalities per year*, or the *Cumulative Frequency of loss of N or more life per year*. In any cases, the calculation of F is done with the risk equations to which the consequences part is modified. For example, in Eq. [2], the *E* is dropped and the equation is not multiplied by the number of fatalities.

A cost-benefit evaluation could lead to a different risk acceptance than the risk assessment made for the loss of life. Ho and Ko (2009) related a case in Hong Kong where the mitigation measure proved not to be economically justifiable compared to risk of loss of life. However, when the evaluation was carried out by quantifying the risk in terms of the different economic losses, the mitigation measures turned out to be justifiable.

Hungr and Wong (2007) discuss about some issues concerning interpretation of risk tolerance based on F-N diagrams. They ask if the curves are dependant or not on the size of the exposed group. They present cases where the interpretation would lead to less safe or safer interpretation depending on the area included in the risk analysis. The authors also discuss about the effects of normalizing the tolerance criteria curves to the size of the exposed group of people. For the Government of Honk Kong, the societal risk tolerance criteria are applied to "Consultation zones", defined as portions of 500 m long natural hillside toe (Ho and Ko 2009; Hungr and Wong 2007).

The risk acceptance criteria should be established before the QRA is performed (Song *et al.* 2007). Most authors state that the use of quantitative risk assessment needs the establishment of unambiguous, easy to understand and uniform criteria values (Fell *et al.* 2005; Glade and Anderson 2005; Hungr and Wong 2007), that are still to be defined. Still, quantitative risk evaluation is useful to compare and to prioritize works and helps to take rational decisions.

4.6 Methodology of the Gascons Rockslide Risk Analysis

4.6.1 Adaptation of the Methodology Proposed by Fell *et al.* (2005)

The risk analysis of the Gascons rockslide is limited to the active slide area. The elements exposed to the danger are the railroad, the retaining walls, the train and its travellers, fishermen near the beach, visitors, and pedestrians. No house near or uphill the crest of the landslide is endangered. For the following analysis, the only elements at risk considered are the train's passengers, presented in terms of fatalities due to the derailment or partial derailment of the train.

The risk estimation considers that the cause of a derailment is an operational failure of the railroad caused by the landslide. As the railroad is traversing the active slide, the operational failure can result from debris accumulation on the railroad or by the loss of track support due to sliding of supporting material under or below the railroad, thereby affecting its foundation's stability. In this study, the author is using the term *collapse event* to describe a situation that involves an acceleration of all or part of the rockslide and that have potential consequences on the railroad. Other possible terms could have been rapid failure/slide, catastrophic event/failure, etc. The author tried to avoid using the term failure to stick to the definition of Leroueil *et al.* (1996): "failure is characterised by the formation of a continuous shear band or surface through the entire soil or rock mass". In the Gascons rockslide, the main sliding surface is assumed to be already defined.

The methodology presented by Fell *et al.* (2005) is adapted to the Gascons situation. The equation used to calculate the probability of loss of life (P_{LOL}) per year for the Gascons risk estimation is now expressed in the following way:

$$P_{LOL} = P_{(L)} \sum_1^N (P_{sN} \times P_{(S:T),N} \times P_{(T:L),N} \times V_{e:T,N}) \quad [4]$$

The terms in the equation stand for:

$P_{(LOL)}$: Annual probability of loss of life;

$P_{(L)}$: Annual probability of a collapse event;

P_{sN} : Relative probability of occurrence of dangerous scenarios 1 to N defined for the Gascons sector.

$P_{(S:T)}$: Annual temporal spatial probability: the probability that the element at risk is in the danger zone at the time of its occurrence.

$P_{(T:L)}$: Probability of landslide reaching the element at risk, *i.e.* that the landslide will affect the area in which the element at risk is located.

$V_{(e:T)}$: Vulnerability of the element at risk if it is touched by the danger.

The risk could be estimated for the infrastructure, but as the railway is fixed and traversing completely the landslide, the probability of landslide reaching the element at risk and the temporal spatial probability are fixed to one ($P_{(T:L)} = P_{(S:T)} = 1$). In the case of the risk to the railroad, the equation reduces to:

$$R_{T,infrastructure} = P_{(L)} \sum_1^N (P_{sN} \times V_{infrastructure:T,N}) \quad [5]$$

The monetary value (E) of the element at risk is not taken into consideration, as the risk value will be presented as the probability of loss of life. Moreover, the author is not in a position to determine the cost of the elements at risk. This consideration is similar for Corominas *et al.* (2005) who, in a risk evaluation four houses in a rockfall prone area, have excluded the term E from the equation and called the resulting value the annual potential loss of property value. The following sections (4.6.2 and 4.6.3) explain how the different parameters are estimated.

4.6.2 Hazard Analysis

The equation's first term (Eq. [4]), $P_{(L)}$, is the annual probability of a danger occurrence. This term has been introduced in the equation to compute the potential loss of life on an annual basis in order to compare it with values found in the literature. The probability has been determined by expert judgement based on the knowledge of the instability, described in the two previous chapter of this thesis and in section 4.4 of the present chapter. First, a return period of a phenomenon that has the potential to cause an operational failure of the railroad is determined. Then, a power law is used to convert this return period into an annual probability. It is the power law proposed by Raetzo *et al.* (2002) in Switzerland:

$$P_{(L)} = 1 - \left(1 - \frac{1}{T}\right)^n \quad [6]$$

where T is the returned period of a slide event and n the time length considered. The concept of a return period is judge valid here since the slide is active and that the main factor responsible for the sliding activity, the erosion, is still an ongoing process at Gascons. A parametric study is carried on $P_{(L)}$ to evaluate its impact on the risk value.

The evolution of the active rockslide could lead to different dangerous events. Five scenarios of the evolution of the rockslide were determined and are detailed in section 4.7.2. For each of the scenarios, a relative probability of occurrence is associated (P_{SN}). The sum of the P_{SN} equals 1, because if a dangerous event happens, it must be one of those stipulated by the author. To associate probabilities to the scenarios, a list of qualitative terms associated to probabilities values and suggested in Lacasse (2008) was used. The list is presented in Table 4-2.

The work of Lacasse (2008) indicates that such probabilities were determined in discussion groups, where participants were debating on the appropriate relative probability of a scenario compared to other scenarios based on all the data available on a rockslide. In the Gascons rockslide, the P_{SN} were determined by discussion between the author, her supervisor and other colleagues, but not in a discussion group such as the one described by Lacasse (2008).

Table 4-2 Probability values associated to qualitative terms describing the occurrence potential of a dangerous event after Lacasse (2008).

Descriptor of uncertainty	Event probability
Virtually impossible	0.001
Very unlikely	0.01
Unlikely	0.10
Uncertain	0.50
Likely	0.90
Very likely	0.99
Virtually certain	0.999

4.6.3 Consequence Analysis

The two previous terms, $P_{(L)}$ and P_{SN} , were associated with the hazard evaluation. The remaining terms are associated to the consequences on the element at risk.

The probability of landslide reaching the element at risk ($P_{(T,L)}$) is fixed to 1. In fact, this term depends on the path taken by the element at risk and the path taken by the landslide. The train crosses the whole landslide every time it circulates on the rail. Thus, if a dangerous event occurs, it will be on the path of the train.

For the purpose of this analysis, the vulnerability of the train's passengers is fixed to 1, because the author does not have the required knowledge and expertise to determine this value. Moreover, the train circulates at an elevation of 63 m and the derailment could cause the train to fall down the cliff, thus motivating the use of a conservative approach. Moreover, the recommended vulnerability value for a person in a vehicle being buried or crushed by a landslide in Table 4-1 is also 1. However, as will be discussed further, it is not certain that all scenarios will cause sufficient damages to the railroad to cause a derailment and motivate a vulnerability value of 1.

Since both the vulnerability and $P_{(T,L)}$ are fixed to 1, the consequences analysis only depends on the term $P_{(S,T)}$, *i.e.* the probability that the element at risk is in the area affected by the danger at the time of its occurrence. This term represents the annual exposure time of the element at risk to the danger. It is dependant of the capacity of the train to be aware of the danger in time to stop before circulating on a damaged railroad. The variables to be accounted in the computation of $P_{(S,T)}$ are:

- train can or cannot stop if it sees the danger;
- train's frequency;
- train's speed and length to determine the time spent in the zone;
- railway inspection: they diminished the exposure time of the train. In fact, if an inspection is done ten minutes before the train enters the zone, then the threat most occur in these ten minutes to be a danger for the train. If it happened before the inspection, then the train will be informed of the danger prior to entering the zone.

The $P_{(S,T)}$ is computed using the following equation:

$$P_{(S:T)} = \frac{(d+t_p+t_v) \times f_p}{525\ 600} \xrightarrow{\text{dimensional analysis}} \left[\frac{(\text{min}+\text{min}) \times \text{passage}/\text{year}}{\text{min}/\text{year}} \right] \Rightarrow [\text{dimensionless}] \quad [7]$$

where:

$P_{(S:T)}$: Annual temporal spatial probability: the probability that the element at risk is in the danger zone at the time of its occurrence;

d : the time, or delay, in minutes between the last inspection and the train entering the zone. It is also the time without monitoring;

f_p : yearly train frequency;

t_v : time (in minutes) for the train to travel the critical stopping distance. This term depends on the stopping distance of the train. If the collapse event occurs when the train is closer to the zone than this distance, it will be touched as it will not have enough time/distance to stop;

t_p : time (in minutes) for the train to cross the rockslide, calculated as follow:

$$t_p = \frac{\text{danger zone length}}{\text{train's speed}} + \frac{\text{train length}}{\text{train's speed}} \quad [8]$$

Some situations could lead to the train circulating on damaged rails: if a collapse event occurs at the same moment than that the train enters the zone, or if for some reasons, as fog, the train cannot see the danger or cannot see the danger early enough to stop the train before circulating on the damaged rails. For these reasons and to evaluate the impact of this variable on the risk calculation, different values of $P_{(S:T)}$ are estimated, one of them being defined as the *minimum $P_{(S:T)}$ without forecasting*.

The *minimum $P_{(S:T)}$ without forecasting* corresponds to the situation that the train can only be attained if the danger occurs at the same time than the train is circulating in the zone. If the danger occurs before the train enters the zone, the train will be informed and stop before entering the zone, a 100% of time. In other words, it is the minimum value that can be reached while monitoring continuously. In fact, as will be discussed later, to lower the $P_{(S:T)}$ below the minimum value without forecasting, prediction the hazard occurrence is needed to stop the train before the danger occurs.

The concept of *the minimum $P_{(S:T)}$ without forecasting* was created during the analysis, when discussing about the effect of an early warning system on the risk.

As $P_{(T:L)}$ and the vulnerability are fixed to one for all collapse event scenarios, the risk equation for the probability of loss of life (Eq. [4]) is now simplified to:

$$P_{LOL} = P_{(L)} \times P_{(S:T)} \quad [9]$$

4.6.4 Evaluation of Failure Scenarios by Event Tree

An event tree was developed to evaluate the impact of an initial failure on the rest of the instability (*i.e.* failing mass). We call it the domino effect. An event tree analysis provides an intuitive structure to represent schematically the various event sequences following the initial danger. This technique requires breaking the complex situations into smaller pieces and organizes them into chronological order leading to an increase understanding of the problem as one must debate and confront the various possible alternatives. It reflects also the uncertainty about the system's evolution.

According to Baecher and Christian (2003), an event tree is composed of branches and nodes and represents the various event chains that could result from an initial event. The chains, or branches, might or might not lead to the failure of the system. The event tree technique is used to associate a conditional occurrence probability to each event, given the previous event on the branch, *e.g.* there are more chances for B to happen if A has happened previously. A joint probability is obtained by the multiplication of every probability along a branch. The probability must obey these rules: (1) the sum of the probabilities of the nodes' branches equals 1 and (2) the sum of the joint probabilities equals 1. The outcome of a node must be mutually exclusive and collectively exhaustive. The initializing event is the active rockslide and on the first level of nodes are the five dangerous scenarios defined for the Gascons rockslide's evolution and described in section 4.7.2.

The determination of the P_{SN} enables computing the risk relative to a specific scenario and identifying the most critical one. In fact, each scenario could consider different kinds of damage to the railroad and the vulnerability to the train could be adjusted consequently. For example, a collapse event damaging the retaining walls would probably lead to greater consequences for the train than a collapse event occurring on the western part of slide. The derailment in the first case would likely imply the train's fall down the cliff, while the second case would very likely not result in the train falling down the cliff, because the cliff is further from the railroad in the western part of rockslide.

However, for the risk estimation conducted in this study, the vulnerability is not modified with the scenarios. In fact, as indicated in Eq. [9], the total risk is evaluated using the sum of the P_{SN} which equals 1 and a vulnerability of 1.

The event tree analysis helps to develop knowledge of the hazard and clarifies its prediction. It informs the decision makers of the most probable evolution, based on engineering judgement, and should be useful in their selection of mitigation methods.

4.6.5 Risk Mitigation and Warning Criteria Definition

The risk can be lowered of various ways: (1) reduce the probability that the train is in the dangerous zone as the danger happens ($P_{(S:T)}$), (2) apply active measure to increase the stability of the rock mass and decrease the hazard to acceptable levels ($P_{(L)}$), and (3) relocate the railroad to avoid the danger ($P_{(T:L)}$). In this study, the possibility to develop a warning system with the monitoring system in place is evaluated. A warning system will decrease the risk by reducing the $P_{(S:T)}$ by advising the train if the danger occurs or by predicting the occurrence of the danger.

In order to develop an early warning system, the definition of warning criteria must be achieved. The warning criteria were defined by observing the actual kinematic behaviour of the rockslide and the instruments response. Threshold values found in the literature were also taken into consideration.

4.7 Hazard Evaluation

4.7.1 Probability of Occurrence of a Collapse Event ($P_{(L)}$)

The slide is active and the deformations are cumulating, thus increasing continuously the rock's damage. Therefore, the return period is not obtained from the average frequency of past dangerous events but from a forecast based on the history of the landslide, its current state, and behaviour described previously.

By considering that the displacement rates will remain similar in the future, the displacement that will cumulate in the next years can be calculated. As the displacement rates vary from one place to another, the time to cumulate a metre of displacement is also varying in space and in time and presented in Table 4-3. Nine or ten years is needed to cumulate an extra metre of displacement in the East-Centre and in Block-E, while it is between 17 and 70 years for the blocks in the Petit-massif.

Because of the morphology of the Petit-massif's blocks, it is almost certain that a metre of displacement would cause the upper blocks to topple and that would probably damage the railroad. The average time needed to cumulate a supplementary metre of displacement is of 29 years and is used to estimate the return period. Moreover, the fact that the last major event happened more than 10 years ago was also taken into consideration, meaning that more displacement cumulated since the last event. On the other hand, it is the only documented event since the railroad construction around 1911, which means that the historical frequency of occurrence is low. From the above analysis, the author believes, based on engineering judgement that a collapse event will happen in the next 20 years.

In summary, for the purpose of this study, the return period of a collapse event in the Gascons rockslide has been evaluated to be an event every 20 years, corresponding to a probability of 0.05 calculated with Eq. [6], *i.e.* $P_{(L)} = 0.05$. The following analysis will present a parametric study on this parameter ($P_{(L)}$).

Table 4-3 Time needed to cumulate an extra meter of displacement, if the displacement rates stay constant in time. For more information about the displacement rates, read Chapter three of this thesis.

Instrument (see Figure 4-3 for location)	Rate	Time to cumulate
	mm/yr	1 m (yr)
Absolute displacement rates		
Inclinometer	14.3	70
CR11	21.5	47
CR3	73	14
C1PM	59	17
CR12	107	9
HB8	99	10
CR13	111	9
Relative displacement rates		
EX6-7	16.3	61
F11	43.5	23
	Average	29

4.7.2 Description of Collapse Event Scenarios

The analysis resulted in the definition of five different collapse events that could occur at the Gascons rockslide. This section describes the scenarios and the relative probability associated to each scenario. The relative probability values given to the scenario were inspired from the one suggested in Table 4-2. However, as the relative probabilities must sum to 1, the values in Table 4-2 could not be directly applied. The relative probabilities are used to compare one scenario the others.

4.7.2.1 *Petit-massif Partial Collapse*, $P_{s1} = 0.5$

The first scenario is an event similar to the 1998 event that would comprise one or a few blocks of the Petit-massif. The blocks that are the most prone to be involved in a collapse are those at the top of the cliff, either to the east but also in the middle of the Petit-massif. These blocks are identified in Figure 4-4. The blocks would fall down to the beach. The velocity acquired by the blocks during the fall would be important, but the elements at risk are not in the travel path of this slide. However, the fall of the eastern blocks could lead to a loss of support of the railroad's foundation, similar to what happened in 1998. To the west in the Petit-massif sector, the railroad is getting further away from the cliff. The fall of the western blocks would not damage the railroad. Considering this, two parameters of the risk equation could be reduced. The first one is the $P_{(T,L)}$, because it is not certain that the partial collapse of the Petit-massif will lead to an operational failure of the track. The

second is the $P_{(S:T)}$, because the damage length would be less than 200 m. However, for this analysis, the $P_{(S:T)}$ and $P_{(T:L)}$ are kept constant through the different scenarios.

As this event is considered the most probable, a relative probability of 0.5 is associated to the event. Precursory signs related to this scenario are widening of cracks, an increase of rockfall, and of displacement rates.

4.7.2.2 *Petit-massif Total Collapse, $P_{s2} = 0.01$*

This scenario refers to the failure of most of the Petit-massif as it is identified in Figure 4-2A. The sliding surface associated to this zone is the one identified at a depth of 10 m in the inclinometer and presented in the cross-section AA' in Figure 4-5. Such a collapse event has a low probability. In fact, the 1998 partial collapse did not cause the whole Petit-massif to collapse. Consequently, a probability of 0.01 is associated. The total failure of the Petit-massif would cause major damage, as the railroad would become without support on a length of 50 to 60 m. The volume is estimated to 13 300 m³.

The mass would accelerate as it starts to fall down the cliff. The railroad is situated near the crest of this sector, thus the train and its passengers would not be hit by the debris. Again, it is the damage to the railroad that is the threat for the train and its passengers.

4.7.2.3 *Block-E Partial Collapse, $P_{s3} = 0.289$*

The railroad is traversing Block-E. The failure surface is situated under the railroad and the retaining walls. Part of Block-E is situated above the railroad and is identified in Figures 4-2A and 4-5. The partial collapse of Block-E would involve small volumes situated in the slope north and above of the railroad pointed out in Figure 4-4. The volumes are estimated between 1 to 10 m³. As the slope is near the railroad and that there is no trench to catch the falling rocks (Figure 4-4), even a small volume could cover the railroad. The probability is fixed to 0.289.

In this case, the threat for the train and its passengers are (1) to be hit by falling material or (2) that the railroad gets partly covered by debris. Both situations could cause a derailment. Where the railroad is circulating in Block-E the corridor is relatively narrow and it overlooks the retaining walls (Figures 4-3, 4-4, and 4-5). Thus, if the train derails in this sector, it is assumed that it would most likely fall down the cliff.

4.7.2.4 *Block-E Total Collapse, $P_{s4} = 0.2$*

The total collapse of Block-E would involve the volume delineated in Figures 4-2A and 4-5 (23 400 m³), including both retaining walls. It would damage the railroad on a portion of 75 metres. The probability associated to the total collapse of Block-E is 0.2.

4.7.2.5 Major Acceleration of the Slide, $P_{s5} = 0.001$

A major acceleration of the slide would be an acceleration of a large volume, as the East-Centre or the total active slide as illustrated in Figure 4-2A. The railroad would be taken away by a major rockslide and repairs would not be possible. This scenario is considered less probable than all the other scenarios and is given a probability of 0.001, related to virtually impossible in Table 4-2. The author considered that the slide will most likely break down into smaller volumes rather than as a single mass. The overall sliding mass has a volume of 410 000 m³ and the East-Centre sector a volume of 75 600 m³.

4.7.3 Event Tree Analysis and Evaluation of the Domino Effect

The event tree analysis, presented in Figure 4-10, shows many possible evolutions of the rockslide and enables the evaluation of the impact of a collapse on the stability of other sectors by means of engineering judgement. It gives a means to evaluate the domino effect, i.e. secondary consequences of an initial sliding event. The five scenarios presented in section 4.7.2 are taken into consideration.

A branch finishes with either one of these possibilities: (1) Slow Evolution, i.e. following the preceding events the slide returns in a situation slow enough to maintain a functional railroad or (2) Major Collapse i.e. the collapse of a large portion or the overall sliding mass. The ending into Slow Evolution does not signify that the slide is returning to its actual situation or that it is safe for the train, because in certain branches, the preceding events imply a major change in the slide's geometry. However, the return to a Slow Evolution would provide time to undertake repair works in the zone or to re-evaluate the situation. Whereas a Major Collapse does prevent any access to the zone as the displacement rates would be too high or because the mass has already slid down.

The values associated with the scenario's probability depend partly on the time period on which the analysis is based. In this case, the return period designated for the computation of $P_{(L)}$, 20 years, is used.

The Partial Collapse of the Petit-massif's branch is dividing into four branches. A return to Slow Evolution is the branch considered the most probable with a value of 0.89. It is an event very similar to the 1998 one, with important consequences for the railroad, but not on the slide's immediate evolution. The second branch evaluates the probability that the failure of Block-E is triggered by the Partial Petit-massif collapse. A low probability of 0.09 is associated as Block-E's stability is believed to be little influenced by the blocks that are up the cliff in the Petit-massif. However, depending on which blocks of the Petit-massif are involved, the consequences could be different. The Total Petit-massif collapse is considered again less probable with an associated value of 0.01. Finally, it is thought very unlikely that a Partial Collapse of Petit-massif could trigger a Major Collapse.

The second major branch is the Total Collapse of Petit-massif. Such an event would most likely (0.8) cause the collapse of Block-E, because Block-E would become without lateral support. A return to a Slow Evolution is unlikely (0.01) following the collapse of the Total Petit-massif and of Block-E, because this event sequel would cause a major modification of the rockslide's geometry.

The Total Collapse of Block-E and the Partial Collapse of Block-E are strongly correlated. They were separated into two events because the partial failures are enough to cause the railroad's operational failure. In all the branches implying the collapse of Block-E, the Major Collapse is considered probable as the failure of Block-E could lead to the acceleration of the East-Centre. In the opposite, it is uncertain that the failure of Block-E could trigger the Total Collapse of Petit-massif.

The sum of all the branches ending by a Major Collapse is about 0.40. This value comes in great part from the two branches involving the Block-E, because the failure of Block-E can destabilize the East-Centre. If the East-Centre accelerates this is considered as a Major Collapse. The sum of all the branches ending by a Slow Evolution is about 0.60.

4.8 Evaluation of the Consequences: $P_{(S:T)}$, $P_{(T:L)}$, and $V_{E:T}$

The consequences of the hazard are related to the elements at risk and factors such as its presence, the possibility of being hit by the danger and its vulnerability. The element at risk considered in this analysis is the train's passengers. Since both the vulnerability and $P_{(T:L)}$ are fixed to 1, the consequence terms simplify to the term $P_{(S:T)}$, i.e. the probability that the element at risk is in the area affected by the danger at the time of its occurrence and is evaluated using Eq. [7].

The *minimum $P_{(S:T)}$ without forecasting*, defined in section 4.6.3, represents the case that if the danger occurs before the train passage, the train chauffeur will see the danger and proceed successfully to stop the train before entering the dangerous zone. Thereby, the rockslide is only a threat for the train if it occurs during the train passage. The parameters used to compute this value are presented in Table 4-4. The *minimum $P_{(S:T)}$ without forecasting* is 0.0009.

The *minimum $P_{(S:T)}$ without forecasting* is the smallest $P_{(S:T)}$ value presented in this analysis, which assumes that, contrary to what happened in 1998, the operator cannot use his observation of the evolution of the damages to stop the train. It could also be lower if the train frequency considered is lower, or if the length of the dangerous zone is shorter. The $P_{(S:T)}$ could also be increased, for example, if for some reason, such as fog or snowstorm, the train is not able to stop before entering the rockslide. Values of $P_{(S:T)}$ representing that for 1% and 5% of the passages, the train is not able to see the danger in time to stop are evaluated with this equation:

$$P_{(S:T),1\%} = 1\% \times P_{(S:T),max} + 99\% \times P_{(S:T),residual} \quad [10]$$

The parameter $P_{(S:T), max}$ used in the above equation, represents the case that the train does not see the danger and/or does not attempt to stop the train before entering the dangerous zone. In this case, the slide has more time than in the minimum without forecasting situation to occur and still be a danger for the train. As the integrity of the railroad is verified before the train passage, if the danger occurs between the last inspection and the train passage, the train will circulate on the damaged railway. In case of no inspection, the delay parameter (d in Eq [7]) will take a maximum value corresponding to the time span between two trains. In fact, it is considered that the previous train is carrying the inspection. This time period is called the delay and is part of Eq. [7]. The maximum $P_{(S:T)}$ is computed using the same parameters than the *minimum $P_{(S:T)}$ without forecasting* except for the delay that is increase to 360 minutes. Considering that for some reason, the maintenance crew is unable to foresee the danger and the train cannot see the danger 1 or 5 % of the travels, the intermediate values of $P_{(S:T)}$ could be:

$$P_{(S:T),1\%} = 0.002991$$

$$P_{(S:T),5\%} = 0.01136$$

Table 4-4 Parameter values used to calculate the *minimum $P_{(S:T)}$ without forecasting*.

Parameter	Value
f_p (train/year)	312
Train's speed (km/h)/ train's length (m)	16.09/ 200
Dangerous zone length (m)	200
t_p (minutes)	1.3
t_v (minutes)	0.16
d (minutes)	0
Minimum $P_{(S:T)}$ without forecasting	0.0009

4.9 Risk Analysis Results

For the annual probability of loss of life (P_{LOL}), also called the risk in this study, the computation is straight forward using Eq. [9]. When using the *minimum $P_{(S:T)}$ without forecasting* in Eq. [9] the result is called the total risk without forecasting and is equal to 4.5×10^{-5} . This risk is shown in Figure 4-11. The number of fatalities (N) can be modified depending of the number of fatalities evaluated (number of passengers). A value of 20, chosen arbitrarily, is used in this plot.

In this analysis, the total risk depends on the occurrence probability ($P_{(L)}$) and the $P_{(S:T)}$. If the limits proposed by the Geotechnical Office of Hong Kong in 1998 apply to the railroad in Gascons, then the risk without forecasting calculated for a return period of 20 years and for 20 fatalities is just below the limit between the ALARP and the unacceptable zones in the F-N diagram (Figure 4-9B).

The risk calculated with the $P_{(S:T),1\%}$ is 1.5×10^{-4} . For the $P_{(S:T),5\%}$ the risk increases to 5.7×10^{-4} . The computation of these other $P_{(S:T)}$ shows that the train's chauffeur capacity to see the danger and stop in time is very important in reducing the risk. The $P_{(S:T), 1\%}$ and $P_{(S:T), 5\%}$ were computed to study the effect of the train's capacity to see the danger and stop before entering the dangerous zone. However, these values might not reflect the reality.

A parametric study is also made for the occurrence probability, $P_{(L)}$, that is varied between two extreme values : 0.11 and 0.014. They correspond to return periods of 9 and 70 years, the minimum and maximum values of Table 4-3 representing the time to cumulate an extra metre of displacement. The return period of 70 years reduces the risk to 1.25×10^{-5} , which falls into the tolerable zone on the F-N diagram of Figure 4-9B, considering 20 fatalities. The risk is 9.9×10^{-5} when using the minimum return period of 9 years for a collapse event that falls into the unacceptable zone on the F-N diagram, considering 20 fatalities. Still, this value is lower than the risk computed using $P_{(S:T),1\%}$.

The calculated risk using the *minimum* $P_{(S:T)}$ *without forecasting* is the lowest that can be attained doing inspection and monitoring, but no forecasting. To lower the risk under this value, prediction of the time of collapse is necessary. With a perfect prediction system, the $P_{(S:T)}$ could be reduced to zero. However, a perfect warning system is not achievable and a certain risk will always remain. The next section discussed about warning system requirement and development.

4.10 Warning System and Warning Criteria Determination

4.10.1 The Idea behind a Warning System

A warning system can reduce the risk caused by the landslide to the train and its passengers; it acts on the risk by reducing the spatial temporal probability term ($P_{(S:T)}$) in the risk equation. The risk without forecasting, computed with conservative parameters, is 4.5×10^{-5} and falls on the boundary of the ALARP and unacceptable zone in the F-N diagram of Figure 4-9B, considering 20 fatalities. The warning system aims at lowering the risk to an acceptable value, such as the targeted risk presented in Figure 4-11. To obtain a risk equal to a the targeted value of 4×10^{-7} , for example, the $P_{(S:T)}$ must be reduced to 8×10^{-6} , this would mean a reduction of the risk by about 99%, *i.e.* the collapse event would have to be predicted 99 times out of 100.

The concept behind the monitoring and the warning system is that there will be precursory signs prior to a collapse event and that these signs can be monitored and interpreted to predict a collapse event, before it damages the track. The monitoring system was put in place in order to understand and monitor the rockslide displacements and pore water pressures. The decision of monitoring the rockmass and not the infrastructure is based on the fact that we need to predict a collapse event in order to lower the risk. To do so, we need to foresee the occurrence of the danger by monitoring the displacement of the rockslide. Monitoring of the infrastructure would only enable to notice the slide once it happened.

The event tree analysis showed that the events more prone to affect the railroad are the Partial Collapse of the Petit-massif and the Partial or Total Collapse of Block-E. It is this type of collapse event that the warning system aims to predict. For that reason among others, the inspection of the railroad and retaining walls are still mandatory to noticed damages caused by cumulative displacements, such as rail alignment and undermining of the ballast.

4.10.2 Approach of the WEB-based Warning System

A system has been developed in order to notice and warn someone of changes in the kinematic behaviour of part or the overall rockslide in order to forecast a collapse event that could damage the railroad. Only instruments with automatic acquisition were judged to have a sufficient reading frequency to be part of the warning system. However, the system also relies on the understanding of the overall rockslide which must be based on a nearly complete coverage of the slide area and, at Gascons this has been achieved by integrating results from manual measurements and remote sensing in the analysis.

The literature review on rockslide's warning systems mentioned the use of different warning levels leading to a catastrophic situation (Blikra 2008; Crosta and Agliardi 2002; Froese and Moreno 2011; Froese *et al.* 2009). The same approach is used here. Three levels of warning are proposed to represent the general state of the instability in addition to a technical alert. Thresholds on individual sensors are coupled to determine the general alert level of the instability.

The first one is a green situation which indicates that the rockslide conditions remain normal and that no peculiar behaviour outside the known limits is detected. The second level, yellow, means that part of the instability requires a special attention. This situation occurs if seasonal variations are exceeded on more than one sensor, or on a critical sensor. Finally, the third level is red and is kept for a situation showing clear signs that a collapse event is near, so the situation requires an immediate response.

The technical alert will inform the users if one or multiple instruments are not working or giving out of range data. It will also inform the users of loss of communication, power outage, and if the transfer to the external

server is not working. If the warning system is out of function, proper actions must be taken as the risk will increase when the warning system is out.

The thresholds are developed in order to warn the manager of a change in the behaviour of the sliding mass, such as a fast acceleration or a velocity higher than the ones observed previously. The threshold could not be based directly on velocity of previous collapses in the active slide. However, the rates measures in 1994 in the sector that collapsed in 1998 were used as an indication that the slide is still slower than what it was four years before the event, except for the East-Centre and Block-E sectors.

The automatic instruments are mostly installed in the Petit-massif sector. In fact, at the time of installation the Block-E and East-Centre were not yet recognized, and the Petit-massif was considered as the most important short term threat, considering that the only known collapse event occurred in the Petit-massif in 1998. The lack of automatic instrumentation in the upper part of the slide and in the East-Centre part creates a dependency on regular manual reading of other instruments to understand and detect the behaviour of these sectors.

For these reasons, the expert judgement has an important role in the warning system and expert must analyze and interpret the changes in the rock mass behaviour. Moreover, as new information is acquired, the thresholds should be adapted accordingly.

Through the warning system design process, it became clear that analysis of the data by an expert was essential. Thus, it was decided to focus on creating tools, such as a website, to help the experts in their analyses and, most of all, to accelerate the data interpretation. The website opens with a daily report of the data, presenting comprehensive graphs that are coupling instruments in order to facilitate the interpretation and a table with the state of the alerts. In this way, the expert can see quickly the individual sensors' alert level. The data process is all automated. If the expert needs to access more detail information, pages showing graphs with longer time periods, detailed information, pictures, geotechnical information on the rockslide, including cross-sections, 3D views of the rockslide, information on volumes, and etc. are included in the web site. The objective is that the expert finds all the information needed on the website to correctly interpret the evolution of the rockslide.

4.10.3 Threshold Values

Thresholds have been developed for the crackmeters, the tiltmeter, and horizontal SAA. No threshold alerts have been implemented for water pressures, thus on the piezometers. Characteristics of each instrument, as noise level and acquisition frequency, were taken into account in the implementation of threshold algorithms.

4.10.3.1 Tiltmeter

The definition of threshold values for the tiltmeter was straightforward, as the noise level is very regular and the measurements follow an annual cycle, returning approximately to the same inclination angle in the same period of the year.

The tiltmeter is biaxial, meaning that there are two sensors mounted perpendicularly. The same threshold values are used for both axes. The tiltmeter is installed on one part of the retaining wall built in 1998. The inclination measured by the tiltmeter is thus linked to the inclination of one pillar of the retaining wall.

The yellow threshold is just above the seasonal variation, $[-0.2; 0.2]^{\circ}$ for at least two subsequent data, while the red alert is of $[-1; 1]^{\circ}$.

4.10.3.2 Crackmeter

The crackmeters are all installed in the Petit-massif sector (Figure 4-2), on open cracks, as the one seen in Figure 4-4. The top of the cliff in the Petit-massif is made up of multiple blocks separated by open fractures. The thickness of the sliding mass is the largest in the Petit-massif sector, but the failure surface of the blocks monitored by the crackmeters is much higher than the deepest sliding surface (Figure 4-5, cross-section AA'). Their volumes are limited to a few 1000 m³ per block.

The blocks are all sliding down. Some cracks are closing and other are opening which means that the blocks are individualized and not necessarily moving as neighboring blocks. The final behaviour before their failure and fall down the cliff can have two different patterns. One pattern is an acceleration of the displacement rates that could form over a week period or even over months. The other pattern is an abrupt acceleration, a step-like behaviour that can happen if the blocks attain a step in the sliding surface. As so, two types of criteria are designed. One will notice a change of trend in the rates of displacements, while the other is designed to notice quick change in displacements.

The design of the criteria had to take into account the daily variations on the crackmeter sensors that are important compared to the displacement rates. In fact, the magnitude of daily variation reaches 0.08 to 1.91 mm while the long term trend of displacements is between 0.004 and 0.18 mm/d (1.5 to 66 mm/yr). The daily variations vary from sensor to sensor and also from season to season. This oscillation, that is link to temperature effects on all the system components (including the rock mass), has an important effect on the calculation of the first and second order derivative (speed and acceleration) used for the criteria definition.

Thus, the first type of criteria, the velocity-type criteria, is a linear trend calculated on 20 days of daily arithmetic averages. The 20 day period was chosen after testing different time span. The velocity thresholds

values for crackmeters are of 0.06 mm/d to 0.1 mm/d for yellow alarm and of 0.15 to 0.2 mm/d for red alarm. The criteria uses 20 days of data so it will take multiple days before the change of trend is noticed.

The second type of criteria, the displacement-type criteria, was put in place to notice quick change in the behaviour. The average daily displacement is compared with a predicted value. If the difference between the measured and predicted values is more than 1 mm (yellow level) or 2 mm (red level) an alert is issued. The predicted value is calculated using the trend of the displacement-time curve computed 3 days earlier. The trend computed for the velocity criteria, described in the previous paragraph is used. In this way, if the trend changes, the predicted value will be wrong. Closing or opening will both cause an alert to be issued as it is believed that the closing of a fracture is also the sign of a displacement.

The range of the crackmeters is between 100 and 300 mm, so they can support a limited amount of displacement. If the displacement rates accelerate, the life expectancy of the instrument will reduce as it will reach its full opening faster. Thus, the crackmeters are useful to measure the onset of the acceleration.

4.10.3.3 Horizontal SAA

The only automatic sensor in the Block-E vicinity is the horizontal 60 m SAA chain, read every hour. This instrument measures its vertical displacements, thus either swelling or settling of the railway ballast. The data acquired correspond well to the morphology of the slide. The east side of SAA1 is settling compared to the western side and this movement is linked to the Block-E (see Figure 3-17, in Chapter 3). As the collapse of Block-E would affect the retaining wall, the ballast will also be affected. Consequently, the acceleration of Block-E should be detected by SAA1. The two horizontal SAA should be part of the warning system.

However, there is a slight change that Block-E's acceleration will not cause the predicted effect on the ballast and the instrument. For example, the ballast could readjust slowly around the SAA not carrying it with it.

4.10.4 Limitations of the Warning System

The warning system in the Gascons case is seen as a good mitigation method for short term purposes. As there should be no self-stabilisation of the rockslide, increasing deformation of the rails is forecasted, thus, inexorably, major works will become necessary to keep the railroad in function due either to cumulative displacements or to a major collapse event. Moreover, a warning system does not reduce the occurrence probability ($P_{(L)}$).

Looking at reported behaviour prior to failure in the literature, the system should foresee a collapse event in the Petit-massif sector. In fact, acceleration prior to the final acceleration phase seems to be the norm in rockslides and numerous examples are reported in the literature (Crosta and Agliardi 2003; Cruden and

Masoumzadeh 1987; Froude 2011; Masoumi and Douglas 2010; Mufundirwa *et al.* 2010; Rose and Hungr 2007; Saito 1969). The inverse velocity method has been developed from observation of this behaviour (Rose and Hungr 2007).

Values of criteria found in the literature are presented in Figure 4-12. From this review, it appears that the lowest velocity criterion is around 1.5 mm/day. Thereby, the onset of a rapid failure should reach rates of 1.5 mm/day long enough before the collapse event. The monitoring system is sensitive enough to monitor such displacement rates. In that perspective, the monitoring system will permit to see the acceleration prior to a collapse event. The defined thresholds for the crackmeters are much lower than 1.5 mm/day. The choice of such conservative values is motivated by the fact that the elements at risk, which are the train and the rails are both sensible to small deformations and located inside the instability. Again, the proposed warning system is not totally independent and before an alarm is issued, the situation must be evaluated by an expert. This is why the warning criteria are designed to warn the expert that the rockslide is changing behaviour. When the defined thresholds will be reached, the situation will need a re-evaluation.

The study permitted to find the warning system's limitations that are:

1. The lack of confrontation of the system with real events. Its performance to predict a collapse event is theoretical. Up to date, there have only been yellow alerts on single instruments and technical alerts.
2. The limited automatic instrumentation of the Block-E and the East-Center. Block-E was identified as the most critical sector for the railway safety, but it is only monitored by one automatic sensor, SAA1. Consequently, the manual displacement measurements and PTA-InSAR monitoring must be continued to follow these sectors, or instrumentation must be added.
3. The warning system does not predict the undermining of the ballast. The undermining will be seen once it has happened. In the case of that particular danger, the warning system will not reduce the risk below its residual value.
4. It has not been possible to establish a relation between the rockslide's displacement and the induced rails deformation. This is why the system focuses on predicting a rapid slide event. Consequently, the warning system does not replace the visual inspections done by the railroad maintenance crew; it completes their work.
5. The analysis by an expert of the warning issued by the system is necessary in order to understand the situation and alert the train operator if needed, to judge if the situation is a threat for the railway and also to update the threshold values as new information is coming in.

4.11 Discussion on the Risk Analysis Uncertainties

As the slide is active, one could ask the question if the risk value also vary in time. If the same analysis (with the same amount of data) would have been done in early 1990's would the risk be higher or lower? The estimation of the probability of occurrence of a collapse event, $P_{(L)}$, is based on subjective probability. Subjective probability is affected by the degree of comprehension of the process, judgement regarding an evaluation, and the quality and quantity of information available. This kind of probability might change in time as the state of knowledge changes (Fell *et al.* 2005). Even though the concept of a return period was used to determine the $P_{(L)}$, the $P_{(L)}$ does not reflect the historic frequency of events, because, active slides are not recurrent processes as avalanches or debris flows.

The uncertainty on the occurrence probability is hard to quantify. In this analysis, the uncertainty was represented by the use of a maximum and minimum value. The risk computed with these $P_{(L)}$ values varied from 1.26×10^{-5} and $9,9 \times 10^{-5}$. However, the use of extreme values is not representative of the reality and over or under estimates the risk. The author is confident in the use of a return period of 20 years to represent the best estimate if the analysis is carried on a mid-term length, such as 50 years. Moreover, if no active mitigation measure is put in place, the state of instability will keep degrading towards a more unstable situation, as the displacement is continuous and erosion is still an active process.

The spatial temporal probability is probably the most important source of uncertainty in the equation. The difference of two orders of magnitude between the *minimum without forecasting* and $5\% P_{(S:T)}$ shows how the operation mode of the railroad influences the risk associated to the train and its passengers.

In the case of the 1998 collapse event, the failure was forecasted. The prediction of the collapse event reduced the $P_{(S:T)}$ to zero and, consequently, the risk was also zero. Such an example indicates that even without an automatic warning system, forecasting can be done by the employees. If we take for granted that precursory signs will precede a collapse event, then, the risk without forecasting is an overestimation of the reality, because it considers that the railroad employees will not use these signs to forecast the event. In any case, the risk without forecasting definition proposed in this chapter is useful to evaluate the risk related to a rapid collapse event that could not be predicted and to evaluate the forecasting capabilities that must be achieved to lower the risk to a targeted level.

The vulnerability was fixed to a value of 1 for all the scenarios. The risk could also be calculated for a specified scenario, using Eq. 11 and varying the vulnerability accordingly:

$$R_{T,e} = P_{(L)} \times P_{SN} \times P_{(S:T),N} \times P_{(T:L),N} \times V_{e:T,N} \quad [11]$$

The consideration of different consequences for each scenario would involve that:

- The chances that a particular scenario affects the railroad should be discussed. This would modify the value of $P_{(T,L)}$.
- The length of the railroad affected by a particular scenario can be estimated and the $P_{(S,T)}$ computed accordingly;
- The vulnerability of the train could be evaluated for each scenario. For example, if there is a known critical length of railroad that needs to be affected to cause a derailment, this information could be used to reduce the vulnerability for scenarios that impact a shorter length.

The number of passengers in the train will influence the tolerable limit of risk. As can be seen in the F-N diagram (Figure 4-9), the tolerable risk reduces when the consequences increase. This means that the acceptable risk is higher for a merchandise train than for a full passenger train. This needs to be taken into consideration by the railroad managers.

4.12 Concluding Remarks and Recommendations

A quantitative risk analysis has been conducted for the train circulating in the active Gascons rockslide. No methodologies found in the literature could be directly applied to the Gascons case, so an approach has been developed based on the one proposed by Fell *et al.* (2005).

In order to characterize the hazard, potential dangerous failure scenarios were defined and a relative probability of occurrence was associated to each scenario based on engineering judgement. The event tree analysis showed that the scenario which can generate the greatest domino effect, *i.e.* the potential to induce a major collapse of the sliding mass would be the partial collapse of Block-E. The occurrence probability ($P_{(L)}$) was evaluated with regard to the return period of a collapse event based on the author's knowledge and judgement and defined a value of 0.05.

The risk without forecasting concept is proposed to represent the risk related to the situation that the slide occurs at the same time than the train is circulating in the zone. It is computed using the minimum spatial temporal probability without forecasting ($P_{(S,T)}$). The risk computed is 4.5×10^{-5} . This can be used as a reference value from which to compare the performance of various mitigation methods.

In terms of risk mitigation, the risk calculated using the minimum spatial temporal probability without forecasting ($P_{(S,T)}$) is the lowest value that can be achieved doing monitoring only, thus without forecasting. To reduce $P_{(S,T)}$ furthermore, it is necessary to proceed to the prediction of the danger. Then, if the slide is predicted, the train can be stop before the slide happens.

This study should be carefully looked at by the management team (formed by government representatives and railroad management) to set appropriate values of the vulnerability, the $P_{(S,T)}$, and acceptance criteria. This study was mostly focused on the evaluation of the hazards, the consequences analysis is somewhat outside of the expertise field of the author. Even though there is lots of uncertainty, the QRA results should be sufficiently reliable and representative for use in risk evaluation and formulation of risk mitigation strategies.

The actual monitoring system, the development of warning threshold values and the awareness of the railroad maintenance crew workers are elements that should ensure the maintenance of the risk for users to an acceptable level. However, the author believes that the warning system should only be considered as a short term mitigation method. Referring to the comments on risk acceptance presented in section 4.5.3-g, the population should be less tolerant for the Gascons rockslide as it is now a monitored slope.

It is recommended to keep doing the manual and PTA-InSAR monitoring on a regular basis to follow the East-Centre and Block-E sectors, since they were both identified as critical sectors. Installing automatic instruments in these sectors would certainly be an improvement of the monitoring system and it would help increasing the prediction capabilities and consequently lower the risk.

It is suggested to run the risk analysis again as new data and interpretation are obtained, and also on periodic basis as the slide is evolving and the evolution should bring the instability or part of the instability closer to collapse. Moreover, before using the results of this study, a person must be aware of the uncertainties, limitation, and must understand the methodology used.

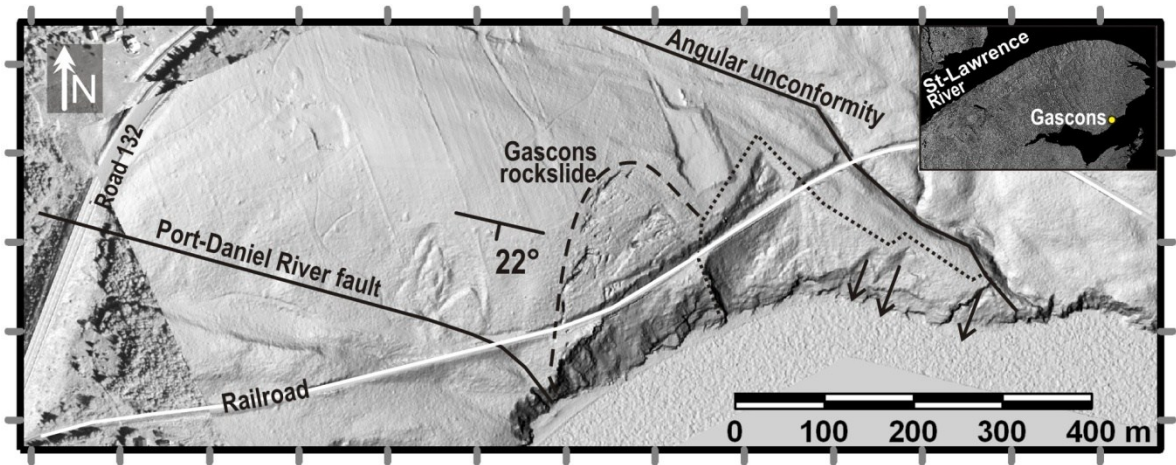


Figure 4-1 The Gascons rockslide's location in the Gaspé Peninsula is indicated in the inset (© Natural Resources Canada. All rights reserved.). The elevation model of the rockslide and its surroundings is showing the railroad, the road, past rockslides (black arrows) and geological features (angular unconformity and Port-Daniel River fault).

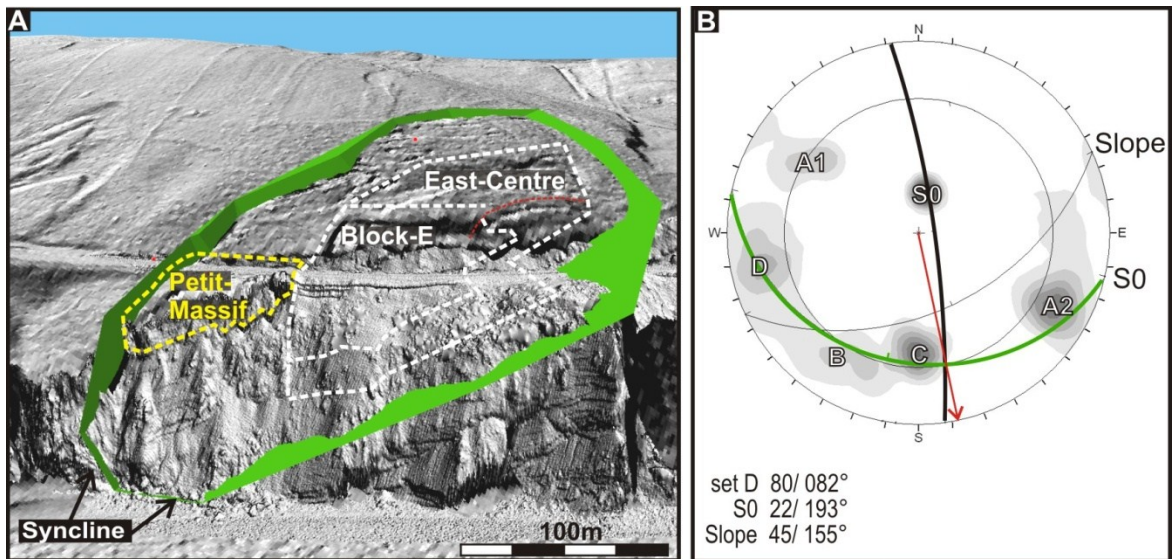


Figure 4-2 A) Oblique view of the elevation model of the Gascons rockslide. The main sliding surface appears in green and the rockslide different sectors are identified. B) Stereographic representation of the discontinuity sets. The failure surface is a wedge formed by the bedding planes (S0) and discontinuity set D. The lateral surface has a stepped morphology and is formed by the intersections of sets A and D.

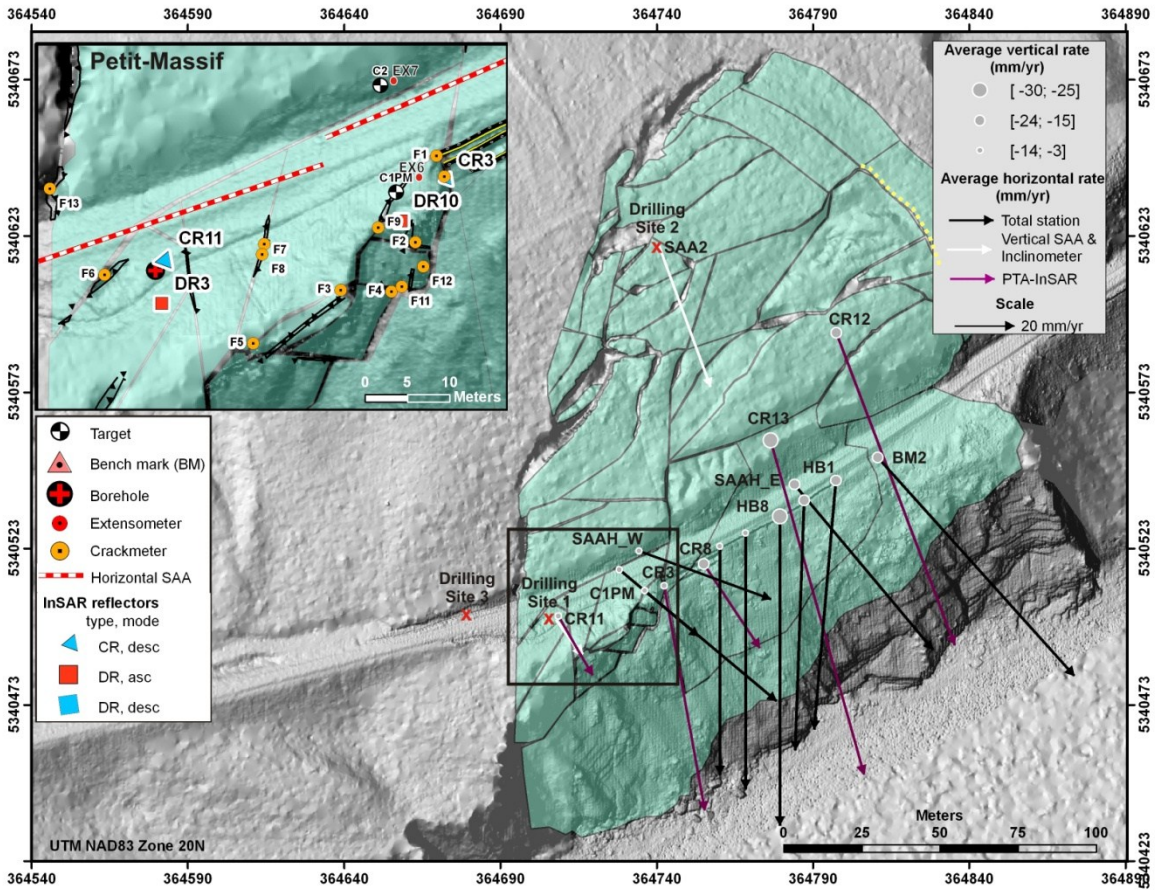


Figure 4-3 Instrumentation map, displacement vectors and block representation of the rockslide presented over the hill shade of the elevation model. The inset presents a zoom of the Petit-massif sector.

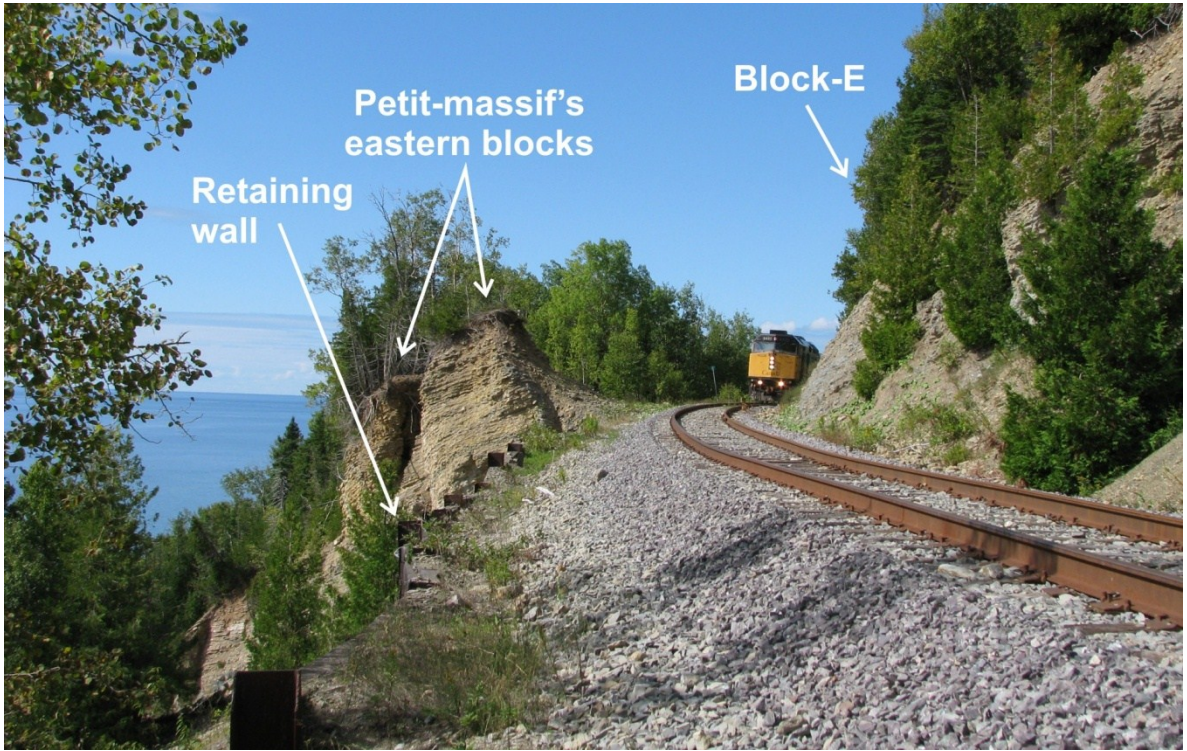


Figure 4-4 Photography taken in 2009 before the installation of the monitoring system looking towards the west and the Petit-massif sector.

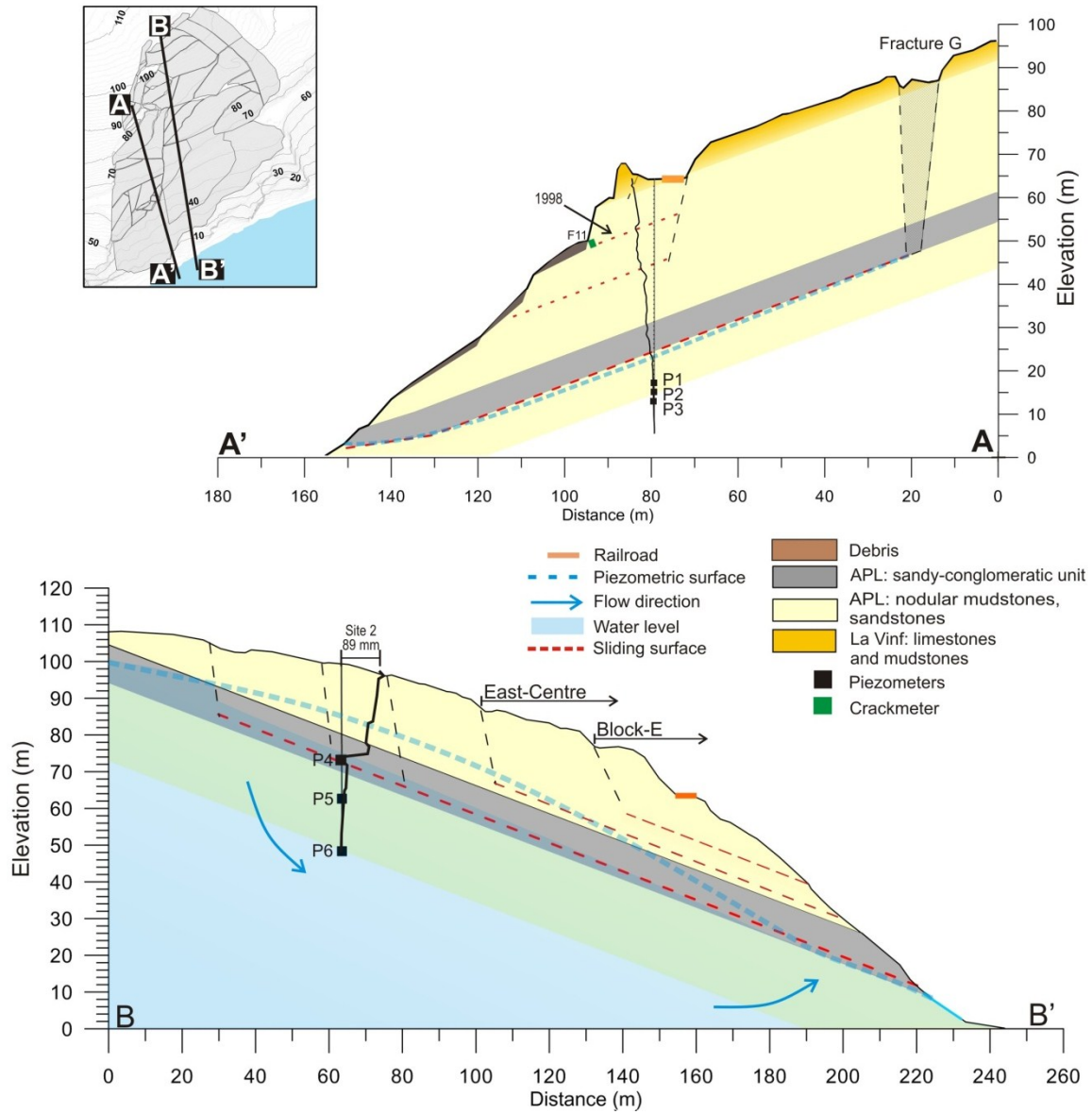


Figure 4-5 Cross-sections AA' and BB' locations are indicated in the top corner image. Cross-sections show the sliding surfaces, vertical profiles of displacements, piezometers locations and the water level. AA' shows the Petit-massif, while BB' shows East-Centre and Block-E sectors.

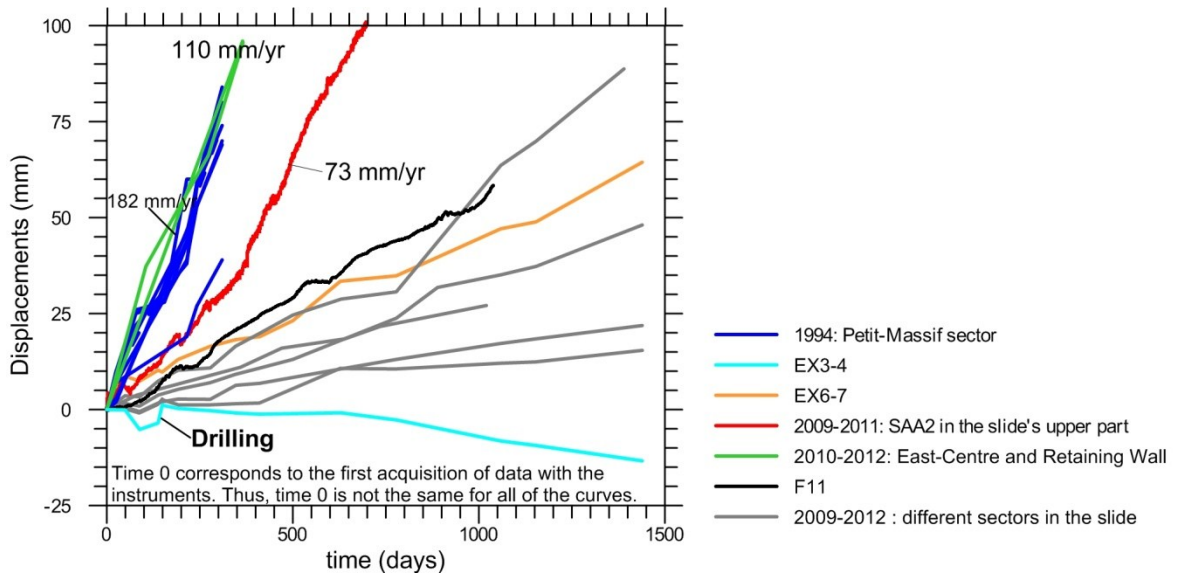


Figure 4-6 Displacement measurements: Blue curves are measurements taken in 1993-1994 and the other ones between 2009 and 2012. All reading sequences are starting at a time value of 0.



Figure 4-7 Examples of damage caused by the accumulation of displacements on the infrastructures and of the 1998 collapse event. A) Undermining of the railway ballast in an underlying fissure in February 2011. B) Deformation of the retaining wall and of the railway. C) Deformation in the retaining wall built in 1998 D) Newspaper cut showing the damaged railroad after the 1998 slide event (Le Soleil, 1998).

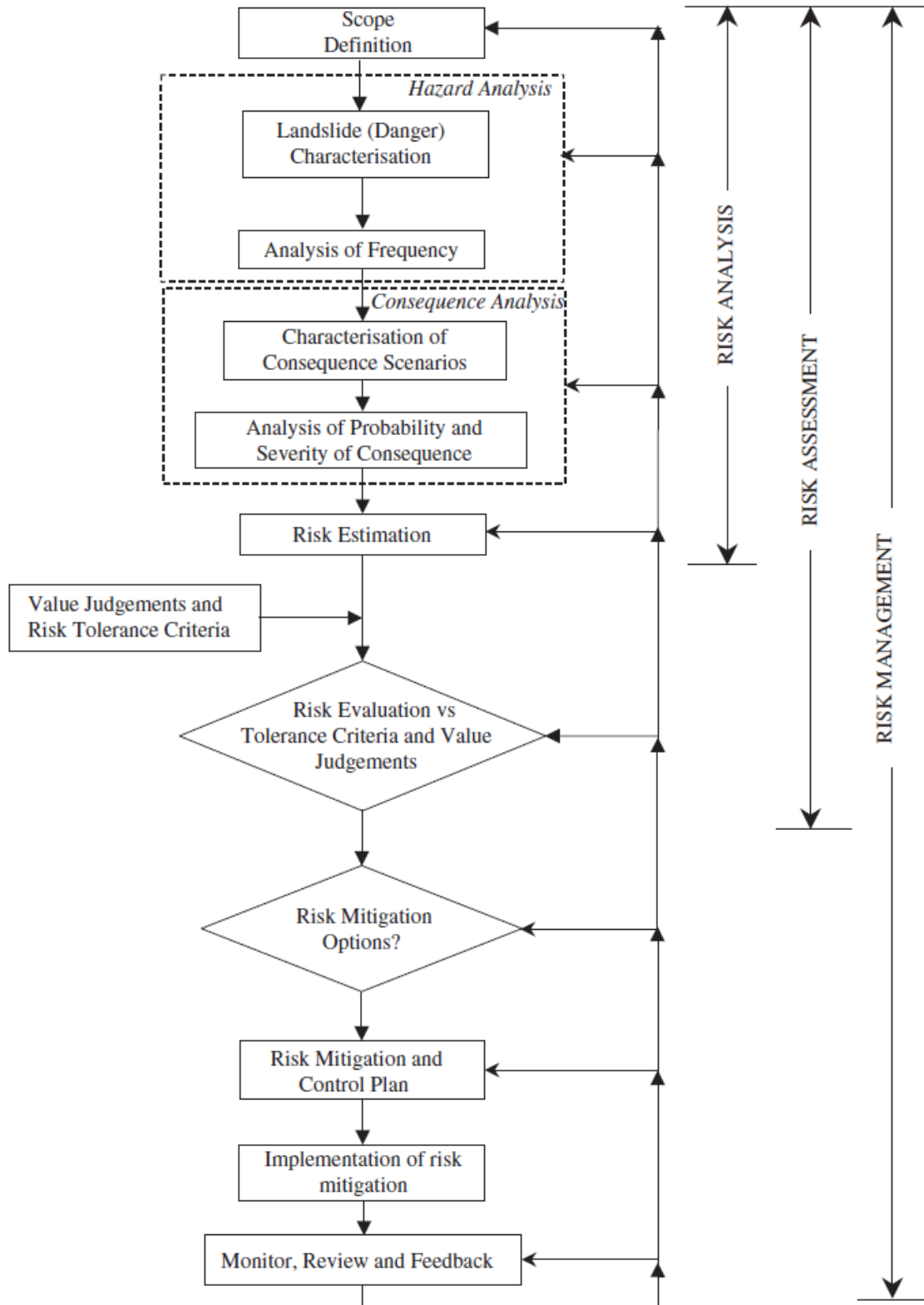
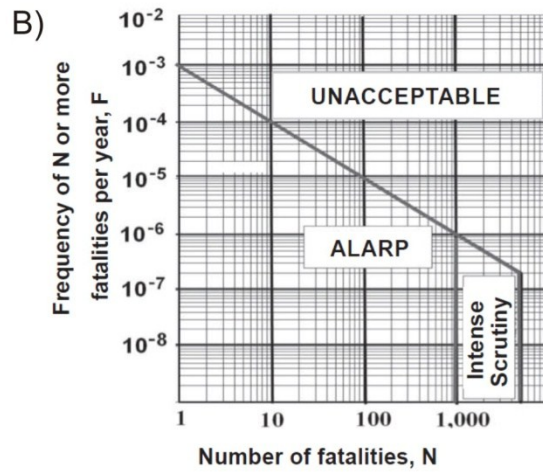
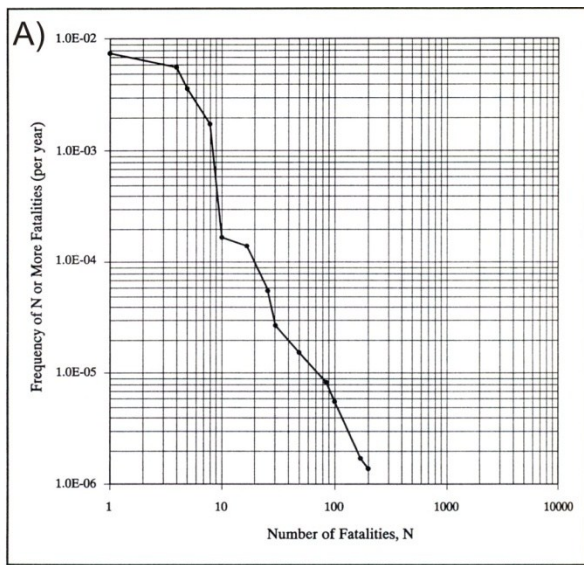


Figure 4-8 Flow chart of landslide risk management as proposed by Fell *et al.* (2005).



Note: The above societal risk criteria are to be used in conjunction with a reference natural hillside toe length of 500 m. Appropriate scaling of the risk criteria should be made where the actual toe length is greater than 500 m, see ERM (1998) for details.

Figure 4-9 A) Example of a cumulative frequency curve in a risk analysis of a road threaten per landslides presented by Wong (1997) and B) Societal risk tolerability criteria in Hong Kong presented in Ho and Ko (2009).

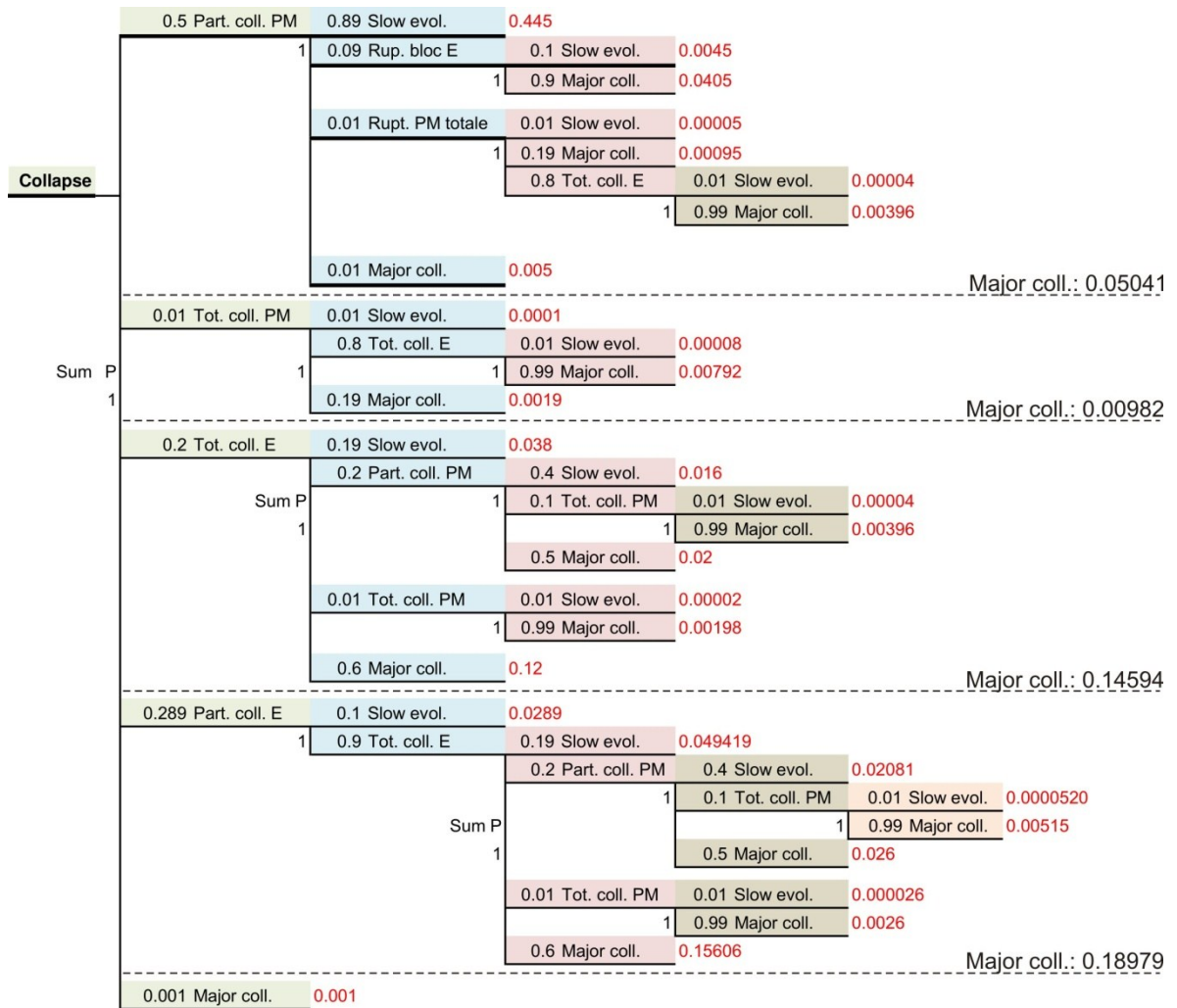


Figure 4-10 Event tree analysis to evaluate the domino effect. Every event is described in section 4.7.2. The sum of the joint probabilities (in red) leading to a major collapse are indicated in black for each of the five initial events.

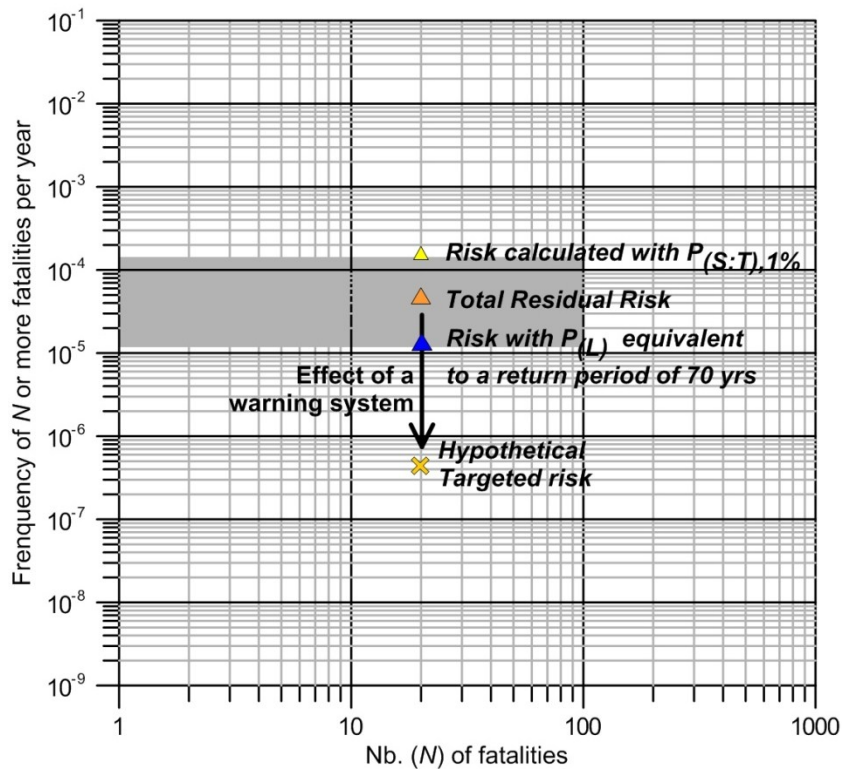


Figure 4-11 The grey zone presents the range of risk values computed in this study. The estimated residual risk, the risk considering that 1% of the time the train will not be able to stop if a danger occurs and the risk computed with a return period of 70 years are plotted for an arbitrary number of fatalities (N) of 20.

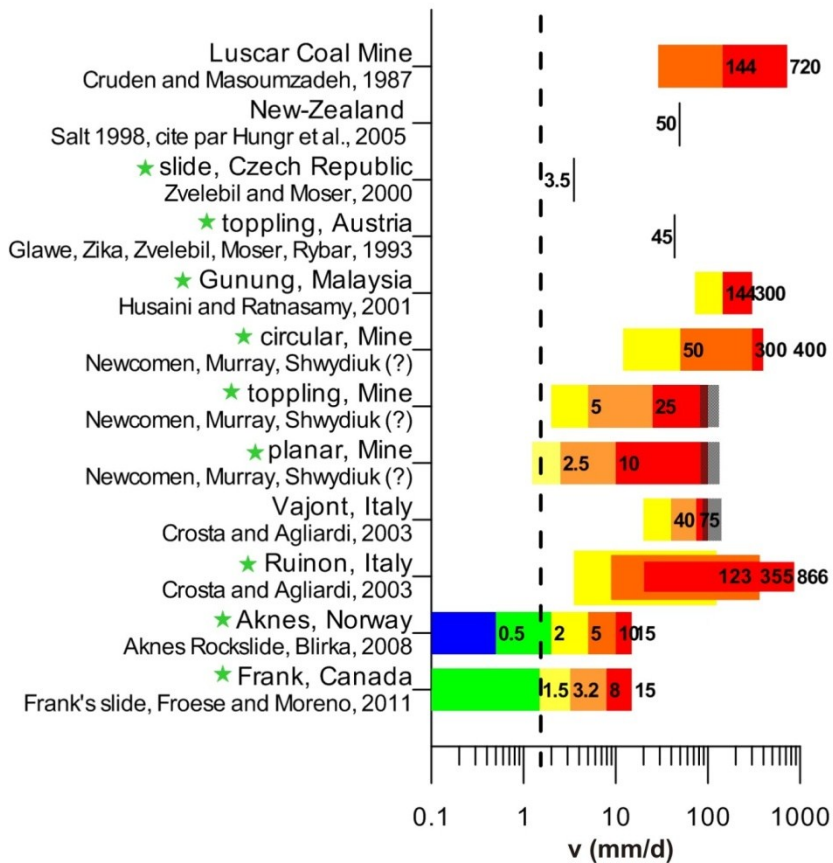


Figure 4-12 Proposed velocity based warning criteria found in the literature. The green stars show the criteria that were defined prior to brutal failure. In the vast majority of cases, the authors proposed intervals associated with different alert levels. The author associated colors to the values, even though some authors have not. Green and blue colors are used to represent situations considered normal, yellow is use for an increase activity, orange is a preoccupying situation and must be evaluated by an expert while red is the superior alert level associated with immediate actions. The red warning criteria were generally presented as “more than”. In the figure, the maximum values have been limited to facilitate presentation.

Conclusions (English version)

Les conclusions rédigées en français suivent la version anglaise.

The instrumentation of the Gascons rockslide was an excellent opportunity to document in details and for the first time the post-failure behaviour of an active rockslide in the sedimentary rocks of eastern Québec. Therefore, this research contributed in developing an expertise in rockslide instrumentation for the province of Québec. Moreover, now a unique set of data is available for the scientific community.

The detailed study of the kinematic behaviour of the Gascons rockslide provides general knowledge on rockslides undergoing very slow displacement and also helps to understand the mechanisms involved. The displacement analysis proved to be a good tool to provide data to explore potential scenarios of the slide. Critical sectors for the railroad were identified. It results into a better evaluation of the hazard and risk associated to an active rockslide. Moreover, this study will be an excellent tool for the railroad managers to design and evaluate mitigation avenues.

The findings of this thesis are grouped under the different research objectives which were (1) to characterize the rockslide, (2) to describe its kinematic behaviour, (3) to identify critical zones for the railroad by defining possible dangerous scenarios, (4) to undertake a risk analysis, and (5) to share the knowledge on the instrumentation of a rockslide and to discuss the contributions of different instruments to an early warning system. A set of recommendation follows the conclusions.

Geological and Hydrogeological Characterization

- The study showed that the Gascons rockslide is an asymmetrical wedge failure of 410 000 m³ with a bedding-controlled sliding surface. Discontinuity sets D and A are forming the lateral releasing surfaces.
- Conditions prevailing in the lower wedge corner are contributing to decrease the displacements on the main sliding surface. Firstly, active erosion processes are needed to provide additional displacement as the sliding surface daylight at sea level. Secondly, the syncline fold contributes in reducing the dip of the sliding surface and therefore act as a buttress.
- Because the displacements are limited by the conditions in the lower wedge corner, two intermediate sliding surfaces developed in the Petit-massif sector to accommodate more displacements. It results into a less constrained geometry. Moreover, East-Centre and Block-E sectors both slide on their own sliding surface. These intermediate rupture surfaces daylight high in the slope, their movements are not constrained, and thereby erosion is not needed to provoke displacement.

- A conceptual hydrogeological model based on piezometer records was proposed and the groundwater level variations were detailed. It was found that because the slide is well drained it prevents groundwater level to rise in the slide. Therefore, the groundwater level is generally below the main sliding surface. However, it was demonstrated that precipitation events and snow melt lead to increase groundwater pressures in fissures below the sliding surface. The pressure rises can reach up to 9 m in the uphill part of the slide, which means that the equivalent water column is well above the sliding surface in this sector during these events. The rise of pressure is always faster than the decrease.
- From the observations available, the slide would be active since about a hundred years. However, it was not possible to associate the failure to the railroad construction from available data, among others, caused by the lack of information on the blasting operation conducted during the construction limit.. On the other hand, the blasting required for the railroad construction could have contributed to create the intermediate sliding surfaces in the Petit-massif and of Block-E, but most likely had no effect on the main sliding surface which is located 40 m under the railroad.

Kinematic Characterization

- The Gascons rockslide is classified as a very slow rockslide in the classification proposed by Cruden and Varnes (1996) and has been active for the whole observation period; thereby we conclude that it is continuously moving with displacement rates ranging from 6 to 111 mm/yr.
- Based on the displacement rate spatial variations, the rockslide has been divided into sectors that are in good agreement with the ones interpreted from the morphological study. Of these sectors, East-Centre and Block-E are the fastest. The vertical downward displacements of Block-E are more important than those measured elsewhere in the slide which might indicate a different sliding mechanism. The H-Beam retaining wall is part of Block-E.
- It was shown that groundwater pressures influenced the displacement in the upper part of the slide, near Site 2. In the Petit-massif sector, some accelerating and decelerating phases can be related to events such as heavy rainfall and snowmelt, but it is not repeated for every similar events. Thereby, it was concluded that the role of water is complex and vary through the rockslide.
- The slide is sensitive to external factors. For example, the period from fall 2010 to winter 2011 was the most active period and it was the fall with the higher precipitations and with particularly erosive high tides.
- The annual patterns observed on the crackmeters were not successfully linked to external factors, except for crackmeter F11. The suggested hypothesis is that these patterns could reflect block

interactions resulting in changes of the direction of movement, creating an apparent difference in displacement rates.

- At first, the directions were supposed to be towards the south and mostly constant through time, but the results indicate a component of displacement towards the east, which can be explained by a rotation of the wedge, caused, in part, by the buttress created by the presence of the fault and fold in the lower wedge corner.

Risk Analysis and Definition of Potential Dangerous Scenarios

- The methodology proposed by Fell *et al.* (2005) was modified to be able to apply to an active rockslide.
- The hazard determination is divided in two parts: (1) the designation of a return period which is then transformed into an annual occurrence probability, and (2) the evaluation of relative occurrence probability for potential scenarios of a collapse event.
- The occurrence probability of a collapse event proposed is 0.05 equivalents to a 20-year return period.
- An event tree analysis was carried out to evaluate the potential domino effect of a partial collapse on the stability of the rest of the slide. This work led to the conclusion that Block-E is the most preoccupying sector for the railroad integrity, followed by a partial collapse of the Petit-massif. It was concluded that the acceleration of the overall slide is very unlikely.
- The risk without forecasting concept is proposed to represent the risk related to the situation that the slide occurs at the same time than the train is circulating in the zone. It is computed using the minimum value of the spatial temporal probability ($P_{(S,T)}$) without forecasting. This risk represents the lowest value that can be achieved doing monitoring only, thus without forecasting. It can be used as a reference value to compare the performance of various mitigation methods. In terms of risk mitigation, to reduce $P_{(S,T)}$ below this value, it is necessary to predict the danger. Then, if the slide is predicted, the train can be stopped before the slide occurs.

Instrumentation, Monitoring and Warning Systems

- The analysis concludes that warning system better adapted to the current situation of the Gascons rockslide should include the analysis of the data by an expert before a warning is issued. With that idea in mind, the suggested threshold values aim at warning the expert that the slide is evolving towards an unfavorable situation for the railroad.
- From the experience gained at Gascons, some general suggestions concerning instrumentation of a slow rockslide are listed hereunder:

- a) The instrumentation of a rockslide should provide sufficient spatial and temporal coverage to identify if some sectors are moving faster or if it moves as a whole, and if seasonal patterns or environmental forcing exist. The combination of manually measured and remotely monitored instruments turned out to be a convenient way to reach these objectives at Gascons.
- b) Reading of an instrument will become meaningful only when the total amplitude of the signal will be greater than the noise and errors. The slower the displacement, the longer it will take before a movement is observed by the instruments. In the Gascons case, the data became meaningful after six months for SAA2. It took almost a year before clear trends could be observed on all the crackmeters, SAA3 and inclinometer and about two years for the total station surveys. The study of post-failure behaviour of a very slow rockslide should ideally be carried on data sets longer than a few years.
- c) The integration of redundancy in the monitoring system is essential and allows data validation. In this study, the redundancy increased the confidence in values obtained of monitoring methods with higher uncertainties.
- d) Measuring absolute displacement is essential to characterize the overall kinematic of the slide. Relative displacements are only well interpreted once the overall kinematic is well understood. For example, closing of a fracture measured by a crackmeter must be integrated into a general displacement scheme to understand its real signification.

Recommendations

- As there should be no self-stabilisation of the rockslide, increasing deformation of the rails is forecasted, thus, inexorably, major works will become necessary to keep the railroad in function due either to cumulative displacements or to a major collapse event. In that perspective, a warning system is seen as a good mitigation method for short term planning only, such as on a 50 year period.
- It is suggested that the Gascons slides become a permanent observatory, as a longer data set will certainly help to validate certain hypotheses and to better understand rockslides with slow post-failure stages. Moreover, it will contribute in reducing the risk to the train.
- Manual readings must be carried on periodically. They bring important knowledge on displacements and on the evolution of the site, because they offer a good spatial coverage. These records are important both for the operation of the railroad and for future investigations of the rockslide.
- The same recommendation is true for PTA-InSAR monitoring, which is the best technique on site to measure three-dimensional displacement in the upper part of the slide.
- Increase the instrumentation of Block-E and East-Centre, maybe with one or two boreholes, to follow closely their displacements and locate their sliding surface. To monitor the displacement of Block-E

automatically, GPS could be considered or to increase the frequency of the PTA-InSAR monitoring. Furthermore, the replacement of the actual retaining wall by one that would be anchored upstream of Block-E sliding surface could be considered as an active mitigation mean to increase the resisting forces acting on Block-E.

- Numerical modelling of the Gascons rockslide would certainly be an interesting research axis to answer some questions that were raised in this thesis. This thesis should contain enough information to allow calibration of the chosen models.

Perspectives

This thesis presents a detailed characterization of an active very slow rockslide. It brings interesting observations which contributes to improve the theoretical understanding of the mechanisms associated with the post-failure stage. The detailed behaviour of groundwater levels in this environment provides crucial information to understand the role of water in the progression of an active rockslide. Hopefully, the experience gained at Gascons site will be useful for future instrumentations in similar terrains. Finally, this research is meaningful for the operation of the railroad, the risk management and the evaluation of mitigation methods

Conclusions (version française)

L'instrumentation du glissement de Gascons était une excellente opportunité de documenter pour la première fois et de façon très détaillée le comportement post-rupture d'un glissement actif dans les roches sédimentaires de l'est du Québec. Ainsi, cette recherche a permis d'apporter une certaine expertise en instrumentation de mouvements rocheux au Québec. De plus, une série de données unique est maintenant disponible pour la communauté scientifique.

L'étude détaillée du comportement cinématique du glissement de Gascons augmente les connaissances générales relatives à un massif soumis à des déplacements très lents et des mécanismes impliqués. L'analyse des déplacements s'est avérée être un bon outil pour explorer les scénarios d'évolution du glissement. Des secteurs critiques pour la voie ferrée ont été identifiés. Il en découle une meilleure évaluation de l'aléa et du risque associé à un tel glissement. De plus, cette étude sera une aide précieuse pour les propriétaires de la voie ferrée pour analyser les avenues de mitigation du risque.

Les conclusions de cette thèse sont regroupées ci-dessous selon les objectifs de recherche qui étaient de (1) caractériser le glissement, (2) de décrire son comportement cinématique, (3) de cerner les zones critiques pour le chemin de fer en proposant des scénarios de rupture et d'évaluer le risque et (4) de partager des

connaissances acquises sur l'instrumentation d'un massif rocheux et leur applicabilité pour le développement d'un système d'alerte. Une série de recommandations suit les conclusions.

Caractérisations géologique, géométrique et hydrogéologique

- L'étude a permis de déterminer que le glissement de Gascons est un dièdre asymétrique de 410 000 m³ et qu'il glisse sur le litage. Les familles de discontinuités D et A forment les surfaces de détachement.
- Les conditions du coin inférieur du dièdre contribuent à augmenter sa stabilité. Premièrement, une érosion active est nécessaire puisque la surface de rupture voit le jour au niveau de la plage. Deuxièmement, le pli synclinal aplani la surface de rupture et agit comme une butée.
- Puisque les déplacements sont limités au niveau du coin inférieur du dièdre, deux surfaces de rupture intermédiaires sont présentes dans le secteur du Petit-massif et permettent d'accommoder plus de déplacements. De plus, les secteurs Centre-Est et Bloc-E glissent chacun sur une surface de rupture qui leur est propre. Puisque ces surfaces de rupture intermédiaire voient le jour haut dans la pente, leur mouvement n'est pas contraint et l'érosion en pied de talus n'est pas nécessaire.
- L'étude des données piézométriques a permis de proposer un modèle conceptuel de l'hydrogéologie et de décrire les fluctuations de la nappe. Puisque le glissement est très drainant, ceci empêche la nappe phréatique de se former dans le glissement. Elle se situe donc généralement sous le niveau de la surface de rupture. Par contre, lors des précipitations et de la fonte des neiges, des pressions se construisent dans les fissures sous le glissement. Elles peuvent atteindre 9 m dans la partie amont du glissement, ce qui signifie que le sommet de la colonne d'eau est bien au-dessus de la surface de rupture dans ce secteur. L'augmentation des pressions est toujours plus rapide que leur diminution. Les données piézométriques ont aussi permis de caractériser l'écoulement dans le glissement.
- D'après l'ensemble de nos observations, le glissement serait actif depuis environ une centaine d'années. Par contre, il n'est pas possible avec les données disponibles d'associer la rupture à la construction de la voie ferrée, entre-autre due à l'absence d'information sur le dynamitage réalisé à l'époque de la construction. Toutefois, il semble peu probable que le dynamitage ait pu engendrer une surface de rupture située 40 m sous la voie ferrée. Par contre, le dynamitage a pu avoir un effet sur les surfaces de ruptures intermédiaires du Petit-massif et du Bloc-E, mais probablement pas sur la surface de rupture générale.

Caractérisation cinématique

- Le glissement de Gascons est classifié selon la nomenclature de Cruden et Varnes (1996) comme un glissement très lent et il est demeuré en mouvement sur toute la période d'observation, donc on conclut qu'il est continuellement en mouvement avec des taux de déplacements moyens de 6 à 111 mm/an.
- Les taux de déplacement varient spatialement, ce qui permet d'identifier des secteurs dans le glissement, qui concordent bien avec ceux déterminés de l'étude de la morphologie. De ces secteurs, ceux du Centre-Est et du Bloc-E se déplacent plus rapidement que les autres secteurs. De plus, les déplacements verticaux du Bloc-E sont plus importants que ceux mesurés dans le restant du glissement. Les données de déplacements ont montré que le mur de soutènement en H-Beam se déplace avec le Bloc-E.
- Il a été possible de démontrer que les pressions d'eaux influencent les déplacements dans le haut du glissement, à proximité du Site 2. Dans le secteur du Petit-massif, certaines accélérations et décélérations sont associées avec des événements tels que de fortes pluies ou la fonte des neiges, mais cela ne se répète pas pour chaque événement. Ainsi, le rôle de l'eau sur les déplacements est complexe et varie spatialement dans le glissement.
- Le glissement est sensible aux facteurs extérieurs, d'ailleurs l'automne 2010 et l'hiver 2011 a été la période la plus active et est associée aux précipitations importantes de l'automne 2010 ainsi qu'aux grandes marées.
- Il n'a pas été possible d'expliquer avec certitudes les cycles annuels de déplacements observés dans les données des fissuromètres, à l'exception du fissuromètre F11. L'hypothèse suggérée est que ces cycles pourraient refléter l'interaction entre les blocs et indiquer des changements de directions des déplacements.
- L'hypothèse à priori était que la direction des déplacements serait vers la mer et constante dans le temps. Toutefois, les résultats obtenus indiquent une composante des déplacements vers l'est, qui peut être expliquée par la rotation du dièdre, causée en partie par la butée créée par la faille et le plissement des strates sédimentaires dans le coin inférieur du dièdre.

L'analyse du risque et la définition des scénarios d'évolution du glissement

- L'approche proposée par Fell *et al.* (2005) a été adaptée pour être appliquée à un glissement actif.
- La détermination de l'aléa est divisée en deux parties : (1) l'évaluation d'une période de retour qui est ensuite transformée en probabilité d'occurrence annuelle et (2) la détermination d'une probabilité d'occurrence relative pour des scénarios de rupture prédéterminés.

- La probabilité d'occurrence $P_{(L)}$ proposée est de 0.05, équivalente à une période de retour de 20 ans.
- La construction d'un arbre d'évènement a permis d'évaluer l'effet domino des ruptures partielles sur la stabilité du glissement. Ce travail mène à la conclusion que le Bloc-E est le secteur le plus préoccupant pour la stabilité du chemin de fer, suivi par une rupture partielle du Petit-massif. Il a été conclu que l'accélération du glissement global est très improbable.
- Le concept du *risque sans prédiction* associé à la probabilité spatio-temporelle résiduelle ($P_{(S:T)}$) minimale sans prédiction est défini comme le risque correspondant au cas où le glissement se produit au même moment que le train y circule. Le risque sans prédication et sa $P_{(S:T)}$ représentent les valeurs minimales qui peuvent être atteintes en faisant seulement de la surveillance, *i.e.* d'autres méthodes de mitigations actives ou passives ne sont pas mises en place. Le risque sans prédiction est un point de référence qui aide à évaluer les performances qui doivent être atteintes par un système de surveillance. Pour diminuer le risque sous sa cette valeur, il faut prédire le danger. Ainsi, le train peut être arrêté avant que le glissement ne se produise.

Instrumentation, systèmes de surveillance et d'alerte

- L'analyse conclut que le système d'alarme le mieux adapté à la situation actuelle devrait inclure l'analyse des données de déplacement par un expert avant le déclenchement d'une alerte. En ce sens, les valeurs seuil sont suggérées de façon à avertir l'expert que le glissement évolue vers une situation défavorable pour la voie ferrée.
- Suite à l'expérience acquise à Gascons, quelques suggestions par rapport à l'instrumentation de glissements lents sont énumérées ci-dessous. Elles sont inspirées de difficultés et de réussites du système de Gascons.
 - a) La caractérisation adéquate d'un glissement nécessite des données avec une couverture spatiale ainsi qu'une résolution temporelle suffisantes pour être en mesure de déterminer s'il existe des secteurs plus rapides ou si le glissement se déplace comme un tout et s'il existe des changements saisonniers ou des changements reliés à des facteurs extérieurs, comme l'eau. Le couplage de données manuelles et automatiques est une bonne façon d'atteindre les objectifs en diminuant les coûts d'achats et d'entretien des instruments.
 - b) Un instrument ne détecte un mouvement significatif que lorsque son amplitude totale (le signal) dépasse le bruit. Plus le glissement est lent et plus il est long avant d'observer un mouvement général. Dans le cas de Gascons, les données sont devenues significatives après six mois pour le SAA2. Il a fallu près d'un an pour qu'une tendance claire se dégage des données de tous les fissuromètres, du SAA3 et de l'inclinomètre traditionnel et deux ans pour les données de la

station totale. L'étude d'un glissement lent doit idéalement être réalisée à partir de séries de données d'une durée de plusieurs années.

- c) L'intégration de redondance dans le système est un élément essentiel qui permet de valider les données et, dans le cadre de cette étude, d'augmenter la confiance dans les valeurs obtenues de méthodes de suivi dont les incertitudes sont plus grandes.
- d) Il est essentiel de mesurer des déplacements absolus pour connaître l'allure générale des déplacements. Les déplacements relatifs sont bien interprétés seulement une fois que le comportement général du glissement est bien compris. Par exemple, la fermeture d'une fissure mesurée par un fissuromètre doit être intégrée à un schéma de déplacement global du glissement pour en comprendre la signification.

Recommandations

- À la lumière des scénarios de rupture développés, il semble clair que si aucune méthode de mitigation active n'est mise en place, un évènement qui endommagera la voie ferrée va survenir. Dans cette optique, l'utilisation d'un système d'alerte comme moyen de mitigation semble uniquement valide dans le cadre d'une planification à court-terme (moins de 50 ans).
- Il est suggéré que le site de Gascons devienne un observatoire permanent, car une plus longue série temporelle permettra certainement de valider certaines hypothèses et d'acquérir de nouvelles connaissances sur la cinétique des glissements lents. De plus, cet observatoire va contribuer à diminuer le risque pour le train.
- Les lectures manuelles doivent être continuées. Elles apportent des connaissances importantes sur les déplacements et sur l'évolution du site, car elles offrent la meilleure couverture spatiale. Cette continuité est tout aussi essentielle du point de vue opérationnel que de celui de futures investigations et recherches.
- La même recommandation est aussi faite pour le suivi par PTA-InSAR qui est la meilleure technique sur le site pour avoir les déplacements tridimensionnels dans le secteur amont du glissement.
- Il est recommandé d'instrumenter davantage le Bloc-E et le Centre-Est, possiblement en réalisant un ou deux forages, afin de discerner avec certitude la profondeur de la surface de glissement et de suivre de près leurs déplacements et ceux des murs de soutènement. Un suivi par GPS pourrait être considéré pour le Bloc-E, ou encore d'augmenter la fréquence du suivi par PTA-InSAR. D'ailleurs, le remplacement du mur de soutènement actuel par un mur qui irait s'ancrer en amont de la surface de

rupture du Bloc-E pourrait être envisagé comme moyen de mitigation active afin d'augmenter la stabilité du Bloc-E.

- La modélisation numérique du glissement de Gascons serait certainement un axe de recherche intéressant pour permettre de répondre à certaines questions soulevées dans cette thèse. L'étude présentée dans cette thèse devrait permettre de calibrer les divers modèles.

Perspectives

Cette étude présente en détail le cas d'un glissement rocheux actif très lent. Elle apporte des observations qui contribuent à améliorer la compréhension théorique des mécanismes de rupture et des instabilités dans le domaine de la post-rupture. Le comportement détaillé des pressions d'eau dans un glissement rocheux très lent et hautement fracturé apporte des informations cruciales à la compréhension du rôle de l'eau dans la progression d'une instabilité active. Les comportements observés à Gascons seront utiles pour le design de futurs sites d'instrumentation dans des terrains similaires. Enfin, cette recherche est utile du point de vue opérationnel pour la voie ferrée, pour la gestion du risque et pour l'évaluation de méthodes de mitigation.

Références

- Agliardi, F., Crosta, G., Sosio, R., Rivolta, C. et Mannucci, G., 2013. In Situ and Remote Long Term Real-Time Monitoring of a Large Alpine Rock Slide, *Éditeurs: C. Margottini, P. Canuti, et K. Sassa, Landslide Science and Practice*. Springer Berlin Heidelberg, pp. 415-421.
- Barla, G., Antolini, F., Barla, M., Mensi, E. et Piovano, G., 2010. Monitoring of the Beauregard landslide (Aosta Valley, Italy) using advanced and conventional techniques. *Engineering Geology*, 116(3-4), pp. 218-235.
- Baecher, G. B. et Christian, J. T., 2003. *Reliability and Statistics in Geotechnical Engineering*: John Wiley & Sons
- Binet, S., Mudry, J., Scavia, C., Campus, S., Bertrand, C., et Guglielmi, Y., 2007. In situ characterization of flows in a fractured unstable slope. *Geomorphology*, 86(1-2), pp. 193-203.
- Blikra, L. et Kristensen, L., 2013. Monitoring Concepts and Requirements for Large Rockslides in Norway, *Éditeurs: C. Margottini, P. Canuti, et K. Sassa, Landslide Science and Practice*. Springer Berlin Heidelberg, pp. 193-200.
- Blikra, L. H., 2008. The Aknes rockslide; monitoring, threshold values and early-warning. *Éditeurs: Z. Chen, J. Zhang, Z. Li, F. Wu, et K. Ho, Présenté à 10th International Symposium on Landslides and Engineered Slopes, Xi'an, China*, pp. 1089-1094.
- Bourque, P.-A. et Lachambre, G., 1980. *Stratigraphie du Silurien et du Dévonien basal du sud de la Gaspésie*. Direction de la géologie, Direction générale de la recherche géologique et minérale, Ministère de l'énergie et des ressources du Québec, Québec, p. 123.
- Brideau, M.-A., Sturzenegger, M., Stead, D., Jaboyedoff, M., Lawrence, M., Roberts, N., Ward, B., Millard, T. et Clague, J., 2012. Stability analysis of the 2007 Chehalis lake landslide based on long-range terrestrial photogrammetry and airborne LiDAR data. *Landslides*, 9(1), pp. 75-91.
- Brodu, N. et Lague, D., 2012. 3D terrestrial lidar data classification of complex natural scenes using a multi-scale dimensionality criterion: Applications in geomorphology. *ISPRS Journal of Photogrammetry and Remote Sensing*, 68(0), pp. 121-134.
- Bunce, C. M., Cruden, D. M. et Morgenstern, N. R. 1997. Assessment of the hazard from rock fall on a highway. *Canadian Geotechnical Journal*, 34(3), pp. 344-356.
- Canadian Standard Association (CSA), 1997. Risk Management: Guidelines for Decision-Makers, Ontario, Canada, 46p.
- Canadian Standard Association (CSA), 2011. Implementation Guide to CSA/CAN-ISO 31000, Risk Management - Principles and Guidelines, 47p.
- Cloutier, C., Locat, J., Lord, P.-É. et Couture, R., 2010. Caractérisation des instabilités côtières dans le secteur de Port-Daniel-Gascons, Gaspésie, Québec. *63rd Canadian Geotechnical Conference and 6th Canadian Permafrost Conference*, Calgary, AB, pp. 71-79.
- Cloutier, C., Locat, J., Couture, R., et Lord, P.-É., 2011. Analysis of one year of monitoring data for the active Gascons rockslide, Gaspé Peninsula, Québec. *5th Canadian Conference on Geotechnique and Natural Hazards*, Kelowna, BC, 8p.
- Cloutier, C., Locat, J., Lord, P.-É., Couture, R. et Jaboyedoff, M., 2012. Kinematic considerations of the Gascons rockslide, Québec (Gaspésie), Canada. *Éditeurs: E. Eberhardt, C. Froese, A. K. Turner, et S. Leroueil, 11th International Symposium on Landslides and 2nd North American Symposium on Landslides*, Banff, pp. 1264-1270.

- Cloutier, C., Lord, P.-É. et Locat, J., 2009. *Rapport 01: Données historiques et récentes*. LERN-GASCONS-09-02 Rapport technique, Université Laval, Québec. 406p.
- Corominas, J., Copons, R., Moya, J., Vilaplana, J., Altimir, J. et Amigó, J., 2005. Quantitative assessment of the residual risk in a rockfall protected area. *Landslides*, 2(4), pp. 343-357.
- Corominas, J., Moya, J., Ledesma, A., Lloret, A. et Gili, J., 2005. Prediction of ground displacements and velocities from groundwater level changes at the Vallcebre landslide (Eastern Pyrenees, Spain). *Landslides*, 2(2), pp. 83-96.
- Corsini, A., Pasuto, A., Soldati, M. et Zannoni, A., 2005. Field monitoring of the Corvara landslide (Dolomites, Italy) and its relevance for hazard assessment. *Geomorphology*, 66(1-4), pp. 149-165.
- Cotecchia, V., 2006. The Second Hans Cloos Lecture. Experience drawn from the great Ancona landslide of 1982. *Bulletin of Engineering Geology and the Environment*, 65(1), pp. 1-41.
- Couture, R., Charbonneau, F., Murnaghan, K., Singhroy, V., Locat, J. et Lord, P.-É., 2010. PTA-InSAR rock slope monitoring at the Gascons site, Gaspé Peninsula, Quebec. *63rd Canadian Geotechnical Conference and 6th Canadian Permafrost Conference*, Calgary, AB, 8p.
- Couture, R., Charbonneau, F., Singhroy, V., Murnaghan, K., Drouin, H., Locat, J., Lord, P.-É. et Cloutier, C., 2011. PTA-InSAR rock slope monitoring at the Gascons site, Gaspé Peninsula Quebec: Preliminary results. *5th Canadian Conference on Geotechnique and Natural Hazards*, Kelowna, BC, 8p.
- Crosta, G. B. et Agliardi, F., 2002. How to obtain alert velocity thresholds for large rockslides. *Physics and Chemistry of the Earth, Parts A/B/C*, 27(36), pp. 1557-1565.
- Crosta, G. B. et Agliardi, F., 2003. Failure forecast for large rock slides by surface displacement measurements. *Canadian Geotechnical Journal*, 40(1), pp. 176-191.
- Crosta, G. B., di Prisco, C., Frattini, P., Frigerio, G., Castellanza, R., et Agliardi, F., 2013. Chasing a complete understanding of the triggering mechanisms of a large rapidly evolving rockslide. *Landslides*, pp. 1-18.
- Cruden, D. M. et Masoumzadeh, S., 1987. Accelerating creep of the slopes of a coal mine. *Rock mechanics and rock engineering*, 20(2), pp. 123-135.
- Cruden, D. M. et Varnes, D. J., 1996. Landslide types and processes, in A. K. Turner et R. L. Schuster, (eds.), *Landslides : Investigation and mitigation Transportation Research Board Special Report 247*. Washington, D.C.: National Academy Press, pp. 36-71.
- Dai, F. C., Lee, C. F. et Ngai, Y. Y., 2002. Landslide risk assessment and management: an overview. *Engineering Geology*, 64(1), pp 65-87.
- Danisch, L., Patterson, T., Cloutier, C., Locat, J., Lord, P.-É. et Bond, J., 2010. Integration of SAA technology for coastal rock slope movement monitoring at Gascons, Gaspé Peninsula, Québec, Canada. *63rd Canadian Geotechnical Conference and 6th Canadian Permafrost Conference*, Calgary (AB)
- Derron, M.-H., Jaboyedoff, M. et Blikra, L. H., 2005. Preliminary assessment of rockslide and rockfall hazards using a DEM (Oppstadhornet, Norway). *Natural Hazards and Earth System Science*, 5(2), pp. 285-292.
- Eberhardt, E. 2008. Twenty-ninth Canadian Geotechnical Colloquium: The role of advanced numerical methods and geotechnical field measurements in understanding complex deep-seated rock slope failure mechanisms. *Canadian Geotechnical Journal*, 45(4), pp. 484-510.

- Eberhardt, E., Bonzanigo, L. et Loew, S., 2007. Long-term investigation of a deep-seated creeping landslide in crystalline rock. Part II. Mitigation measures and numerical modelling of deep drainage at Campo Vallemaggia. *Canadian Geotechnical Journal*, 44(10), 1181-1199.
- Eberhardt, E., Stead, D., et Coggan, J. S., 2004. Numerical analysis of initiation and progressive failure in natural rock slopes—the 1991 Randa rockslide. *International Journal of Rock Mechanics and Mining Sciences*, 41(1), pp. 69-87.
- El Bedoui, S., Guglielmi, Y., Lebourg, T. et Pérez, J.-L., 2009. Deep-seated failure propagation in a fractured rock slope over 10,000 years: The La Clapière slope, the south-eastern French Alps. *Geomorphology*, 105(3–4), pp. 232-238.
- Esri Inc., 2009. ArcGIS v. 9.3.1, Toronto.
- Faillietaz, J., Sornette, D. et Funk, M., 2010. Gravity-driven instabilities: Interplay between state- and velocity-dependent frictional sliding and stress corrosion damage cracking. *Journal of Geophysical Research*, 115(B3), B03409.
- Fell, R., Ho, K. K. S., Lacasse, S. et Leroi, E., 2005. A framework for landslide risk assessment and management, *Éditeurs: O. Hungr, R. Fell, R. Couture, et E. Eberhardt, Landslide Risk Management*. Taylor and Francis, pp. 3-25.
- Ferretti, A., Prati, C. et Rocca, F., 2001. Permanent scatterers in SAR interferometry. *Geoscience and Remote Sensing, IEEE Transactions on*, 39(1), pp. 8-20.
- Finlay, P. J., 1996. *The Risk Assessment of Slopes*, Ph.D. Thesis, School of Civil Engineering, University of New South Wales.
- Froese, C. et Moreno, F., 2011. Structure and components for the emergency response and warning system on Turtle Mountain, Alberta, Canada. *Natural Hazards*, pp. 1-24.
- Froese, C. R., Moreno, F., Jaboyedoff, M. et Cruden, D. M., 2009. 25 years of movement monitoring on South Peak, Turtle Mountain: understanding the hazard. *Canadian Geotechnical Journal*, 46(3), pp. 256-269.
- Froude, M., Jane., 2011. *Capturing and characterising pre-failure strain on failing slopes*, M. Sc Thesis, Durham University. Available at Durham E-Theses Online: <http://etheses.dur.ac.uk/3272/>. 200p.
- Fukuzono, T., 1985. A New Method for Predicting the Failure Time of a Slope. *Fourth International Conference and Field Workshop on Landslides*, Tokyo, Japan pp. 145-150.
- Ganerød, G. V., Grøneng, G., Rønning, J. S., Dalsegg, E., Elvebakk, H., Tønnesen, J. F., Kvelde, V., Eiken, T., Blikra, L. H., et Braathen, A., 2008. Geological model of the Åknes rockslide, western Norway. *Engineering Geology*, 102(1–2), pp. 1-18.
- Geotechnical Engineering Office, 1998. *Landslides and Boulder Falls from Natural Terrain: Interim Risk Guidelines*. Geotechnical Engineering Office, The Government of the Hong Kong Special Administrative Region
- Gigli, G., Fanti, R., Canuti, P. et Casagli, N., 2011. Integration of advanced monitoring and numerical modeling techniques for the complete risk scenario analysis of rockslides: The case of Mt. Beni (Florence, Italy). *Engineering Geology*, 120(1–4), pp. 48-59.
- Girardeau-Montaut, D., 2012. CloudCompare, Grenoble.
- Gischig, V., Moore, J. R., Evans, K. F. et Loew, S., 2010. Seasonal changes of rock mass deformation rate due to thermal effect at the Randa rock slope instability, Switzerland, *Geologically Active*. London: Taylor & Francis Group, pp. 179-186.

- Glade, T. et Anderson, M., 2005. Landslide Hazard and Risk: Issues, Concepts and Approach, *Éditeurs: T. Glade, M. Anderson, et M. J. Crozier, Landslide Hazard and Risk*. Chichester, West Sussex, England: John Wiley & Sons, Ltd, pp. 1-40.
- Glastonbury, J. et Fell, R., 2008. A decision analysis framework for the assessment of likely post-failure velocity of translational and compound natural rock slope landslides *Canadian Geotechnical Journal*, 45(3), pp. 329-350.
- Grøneng, G., Christiansen, H., Nilsen, B. et Blikra, L., 2011. Meteorological effects on seasonal displacements of the Åknes rockslide, western Norway. *Landslides*, 8(1), pp. 1-15.
- Grøneng, G., Lu, M., Nilsen, B. et Jenssen, A. K., 2010. Modelling of time-dependent behavior of the basal sliding surface of the Åknes rockslide area in western Norway. *Engineering Geology*, 114(3-4), pp. 414-422.
- Ho, K. K. S. et Ko, F. W. Y., 2009. Application of quantified risk analysis in landslide risk management practice: Hong Kong experience. *Georisk: Assessment and Management of Risk for Engineered Systems and Geohazards*, 3(3), pp. 134-146.
- Hoek, E. et Bray, J. W., 1981. *Rock Slope Engineering*, London: The Institution of Mining and Metallurgy. 358p.
- Helmstetter, A. et Garambois, S., 2010. Seismic monitoring of Séchilienne rockslide (French Alps): Analysis of seismic signals and their correlation with rainfalls. *Journal of Geophysical Research: Earth Surface*, 115(F3), F03016.
- Helmstetter, A., Sornette, D., Grasso, J. R., Andersen, J. V., Gluzman, S., et Pisarenko, V., 2004. Slider block friction model for landslides: Application to Vaiont and La Clapière landslides. *Journal of Geophysical Research*, 109(B2), B02409.
- Hungr, O. et Amann, F., 2011. Limit equilibrium of asymmetric laterally constrained rockslides. *International Journal of Rock Mechanics and Mining Sciences*, 48(5), pp. 748-758.
- Hungr, O. et Wong, H., 2007. Landslide risk acceptability criteria: are FN plots objective. *Geotechnical News*, 25(4), 47p.
- Innovmetric, 2011. Polyworks v12, ImAlign and ImSurvey, Québec.
- ISRM, International Society for Rock Mechanics, 1978. Commission on Standardization of Laboratory and Field Tests : Suggested Methods for the Quantitative description of Discontinuities in Rock Masses. *International Journal of Rock Mechanics, Mining Sciences and Geomechanics Abstracts*, 15, pp. 319-368.
- IUGS Working Group on Landslides, 1997. Quantitative Risk Assessment for Slopes and Landslides - The State of the Art. D. M. Cruden et R. Fell, *Presented at The International Workshop on Landslide Risk Assessment*, Honolulu, Hawaii, pp. 3-12.
- Jaboyedoff, M., 2002. International Independent Center of Climate Change Impact on Natural Risk Analysis in Mountainous Areas, Lausanne.
- Jaboyedoff, M., Couture, R. et Locat, P., 2009. Structural analysis of Turtle Mountain (Alberta) using digital elevation model: Toward a progressive failure. *Geomorphology*, 103(1), pp. 5-16.
- Jaboyedoff, M., Oppikofer, T., Abellán, A., Derron, M.-H., Loye, A., Metzger, R. et Pedrazzini, A. 2012. Use of LIDAR in landslide investigations: a review. *Natural Hazards*, 61(1), pp. 5-28.
- Journeaux, N., Bédard et Associés, 2000. *Rapport S-00-1133, Évaluation du site de l'affaissement P.M. 30.5 (Gascons est) Ligne Matapédia-Gaspé*. Journeaux, Bédard et associés, Inc., Dorval, Qc. 13p.

- Journeaux, N., Bédard et Associés, 2003a. *Rapport S-02-1315, Rapport de stabilisation, mouvement des fissures ouvertes, éboulement de roches, Gascon au P.M. 30.5 S/D Chandler*. Journeaux, Bédard et associés, Inc., Dorval, Qc. 12p.
- Journeaux, N., Bédard et Associé, 2003b. *Rapport S-03-1460, Inspection des zones d'instabilité Mile 30.6 Chandler ouest et mile 96.28 Chandler est*. Journeaux, Bédard et associés, Inc., Dorval, Qc. 28p.
- Kalenchuk, K., 2010. *Multi-Dimensional Analysis of Large, Complex Slope Instability*, Queen's University, Kingston. 449p.
- Kalenchuk, K., Hutchinson, D. et Diederichs, M., 2009. Application of spatial prediction techniques to defining three-dimensional landslide shear surface geometry. *Landslides*, 6(4), pp. 321-333.
- Kristensen, L. et Blikra, L., 2013. Monitoring Displacement on the Mannen Rockslide in Western Norway, *Éditeurs: C. Margottini, P. Canuti, et K. Sassa, Landslide Science and Practice*. Springer Berlin Heidelberg, pp. 251-256.
- Lacasse, S., 2008. Event Tree Analysis of Aknes Rock Slide Hazard. D. P. J. Locat, D. Turmel, D. Demers, S. Leroueil, *4th Canadian Conference on Geohazards: From Causes to Management*, Québec 594p.
- Lato, M., Diederichs, M. et Hutchinson, D. J., 2010. Bias Correction for View-limited Lidar Scanning of Rock Outcrops for Structural Characterization. *Rock mechanics and rock engineering*, 43(5), pp. 615-628.
- Lato, M., Diederichs, M., Hutchinson, D. J. et Harrap, R., 2012. Evaluating roadside rockmasses for rockfall hazards using LiDAR data: optimizing data collection and processing protocols. *Natural Hazards*, 60(3), pp. 831-864.
- Leone, F., Aste, J. P. et Leroi, E., 1996. Vulnerability assessment of elements exposed to mass-moving: working toward a better risk perception. *Éditeurs: K. Senneset, Seventh International Symposium on Landslides*, Trondheim, Norway pp. 263-269.
- Leroueil, S., Vaunat, J., Picarelli, L., Locat, J., Lee, H. et Faure, R., 1996. Geotechnical characterization of slope movements. *Éditeurs: K. Senneset, Seventh International Symposium on Landslides*, Trondheim, pp. 53-74.
- Li, Z., Nadim, F., Huang, H., Uzielli, M. et Lacasse, S., 2010. Quantitative vulnerability estimation for scenario-based landslide hazards. *Landslides*, 7(2), pp. 125-134.
- Locat, J., Cloutier, C., Lord, P.-É., Therrien, P., Jacob, C., Nadeau, A., Hébert, D., Couture, R., Charbonneau, F., Singhroy, V., Murnaghan, K., Danisch, L., Jaboyedoff, M., Pedrazzini, A. et Gravel, S., 2010. An integrated mass movement monitoring system for rockslide hazard assessment at Gascons, Gaspé Peninsula, Québec: An Overview. *63rd Canadian Geotechnical Conference and 6th Canadian Permafrost Conference*, Calgary, AB, 8p.
- Locat, J., Cloutier, C., et Jaboyedoff, M., 2013. A risk evaluation approach for an active rock slide: the Gascons coastal rock slide, Québec. *66^e Conférence annuelle canadienne de géotechnique et la 11^e conférence conjointe SCG/AIH-SNC, GeoMontréal*, Montréal, Qc, 8p.
- Locat, J. et Couture, R., 1995a. Analyse de la stabilité d'un talus rocheux à Anse-aux-Gascons, Gaspésie, Québec, *48^e Conférence canadienne de géotechnique*, Vancouver, 9p.
- Locat, J. et Couture, R., 1995b. *Rapport final : Analyse de la stabilité du massif rocheux au millage 30.5, Division de Chandler, Anse-aux-Gascons, Gaspésie, Québec*. Groupe de recherche en Environnement et en Géomécanique, Université Laval, Québec. 95p.
- Lord, P.-É., 2011. *Analyse des déplacements du glissement rocheux de Gascons, Gaspésie, Québec*, Thèse M.Sc, Université Laval, Québec. 290p.

- Lord, P.-É., Locat, J., Couture, R., Charbonneau, F., Cloutier, C., Singhroy, V. et Pedrazzini, A., 2010. Analyse des déplacements du glissement de Gascons, Gaspésie, par couplage d'observations aéroportées et terrestres. *63rd Canadian Geotechnical Conference and 6th Canadian Permafrost Conference*, Calgary, AB, 8p.
- Masoumi, H. et Douglas, K. J. 2010. Review of Rock Slope Displacement-Time Curve and Failure Prediction Models, *Éditeur: J. Brune, Extracting the Science: A Century of Mining Research*. Society for Mining Metallurgy, pp. 247-259.
- McKenna, G. T., 1995. Grouted-in installation of piezometers in boreholes. *Canadian Geotechnical Journal*, 32(2), pp. 355-363.
- Mikkelsen, E. P. et Green, G. E., 2003. Piezometers in Fully Grouted Boreholes. F. Myrvoll, *Symposium on Field Measurements in Geomechanics*, Oslo, Norway pp. 545-554.
- Mufundirwa, A., Fujii, Y. et Kodama, J., 2010. A new practical method for prediction of geomechanical failure-time. *International Journal of Rock Mechanics and Mining Sciences*, 47(7), pp. 1079-1090.
- Nordvik, T., Blikra, L. H., Nyrnes, E. et Derron, M.-H., 2010. Statistical analysis of seasonal displacements at the Nordnes rockslide, northern Norway. *Engineering Geology*, 114(3-4), pp. 228-237.
- Nordvik, T. et Nyrnes, E., 2009. Statistical analysis of surface displacements - an example from the Åknes rockslide, western Norway. *Natural Hazards and Earth System Sciences*, 9(3), pp. 713-724.
- Norrish, N. I. et Wyllie, D. C., 1996. Rock Slope Stability Analysis, *Éditeurs: K. A. Turner et R. L. Schuster, Landslides, Investigation and Mitigation. Transportation Research Board, Special Report 247*. Washington, D.C.: National Academy Press, pp. 391-424.
- Oppikofer, T., Jaboyedoff, M., et Keusen, H.-R., 2008. Collapse at the eastern Eiger flank in the Swiss Alps. *Nature Geoscience*, 1(8), pp. 531-535.
- Oppikofer, T., Jaboyedoff, M., Pedrazzini, A., Derron, M.-H. et Blikra, L. H., 2011. Detailed DEM analysis of a rockslide scar to characterize the basal sliding surface of active rockslides. *Journal of Geophysical Research: Earth Surface*, 116(F2), F02016.
- Optech, 2006. Ilris 3D Scanner, Toronto.
- Pedrazzini, A., 2012. *Characterization of gravitational rock slope deformations at different spatial scales based on field, remote sensing and numerical approaches*, Université de Lausanne, Lausanne. 348p.
- Petley, D.N., Higuchi, T., Dunning, S.A., Rosser, N.J., Petley, D.J., Bulmer, M.H.K. et Carey, K.J., 2005. *A new model for the development of movement in progressive landslides*, *Éditeurs: O. Hungr et al.*, Amsterdam: A.A. Balkema.
- Picarelli, L., 2007. Considerations about the Mechanics of Slow Active Landslides in Clay, *Éditeurs: K. Sassa, H. Fukuoka, F. Wang et G. Wang, Progress in Landslide Science*. Springer Berlin Heidelberg, pp. 27-45.
- Raetzo, H., Lateltin, O., Bollinger, D. et Tripet, J., 2002. Hazard assessment in Switzerland – Codes of Practice for mass movements. *Bulletin of Engineering Geology and the Environment*, 61(3), pp. 263-268.
- Remondo, J., Bonachea, J. et Cendrero, A., 2008. Quantitative landslide risk assessment and mapping on the basis of recent occurrences. *Geomorphology*, 94(3-4), pp. 496-507.
- Rocscience, 2005. Dips 5.1, Toronto, Stereonet Analysis program.
- Rocscience, 2003, Swedge 5.0, Toronto, 3D Surface Wedge Analysis for Slopes and Swedge Theory Manual.

- Roberge, C., 1995. *Projet de fin d'étude, Essai à la boîte de cisaillement*. Rapport présenté à Jacques Locat et Réjean Couture, Université Laval. 38p.
- Rondeau, M., 2010. Centre interdisciplinaire de développement en cartographie des océans, Rimousky.
- Rose, N.D. et Hungr, O., 2007. Forecasting potential rock slope failure in open pit mines using the inverse-velocity method. *International Journal of Rock Mechanics and Mining Sciences*, 44(2), pp. 308-320.
- Saito, M., 1969. Forecasting time of slope failure by tertiary creep, *Seventh international conference on soil mechanics and foundation engineering*, Mexico city, pp. 677 - 683.
- Song, Q., Liu, D. et Wu, Y., 2007. Study on acceptable and tolerable risk criteria for landslide hazards in the Mainland of China. *Proceeding of the First international symposium on geotechnical safety & risk*, pp. 363-374.
- Sornette, D., Helmstetter, A., Andersen, J. V., Gluzman, S., Grasso, J.R. et Pisarenko, V., 2004. Towards landslide predictions: two case studies. *Physica A: Statistical Mechanics and its Applications*, 338(3-4), pp. 605-632.
- Stead, D. et Eberhardt, E., 2013. Understanding the Mechanics of Large Landslides. R. Genevois et A. Prestininzi, *Presented at International Conference on Vajont - 1963-2013 Thoughts and analyses after 50 years since the catastrophic landslide*, Padova, Italy, pp. 85-112.
- Stead, D., Eberhardt, E. et Coggan, J.S., 2006. Developments in the characterization of complex rock slope deformation and failure using numerical modelling techniques. *Engineering Geology*, 83(1-3), pp. 217-235.
- Strozzi, T., Farina, P., Corsini, A., Ambrosi, C., Thüring, M., Zilger, J., Wiesmann, A., Wegmüller, U. Et Werner, C., 2005. Survey and monitoring of landslide displacements by means of L-band satellite SAR interferometry. *Landslides*, 2(3), pp. 193-201.
- Sturzenegger, M. et Stead, D., 2009. Quantifying discontinuity orientation and persistence on high mountain rock slopes and large landslides using terrestrial remote sensing techniques. *Nat. Hazards Earth Syst. Sci.*, 9(2), pp. 267-287.
- Sturzenegger, M. et Stead, D., 2012. The Palliser Rockslide, Canadian Rocky Mountains: Characterization and modeling of a stepped failure surface. *Geomorphology*, 138(1), pp. 145-161.
- Syvitski, P.M.J., 1992. Marine Geology of Baie des Chaleurs. *Géographie physique et Quaternaire*, 46(3), pp. 331-348.
- Terr@num, 2011. Coltop 3D, Lausanne, Designed for the interactive analysis of orientation of airborne and terrestrial LiDAR data and digital elevation models (DEM) at local and regional scale.
- Van Westen, C., Van Asch, T. W. et Soeters, R., 2006. Landslide hazard and risk zonation—why is it still so difficult? *Bulletin of Engineering Geology and the Environment*, 65(2), pp. 167-184.
- Voight, B., 1988. A method for prediction of volcanic eruptions. *Nature*, 332, pp. 125-130.
- Voight, B., 1989. A Relation to Describe Rate-Dependent Material Failure. *Science*, 243(4888), pp. 200-203.
- Watson, A. D., Moore, D. P. et Stewart, T. W., 2004. Temperature influence on rock slope movements at Checkerboard Creek. *Éditeurs: W. Lacerda, M. Ehrlich, S. Fontoura et A. Sayao, Proceedings of the Ninth International Symposium on Landslides*, Rio de Janeiro, pp. 1293-1298.
- Willenberg, H., Evans, K. F., Eberhardt, E., Spillmann, T. et Loew, S., 2008a. Internal structure and deformation of an unstable crystalline rock mass above Randa (Switzerland): Part II - Three-dimensional deformation patterns. *Engineering Geology*, 101(1-2), pp. 15-32.

- Willenberg, H., Loew, S., Eberhardt, E., Evans, K. F., Spillmann, T., Heincke, B., Maurer, H. et Green, A.G., 2008b. Internal structure and deformation of an unstable crystalline rock mass above Randa (Switzerland): Part I — Internal structure from integrated geological and geophysical investigations. *Engineering Geology*, 101(1–2), pp. 1-14.
- Wong, H.N., Ho, K.K.S. et Chan, Y.C., 1997. Assessment of Consequences of Landslides. *Éditeurs: D.M. Cruden et R. Fell, The International Workshop on Landslide Risk Assessment*, Honolulu, Hawaii, pp. 111-149.
- Yueping, Y., Wang, H., Gao, Y. et Li, X., 2010. Real-Time Monitoring and Early Warning of Landslides at Relocated Wushan Town, The Three Gorge Reservoir, China. *Journal of Southeast Asian Applied Geology*, 2(3), pp. 170-184.
- Zangerl, C., Eberhardt, E. et Perzmaier, S., 2010. Kinematic behaviour and velocity characteristics of a complex deep-seated crystalline rockslide system in relation to its interaction with a dam reservoir. *Engineering Geology*, 112(1-4), pp. 53-67.
- Zvelebil, J., et Moser, M., 2001. Monitoring Based Time-Prediction of Rock Falls: Three Case-Histories. *Physics and Chemistry of the Earth (B)*, 26(2), pp. 159-167.

Annexes

Annexe A. Mise en place et validation du système de surveillance de Gascons

Cette annexe décrit les composantes du système d'instrumentation en place à Gascons. Il s'agit de la Section 5 du Rapport final du Projet Gascons, dont la référence est :

Locat, J., Cloutier, C., Turmel, D., 2013. Rapport 10 : Développement d'outils de gestion du risque de mouvements de terrain dans le secteur Gascons de la société du Chemin de fer de la Gaspésie (Projet Gascons), LERN-GASCONS-13-01, Laboratoire d'études sur les risques naturels, Université Laval, 112p.

Cette section présente une synthèse de l'instrumentation mise en place et de ses performances. Les détails de la conception et les travaux de mises en place sont détaillés dans les documents suivants :

- Conception du système de surveillance (Lord et al., 2009a);
- Système de surveillance couplant les données terrestres et satellitaires (Lord et al., 2010);
- Analyse des données de surveillance et définition des critères d'alerte (Cloutier et Locat, 2012a);
- Rapport de visite 01 : Visite de terrain, cartographie des fractures et mise en place du réseau extensométrique (Cloutier et al., 2009b);
- Rapport de visite 04 : Installation du système d'observation du massif rocheux (Lord et Cloutier, 2009);
- Rapport de visite 08 : Lectures, installation d'instruments et modifications du système d'acquisition du système d'observation (Lord et Cloutier, 2010c);
- Rapport de visite 10 : Entretien et ajouts au système d'instrumentation et levés manuels (Cloutier et Locat, 2011b);
- Rapport de visite 12 : Entretien et levés manuels (Cloutier, 2012b).

Les composantes du système de surveillance

Le système de surveillance est composé d'instruments à lecture manuelle, donc la mesure nécessite de se déplacer au site et d'instruments reliés à un système d'acquisition qui permet une lecture automatisée. Le système d'acquisition est situé à Gascons à 50 mètres du glissement actif dans une guérite climatisée et chauffée, qui est reliée au réseau électrique d'Hydro-Québec et au réseau téléphonique de Telus. Les instruments à lecture automatique sont reliés par câbles au système d'acquisition.

D'abord, les instruments à lecture manuelle sont présentés puis ceux à lecture automatique. Pour chacun des instruments, l'entretien nécessaire à son bon fonctionnement est mentionné, ainsi que l'intervalle de temps pour lesquels des données sont disponibles. Ensuite, le système d'acquisition et de transfert des données est présenté. Enfin, le suivi par interférométrie radar, mené par le Centre canadien de télédétection, en collaboration avec l'Agence spatiale canadienne et la Commission géologique du Canada est brièvement présenté.

Instruments à lectures manuelles

Réseau extensométrique

Le terme extensomètre réfère au couple d'ancrages fixes munis d'un œillet dont l'espacement est mesuré manuellement par un ruban de mesure ayant une grande précision. Le ruban utilisé est le modèle Convex-Ealey de la compagnie RocTest. La résolution de l'appareil est de l'ordre de 0.01mm. Cet appareil permet de mesurer des couples d'ancrages situés à une distance maximale de 30m.

Les ancrages ont été placés dans deux types d'emplacement. Lorsque possible, les ancrages étaient cimentés dans la roche à l'intérieur d'un trou réalisé avec une foreuse à percussion, trou d'une profondeur variant entre 20 et 30 centimètres. Lorsque le roc n'était pas atteignable, les tiges étaient enfoncées jusqu'au refus dans le mort terrain. Une autre tige à angle avec cette première était aussi enfoncée pour que, une fois rattachée à la première, l'ensemble soit relativement solide. Un œillet était aussi installé à l'extrémité de ces tiges.

Le réseau extensométrique est composé de tiges métalliques ancrées dans le roc ou enfoncées jusqu'au refus dans le mort-terrain et comprend des tiges installées en 1993, en 2009 et en 2010. Le réseau s'étend sur la totalité de la zone instable de Gascons (figures 1 et 2). La distance entre les couples de tiges installées en 2009 et 2010 est mesurée avec le ruban Convex-Ealey, alors que la distance entre les couples encore stables de 1993 est mesurée avec un ruban traditionnel. Le ruban Convex-Ealey permet de mesurer une distance avec une précision de 0.1 mm, à condition que les tiges soient stables.

Le levé extensométrique est effectué à chacune des visites, ainsi les données sont disponibles en fonction du moment de l'installation et des visites de terrain. Certains couples ne sont pas accessibles en hiver et n'ont donc pas été mesurés lors des visites hivernales (visites 05, 06 et 09).

Inclinomètre

L'inclinomètre est un instrument utilisé dans un forage équipé de tubes rainurés, permettant de faire le suivi des déplacements d'un massif rocheux en profondeur et permettant ainsi de localiser le ou les plans de glissement. L'inclinomètre est un instrument de mesure manuelle qui doit être descendu dans le tube rainuré à deux reprises, pour pouvoir déterminer les déplacements dans toutes les directions.

Le système inclinométrique est composé d'un tube rainuré (RocTest, GEO-LOK, 70mm) d'une profondeur de 60 m et d'une sonde (RocTest, DIS-500, câble de 75 m) qui permet de mesurer les déformations du tubage par incréments de 50 cm. Il a été mis en place au site de forage 1 (figure 1) par la compagnie Vincent Fournier & Associés à l'automne 2009. L'orientation des rainures est indiquée à la figure 3.

Les profils des déplacements avec la profondeur sont obtenus en effectuant quatre passages de la sonde manuellement. La fréquence d'acquisition d'un profil dépend donc du nombre de visites effectuées sur le site. La précision de la sonde est de 2 mm sur une étendue de 25 m.

On s'aperçoit que les mesures effectuées en juillet sont affectées par une dérive instrumentale qui est possiblement reliée au changement de température le long du tubage. Les données prises dans les autres mois de l'année ne présentent pas cette dérive.

Levés à la station totale

Un suivi de certains marqueurs présents sur le site est effectué à l'aide de la station totale Leica TS06. Trois bornes d'arpentages, des cylindres bétonnés avec en leur centre une tige métallique, sont présents à Gascons et nommés BM1, BM2 et BM3. De plus, cinq cibles réfléchissantes ont été installées en 2010 pour effectuer un suivi des déplacements à l'aide d'une station totale. À chaque visite où les conditions le permettent, une première série de visées est faite à partir de BM1 avec comme référence angulaire la cible réfléchissante sur la guérite (figure 1), puis une seconde série de visée à partir de BM2 avec BM1 en référence. En plus des cibles réfléchissantes, des marques gravées sur les pieux en H du mur de soutènement sont relevées.

Les résultats sont mitigés, possiblement entre autre à cause du changement fréquent de l'opérateur. Quoiqu'il en soit, cette méthode semble très efficace pour suivre les déformations du mur de soutènement relatif à BM1 et entre les sections des murs.

Instruments à lecture automatique

Clinomètre

Les clinomètres bi-axiaux permettent de mesurer des changements d'angles selon deux plans orthogonaux définis au préalable. Le modèle 6160, fonctionnant avec des capteurs MEMS de la compagnie Geokon a été retenu.

Un clinomètre biaxial du modèle 6160-2-30 de Geokon est vissé au mur de soutènement en caisson de bois. Il renferme deux capteurs MEMS qui permettent de mesurer l'inclinaison dans deux axes perpendiculaires. L'axe A du capteur est orienté vers la mer et l'axe B est parallèle au mur et pointe vers le Petit-massif. La plage de lecture est de $\pm 20^\circ$ et la précision est de 0.1 % de sa plage donc de 0.04° . L'acquisition des données se fait aux 5 minutes.

L'entretien du clinomètre est minimal. Il faut s'assurer que tous les éléments soient en bon état : le boîtier protecteur en bois, le câble qui longe le mur de soutènement et l'ancrage vissé qui relie le clinomètre au mur de soutènement.

Fissuromètre

Le fissuromètre est un appareil électronique ancré de part et d'autre d'une fissure et qui mesure son déplacement. Les mesures du fissuromètre, contrairement aux mesures de l'extensomètre, sont prises automatiquement par le système d'acquisition de données. Les fissuromètres ont donc comme avantage, par rapport à l'extensomètre, de permettre une acquisition plus fréquente et à distance. Les fissuromètres utilisés sont le modèle 4420 à corde vibrante de Geokon ayant des intervalles de mesure de 150 ou de 300 mm. Le désavantage comparativement à l'extensomètre est donc l'ouverture maximale de la fissure à mesurer qui est beaucoup plus faible.

Les treize fissuromètres sont installés dans la roche à l'aide d'ancrages injectés à l'époxy et de façon à mesurer deux types de déplacement. Dix fissuromètres ont été installés de part et d'autres de fissures préexistantes et ouvertes en moyenne de 22 cm. Ces fissuromètres permettent de suivre l'évolution de l'ouverture d'une fissure. De ces dix appareils, deux sont installés sur la même fissure à un angle de 90° afin de mesurer deux composantes du déplacement. Il s'agit des fissuromètres F7 et F8. Les fissuromètres F10 et F12 ont été installés de façon à suivre un mouvement de cisaillement sur un plan du litage susceptible de devenir une surface de rupture. Le fissuromètre F1 a une de ses extrémités vissée au mur de soutènement en caisson de bois et l'autre ancrée au compartiment est du Petit-massif. Tous

les fissuromètres sont recouverts d'un capot protecteur et reliés au système d'acquisition par un câble électrique quatre brins avec une gaine en PVC du modèle 02-250V6-M de Geokon. Les lectures sont réalisées aux cinq minutes. La plage de lecture des fissuromètres, indiquée au tableau 1, est de 100, 150 ou 300 mm. Les fissuromètres ont été installés à 50% de leur élongation initiale pour accommoder des mouvements en fermeture et en ouverture des fissures.

Les fissuromètres ont une précision de 0.1 % et une résolution de 0.025 % à pleine échelle, ce qui correspond à 0.3 et 0.075 mm pour les plages de 300 mm. Étant donné les vitesses actuelles de déplacement, une telle précision est nécessaire afin de cerner les variations saisonnières. Les fissuromètres seront utiles pour déceler une phase précoce de l'accélération et pour caractériser les vitesses faibles actuelles.

Les fissuromètres ont une plage de lecture limitée et il est nécessaire de veiller à ce que cette plage ne soit pas dépassée, ce qui entraînerait la perte de l'instrument. Il faut donc procéder à des ré-ancrages des appareils avant qu'ils atteignent leur limite. Les fissuromètres qui sont installés à l'intérieur de fissures sont susceptibles de recevoir des chutes de blocs. Le F12 a reçu un bloc rocheux qui a légèrement plié sa tige coulissante, mais l'appareil est demeuré fonctionnel. De plus, il faut procéder à l'inspection générale de leur état : solidité des ancrages, capot de protection, conduits électriques et écaillage préventive de la paroi, et cela au moins une fois par année ou après un événement qui aurait endommagé un capteur.

Piézomètres

Les piézomètres permettent de mesurer les pressions d'eau dans le sol ou dans le roc et sont placés à l'intérieur d'un forage. Ils donnent des informations sur le niveau de la nappe phréatique et permettent de modéliser l'écoulement vertical et horizontal dans le massif. Les piézomètres sont installés de manière permanente et sont reliés au système d'acquisition de données, permettant des lectures automatiques. Dans le cadre de ce projet, trois forages sont instrumentés avec chacun trois piézomètres placés à trois élévations différentes tout en s'assurant que ces derniers soient sous le niveau connu de la nappe phréatique, avec le plus profond au fond du trou.

Les neuf piézomètres du modèle 4500S à corde vibrante de Geokon sont installés dans trois forages, dont la position est indiquée à la figure 1. La mise en place a été faite par la compagnie Vincent Fournier & associés à l'automne 2009. Ils sont installés dans un forage complètement cimenté par la méthode «fully-grouted» (McKenna, 1995, Mikkelsen et Green, 2003). Leur profondeur est indiquée au tableau 2. Ces capteurs mesurent la pression d'eau ressentie à la profondeur où ils sont installés. Pour chacun des forages, le piézomètre le moins profond a une plage de lecture qui s'étend jusqu'à 350 kPa, i.e. équivalent à une colonne d'eau maximale de 35 m, alors que les deux appareils les plus profonds sont calibrés pour une pression maximum de 700 kPa (i.e. Colonne d'eau de 70m). La sensibilité des appareils est de 0.025% de la plage de lecture, soit de 2 cm pour une plage de 700 kPa et de 1 cm pour une plage de 350 kPa. La fréquence d'acquisition est aux six heures et permet de bien cerner les variations des pressions d'eau causées par les précipitations et la fonte des neiges.

L'entretien des piézomètres se limite à l'inspection des boîtes de jonction et parafoudres situés au-dessus des forages et protégés par des boîtiers métalliques verts. Un plan de branchement type d'une boîte de jonction est montré à la figure 4. À la sortie du forage, chaque piézomètre a son câble électrique (trois câbles sortent du forage). Cette boîte de jonction permet de passer de trois à un fils multiconducteur.

Shape Accel Array (SAA)

Le SAA se veut, à l'instar du fissuromètre vis-à-vis de l'extensomètre, le vis-à-vis de l'inclinomètre. Le SAA (Shape Accel Array) de la compagnie Mesurand est un appareil permettant de suivre et de quantifier les déplacements d'un massif rocheux en profondeur. Les SAA sont composés d'une série de segments rigides liés par des joints qui sont installés de façon permanente dans un forage (vertical), ou déposés de manière permanente dans un remblai (horizontal). Chaque segment rigide de 500 mm est composé d'un capteur et est relié aux autres par des joints permettant les mouvements dans toutes les directions. Les capteurs permettent de détecter ces mouvements donc de suivre la déformation du SAA dans le temps.

Quatre Shape Accel Array (SAA) de la compagnie Measurand sont installés sur le site. Ces appareils permettent de suivre et de quantifier les déplacements du massif en profondeur, un peu comme le fait un inclinomètre. Les SAA sont composés d'une série de segments rigides de 50 cm reliés entre eux par des joints rotulés et munis de senseurs MEMs qui mesurent leur inclinaison. Le chapelet peut aussi mesurer les vibrations. À Gascons, deux chaînes sont installées verticalement aux sites 1 et 2 (SAA2 et SAA3) et deux autres sont enfouis horizontalement (SAA1 et SAA4) dans le ballast de la fondation qui supporte les rails (figure 1). Les SAA1, 2 et 3 ont été installés à l'automne 2009 alors que le SAA4 est installé depuis l'été 2011.

Les SAA verticaux suivent les mouvements du massif en profondeur et permettent de déterminer la position des surfaces de glissement, ainsi que la direction du mouvement du massif. La chaîne est dans un tube de PVC de 1 pouce de diamètre qui est cimenté dans le forage. Ils sont lus toutes les six heures.

Pour leur part, les SAA horizontaux remplissent une fonction de surveillance de l'intégrité du remblai et devraient détecter des affaissements, comme ceux qui ont eu lieu en 1998, en 2000 (Journeaux et al., 2000) et en 2011 (Cloutier, 2011a). Ils sont lus à toutes les heures. Avant d'être enfouis, les SAA horizontaux sont aussi insérés dans un conduit de PVC de 1 pouce de diamètre, qui est entouré d'une couche protectrice de sable, puis d'un géotextile.

La partie supérieure du SAA2 (site de forages 2, figure 2) a cessé de fonctionner le 25 juillet 2012. Le bris est survenu dans les segments entre les profondeurs de 22 à 24 m, ce qui correspond à la zone de cisaillement. Ainsi, la quantité de déplacement maximum qu'a pu subir le capteur avant de rompre, dans le cas d'un plan de cisaillement franc est d'environ 80 mm. Le SAA2 est toujours en place dans le massif, mais les segments au-dessus de 24m de profondeur ne fonctionnent plus. La partie plus profonde fonctionne toujours.

À son sommet (extrémité à l'ouest sur le site), le SAA4 est doté d'un SAAtop. Il s'agit d'un module qui mesure et enregistre l'ampérage et le voltage. Ces données sont utiles pour poser des diagnostics dans le cas de problèmes. Ce module a aussi été ajouté au SAA1. Pour des raisons techniques évidentes, le module n'a pas été ajouté directement au bout du SAA1, mais plutôt à la jonction entre le câble électrique et l'acquisition de données (dans la guérite).

Les SAA ne demandent pas d'entretien particulier, sauf en cas de bris. À ce moment, une réparation ou un remplacement pourraient être nécessaires. Les SAA horizontaux sont situés sous l'extrémité des dormants qui supportent la voie ferrée. En cas de travaux effectués sur la voie ferrée, il faut s'assurer de ne pas les endommager. Il pourrait être nécessaire de retirer, puis de replacer les SAAs horizontaux.

Station météorologique

Une station météorologique est située sur le toit de la guérite et comprend une sonde de température et d'humidité relative, un baromètre, un capteur de vitesse du vent et une jauge de précipitations (tableau

3). La jauge de précipitation munie d'un élément chauffant permet de mesurer les précipitations sous forme de pluie et de neige. Tous les capteurs de la station météorologique sont lus aux demi-heures.

Les instruments de la station météo demandent tous un entretien régulier. La jauge de précipitation doit être nettoyée à chaque année et calibrée aux deux ans. Au printemps et à l'automne, il faut enlever ou mettre une grille grossière selon le type de précipitation attendu. Le baromètre et la sonde de température doivent être nettoyés à chaque année. Enfin, le roulement à bille de l'anémomètre doit être remplacé aux deux ans, et la compagnie suggère de leur retourner aux trois ans pour une remise à neuf.

Système d'acquisition et de transfert des données

Composantes physiques

Le système d'acquisition et de transfert des données est situé dans la guérite, dont l'emplacement est indiqué à la figure 1. Le schéma général du système est indiqué à la figure 5, tandis que les modules sont détaillés dans le tableau 4. Tous les appareils sont reliés par câbles au système d'acquisition. Les câbles circulent dans un réseau de tuyaux enfouis à quelques centimètres sous la surface. Les tuyaux sont en ABS ou en PVC et la position du réseau est indiquée à la figure 1. Il faut vérifier à chaque année que l'eau ne s'accumule pas dans les conduites. À cet effet, des regards ont été installés à plusieurs endroits.

Les composantes du système d'acquisition tirent leur alimentation électrique du réseau en courant alternatif d'Hydro-Québec. Deux systèmes d'énergie alternative sont présents : un UPS pour l'ordinateur et un système de batterie 12V et chargeur pour alimenter le CR1000. Les autres composantes acquièrent leur énergie du CR-1000.

Les instruments à corde vibrantes, i.e. les 13 fissuromètres et les 9 piézomètres, sont d'abord raccordés dans un multiplexeur, puis dans un module de transformation du signal avant d'être relié au CR-1000. Le plan de branchement des multiplexeurs est présenté à la figure 6.

Un certain entretien est nécessaire pour assurer que le système d'acquisition demeure performant et ne fasse pas défaut. Les batteries internes du CR-800 et du CR-1000 doivent être changées. Les batteries des systèmes alternatifs d'énergie doivent être changées aux 2 ans pour le UPS et aux 5 ans pour la batterie 12V. Enfin, il est recommandé de changer l'ordinateur aux 5 ans.

Logiciels

Le logiciel Loggernet, de Campbell Scientific est utilisé pour programmer et communiquer avec les modules d'acquisition CR-1000 et CR-800. Le logiciel est installé sur l'ordinateur présent au site et aussi sur la base de données présentement hébergée à l'Université Laval.

Transfert et sauvegarde des données

La mémoire interne du CR-1000 est limitée. Le module NL115, jumelé avec une carte mémoire devait permettre d'augmenter la capacité de sauvegarde des données. Par contre, malgré plusieurs essais et modifications, le module n'a pas été en mesure de fonctionner avec la carte mémoire. Ainsi, la mémoire du module est limitée à celle interne du CR-1000, ayant pour conséquence que si les données ne sont pas récupérées approximativement à toutes les 72h, elles sont perdues puisque le CR-1000 réécrira par-dessus les données présentes.

La récupération et sauvegarde fréquente des données est assurée par l'ordinateur situé dans la guérite qui est relié directement au système d'acquisition. Les données brutes sont ensuite transférées par un lien internet de l'ordinateur vers le site ftp du département de géologie et de génie géologique et sauvegarder dans une base de données. De plus, les données brutes sont aussi envoyées à une adresse courriel Gmail.

Enfin, un second lien existe avec le CR-1000. Il s'agit d'un lien par modem téléphonique. Les données sont transférées via ce lien à tous les 4 jours.

Il est possible d'accéder au CR-1000, par exemple, pour récupérer des données manuellement, le code d'acquisition ou pour mettre un nouveau code, par la ligne téléphonique et par internet via le PC sur le site. Il est à noter que l'insertion d'un nouveau code efface toutes les données de la mémoire du CR-1000.

Suivi PTA-InSAR

La technique de suivi InSAR est utilisée pour le suivi des déplacements au site de Gascons. Cette technique utilise les principes de l'imagerie radar, données acquises dans ce cas-ci de manière satellitaire (Lord et al. 2010). Dans ce projet, des réflecteurs en coin, soit des réflecteurs artificiels ont été installés sur le site pour les besoins de la méthode PTA qui permet d'imager les déplacements d'un terrain de manière ponctuelle en se basant sur des réflecteurs permanents, et ce avec une précision de l'ordre du millimètre. Les réflecteurs en coin sont des points au sol dont le signal radar (phase et amplitude) est constant tout au long d'une série temporelle.

Au site de Gascons, 23 cibles réfléchissantes ont été installées (figure 1) pour effectuer un suivi satellitaire par PTA-InSAR (Point Target Analysis – Interferometric Synthetic Aperture Radar). Cette technique utilise une série temporelle d'images prises par un radar satellite (Radarsat-2, dans le cas de Gascons) pour calculer des déplacements sur des cibles fixes. La technique permet de mesurer le déplacement dans la direction de la ligne de visée entre le satellite et la cible à partir de la phase et de l'intensité de l'onde électromagnétique retournée au satellite.

Le suivi satellitaire est effectué par le Centre canadien de télédétection en collaboration avec la commission géologique du Canada et l'Agence spatiale canadienne. Pour plus d'information sur la technique, deux articles du PTA-InSAR à Gascons sont parus dans des comptes-rendus de conférence sur le cas de Gascons (Couture et al., 2010, 2011).

Les réflecteurs en coin, surtout ceux triangulaires, doivent être nettoyés périodiquement pour enlever les débris qui s'y accumulent et affecteront les déplacements calculés.

Capacité et performance du système

Le secteur de la voie ferrée est celui qui est le plus instrumenté, puisque l'élément mis à risque par le glissement est la voie ferrée. Les instruments du système de surveillance automatisé sont tous situés à proximité de la voie ferrée. Initialement, le SAA2 permettait d'obtenir des informations sur les déplacements de la partie amont du massif, mais le SAA2 a atteint sa limite de cisaillement et n'est plus fonctionnel. Ainsi, le levé extensométrique est essentiel puisqu'il permet d'acquérir de l'information dans le secteur centre-est du glissement, où aucun instrument du système automatisé n'est installé. Un autre point important à noter avec le levé extensométrique, c'est qu'il oblige à marcher tout le secteur du glissement et permet donc d'observer visuellement l'évolution du glissement et des fractures ouvertes. Les réflecteurs en coin ont une aussi bonne répartition spatiale que le réseau extensométrique, ce qui assure tout de même une méthode de suivi à distance de la partie amont du glissement.

Tous les instruments à lecture manuelle (inclinomètres, extensomètres et station totale) ne sont pas appropriés pour déceler l'imminence de dommages à la voie ferrée : la fréquence de lecture est trop faible pour le moment et puisqu'il faut se rendre sur le site pour effectuer le levé, l'évènement sera d'abord constaté visuellement. Toutefois, ces instruments sont utiles pour la compréhension globale du mouvement et de son évolution à long terme, entre autre parce qu'ils couvrent une grande superficie de la masse instable (les extensomètres). Le ruban extensométrique permet de mesurer des déplacements entre deux points distancés de près de 30 m et demande peu d'entretien ; il s'avère donc un outil privilégié pour un suivi à long terme.

En février 2011, l'instrumentation en place n'avait pas permis de prédire ou de constater qu'une dépression s'était formée sous le rail sud (Cloutier, 2011a). C'est pourquoi le SAA4 a été installé horizontalement à l'ouest des murs de soutènement dans le secteur du Petit-massif. Depuis son installation, un tassement est mesuré à l'endroit où la dépression s'était formée. Étant donné qu'un tel évènement ne s'est pas reproduit, il demeure toujours une incertitude à savoir si le SAA pourra détecter la formation d'une nouvelle dépression, bien que l'on constate que des déformations se produisent au même endroit.

La fréquence de lecture des SAA horizontaux qui est aux heures, est limitée par le système d'acquisition et par l'appareil lui-même. Étant donné que l'objectif de ces appareils est de caractériser l'intégrité du ballast soutenant la voie et que le train circule uniquement quelques fois par semaine, cette vitesse d'acquisition est considérée suffisante pour l'instant pour le développement de seuils d'alerte.

La fréquence de lecture des fissuromètres et du clinomètre est très rapide (cinq minutes), ce qui permet de cerner un changement qui se produirait dans un court laps de temps. Toutefois, leur signal montre une variation journalière de type sinusoïdale qui est influencée entre autre par la température et qui peut rendre leur interprétation difficile.

Le système d'acquisition des données a toujours bien fonctionné. Les quelques périodes sans données sont associées aux périodes de travaux sur le terrain qui nécessitaient d'arrêter l'acquisition pour ajouter des instruments et modifier le programme. Le site web qui permet de visualiser les données est mis à jour quatre fois par jour.

Visite de terrain et levés manuels

#	Titre	Dates de la visite	Référence
01	Visite de terrain, cartographie des fractures et mise en place du réseau extensométrique	1 au 10 juin 2009	(Cloutier et al., 2009b)
02	Rapport de visite 02, Mesures extensométriques, levés LIDAR terrestre et levés structuraux.	26 au 30 juillet 2009	(Cloutier et al., 2009c)
03	Mesures extensométriques, conception du système de surveillance et échantillonnage.	2 au 6 septembre 2009	(Cloutier et Lord, 2009)
04	Installation du système d'observation du massif rocheux	24 octobre au 9 novembre 2009	(Lord et Cloutier, 2009)
05	Mesure du réseau extensométrique et mise au point du système de surveillance	16 au 18 décembre 2009	(Cloutier et Lord, 2010)
06	Lecture du réseau extensométrique et des données inclinométriques	12 au 14 mars 2010	(Lord et Cloutier, 2010a)
07	Lecture du réseau extensométrique et des données inclinométriques	21 au 23 mai 2010	(Lord et Cloutier, 2010b)
08	Lectures, installation d'instruments et modification du système d'acquisition du système d'observation	24 juillet au 1 août 2010	(Lord et Cloutier, 2010c)
09	Évènement du 24 février 2011 et mesures manuelles	25 février au 1 mars 2011	(Cloutier, 2011a)
10	Entretien et ajouts au système d'instrumentation et levés manuels	25 juillet au 6 août 2011	(Cloutier et Locat, 2011b)
11	Entretien et levés manuels	13 au 16 novembre 2011	(Cloutier, 2011b)
12	Entretien et levés manuels	30 avril au 4 mai 2012	(Cloutier, 2012a)
13	Entretien, ajouts au système d'instrumentation et levés manuels	4 au 11 août 2012	(Cloutier, 2012b)
14	Entretien et levés manuels	15 au 19 mai 2013	Cloutier, 2013

Conclusions

Un système de surveillance en quasi-temps réel du glissement de Gascons a été mis en place en plus d'un site internet de visualisation des données. Les données acquises des instruments ont permis de caractériser les vitesses de déplacements, leurs variations saisonnières et leur direction. Les profils de déplacements obtenus des SAA verticaux et de l'inclinomètre ont été utilisés pour déterminer la géométrie du glissement et la position de la surface de rupture. Les levés Lidar aéroportés et terrestres qui ont été couplés pour former un modèle numérique de terrain haute résolution ont aussi été utilisés pour déterminer la géométrie du glissement et pour calculer son volume. Une connaissance accrue des propriétés et du comportement du glissement était essentielle pour mener l'analyse du risque, présentée

dans le rapport 09 (Cloutier et Locat, 2012b). La situation actuelle du glissement est très bien connue et détaillée par de nombreux documents (photos, cartes, géométrie et dimensions des fissures, etc). Ces données seront utiles pour comparer avec des mesures futures afin de constater l'évolution du glissement.

Les travaux ont permis de tester les capteurs SAA de la compagnie Measurand en milieu rocheux. La comparaison avec les mesures inclinométriques a permis de constater que le SAA est efficace pour situer les zones de cisaillements. De plus, une première approximation de la capacité des SAA à subir du cisaillement sur un plan mince a été obtenue puisque le SAA2 a cessé de fonctionner à cause du cisaillement. Cette valeur est certainement plus grande que celle qui aurait pu être tolérée avec un inclinomètre traditionnel. Par contre, l'instrument est perdu, il ne peut pas être retiré du trou toujours à cause du cisaillement important. De plus, les installations à Gascons des SAA verticaux ont permis de développer une nouvelle méthode de mise en place des SAA en milieu rocheux (Lord et Cloutier, 2009). Enfin, ces installations ont aussi mené la compagnie Measurand à apporter des changements pour faciliter l'identification de la direction des axes de mesures lors de l'installation.

Des critères d'alerte ont été développés pour le suivi et la prédiction d'un mouvement causant des dommages à la voie ferrée et sont en cours de validation. Le rapport 08 présentait ces critères (Cloutier et Locat, 2012a).

L'acquisition et l'analyse des données de déplacement et de pressions interstitielles a permis d'améliorer la compréhension du comportement rhéologique (déformation) d'un massif rocheux, dont l'origine de l'instabilité est liée principalement à l'érosion côtière. Les travaux ont aussi démontré l'absence de réseau karstique dans le secteur du glissement de Gascons. Enfin, les travaux de recherche réalisés dans le cadre du doctorat de Catherine Cloutier devraient augmenter la compréhension liés aux déplacements observés à Gascons.

Enfin, le bon fonctionnement du système de surveillance dépend d'un bon entretien. De plus, pour effectuer une analyse adéquate des mesures, il est nécessaire d'avoir une bonne compréhension du fonctionnement des appareils et une connaissance du type d'installation (ancrages, localisation).

Références

Cloutier, C., Lord, P.-É. et Locat, J. (2009a) Rapport 01: Données historiques et récentes, Projet Gascons, LERN-GASCONS-09-02, Université Laval (Québec) 406p.

Cloutier, C., Lord, P.-É., Lacroix-Beaupré, M.-P. et Locat, J. (2009b) Rapport de visite 01, Visite de terrain, cartographie des fractures et mise en place du réseau extensométrique, Développement d'outils de gestion du risque de mouvements de terrain dans le secteur Gascons de la Société du Chemin de fer de la Gaspésie., Université Laval (Québec).

Cloutier, C., Lacroix-Beaupré, M.-P. et Lord, P.-É. (2009c) Rapport de visite 02, Mesures extensométriques, levés LIDAR terrestre et levés structuraux, Développement d'outils de gestion du risque de mouvements de terrain dans le secteur Gascons de la Société du Chemin de fer de la Gaspésie, LERN-GASCONS-09-06, Université Laval (Québec) 57p.

Cloutier, C. et Lord, P.-É. (2009) Rapport de visite 03, Mesures extensométriques, conception du système de surveillance et échantillonnage, Développement d'outils de gestion du risque de mouvements

de terrain dans le secteur Gascons de la Société du Chemin de fer de la Gaspésie, LERN-GASCONS-09-07, Université Laval (Québec) 36p.

Cloutier, C. et Locat, J. (2010) Rapport 04: Modèle géologique, Projet Gascons, LERN-GASCONS-10-01, Université Laval (Québec) 39p.

Cloutier, C. et Lord, P.-É. (2010) Rapport de visite 05, Mesure du réseau extensométrique et mise au point du système de surveillance, Développement d'outils de gestion du risque de mouvements de terrain dans le secteur Gascons de la Société du Chemin de fer de la Gaspésie, LERN-GASCONS-10-01, Université Laval (Québec) 23p.

Cloutier, C. et Locat, J. (2011a) Rapport 06: Modèle Hydrogéologique, Projet Gascons, LERN-GASCONS-11-01, Université Laval (Québec) 41p.

Cloutier, C. (2011a) Rapport de visite 09 : Évènement du 24 février 2011 et mesures manuelles, Projet Gascons, LERN-GASCONS-11-02, LERN, Université Laval (Québec) 29p.

Cloutier, C. et Locat, J. (2011b) Rapport de visite 10: Entretien et ajouts au système d'instrumentation et levés manuels, Développement d'outils de gestion du risque de mouvements de terrain dans le secteur Gascons de la Société du Chemin de fer de la Gaspésie, LERN-GASCONS-11-04, Université Laval (Québec) 38p.

Cloutier, C. (2011b) Rapport de visite 11: Entretien et levés manuels, Développement d'outils de gestion du risque de mouvements de terrain dans le secteur Gascons de la Société du Chemin de fer de la Gaspésie, LERN-GASCONS-11-06, Université Laval (Québec) 32p.

Cloutier, C. et Locat, J. (2011c) Rapport 07 : Analyse de l'aléa mouvement de terrain, Projet Gascons, LERN-GASCONS-11-03, LERN, Université Laval (Québec) 47p.

Cloutier, C. et Locat, J. (2012a) Rapport 08 : Analyse des données de surveillance et définition des critères d'alerte, Projet Gascons, LERN-GASCONS-12-01, LERN, Université Laval (Québec) 75p.

Cloutier, C. (2012a) Rapport de visite 12: Entretien et levés manuels, Développement d'outils de gestion du risque de mouvements de terrain dans le secteur Gascons de la Société du Chemin de fer de la Gaspésie, LERN-GASCONS-12-01, LERN, Université Laval (Québec) 32p.

Cloutier, C. (2012b) Rapport de visite 13: Entretien, ajouts au système d'instrumentation et levés manuels, Développement d'outils de gestion du risque de mouvements de terrain dans le secteur Gascons de la Société du Chemin de fer de la Gaspésie, LERN-GASCONS-12-03, LERN, Université Laval (Québec) 90p.

Cloutier, C. (2013) Rapport de visite 14: Entretien et levés manuels, Développement d'outils de gestion du risque de mouvements de terrain dans le secteur Gascons de la Société du Chemin de fer de la Gaspésie, LERN-GASCONS-13-02, LERN, Université Laval (Québec) 15p.

Cloutier, C. et Locat, J. (2012b) Rapport 09: Pour une approche de l'analyse du risque associé à un mouvement de terrain actif, Projet Gascons, LERN-GASCONS-12-04, LERN, Université Laval (Québec) 62p.

Lord, P.-É., Cloutier, C. et Locat, J. (2009a) Rapport 02 : Conception du système d'observation, Projet Gascons, LERN-GASCONS-09-03, Université Laval (Québec) 52p.

Lord, P.-É., Cloutier, C. et Locat, J. (2009b) Rapport 03: Modèle de terrain et SIG de base, Projet Gascons, Université Laval (Québec) 29p.

Lord, P.-É. et Cloutier, C. (2009) Rapport de visite 04, Installation du système d'observation du massif rocheux, Développement d'outils de gestion du risque de mouvements de terrain dans le secteur Gascons de la Société du Chemin de fer de la Gaspésie, LERN-GASCONS-09-09, Université Laval (Québec) 46p.

Lord, P.-É. et Cloutier, C. (2010a) Rapport de visite 06, Lecture du réseau extensométrique et des données inclinométriques, Développement d'outils de gestion du risque de mouvements de terrain dans le secteur Gascons de la Société du Chemin de fer de la Gaspésie, LERN-GASCONS-10-02, Université Laval (Québec) 21p

Lord, P.-É. et Cloutier, C. (2010b) Rapport de visite 07, Lecture du réseau extensométrique et des données inclinométriques, Développement d'outils de gestion du risque de mouvements de terrain dans le secteur Gascons de la Société du Chemin de fer de la Gaspésie, LERN-GASCONS-10-04, Université Laval (Québec) 29p.

Lord, P.-É., Cloutier, C., Locat, J., Couture, R. et Charbonneau, F. (2010) Rapport 05: Système de surveillance couplant les données terrestres et satellitaires, LERN-GASCONS-10-06, Laboratoire d'études sur les risques naturels, Université Laval (Québec) 58p.

Lord, P.-É. et Cloutier, C. (2010c) Rapport de visite 08 :Lectures, installation d'instruments et modification du système d'acquisition du système d'observation, LERN-GASCONS-10-05, Laboratoire d'études sur les risques naturels, Université Laval (Québec) 40p.

Tableau 1 Information relatives aux fissuromètres installés sur le site de Gascons

#	# de série	emplacement	élongation initiale	date de mise en place	Direction de lecture (°)	Pendage de l'instrument (°)	Largeur fissure à l'installation (mm)
F1-original	08 27522	Amont P-M	± 50% (150 mm)	26/10/2009	305	0	200
F1	08 27522	Amont P-M et mur caisson	(150mm)	06/08/2012	200	21	ne s'applique pas
F2	08 27521	Trou int. P-M	± 50% (150 mm)	27/10/2009	143	0	210
F3	08 27520	Gravel Est	± 50% (150 mm)	28/10/2009	0	29	250
F4	08 23206	2e pallier	± 50% (75 mm)	29/10/2009	190	24	50
F5	08 23207	Gravel Ouest	± 50% (75 mm)	30/10/2009	107	22.5	300
F6	08 27523	Fissure B	± 50% (150 mm)	30/10/2009	146	0	300
F7	1013167	Fissure D	± 50% (75 mm)	29/07/2010	337	0	200
F8	1013168	Fissure D	± 50% (75 mm)	29/07/2010	245	0	200
F9	1013166	Petit Massif ouest	± 50% (75 mm)	28/07/2010	125	3	50
F10	1013170	Petit M cisaillement	± 50% (75 mm)	28/07/2010	190	22.8	0
F11	1013169	Facture pied PM ouest	± 50% (75 mm) + tige d'extension de 30cm	28/07/2010	274	8	460
F12	1011371	Pied Pm Est cisaillement	± 50% (50 mm)	28/07/2010	190	22.8	0
F13	1210097	Fissure A	± 50% (75mm) + tige d'extension 20cm	09/08/2012	293	12	620

Tableau 2 Données relatives aux neuf piézomètres installés à Gascons

Site	# de forage	élévation surface (m)	# de série	position	Elévation (m)	Profondeur (m)	# Piezo
1	F6	63.39	09 24300	HAUT	17.4	46.0	1
			09 18635	MILIEU	15.4	48.0	2
			09 18632	FOND	13.4	50.0	3
2	F1	99.25	09 24302	HAUT	76.05	23.2	4
			09 18367	MILIEU	62.65	36.6	5
			09 18634	FOND	48.35	50.9	6
3	F5	63.58	09 24301	HAUT	20.58	43.0	7
			09 18636	MILIEU	17.08	46.5	8
			09 18633	FOND	13.58	50.0	9

Tableau 3 Instruments de la station météorologique

Paramètre mesuré	Modèle	Marque
Température et humidité relative	HMP45C	Campbell Scientific
Vitesse du vent	014A	Met One Instruments, Inc.
Pression atmosphérique	92	Met One Instruments, Inc.
Jauge de précipitations eau et neige	385	Met One Instruments, Inc.

Tableau 4 Composantes physiques du système d'acquisition

Modèle	Compagnie	Année d'installation	Fonction	Coût (\$)
PC avec 2 cartes réseau		2009	Sauvegarder et transférer les données	300
CR-1000	Campbell Scientific	2009	module principal d'acquisition	2350
CR-800	Campbell Scientific	remplacé en 2012	acquisition des SAA	1850
AVW200	Campbell Scientific	2009	transformation du signal des appareils à corde vibrante	705
MUX AM16/32B	Campbell Scientific	2009	multiplexeur	1075
MUX AM16/32B	Campbell Scientific	2009	multiplexeur	1075
Carte NL115	Campbell Scientific	2010	Relier CR-1000 à internet et ajouter de la mémoire au CR-1000	
Modem téléphonique	Campbell Scientific	2009	connecter le CR1000 au réseau téléphonique	625
Modem internet DSL	Telus	2010	relier le PC à internet	
5-SAA232	Measurand	2011	Transformer le signal de SAA pour compatibilité avec CR-800	
Back-UPS XS	APC	2010 (batterie 2012)	source alternative d'énergie pour le PC	300 (50 batterie)
Système alternatif d'énergie (acheté chez Measurand)				
17 Ah batterie		2012	Batterie	50
SAAREg	Measurand	2012	Contrôleur de charge	300
Chargeur	Measurand	2012	Chargeur	150

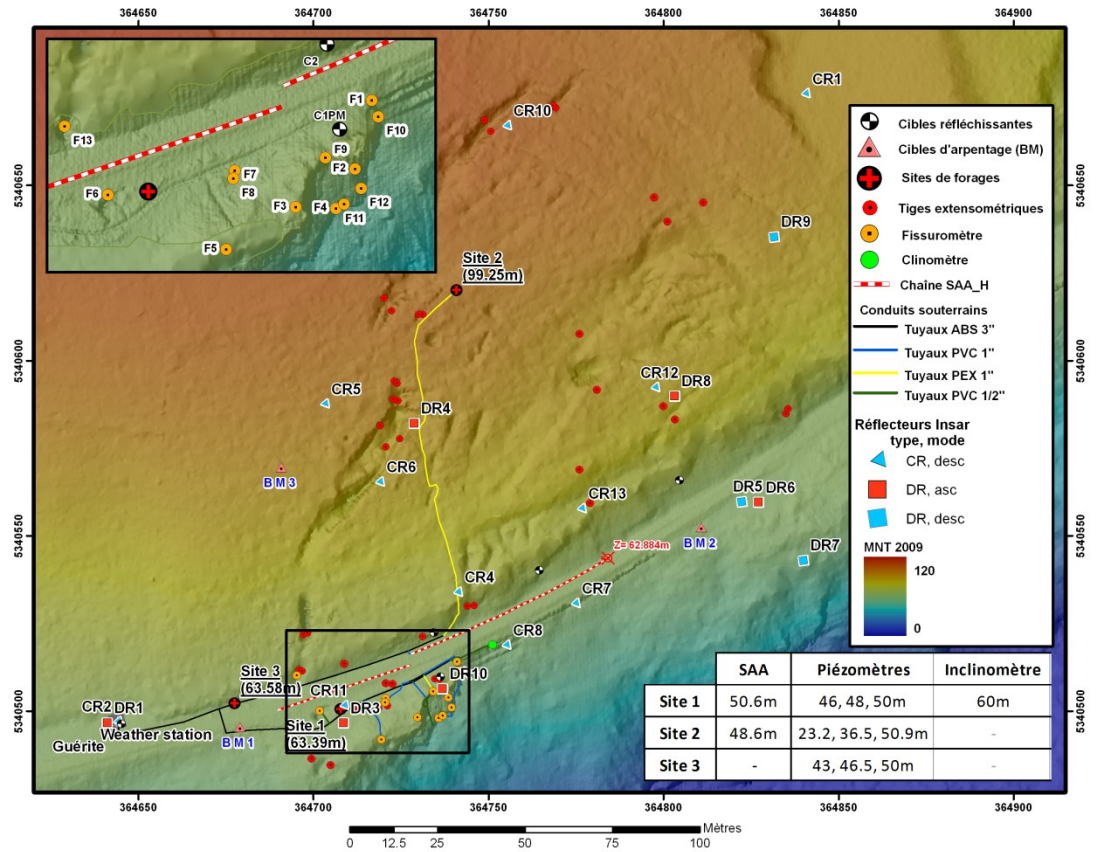


Figure 1 Plan d'instrumentation du glissement de Gascons, les chiffres dans le tableau sont des profondeurs. L'encadré est un agrandissement du secteur du Petit-massif.

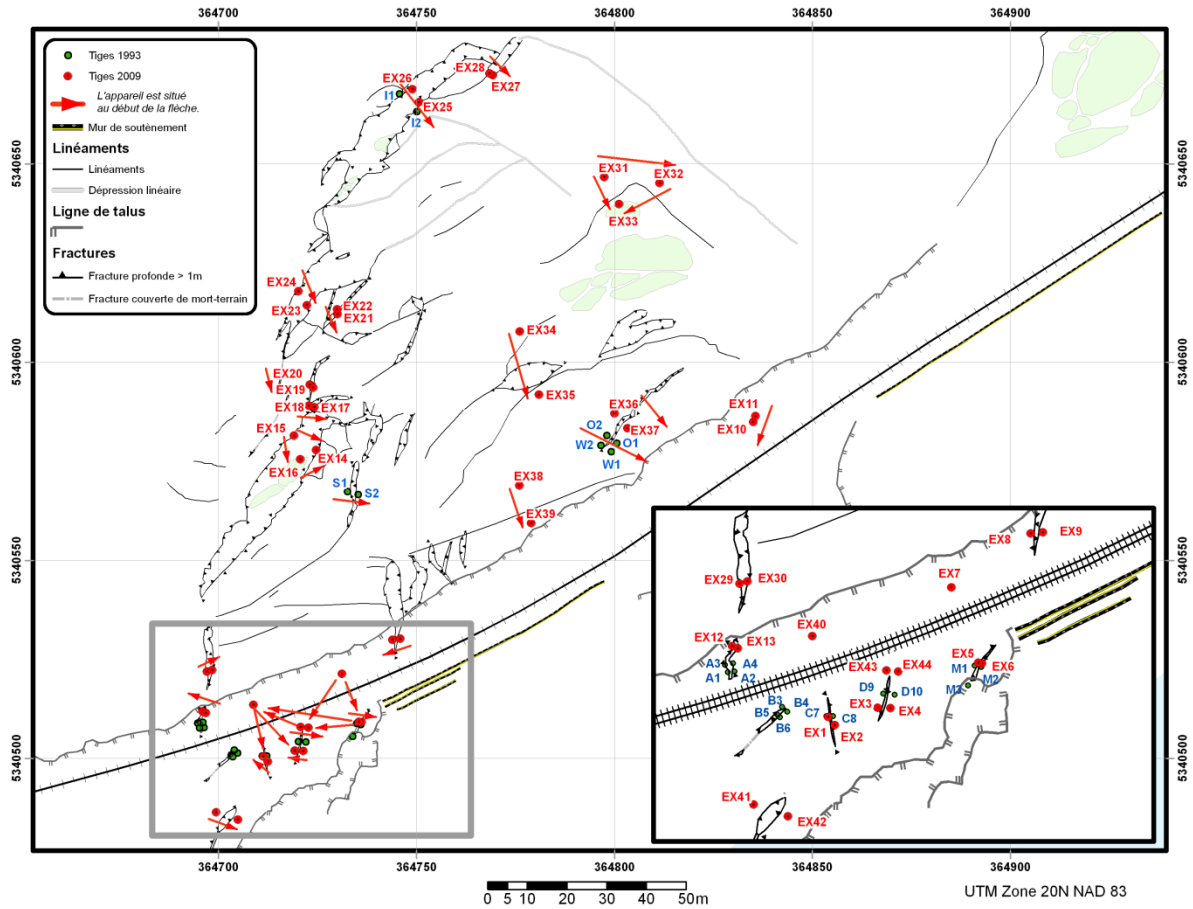


Figure 2 Plan du réseau extensométrique.

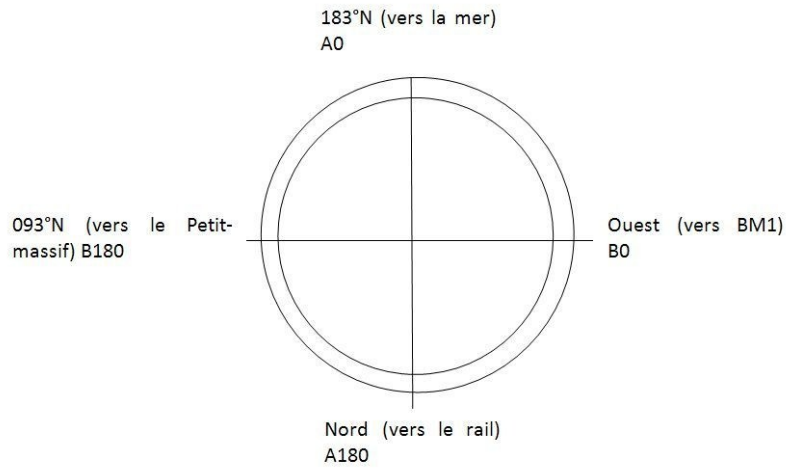


Figure 3 Orientation et noms des rainures du tube inclinométrique.

Multiconducteur		Piézomètres	
Rouge	1	1	Rouge VW +
Noir	2	2	Noir VW -
Vert	3	3	Blanc TH +
Noir	4	4	Vert TH -
Rien	5	5	Shield
Ground	E	E	Rien
HAUT			
Blanc	1	1	Rouge VW +
Noir	2	2	Noir VW -
Brun	3	3	Blanc TH +
Noir	4	4	Vert TH -
Tous les shields	5	5	Shield
Ground	E	E	Rien
MILIEU			
Jaune	1	1	Rouge VW +
Noir	2	2	Noir VW -
Bleu	3	3	Blanc TH +
Noir	4	4	Vert TH -
Rien	5	5	Shield
Ground	E	E	Rien
FOND			

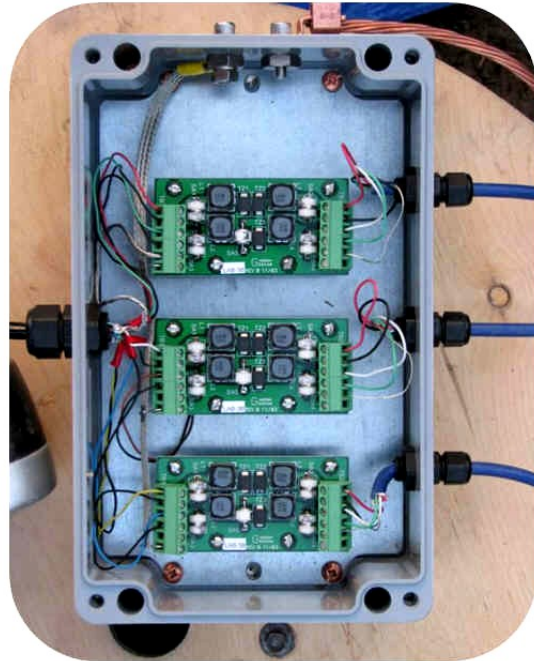


Figure 4 Plan de branchement des boîtes parafoudres. À la sortie du forage, chaque piézomètre a son câble électrique (trois câbles sortent du forage). Cette boîte de jonction permet de passer de trois à un fils multiconducteurs.

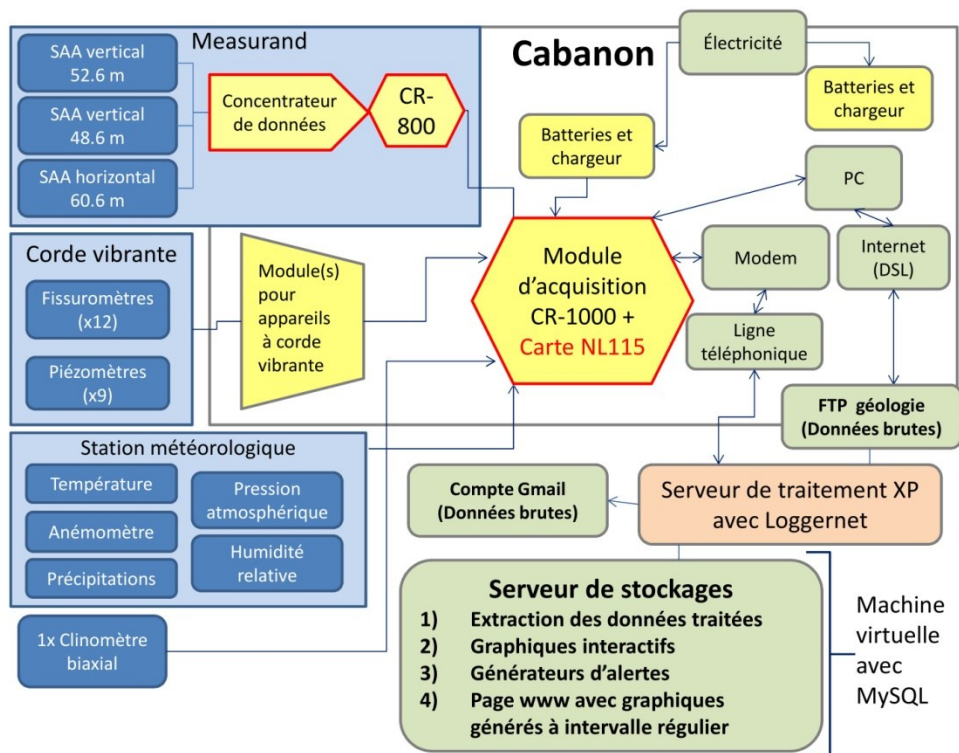


Figure 5 Schéma général du système d'acquisition des données installé dans la guérite (bungalow).

MUX 1						MUX 2					
#entrée	what	color	#entrée	what	color	#entrée	what	color	#entrée	what	color
1	1	PZ1 -VW +	9	17	PZ9-VW +	1	1	F1-VW	9	17	F9-VW
		black			black			black			black
2	2	PZ1-Th +	10	18	PZ9-Th	2	2	F1-Th	10	18	F9-Th
		green			blue			green			green
3	3	PZ2-VW +	11	19	PZ9-Th -	3	3	F2-VW	11	19	F10-VW
		white			black			red			red
4	4	PZ2-VW -	12	20		4	4	F2-VW	12	20	F10-VW
		black						black			black
5	5	PZ2-Th	13	21		5	5	F2-Th	13	21	F10-Th
		brown						green			green
6	6	PZ2-Th -	14	22		6	6	F2-Th	14	22	F10-Th
		black						white			white
7	7	PZ3-VW +	15	23		7	7	F3-VW	15	23	F11-VW
		yellow						red			red
8	8	PZ3 -VW -	16	24		8	8	F3-VW	16	24	F11-VW
		black						black			black
9	9	PZ3-Th	17	25		9	9	F3-Th	17	25	F11-Th
		blue						green			green
10	10	PZ3-Th -	18	26		10	10	F3-Th	18	26	F11-Th
		black						white			white
11	11	PZ4-VW +	19	27		11	11	F4-VW	19	27	F12-VW
		red						red			red
12	12	PZ4-VW -	20	28		12	12	F4-VW	20	28	F12-VW
		black						black			black
13	13	PZ4-Th +	21	29		13	13	F4-Th	21	29	F12-Th
		green						green			green
14	14	PZ4-Th -	22	30		14	14	F4-Th	22	30	F12-Th
		black						white			white
15	15	PZ5-VW +	23	31		15	15	F5-VW	23	31	F13-VW
		white						red			red
16	16	PZ5-VW -	24	32		16	16	F5-VW	24	32	F13-VW
		black						black			black
17	17	PZ5-Th	25	33		17	17	F5-Th	25	33	F13-Th
		brown						green			green
18	18	PZ5-Th -	26	34		18	18	F5-Th	26	34	F13-Th
		black						white			white
19	19	PZ6-VW +	27	35		19	19	F6-VW	27	35	Tilt-Th
		yellow						red			blue
20	20	PZ6-VW -	28	36		20	20	F6-VW	28	36	Tilt-Th
		black						black			black
21	21	PZ6-Th	29	37		21	21	F6-Th	29	37	
		blue						green			
22	22	PZ6-Th -	30	38		22	22	F6-Th	30	38	
		black						white			
23	23	PZ7-VW +	31	39		23	23	F7-VW +	31	39	
		red						red			
24	24	PZ7-VW -	32	40		24	24	F7-VW -	32	40	
		black						black			
25	25	PZ7-Th	33	41		25	25	F7-Th +	33	41	
		green						green			
26	26	PZ7-Th -	34	42		26	26	F7-Th -	34	42	
		black						white			
27	27	PZ8-VW +	35	43		27	27	F8-VW	35	43	
		white						red			
28	28	PZ8-VW -	36	44		28	28	F8-VW	36	44	
		black						black			
29	29	PZ8-Th	37	45		29	29	F8-Th	37	45	
		brown						green			
30	30	PZ8-Th -	38	46		30	30	F8-Th	38	46	
		black						white			

Figure 6 Plan de branchement des multiplexeurs.

Annexe B. Caractérisation des instabilités côtières dans le secteur de Port-Daniel-Gascons, Gaspésie, Québec

Cloutier, C., Locat, J., Lord, P.-É., et Couture, R., 2010. Caractérisation des instabilités côtières dans le secteur de Port-Daniel-Gascons, Gaspésie, Québec. Comptes rendus de la 63^e Conférence canadienne de géotechnique, Calgary, pp. : 71-79.

Caractérisation des instabilités côtières dans le secteur de Port-Daniel-Gascons, Gaspésie, Québec



Catherine Cloutier, Jacques Locat & Pierre-Étienne Lord
Département de géologie et de génie géologique – Université Laval, Québec, QC, Canada
Réjean Couture
Commission géologique du Canada, Ottawa, ON, Canada

ABSTRACT

The Gaspésie railroad runs directly across an active rock slide along the coast of Baie des Chaleurs, Gaspésie. The volume is estimated at more than 500 000 m³. The rock cliff shows scars in the order of 1000 m³ associated with planar slides, which are all located within a more impressive scar with dimensions similar to the active rock slide. It has been observed from the DEM generated from an airborne LiDAR survey. In fall 2009, instruments have been installed in boreholes and on the slope surface to monitor this gravitational movement.

RÉSUMÉ

Le chemin de fer de la Gaspésie traverse un glissement rocheux actif en bordure de la Baie des Chaleurs, dont le volume est estimé à plus de 500 000 m³. Sur la pointe est de l'anse, quelques cicatrices de l'ordre de 1000 m³ sont situées à l'intérieur d'une cicatrice de dimension plus importante et similaire au glissement actif. Un levé LiDAR aéroporté a permis de mettre en évidence certaines structures qui étaient jusqu'ici passées inaperçues. À l'automne 2009, une série d'instruments en forage et en surface a été mise en fonction afin d'effectuer un suivi du glissement.

1 INTRODUCTION

La côte de la Baie des Chaleurs en Gaspésie montre par endroit de hautes falaises rocheuses générées par l'érosion côtière et marquées de divers signes d'instabilités. C'est le cas d'une section de la côte de l'anse à Pierre-Loiselle située dans la municipalité de Port-Daniel-Gascons (figure 1) qui exhibe une falaise de 60 mètres de hauteur. La présence d'un glissement actif couvrant un secteur de 200 x 200 mètres y est connu depuis 1988 (Génilab BSLG Inc. 1988). Depuis, plusieurs cicatrices de glissements rocheux de diverses dimensions ont été repérées à proximité (figure 1).

Le glissement de Gascons menace l'intégrité d'une portion d'une longueur de 200 mètres du chemin de fer de la Gaspésie. La compréhension des mécanismes impliqués dans cette instabilité est essentielle à la mise en place et à la validation d'un système de surveillance à distance.

Cet article décrit la géologie et la morphologie du secteur en tentant de lier les observations à la compréhension de la cinématique du mouvement. Certaines observations viennent s'appuyer sur des données acquises par l'instrumentation installée à l'automne 2009. Enfin, l'article débute avec une présentation du contexte général des travaux de recherche qui met en perspective les enjeux reliés à l'instabilité.

2 CONTEXTE GENERAL ET HISTORIQUE

Afin de comprendre les processus affectant la stabilité du secteur, le projet Gascons a été initié. Il vise deux

objectifs principaux : (1) la mise en place et la validation d'un système de surveillance à distance et (2) la compréhension des mécanismes de rupture associés à cette instabilité dans le but de réaliser une analyse du risque (voir Locat et al., cette conférence). Le site a d'abord été étudié en 1993 par une équipe de l'université Laval (Locat et Couture 1995b) qui a cartographié le réseau complexe de fractures et installé des tiges métalliques qui permettaient de faire un suivi des déplacements des fissures. Ces mesures ont été effectuées à plusieurs reprises en 1993 et, bien qu'il s'agisse d'une instrumentation rudimentaire, ils ont réussi à délimiter un compartiment dont les déplacements étaient plus importants [3 à 13 mm/mois]. Une section de ce bloc, nommé le Petit-massif, a atteint la rupture en juillet 1998 entraînant dans sa chute le remblai qui soutient la voie ferrée sur quelques mètres. Suite à cet événement, la voie ferrée est demeurée fermée le temps de construire un mur de soutènement en caissons de bois (figure 2).

En 2000, une cavité de deux mètres de diamètre s'est formée sous les rails lorsque le matériel du remblai s'est évidé dans l'une des fractures qui passent sous la voie. Occasionnellement, des ajouts de matériel sont nécessaires pour combler certaines dépressions mineures sous les rails et cela depuis longtemps avant même la première instrumentation dans les années 1990 (comm. pers. CN, 1993).

En 2008, un projet de recherche est confié à l'Université Laval pour développer un système de surveillance à distance. À l'automne 2009, une série d'instruments a été mise en place afin d'acquérir des informations sur (1) la position de la surface de rupture, (2) les déplacements associés aux diverses fissures, en

priorité celles du Petit-massif (3) l'intégrité du remblai et du mur de soutènement (4) les conditions d'eau

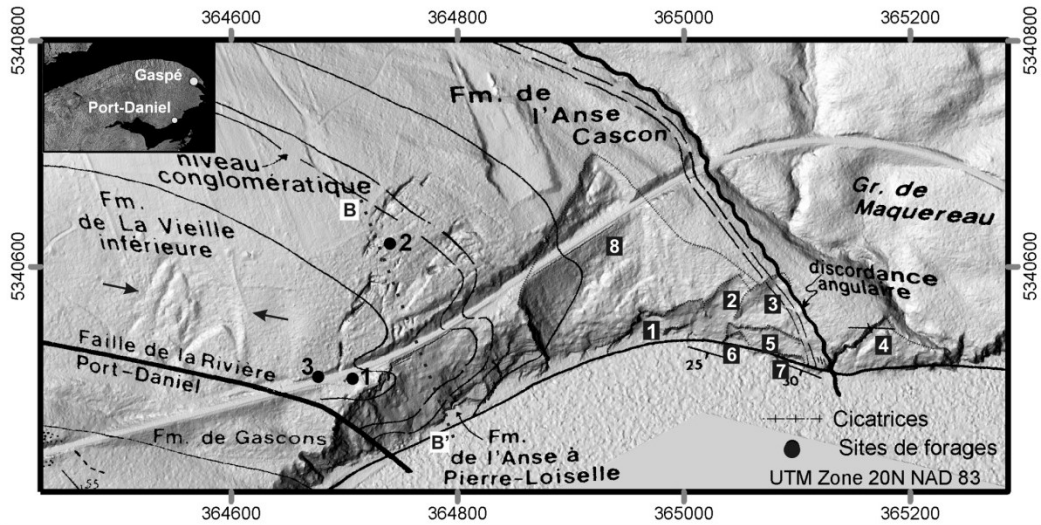


Figure 1. Modèle de terrain avec la carte géologique (modifiée de Bourque et Lachambre 1980) superposée. À l'est, les cicatrices de la pointe au Maquereau sont numérotées de 1 à 8 en blanc sur fond noir. Positionnement de la coupe géologique B-B' en tireté (figure 5) (encadré: © Ressources naturelles Canada. Tous droits réservés).

souterraine et (5) les conditions météorologiques. Trois types de suivis sont effectués. Le premier est un suivi manuel qui consiste à mesurer avec un ruban extensométrique des couples de tiges métalliques et à suivre les déplacements en profondeur avec un inclinomètre traditionnel. Deuxièmement, une série d'appareils électroniques reliés à un système d'acquisition permet d'obtenir des informations relatives aux mouvements et aux conditions hydrogéologiques à une fréquence élevée. Il s'agit d'appareils en forage (piézomètres, chaîne de capteurs «ShapeAccelArray ou SAA») et en surface (fissuromètres et clinomètre). Enfin, le dernier type de suivi est effectué par satellite radar (PTA-InSAR) sur des réflecteurs en coin (voir Couture et al., cette conférence).

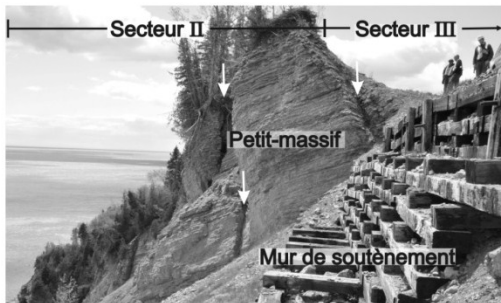
Figure 2. Vue vers l'ouest du Petit-massif en 2009 et du mur de soutènement construit en 1998. Les flèches pointent des fissures et les secteurs sont décrits à la section 4.1.

L'instrumentation présentement en place n'agit pas encore en tant que système de surveillance à distance. Il s'agit plutôt d'un système d'observation du massif, qui permet de réunir les données nécessaires à l'étude détaillée de la cinématique du mouvement. Au moment de rédiger ces lignes, les données sont acquises à distance, mais le suivi des déformations n'est pas encore automatisé. Une fois le comportement du massif cerné, des critères d'alertes pourront être établis et le passage de l'observation à la surveillance sera amorcé.

3 GEOLOGIE

La géologie du secteur a été étudiée par Bourque et Lachambre (1980) qui ont identifié deux éléments géologiques qui délimitent de part et d'autre le secteur instable de l'anse à Pierre-Loiselle. Il s'agit à l'ouest de la faille de la rivière Port-Daniel et à l'est d'une discordance angulaire marquant la limite entre des roches du Silurien et du Cambrien. Les deux éléments géologiques sont délimités sur la carte de la figure 1 (modifiée de Bourque et Lachambre 1980).

Le site de Gascons est constitué de roches sédimentaires associées à trois formations faisant partie du groupe de Chaleurs: Cascon, l'Anse à Pierre-Loiselle (APL) et la Vieille inférieure (La Vinf). La formation de



Gascons et le groupe de Maquereau sont situés à l'extérieur des limites géologiques nommées précédemment (discordances et faille).

La formation de Cascon est visible à la base de la falaise et est constituée de bancs de grès en alternance avec des lits de mudstone. Les grès ont des épaisseurs entre 10 et 50 cm et sont fortement bioturbés par endroits. Quelques lits conglomératiques sont présents. Un niveau à mudstone verdâtre à nodules calcaires est utilisé comme unité repère.

La formation de l'Anse à Pierre-Loiselle (APL) compose la majeure partie de la falaise rocheuse instable, où elle a une épaisseur de 60 mètres. A sa base, elle est constituée de bancs de grès fin calcaireux en alternance avec des mudstones arénacés et bioturbés. Les lits ont une épaisseur de 3 à 20 cm et établissent la transition entre la formation de Cascon et de l'APL. Les mudstones deviennent ensuite plus présents et contiennent de 30 à 80% de nodules calcaires et quelques grands coraux coloniaux et stromatopores.

En son centre, cette formation est marquée par une unité de conglomérats et de grès constitués de grains de quartz, de feldspath et de chert avec une matrice calcaireuse. Ensuite, la formation est constituée essentiellement de mudstones noduleux, dont certains bancs sont non-calcaireux avec des épaisseurs de 3 à 10 cm. À son sommet, elle présente des caractéristiques de la formation de la Vieille inférieure, avec une abondance de *Costistricklandia gaspensis* et une biolithite à coraux halysitidés de 90 cm. La présence de pyrite et de veines de calcite explique l'altération orangée (oxyde de fer) qui caractérise les faces des fissures.

La formation de la Vieille inférieure (La Vinf) n'est pas très répandue sur le site et se limite aux secteurs en altitude. Elle est présente dans le haut de la falaise et compose une partie du Petit-massif (figure 2). Elle est décrite comme une unité de calcilutite à nodules calcaires de 5 à 10 cm avec des interlits de mudstones et avec des stromatopores tabulaires, des coraux rugueux et coloniaux ainsi que des *Costistricklandia gaspensis*.

La pointe au Maquereau, qui délimite l'est de l'anse, est formée de roches métasédimentaires du groupe de Maquereau.

Puisque la formation de l'Anse à Pierre-Loiselle présente des caractéristiques des deux formations qui y sont adjacentes, les contacts ne sont pas francs et il est difficile de placer une délimitation sur le terrain.

Des carottes provenant de trois forages ont été analysées. Dans ces trois forages, la formation de la Vieille inférieure a été observée au-dessus d'un banc de haute densité en fossiles, associé à la biolithite de la formation de l'APL. Enfin, l'unité conglomératique a été repérée dans tous les forages, mais n'a pas été vue dans la falaise possiblement à cause de la présence des débris d'éboulis.

Il est intéressant de noter qu'à différents niveaux, les strates présentent des surfaces de glissements polies fort probablement créées lors de la formation de la faille de la rivière Port-Daniel. De telles surfaces peuvent donc

fournir une résistance au cisaillement du massif proche des valeurs résiduelles.

4 DESCRIPTION DES INSTABILITES

Les instabilités du secteur peuvent être regroupées en deux types, instabilités actives et passives (cicatrices de mouvement). Dans un premier temps, le glissement actif instrumenté est décrit et dans un deuxième temps, les cicatrices repérées à proximité sont présentées.

4.1 Glissement actif

La masse rocheuse impliquée dans le mouvement est estimée à 500 000 m³ (Locat et Couture 1995a) et est subdivisée en trois secteurs délimités à la figure 8. Le secteur II (figure 2) est une falaise de 63 mètres de hauteur, inclinée entre 40 et 60° et dont le pied se termine dans la mer. Dans certaines sections de la falaise, les strates sédimentaires sont visibles alors qu'ailleurs dans d'autres des débris d'éboulement cachent la roche en place. Les strates de la formation de l'Anse à Pierre-Loiselle sont orientées sud-est dans la falaise avec un pendage de 23° vers le sud-ouest, donc vers la mer. Cette morphologie est favorable à une érosion différentielle qui découpe le rivage en forme de dents de scie selon les propriétés mécaniques et les caractéristiques structurales des formations. Les strates formées de roches plus friables se détériorent plus rapidement que leurs voisines plus résistantes. Cette érosion mène à la formation de surplombs instables pouvant localement entraîner des chutes de blocs et l'éventuel recul de la falaise.

Au bas de la falaise, approximativement à trois mètres au-dessus du niveau de la mer, un suintement est visible sur une largeur de cinq mètres. Cette résurgence est alignée avec le mur de soutènement construit suite à l'éboulement de 1998 (figure 2) et pourrait correspondre à un drainage souterrain localisé le long de fissures enfouies sous le remblai.

Le nom Petit-massif réfère à une section de la falaise à l'ouest du mur de soutènement dont une partie est plus élevée que la voie ferrée. Plusieurs fissures verticales sont présentes près du Petit-massif, mais ne sont pas visibles sur le modèle de terrain. La figure 2 en présente quelques unes qui sont pointées par des flèches blanches. Le Petit-massif chevauche les secteurs II et III.

Le secteur III (figures 2 et 8) est un replat sur lequel est construite la voie ferrée. À l'ouest de l'instabilité, ce replat fait une vingtaine de mètres de largeur et est traversé par trois fissures sub-verticales ouvertes de 20 à 70 cm. En amont de la voie ferrée, la pente est de 45° et a une hauteur de cinq à vingt mètres. Puis, la pente s'adoucit jusqu'à environ 15° dans la partie amont qui constitue le secteur I.

Le secteur I est une forêt dans laquelle d'importantes fissures et linéaments ont été cartographiés jusqu'à une distance de 115 mètres au nord du chemin de fer. La zone considérée active est particulièrement bien délimitée par un réseau de fractures sub-verticales et

profondes de plusieurs mètres. Ce réseau intense de fractures ainsi qu'un pendage général des strates vers la mer assurent ainsi un drainage efficace de cette portion du massif rocheux.

Les fissures délimitant l'ouest du mouvement de terrain sont plus ouvertes que celles à l'est, laissant croire que le mouvement global ne s'effectue pas nécessairement dans le sens du pendage maximal du litage.

4.2 Cicatrices

Sur la pointe au Maquereau, la côte change de direction pour s'orienter est-sud-est. Ainsi, la direction de la côte se rapproche de celle du litage de telle sorte que le pendage des strates est dans la même direction que la pente du talus, favorisant les glissements planaires. En tout, huit cicatrices ont été dénombrées (figure 1) et semblent s'être produites le long d'un plan conforme au litage (i.e., rupture planaire). Les escarpements latéraux de ces glissements sont tous orientés de façons similaires, laissant supposer un contrôle structural de leur géométrie. Il est à noter que pour plusieurs cicatrices l'escarpement latéral gauche est absent. Les dimensions des cicatrices numérotées de 1 à 7 sur la figure 1 varient de 1000 à 20 000 m³ et elles sont situées à l'intérieur d'un amphithéâtre de dimensions beaucoup plus importantes et dont la géométrie s'apparente au glissement décrit à la section 4.1.

L'amphithéâtre le plus important est associé à une cicatrice ancienne présente avant la construction du chemin de fer dans les années 1920 (numéro 8, figure 1). Elle est située immédiatement à l'est du glissement actif et la voie ferrée la traverse sur 124 mètres. Dans cette section, le remblai est contenu par un mur de soutènement. Le modèle de terrain permet de constater que le remblai vient remplir une partie de la dépression causée par ce glissement.

Il est difficile de le dater, mais il pourrait avoir été initié à un moment où le niveau marin relatif était plus élevé qu'aujourd'hui, possiblement lors du niveau maximum qui semble être aux environs de 60 mètres au-dessus du niveau actuel de la mer (Syvitski 1992). Au sommet de cette cicatrice ancienne, des blocs semblent avoir subi un faible déplacement faisant en sorte qu'ils n'ont pas été évacués complètement de la zone de glissement.

À la connaissance des auteurs, cette cicatrice n'avait jamais été identifiée, ni par l'observation des photographies aériennes, ni même sur le terrain. C'est le levé LiDAR aéroporté réalisé à l'automne 2009 qui a permis son observation. Sa similitude avec le glissement présentement actif est frappante, tant par sa géométrie que par ses dimensions. Elle s'apparente à une rupture par dièdre. La végétation a complètement recouvert la cicatrice, sauf où d'autres mouvements plus récents se sont produits, numérotés de 1 à 7 sur la figure 1.

L'analyse des photographies aériennes permet d'affirmer que les glissements 3 et 4 (figure 1) sont survenus avant 1934, alors que la cicatrice numérotée 2

est apparue entre 1948 et 1963. La cicatrice 3 n'est pas visible sur les photographies aériennes, car elle est couverte de végétation. Le glissement 4 au contraire ne s'est jamais reboisé et est facilement repérable sur chacune des photographies. Sa cicatrice est remplie de débris, qui sont des blocs rectangulaires dont les plus petits ont une quinzaine de centimètres de côté alors que les plus grands sont de l'ordre du mètre.

À l'ouest du glissement étudié, un autre type de formes linéaires est observé sur le modèle de terrain (figure 1, pointé par des flèches), qui laisse croire que d'autres portions du territoire sont aussi sujettes à des instabilités. Le terrain semble avoir été soumis à un mouvement gravitaire qui s'est stabilisé. Cette partie est boisée. Cette indication d'instabilité n'avait pas été reconnue avant l'obtention des données LiDAR aéroporté.

5 MORPHOLOGIE DES LINEAMENTS ET STRUCTURE

5.1 Analyse structurale

La roche sédimentaire formant les côtes de l'anse-à-Pierre-Loiselle est fortement fracturée à diverses échelles. L'analyse présentée ici est effectuée sur les discontinuités aux niveaux des strates ou de plusieurs strates, mais n'inclut pas les grandes fractures ouvertes et linéaments qui sont traités à la section suivante. La morphologie des instabilités du secteur est fortement influencée par les familles de discontinuités. La famille la plus évidente correspond au litage et à un pendage et une direction du pendage de 23/193°. Deux autres familles principales sont orthogonales au litage et découpent les strates sédimentaires, il s'agit des familles A et B toutes deux à fort pendage. La famille A se divise en deux sous-groupes, résultant de l'inversion de la direction du pendage.

Deux autres familles secondaires de joints sont identifiées, les familles D et E. La dernière comporte peu de données. La famille C est similaire à la famille B, mais elle se démarque clairement lors de l'étude des grands linéaments. Ainsi, elle est considérée comme une famille à part entière. Le stéréogramme de la figure 3 et le tableau 1 présentent ces familles de discontinuités.

5.2 Familles de linéaments

Les linéaments dont il est question dans cette section regroupent les grandes fractures ouvertes, les dépressions linéaires et les escarpements des cicatrices de glissements. Ces structures sont classées en quatre familles, décrites au tableau 2 et représentées sur une rosette à la figure 4. Ces groupes peuvent être reliés aux familles de discontinuités mentionnées à la section précédente.

Les grandes fractures ouvertes permettent de poser des limites au glissement. Le glissement est délimité par les membres des familles 1 à l'est, ainsi que 2 et 3 au nord-ouest. Le même agencement se répète pour la

grande cicatrice et pour les plus petites de la pointe au Maquereau. Les groupes de linéaments sont associés aux familles de discontinuités A, B, C et D

6 ÉTUDE DES INSTABILITES

6.1 Mécanismes de rupture

Les secteurs décrits à la section 4.1 (figure 8) sont soumis à différents types de rupture. Dans le massif en général, il semble se former une rupture planaire et une décompression du massif. L'analyse cinématique montre qu'une rupture serait possible avec le litage comme surface de rupture, si la direction de pendage de la côte est modifiée pour se rapprocher de la direction du

Tableau 1. Caractéristiques des familles de discontinuités.

	Nombre d'éléments	Pendage(°)	Direction du pendage (°)
S0	43	23	193
Famille A	53	80	121
Famille B	52	72	026
Famille C	9	79	348
Famille D	15	76	089
Famille E	12	74	187

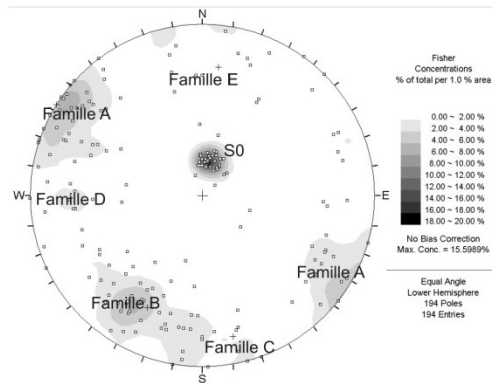


Figure 3. Stéréogramme des pôles des familles de discontinuités (hémisphère sud)

pendage du litage. Les familles A, B et D correspondent aux fractures latérales.

Dans la falaise, les blocs désarticulés semblent se détacher pour former des éboulements rocheux, dont le mécanisme serait associé à du basculement et à des ruptures par dièdres évoluant finalement en chutes de blocs. Les ruptures par basculement sont associées aux familles A et C et se produisent sur le plan formé par le litage. Les ruptures par dièdres sont possibles avec plusieurs couples de discontinuités, selon l'inclinaison du

talus qui varie entre 40 et 70°. Les couples les plus sensibles à la rupture par dièdre sont formés par le litage et la famille de discontinuités D et par les familles de discontinuités B et E.

6.2 Analyse de la cinétique globale

Aucun des mécanismes mentionnés ne peuvent expliquer une rupture de dimensions aussi importantes que celle qui est présentement en cours. Ainsi, il est fort probable que le mouvement implique plus d'un type de mécanismes. L'une des hypothèses proposée implique une rotation de la masse en mouvement. Le glissement planaire ne peut se produire pleinement selon la direction du pendage du litage. En fait, les couches sont plissées en bordure de la faille de la rivière Port-Daniel et le pendage des strates se renverse vers l'intérieur du talus.

Tableau 2. Caractéristiques des structures linéaires visibles sur le modèle de terrain.

Groupe de linéaments	Famille de discontinuités associées	Nombre d'éléments	Orientation moyenne (°)	Écart-type (°)
1	Famille B	7	125	8
2	Famille A	17	042	8
3	Famille D	13	007	13
4	Famille C	7	078	9

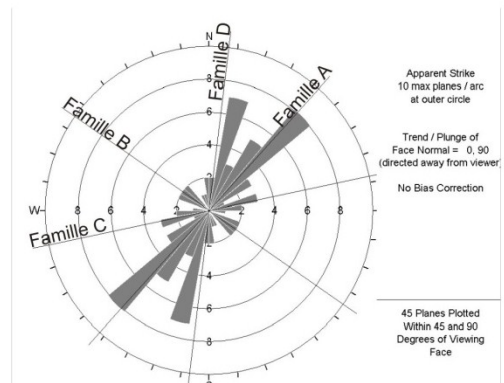


Figure 4. Rosette présentant l'orientation des linéaments et les familles auxquelles ils sont associés.

Ainsi, le mouvement est contraint vers le sud-ouest où ce secteur forme une sorte de butée contre la rupture planaire. Pour compenser, la masse effectue une rotation horaire. Cette rotation peut expliquer que les fractures à l'ouest sont plus ouvertes que celles à l'est

Une seconde hypothèse émise associe les mouvements à un mécanisme composite entre une rupture par dièdre et planaire. Le dièdre serait formé avec les discontinuités de la famille D et le litage. Les

familles A et B contrôlent l'extension du glissement en formant des ruptures par tension.

Pour le moment, encore plusieurs questions demeurent sans réponse. Une analyse plus détaillée des données récemment acquises est nécessaire pour faire la lumière sur les mécanismes permettant de mettre en mouvement cette masse rocheuse et leur rôle respectif. A ce propos, le positionnement de la surface de rupture est une information essentielle à obtenir pour cerner la cinématique des compartiments impliqués dans le mouvement global.

6.3 Surface de rupture

L'un des objectifs fixés lors de l'instrumentation de l'instabilité était de localiser la surface de rupture. À ce jour, les déplacements enregistrés par la chaîne de capteurs SAA permettent de déterminer sa profondeur au site de forages 2, situé en amont du mouvement (figure 1). En fait, les déplacements au-dessus de 23 mètres sont plus importants (10 mm) que ceux des capteurs inférieurs qui sont quasiment nul (2 mm). La surface de rupture serait à une profondeur de 23 mètres, ce qui la situe à l'intérieur de l'unité de conglomérat alterné avec des couches de mudstone très fragiles, tel qu'illustré sur la coupe de la figure 5. À ce moment, il n'est pas possible de positionner la surface de rupture avec certitude au site de forages 1 situé au niveau de la voie ferrée.

La surface de rupture est considérée conforme au litage et donc inclinée à 23°, dans une direction de 193°. En suivant ce raisonnement la surface de rupture serait à une profondeur approximative de 25 mètres en bordure de la voie ferrée le long du profil BB' (figure 1 et 5).

Sur l'une des faces du Petit-massif, il est possible d'observer des discontinuités formant des échelons (figure 6). Comme la structure locale est représentative de la géométrie du glissement, il est fort probable que cette structure soit associée à la rupture générale. Si c'est le cas, l'épaisseur de la zone instable est probablement plus importante en aval qu'en amont.

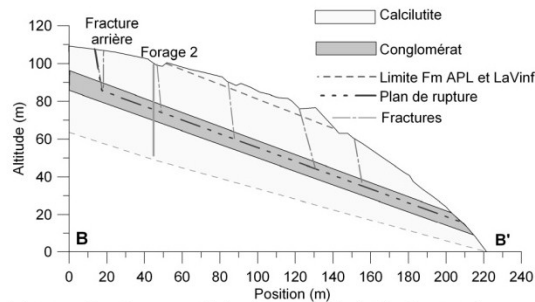


Figure 5. Coupe géologique BB' (voir figure 1 pour localisation). Les fissures observées en surface ont été prolongées jusqu'au plan de rupture estimé.



Figure 6. Formes en échelons (traits pointillés). Le fissuromètre 1 se referme depuis son installation. Les flèches indiquent les déplacements mesurés sur les tiges extensométriques, EX5, 6 et 7 (vue vers l'ouest).

6.4 Conditions hydrogéologiques

L'impact du réseau de fractures sur les conditions hydrogéologiques est encore peu connu. Aux trois sites de forages (figures 1 et 8), trois piézomètres à corde vibrante ont été installés à l'intérieur d'un même forage. Ces piézomètres fournissent des éléments cruciaux permettant d'évaluer les niveaux relatifs de la nappe phréatique entre la zone du glissement et celle intacte. Les résultats préliminaires tendent à souligner une différence dans les conditions hydrogéologiques, puisque l'on observe un changement d'environ dix mètres entre le niveau de la nappe phréatique des sites 1 (dans le glissement) et 3 (à l'extérieur du glissement) lesquels ne sont distants que de 31 mètres en surface.

Au mois d'avril 2010, suite à un épisode de pluie et à un réchauffement auquel est associée la fonte des neiges, un des piézomètres du forage situé en amont du massif a indiqué une augmentation de neuf mètres du niveau d'eau (en équivalent pression). Cette mesure indiquerait un niveau piézométrique temporairement au-dessus de la surface de glissement.

Le comportement des piézomètres au site 2 est particulier. Comme il est montré à figure 7, le piézomètre le plus en surface (P1) est situé juste au-dessus du plan de glissement et il mesure un niveau d'eau à peu près constant. Au contraire, les deux piézomètres situés sous la surface de glissement montrent une variation importante des pressions d'eau. Le P1 n'est pas soumis aux mêmes variations de pressions d'eau que P2 et P3 ce qui laisse supposer que la surface de rupture influence l'écoulement de l'eau (Binet *et al.* 2007).

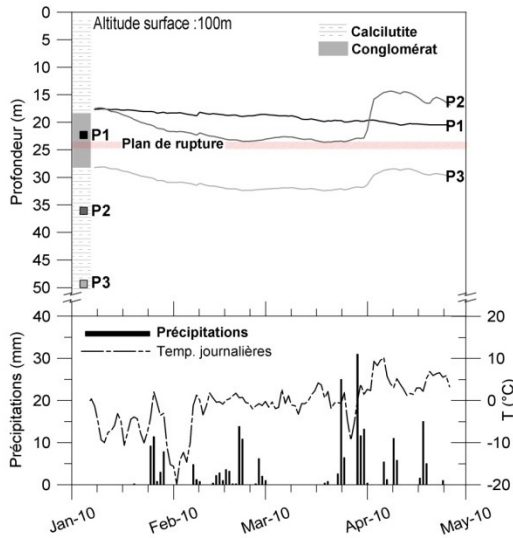


Figure 7. Niveaux piézométriques des piézomètres 1, 2 et 3 du site de forages 2 et précipitations (cumulées sur 24 heures) et températures (moyenne 24 heures). La position de la surface de rupture est déduite des résultats du chapelet SAA dans un forage voisin.

Le suivi à long terme de l'ensemble des piézomètres ne fait que commencer et les données futures devraient permettre de mieux comprendre les variations de la nappe phréatique et son rôle sur la stabilité du talus et éventuellement sur les mouvements. Par contre, à ce même suivi devra s'ajouter une analyse et possiblement d'autres mesures sur le terrain visant à valider ces observations à l'ensemble du talus.

7 ANALYSE DES DEPLACEMENTS

Les déplacements associés à ce massif sont lents et sont de l'ordre du millimètre au centimètre par année. Les données présentement disponibles sont encore limitées. Les observations sur le mouvement du Petit-massif en 1993 et 1994 indiquaient que les vitesses de déplacements étaient de l'ordre de 3 à 13 mm/mois (Locat et Couture 1995b).

En juin 2009, des couples de tiges ont été installés en vue de mesurer leur espacement avec un ruban extensométrique qui peut détecter des variations sous le millimètre. Entre juin 2009 et mars 2010, une série de six mesures a été réalisée avec cet appareil. Les conditions du terrain, telles que l'épaisseur de neige et la présence de glace ont empêché certaines lectures. Les mesures, bien qu'elles soient échelonnées sur une courte période de temps, montrent des déplacements significatifs.

Les déplacements les plus importants sont ceux des fissures du secteur I (figure 8) orientées nord-est. Chacun des couples montrent un déplacement régulier dont la vitesse se situe entre 0.2 mm/mois à 2 mm/mois.

La fissure montrant les déplacements les plus importants est celle des tiges EX14 et 15 avec une ouverture de 19 mm en 9 mois (figure 8).

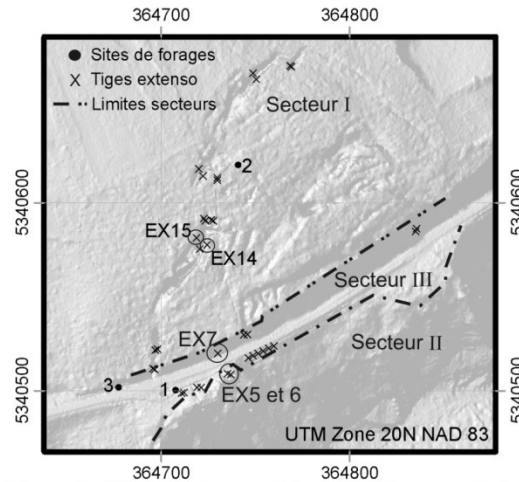


Figure 8. Réseau extensométrique, positionnement des sites de forages et délimitation des secteurs décrits à la section 4.1.

Les couples situés dans les fissures près de la voie ferrée (secteur III) ne montrent pas tous des comportements réguliers. Trois tiges indiquent des déplacements significatifs. Il s'agit de EX5, 6 et 7 indiqués aux figures 6 et 8.

En novembre, six fissuromètres à corde vibrante ont été installés dans le Petit-massif et en bordure de la voie ferrée. Depuis, une lecture est enregistrée à toutes les heures.

Deux fissuromètres indiquent des ouvertures constantes de 1.4 et 1.6 mm sur une période de novembre à avril. Trois fissuromètres se sont refermés depuis leur mise en place de 1, 2 et 3.5 mm. Ce dernier fissuromètre est localisé sur la fracture amont du Petit-massif (figure 6). La fermeture de cette fracture peut résulter du basculement du bloc supérieur du Petit-massif. Cette dernière hypothèse permet, en partie, d'expliquer les déplacements observés sur le réseau extensométrique. Enfin, l'un des fissuromètres ne montre pas encore de mouvement significatif.

8 ALEA ET RISQUE

L'aléa est associé à la probabilité temporelle et spatiale d'occurrence d'une rupture complète ou partielle du massif rocheux. Pour le cas présent, le facteur de sécurité est déjà inférieur à l'unité, puisque le glissement est actif. L'aléa devra donc être défini pour divers secteurs, selon l'intensité du mouvement anticipé et ses conséquences sur l'évaluation de la rupture. Par

exemple, l'hypothèse principale associée au mouvement du compartiment supérieur du Petit-massif est une rupture par basculement (figure 6). Pour définir la probabilité que le centre de masse dépasse le pied du bloc et bascule, il faudra relier ce moment aux déplacements mesurés (Zvelebil et Moser 2001).

L'aléa est associé à la cinématique du mouvement et à la progression des déplacements qui peuvent accélérer ou ralentir. Ainsi, les déplacements ont une dépendance non linéaire en fonction du temps, qui peut résulter de phénomènes saisonniers tels que la fonte des neiges et de mécanismes de rupture à long terme (Crosta et Agliardi 2003). De plus, il est influencé par les paramètres qui font varier l'état des contraintes, dont l'érosion par la mer du bas de la falaise et les pressions interstitielles qui semblent être importantes en haut de talus. Tous ces paramètres devront être considérés pour effectuer une approximation de la probabilité d'occurrence d'une rupture donnée.

Deux évènements qui ont portés atteinte à la voie ferrée sont répertoriés, soit la rupture partielle du Petit-massif de 1998 et un affaissement du remblai sous la voie ferrée en 2000. Ces évènements ont causé l'arrêt temporaire du trafic ferroviaire en plus de nécessité des travaux. Ainsi, même une rupture partielle en aval de la voie ferrée a des conséquences sur l'intégrité de la voie ferrée. Si une telle rupture est correctement anticipée, elle pourra être prise en compte pour les opérations ferroviaires et la sécurisation du secteur.

9 DISCUSSION

L'analyse du glissement rocheux de Gascons en est encore à ses premières étapes. La cinématique du glissement est complexe et semble faire intervenir plusieurs compartiments désarticulés et délimités par les grandes fractures sub-verticales. Les déplacements sont lents et ceux observés sur une période de moins d'une année sont significatifs.

Les lectures de l'inclinomètre installé à l'automne 2009 au site de forages 1 ne permettent pas encore de déceler des mouvements significatifs. Par contre, certaines indications permettent de poser des hypothèses quant à la localisation de la surface de rupture. Le forage traverse une cavité de près de deux mètres de 24 à 26 mètres de profondeur, indiquant que la zone au-dessus est en mouvement. Une zone hautement fracturée et située de 27 à 29 mètres de profondeur pourrait être associée à la surface de rupture. Enfin, il n'est pas écarté que plus d'un plan découpe le massif à diverses altitudes à proximité de la falaise. En fait, une zone très fragile constituée de mudstone est présente de 44.7 à 49.6 mètres et correspond à la même unité qui est reliée à la surface de rupture au site de forage 2.

Les pressions d'eaux exercées sur la surface de rupture apparaissent importantes à l'amont du glissement et plus faibles près de la falaise, ce qui laisse présager que le mouvement est peut être contrôlé non seulement par l'érosion en pied de talus, mais aussi par

une poussée de la masse mise en mouvement dans la partie amont du glissement.

Enfin, le suivi des déplacements sur une plus longue période permettra de mieux cerner la dynamique du mouvement. Une analyse en trois dimensions est nécessaire afin de cerner correctement les mouvements impliqués.

10 CONCLUSION

Le glissement de Gascons en Gaspésie implique un volume approximatif de 500 000 m³ de roche qui se déplace lentement et qui est traversé par un chemin de fer côtier. Immédiatement à l'est du glissement, une grande cicatrice ancienne similaire au glissement actif a été observée suite au levé LiDAR aéroporté. De nombreuses cicatrices de dimensions moins importantes recoupent cette cicatrice, là où la morphologie de la côte est susceptible aux glissements planaires.

Dans la falaise, certains compartiments rocheux semblent être soumis à du basculement et un éboulis semblable à celui de 1998 est envisageable. La rupture du massif global s'apparente à une rupture planaire, mais ce mécanisme ne permet pas d'expliquer correctement les déplacements observés.

L'instrumentation installée en 2009 permet d'acquérir des données sur les déplacements de surface et en profondeur, ainsi que sur les pressions d'eau. Toutes ces informations seront colligées pour déterminer les mécanismes de rupture impliqués et éventuellement pour déterminer l'aléa associé aux ruptures partielles et complètes de la falaise de l'anse à Pierre-Loiselle.

REMERCIEMENTS

Nous remercions nos partenaires financiers sans qui ce projet serait impossible : le ministère des Transports du Québec et le ministère de l'Éducation des Loisirs et du Sport du Québec. Nous tenons à souligner la participation de Transports Canada. Merci aux employés de la compagnie Measurand et à Pierre Therrien pour leur aide avec le développement, ainsi qu'à tous ceux qui ont participé aux travaux de terrain: Andrea Pedrazzini (Université de Lausanne), les étudiants du LERN, les gens de la Société des Chemins Fer de la Gaspésie et Stéphan Gravel. Merci à la compagnie Fournier et associés pour la réalisation des forages. Les auteurs remercient Didier Perret pour la révision de l'article, ainsi que le secteur des Sciences de la terre pour sa contribution (No. 20100061).

REFERENCES

Binet, S., Mudry, J., Scavia, C., Campus, S., Bertrand, C. and Guglielmi, Y. 2007. In situ characterization of flows in a fractured unstable slope. *Geomorphology*, 86: 193-203.

- Bourque, P.-A., et Lachambre, G. 1980. *Stratigraphie du Silurien et du Dévonien basal du sud de la Gaspésie*, Rapport ES-30, Direction de la géologie, Direction générale de la recherche géologique et minérale, Ministère de l'énergie et des ressources du Québec, Canada.
- Crosta, G.B. and Agliardi, F. 2003. Failure forecast for large rock slides by surface displacement measurements. *Can. Geotech. J.*, 40: 176-191.
- Génilab BSLG Inc. 1988. Rapport 88805 Stabilité et crevasses pour le Bureau de la protection civile du Québec. Rimouski, Qc, Canada : 10, non publié.
- Locat, J. et Couture, R. 1995a. Analyse de la stabilité d'un talus rocheux à Anse-aux-Gascons, Gaspésie, Québec, *48e Conférence canadienne de géotechnique*, Vancouver, BC, Canada : 8.
- Locat, J. et Couture, R. 1995b. Rapport final : Analyse de la stabilité du massif rocheux au millage 30.5, Division de Chandler, Anse-aux-Gascons, Gaspésie, Québec. Groupe de recherche en Environnement et en Géo-ingénierie, Université Laval, non-publié.
- Syvitski, J.P.M. 1992. Marine Geology of Baie des Chaleurs. *Revue Géographie physique et Quaternaire*, vol. 46, n° 3: 331-348.
- Zvelebil, J. and Moser, M., 2001. Monitoring Based Time-Prediction of Rock Falls: Three Case-Histories. *Phys. Chem. Earth (B)*, Vol. 26, No 2: 159-167.

Annexe C. Analysis of one year of monitoring data for the active Gascons rockslide, Gaspé Peninsula, Québec

Cloutier, C., Locat, J., Couture, R. et Lord, P-E., 2011. Analysis of one year of monitoring data for the active Gascons rockslide, Gaspé Peninsula, Québec. 5th Canadian Conference on Geotechnique and Natural Hazards, Kelowna, BC, Canada, 8p.

Analysis of one year of monitoring data for the active Gascons rockslide, Gaspé Peninsula, Québec

Catherine Cloutier, Jacques Locat & Pierre-Étienne Lord
Département de géologie et de génie géologique, Université Laval, Québec, Qc, Canada
Réjean Couture
Natural Resources Canada, Ottawa, Ontario, Canada

ABSTRACT

Along the coast of the Gaspé Peninsula, in Quebec, Canada, a railroad runs directly across an active rockslide involving a volume of 0.5Mm³. A near real time monitoring system has been installed in 2009 and 2010 in order to develop an early-warning system. After more than a year of data acquisition, an overall seasonal trend has been observed, with slower movements in the summer months and acceleration in fall through early winter. Information acquired by the monitoring system and other sources enables the evaluation of the failure surface geometry with good confidence.

RÉSUMÉ

Sur la côte de la baie des Chaleurs gaspésienne, au Québec, Canada, la voie ferrée traverse un glissement rocheux actif, d'un volume de 0.5Mm³. Un système d'observation, en quasi temps réel, a été mis en place en 2009 et en 2010 dans le but de développer un système de surveillance et d'alerte. Avec plus d'un an de données en main, une variation saisonnière des taux de déplacement est observée. Elle est caractérisée en été par un ralentissement et par des déplacements plus rapides qui débutent en automne et perdurent l'hiver. Les données acquises du système d'observation et d'autres sources permettent d'établir avec confiance la forme géométrique de la surface de rupture.

1 INTRODUCTION

Along the coast of the Gaspé Peninsula, in Quebec, Canada, a railroad runs directly across an active rockslide involving a volume of 0.5 Mm³ (Figure 1). First geotechnical studies in the early 1990's revealed an important fissures network and significant displacements of up to 13mm/month (Locat and Couture 1995a and b). In the municipality of Port-Daniel-Gascons, the locals have been aware of the rockslide for a longer time. The expression "thunder holes" is used by older people to refer to the fractures.

The Gascons rockslide is an active composite extremely slow to very slow rock slide-rock topple and is in its post-failure stage (Leroueil et al. 1996). In 2009 and 2010, a monitoring system was designed and installed. The monitoring effort is addressing two main aspects: (1) understanding and (2) mitigating, the mitigation component being part of risk management decision. The analysis of the rockslide will be based on knowledge generated by field techniques providing information on: the stratigraphy, the position of the failure surface, the types of mass movements involved, the role of groundwater and the displacements of the various blocks involved in the slide. Because the slide is undergoing post-failure displacements, the various in situ instruments are put in place not to evaluate the factor of safety of the slope, but to understand what affects its kinematics in order to be able to develop warning criteria based on displacement observations and their response to the various contributing factors such as erosion and pore pressure variations.

This paper presents the analysis of data from one year of monitoring. It starts with a general description of the rockslide and then continues with the analysis of the failure surface geometry, pore water pressures and displacements.

2 THE GASCONS ROCKSLIDE

The cliff of the Pierre-Loiselle bay is cut into Silurian to Devonian sedimentary rocks lying as an angular unconformity on the Cambrian Maquereau group (Bourque and Lachambre 1980). The sector of interest (Figure 1) is limited by the Port-Daniel River fault to the west and by the angular unconformity to the east.

The active rockslide is mostly taking place in the Anse-à-Pierre-Loiselle formation described by Bourque and Lachambre (1980) as a transition unit between the Anse Cascons formation (sandstones) and La Vieille inférieure (limestones) that are part of the Chaleurs Bay synclorium (Figure 2). The Anse-à-Pierre-Loiselle is comprised of sandstones alternating with mudstones, to fossiliferous units with increasing percentage of limestone concretions going upward. Bourque and Lachambre (1980) mention the presence of a conglomeratic unit in the middle of the Anse-à-Pierre-Loiselle formation. Strata are dipping 23° south-south-east (Figure 1) until they approach the fault, where the bedding planes curve upwards forming a syncline (red arrow in Figure 2).

East of the Gascons rockslide, scars of past translational slides are observed (Figure 1). Erosion of the toe of the slope by the action of the sea is certainly the key factor leading to instability. A strong structural

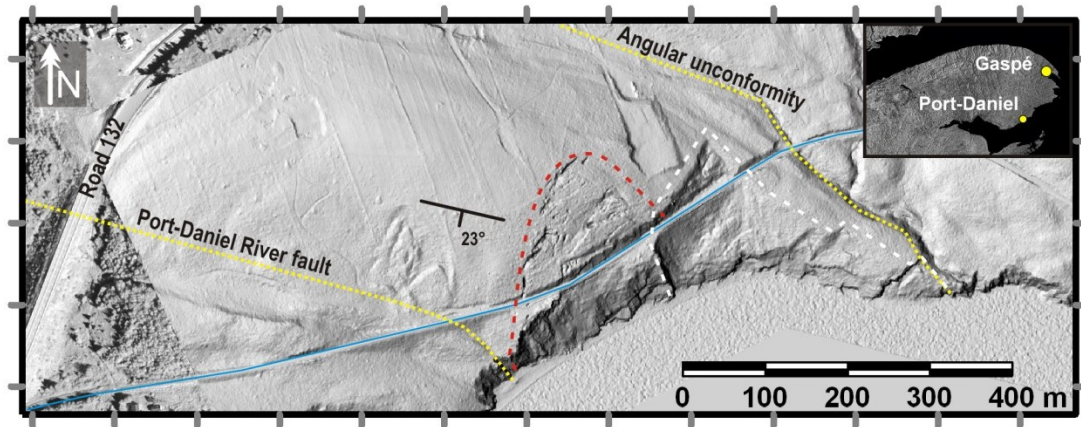


Figure 1. LiDAR survey of the Gascons rockslide (dashed line in red) area, showing in blue the railroad and other rockslide scars within the area defined by the white dashed line. (© Natural Resources Canada. All rights reserved.)

control is suggested by the repeating patterns in the active rockslide and the similar morphology with the ancient scar directly east of the Gascons rockslide.

Moreover, the main lineaments forming the opened fractures correspond with discontinuity sets of the rock mass (Cloutier et al. 2010). Those fractures are clearly visible on the elevation model produced from airborne LiDAR survey visible on Figures 1, 2, and 4. It is interesting to note that on the 1933 aerial photograph the terrain is clear of trees and the large fractures are not visible.

The sliding mass is divided into compartments, which are individualized from the main body to different degrees (Lord et al. 2010). In fact, near the top of the cliff, a sector of blocks of precarious stability is named the Petit-massif (Figure 3B and Figure 9A). Planar and wedge sliding, as well as toppling, are possible failure modes for those compartments; as for example the upper-eastern bloc of the Petit-Massif is kinematically free for planar failure (Figure 9A). The possible evolution of those compartments in rock falls is a threat to the railway integrity, because it could destabilize the foundation. In July 1998, such a phenomenon happened. The failed rock mass and the railroad were situated approximately at the same elevation (60 m above sea level); as a result, the granular material supporting the tracks followed the block down the cliff. This event caused damage to the track and interrupted the traffic for several days. The construction of a retaining wall was necessary.

Possible rock falls in the cliff area and ballast falling inside fissures leaving the rail without support represent short term risks for the railway. The main sliding mass, which is moving slowly, is not seen yet as a short term threat to the railway, but the effect of cumulate displacements over the years will affect the railway. Moreover, if the slide evolves towards faster rates of displacement, then the risk associated with the main body of the instability would increase.



Figure 2. Geological formations are identified on a photograph taken from the Chaleurs Bay. The red arrow is showing the curving of the bedding (the width of the photograph shows about 400m of the coastline).

3 MONITORING SYSTEM

The approach used to monitor the rockslide can be separated in two parts: direct and remote monitoring. The direct monitoring part is composed of sensors installed in-situ (Figure 3), while remote monitoring refers to satellite monitoring with the InSAR technique. The monitoring enables one to follow surface and in depth displacements (magnitude and direction), pore water pressures, tilting of the retaining wall, settlement of the railway ballast, and weather. The following presents briefly the monitoring techniques used to gain information on the six parameters mentioned above. A complete description of the system design is available in Locat et al. (2010).

The surface displacements are measured by an extensometer network, which consists of 44 rods anchored in rock and in soil. The distance between pairs of rods is measured manually. In 2009 and 2010 a total of nine measurements were taken. Because monitoring points can be added with relatively low cost and because the installation offers a lot of flexibility, this type of instrument has the best spatial dispersion, and therefore, gives very useful information. Surface displacements are also followed by the twelve crackmeters, read automatically every five minutes. They are installed in the railroad and in the cliff area (Figures 3 and 9A). In the short term, the movements in this sector appear to be the

most critical hazard for the immediate railroad safety. This is the sector of the 1998 instability.

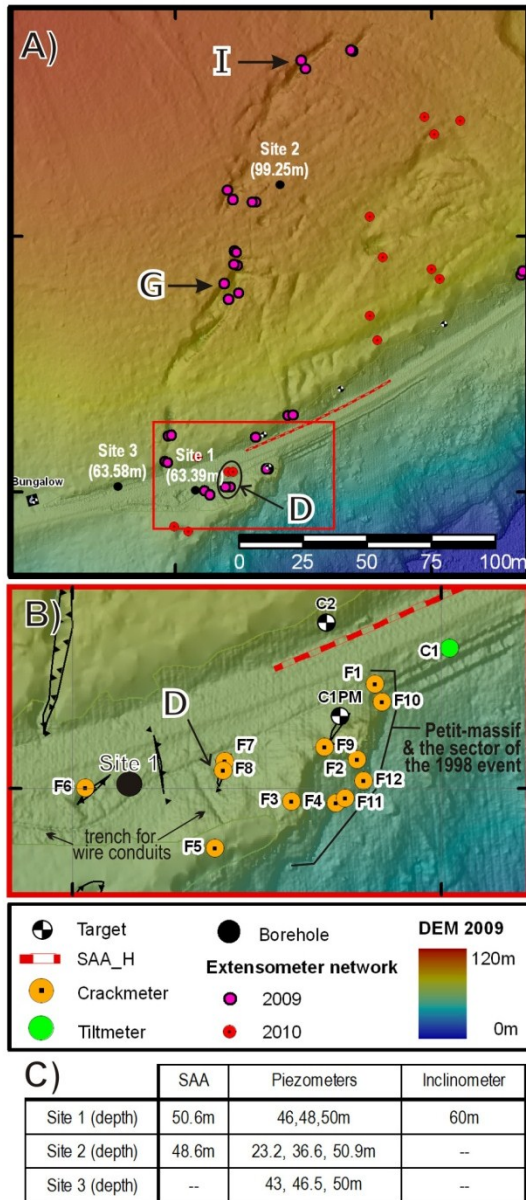


Figure 3. A) Location of in-situ instruments with borehole sites 1, 2 and, 3. B) Railway vicinity and Petit-massif area. C) Instruments in boreholes.

Surveys with a total station instrument are done on a number of targets that are either reflective plates or

marks on boreholes and other structures. Displacements are also followed by satellite radar techniques. Artificial radar reflectors have been installed to allow the use of the PTA-InSAR technique (Couture et al. 2010). This will not be addressed in this paper, but the reader is referred to the paper by Couture et al. (2011) presented in this conference.

At site 1 (Figure 3A), displacement profiles with depth are obtained from a traditional inclinometer reaching a depth of 60m and from a 52m shape-accel-array (SAA) (Danisch et al. 2010) acting as a permanent inclinometer. At site 2 (Figure 3), a 48m SAA is installed. The two vertical SAA are read automatically every six hours.

Crackmeters and extensometers are, in most cases, measuring opening and closing of fractures. Such readings are taken between two points inside the moving mass. These measurements are referred to as relative displacements. Moreover, an increase in distance means that the two points are moving apart but it does not give the direction of movement. To overcome this limitation, one rod can be paired with many others to have more than one direction of measurement, and some of the extensometer points are situated at the limit of the unstable mass. A pair of crackmeters has been installed at a 90° angle to read two components of displacement. Surface displacements obtained from PTA-InSAR and the total station surveys will be providing absolute displacements and directions. Therefore, the coupling of the crackmeters and extensometers with the PTA-InSAR and total station measurements will provide the necessary information to create a kinematic model.

At sites 1, 2, and 3, pore water pressures are measured. At each site, a borehole 50m deep contains three vibrating wire piezometers read every six hours. Depths of the installation are mentioned in Figure 3C. Every hour, a weather station (installed at the bungalow, Figure 3a) acquires data on air temperature, relative humidity, barometric pressure, snow and rain precipitation and wind speed.

For mitigating purposes, the integrity of one of the retaining walls and the ballast are monitored. Every five minutes, a biaxial tiltmeter is measuring changes in tilt of the retaining wall. A 60m SAA is buried horizontally parallel to the railroad and is measuring vertical displacements (Figure 3B). The horizontal SAA is read every half hour.

The instruments were not all installed at the same time, which explains why the data sets are not of equal time lengths. This was motivated by design objectives. Each instrument brings a better understanding of the rockslide; therefore, better design results from enhanced knowledge. At first, in June 2009 part of the extensometer network was installed to gain knowledge on the magnitudes of displacements in order to properly choose the automatic instruments. Then in Fall 2009, the electrical instruments, automatic acquisition and transmission were put in place, as well as eight permanent targets for remote sensing monitoring. In summer 2010, the monitoring system was enhanced with fourteen extensometer rods, six crackmeters, and the acquisition system was modified. Finally, in fall 2010 fifteen permanent reflectors for PTA-InSAR were added. The rockslide is monitored by multiple means and this

assures a useful redundancy in measurements. A year of data is now available and the next section presents the first results and interpretations.

4 DATA ANALYSIS

4.1 Failure surface

In this section, the sliding mass morphology will be presented, with emphasis on the failure surface geometry which is determined from detailed mapping of the fissure network, from borehole stratigraphy and from profile of displacements obtained from instruments in the boreholes. The main mass movement is a translational slide, with a wedge shape (Figures 4 and 5) and it slides mostly along the bedding planes of the Anse-à-Pierre-Loiselle formation.

Figures 4 and 5 present the failure surface morphology obtained by fitting a plane to the eastern limits of the slide. Those limits are determined from the detailed mapping of fissures and lineaments (Figures 1 and 4). A plane with the mean dip and dip direction of the bedding has been created and moved vertically, until the best fit with the eastern limits was obtained.

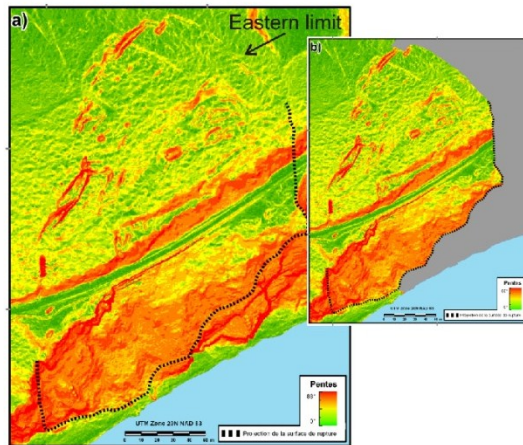


Figure 4. A) Delimitation of the unstable area in black determined by the grey plane in B) In grey, plane with direction and dip direction of bedding fitted to the eastern limit of the rockslide.

As can be seen on Figure 4B, the plane in grey matches well the eastern lineaments of the instability. This plane is also used to trace the limit of the unstable sector in the cliff (black line in Figure 4). Figure 5 presents the sector with the unstable mass removed. Of course, to use this method the hypothesis that the failure surface follows only one bedding surface is imposed. This exercise also enables the evaluation of the volume of the sliding mass to be 561 300m³.

From this analysis, the depths of the failure surface at the borehole positions are computed. At site 1, the failure surface would be at 46.5m under the surface (16.5m a.s.l.) and at 28m at site 2 (71.3m a.s.l.)(Figure 3). At site 1, the core from 44.7 to 49.6m is a highly fractured, non-calcareous mudstone unit alternated with thinner (approx. 1 cm) calcareous sandstone units. It is overlaid by a 6m thick coarser unit of mudstone alternated with sandstones and conglomerates, which is associated with the conglomerate mentioned by Bourque and Lachambre (1980). At site 2, the situation is very similar. The conglomerate unit is present from 19 to 29m and is characterized by coarser lithic fragments compared to site 1. Non calcareous mudstones are also found in and under the conglomerate unit from 25.6 to 34m. In both cases, it is the only section in the cores where the rock does not react to hydrochloric acid.

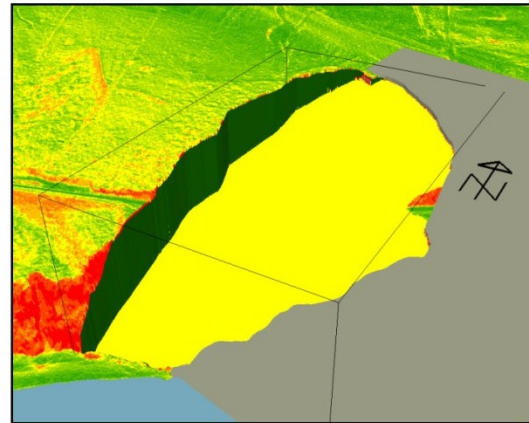


Figure 5. Morphology of the rockslide sector, if the unstable mass determined by the plane fitting technique is removed.

Instruments installed in the boreholes also give information about the geometry of the sliding mass. At site 2, the vertical SAA is showing a clear separation at 22m under the surface (Figure 6). The section shallower than 22m has experienced a total displacement of 43mm in a year and appears to be moving as a block. From 22 to 31m the annual magnitude of displacement is less important, but significant, with an integrated value less than 20mm. These observations are in good agreement with the maximum depth estimated above from the projection of the plane of the failure surface. As will be mentioned in the next section, the displacements above and below 22m have different patterns and directions of movement.

The situation is different for the inclinometer and the SAA installed at site 1. Both instruments are showing similar trends, but the trends are different from what is observed at site 2 and for multiple reasons the interpretation is not as self-explanatory. In fact, for the

boreholes at site 1 it is important to take into consideration

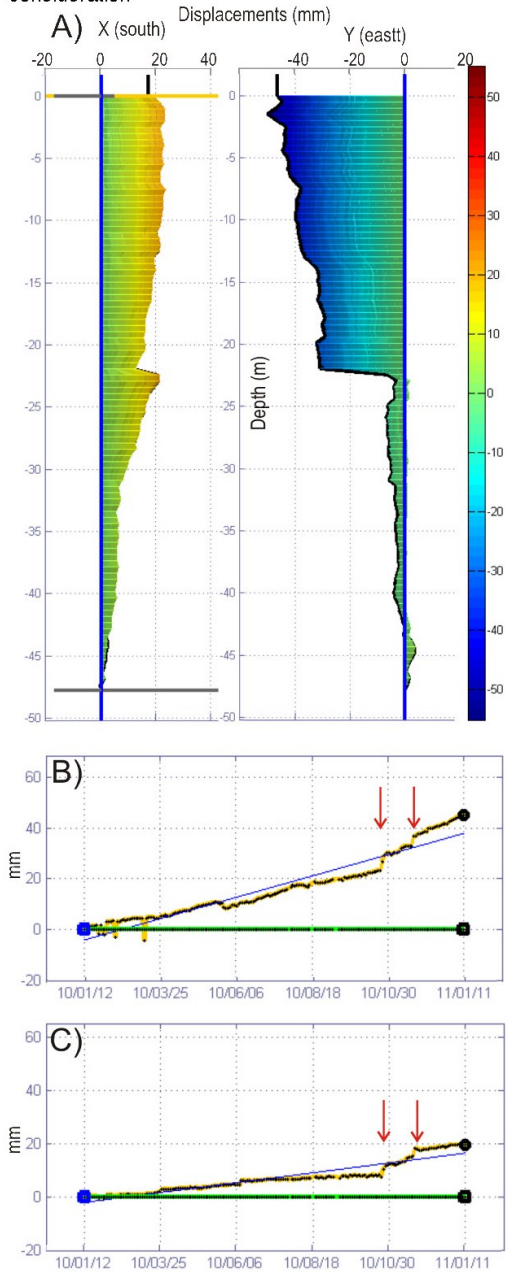


Figure 6. A) Displacement vs depth profile for SAA at site 2 in the X(south) and Y(east) direction. B) Displacement vs time at a depth of 10m. C) Displacement vs time at a depth of 25m.

that a cavity of 2m was encountered while drilling and that the quality of the rock mass overall is lower than at site 2 as estimated from RQD and core recovery data (Danisch et al. 2010). Such void spaces in the rock prevent adequate grouting of the inclinometer tubing and of the SAA in that portion of the borehole. Therefore, part of the displacement measured would be due to the deformation of the tubing in those void spaces. This hypothesis is also supported by the “S” shape of the SAA, suggesting that some deformation of the tubing under gravity may have taken place soon after the installation.

The inclinometer data set is composed of four measurements distributed from December 2009 to July 2010. For the SAA, the data set is longer and starts in October 2009 and continuous monitoring is done, at a rate of every 6 hours. One thing that can be seen from the results is that the displacements are more chaotic and are not indicative of monolithic block movement. The deeper displacements are observed at a depth of 43m, which is in good agreement with the position of the failure plane shown in Figures 4 and 5. The preliminary analysis of the displacement direction shows that it is not parallel to the dip direction of the bedding planes. Both the SAA and the inclinometer data are showing maximum displacement in the east-south-east direction, which may indicate that in that portion of the rock mass, the slide mass is also moving in the direction of the main escarpment.

It is believed that the main failure surface position and shape is established with a significant confidence level. It is also becoming clear that shallower failure planes exist and movements are happening in more than one direction. Other types of data are also providing information to help to understand the rock mass morphology, behaviour and failure surfaces.

4.2 Pore water pressures

Pore water pressures are measured in three boreholes located at sites 1 (near the cliff), 2 (uphill) and 3 (outside of the sliding mass) (Figure 3). The first year of data reveals differences in the piezometer responses.

At site 1, an equivalent water level of 18m a.s.l. is calculated from the data from the three piezometers. The failure surface is estimated to be at an elevation around 16.5m a.s.l.. No variation is seen through the year, and the water level shows very little response to external factors (precipitation and snow melt). This is in complete contradiction with what is observed uphill (site 2).

At site 2, three piezometers are installed at depths of 23.3, 36.6 and 50.9m (Figures 3 and 7). Piezometer P4, situated above the failure surface, shows very different behaviour compared to P5 and P6, installed under the failure surface. As seen in Figure 7, P4 data are slightly influenced by precipitation and snow melt; it shows a constant water pressure with a slight decrease stabilizing in late summer 2010. On the contrary, P5 and P6 are showing fluctuations that can be linked with external events, such as the snow melt period indicated in Figure 7. This is suggesting that the sliding mass acts as a very effective drain. Pore pressure variations at P5 and P6 are probably linked to fissures filling with water. In a parametric study on the effect of water level on stability,

Locat and Couture (1995b) have shown that the factor of safety gets close to one or less once the water level reaches the failure surface.

Those observations would not be possible without the automatic acquisition of the pore water pressures every 6 hours.

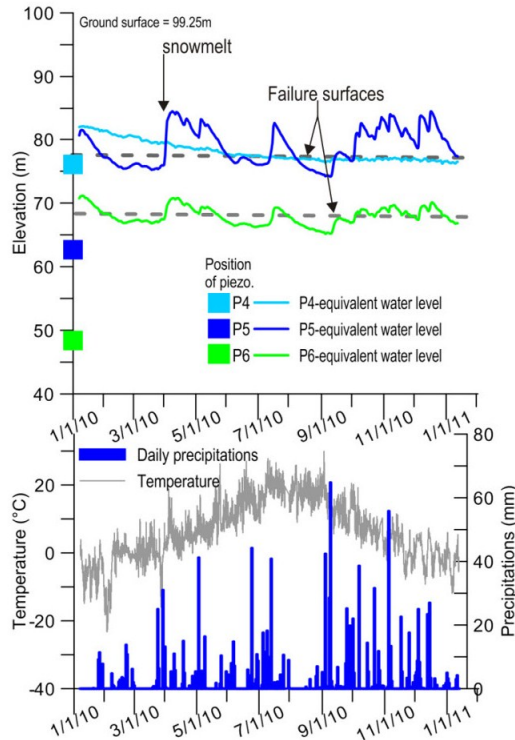


Figure 7. Pore water pressures measured at site 2 by piezometers P4, P5, and P6 and temperature and daily precipitations observed for the same period.

4.3 Displacements

As said earlier, a clear failure surface is observed at 22m depth on the vertical SAA at site 2, but significant displacements are occurring until 31m depth (Figure 6A). The mass above 22m depth reached a total displacement of 43mm in a year, while the magnitude of displacement increases regularly from 31 to 22m to reach a maximum value of 20mm.

The displacements of the lower mass are episodic. In between those events, the mass is coming almost to a halt as can be seen from the graphic in Figure 6C. Those episodic movements are also observed in the upper part, but a continuous movement is added to the trend (Figure 6B) of 2.5 to 4mm/month. The direction of the episodic

movements is south, while the regular displacements of the mass above are towards the west.

The episodic displacement pattern of the lower part became clear late in fall 2010 after the two events indicated by arrows on Figures 6B and 6C. At the time of writing, no clear relations have been established with water pressures or precipitation. A possible explanation would be that the shape of the profile in Figure 6 might be due to a toppling of the lower block, while the upper part is sliding. The rock mass above could be dragged by the lower part.

The displacements measured by the vertical SAA situated uphill are absolute because they are measured from a point below the unstable mass. They can be compared to displacements obtained from extensometer pairs situated in fissures named G and I (Figure 3A), that have annual displacements of 17 and 10mm respectively. The displacements are smaller but of the same order of magnitude. Because there is a fissure uphill of fissure G, relative displacements are measured. In the case of fissure I, no fissures have been observed uphill.

The extensometer measurements of fissures G and I show mostly regular and continuous patterns, which is not the case for all of the extensometer pairs (Figure 8). In the railway vicinity, chaotic patterns are observed on some fissures, such as fissure D (Figures 3 and 8). Moreover, displacements measured by crackmeters F2, F3, F4, F5, and F6 are much smaller than what is measured with extensometers in larger fissures. Those crackmeters are installed on opened fissures in the cliff and railway vicinity and the measured displacements vary from 1.2 to 2.3mm in a year. Those measurements do not represent the total displacement of a rock compartment, but the relative displacement between two blocks.

F11 and F12, two crackmeters installed in July 2010, show particular displacements (Figure 8A). The mean rate of displacement of F11, for five months of operation, is 1.7 mm/month, which is much higher than what is observed on the other crackmeters. F12 has been installed to measure displacement on a sliding plane instead of the opening of a fracture as shown in Figure 8B. The displacement observed is concentrated in one event, as is the case for the vertical SAA at site 2 (Figure 6C).

The chaotic pattern is related to subsequent closing and opening of fissures that are either due to changes in direction, rotation or unsynchronised movements of blocks. This probably reflects a higher degree of individualization of the compartments closer to the cliff.

For the instruments installed in November 2009, over a year of data has been acquired and seasonal variations are observed on most of the sensors. They are characterized by a decrease in movement rates from June to September. Figure 8 shows two examples of the data showing seasonal variations, the crackmeter F6 and the horizontal SAA (Figure 3).

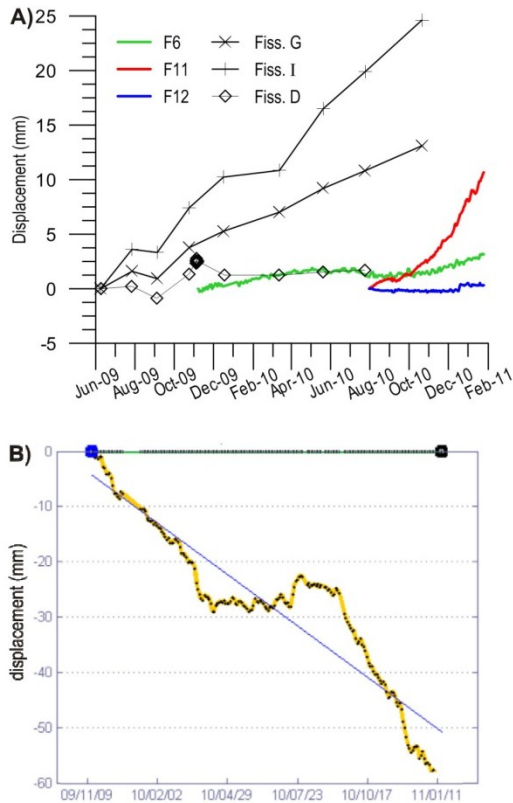


Figure 8. A) Displacement of extensometer in fissures G, I, and D, as well as crackmeters F6, F11 and F12. B) Vertical displacement of the horizontal SAA buried in the ballast.

5 DISCUSSION

For the instruments installed in 2009, more than one year of data is now available. We are starting to get more familiar with what the measurements of every sensor mean and what information can be determined in terms of the rock mass behaviour.

From the beginning, it was planned that the installation of instruments would be conducted in two steps almost a year apart. The data obtained from the first instruments was very useful for the design of the second installation effort. In summer 2010, instruments were added to answer the questions that arose from those initial data and also to correct some flaws that were noticed through the validation phase of the system.

The extensometer network has been extended to the eastern side of the slide (purple dots in Figure 3). Along the eastern limit of the instability, the rock is not visible and the fracture network is limited to linear depressions in the ground. It is in contrast with the western side, where

fractures are clearly developed and opened. Only two measurements have been taken so far on the new extensometer pairs and those data are not included in this paper.

The seasonal pattern described above is relying only on one year of data. The seasonal variation observed shows a decrease in movements in summer, but a longer period of observation is needed to support the hypothesis. It has to be noted that the 1998 event happened in July, so the summer months are not necessarily free of movements.

Not only the magnitude of displacement is useful, but the direction of movement is also of prime relevance to correctly understanding the kinematic behaviour of the sliding mass and the interactions of compartments. Already, data from the SAA and inclinometers are giving meaningful information about the direction of sliding.

All the data obtained enable a better understanding of the kinematic behaviour of the rockslide. The analysis presented in this paper is preliminary and a lot of interesting analysis is still to be done.



Figure 9. A) Position of the crackmeter F12 and looking west at the Petit-massif B) F12 is installed to monitor a translational movement of the upper block relative to the lower block. F11 is measuring the opening of the crack below F12.

6 CONCLUSION

A railroad runs directly across the active Gascons rockslide in the municipality of Port-Daniel-Gascons. A monitoring system was installed in 2009 and 2010 to investigate the post-failure behaviour of an active rockslide in order to create an early-warning system.

The monitoring system is coupling direct (in-situ geotechnical instruments) and remote (InSAR) monitoring. The failure surface geometry is determined from stratigraphy, morphology and displacement profiles with depth. The rock mass is sliding on bedding planes of the Anse-à-Pierre-Loiselle formation associated with the conglomeratic unit and non-calcareous mudstone.

Pore water pressure measurements show that, in the upper part of the slide, water pressure developing near the failure surface might be an important factor. The increase in pressure is related to snow melt and precipitation. Such responses to external factors are not seen by the piezometers at site 1, situated on the seaside of the railroad.

Displacement rates are subject to seasonal variations, and they vary throughout the instability. Moreover, the direction of movement is not continuous across the rockslide.

To conclude, this paper presents the advancements of the Gascons project and preliminary results obtained from the monitoring system as of January 2011. Continuous acquisition of data is ongoing and field work is planned to get measurements from manual reading instruments twice a year. The reader is referred to the paper by Couture et al. (2011) presented in this conference for information about the indirect monitoring realised with the PTA-InSAR technique.

ACKNOWLEDGEMENTS

The writers would like to acknowledge the support of the Ministère des transports du Québec, Transport Canada, the Ministère de l'éducation des loisirs et des sports du Québec, and the Canadian Space Agency. The writers would like to thank Lee Danisch from Measurand and Pierre Therrien from Laval University for the development of data management tools and acquisition system, and Dominic Turmel from Laval University for his help with field work. Thanks also to the Chemin Fer de la Gaspésie and Railterm for their logistic support. Thanks to Baolin Wang for his review. The Earth Science Sector contribution number is 20100448.

REFERENCES

- Bourque, P.-A. and Lachambre, G. 1980. *Stratigraphie du Silurien et du Dévonien basal du sud de la Gaspésie. Rapport ES-30*. Québec, Direction de la géologie, Direction générale de la recherche géologique et minérale, Ministère de l'énergie et des ressources du Québec: 123.
- Cloutier, C., Locat, J., Lord, P.-É., and Couture, R. 2010. Caractérisation des instabilités côtières dans le secteur de Port-Daniel-Gascons, Gaspésie, Québec. *63rd Canadian Geotechnical Conference and 6th Canadian Permafrost Conference*, Calgary, AB, Canada, 71-79.
- Couture, R., Charbonneau, F., Murnaghan, K., Singhroy, V., Locat, J., and Lord, P.-É. 2010. PTA-InSAR rock slope monitoring at the Gascons site, Gaspé Peninsula, Québec. *63rd Canadian Geotechnical Conference and 6th Canadian Permafrost Conference*, Calgary, AB, Canada, 102-110.
- Couture, R., Charbonneau, F., Singhroy, V., Murnaghan, K., Drouin, H., Locat, J., Lord, P.-É., and Cloutier, C. 2011. PTA-InSAR rock slope monitoring at the Gascons site, Gaspé Peninsula, Québec: Preliminary results. *5th Canadian Conference on Geotechnique and Natural Hazards*, Kelowna, BC, Canada.
- Danisch, L., Patterson, T., Cloutier, C., Locat, J., and Lord, P.-É. 2010. Integration of SAA technology for coastal rock slope movement monitoring at Gascons, Gaspé Peninsula, Québec, Canada. *63rd Canadian Geotechnical Conference and 6th Canadian Permafrost Conference*, Calgary, AB, Canada, 86-93.
- Leroueil, S., Vaunat, J., Picarelli, L., Locat, J., Lee, H., and Faure, R., 1996. Geotechnical characterization of slope movements, in Senneset, K., ed., *Seventh International Symposium on Landslides*, Volume 1: Thronheim, A.A. Balkema, p. 53-74.
- Locat, J., and Couture, R. 1995a. Rapport final : Analyse de la stabilité du massif rocheux au millage 30.5, Division de Chandler, Anse-aux-Gascons, Gaspésie, Québec: Québec, Groupe de recherche en Environnement et en Géo-ingénierie, Université Laval, p. 95.
- Locat, J. and Couture, R. 1995b. Analyse de la Stabilité d'un Talus Rocheux à l'Anse-aux-Gascons, Gaspésie, Québec, *48th Canadian Geotechnical Conference*, Vancouver, BC, Canada: 885-892.
- Locat, J., Cloutier, C., Lord, P.-É., Therrien, P., Jacob, C., Nadeau, A., Hébert, D., Couture, R., Charbonneau, F., Singhroy, V., Murnaghan, K., Danisch, L., Jaboyedoff, M., Pedrazzini, A., and Gravel, S. 2010. An integrated mass movement monitoring system for rockslide hazard assessment at Gascons, Gaspé Peninsula, Québec: An Overview. *63rd Canadian Geotechnical Conference and 6th Canadian Permafrost Conference*, Calgary, AB, Canada, 35-43.
- Lord, P.-É., J. Locat, et al. 2010. Analyse des déplacements du glissement de Gascons, Gaspésie, par couplage d'observations aéroportées et terrestres. *63rd Canadian Geotechnical Conference and 6th Canadian Permafrost Conference*, Calgary, AB, Canada, 56-64.

Annexe D. Kinematic considerations of the Gascons rockslide, Québec (Gaspésie)

Cloutier, C, Locat, J. Lord, P-É, Couture, R., et Jaboyedoff, M., 2012. Kinematic considerations of the Gascons rockslide, Québec (Gaspésie), Canada, 11th International Symposium on Landslides and 2nd North American Symposium on Landslides, Eds.: E. Eberhardt, C. Froese, A. K. Turner, S. Leroueil, Taylor and Francis Group, London, Banff, 2012, vol. 2, pp. 1264-1270.

Kinematic considerations of the Gascons rockslide, Québec (Gaspésie), Canada

C. Cloutier, J. Locat & P-E. Lord

Laboratoire d'études sur les risques naturels, LERN, Université Laval, Québec, Qc, Canada

R. Couture

Geological Survey of Canada, Natural Resources Canada, Ottawa, On, Canada

M. Jaboyedoff

Institute of Geomatics and Analysis of Risk (IGAR), University of Lausanne, Switzerland

ABSTRACT: An integrated mass movement monitoring system including ground and satellite observations has been developed for an active coastal rockslide threatening a railroad in the Gaspé Peninsula, Québec, Canada. The slide consists of an overall wedge failure, involving a volume of 560 000 m³, composed of multiple compartments that are more or less well individualized. A first model to define the blocks forming the sliding mass is discussed and tested with displacement data. In the south part of the slide, the blocks are moving individually, while in the north part, they move as a whole and faster. Changes in the movement's direction have also been observed. Fine analysis of the kinematic behaviour of the slide will lead to a better evaluation of risk associated with this active rockslide and to the implementation of warning criteria.

1 INTRODUCTION

Post-failure displacements of a landslide can take many forms, in terms of speed. Some active landslides are known to accelerate with external factors such as rain events or freezing cycles (Blikra 2008, Cruden & Varnes 1996, Crosta & Agliardi 2003, Rose & Hungr 2007, Zangerl et al. 2010). The understanding of post-failure behaviour of landslides is important to assess hazards and risks as a very slow landslide, if velocity remains constant, will not have the same consequences than an extremely fast one.

In the Gaspé Peninsula in Québec, Canada (Fig. 1), an active rockslide, involving a volume of 560 000 m³, has been identified in 1980 and first geotechnical investigation has been made in 1994 (Locat & Couture 1995a, b). The only railroad that reaches the town of Gaspé is running directly across this coastal instability. Frequent maintenance is needed in the sector due to the movements of the rockslide. In order to contribute to the safe operation of the railroad, the Gascons project was initiated in 2009. A monitoring system has been put in place to understand the various types of movements in an attempt to develop both warning criteria and risk assessment scenarios to be considered as part of a risk management for the Gascons site (Locat et al. 2010).

This paper presents briefly the advances made in the integration of slope displacements by coupling different sensors in a kinematic analysis of the rockslide. Descriptions of the monitoring system and of

the rockslide and examples of the data acquired are presented and discussed.

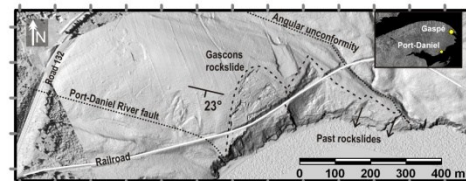


Figure 1. Localisation of the Gascons rockslide.

2 MONITORING SYSTEM

The actual monitoring system of the Gascons rockslide has been put in place in multiple phases from June 2009 to summer 2011, as we felt that more information was needed in order to finalize the conception. The system is composed of sensors connected to an automatic acquisition system and of manually made measurements.

The monitoring enables one to follow surface and in depth displacements (magnitude and direction), pore water pressures, tilting of the retaining wall, settlement of the railway ballast, and weather. Figure 2 presents the instrumentation map. Six boreholes have been drilled for instrumentation and to study the stratigraphy. A complete description of the system design is available in Locat et al. (2010).

Profile of displacements with depth is obtained from a traditional inclinometer casing and probe, and from two shape accelerometers arrays (SAA). The

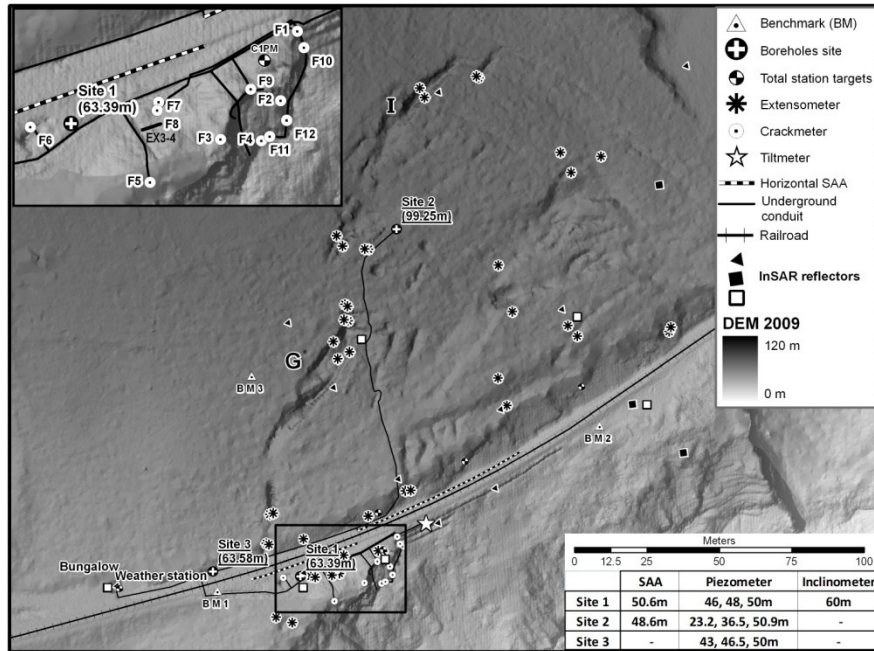


Figure 2. Instrumentation map of the Gascons monitoring system. The position of the data logger is marked on the map as bungalow and the letters G and I refer to fissures name.

SAA is a chain of 50 cm joint-linked rigid segments (Danisch et al. 2010). Each segment has accelerometers that enable to calculate its inclination and the shape of the chain. It acts as an in-place inclinometer.

The surface displacements are measured by an extensometer network, which consists of 44 rods of 45.7 cm anchored in rock and in soil. The distance between pairs of rods is measured manually with a sub-millimetric precision. Surface displacements are also followed by twelve crackmeters, read automatically every five minutes. They are installed along the railroad and in the cliff area, south of the railroad (Fig. 2). Nine vibrating wire piezometers are installed in three boreholes located on Figure 2. Piezometric measurements are collected four times a day.

An automated system has been programmed and deployed for data collection, transfer, correction, and conversion. The processed data can be visualized on a website with private access and exported for further analysis. Raw data are also accessible to users.

Along with direct in situ monitoring, satellite monitoring with the InSAR technique is done (Couture et al. 2010, 2011) and will enhance the knowledge on displacements.

3 ROCKSLIDE DESCRIPTION

The active Gascons rockslide is a translational slide, with a wedge shape. Fissures are clearly visible on the elevation model produced from airborne and terrestrial LiDAR surveys (Figs. 1, 2). The wedge failure slides mostly on the bedding plane of the Anse-à-Pierre-Loiselle formation dipping 23° south-south-west. Near the fault shown on Figure 1, the bedding planes curve upwards forming a syncline (Cloutier et al. 2010).

Bourque and Lachambre (1980) describe this formation as a transition unit between the Anse Cascons formation (sandstones) and La Vieille inférieure (limestones). The Anse-à-Pierre-Loiselle is composed of sandstones alternating with mudstones, to fossiliferous units with an upward increasing percentage of limestone concretions. A conglomeratic unit marks the middle of the Anse-à-Pierre-Loiselle formation.

Discontinuity sets of the rockslide are shown on the stereonet of Figure 3a. The two sets forming the wedge are in bold character. From this interpretation, the main direction of movement is believed to be south/south-east.

Considering that the shape of the slide is a wedge, a three dimensional understanding is necessary to analyze the displacement data. In fact, the thickness of the sliding material is thinning from west to east and the direction of movement is strongly influenced by the structure of the rock.

The depth of the failure surface is known with a good level of confidence. The geometry of the sliding mass has been interpreted from instruments installed at borehole sites 1 and 2, from stratigraphy and from morphological studies (Cloutier et al. 2011). Displacement profiles obtained at the borehole site 2 (Fig. 2) is shown in Figure 3b. In this sector, the failure surface's depth is 22m.

East of the Gascons rockslide, the combination of cliff and bedding dip directions creates a favorable structure for planar slides. Indeed, scars of older translational slides are observed (Fig. 1). Erosion of the toe of the slope by the action of the sea is the key factor leading to instabilities.

4 APPROACH FOR DISPLACEMENT ANALYSIS

4.1 Fracture versus block framework

In the field, the activity of the rockslide is represented mostly by open fissures, depressions and lineaments. Measuring the distance between markers set on both sides of a fissure is an easy and convenient way of following its evolution, as it is done with crackmeters or extensometers. But the real interest lies in the rock's movement. Thus, it is necessary to be able to relate the measures on cracks to the actual displacement of blocks and their impact on the evolution of the rockslide and of course, on the elements at risk. This requires the identification and clear definition of the geometry of the blocks involved which remains an ongoing challenge.

4.2 Hypothesis for block diagram

A first hypothesis for the block representation of the rockslide has been made based on morphological criteria and is presented in Figure 4 (modified from Lord et al. 2010). The criteria followed are that; (1) a block is delimited by cracks, lineaments and depressions, (2) all the fissure reach the failure surface, and (3) a fracture stops when it intercepts another one. With those rules, a first model is created. Then, the model is tested with displacement data and appropriately modified with incoming new information (displacements and field evidences). The model presented here is a 2D block model which assumes that the surface fissures project onto the failure plane underneath. Issues related with this method are discussed in Section 6.

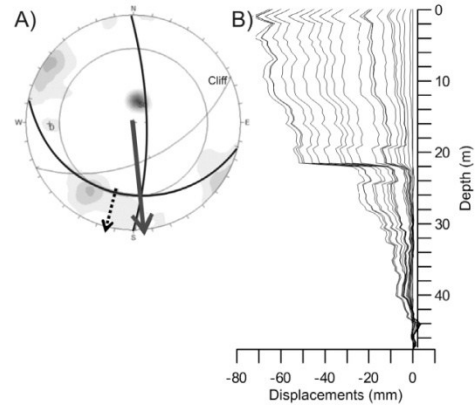


Figure 3. a) The grand circles of the bedding (S0) and the discontinuity set (D) defining the wedge are in a bold on the stereonet (lower hemisphere). The longer arrow is the wedge's direction of movement; the other arrow is planar sliding direction. b) Monthly displacement profiles of SAA at borehole site 2, from January 2010 to September 2011.

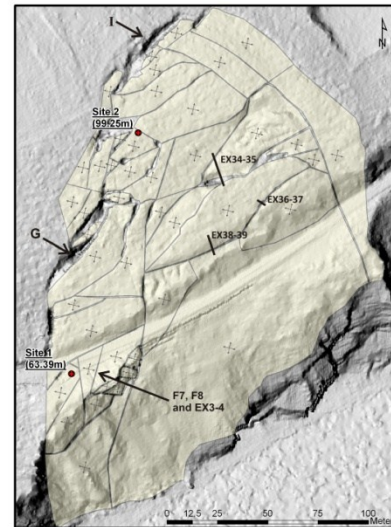


Figure 4. First block model of the Gascons rockslide. The axes in the blocks center are oriented with the bedding structure. The fissure measured by F7, F8, and EX3-4 is pointed as well as fissures G and I.

5 OBSERVED DISPLACEMENTS

Some examples of displacements measured at the Gascons rockslide are presented in Figures 3b, 5a, b

and 6 and discussed in Section 6. In Figures 5a and b, the width of the fissure at the beginning of monitoring is written beside each curve. The three crackmeters F1, F7, and F8 are physically near each other, but their displacements in time are different in terms of maximum and rates of opening (or closing). Extensometer pair EX3-4, F7, and F8 are monitoring the same crack, pointed in Figure 4. The directions of measurement of EX3-4 and F7 are respectively within a 15° and 90° angle of F8. The other extensometer data, EX34-35, EX36-37, EX38-39, G, and I, are coming from the forested sector north of the rails (Fig. 4). Fissures I and G are approximately delimiting the extension of the sliding mass to the north and the west (Fig. 2). The displacement versus time measured by the SAA chain at site 2 is also plotted on Figure 5b.

Figure 6 represents the displacement in the horizontal plane at a depth of 24 m of the SAA chain at site 1 (Fig. 2). The graph shows that the movement of the block monitored is not constant. The mean direction turns of 90° in March 2010, to returns to its original direction in October 2010

6 DISCUSSION

6.1 Hypotheses made to conduct the kinematic analysis

Where there is a lot of field evidences, the block model will be more refined and block will be of smaller area. In sectors where almost no fissures are visible (in the forest or in the cliff where debris hide the structure) the blocks will be bigger.

Displacement of blocks should always be in a downward direction, as it is driven by gravity. At the most, the block can slide along an axis perpendicular to the dip direction of the bedding surface. This fact is represented on Figure 4, by a set of axis in the center of each block. Most rockslides seem to involve individualized blocks and it is not unusual to see chaotic pattern of movement, with blocks apparently not moving in the direction of the main mass movement (Rose & Hungr 2007, Crosta & Agliardi 2003).

The blocks are moving in x, y and z, but not all of the surface displacement measurements are in real 3D. Crackmeters and extensometers are, in most cases, measuring opening and closing of fractures. Such readings are taken between two points inside the moving mass and they are referred to as relative displacements.

An increase in distance means that the two points are moving apart but it does not give the direction of movement. To overcome this limitation, one marker can be paired with many others to have more than one direction of measurement (e.g. F7 and F8 in-

stalled at a 90° angle to read two components of displacement), and some of the extensometer points are located outside of the limit of the unstable mass (not shown).

Along the same line, the closing of a fracture does not mean stabilization. It can represent a change in direction, or simply that the block uphill is going down faster than the one downhill. Thus, the direction of displacement is a function of time. This means that the integration of displacement must take in account the time laps of the different sets of data.

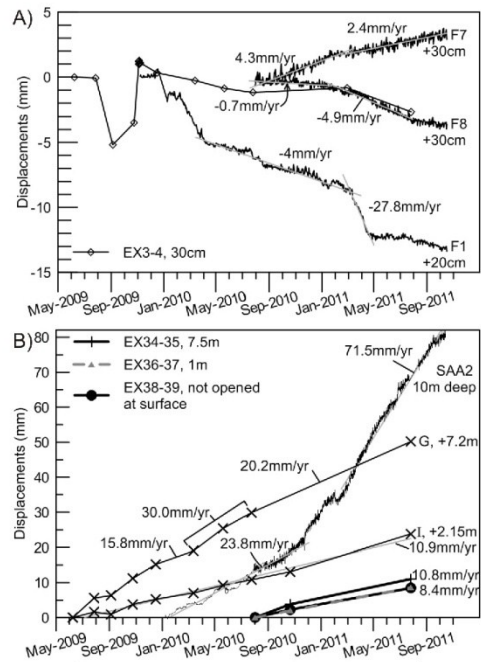


Figure 5. Displacement vs time curves of certain crackmeters, extensometer pairs, and SAA at borehole site 2. a) South of the rails b) North of the rails.

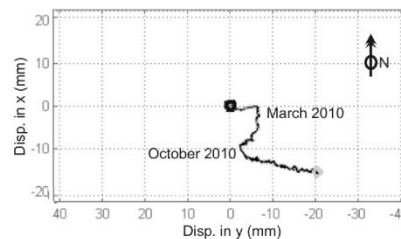


Figure 6. Displacement in the horizontal plane of the SAA at borehole site 1, south of the railroad, at 24m deep, from January 2010 to September 2011.

In the block representation of Figure 4, the edges are smooth and linear. Of course, fissures are not necessarily straight and they have a roughness. Locally, their irregular shape can cause a closing, while it is opening a few meters further. In the Gascons rockslide, the magnitude of movement in a year is often less than a cm, so this might lead to such errors. If the displacements are in the order of meters per year, such localized phenomenon are less likely to influence the data, because they are small compared to the total movement. So, as time goes on, this may be less of an issue.

The compartments are inter-related and they certainly influence each other. A fracture seen at the surface does not necessarily reach the failure surface and there might be blocks on top of blocks. This situation is observed in the cliff area, south of the railroad. The blocks are not completely rigid, but deformable to a certain extent due to their inner discontinuities. Thus, displacement might be attenuated inside a block, i.e. a 10 mm movement on one edge is not always completely transferred to the opposite edge. The points stated in this section are illustrated by examples in sections 6.2 and 6.3.

6.2 Block movement south of the railroad

The EX3-4 data set is the longest in time and presents a chaotic pattern of displacement (Fig. 5a). There is a good agreement between EX3-4 and F8 installed in the same direction, for the overlapping time. In February 2011, F7 and F8 rates of displacement varied; F7 slowed down while F8 accelerated (Fig 5a). As mentioned in Section 6.1, the chaotic pattern of F7, F8 and EX3-4 might represent a change in direction and this is the current explanation. The actual displacement is parallel to the fissure monitored. West of the blocks on which are anchored F7 and F8, is the block monitored by SAA at site 1 (Fig. 4). The pattern of displacement of this block also shows similar variations in displacement (Fig. 6). Thus, the explanation of changes in direction to explain the observed displacement is coherent with data coming from different instruments on different blocks.

Special care is to be taken to make sure that what the sensor is measuring is well understood. This is particularly important with crackmeter analysis. For example, F1 is closing and the rates are accelerating in winter and slowing down in summer (Fig. 5a). During a yearly inspection, it has been noticed, that a fissure opened just uphill of F1. This new information changes the interpretation of the displacement and explains the closing state observed at F1, as well as the importance of this sensor for risk management. In fact, it is following a small block (30x30 cm²) and the significance for the safety of the element at risk, the railroad, is low. The fissure was unnoticed partly because of the high level of weather-

ing of the rock in place. The rock is of poor quality and this makes it difficult to find places to anchor the crackmeters.

6.3 Block movement north of the railroad

The maximum displacement is measured by the SAA chain at borehole site 2 (Figs 3b, 5b). From January 2010 to January 2011 total displacement is of 30 mm. Since December 2010, the rate accelerated and reached a value of 71.5 mm/yr (Fig. 5b). The bottom of the chain is fixed, as it extends in stable rock below the failure surface. Thus, the sensor is measuring the total displacement of this block. Extensometer pairs G and I (Fig. 5b) are located in the same sector, but are showing a smaller amount and slower mean rate of displacements. This might be due to the fact that the markers do not extend in stable ground as it was initially believed, giving the impression that the movements are smaller.

Extensometer pairs EX34-35, EX36-37, and EX38-39, installed in July 2010, are showing similar rates of displacement. In Section 6.2, the comparison of three crackmeters located in the same sector south of the rail (inside a circle of 10 m) showed that they were not moving as whole. EX34-35, EX36-37, and EX38-39 are further from each other but their curves are similar. So, this sector is moving as a whole compared to the blocks south of the rails.

6.4 Tentative assumption for further analysis

In order to develop a sort of algorithm to process and to integrate displacement data, a set of assumptions must be defined. The analysis is ongoing, and the first assumptions are mentioned below.

- Displacements can be in two directions: (1) the one of planar sliding (dip direction of the bedding planes), and (2) in the direction of the wedge failure (Figs. 3 and 4);
- The blocks are sliding on a plan with dip and dip direction of the bedding planes;
- The blocks are rigid (no deformation);
- Outside of the defined limits of the slide the ground is stable.

Some instruments are monitoring blocks and not fissures: the two vertical SAAs, the traditional inclinometer, the total survey markers and the point target analysis (PTA) InSAR monitoring. The permanent reflectors installed for this last technique (Fig. 2) are widely spread in the field. It will bring essential knowledge on directions of displacements of blocks across the rockslide. Thus, as a last assumption, the displacement of blocks must be coherent with PTA-InSAR displacement data.

7 CONCLUDING REMARKS

Along the coast of the Gaspé Peninsula, in Quebec, Canada, a railroad runs directly across an active rockslide involving a volume of 560 000 m³. A near real time monitoring system has been installed in order to develop an early-warning system and to investigate the post-failure behaviour of this active slide.

The monitoring system is coupling direct (in-situ geotechnical instruments) and remote (InSAR) monitoring. The wedge type failure slides on the bedding plane of the Anse-à-Pierre-Loiselle formation.

Preliminary analysis of displacement shows some coherency in movement:

- In the south part of the slide, the blocks are moving individually;
- In the north part, blocks appear to move faster and as whole;
- Some blocks are changing direction with time;
- The monitoring system is relatively young and as more data is collected, tendencies will become better defined;
- Upcoming PTA-InSAR data will help to reduce the uncertainty on movement of particular blocks.

The system is continuously acquiring new data and before defining meaningful warning criteria, the data of the instrumentation must be well understood.

ACKNOWLEDGEMENTS

The writers would like to acknowledge the support of the Ministère des transports du Québec (C. Jacob), Transport Canada (D. Hébert), the Ministère de l'éducation des loisirs et des sports du Québec, the Canadian Space Agency (V. Singhroy) and the Fonds de recherche du Québec. Thanks also to L. Danisch (Measurand), P. Therrien (U. Laval) and A.M LeBlanc (NRCAN-CGC). The Earth Science Sector contribution number is 20110311.

REFERENCES

- Blikra, L.H. 2008. The Aknes rockslide; monitoring, threshold values and early-warning. 10th International Symposium on Landslides and Engineered Slopes, Xi'an, China, 1089-1094.
- Bourque, P.-A. & Lachambre, G. 1980. Stratigraphie du Silurien et du Dévonien basal du sud de la Gaspésie. Rapport ES-30. Québec, Direction de la géologie, Direction générale de la recherche géologique et minérale, Ministère de l'énergie et des ressources du Québec: 123p.
- Cloutier, C., Locat, J., Lord, P.-É., & Couture, R. 2010. Caractérisation des instabilités côtières dans le secteur de Port-Daniel-Gascons, Gaspésie, Québec. 63rd Canadian Geotechnical Conference and 6th Canadian Permafrost Conference, Calgary, AB, Canada: 71-79.
- Cloutier, C., Locat, J., Couture, R., & Lord, P.-E. 2011. Analysis of one year of monitoring data for the active Gascons rockslide, Gaspé Peninsula, Québec. 5th Canadian Conference on Geotechnique and Natural Hazards, Kelowna, BC, Canada.
- Couture, R., Charbonneau, F., Murnaghan, K., Singhroy, V., Locat, J., & Lord, P.-É. 2010. PTA-InSAR rock slope monitoring at the Gascons site, Gaspé Peninsula, Québec. 63rd Canadian Geotechnical Conference and 6th Canadian Permafrost Conference, Calgary, AB, Canada: 102-110.
- Couture, R., Charbonneau, F., Singhroy, V., Murnaghan, K., Drouin, H., Locat, J., Lord, P.-É., & Cloutier, C. 2011. PTA-InSAR rock slope monitoring at the Gascons site, Gaspé Peninsula, Québec : Preliminary results. 5th Canadian Conference on Geotechnique and Natural Hazards, Kelowna, BC, Canada.
- Crosta, G.B. & Agliardi, F. 2003. Failure forecast for large rock slides by surface displacement measurements. Canadian Geotechnical Journal, 40(1): 176-191.
- Cruden, D.M. & Varnes, D.J. 1996. Landslide types and processes, in A. K. Turner et R. L. Schuster, (eds.), Landslides : Investigation and mitigation Transportation Research Board Special Report 247. Washington: National Academy of Sciences: 673
- Danisch, L., Patterson, T., Cloutier, C., Locat, J., & Lord, P.-É. 2010. Integration of SAA technology for coastal rock slope movement monitoring at Gascons, Gaspé Peninsula, Québec, Canada. 63rd Canadian Geotechnical Conference and 6th Canadian Permafrost Conference, Calgary, AB, Canada: 86-93.
- Locat, J., & Couture, R. 1995a, Rapport final : Analyse de la stabilité du massif rocheux au millage 30.5, Division de Chandler, Anse-aux-Gascons, Gaspésie, Québec: Québec, Groupe de recherche en Environnement et en Géomécanique, Université Laval : 95.
- Locat, J. & Couture, R. 1995b. Analyse de la Stabilité d'un Talus Rocheux à l'Anse-aux-Gascons, Gaspésie, Québec, 48th Canadian Geotechnical Conference, Vancouver, BC, Canada: 885-892.
- Locat, J., Cloutier, C., Lord, P.-É., Therrien, P., Jacob, C., Nadeau, A., Hébert, D., Couture, R., Charbonneau, F., Singhroy, V., Murnaghan, K., Danisch, L., Jaboyedoff, M., Pedrazzini, A., & Gravel, S. 2010. An integrated mass movement monitoring system for rockslide hazard assessment at Gascons, Gaspé Peninsula, Québec: An Overview. 63rd Canadian Geotechnical Conference and 6th Canadian Permafrost Conference, Calgary, AB, Canada: 35-43.
- Lord, P.-É., J. Locat, et al. 2010. Analyse des déplacements du glissement de Gascons, Gaspésie, par couplage d'observations aéroportées et terrestres. 63rd Canadian Geotechnical Conference and 6th Canadian Permafrost Conference, Calgary, AB, Canada: 56-64.
- Rose, N.D. & Hungr, O. 2007. Forecasting potential rock slope failure in open pit mines using the inverse-velocity method. International Journal of Rock Mechanics and Mining Sciences, 44(2): 308-320.
- Zangerl, C., Eberhardt, E. & Perzlmaier, S. 2010. Kinematic behaviour and velocity characteristics of a complex deep-seated crystalline rockslide system in relation to its interaction with a dam reservoir. Engineering Geology, 112(1-4): 53-67

Annexe E. Preliminary numerical modelling with the distinct element code *3DEC*

Numerical modelling strategy

The three-dimensional distinct element code 3DEC (Itasca, manual reference) was used to test the geometry of the slide, to evaluate the influence of the fault and of the block size on the stability. The 3DEC code represents the rock mass as an assemblage of three-dimensional blocks that can be subjected to static or dynamic loading (Cundall 1988; Hart et al. 1988). The strengths of the material and of the discontinuities making up the blocks are specified by the user using built in models. Large displacement and rotation along the discontinuities bounding the blocks are permitted.

The Gascons rockslide is structurally controlled and has already cumulated important displacements. The movement occurs on pre-existing discontinuities; consequently, failure into intact rock is not a dominant mechanism in the actual evolution of the rockslide. For these reasons, rigid block conditions were assumed for the analysis. These conditions imply that the block cannot deform or break into smaller blocks. Thus, the study is interested in the actual shape of the rockslide. The locations of fractures and sliding surfaces are imposed in order to build the observed geometry.

Various geometries were tested in order to identify their effect on the behaviour of the mass. The modelling started with the simplest geometry, representing the slide as one block of 334 920 m³. The approach was to increase the complexity of the wedge by adding features, based on the location of existing sliding surfaces and fractures recognised in the field. A model was also created using the built-in algorithms to create fully persistent joint sets. To do so, the user needs to specify the orientation and spacing of the joint set.

A simplified slope was created to represent the topography of the Gascons sector and compared with the real topography using Polyworks (Figure 1A). This simplified topography does not include the Petit-Massif sector or the railway cut.

To model the creation of the slope by erosion, the analysis starts with three phases of gravity loading, in between which one slice of the slope is taken off (Figure 1B). The discontinuity representing the Port-Daniel-River fault is imposed to the model from the beginning. On the south side of the fault, the model is fixed and not allowed to move in subsequent steps.

Once the three phases of erosions and gravity loading are done, the next step is to create the sliding surface. The block (or blocks) forming the slide are created before the gravity loading, but are joined to the rest of the model for the erosion steps. Then they are un-joined and a high cohesion is imposed to the joints. After another gravity loading, the cohesion is lowered to zero for all the joints forming the sliding surface. The last step is to lower the friction angle gradually until significant displacements are observed to qualify the slope as failed.

As the blocks are rigid, only the density is specified to 2500 kg/m³. The joint properties are set with the Coulomb Slip Model. The properties imposed in this model are: (1) cohesion, c , (2) friction angle, ϕ , and (3) joint normal and shear stiffness (j_{kn} and j_{ks}). The cohesion is set to 0 while the friction angle is lowered during the analysis. The analysis starts with a value of 30°. The joint normal and shear stiffness

were both set to 1×10^9 Pa/m. Values were determined by research in the literature (Kalenchuk 2010; Brideau and Stead 2012; Brideau, Sturzenegger et al. 2012) and were kept constant through the analysis.

A major limitation to this model is that the same set of joint properties is applied to all the joints forming the sliding surface, including the bedding surface and the vertical joints. The vertical joints that cross different lithologies have a higher roughness. In fact, they are certainly less polished than the shale units forming the sliding surface. However, the force acting on vertical joints is low, so the effect on the modelling might be limited.

Results

The simplest geometry models the slide as one block. The required friction angle to initiate failure is of 19.2° . The displacement of the wedge is limited. The movement stops, when the wedge corner hits the beach. In fact, the block is physically restrained because it is rigid and not being permitted to fracture internally. This points out that as the failure surface is supposed to be at the same level than the beach in the lower wedge corner, erosion of the wedge corner is necessary to accommodate displacements.

The impact of the softening of the slope angle of the bedding plane near the Port-Daniel-River fault was tested by adding a plane in the corner of the wedge with different slope and aspect. The addition of a low angle plane in the corner of the wedge increases the stability. When tested with a plane according to the geometry interpreted from elevation model shown by the green surface in Figure 2-13A (Chapter 2 of the thesis), then the slide is not happening. The geometry has been tested with planes at dip/dip direction of $05/189^\circ$, $10/189^\circ$, $15/189^\circ$ and $18/189^\circ$. An example is show in Figure 1C. The friction angles necessary to initiate failure are respectively of 7, 13.4, 15.6, and 17° . As the block is rigid, part of the block has to be lifted in order to slide (Figure 1C).

The syncline is affecting only a small portion of the rupture surface area; however it increases the stability of the wedge that is already constrained because the corner is as the same level then the beach. These two elements explain the limited displacement observed on the deepest sliding surface in the Petit-Massif sector.

In the Petit-massif multiple shearing surfaces are detected with the inclinometer and the vertical SAA3, indicating that the mass is breaking down not only due to the vertical fractures, but also forming stacks of blocks, increasing the complexity of the mass. Thus, an analysis is run with two extra bedding planes, acting as intermediate sliding surfaces (Figure 1D). Displacement on the middle and deeper failure surface starts at the same moment. Movement on the middle failure surface continues when the lower surface hits the beach. Displacement on the higher sliding surface starts only once the middle block hits the beach too.

This vertical breakdown is an answer to this buttressing at the bottom of the cliff. The fact that the two top blocks do not individualize in the simulation is not contraire to what is observed on site, as the top sliding surface is associated to a toppling mechanism, while no toppling is possible in the imposed geometry of this simulation because the vertical fractures perpendicular to the slope face are not modeled.

Geometries with more blocks are created by adding a repeating pattern of fully persistent discontinuities in the sliding mass. In these simulations, the main slide is not creating (Figure 1E). The model involves towards smaller wedge failures forming in the upper part of the cliff. This is similar to what is observed in the field where major fractures open everywhere dividing the rockslide into separated blocks. However, through the simulation, the friction angle must be constantly lower to permit retrogression of the failure.

Numerical Modelling Discussion

The numerical modelling presented here only uses the basic capacities of the modelling software. These analyses were carried on to get a better understanding of the kinematic constraints related to the geometry of the slide and to explore what could be done with numerical modelling to better understand the Gascons rockslide.

The simulations were run in dry conditions, because the slide keeps moving when the water pressures are at their lowest, which corresponds to a water table below the rupture surface. However, as the water pressures influence displacement in the upper part of the slide, an analysis including water flow and water pressure would be closer to reality.

In the 3DEC simulations, the blocks were considered rigid as we felt that the evolution of the rockslide depends upon existing discontinuities and not on intact material fracturing. Another reason that motivated a rigid block analysis is the changing nature of the rock through the rockslide. In fact, the Anse-à-Pierre-Loiselle Formation is a transition unit, varying through the rockslide from sandstone to limestone. The bed layers are 3 to 20 cm thick. In the field, thin beds of highly weathered soil-like material and very soft shale units were observed. The failure surfaces are associated with these low strength units, but little is known about their mechanical properties. Representing correctly the rock mass mechanical behaviour would demand to add a lot of complexity to the model, which demands more time, more data, and it complicates the interpretation of the model response.

The rigid block condition impacts the results: (1) the block has to lift when the failure surface corner is flattened (Figure 1C) and (2) the rigidity of the block causes it to stop when the wedge's corner hits the beach.

References

Brideau, M.-A. and Stead, D., 2012. "Evaluating Kinematic Controls on Planar Translational Slope Failure Mechanisms Using Three-Dimensional Distinct Element Modelling." *Geotechnical and Geological Engineering*, 30(4), 991-1011.

Brideau, M.-A., Sturzenegger, M., Stead, D., Jaboyedoff, M., Lawrence, M., Roberts, N., Ward, B., Millard, T., and Clague, J., 2012. "Stability analysis of the 2007 Chehalis lake landslide based on long-range terrestrial photogrammetry and airborne LiDAR data." *Landslides*, 9(1), 75-91.

Cundall, P. A., 1988. "Formulation of a three-dimensional distinct element model—Part I. A scheme to detect and represent contacts in a system composed of many polyhedral blocks." *International Journal of Rock Mechanics and Mining Sciences & Geomechanics Abstracts*, 25(3), 107-116.

Hart, R., Cundall, P. A., and Lemos, J., 1988. "Formulation of a three-dimensional distinct element model—Part II. Mechanical calculations for motion and interaction of a system composed of many polyhedral blocks." *International Journal of Rock Mechanics and Mining Sciences & Geomechanics Abstracts*, 25(3), 117-125.

Kalenchuk, K., (2010). *Multi-Dimensional Analysis of Large, Complex Slope Instability*, Queen's University, Kingston.

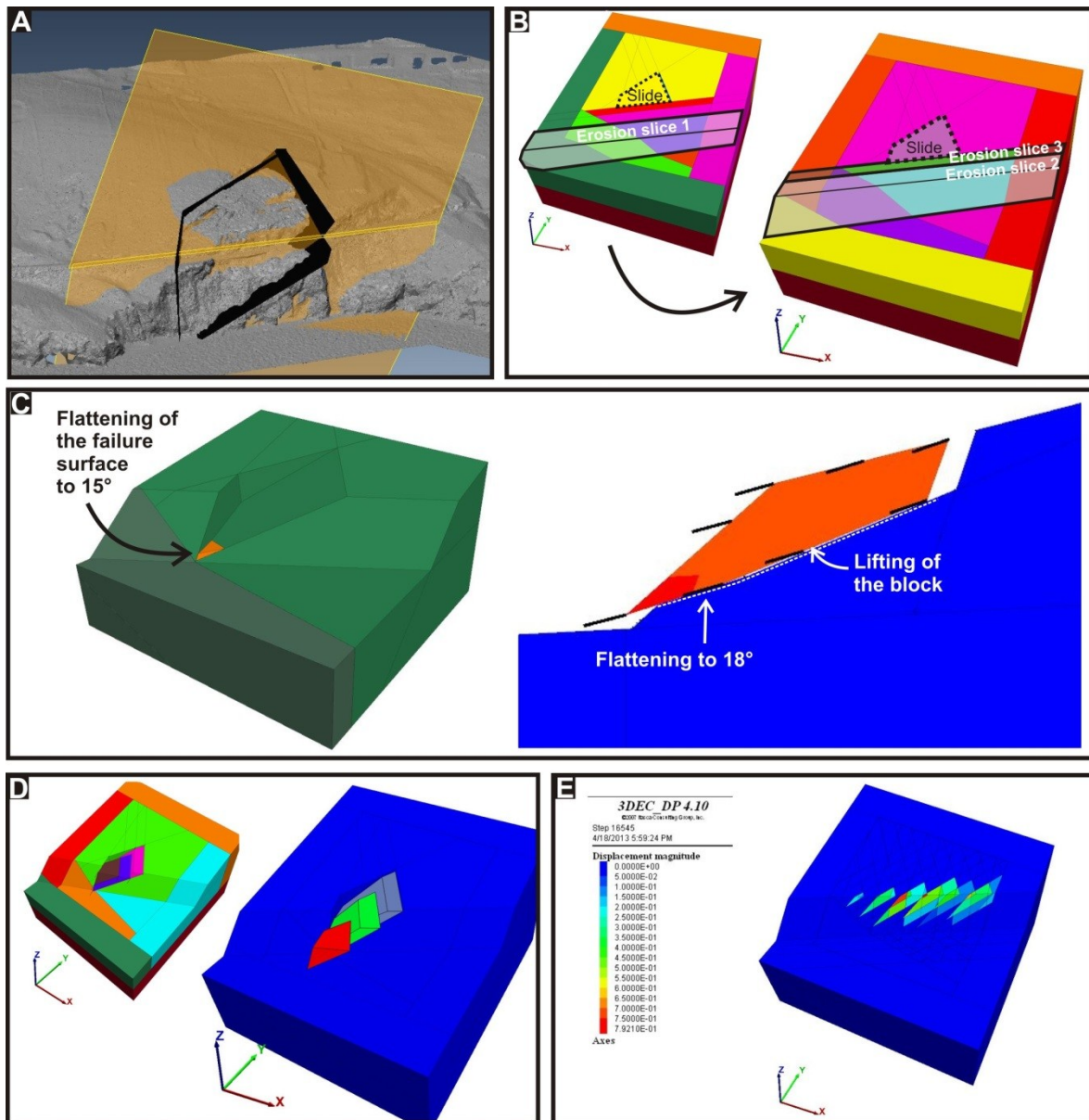


Figure 1. A) Comparison of the topography created for the modelling with the real elevation model in Polyworks (Innovmetric). B) Three slices are taken off successively to model the creation of the modern slope by erosion. C) Flattening of the failure surface to represent the effect of the syncline. The block lifts when it slides. D) Two bedding discontinuities are added to the model. E) One of the models created with repeating patterns of fully persistent joint sets.

Numerical codes for 3DEC modelling

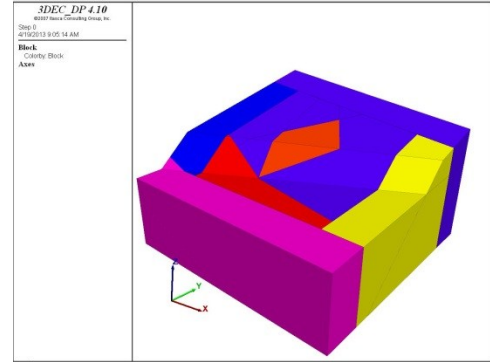
1. Dièdre simple avec erosion

```
new
poly brick (-300,300) (-300,300) (-200,200)

; create sea floor
jset dip 3 dd 180 origin 0,-72,0

;creat the cliff
jset dip 45 dd 155 origin 0,0,72
jset dip 45 dd 155 origin 0,-20,72
jset dip 45 dd 155 origin 0,-50,72
jset dip 45 dd 155 origin 0,-100,72
delete range y -120,-300 z 72,200

;create the upper part of the slope
hide y -120,-300
jset dip 16 dd 155 origin 0,0,72
delete range z 72,200
;
seek
join on
;
;cut the external blocks that will be fixed for the boundary conditions
jset dip 90 dd 180 origin 0,200,0
jset dip 90 dd 180 origin 0,-200,0
hide range y 200,300
hide range y -200,-300
;
jset dip 90 dd 90 origin -200,0,0
jset dip 90 dd 90 origin 200,0,0
hide range x -200,-300
hide range x 200,300
;
jset dip 0 dd 0 origin 0,0,-100
hide range z -10,-200
;
hide
seek range x -200,200 y -200,200 z -100,200
;
jset dip 90 dd 191 origin -200,-85,72
hide
seek block 12379,36752,26540,18972,217
```



```

mark region 10
hide
seek block 11587,35928,27450,19542,9525
mark region 11
hide
seek block 8459,35114,28356,20541,10139
mark region 12
seek
;
;hide inside regions to mark the outside blocks as region 0
seek
hide range x -200,200 y -200,200 z -200,200
mark region 1
hide
seek range x -200,200 y -200,200 z -200,-100
mark region 2
seek
hide region 1,2
hide range y -130,-200
hide range x -200,-100
jset dip 23 dd 192 spacing 10 num 10 origin 0,0,50
jset dip 81 dd 84 spacing 40 num 15 origin 0,0,0
jset dip 79 dd 125 spacing 30 num 10 origin 0,0,0
;
seek
; assign material properties to run initial conditions
prop mat=1 k 2e8 g 1e8 den 2500
;jmat 2 is for vertical external boundaries, jmat 3 for the bottom external boundary, jmat 1 for the joints for
initial loading under gravity
prop jmat=1 jkn 1e10 jks 1e9 coh 1e20 fric 20
prop jmat=2 jkn 1e9 jks 1e9 coh 0 fric 0
prop jmat=3 jkn 1e9 jks 1e9 coh 1e20 fric 1e20
; assign boundary conditions
hide range x -200,200 y -200,200 z -100,200
fix
;assign the right properties to the different joints
seek
change jmat 2 range x -201,-199
change jmat 2 range y -201,-199
change jmat 2 range x 199,201
change jmat 2 range y 199,201
change jmat 3 range z -99,-101
;
;initialize gravity

```

```

;grav 0 0 -9.8
;damp local
;histories
;hist unbal
;hist zdis 0,0,72
; equilibrate
;solve
;
;get rid of one layer of erosion
;delete region 10
;delete block 12379,18972,217
;hide range x -200,200 y -200,200 z -100,200
;fix
;solve
;delete region 11
;delete block 9525,19542,11587
;hide range x -200,200 y -200,200 z -100,200
;fix
;seek
;solve
;delete range 12
;delete block 8459,20541,10139
;hide range x -200,200 y -200,200 z -100,200
;fix
;seek
;solve
; reduce the joint properties material of jmat 1. For the moment, all the joints have the same properties.
;prop jmat 1 coh 0
;reset disp

```

2. *Dièdre monolithique avec la surface de rupture aplanie dans le coin inférieur du dièdre pour correspondre avec celle interprétée de la morphologie*

```

new
poly brick (-300,300) (-300,400) (-200,300)

; create sea floor
jset dip 3 dd 180 origin 0,-72,0
hide range z 0,-200
;creat the cliff and erodable blocks
jset dip 45 dd 155 origin 0,0,72

delete range y 0,-300 z 72,200

```

```

;create the upper part of the slope
jset dip 16 dd 155 origin 0,0,72
delete range z 72,300
;
seek
;
;cut the external blocks that will be fixed for the boundary conditions
jset dip 0 dd 0 origin 0,0,-100
hide range z -100,-200
jset dip 90 dd 180 origin 0,300,0
jset dip 90 dd 180 origin 0,-200,0
hide range y 300,400
hide range y -200,-300
;
jset dip 90 dd 90 origin -200,0,0;
jset dip 90 dd 90 origin 200,0,0
;
hide
seek range x -200,200 y -200,200 z -100,300
;
jset dip 90 dd 191 origin -200,-85,72
hide
seek range x -300,-200 y -200,300
join on
hide
seek range x 200,300 y -200,300
join on
hide
seek range y -200,-300
join on
hide
seek range y 300,400
join on
hide
seek range x -200,200 y -100,-200
join on
hide
seek range x -200,200 y 0,300 z 0,200
; cut the geometry of the slide
jset dip 23 dd 192 origin 0,0,51
jset dip 81 dd 84 origin -80,-75,72
jset dip 79 dd 125 origin 0,150,115
seek range x -75,50 y -70,100 z 10,100
jset dip 04 dd 009 origin -65 -110 5

```



```

seek range x -200,200 y -200,300 z -100,200
hide block 8987
join on
mark region 2
;
; Impose the different limits of the slide
seek
; assign properties mat and jmat
prop mat=1 k 2e8 g 1e8 den 2500
;jmat 2 is for vertical external boundaries, jmat 3 for the bottom external boundary, jmat 1 for the joints for
initial loading under gravity
prop jmat=1 jkn 1e10 jks 1e9 jcoh 1e20 jfric 50
prop jmat=2 jkn 1e9 jks 1e9 jcoh 0 jfric 0
prop jmat=3 jkn 1e9 jks 1e9 jcoh 1e20 jfric 1e20
;
hide range x -200,200 y -200,300 z -100,300
fix
change jmat 3
seek
change jmat 2 range x -201,-199
change jmat 2 range x 199,200
change jmat 3 range x -200,200 y -200,300 z -99,-101

; initialize gravity
;grav 0 0 -9.8
;damp local
; histories
;;hist unbal
;hist zdis 0,0,72

; equilibrate for the first geometry (without erosion)
; solve

; Preparation to run a first stability analysis
;hide range x -200,200 y -200,300 z -100,300
;fix
;seek
;prop jmat=1 jkn 1e10 jks 1e9 jcoh 0 jfric 50
;reset disp
;reset hist
;hist unbal
;hist zdis 0,0,72

```

```

;cycle 10000
;prop jmat 1 jfr 30
;cycle 20000
;prop jmat 1 jfr 25
;cycle 20000
;cycle 20000
; keep lowering the friction angle. This geometry does not slide.

```

3. *Dièdre monolithique avec la surface de rupture aplanie dans le coin inférieur du dièdre. Dans cet exemple la surface est à 18°. Sans érosion.*

```

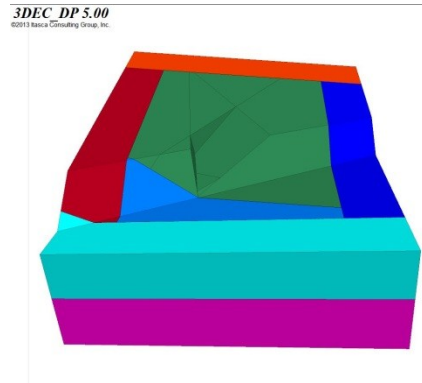
new
poly brick (-300,300) (-300,400) (-200,300)

; create sea floor
jset dip 3 dd 180 origin 0,-72,0
hide range z 0,-200
;creat the cliff and erodable blocks
jset dip 45 dd 155 origin 0,0,72

delete range y 0,-300 z 72,200

;create the upper part of the slope
jset dip 16 dd 155 origin 0,0,72
delete range z 72,300
;
seek
;
;cut the external blocks that will be fixed for the boundary conditions
jset dip 0 dd 0 origin 0,0,-100
hide range z -100,-200
jset dip 90 dd 180 origin 0,300,0
jset dip 90 dd 180 origin 0,-200,0
hide range y 300,400
hide range y -200,-300
;
jset dip 90 dd 90 origin -200,0,0;
jset dip 90 dd 90 origin 200,0,0
;
hide
seek range x -200,200 y -200,200 z -100,300
;
jset dip 90 dd 191 origin -200,-85,72

```



```

hide
seek range x -300,-200 y -200,300
join on
hide
seek range x 200,300 y -200,300
join on
hide
seek range y -200,-300
join on
hide
seek range y 300,400
join on
hide
seek range x -200,200 y -100,-200
join on
hide
seek range x -200,200 y 0,300 z 0,200
; cut the geometry of the slide
jset dip 23 dd 192 origin 0,0,51
jset dip 81 dd 84 origin -80,-75,72
jset dip 79 dd 125 origin 0,150,115
hide
seek range x -75,50 y -70,100 z 10,100
; change the dip to do the parametric study
jset dip 18 dd 189 origin -65 -110 5
hide
seek range x -200,200 y -100,300 z -100,200
hide block 8987
join on
mark region 2
;
; Impose the different limits of the slide
seek
; assign properties mat and jmat
prop mat=1 k 2e8 g 1e8 den 2500
;jmat 2 is for vertical external boundaries, jmat 3 for the bottom external boundary, jmat 1 for the joints for
initial loading under gravity
prop jmat=1 jkn 1e10 jks 1e9 jcoh 1e20 jfric 50
prop jmat=2 jkn 1e9 jks 1e9 jcoh 0 jfric 0
prop jmat=3 jkn 1e9 jks 1e9 jcoh 1e20 jfric 1e20
;
hide range x -200,200 y -200,300 z -100,300
fix
change jmat 3

```

```

seek
change jmat 2 range x -201,-199
change jmat 2 range x 199,200
change jmat 3 range x -200,200 y -200,300 z -99,-101

```

```

; initialize gravity
grav 0 0 -9.8
damp local
; histories
hist unbal
hist zdis 0,0,72
; equilibrate for the first geometry (without erosion)
solve
; Preparation to run a first stability analysis
;hide range x -200,200 y -200,300 z -100,300
;fix
;seek
prop jmat=1 jkn 1e10 jks 1e9 jcoh 0 jfric 50
;reset disp
;reset hist
;hist unbal
;hist zdis 0,0,72

```

```

cycle 10000
prop jmat 1 jfr 30
cycle 20000
prop jmat 1 jfr 25
cycle 20000

```

```

prop jmat 1 jfr 20
;reset disp
cycle 20000

```

4. Glissement avec trois niveaux de surface de rupture

```

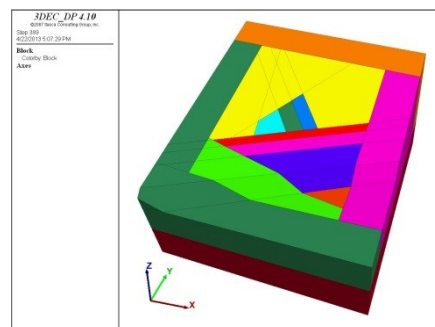
new
poly brick (-300,300) (-300,400) (-200,300)

```

```

; create sea floor
jset dip 3 dd 180 origin 0,-72,0
hide range z 0,-200
;creat the cliff and erodable blocks
jset dip 45 dd 155 origin 0,0,72
jset dip 45 dd 155 origin 0,-20,72

```



```

jset dip 45 dd 155 origin 0,-50,72
jset dip 45 dd 155 origin 0,-100,72
delete range y -120,-300 z 72,300

;create the upper part of the slope
jset dip 16 dd 155 origin 0,0,72
delete range z 72,200
;
seek
;
;cut the external blocks that will be fixed for the boundary conditions
jset dip 0 dd 0 origin 0,0,-100
hide range z -100,-200
jset dip 90 dd 180 origin 0,300,0
jset dip 90 dd 180 origin 0,-200,0
hide range y 300,400
hide range y -200,-300
;
jset dip 90 dd 90 origin -200,0,0
jset dip 90 dd 90 origin 200,0,0
;
hide
seek range x -200,200 y -200,200 z -100,300
;
jset dip 90 dd 191 origin -200,-85,72
hide
seek range x -300,-200 y -200,300
join on
hide
seek range x 200,300 y -200,300
join on
hide
seek range y -200,-300
join on
hide
seek range y 300,400
join on
hide
seek range x -200,200 y -100,-200
join on
hide
seek range x -200,200 y -10,300 z -20,200
; cut the geometry of the slide
jset dip 23 dd 192 origin 0,0,51

```

```

jset dip 23 dd 192 origin 0,0,61
jset dip 23 dd 192 origin 0,0,73
jset dip 81 dd 84 origin -80,-75,72
jset dip 79 dd 125 origin 0,150,115
hide block 18595,24473,23595
join on
seek
;
; Impose the different limits of the slide
; assign properties mat and jmat
prop mat=1 k 2e8 g 1e8 den 2500
;jmat 2 is for vertical external boundaries, jmat 3 for the bottom external boundary, jmat 1 for the joints for
initial loading under gravity
prop jmat=1 jkn 1e10 jks 1e9 coh 1e20 fric 50
prop jmat=2 jkn 1e9 jks 1e9 coh 0 fric 0
prop jmat=3 jkn 1e9 jks 1e9 coh 1e20 fric 1e20
;
hide range x -200,200 y -200,300 z -100,300
fix
change jmat 3
seek
change jmat 2 range x -201,-199
change jmat 2 range x 199,200
seek
change jmat 3 range x -200,200 y -200,300 z -99,-101

; initialize gravity
grav 0 0 -9.8
damp local
; histories
hist unbal
hist zdis 0,0,72
hist zdis 0,0,68
hist zdis 0,0,62
hist zdis 0,0,55
hist zdis 0,0,25
; equilibrate for the first geometry (without erosion)
; solve

; remove the first layer of erosion
;delete block 9153,20821,15597,217,11631
;hide range x -200,200 y -200,300 z -100,300
;fix
;reset disp

```

```

;reset hist
;hist unbal
;hist zdis 0,0,72
;seek
;solve

; remove the next erodible layer
;delete block 8309,20065,16329,12201,5813
;hide range x -200,200 y -200,300 z -100,300
;fix
;reset disp
;reset hist
;hist unbal
;hist zdis 0,0,72
;seek
;solve

; remove the next erodible layer
;delete block 7807,19319,17099,13132,6461
;hide range x -200,200 y -200,300 z -100 300
;fix
;reset disp
;seek
;solve

; Preparation to run a first stability analysis
;hide range x -200,200 y -200,300 z -100,300
;fix
;prop jmat=1 jkn 1e10 jks 1e9 coh 0 fric 50
;reset disp
;reset hist
;hist unbal
;hist zdis 0,0,72
;hist zdis 0,0,72
;hist zdis 0,0,68
;hist zdis 0,0,62
;hist zdis 0,0,55
;hist zdis 0,0,25
;seek
;solve
;prop jmat 1 fr 30
;reset disp
;solve
;prop jmat 1 fr 25

```

```

;cycle 20000
;cycle 20000
; keep reducing friction angle.

```

5. *Géométrie avec des joints avec une persistance infinie. Les familles A et D sont les joints inclus dans cet exemple.*

```

new
poly brick (-300,300) (-300,300) (-200,200)

```

```

; create sea floor
jset dip 3 dd 180 origin 0,-72,0

```

```

;creat the cliff
jset dip 45 dd 155 origin 0,0,72
jset dip 45 dd 155 origin 0,-20,72
jset dip 45 dd 155 origin 0,-50,72
jset dip 45 dd 155 origin 0,-100,72
delete range y -120,-300 z 72,200

```

```

;create the upper part of the slope
hide y -120,-300
jset dip 16 dd 155 origin 0,0,72
delete range z 72,200

```

```

;
seek
join on
;

```

```

;cut the external blocks that will be fixed for the boundary conditions

```

```

jset dip 90 dd 180 origin 0,200,0
jset dip 90 dd 180 origin 0,-200,0
hide range y 200,300
hide range y -200,-300

```

```

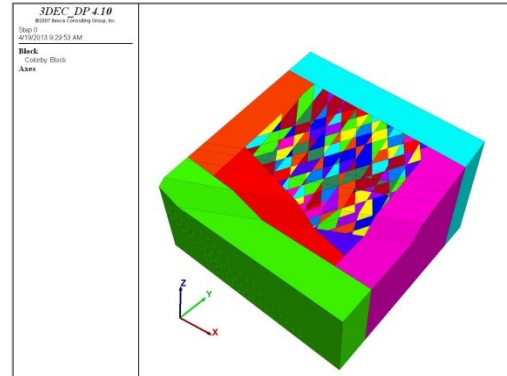
;
jset dip 90 dd 90 origin -200,0,0
jset dip 90 dd 90 origin 200,0,0
hide range x -200,-300
hide range x 200,300

```

```

;
jset dip 0 dd 0 origin 0,0,-100
hide range z -10,-200
;
hide

```




```

seek range x -200,200 y -200,200 z -100,200
;
jset dip 90 dd 191 origin -200,-85,72
hide
seek block 12379,36752,26540,18972,217
mark region 10
hide
seek block 11587,35928,27450,19542,9525
mark region 11
hide
seek block 8459,35114,28356,20541,10139
mark region 12
seek
;
;hide inside regions to mark the outside blocks as region 0
seek
hide range x -200,200 y -200,200 z -200,200
mark region 1
hide
seek range x -200,200 y -200,200 z -200,-100
mark region 2
seek
hide region 1,2
hide range y -130,-200
hide range x -200,-100
jset dip 23 dd 192 spacing 10 num 10 origin 0,0,50
jset dip 81 dd 84 spacing 40 num 15 origin 0,0,0
jset dip 79 dd 125 spacing 30 num 10 origin 0,0,0
;
seek
; assign material properties to run initial conditions
prop mat=1 k 2e8 g 1e8 den 2500
;jmat 2 is for vertical external boundaries, jmat 3 for the bottom external boundary, jmat 1 for the joints for
initial loading under gravity
prop jmat=1 jkn 1e10 jks 1e9 coh 1e20 fric 20
prop jmat=2 jkn 1e9 jks 1e9 coh 0 fric 0
prop jmat=3 jkn 1e9 jks 1e9 coh 1e20 fric 1e20
; assign boundary conditions
hide range x -200,200 y -200,200 z -100,200
fix
;assign the right properties to the different joints
seek
change jmat 2 range x -201,-199
change jmat 2 range y -201,-199

```

```

change jmat 2 range x 199,201
change jmat 2 range y 199,201
change jmat 3 range z -99,-101
;
;initialize gravity
;grav 0 0 -9.8
;damp local
;histories
;hist unbal
;hist zdis 0,0,72
; equilibrate
;solve
;
;get rid of one layer of erosion
;delete region 10
;delete block 12379,18972,217
;hide range x -200,200 y -200,200 z -100,200
;fix
;solve
;delete region 11
;delete block 9525,19542,11587
;hide range x -200,200 y -200,200 z -100,200
;fix
;seek
;solve
;delete range 12
;delete block 8459,20541,10139
;hide range x -200,200 y -200,200 z -100,200
;fix
;seek
;solve
; reduce the joint properties material of jmat 1. For the moment, all the joints have the same properties.
;prop jmat 1 coh 0
;reset disp

```

Annexe F Données brutes des instruments à lectures manuelles

Les données des levés à la station totale sont d'abord présentées sous forme de tableaux, puis dans un graphique des déplacements en fonction du temps. Ensuite, les mesures prises au ruban extensométriques sont présentées sous forme de tableaux, puis en graphiques.

Visite 04Octobre 2009

Station DE	à	Angle H (hz) en degrés	Dist. en pente	hauteur de l'instrument (m)	hauteur du jalon (m)
BM1					
	BM2	0	143.629	1.28905	1.3
	REG1	24.32412	16.531	1.28905	1.3
	FRB	24.93126	18.076	1.28905	1.3
	ABS1	25.69248	20.242	1.28905	1.3
	ABS2	23.52357	23.876	1.28905	1.3
	REG2	21.03084	25.553	1.28905	1.3
	REG3	14.778	30.474	1.28905	1.3
	REG4	11.1474	36.627	1.28905	1.3
	REG5	9.00999	47.023	1.28905	1.3
	REG6	8.80965	51.016	1.28905	1.3
	REG7	5.75883	62.91	1.28905	1.3
	S2	359.19513	63.771	1.28905	1.3
	RS2	0.90306	63.753	1.28905	1.3
	REG8	359.0289	52.86	1.28905	1.3
	RREG8	0.75861	52.553	1.28905	1.3
	REG9	357.66117	41.648	1.28905	1.3
	RREG9	0.30501	41.62	1.28905	1.3
	REG10	354.75075	30.698	1.28905	1.3
	RREG10	358.87644	30.465	1.28905	1.3
	REG11	344.53827	16.645	1.28905	1.3
	RREG11	352.64781	16.073	1.28905	1.3
	REG12	281.36079	6.86	1.28905	1.3
	RREG12	287.27604	4.105	1.28905	1.3
	90BUNG	199.61406	34.383	1.28905	1.3
	BUNG	202.9212	34.758	1.28905	1.3
	TRAVRS	179.70093	4.285	1.28905	1.3
	RTRAVRS	217.09683	4.595	1.28905	1.3
	TRAVRN	244.55106	7.967	1.28905	1.3
	RTRAVRN	230.21613	5.914	1.28905	1.3
BM2					
	BM1	0	143.636	1.2585	1.3
	SAAH_LECTURE1	5.337	28.1	1.2585	1.3
	SAAH_LECTURE2	5.33808	28.094	1.2585	1.3
	AM189 (MUR SOUTENEMENT)	354.74688	15.129	1.2585	1.3

Visite 08 – Août 2010

Opérateur : Pierre-Étienne Lord et Catherine Cloutier

Station	hauteur de		Angle H (hz)	Angle V	Dist.	Dist.	hauteur du
DE	l'instrument (m)	à	en degrés	en degrés	horizontale	en pente	jalon (m)
BM1	1.272						
		BM2	0	90.52525	143.622		1.48
		Cbung1	204.9816389	88.07958333	33.912737	33.9318	0
BM1	1.272						
		Cbung1	0	88.07894444	33.912424	33.9315	0
		EX1	169.45525	90.2665	32.843345	32.8437	1.48
		EX2	170.3826944	90.13163889	34.20451	34.2046	1.48
		EX3	170.4691944	90.16738889	40.03723	40.0374	1.48
		EX4	170.1287778	90.03783333	42.637291	42.6373	1.48
		EX5	164.4444167	88.31541667	57.396069	57.4209	1.48
		EX6	164.9113056	87.69577778	58.743444	58.791	1.48
		EX43	161.6965556	90.07658333	43.588161	43.5882	1.48
		EX44	162.5987778	90.22466667	45.414352	45.4147	1.48
		EX42	201.1553333	92.88258333	28.131565	28.1672	1.48
		EX41	202.12075	93.54269444	22.315479	22.3582	1.48
		EX40	147.2158056	88.80652778	34.902523	34.9101	0
		SAAH_Ouest	155.2889722	89.96588889	53.23489	53.2349	1.48
		EX7	152.0440833	89.21002778	58.262755	58.2683	0
		BM2	155.0198333	90.52369444	143.605628	143.6116	1.48
		SAAH_EST	153.7235278	89.94869444	115.690552	115.6906	2.05
		CBUNG1	0.084944444	88.08072222	33.912159	33.9312	0
		C1PM	164.3080833	89.15411111	59.058356	59.0648	0
		C2	152.4004167	88.63633333	61.685012	61.7025	0
	152.4003889		88.63633333	61.684812	61.7023	0	
	152.4003889		88.63663889	61.685319	61.7028	0	
		C3	N/D	N/D	N/D	N/D	N/D
		C4	N/D	N/D	N/D	N/D	N/D
		Incl	165.2719167	89.74977778	28.956423	28.9567	1.48
BM2	1.327						
		BM1	0	89.3365	143.612536	143.6222	1.48
		SAAH_Ouest	359.8417222	89.00836111	90.381763	90.3942	1.48
			359.8344722	89.05038889	90.376666	90.3891	1.48
		SAAH_Est	5.759277778	87.96547222	28.080384	28.0981	1.48
			5.810111111	87.96508333	28.072482	28.0902	1.48
		C1PM	353.6185556	88.43744444	85.781561	85.8135	0
		C2	N/D	N/D	N/D	N/D	N/D
		C3	8.610222222	84.91225	47.902192	48.0917	0
		C4	89.35580556	71.00988889	14.41691	15.1719	0

Visite du Centre Canadien de Télédétection en Octobre 2010
 Opérateur : Hugo Drouin et François Charbonneau

De	À	Hz				Vz				Dist horizontale calculée	Dist Inclinée	Diff. Altitude	HI	HR
		D	M	S	DD	D	M	S	DD					
BM1													0.984	
	R_BM1_CBUN1	0	0	0.0	0.000000	87	36	39.3		33.91529	33.9448	2.3991	0.984	0
	R_BM1_CBUNG1	0	0	0.0	0.000000	87	36	38.4		33.91549	33.945	2.3992	0.984	
	1	165	16	51.9	165.281083	88	10	15.9	88.17108	28.96234	28.9771	1.9089	0.984	0
	INCLINO	165	19	21.0	165.322500	88	10	16.5	88.17125	28.95904	28.9738	-0.0913	0.984	2
	INCLINO1	164	19	14.8	164.320778	88	52	56.1	88.88225				0.984	2
	C1PM	164	19	20.5	164.322361	88	52	56.4	88.88233	59.05756	59.0688	2.1364	0.984	0
	C1PM1	164	19	20.2	164.322278	88	52	56.5	88.88236				0.984	0
	C1PM2	164	19	18.3	164.321750	88	52	53.2	88.88144	59.057640	59.0689	2.1373	0.984	0
	BM2	155	2	0.1	155.033361	90	12	12.8	90.20356	143.614599	143.6155	-1.5248	0.984	2
	C2	152	24	40.9	152.411361	88	22	32.6	88.37572	61.683398	61.7082	2.7334	0.984	0
BM2	R_BM2_BM1	0	0	0.0	0.000000	89	1	54.9	89.03192	143.629573	143.6501	1.5174	1.089	2
	BM1	359	59	58.9	359.999694	89	1	56.5	89.03236	143.602994	143.6235	1.5159	1.089	2
	C4	88	39	11.2	88.653111	71	0	43.9	71.01219	14.416903	15.245	6.0451	1.089	0
	C4	88	39	12.7	88.653528	71	1	43.4	71.02872	14.416903	15.245	6.0451	1.089	0
	C4	88	39	13.7	88.653806	71	1	42.2	71.02839	14.416797	15.2449	6.0451	1.089	0
	C5	88	39	14.4	88.654000	71	1	41.4	71.02817	14.416869	15.245	6.0452	1.089	0
	C4	88	39	16.1	88.654472	71	1	41.5	71.02819	14.416692	15.2448	6.0451	1.089	0
	SAA_EST	5	23	27.3	5.390917	86	25	37.5	86.42708	28.070228	28.1249	0.8418	1.089	2
BM2	R_BM2_BM2	0	0	0.0	0.000000	89	1	51.5	89.03097	143.626632	143.6472	1.5198	1.089	2
	BM1	0	0	29.4	0.008167	89	1	50.1	89.03058	143.609819	143.6304	1.5204	1.089	2
	C1PM	353	36	59.5	353.616528	88	16	52.4	88.28122	85.780872	85.8195	3.6636	1.089	0
	C3	8	0	55.6	8.015444	84	38	4.5	84.63458	47.935235	48.1462	5.5912	1.089	0
	C4	88	38	50.9	88.647472	71	1	49.3	71.03036	14.449212	15.279	6.0557	1.089	0
	SAA1_est	5	21	10.4	5.352889	86	31	23.3	86.52314	28.080418	28.1322	0.7951	1.089	2

Visite 09 – Février 2011
 Opérateur Dominique Turmel et Catherine Cloutier
 Hauteur instrument :

DE	À	Hz				Vz				dist. Hori. Calculée	ist Incliné	Diff. Altitude	HI	HR
		D	M	S	DD	D	M	S	DD					
De BM1					0.000000								1.24	
	R_BM1_CBUNG1	0	0	0	0.000000	272	6	44.5	272.11236	33.9097	33.9328	2.4908	1.24	0
	Cbung1	0	0	0.7	0.000194	272	6	46.5	272.11292	33.9097	33.9328	2.4911	1.24	0
	Cbung3	0	0	1.9		272	6	46.4		33.9097	33.9328	2.4911	1.24	
	C2	152	24	0.0	152.400000	271	27	34.8	271.45967	61.6835	61.7035	2.8119	1.24	0
	C1PM	164	19	8.5	164.319028	270	56	47.0	270.94639	59.0580	59.0661	2.2158	1.24	0
	Inclinn	165	15	53.0	165.264722	270	30	49.7	270.51381	28.9521	28.9533	-0.0003	1.24	1.5
	Inclinn1	165	15	53.1	165.264750	270	30	49.3	270.51369				1.24	1.5
	TrouW	156	36	34.0	156.609444	271	27	1.5	271.45042	28.6179	28.6271	0.4647	1.24	1.5
	TrouE	156	47	27.9	156.791083	271	6	20.4	271.10567	30.9043	30.9101	0.3365	1.24	1.5
	BM2	155	1	21.2	155.022556	269	47	55.0	269.79861	143.5823	143.5832	-1.4633	1.24	2.2
	BM2-2	155	2	2.6	155.034056	269	47	3.1	269.78419	143.6212	143.6222	-1.4995	1.24	2.2
	BM2-3	155	3	3.5	155.050972	269	47	2.6	269.78406				1.24	2.2
	EX1	169	28	18.0	169.471667	270	36	56.6	270.61572	32.8773	32.8792	-0.4066	1.24	2
	EX2	170	23	12.5	170.386806	270	43	49.9	270.73053	34.2391	34.2419	-0.3233	1.24	2
	EX43	161	42	6.3	161.701750	270	16	7.0	270.26861	43.6302	43.6307	-0.4553	1.24	1.9
	EX44	162	37	1.9	162.617194	270	6	55.2	270.11533	45.4465	45.4466	-0.5684	1.24	1.9
	EX4	170	5	51.3	170.097583	270	32	49.3	270.54703	42.6548	42.6567	-0.2526	1.24	1.9
	EX3	170	29	6.2	170.485056	270	27	43.7	270.46214	40.0643	40.0656	-0.3367	1.24	1.9
	Sans-neige	157	29	29.9	157.491639	270	58	18.9	270.97192	53.0233	53.0304	0.2089	1.24	1.9
	EX7	152	4	9.4	152.069278	272	12	23.0	272.20639	58.2403	58.2835	1.9841	1.24	1.5
	EX6	164	53	33.8	164.892722	270	58	43.5	270.97875	58.7000	58.7086	2.2431	1.24	0
	EX5	164	25	36.1	164.426694	271	41	1.5	271.68375	57.4164	57.4412	1.428	1.24	1.5

Visite 10 – Juillet et Août 2011

Opérateur : Nicolas Jamin et Catherine Cloutier

DE	À							Dist Inclinée m	Diff. Altitude m	Hi m	Hr m	Dist. hori. calculée m
		D	M	S	D	M	S					
De BM1										1.03		
	R_BM1_CBUNG1	0	0	0	272	20	9.1	33.9834	2.4151	1.03	0	33.9552
	C1PM	164	21	12.3	271	4	35.1	59.1008	2.1405	1.03	0	59.0904
	C2	152	26	37.6	271	34	43.9	61.7441	2.7315	1.03	0	61.7207
	Inclino	165	19	33.5	270	42	51.2	29.0011	-0.0844	1.03	1.476	28.9988
	SAAH1_ouest	155	20	9.5	270	16	44.8	53.2626	-0.1863	1.03	1.476	53.2620
	SAAH1_est	153	46	34.5	270	22	50.5	115.724	-0.7002	1.03	2.5	115.7212
	BM2	155	4	33.7	269	57	58.3	143.649	-1.5533	1.03	2.5	143.6491
De BM2	BM1	136	9	5.6	270	42	34.3	143.659	1.5244	1.244	1.5	143.6481
	Bm1(2)	136	9	6.4	270	42	34.6	143.661	1.5246	1.244	1.5	143.6495
	SAAH1_ouest	136	0	44.1	271	0	7.5	90.4264	1.326	1.244	1.5	90.4126
	SAAH1_est	141	31	18.9	272	15	17.2	28.1357	0.851	1.244	1.5	28.1139
	C1PM	129	46	47.8	271	37	18.2	85.8275	3.6735	1.244	0	85.7931
	C3	144	11	33.2	275	11	5.7	48.1291	5.5936	1.244	0	47.9322
	C4	224	50	4.0	288	25	25.7	15.2298	6.0573	1.244	0	14.4492
	HB1	130	51	53.1	273	2	48.1	15.1448	0.549	1.244	1.5	15.1234
	HB2	131	1	20.9	271	37	3.2	18.2877	0.2602	1.244	1.5	18.2804
	HB3	131	13	7.3	272	36	18.2	21.0536	0.3337	1.244	1.5	21.0453
	HB4	131	16	59.4	271	22	44.9	24.0797	0.3236	1.244	1.5	24.0727
	HB5	129	33	9.4	270	47	35.7	27.14	0.1198	1.244	1.5	27.1374
	HB6	128	39	9.6	270	43	2.5	30.3094	0.1235	1.244	1.5	30.3070
	HB7	128	49	24.3	270	27	47.3	33.4888	0.0148	1.244	1.5	33.4877
	HB8	128	45	29.8	270	12	42.9	36.4688	-0.121	1.244	1.5	36.4686
	HB9	128	47	9.8	270	16	32.1	39.4879	-0.066	1.244	1.5	39.4874
	HB10	129	26	7.1	270	22	33.2	42.4389	0.0225	1.244	1.5	42.4380
	HB11	129	33	56.0	271	4	20.3	45.416	0.5941	1.244	1.5	45.4080
	HB12	129	54	41.3	271	7	51.1	48.6584	0.7045	1.244	1.5	48.6489
	HB13	130	5	51.3	271	8	35.3	51.6072	0.7738	1.244	1.5	51.5969
	HB14	130	12	26.7	271	1	43.9	54.7638	0.7275	1.244	1.5	54.7550
	HB15	130	17	4.5	271	6	51.7	57.9176	0.8706	1.244	1.5	57.9066
SITE 2												
point	ref	43	10	6.4	88	6	40.2	21.5530	21.5647	0.6108	1.4	1.5
	ref(2)	43	4	36.9	88	10	8.4	21.5673	21.5783	0.4895	1.4	1.6
	site2	258	23	41.4	98	58	32.6	34.9765	35.4101	6.3245	1.4	2.2
	site2(2)	258	25	51.4	98	59	15.6	34.9810	35.4158	6.3326	1.4	2.2

Visite 11 – Novembre 2011

Opérateur : Catherine Cloutier et Pierre Therrien

DE	À	Hz			Vz			Dist Inclinée m	Diff. Altitude m	Hi m	Hr m	Dist. hori. calculée m
		D	M	S	D	M	S					
De BM1												
	R_BM1_CBUNG1	0	0	0	272	18	25.9	33.9781	2.3959	1.028	0	33.9506
	C1PM	164	21	49.4	271	3	30.3	59.1071	2.1201	1.028	0	59.0970
	C2	152	26	24.5	271	34	11.3	61.7477	2.7198	1.028	0	61.7245
	Inclino	165	16	57.9	270	44	42.3	28.9381	-0.0716	1.028	1.5	28.9353
	SAAH1_ouest	155	19	17.1	270	17	57.0	53.232	-0.1939	1.028	1.5	53.2313
	EX5	164	26	16.9	271	48	0.4	57.4114	1.3317	1.028	1.5	57.3831
	EX5.2	164	27	39.2	271	48	2.5	57.4228	1.3326	1.028	1.5	57.3944
BM1												
	R_BM1_CBUNG1	0	0	0.0	272	18	25.5	33.9771	2.3958	1.028	0	33.9496
	BM2	155	4	24.6	269	57	27.9	143.6062	-1.5765	1.028	2.5	143.6062
	BM2_2	155	4	20.9	269	57	27.7	143.6044	-1.5766	1.028	2.5	143.6044
De BM2	BM1	0	0	0.0	89	13	50.3	143.6265	1.5579	1.128	1.5	143.6135
	SAAH1_ouest	359	51	37.9	88	54	9.9	90.3978	1.3596	1.128	1.5	90.3812
	SAAH_est	5	22	8.3	87	31	6.5	28.1048	0.8449	1.128	1.5	28.0784
	C1PM	353	36	50.2	88	17	19.3	85.8109	3.6911	1.128	0	85.7726
	C3	8	1	8.0	84	40	3.3	48.1379	5.6018	1.128	0	47.9296
	C4	88	40	28.2	71	9	57.0	15.2673	6.0568	1.128	0	14.4498
	HB1	354	42	44.8	86	30	40.8	15.1475	0.5498	1.128	1.5	15.1194
	HB2	354	48	36.8	88	2	10.0	18.2967	0.255	1.128	1.5	18.2860
	HB3	355	2	52.5	88	6	38.5	21.0541	0.3222	1.128	1.5	18.2860
	HB4	354	4	19.4	88	20	21.4	24.0763	0.3258	1.128	1.5	24.0662
	HB5	353	22	42.5	88	57	54.8	27.1419	0.1182	1.128	1.5	27.1375
	HB6	352	26	30.3	89	3	49.2	30.3074	0.1233	1.128	1.5	30.3034
	HB7	352	36	39.0	89	19	38.2	33.4799	0.0212	1.128	1.5	33.4776
	HB8	352	33	26.5	89	36	48.9	36.4544	-0.1261	1.128	1.5	36.4536
	HB9	352	36	9.1	89	33	8.9	39.4814	-0.0635	1.128	1.5	39.4802
	HB10	353	15	2.1	89	27	57.9	42.4401	0.0236	1.128	1.5	42.4383
	HB11	353	23	44.4	88	47	12.3	45.401	0.5894	1.128	1.5	45.3908
	HB12	353	44	55.8	88	43	33.4	48.6566	0.71	1.128	1.5	48.6446
	HB13	353	58	50.7	88	43	30.2	51.5911	0.7761	1.128	1.5	51.5783
	HB14	354	1	42.3	88	50	16.2	54.7551	0.7388	1.128	1.5	54.7438
	HB15	354	7	48.4	88	45	46.4	57.9221	0.8788	1.128	1.5	57.9086

Visite 12 – Mai 2012

Opérateur : Catherine Cloutier et Agathe Fontaine

DE	À							Dist Inclinée m	Diff. Altitude m	Hi m	Hr m	dist. hori. calculée m
		D	M	S	D	M	S					
De BM1	R_BM1_Cbung1	0	0	0	87	40	46.3	33.9782	2.2028	1.019	0	33.9576
	C1PM	164	23	12.3	88	56	11.3	59.1077	1.9243	1.019	0	59.1008
	C2	152	27	22.6	88	25	36.1	61.7478	2.5226	1.019	0	61.7295
	INCLINO	165	18	23.6	89	13	42.8	28.9715	-0.2829	1.019	1.5	28.9708
	EX5	164	30	19.7	88	11	14.9	57.4479	1.1443	1.019	1.5	57.4249
	SAA1_W_BM1	155	19	40.3	89	41	18.2	53.2335	-0.3833	1.019	1.5	53.2334
	SAA1_E_BM1	153	46	39.0	89	37	0.9	115.6782	-0.8987	1.019	2.5	115.6767
	BM2	155	4	56.9	90	13	25.2	143.612	-1.7322	1.019	2.0	143.6100
	BM2-2	155	4	57.0	90	13	28.5	143.61	-1.7345	1.019	2.0	143.6080
De BM2	R_BM2_BM1	0	0	0.0	89	13	43.2	143.6191	1.3518	1.113	1.5	143.6086
	SAA1_E_BM2	5	22	37.1	87	29	51.8	28.0972	0.6438	1.113	1.5	28.0783
	SAA1_W_BM2	359	51	18.7	88	53	33.2	90.3945	1.1646	1.113	1.5	90.3812
	C4	88	40	23.8	71	10	46.0	15.2679	5.8425	1.113	0	14.5169
	HB1	354	40	56.7	86	28	27.6	15.1579	0.3492	1.113	1.5	15.1400
	HB2	354	49	36.0	88	0	8.8	18.2943	0.0547	1.113	1.5	18.2890
	HB3	355	1	7.7	88	5	1.1	21.0533	0.1211	1.113	1.5	21.0472
	HB4	354	3	55.6	88	19	1.5	24.0784	0.1242	1.113	1.5	24.0730
	HB5	353	21	28.5	88	56	57.5	27.1505	-0.0851	1.113	1.5	27.1488
	HB6	352	25	8.7	89	2	58.8	30.312	-0.0802	1.113	1.5	30.3104
	HB7	352	35	58.3	89	19	28.8	33.5104	-0.188	1.113	1.5	33.5098
	HB8	352	32	37.0	89	36	32.9	36.4661	-0.3341	1.113	1.5	36.4661
	HB9	352	36	8.7	89	32	46.8	39.4859	-0.2702	1.113	1.5	39.4857
	HB10	353	14	14.9	89	28	1.2	42.4429	-0.1881	1.113	1.5	42.4424
	HB11	353	23	14.1	88	46	39.6	45.3894	0.3854	1.113	1.5	45.3828
	HB12	353	46	2.8	88	42	45.2	48.6472	0.5102	1.113	1.5	48.6389
	HB13	353	58	37.6	88	42	33.4	51.6014	0.5795	1.113	1.5	51.5923
	HB14	354	1	37.9	88	49	28.2	54.7497	0.5404	1.113	1.5	54.7418
	HB15	354	7	12.9	88	45	13.1	57.9048	0.6767	1.113	1.5	57.8950
	C3	8	0	41.7	84	40	1.4	48.1373	5.3912	1.113	0	47.9468
Les données suivantes sont prises dans le secteur du site 2.												
Ref_site2	R_BM2_BM2	0	0	0	87	51	54.8	21.5501	0.5418	1.239	1.5	21.5351
	SITE_2	215	10	52.3	98	44	57.8	35.4408	-6.3019	1.239	2.15	35.0284
	SITE_2-2	215	11	3.6	98	45	9.7	35.4363	-6.3033	1.239	2.15	35.0236
	SITE_2-3	215	10	26.7	98	35	15.6	35.4232	-6.3004	1.329	2.25	35.0124

Visite 13 – Août 2012

Opérateur : Catherine Cloutier et Mélanie Mayers

DE	À							Dist Inclinée m	Diff. Altitude m	Hi m	Hr m	Dist. hori. calculée m
		D	M	S	D	M	S					
De BM1	R_BM1_CBUNG	0	0	0	87	51	59.3	33.938	2.4076	1.144	0	33.9149
	C1PM	164	23	35	89	2	27.4	59.107	2.1336	1.144	0	59.0982
	C2	152	27	46.5	88	31	43.7	61.744	2.7295	1.144	0	61.7236
	C2.2	152	27	34.1	88	31	37.2	61.744	2.7315	1.144	0	61.7236
	INCLINO	165	20	49.6	89	27	54.5	28.979	-0.0854	1.144	1.5	28.9773
	EX5	164	30	2.3	88	17	59.7	57.413	1.3475	1.144	1.5	57.3872
	SAAW_BM1	155	20	46.5	89	49	26.5	53.241	-0.1923	1.144	1.5	53.2410
	SAAE_BM1	153	47	58.8	89	56	15.3	115.680	-0.7291	1.144	2	115.6802
	SAAE_BM1.2	153	48	19.5	89	56	17.4	115.667	-0.7303	1.144	2	115.6664
	BM2	155	5	34.9	90	16	55.2	143.619	-1.5615	1.144	2	143.6173
	BM2.2	155	5	32.3	90	17	8.6	143.618	-1.5708	1.144	2	143.6160
	CBUNG	359	59	30.3	87	52	1.9	33.973	2.4084	1.144	0	33.9492
De BM2	R_BM2_BM1	0	0	0.0	89	1	28.8	143.660	1.5468	1.1	2	143.6393
	SAAE_BM2	5	20	54.2	87	28	1.2	28.107	0.8422	1.1	1.5	28.0791
	SAAW_BM2	359	50	44.3	88	53	0.4	90.402	1.3622	1.1	1.5	90.3846
	C4	88	40	16.2	71	5	19.8	15.275	6.0506	1.1	0	14.4503
	HB1	354	41	35.9	86	24	58.3	15.160	0.5476	1.1	1.5	15.1302
	HB2	354	49	37.1	87	57	3.7	18.297	0.2542	1.1	1.5	18.2857
	HB3	355	0	4.7	88	2	37.3	21.053	0.3187	1.1	1.5	21.0406
	HB4	354	3	58.4	88	16	33.8	24.092	0.3248	1.1	1.5	24.0814
	HB5	353	20	33.3	88	54	54.5	27.158	0.1142	1.1	1.5	27.1535
	HB6	352	23	27.1	89	1	37.4	30.352	0.1154	1.1	1.5	30.3473
	HB6.2	352	22	33.7	89	1	34.8	30.335	0.1155	1.1	1.5	30.3303
	HB7	352	34	42.5	89	17	31.9	33.508	0.014	1.1	1.5	33.5053
	HB8	352	32	59.0	89	35	29.6	36.476	-0.1399	1.1	1.5	36.4755
	HB9	352	34	29.5	89	31	39.3	39.503	-0.0742	1.1	1.5	39.5017
	HB10	353	12	48.5	89	26	48.6	42.446	0.0099	1.1	1.5	42.4442
	HB11	353	22	13.9	88	45	33.0	45.430	0.5839	1.1	1.5	45.4193
	HB12	353	43	59.9	88	41	31.0	48.666	0.7111	1.1	1.5	48.6533
	HB13	353	58	25.5	88	41	30.0	51.611	0.7786	1.1	1.5	51.5975
	HB14	354	0	40.4	88	48	19.7	54.765	0.7419	1.1	1.5	54.7535
	HB15	354	6	48.4	88	44	2.0	57.919	0.88	1.1	1.5	57.9051
	C3	8	0	8.5	84	38	10.9	48.136	5.5998	1.1	0	47.9256
	BM1_2	359	59	55.6	89	13	38.0	143.617	1.5384	1.1	1.5	143.6035
	C1PM_BM2	353	35	55.0	88	16	18.8	85.808	3.6882	1.1	0	85.7692

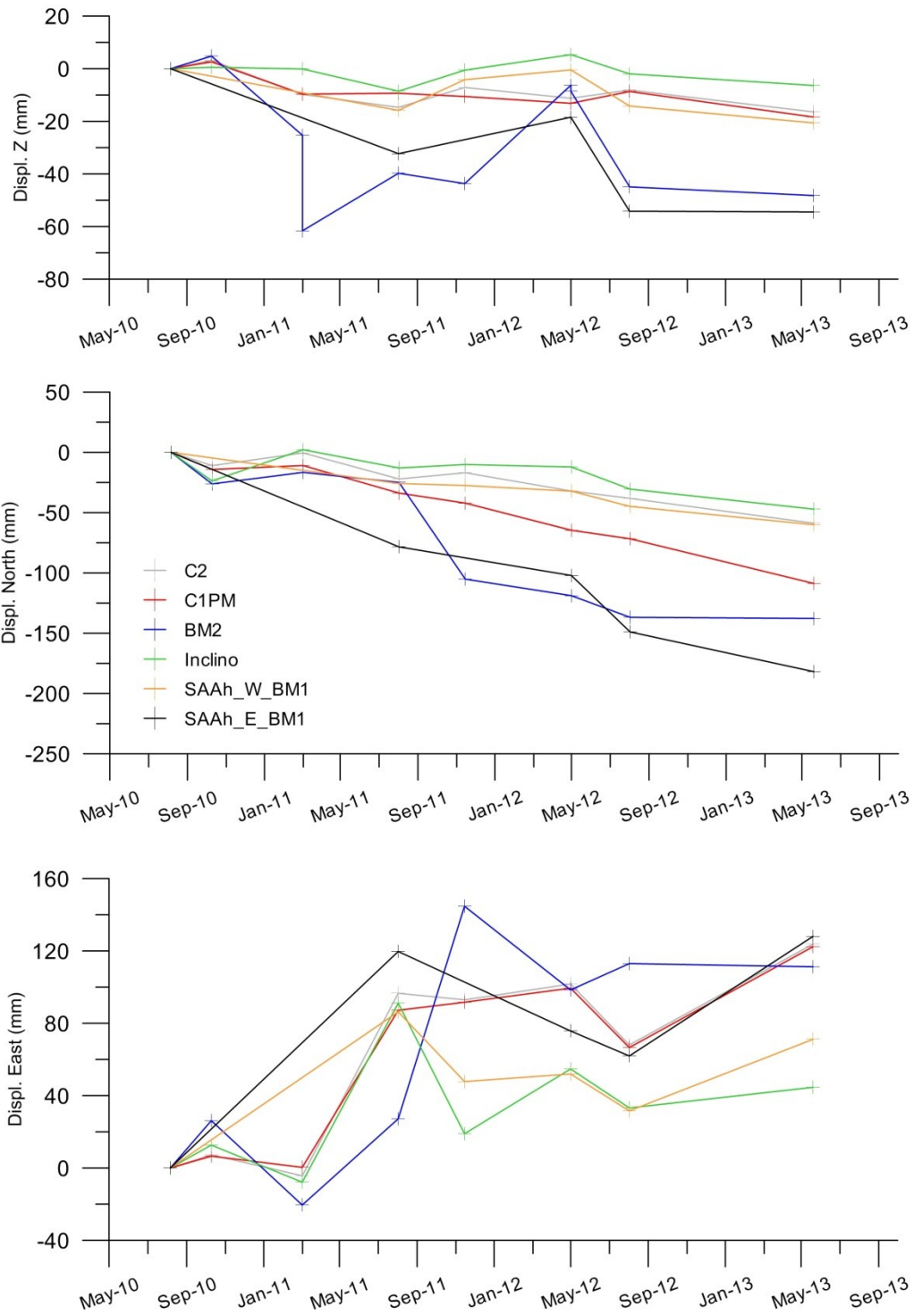
Visite 14 – Mai 2013

Opérateur : Catherine Cloutier et Florence Lanouette

DE	À	Hz			V			Dist. inclinée m	Diff. altitude m	HI m	HR m	Dist. hori. calculée m
		D	M	S	D	M	S					
De BM1	R_BM1_Cbung	0	0	0	87	44	4.6	33.9802	2.4043	1.061	0	33.9536
	C1PM	164	26	0.1	88	58	23.5	59.1126	2.1206	1.061	0	59.1031
	INCLINO	165	21	56.5	89	13	2.4	28.9804	1.4569	1.061	1.55	28.9150
	INCLINO1	165	21	56.1	89	13	3.4	28.9799	-0.0932	1.061	1.55	28.9772
	SAA1.W	155	21	44.7	89	41	28.7	53.2353	-0.202	1.061	1.55	53.2345
	C1	152	29	11.5	88	27	42.5	61.7501	2.7188	1.061	0	61.7278
	SAA1_E	153	48	42.4	89	45	2.1	115.6744	1.5654	1.061	2.3	115.6404
	SAA1_E1	153	48	45.8	89	45	12.8	115.6756	1.5595	1.061	2.3	115.6417
	SAA1_E2	153	48	46.1	89	45	11.1	115.6709	1.5604	1.061	2.3	115.6417
	SAA1_E3	153	48	46.6	89	45	9.7	115.6797	1.5612	1.061	2.3	115.6370
	SAA1_E4	153	48	48.3	89	45	12.7	115.6700	1.5595	1.061	2.3	115.6458
	SAA1_E5	153	48	48.8	89	45	10.2	115.6800	1.5609	1.061	2.3	115.6361
	BM2	155	7	7.9	90	8	7.3	143.5899	-1.5768	1.061	2.3	143.5895
	BM2.2	155	7	6.9	90	8	8.9	143.5825	-1.5779	1.061	2.3	143.5821
	BM2.3	155	7	7.2	90	8	7.5	143.5919	-1.577	1.061	2.3	143.5915
	BM2.4	155	7	4.6	90	7	59.8	143.5969	-1.5717	1.061	2.3	143.5965
	SAA1.E_P2	153	49	25.3	89	47	56.9	115.6760	-0.7326	1.061	2.2	115.6753
	SAA1.E_P3	153	49	27.7	89	48	1.9	115.6829	-0.7353	1.061	2.2	115.6822
	SAA1.E_P4	153	49	24.7	89	47	56.6	115.6924	-0.7324	1.061	2.2	115.6917
	SAA1.E_P5	153	49	25.2	89	47	57.1	115.6779	-0.7327	1.061	2.2	115.6772
	BM2.P2	155	7	23.4	90	10	26.5	143.6043	-1.5738	1.061	2.2	143.6036
	BM2.P2 1	155	7	22.2	90	10	26.9	143.5798	-1.574	1.061	2.2	143.5791
	BM2.P2 2	155	7	22.8	90	10	23.3	143.6071	-1.5716	1.061	2.2	143.6064
	BM2.P2 3	155	7	22.1	90	10	23.5	143.5966	-1.5717	1.061	2.2	143.5959
	BM2.P2 4	155	7	15.3	90	10	22.6	143.5857	-1.571	1.061	2.2	143.5851
	BM2.P2 5	155	7	15.4	90	10	26.3	143.5834	-1.5736	1.061	2.2	143.5827
	BM2.P2 6	155	7	15.3	90	10	25.4	143.5805	-1.5729	1.061	2.2	143.5798
	BM2.P2 7	155	7	15.2	90	10	25.8	143.5932	-1.5732	1.061	2.2	143.5925
De BM2	R_BM2_BM1	0	0	0	89	11	3.1	143.6120	2.3971	1.901	1.55	143.5974
	SAA1_E_BM2.1	359	51	19	88	50	8	90.3784	2.1882	1.901	1.55	90.3597
	SAA1_E_BM2.2	359	51	19.7	88	50	7.7	90.3826	2.1884	1.901	1.55	90.3639
	SAA1_E_BM2.3	359	51	22.5	88	50	7.1	90.3874	2.1888	1.901	1.55	90.3687
	SAA1_E_BM2.4	359	51	22.2	88	50	6.6	90.3695	2.1887	1.901	1.55	90.3508
	SAA1_E_BM2.5	359	51	22.4	88	50	7	90.3835	2.1888	1.901	1.55	90.3648

SAA1_E_BM2.6	359	51	29.7	88	50	6.4	90.3834	2.1890	1.901	1.55	90.3647
SAA1_E_BM2.7	359	51	28.2	88	50	6.9	90.3785	2.1887	1.901	1.55	90.3598
SAA1_E_BM2.8	359	51	28.4	88	50	6.9	90.3830	2.1888	1.901	1.55	90.3643
SAA1_E_BM2	5	21	30.8	87	20	56.5	28.0932	1.6504	1.901	1.55	28.0631
SAA1_E_BM3	5	21	31.2	87	20	56.5	28.1043	1.6509	1.901	1.55	28.0742
HB1	354	39	19.4	86	12	7.3	15.1571	1.3550	1.901	1.55	15.1238
HB2	354	4	20.8	88	8	53.9	24.0827	1.1292	1.901	1.55	24.0701
HB3	353	21	11.2	88	48	56.5	27.1374	0.9119	1.901	1.55	27.1316
HB4	352	21	5.6	88	56	10.6	30.3081	0.9137	1.901	1.55	30.3029
HB5	352	34	7.4	89	13	24.8	33.5046	0.8051	1.901	1.55	33.5015
HB6	352	30	49.4	89	31	12.5	36.4700	0.6565	1.901	1.55	36.4687
HB7	352	32	51.6	89	28	0.4	39.4917	0.7186	1.901	1.55	39.4900
HB8	353	12	31.5	89	23	30.9	42.4429	0.8016	1.901	1.55	42.4405
HB9	353	22	7.3	88	41	16.3	45.4095	1.3910	1.901	1.55	45.3976
HB10	353	43	46	88	37	24.1	48.6531	1.5200	1.901	1.55	48.6391
HB11	353	58	11.1	88	37	11.4	51.5956	1.5939	1.901	1.55	51.5806
HB12	354	0	14.1	88	44	27.5	54.7528	1.5542	1.901	1.55	54.7396
HB13	354	7	38	88	40	17.1	57.9157	1.6941	1.901	1.55	57.9001
C1PM_BM2	353	35	55.4	88	15	18.9	85.8106	4.5142	1.901	0	85.7708
C3	8	0	40.3	84	37	11	48.1284	6.4139	1.901	0	47.9164
C4	88	41	30.7	71	4	42.4	15.2748	6.8542	1.901	0	14.4494

Composantes de déplacement de certains points relevés à la station totale. Les déplacements sont plus réguliers selon l'axe Nord-Sud que selon l'axe Est-Ouest.



Date	Heure	Ruban (m)	Cadran1 (mm)	Cadran2 (mm)	Cadran3 (mm)	Cadran4 (mm)	Cadran5 (mm)	Opérateur	Remarques
bâti									
2010-05-17	10:00:00	0.8	10.26	10.29	10.3	10.28	10.3	PEL	Intérieur du LERN
2010-05-17	10:30:00	0.8	10.33	10.33	10.34	10.34	10.36	PEL	Extérieur du LERN,
2010-05-20	14:08:00	0.8	10.33	10.32	10.33			PEL	Bati dans bunga, sorti faire
2010-05-20	19:06:00	0.8	10.33	10.34	10.33			PEL	
2010-05-21	09:21:00	0.8	10.29	10.27	10.27			PEL	
2010-07-24	14:40:00	0.8	10.22	10.25	10.29	10.3	10.3	PEL	
2010-07-24	18:22:00	0.8	10.23	10.25	10.26			PEL	
2010-07-31	16:15:00	0.8	10.29	10.34	10.32	10.33	10.31	PEL	
2010-07-31	19:00:00	0.8	10.34	10.34	10.34			PEL	
2010-08-01	11:00:00	0.8	10.27	10.27	10.27			PEL	
2010-08-01	15:00:00	0.8	10.29	10.28	10.3			PEL	
2010-10-21	11:23:00	0.8	10.39					RC et FC	Il fait beau
2010-10-21	15:44:00	0.8	9.9	9.79	9.91			RC et FC	L'appareil c'est éteint seul au courant de la journée
2010-10-21	16:21:00	0.8	9.76	9.85	9.85			RC et FC	moyenne du bâti pour corrections est 10.30 mm
2010-10-26	12:00:00	0.8	10.33	10.34	10.34			PEL	Int. LERN Tester au retour de RC et FC
2011-02-26	15:40:00	0.8	10.44	10.43	10.41			CC et DT	
2011-02-26	16:55:00	0.8	10.48	10.46	10.47			CC et DT	
2011-02-27	12:35:00	0.8	10.42	10.39	10.41			CC et DT	
2011-02-27	16:20:00	0.8	10.45	10.52	10.53	10.51		CC et DT	
2011-02-28	8:44:00	0.8	10.45	10.49	10.42	10.48		CC et DT	
2011-03-02	11:40:00	0.8	10.32	10.36	10.34			CC	Int. LERN
2011-03-04	13:20:00	0.8	10.39	10.45	10.43			CC	ext. 5e
2011-07-26	8:33:00	0.8	10.31	10.33	10.31			CC et PT	
2011-07-26	17:15:00	0.8	10.3	10.36	10.37	10.35		CC et PT	
2011-07-28	13:00:00	0.8	10.37	10.36	10.4	10.45	10.38	CC et PT	Très soleil
2011-07-28	15:05:00	0.8	10.37	10.32	10.28	10.3		CC et PT	
2012-05-02	6:51:00	0.8	10.34	10.39	10.36			CC et AF	
2012-05-02	16:09:00	0.8	10.43	10.47	10.48			CC et AF	
2012-05-03	10:39:00	0.8	10.43	10.42	10.44			CC et AF	
2012-08-05	7:52:00	0.8	10.4	10.41	10.38			CC et MM	
2012-08-05	17:08:00	0.8	10.31	10.32	10.29			CC et MM	
2013-05-17	8:13:00	0.8	10.41	10.4	10.42			CC et FL	
2013-05-17	16:18:00	0.8	10.48	10.43	10.39	10.44		CC et FL	
2013-05-18	15:15:00	0.8	10.33	10.34	10.38			CC et FL	
EX1-2									
2009-06-09	12:00:00	1.4	27.72	27.82	27.86			MPLB	
2009-07-27	10:05:00	1.4	27.96	28.01	27.86			MPLB	10h05
2009-09-04	17:00:00	1.4	26.85	26.80	26.82			PEL	17h00 Ensoleillé.
2009-10-24	09:39:00	1.4	29.18	29.19	29.25			PEL	9h39 - nuageux
2009-11-04	08:35:00	1.4	30.36	30.49	30.47			PEL	0835 ombre
2009-11-04	11:00:00	1.4	30.2	30.18	30.28			PEL	1100 vent soleil
2009-11-05	07:25:00	1.4	30.59	30.75	30.61			PEL	725
2009-11-05	14:30:00	1.4	30.19	30.33	30.32			PEL	1430
2009-11-06	13:49:00	1.4	30.27	30.35	30.26			PEL	1349 nuageux
2009-11-07	12:40:00	1.4	30.19	30.26	30.37	30.43		PEL	1240 soleil
2009-12-18	12:00:00	1.4	29.26	29.18	29.19			PEL	Nouvel oeuillet sur EX2 car
2010-03-13	15:20:00	1.4	29.15	29.12	29.09			PEL	Soleil 1520

2010-05-20	17:10:00	1.4	29.27	29.23	29.25			PEL	122/0
2010-07-24	17:20:00	1.4	29.39	29.44	29.41			PEL	
2011-02-27	15:25:00	1.4	38.81	38.78	38.73			CC et DT	
2011-02-28	8:53:00	1.4	38.7	38.7	38.69			CC et DT	
2011-07-26	13:34:00	1.4	38.39	38.32	38.29	38.23	38.29	CC et PT	
2012-05-02	7:00:00	1.4	39.97	39.89	39.95			CC et AF	
2012-08-05	8:06:00	1.4	40.16	40.12	40.05	40.15		CC et MM	
2013-05-18	15:20:00	1.4	43.29	43.33	43.27			CC et FL	EX2 réparé mais tourne légèrement
EX3-4									
2009-06-08	09:28:00	2.55	35.78	35.97	35.86			MPLB	
2009-07-27	10:20:00	2.55	35.67	35.7	35.61			MPLB	
2009-09-04	17:00:00	2.55	30.52	30.5	30.52			PEL	
2009-10-24	09:46:00	2.55	32.54	32.62	32.55			PEL	
2009-11-04	08:39:00	2.55	37.25	37.2	37.29			PEL	
2009-11-04	08:58:00	2.55	37.28	37.14	37.19	37.13	37.28	PEL	
2009-11-04	11:07:00	2.55	36.89	37.05	37.08			PEL	
2009-11-05	07:20:00	2.55	37.37	37.43	37.34			PEL	
2009-11-05	14:35:00	2.55	37.09	37.05	37.16			PEL	
2009-11-06	13:52:00	2.55	37.17	37.21	37.2			PEL	
2009-11-07	13:00:00	2.55	36.98	37.03	36.96			PEL	
2009-12-16	12:45:00	2.55	36.5	36.53	36.48			PEL	
2010-03-13	15:25:00	2.55	35.86	35.8	35.82			PEL	
2010-05-20	17:26:00	2.55	34.91	34.86	34.85			PEL	
2010-07-24	17:25:00	2.55	34.5	34.5	34.5			PEL	
2011-02-27	15:12:00	2.55	35.48	35.54	35.51			CC et DT	
2011-07-26	13:52:00	2.55	33.02	33.01	33.09			CC et PT	
2012-05-02	7:08:00	2.55	27.84	27.84	27.91			CC et AF	
2012-08-05	8:16	2.55	26.29	26.27	26.41	26.42	26.29	CC et MM	
2012-08-05	9:02	2.55	32.99	32.98	32.9			CC et MM	
2013-05-17	10:08	2.55	29.22	29.29	29.33			CC et FL	
EX5-6									
2009-06-09	12:00:00	1.55	12.92	12.89	12.93			MPLB	
2009-07-27	10:26:00	1.55	11.52	11.46	11.44			MPLB	
2009-09-04	17:15:00	1.55	9.73	9.72	9.77			PEL	
2009-10-24	10:10:00	1.55	11.12	11.1	11.07			PEL	
2009-11-04	8:45:00	1.55	11.45	11.5	11.46			PEL	
2009-12-16	12:50:00	1.55	12.3	12.34	12.36			PEL	
2010-03-13	15:40:00	1.55	10.92	10.81	10.81			PEL	
2010-05-20	17:31:00	1.55	9.4	9.39	9.41			PEL	
2010-07-24	17:30:00	1.55	9.11	9.19	9.19	9.2		PEL	
2011-02-27	14:58:00	1.55	10.33	10.33	10.39			CC et DT	
2011-07-26	14:02:00	1.55	7.27	7.36	7.19	7.23		CC et PT	
2012-05-02	7:22:00	1.55	5.32	5.33	5.28			CC et AF	
2012-08-05	8:36	1.55	4.59	4.59	4.6			CC et MM	
2013-05-17	8:30	1.55	3.32	3.3	3.33			CC et FL	
EX5-7									
2009-06-08	12:00:00	12.4	46.54	46.58	46.47			MPLB	
2009-07-27	10:45:00	12.45	3.05	2.77	2.54	2.63		MPLB	
2009-09-04	17:15:00	12.4	51.85	51.86	51.92			PEL	
2009-10-24	09:55:00	12.45	6.46	6.45	6.5			PEL	
2009-11-04	8:55:00	12.4	55.06	54.76	54.99			PEL	

2009-12-16	13:05:00	12.45	7.17	7.1	7.07			PEL	
2010-03-13	15:36:00	12.45	8.04	8.02	7.26	7.66		PEL	
2010-05-20	17:53:00	12.45	7.28	7.3	7.26			PEL	
2010-07-24	17:40:00	12.45	7.12	7.06	7.18	7.09		PEL	
2010-10-21	16:07:00	12.45	12.91	12.17	12.19	11.96		RC et FC	
2011-02-26	16:30:00	12.45	17.24	17.24	17.22			CC et DT	
2011-07-26	14:16:00	12.45	14.02	14.19	14.03	14.05		CC et PT	
02/05/2012	7:29:00	12.45	19.37	19.64	19.44	19.49		CC et AF	
2012-08-05	8:56	12.45	18.41	18.22	18.3			CC et MM	
2013-05-17	8:35	12.45	24.83	24.73	24.67			CC et FL	
EX6-7									
2009-06-08	12:00:00	13	27.92	28.38	28.47			MPLB	
2009-07-27	10:40:00	13	35.94	36.09	35.76			MPLB	
2009-09-04	17:20:00	13	34.57	34.7	34.61			PEL	
2009-10-24	10:00:00	13	39.86	39.49	39.4			PEL	
2009-11-04	08:50:00	13	39.31	39.09	39.09			PEL	
2009-12-16	13:00:00	13	43.15	43.1	43.07	43.02		PEL	VENT PEL
2010-03-13	15:35:00	13	46.28	45.71	45.91			PEL	
2010-05-20	17:59:00	13	45.99	45.94	45.89			PEL	175/0
2010-07-24	17:35:00	13	46.26	46.01	46.06	46.03		PEL	
2010-10-21	16:14:00	13.05	1.67	1.51	1.64			RC et FC	Vent
2011-02-26	16:43:00	13.05	14.4	14.48	14.48			CC et DT	
2011-07-26	14:12:00	13.05	12.17	12.12	12.14			CC et PT	
2012-05-02	7:37:00	13.05	26.18	26.13	26.14			CC et AF	
2012-08-05	8:46	13.05	25.88	26.28	25.98	25.78	25.69	CC et MM	
2013-05-17	8:47	13.05	41.91	41.92	42.05			CC et FL	
EX1-7									
2010-05-20	18:30:00	28.7	18.03	18	17.9	17.78	17.82	PEL	242/12;œillet au sud
2010-07-24	18:02:00	28.7	15.08	15.12	15.12			PEL	
2011-07-28	15:00:00	28.7	10.24	9.83	10.43	9.29		CC et PT	
2012-08-05	11:32:00	28.7	3.63	2.7	2.74	2.76	3.41	CC et MM	
17/05/2013	09:05:00	28.65	50.35	50.31	50.33			CC et FL	
EX2-7									
2010-05-20	18:22:00	28	6.06	5.84	5.98	5.99	5.99	PEL	239/12 œillet au sud-est
2010-07-24	17:56:00	28	3.56	3.44	3.64	3.54	3.53	PEL	
2011-02-27	15:35:00	28	9.21	9.66	9.32			CC et DT	
2011-07-28	14:45:00	27.95	43.37	43.6	43.66	43.62		CC et PT	
2012-08-05	11:40:00	27.95	36.65	36.43	36.6			CC et MM	
2013-05-18	15:36:00	27.95	40.01	40.01	40.12			CC et FL	EX2 réparé mais tourne légèrement
EX3-7									
2010-05-20	18:00:00	23.95	19.55	19.63	19.5	19.48		PEL	238/7°
2010-07-24	17:51:00	23.95	17.35	17.26	17.22	17.26		PEL	
EX4-7									
2010-05-20	18:15:00	22.15	28.45	28.35	28.37	28.4	28.33	PEL	222/07
2010-07-24	17:46:00	22.15	26.89	26.91	26.89			PEL	
EX8-9									
2009-06-08	12:00:00	1.05	28.47	28.67	28.61			MPLB	
2009-07-27	14:45:00	1.05	17.63	17.76	17.88	17.76		MPLB	
2009-09-04	17:30:00	1.05	15.89	16.05	16.04			PEL	
2009-10-24	13:50:00	1.05	17.79	18.02	17.98			PEL	
2009-12-16	13:00:00	1.05	20.16	19.86	19.85	19.9		PEL	

2010-03-13	15:40:00	1.05	18.96	18.71	18.71			PEL	
2010-05-20	18:44:00	1.05	18.4	18.44	18.44			PEL	253/0 Crochet du côté Est vers l'amont sur EX8
2010-07-24	18:06:00	1.05	17.91	17.89	17.86			PEL	
2011-02-27	16:04:00	1.05	18.15	18.13	18.24	18.19		CC et DT	
2011-07-26	15:30:00	1.05	17.54	16.97	16.72	16.63	16.99	CC et PT	
2012-05-02	10:12:00	1.05	12.86	12.5	12.35	12.28	12.28	CC et AF	
2012-08-05	16:46	1.05	11.91	12.07	11.95			CC et MM	
2013-05-17	15:35	1.05	11.76	11.68	11.57	11.7		CC et FL	EX9 plié vers EX8 (- 3mm)
EX10-11									
2009-06-08	12:00:00	0.80	34.21	34.19	34.29			MPLB	
2009-07-28	09:51:00	0.80	34.39	34.60	34.87			MPLB	
2009-09-04	18:20:00	0.80	33.33	33.33	33.33			PEL	
2009-10-24	14:00:00	0.8	35.44	35.51	35.51			PEL	
2009-12-16	13:00:00	0.8	35.84	35.88	35.8			PEL	
2010-03-13	15:46:00	0.8	36.01	36.05	36.12			PEL	
2010-05-20	18:52:00	0.8	36.26	36.29	36.32			PEL	247/11
2010-07-24	18:12:00	0.8	36.39	36.44	36.41			PEL	
2011-07-26	15:51:00	0.8	38.56	38.51	38.54			CC et PT	
2012-05-02	10:12:00	0.8	40.59	40.6	40.62			CC et AF	
2012-08-05	17:00	0.8	40.88	40.95	40.95			CC et MM	
2013-05-17	15:46	0.8	43.21	43.19	43.19			CC et FL	
EX12-13									
2009-06-08	12:00:00	1.00	45.41	45.31	45.30			MPLB	
2009-07-27	10:55:00	1.00	45.94	45.94	45.93			MPLB	
2009-09-04	16:35:00	1.00	44.78	44.80	44.79			PEL	
2009-10-24	13:40:00	1.00	47.17	47.07	47.09			PEL	
2009-11-04	08:28:00	1.00	47.45	47.44	47.41			PEL	
2009-12-16	15:15:00	1.00	48.16	48.2	48.22			PEL	
2010-03-13	15:15:00	1.00	48.1	48.09	48.07			PEL	
2010-05-21	09:27:00	1.00	51.69	51.69	51.68			PEL	Oeillet EX13 changé Dépl pas necess signifi 115/21
2010-07-24	17:15:00	1.00	52.13	52.15	52.15			PEL	
2011-02-27	12:45:00	1.05	6.1	6.05	6.05			CC et DT	
2011-07-26	13:37:00	1.05	8.39	8.36	8.39			CC et PT	
2012-05-02	7:55:00	1.05	12.62	12.59	12.62			CC et AF	
2012-08-05	12:01	1.05	13.65	13.68	13.78			CC et MM	
2013-05-17	10:21	1.05	17.35	17.17	17.31			CC et FL	
EX14-15									
2009-06-08	12:00:00	7.10	26.56	26.61	26.67			MPLB	
2009-07-27	11:35:00	7.10	29.69	29.75	29.71			MPLB	
2009-09-04	15:20:00	7.10	29.26	29.25	29.26			PEL	
2009-10-24	11:25:00	7.10	34.7	34.65	34.6			PEL	
2009-12-16	15:05:00	7.10	38.11	38.01	38.06			PEL	
2010-03-13	15:00:00	7.1	38.14	38.12	38.14			PEL	
2010-05-20	16:45:00	7.1	42.71	42.75	42.68			PEL	151/26,5
2010-07-24	16:42:00	7.10	45.86	45.92	45.93			PEL	
2010-10-21	13:35:00	7.15	1.35	1.34	1.37			RC et FC	
2011-02-28	9:25:00	7.15	1.93	1.98	1.95			CC et DT Anneau plié	
2011-07-26	12:04:00	7.15	6.94	6.86	6.76	6.81		CC et PT	
2012-05-02	13:41:00	7.15	40.43	40.47	40.47			CC et AF	
2012-08-05	13:04	7.15	45.71	45.86	45.58	45.51		CC et MM	
2013-05-17	11:02	7.20	15.82	15.7	15.67	15.82		CC et FL	tige 15 décaussée

EX14-16									
2009-06-08	12:00:00	4.35	15.63	15.53	15.59				MPLB
2009-07-27	11:15:00	4.35	11.92	11.92	11.73				MPLB
2009-09-04	15:20:00	4.35	8.24	8.37	8.35				PEL
2009-10-24	11:20:00	4.35	10.03	10.08	10.11				PEL
2009-12-16	15:15:00	4.35	9.67	9.75	9.81				PEL
2010-03-13	15:00:00	4.35	7.12	7.08	7.02				PEL
2010-05-20	16:50:00	4.35	4.15	4.19	4.16				PEL
2010-07-24	16:45:00	4.3	51.78	51.77	51.78				PEL
2011-07-26	12:19:00	4.3	40.05	39.88	39.88	39.94			CC et PT
2012-05-02	11:04:00	4.3	33.4	33.53	33.52				CC et AF
2012-08-05	13:13	4.3	25.87	26.13	26.02	26.03			CC et MM
2013-05-17	11:12	4.3	19.14	18.99	19.01				CC et FL
EX15-16									
2009-06-08	12:00:00	6.65	13.59	13.77	13.68				MPLB
2009-07-27	11:25:00	6.65	18.79	18.81	18.75				MPLB
2009-09-04	15:20:00	6.65	19.35	19.42	19.31				PEL
2009-10-24	11:20:00	6.65	25.4	25.44	25.37				PEL
2009-12-16	15:15:00	6.65	30.1	29.97	29.97				PEL
2010-03-13	15:00:00	6.65	33.26	33.32	33.28				PEL
2010-05-20	16:40:00	6.65	38.67	38.66	38.62				PEL
2010-07-24	16:36:00	6.65	43	43.05	42.99				PEL
2011-07-26	12:14:00	6.7	13.45	13.35	13.43				CC et PT
2012-05-02	13:37:00	6.7	51.19	51.34	51.33	51.38			CC et AF
2012-08-05	12:58:00	6.75	9.86	9.84	9.75				CC et MM
2013-05-17	11:12	6.75	41.14	41.21	41.12				CC et FL
EX17-18									
2009-06-08	12:00:00	1.75	14.61	14.61	14.63				MPLB
2009-07-27	11:50:00	1.75	15.38	15.39	15.28				MPLB
2009-09-04	15:00:00	1.75	14.68	14.88	14.86				PEL
2009-10-24	11:44:00	1.75	16.89	16.85	16.82				PEL
2009-12-16	14:55:00	1.75	17.72	17.77	17.74				PEL
2010-03-13	14:45:00	1.75	18.62	18.72	18.86	18.85			PEL
2010-05-20	16:20:00	1.75	19.19	19.15	19.18				PEL
2010-07-24	16:14:00	1.75	19.94	19.96	19.9	19.98			PEL
2011-07-26	11:48:00	1.75	24.82	24.69	24.67	24.72			CC et PT
2012-05-02	11:32:00	1.75	25.96	26.06	26.3	26.27			CC et AF
2012-08-05	13:27	1.75	27.32	27.69	27.43	27.46			CC et MM
2013-05-17	11:22	1.75	32.17	32.21	32.34	32.33			CC et FL
EX19-20									
2009-06-08	10:45:00	1.20	24.45	24.36	24.67				PEL
2009-07-28	11:40:00	1.20	25.34	25.22	25.12	25.47			PEL
2009-09-04	14:50:00	1.20	24.66	24.15	24.49	24.38			PEL
2009-10-24	11:37:00	1.2	26.81	26.88	26.88	26.95			PEL
2009-12-16	14:45:00	1.2	27.96	27.8	27.92				PEL
2010-03-13	14:45:00	1.2	27.52	27.61	27.62				PEL
2010-05-20	15:40:00	1.2	29.34	29.32	29.33				PEL
2010-07-24	16:00:00	1.2	29.72	29.73	29.77				PEL
2011-07-26	11:40:00	1.2	37.84	38	37.56	37.88			CC et PT
2012-05-02	11:23:00	1.2	43.64	43.62	43.73				CC et AF
2012-08-05	13:04	1.2	45.33	45.28	45.35				CC et MM
2013-05-17	11:35	1.2	51.45	51.46	51.41				CC et FL

EX21-22									
2009-06-08	11:00:00	0.8	35.2	35.05	34.99			MPLB	
2009-07-28	11:20:00	0.8	35.56	35.56	35.68			MPLB	
2009-09-04	14:45:00	0.8	34.88	34.85	34.84			PEL	
2009-10-24	11:52:00	0.8	36.82	36.89	36.85			PEL	
2009-12-16	14:00:00	0.8	37.14	37.17	37.16			PEL	
2010-03-13	14:10:00	0.8	34.25	34.3	34.35			PEL	
2010-05-20	15:20:00	0.8	34.87	34.85	34.88			PEL	287/6,5 (amont plus bas que l'aval)
2010-07-24	15:48:00	0.8	35.28	35.26	35.28			PEL	
2011-07-26	11:12:00	0.8	35	35.09	35.13	35.24	35.05	CC et PT	
2012-05-02	11:48:00	0.8	29.1	29.18	29.16			CC et AF	Fissure qui s'est remplie
2012-08-05	13:57	0.8	30.6	30.73	30.88	30.82		CC et MM	
2013-05-17	11:45	0.8	28.26	28.45	28.51	28.33		CC et FL	
EX23-24									
2009-06-08	11:00:00	4.70	52.35	52.43	52.53			MPLB	
2009-07-27	12:05:00	4.75	2.94	3.12	2.99			MPLB	
2009-09-04	14:35:00	4.75	1.80	1.86	1.56			PEL	
2009-10-24	11:47:00	4.7	54.45	54.42	54.44			PEL	
2009-12-16	14:00:00	4.75	6.15	6.22	6.15			PEL	
2010-03-13	14:10:00	4.75	6.62	6.65	6.8	6.68		PEL	
2010-05-20	15:07:00	4.75	6.67	6.72	6.71			PEL	169/26
2010-07-24	15:37:00	4.75	6.88	6.92	6.93			PEL	
2010-10-21	12:06:00	4.75	8.71	8.86	8.71			RC et FC	
2011-07-26	11:24:00	4.75	14.33	14.37	14.38			CC et PT	
2012-05-02	14:05:00	4.75	18.92	19.13	18.94	18.99		CC et AF	
2012-08-05	14:10	4.75	19.4	19.52	19.62	19.58		CC et MM	
2013-05-17	12:18	4.75	26.92	27.08	27.15	27.04		CC et FL	
EX25-26									
2009-06-08	11:15:00	2.15	19.43	19.07	19.02	18.93		MPLB	
2009-07-27	12:30:00	2.15	20.82	20.44	20.48			MPLB	
2009-09-04	14:15:00	2.15	19.38	20.04	19.94	20.02		PEL	
2009-10-24	12:07:00	2.15	23.14	23.08	23.01	22.94		PEL	
2009-12-16	13:35:00	2.15	24.52	24.64	24.66	24.72		PEL	
2010-03-13	13:45:00	2.15	26.34	26.29	26.25	26.27		PEL	
2010-05-20	14:20:00	2.15	28.31	28.35	28.31			PEL	172/10 de pendage vers
2010-07-24	15:07:00	2.15	29.71	29.7	29.78	29.78	29.83	PEL	
2010-10-21	11:53:00	2.15	32.14	32.49	32.07	32.18		RC et FC	
2011-07-26	8:24:00	2.15	42.76	43	42.76	42.82	42.69	CC et PT	
2011-11-14		2.201							
2012-05-02	14:17:00	2.2	4.23	4.28	4.235	4.18	4.47	CC et AF	
2012-08-05	14:24	2.2	5.92	6.26	6.5	6.09	6.19	CC et MM	
2013-05-17	12:28	2.2	17.35	17.19	17.24	17.42		CC et FL	
EX27-28									
2009-06-08	11:00:00	0.80	24.95	24.9	24.78			MPLB	
2009-07-27	12:20:00	0.80	25.42	25.56	25.2			MPLB	
2009-09-04	14:00:00	0.80	24.2	24.85	24.88	24.18		PEL	
2009-10-24	12:18:00	0.8	25.48	25.44	25.34			PEL	Nuageux - Terrier à
2009-12-16	13:25:00	0.8	25.69	25.63	25.71			PEL	
2010-03-13	13:35:00	0.8	23.37	23.5	23.69	23.64		PEL	
2010-05-20	14:45:00	0.8	26.89	26.89	26.9			PEL	Dans le haut des oeillet
2010-07-24	15:23:00	0.8	27.49	27.52	27.5			PEL	Haut oeillet

2010-10-21	11:43:00	0.8	28.44	28.46	28.45			RC et FC	
2011-07-26	9:08:00	0.8	36.36	36.34	36.48	36.37		CC et PT	
EX29-30									
2009-07-28	12:30:00	1.05	50.8	50.79	50.93			MPLB	
2009-09-04	16:00:00	1.05	50.48	50.47	50.51			MPLB	
2009-10-24	11:00:00	1.05	52.77	52.75	52.67			PEL	
2010-05-21	09:47:00	1.05	54.28	54.29	54.3			PEL	254/42 -ATTENTION : Un oeillet a crochi
2010-08-01	18:40:00	1.1	5.2	5.2	5.21			PEL	
03/05/2012	11:12:00	1.1	12.42	12.48	12.52			CC et AF	
EX31-32									
2010-08-01	12:45:00	11.25	6.51	6.6	6.55	6.51	6.51	PEL	02/094 de 31 vers 32
2010-10-21	13:14:00	11.25	6.21	5.89	5.97			RC et FC	
2011-07-26	09:38:00	11.25	3.48	3.32	3.47	3.53		CC et PT	
2011-11-14		11.26							
2012-05-02	14:57:00	11.25	2	1.89	1.89			CC et AF	
2012-08-05	15:02:00	11.2	48.61	48.81	48.46	48.45		CC et MM	
2013-05-17	13:46:00	11.2	44.09	44.02	44			CC et FL	
EX31-33									
2010-08-01	12:58:00	7	30.56	30.82	30.65	30.79	30.61	PEL	17/163° de 31 vers 33
2010-10-21	13:19:00	7	31.61	31.33	31.3	31.35		RC Et FC	
2011-07-26	09:24:00	7	31.87	31.70	31.70	31.76		CC et PT	
2011-11-14		7.04							
2012-05-02	14:50:00	7	32.72	32.88	32.76			CC et AF	
2012-08-05	14:56:00	7	31.6	31.6	31.46			CC et MM	
2013-05-17	13:50:00	7	33.25	33.05	32.79	32.86		CC et FL	
EX32-33									
2010-08-01	13:30:00	10.55	22.7	22.75	22.74	22.79	22.71	PEL	04/241° de 32 vers 33
2010-10-21	13:08:00	10.55	24.77	24.58	24.54			RC et FC	
2011-07-26	09:50:00	10.55	24.79	24.94	24.83	24.79		CC et PT	
2011-11-14		10.58							
2012-05-02	15:03:00	10.55	26.51	26.33	26.3	26.19		CC et AF	
2012-08-05	14:51:00	10.55	25.12	25.02	25.06			CC et MM	
2013-05-17	14:00:00	10.55	22.97	23.09	22.97			CC et FL	
EX34-35									
2010-08-01	11:35:00	15.3	12.45	12.29	12.32	12.24	12.36	PEL	06/173° de 34 vers 35
2010-10-21	12:47:00	15.3	17.54	17.48	17.37			RC et FC	
2011-07-26	10:17:00	15.3	23.70	23.40	23.07	23.20	23.49	CC et PT	
2011-11-14		15.33							
2012-05-02	15:20:00	15.3	32.5	32.43	32.34			CC et AF	
2012-08-05	15:21:00	15.3	33.37	33.04	33.04	33.22		CC et MM	
2013-05-17	14:16:00	15.3	41.4	41.51	41.5			CC et FL	
EX36-37									
2010-08-01	12:00:00	6.75	53.99	53.85	53.9	53.85	53.86	PEL	19/170° de 36 vers 37
2010-10-21	12:37:00	6.8	6.44	6.42	6.5			RC et FC	
2011-07-26	10:05:00	6.8	12.46	12.49	12.44			CC et PT	
2011-11-14		6.82							
2012-05-02	15:35:00	6.8	19.77	19.69	19.69			CC et AF	
2012-08-05	15:45:00	6.8	19.75	19.88	19.77			CC et MM	
2013-05-17	14:29:00	6.8	26.48	26.61	26.59			CC et FL	
EX38-39									
2010-08-01	10:49:00	12	22.27	22.26	22.39	22.29	22.33	PEL	37/352° de 38 vers 39

2010-10-21	12:26:00	12	25.5	25.84	25.58	25.63		RC et FC	Vent
2011-07-26	10:46:00	12	30.33	30.76	30.95	30.88	30.93	CC et PT	
2012-05-02	15:49:00	12	39.61	39.08	39.04	38.94		CC et AF	
2012-08-05	16:10:00	12	39.15	38.85	38.75	38.75		CC et MM	
2013-05-17	14:50:00	12	46.56	46.52	46.18	46.06	46.36	CC et FL	
EX40-1									
2010-08-01	13:57:00	13.6	19.77	19.81	19.94	19.7	19.79	PEL	10/185° de 40 vers 1
2011-02-27	13:00:00	13.6	27.18	27	27.05	27.33	27.09	CC et DT	
2011-07-26	16:35:00	13.6	25.75	25.76	25.62			CC et PT	vent instrument instable
2011-07-28	13:10:00	13.6	24.01	23.85	23.96			CC et PT	gros soleil
2012-05-02	08:02:00	13.6	29.45	29.52	30.01	29.57		CC et AF	
2012-08-05	09:09:00	13.6	27.74	27.64	27.64			CC et MM	
2013-05-17	09:57:00	13.6	33.82	33.59	34.02	33.92		CC et FL	
EX40-2									
2010-08-01	14:04:00	14.2	51.99	51.97	51.95	51		PEL	09/184° de 40 vers 2 (clip)
2011-02-27	13:20:00	14.25	11.09	11.21	11.14	11.07		CC et DT	
2011-07-26	16:44:00	14.25	9.52	9.78	9.63	9.70	9.65	CC et PT	vent instrument instable
2011-07-28	13:20:00	14.25	7.78	8.12	8.47	8.18	7.98	CC et PT	soleil instrument instable
2012-05-02	08:10:00	14.25	15.05	15.6	15.18	15.34		CC et AF	
2012-08-05	09:20:00	14.25	14.04	13.91	13.87	13.86		CC et MM	
2013-05-18	15:25:00	14.25	24.64	24.59	24.47			CC et FL	EX2 réparé mais tourne légèrement
EX40-3									
2010-08-01	14:10:00	16.15	20.93	20.93	20.97	20.9		PEL	08/162° de 40 vers 3
2011-07-28	13:38:00	16.15	29.33	29.3	29.4	29.6	29.09	CC et PT	lectures a pris 10minutes
2012-05-02	08:21:00	16.15	39.47	39.88	39.40	39.31		CC et AF	
2012-08-05	09:28:00	16.15	38.41	38.45	38.24	38.31		CC et MM	
2013-05-17	10:04:00	16.15	43.11	43.03	43.24			CC et FL	
EX40-5									
2010-08-01	14:15:00	26	47	47.06	46.94	47.03		PEL	00/291° de 5 vers 40
2011-02-27	13:55:00	26.05	11.65	11.06	11.26	11.34	11.47	CC et DT	mesures instables
2011-07-28	13:55:00	26.05	6.48	6.49	6.60			CC et PT	
2012-05-02	09:06:00	26.05	17.96	17.86	17.73	17.48		CC et AF	
2012-08-05	09:55:00	26.05	16.43	16.48	16.24	16.58		CC et MM	
2013-05-17	09:25:00	26.05	27.15	27.12	27.39	27.06		CC et FL	
EX40-6									
2010-08-01	14:20:00	27.45	20.75	20.77	20.76			PEL	03/295° de 6 vers 40
2011-02-27	13:40:00	27.45	38.07	38.59	39.21	38.54	38.87	CC et DT	
2011-07-28	14:10:00	27.45	31.68	31.61	31.67			CC et PT	
2012-05-02	09:17:00	27.45	42.71	42.75	42.74			CC et AF	
2012-08-05	10:10:00	27.45	40.84	41.2	41.24	40.59	40.22	CC et MM	
2013-05-17	09:34:00	27.5	2.85	2.43	2.45	2.87		CC et FL	
EX40-44									
2010-07-31	16:00:00	15.05	20.43	20.43	20.42			PEL	?/310° de 44 vers 40
2010-10-21	16:02:00	15.05	27.03	26.84	26.89	26.63		RC et FC	vent
2011-02-26	16:15:00	15.05	32.41	32.62	32.61	32.68		CC et DT	
2011-07-28	13:50:00	15.05	28.81	28.58	28.71			CC et PT	
2012-05-02	08:31:00	15.05	36.93	36.57	36.6	37		CC et AF	Vent
2012-08-05	09:39:00	15.05	36.01	36.46	36.17	36.53		CC et MM	
2013-05-17	09:54:00	15.05	46.85	46.88	47.08			CC et FL	
EX41-42									
2010-08-01	10:30:00	5.8	25.98	25.93	25.92	25.86	25.72	PEL	00/130° de 41 vers 42

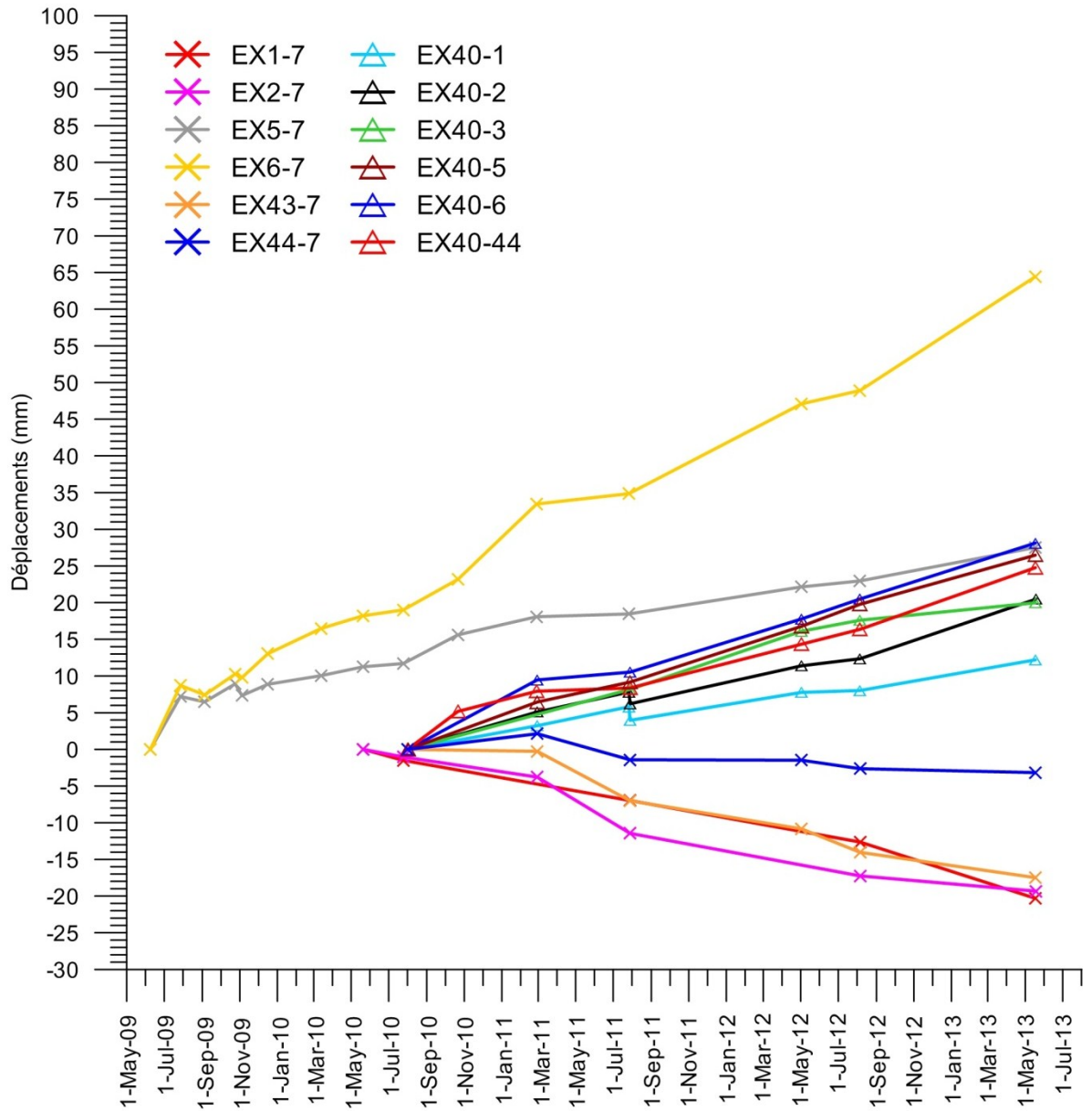
2010-10-21	15:53:00	5.8	28.42	28.52	28.47				RC et FC	
2011-02-27	16:15:00	5.8	28.56	28.68	28.74	28.46	28.56		CC et DT	
2011-07-26	16:24:00	5.8	25.06	25.07	25.02				CC et PT	
2012-05-02	07:45:00	5.8	25.65	25.73	25.77				CC et AF	
2012-08-05	11:54:00	5.8	23.22	23.32	23.18				CC et MM	
2013-05-17	10:17:00	5.8	21.04	21.34	20.88	20.86			CC et FL	
EX43-44										
2010-07-31	16:45:00	1.9	24.77	24.71	24.74	24.76	24.7433		PEL	00/110° de 43 vers 44
2011-02-27	15:03:00	1.9	25.5	25.43	25.33	25.33			CC et DT	
2011-07-26	14:28:00	1.9	22.82	22.76	22.77				CC et PT	
2012-05-02	07:14:00	1.9	19.79	19.72	19.77				CC et AF	
2012-08-05	08:26:00	1.9	18.79	18.69	18.7				CC et MM	
2013-05-17	08:25:00	1.9	16.9	16.85	16.91				CC et FL	
EX43-5										
2010-08-01	14:40:00	14.05	38.03	38.06	37.94				PEL	05/280° de 5 vers 43
2011-02-27	14:50:00	14.05	42.77	42.66	42.62				CC et DT	
2011-07-26	15:23:00	14.05	38.02	37.97	38.14	37.97			CC et PT	
2012-05-02	09:22:00	14.05	37.27	37.32	37.59	37.13	37.24		CC et AF	
2012-08-05	10:20:00	14.05	34.14	34.26	34.09	34.48	34.32		CC et MM	
2013-05-17	09:21:00	14.05	34.51	34.73	34.62	34.67			CC et FL	
EX43-6										
2010-08-01	14:25:00	15.55	24.2	24.26	24.27				PEL	10/284° de 6 vers 43
2011-02-27	14:17:00	15.55	29.45	29.4	29.28	29.49			CC et DT	
2011-07-26	16:55:00	15.55	22.70	22.74	22.75				CC et PT	
2012-05-02	09:33:00	15.55	18.88	18.81	19.16	19.16	19.09		CC et AF	
2012-08-05	10:30:00	15.55	15.13	14.83	15.13	14.76	15.12		CC et MM	
2013-05-17	09:41:00	15.55	13.21	12.66	13.02	13.24			CC et FL	
EX43-7										
2010-07-31	17:00:00	17	49.98	50.15	50.08	50.03	49.95		PEL	05/055° de 7 vers 43 (sud)
2011-02-27	15:50:00	17.05	4.64	4.81	4.54				CC et DT	
2011-07-28	14:32:00	17	42.72	42.69	43.37	43.19	43.06		CC et PT	
2012-05-02	10:05:00	17	41.51	41.64	41.42				CC et AF	
2012-08-05	11:16:00	17	35.41	35.66	35.19	35.17			CC et MM	
2013-05-17	08:59:00	17	34.82	34.85	34.71				CC et FL	
EX44-5										
2010-08-01	14:36:00	12.2	14.22	14.23	14.2				PEL	04/280° de 5 vers 44
2011-02-27	14:40:00	12.2	19.3	19.45	19.41				CC et DT	
2011-07-26	15:13:00	12.2	16.97	17.06	17.16	17.04			CC et PT	
2012-05-02	09:52:00	12.2	20.35	20.54	20.47				CC et AF	
2012-08-05	10:53:00	12.2	18.99	18.89	18.91				CC et MM	
2013-05-17	09:12:00	12.2	21.66	21.47	21.45	21.45			CC et FL	
EX44-6										
2010-08-01	14:32:00	13.7	6.91	7.03	7.02				PEL	10/282° de 6 vers 44
2011-02-27	14:30:00	13.7	12.38	12.04	12.28				CC et DT	
2011-07-26	17:02:00	13.7	7.49	7.75	7.37	7.70	7.67		CC et PT	
2012-05-02	09:43:00	13.7	7.45	7.56	7.42	7.63			CC et AF	
2012-08-05	10:45:00	13.7	4.83	5.21	5.31	5.21			CC et MM	
2013-05-17	09:48:00	13.7	5.1	4.89	5.03				CC et FL	
EX44-7										
2010-07-31	17:00:00	16.05	44.04	43.97	44.05				PEL	03/050° de 7 vers 44 (sud)
2011-02-27	15:58:00	16.1	0.83	0.7	0.75				CC et DT	
2011-07-28	14:19:00	16.05	42.88	42.39	42.53	42.51			CC et PT	

2012-05-02	09:58:00	16.05	44.64	44.77	44.8			CC et AF	
2012-08-05	11:03:00	16.05	40.84	41.18	40.23	40.91	40.7	CC et MM	
2013-05-17	08:54:00	16.05	43	42.93	42.95			CC et FL	
Tige A1-A2									
1993-11-01	12:00:00	0.583						GREGI	
1993-11-26	12:00:00	0.585						GREGI	
1994-01-18	12:00:00	0.582						GREGI	
1994-06-04	12:00:00	0.587						GREGI	
1994-07-01	12:00:00	0.587						GREGI	
1994-09-07	12:00:00	0.587						GREGI	
2009-06-08	12:00:00	0.654						CC	
2009-07-28	13:00:00	0.659						CC	
2009-09-04	14:00:00	0.654						CC	
2009-10-24	15:00:00	0.656						CC	
2010-03-13	16:00:00	0.633						CC	
2010-05-20	17:00:00	0.635						CC	
2010-08-01	15:00:00	0.629						CC	
2011-11-16		0.629						Cc-PT	
2012-08-05		0.628							
2013-05-17		0.629						CC	
Tige A3-A4									
1993-11-01	12:00:00	0.539						GREGI	
1993-11-26	12:00:00	0.543						GREGI	
1994-06-04	12:00:00	0.55						GREGI	
1994-07-01	12:00:00	0.548						GREGI	
1994-09-07	12:00:00	0.5547						GREGI	
2009-06-08	12:00:00	0.63						CC	
2009-07-28	13:00:00	0.628						CC	
2009-09-04	14:00:00	0.624						CC	
2009-10-24	15:00:00	0.625						CC	
2010-03-13	16:00:00	0.604						CC	
2010-05-20	17:00:00	0.61						CC	
2010-08-01	15:00:00	0.6						CC	
2011-11-16		0.604							
2012-08-05		0.602							
2013-05-17		0.605						CC	
Tige A1-A4									
1993-11-01	12:00:00	1.003						GREGI	
1993-11-26	12:00:00	1.114						GREGI	
1994-06-04	12:00:00	1.015						GREGI	
1994-07-01	12:00:00	1.017						GREGI	
1994-09-07	12:00:00	1.107						GREGI	
2009-06-08	12:00:00	1.182						CC	
2009-07-28	13:00:00	1.18						CC	
2009-09-04	14:00:00	1.172						CC	
2009-10-24	15:00:00	1.177						CC	
2010-03-13	16:00:00	1.156						CC	
2010-05-20	17:00:00	1.156						CC	
2010-08-01	15:00:00	1.152						CC	
2011-11-16		1.155							
2012-08-05		1.152							
2013-05-17		1.156						CC et FL	

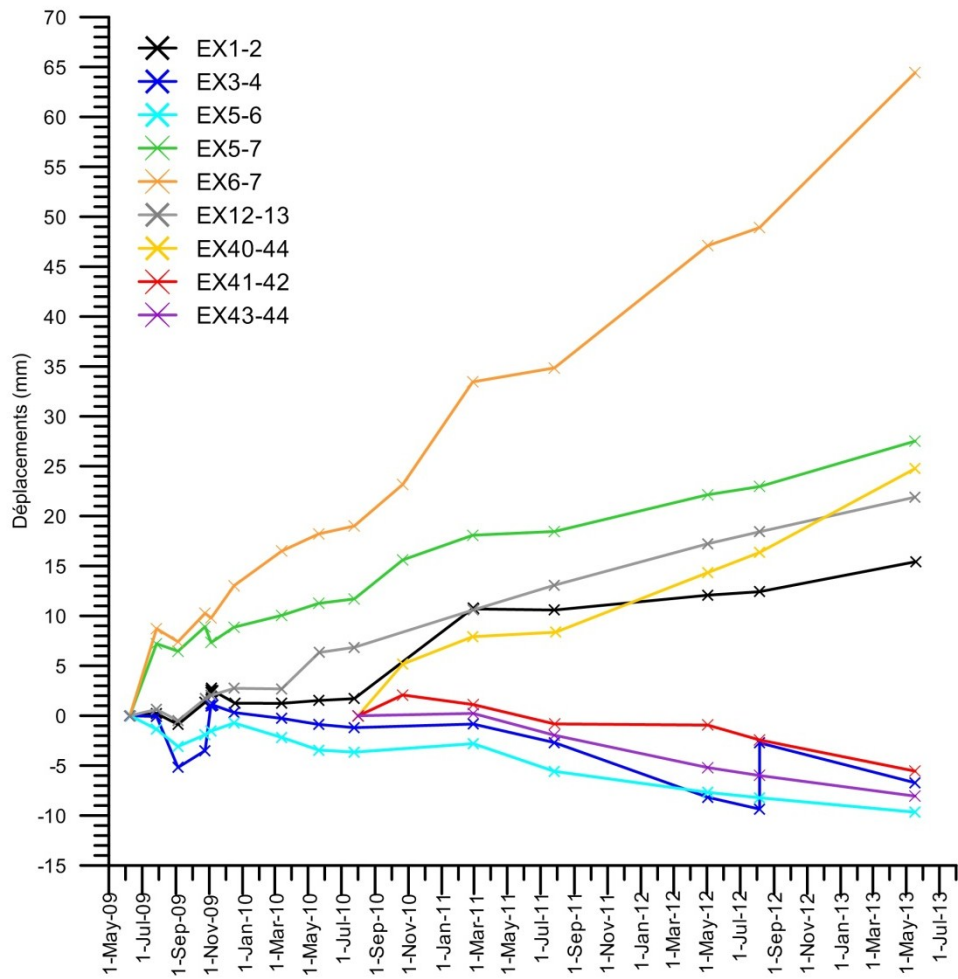
Tige A2-A3								
1993-11-01	12:00:00	1.22						GREGI
1993-11-26	12:00:00	1.22						GREGI
1994-06-04	12:00:00	1.221						GREGI
1994-07-01	12:00:00	1.218						GREGI
1994-09-07	12:00:00	1.216						GREGI
2009-06-08	12:00:00	1.261						CC
2009-07-28	13:00:00	1.272						CC
2009-09-04	14:00:00	1.264						CC
2009-10-24	15:00:00	1.264						CC
2010-03-13	16:00:00	1.245						CC
2010-05-20	17:00:00	1.244						CC
2010-08-01	15:00:00	1.24						CC
2011-11-16		1.242						
2012-08-05		1.239						
2013-05-17		1.24						CC et FL
Tige A1-A3								
2010-05-20	17:00:00	1.037						CC
2010-08-01	15:00:00	1.033						CC
2011-11-16		1.036						
2012-08-05		1.032						
2013-05-17		1.033						CC et FL
Tige A2-A4								
2010-05-20	17:00:00	1.028						CC
2010-08-01	15:00:00	1.025						CC
2011-11-16		1.024						
2012-08-05		1.028						
2013-05-17		1.026						CC et FL
Tige B3-B4								
1993-11-01	12:00:00	1.022						GREGI
1993-11-26	12:00:00	1.024						GREGI
1994-01-18	12:00:00	1.025						GREGI
1994-02-18	12:00:00	1.029						GREGI
1994-04-05	12:00:00	1.025						GREGI
1994-06-04	12:00:00	1.026						GREGI
1994-07-01	12:00:00	1.026						GREGI
1994-09-07	12:00:00	1.025						GREGI
2009-06-08	12:00:00	1.062						CC
2009-07-28	13:00:00	1.058						CC
2009-09-04	14:00:00	10.62						CC
2009-10-24	15:00:00	1.053						CC
2010-05-20	17:00:00	1.05						CC
Tige B5-B6								
1993-11-01	12:00:00	0.183						GREGI
1993-11-26	12:00:00	0.182						GREGI
1994-01-18	12:00:00	0.186						GREGI
1994-02-18	12:00:00	0.186						GREGI
1994-04-05	12:00:00	0.183						GREGI
1994-06-04	12:00:00	0.183						GREGI
1994-07-01	12:00:00	0.185						GREGI
1994-09-07	12:00:00	0.184						GREGI
2010-05-20	17:00:00	0.216						CC

Tige C7-C8								
1993-11-01	12:00:00	1.539						GREGI
1993-11-26	12:00:00	1.541						GREGI
1994-01-18	12:00:00	1.541						GREGI
1994-02-18	12:00:00	1.541						GREGI
1994-04-05	12:00:00	1.539						GREGI
1994-06-04	12:00:00	1.539						GREGI
1994-07-01	12:00:00	1.541						GREGI
1994-09-07	12:00:00	1.542						GREGI
2009-06-08	12:00:00	1.576						CC
2009-07-27	14:45:00	1.58						CC
2009-09-04	17:30:00	1.572						CC
2009-10-24	13:50:00	1.574						CC
2010-05-20	17:00:00	1.558						CC
Tige D9-D10								
1993-11-01	12:00:00	1.578						GREGI
1993-11-26	12:00:00	1.582						GREGI
1994-01-18	12:00:00	1.583						GREGI
1994-02-18	12:00:00	1.583						GREGI
1994-04-05	12:00:00	1.583						GREGI
1994-06-04	12:00:00	1.578						GREGI
1994-07-01	12:00:00	1.583						GREGI
1994-09-07	12:00:00	1.583						GREGI
2009-06-08	12:00:00	1.621						CC
2009-07-27	14:45:00	1.618						CC
2009-09-04	17:30:00	1.615						CC
2009-10-24	13:50:00	1.618						CC
2010-03-13	15:40:00	1.667						CC
2010-05-20	17:00:00	1.668						CC
Tige I1-I2								
1993-11-01	12:00:00	6.6						GREGI
1993-11-26	12:00:00	6.6						GREGI
1994-06-04	12:00:00	6.612						GREGI
1994-09-07	12:00:00	6.614						GREGI
2009-06-08	12:00:00	6.794						CC
2009-07-27	14:45:00	6.76						CC
2009-09-04	17:30:00	6.797						CC
2009-10-24	13:50:00	6.794						CC
2010-03-13	15:40:00	6.773						CC
2010-05-20	17:00:00	6.776						CC
2010-08-01	12:40:00	6.776	6.778					CC
2011-11-14		6.786						
2012-05-02	14:29:00	6.785						CC et AF
2012-08-05		6.789						CC et MM
2013-05-17		6.795						CC et FL
Tige 01-02								
1993-11-01	12:00:00	3.295						GREGI
1993-11-26	12:00:00	3.29						GREGI
1994-06-04	12:00:00	3.272						GREGI
1994-07-01	12:00:00	3.287						GREGI
1994-09-07	12:00:00	3.285						GREGI
2009-06-08	12:00:00	3.252						CC

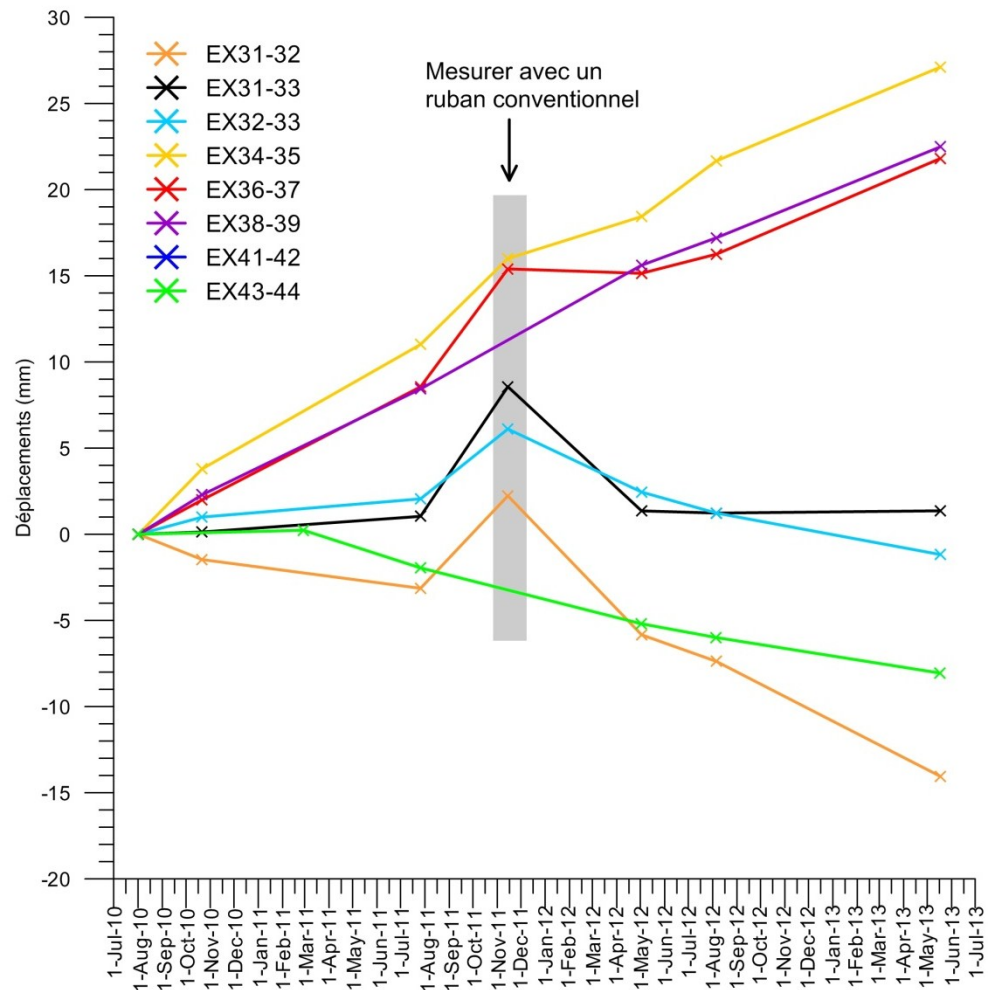
2009-07-27	14:45:00	3.284						CC	
2009-09-04	17:30:00	3.302						CC	
2009-10-24	13:50:00	3.3						CC	
2010-03-13	15:40:00	3.288						CC	
2010-05-20	17:00:00	3.286						CC	
2010-08-01	11:00:00	3.287	3.288					CC	
2011-11-14		3.298							
2012-05-02	15:39:00	3.291						CC et AF	
2012-08-05		3.305						CC et MM	
2013-05-17		3.307						CC et FL	
Tige S1-S2									
1993-11-01	12:00:00	4.882						GREGI	
1993-11-26	12:00:00	4.882						GREGI	
1994-07-01	12:00:00	4.879						GREGI	
1994-09-07	12:00:00	4.883						GREGI	
2009-06-08	12:00:00	4.9						CC	
2009-07-27	14:45:00	4.882						CC	
2009-09-04	17:30:00	4.901						CC	
2009-10-24	13:50:00	4.902						CC	
2010-03-13	15:40:00	4.881						CC	
2010-05-20	17:00:00	4.884						CC	
2011-11-14		4.874							
2012-05-02	13:49:00	4.870						CC et AF	
2012-08-05		4.879						CC et MM	
2013-05-17		4.878						CC et FL	
Tige W1-W2									
1993-11-01	12:00:00	3.847						GREGI	
1993-11-26	12:00:00	3.852						GREGI	
1994-06-04	12:00:00	3.85						GREGI	
1994-07-01	12:00:00	3.864						GREGI	
1994-09-07	12:00:00	3.85						GREGI	
2009-06-08	12:00:00	3.925						CC	
2009-09-04	17:30:00	3.91						CC	
2009-10-24	13:50:00	3.925						CC	
2010-03-13	15:40:00	3.893						CC	
2010-05-20	17:00:00	3.899						CC	
2010-08-01	11:00:00	3.892						CC	
2011-11-14		3.906							
2012-05-02	15:43:00	3.899						CC et AF	
2012-08-05		3.909						CC et MM	
2013-05-17		3.916						CC et FL	



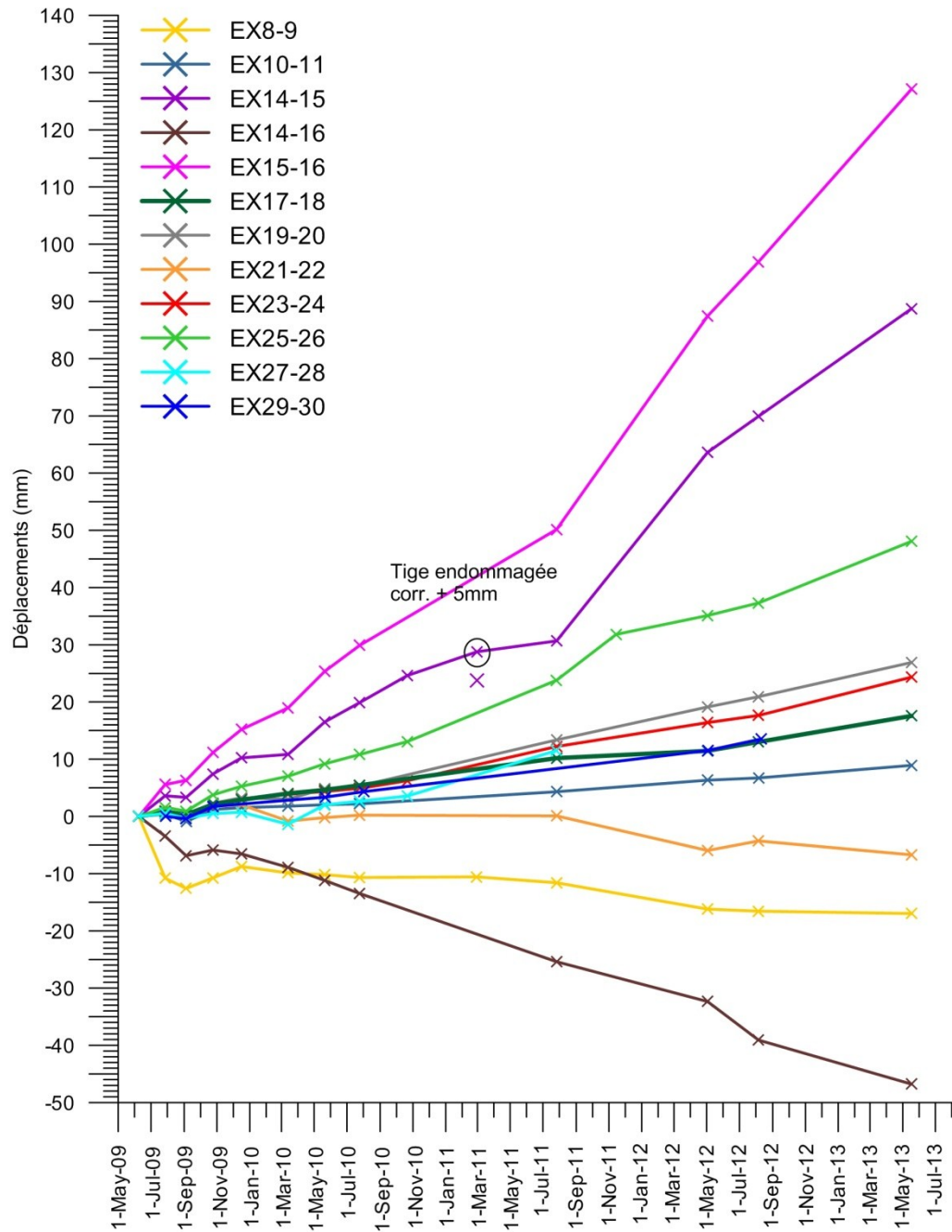
Déplacements obtenus à partir de mesures de distance réalisées à l'aide du ruban extensométrique, pour les tiges dans le secteur du Petit-massif.



Déplacements obtenus à partir de mesures de distance réalisées à l'aide du ruban extensométrique, pour les tiges dans le secteur du Petit-massif.



Déplacements obtenus à partir de mesures de distance réalisées à l'aide du ruban extensométrique, pour les tiges dans le secteur du Centre-Est.



Déplacements obtenus à partir de mesures de distance réalisées à l'aide du ruban extensométrique, pour les tiges dans le secteur en amont du Petit-massif.

Annexe G : Logs des trois forages échantillonnés

Les logs fournis par la compagnie ayant réalisés les forages sont fournis ici (Vincent Fournier et associés, 2009), suivis du synthèse réalisée par l'auteure de la thèse groupant les données RQD et de récupération en plus de la caractérisation géologique refait par l'auteure. Certaines différences notables existent entre les deux interprétations par rapport à la position des contacts des unités géologiques.

Forage F1 : Site 2 pp.264-276

Forage F3 : Site 1 pp.277-289

Forage F3 : Site 3 pp.290-302

FORAGE F-1

ÉLÉVATION DE LA SURFACE: 99,25 MÈTRES

PROFONDEUR EN MÈTRES	ANALYSES ET ESSAIS						
	RÉSULTATS PRÉSENTÉS AILLEURS	LIMITES D'ATTERBERG		ESSAI DE RÉSISTANCE		TENEUR EN EAU (%)	POIDS VOLUMIQUE TOTAL (KN/m³)
		LIMITE DE LIQUIDITÉ (%)	INDICE DE PLASTICITÉ (%)	TYPE D'ESSAI	RÉSISTANCE AU CISAILEMENT		
0							
1							
2							
3							
4							
5							
6							
7							
8							

COUPS/0,3m
ÉCHANTILLON

SYMBOLE	DESCRIPTION	ÉLÉVATION EN MÈTRES
SM	SABLE SILTEUX BRUN AVEC UN PEU DE GRAVIER	99,25
	SOCLE ROCHEUX: CALCILUTITE À NODULES, GRISE, AVEC MINCES LENTILLES DE CALCITE. LE PENDAGE VARIE ENTRE 20 ET 25 DEGRÉS VERS LE SUD, LES LITHOLOGIES SONT D'ÉPAISSEUR INFÉRIEURE À 0,3 MÈTRE. TRÈS MAUVAISE QUALITÉ DURETÉ INFÉRIEURE À 3	97,45
		91,25

($\frac{66}{0}$)

RAPPORT DE FORAGE

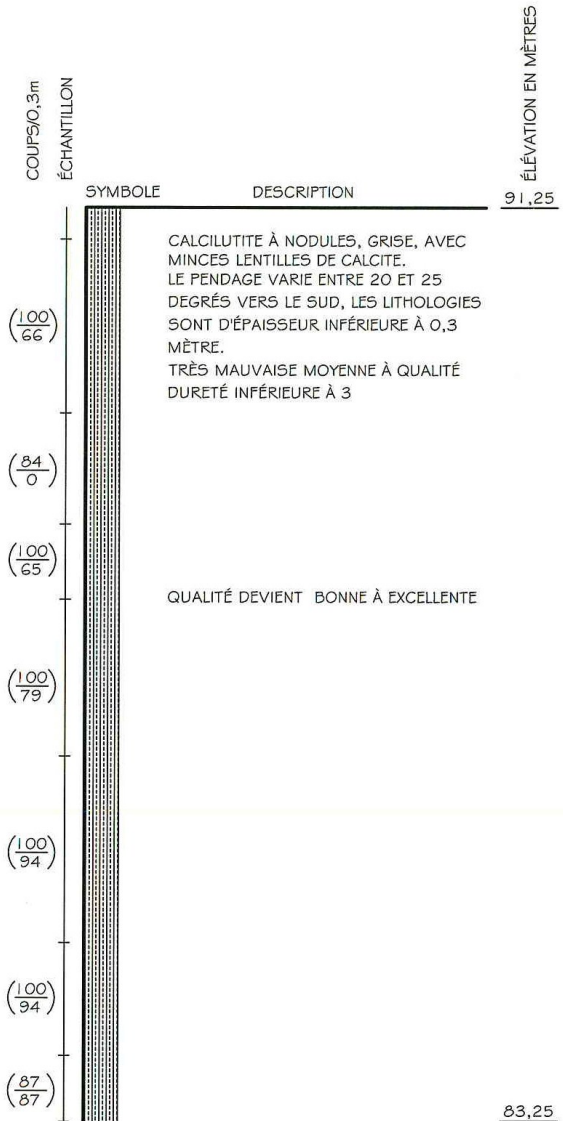
V.Fournier & Associés

FORAGE F-1 (SUITE)

ÉLÉVATION DE LA SURFACE: 99,25 MÈTRES

DOSSIER _____ DATE _____ VERIFIÉ PAR _____ DATE _____ PAR _____

PROFONDEUR EN MÈTRES	ANALYSES ET ESSAIS						
	RÉSULTATS PRÉSENTÉS AILLEURS	LIMITES D'ATTERBERG		ESSAI DE RÉSISTANCE		TENEUR EN EAU (%)	POIDS VOLUMIQUE TOTAL (KN/m ³)
		LIMITE DE LIQUIDITÉ (%)	INDICE DE PLASTICITÉ (%)	TYPE D'ESSAI	RÉSISTANCE AU CISAILLEMENT		
8							
9							
10							
11							
12							
13							
14							
15							
16							



RAPPORT DE FORAGE

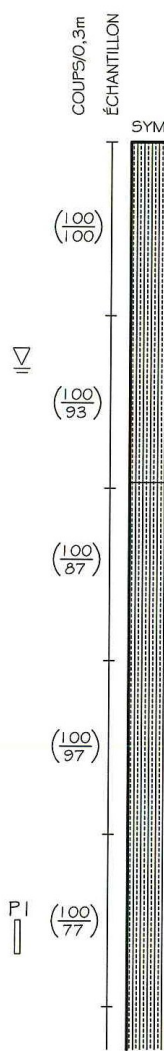
V.Fournier & Associés

DOSSIER _____ DATE _____
 PAR _____ DATE _____
 VÉRIFIÉ PAR _____

FORAGE F-1 (SUITE)

ÉLÉVATION DE LA SURFACE: 99,25 MÈTRES

PROFONDEUR EN MÈTRES	ANALYSES ET ESSAIS						
	RÉSULTATS PRÉSENTÉS AILLEURS	LIMITES D'ATTERBERG		ESSAI DE RÉSISTANCE		TENEUR EN EAU (%)	POIDS VOLUMIQUE TOTAL (KN/m ³)
		LIMITE DE LIQUIDITÉ (%)	INDICE DE PLASTICITÉ (%)	TYPE D'ESSAI	RÉSISTANCE AU CISAILEMENT		
16							
17							
18							
19							
20							
21							
22							
23							
24							



SYMBOLE	DESCRIPTION	ÉLÉVATION EN MÈTRES
(100/100)	CALCULITE À NODULES, GRISE, AVEC MINCES LENTILLES DE CALCITE. LE PENDAGE VARIE ENTRE 20 ET 25 DEGRÉS VERS LE SUD, LES LITHOLOGIES SONT D'ÉPAISSEUR INFÉRIEURE À 0,3 MÈTRE. EXCELLENTE QUALITÉ DURETÉ INFÉRIEURE À 3	83,25
(100/93)		80,25
(100/87)	CONGLOMÉRAT LITHIQUE À MATRICE CALCAIREUSE, GRIS PENDAGE DES STRATES VARIE ENTRE 20 25 DEGRÉS, PRÉSENCE DE CRISTAUX DE QUARTZ ET DE CALCITE QUALITÉ BONNE À EXCELLENTE	75,25

PI : PIÉZOMÈTRE SUPÉRIEUR

RAPPORT DE FORAGE

V.Fournier & Associés

05.009.07F rév. 0.0

DOSSIER _____ PAR _____ DATE _____ VERIFIÉ PAR _____ DATE _____

1504-001 \F-1.DWG

FORAGE F-1 (SUITE)

ÉLÉVATION DE LA SURFACE: 99,25 MÈTRES

PROFONDEUR EN MÈTRES	ANALYSES ET ESSAIS					
	RÉSULTATS PRÉSENTÉS AILLEURS	LIMITES D'ATTERBERG		ESSAI DE RÉSISTANCE		TENEUR EN EAU (%)
		LIMITE DE LIQUIDITÉ (%)	INDICE DE PLASTICITÉ (%)	TYPE D'ESSAI	RÉSISTANCE AU CISAILEMENT	
24						
25						
26						
27						
28						
29						
30						
31						
32						

COUPS/O,3m
ÉCHANTILLON

SYMBOLE	DESCRIPTION	ÉLÉVATION EN MÈTRES
(100/80)	CONGLOMÉRAT LITHIQUE À MATRICE CALCAIREUSE, GRIS PENDAGE DES STRATES VARIE ENTRE 20 25 DEGRÉS, PRÉSENCE DE CRISTAUX DE QUARTZ ET DE CALCITE QUALITÉ BONNE À EXCELLENTE	75,25
(100/84)		
(100/93)		
(100/73)		69,85
(100/92)	CALCULITE À NODULES, GRISE, AVEC MINCES LENTILLES DE CALCITE. LE PENDAGE VARIE ENTRE 20 ET 25 DEGRÉS VERS LE SUD, LES LITHOLOGIES SONT D'ÉPAISSEUR INFÉRIEURE À 0,3 MÈTRE. EXCELLENTE QUALITÉ DURETÉ INFÉRIEURE À 3	67,25

RAPPORT DE FORAGE

V.Fournier & Associés

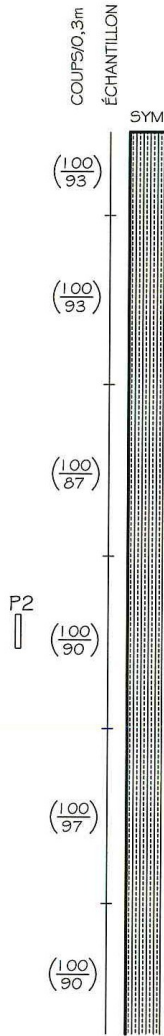
DOSSIER _____ DATE _____ VERIFIÉ PAR _____ DATE _____ PAR _____

FORAGE F-1 (SUITE)

ÉLÉVATION DE LA SURFACE: 99,25 MÈTRES

PROFONDEUR EN MÈTRES	ANALYSES ET ESSAIS						
	RÉSULTATS PRÉSENTÉS AILLEURS	LIMITES D'ATTERBERG		ESSAI DE RÉSISTANCE		TENEUR EN EAU (%)	POIDS VOLUMIQUE TOTAL (KN/m ³)
		LIMITE DE LIQUIDITÉ (%)	INDICE DE PLASTICITÉ (%)	TYPE D'ESSAI	RÉSISTANCE AU CISAILLEMENT		
32							
33							
34							
35							
36							
37							
38							
39							
40							

P2 : PIÉZOMÈTRE MÉDIAN



SYMBOLE	DESCRIPTION	ÉLÉVATION EN MÈTRES
(100/93)	CALCILUTITE À NODULES, GRISE, AVEC MINCES LENTILLES DE CALCITE. LE PENDAGE VARIE ENTRE 20 ET 25 DEGRÉS VERS LE SUD, LES LITHOLOGIES SONT D'ÉPAISSEUR INFÉRIEURE À 0,3 MÈTRE. EXCELLENTE QUALITÉ DURETÉ INFÉRIEURE À 3	67,25
(100/93)		
(100/87)		
(100/90)		
(100/97)		
(100/90)		59,25

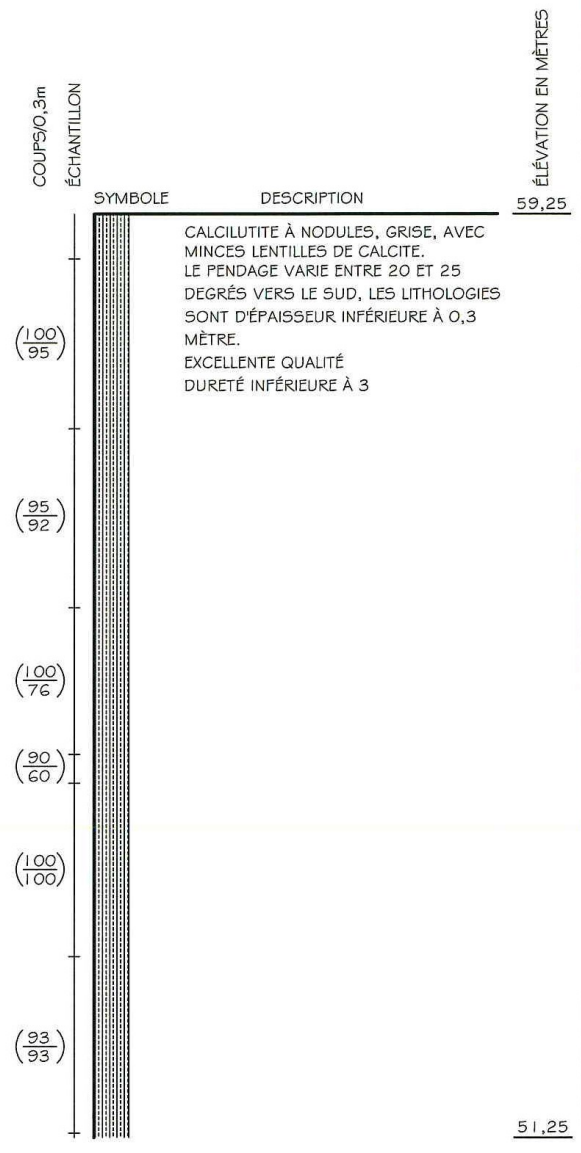
RAPPORT DE FORAGE

V.Fournier & Associés

DOSSIER _____ PAR _____ DATE _____ VÉRIFIÉ PAR _____ DATE _____

FORAGE F-1 (SUITE)
ÉLÉVATION DE LA SURFACE: 99,25 MÈTRES

PROFONDEUR EN MÈTRES	ANALYSES ET ESSAIS						
	RÉSULTATS PRÉSENTÉS AILLEURS	LIMITES D'ATTERBERG		ESSAI DE RÉSISTANCE		TENEUR EN EAU (%)	POIDS VOLUMIQUE TOTAL (kNm ³)
		LIMITE DE LIQUIDITÉ (%)	INDICE DE PLASTICITÉ (%)	TYPE D'ESSAI	RÉSISTANCE AU CISAILLEMENT		
40							
41							
42							
43							
44							
45							
46							
47							
48							



RAPPORT DE FORAGE

V.Fournier & Associés

FORAGE F-1

ÉLÉVATION DE LA SURFACE: 99,25 MÈTRES

PROFONDEUR EN MÈTRES

48

49

50

51

ANALYSES ET ESSAIS						
RÉSULTATS PRÉSENTÉS AILLEURS	LIMITES D'ATTERBERG		ESSAI DE RÉSISTANCE		TENEUR EN EAU (%)	POIDS VOLUMIQUE TOTAL (KN/m ³)
	LIMITE DE LIQUIDITÉ (%)	INDICE DE PLASTICITÉ (%)	TYPE D'ESSAI	RÉSISTANCE AU CISAILLEMENT		


COUPS/0,3m

ÉCHANTILLON

(100/95)

(100/97)

P3

SYMBOLE	DESCRIPTION
	<p>CALCILUTITE À NODULES, GRISE, AVEC MINCES LENTILLES DE CALCITE. LE PÉNDAGE VARIE ENTRE 20 ET 25 DEGRÉS VERS LE SUD, LES LITHOLOGIES SONT D'ÉPAISSEUR INFÉRIEURE À 0,3 MÈTRE. EXCELLENTE QUALITÉ DURETÉ INFÉRIEURE À 3</p>

P3 : PIÉZOMÈTRE INFÉRIEUR

FORAGE TERMINÉ À 51,00 MÈTRES DE PROFONDEUR LE 09/10/28

EAU SOUTERRAINÉ À 18,00 MÈTRES DE PROFONDEUR LE 09/10/29

PIÉZOMÈTRES À CORDE VIBRANTE INSTALLÉS À 23,2, 36,6 ET 50,9 MÈTRES DE PROFONDEUR LE 09/10/29

ÉLÉVATION EN MÈTRES

51,25

48,25

RAPPORT DE FORAGE

V.Fournier & Associés

DESCRIPTION STRUCTURALE DU ROC

02.002.07F r.év. 0.0

CLIENT		UNIVERSITÉ LAVAL										PROJET No		1504-001			
PROJET		FORAGES ET INSTALLATION D'INSTRUMENT, DONT DES PIÉZOMÈTRES ET UN INCLINOMÈTRE DANS LE MASSIF ROCHEUX										FORAGE No		F-1			
ENDROIT		GASCONS, GASPÉSIE										PAGE		1 DE 2			
COURSE					DESCRIPTION ET OBSERVATIONS												
PROFONDEUR (m)		ROD (%)	RECUPÉRATION (%)	PERTE D'EAU (%)	PROFONDEUR (m)		ÉLÉMENT D'ORIT	NOMBRE DE NODURES, JOINTS	ANGLE P/R À L'HORIZONTAL	FERMÉ	OUVERT	COURBE	IRRÉGULIER	MIROIR DE FAILLE	RECOUVERT DE (X)	ALTERATION	COULEUR (XX)
DE	À				DE	À											
7,16	8,28	0	66														
8,28	9,80	66	100														
9,80	10,77	0	84														
10,77	11,43	65	100		11,20	11,43	FRACTURE	1	90°		X	X	X		R	X	b
11,43	12,80	79	100														
12,80	14,43	94	100														
14,43	15,42	94	100														
15,42	16,00	87	87		15,60	15,67	FRACTURE	1	45°		X	X	X		R	X	b
16,00	17,53	100	100														
17,53	19,05	93	100		17,91	18,00	FRACTURE	1	45°	X		X	X				
					18,21	18,31	FRACTURE	1	80°		X	X	X				g
					18,67	18,80	FRACTURE	1	60°		X	X	X		R	X	b
19,05	20,57	87	100		20,07	20,14	FRACTURE	1	60°		X				R	X	b
20,57	22,10	97	100														
22,10	23,62	77	100		22,73	22,86	FRACTURE	1	90°		X	X	X		R	X	b
23,62	25,12	80	100		24,05	24,26	FRACTURE	1	90°		X	X	X				j
					24,69	24,79	FRACTURE	1	60°		X	X	X		C	x	g
25,12	26,67	84	100														
26,67	28,17	93	100		26,82	26,97	FRACTURE	1	60°		X	X	X		C,R	X	b
28,17	29,69	73	100		28,42	28,52	FRACTURE	1	60°		X	X	X		C,R	X	g,b
29,69	31,19	92	100														
31,19	32,74	93	100		31,34	31,44	FRACTURE	1	45°		X	X	X		C		g
32,74	34,24	93	100														
34,24	35,76	87	100		34,24	34,39	FRACTURE	1	60°		X				C,R	X	b
35,76	37,44	90	100														
37,44	38,84	97	100														
38,84	40,39	90	100														
40,39	41,86	95	100		40,48	40,54	FRACTURE	1	45°		X				R	X	g,b
41,86	43,41	92	95		43,10	43,18	FRACTURE	1	60°		X				R	X	g,b
REMARQUES :																	
(X) : C = CALCITE R = ROUILLE (XX) : b = BLANC G = GRAPHITE P = PYRITE r = ROSE I = OXYDE DE FER S = SALBANDE g = GRIS K = CHLORITE A = SILT / ARGILE v = VERT E = EPIDOTE J = JAUNE B = BIOTITE b = BRUN																	
DESCRIPTION QUALITATIVE DU ROC (RGD) $RGD \% = \frac{TOTAL > 100mm}{LONGUEUR DE LA COURSE} \times 100$																	
DESCRIPTION PAR :				DATE :				VÉRIFIÉ PAR :				DATE :					
PHILIPPE BERGERON				09/12/04				VINCENT FOURNIER				09/12/17					

1504-001 \ FICHER.DWG

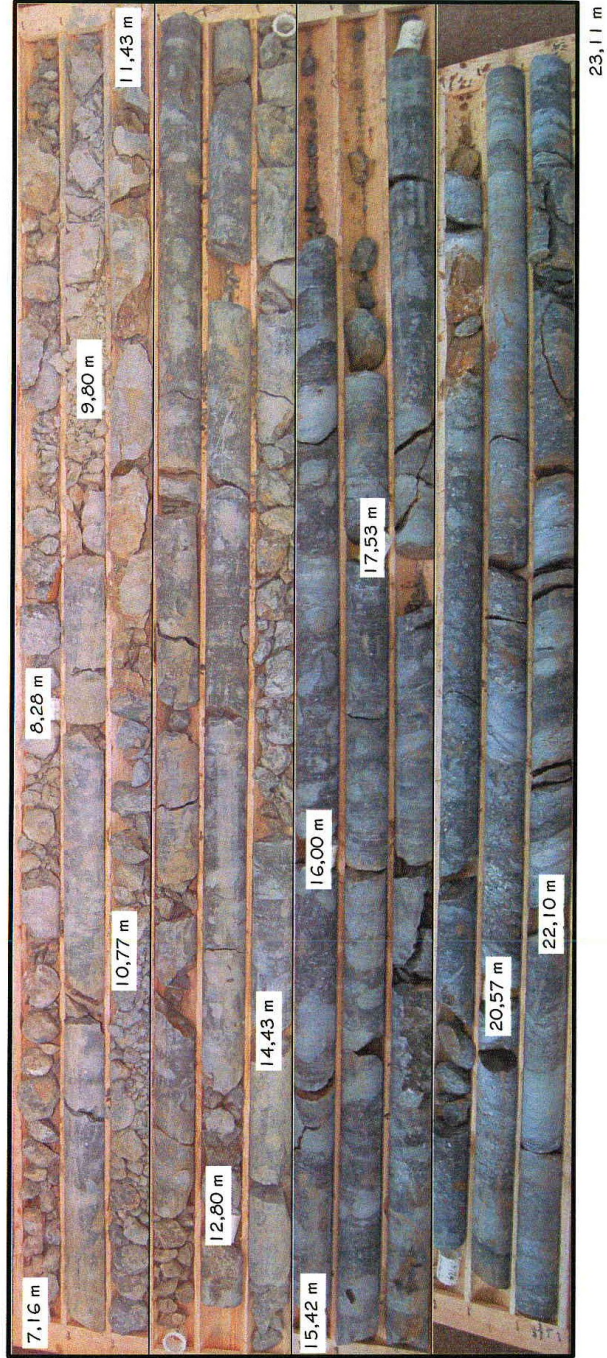
DESCRIPTION STRUCTURALE DU ROC

02.002.07F r & v. 0.0

CLIENT UNIVERSITÉ LAVAL										PROJET No 1504-001							
PROJET FORAGES ET INSTALLATION D'INSTRUMENT, DONT DES PIÉZOMÈTRES ET UN INCLINOMÈTRE DANS LE MASSIF ROCHEUX										FORAGE No F-1							
ENDROIT GASCONS, GASPÉSIE										PAGE 2 DE 2							
COURSE					DESCRIPTION ET OBSERVATIONS												
PROFONDEUR (m)		RQD (%)	RÉGULARITÉ (%)	PERTE D'EAU (%)	PROFONDEUR (m)		ÉLÉMENT DÉCRIT	NOMBRE DE (FRACTURES, JOINTS)	ANGLE P/R À L'HORIZONTAL	FERMÉ	OUVERT	COURBE	IRRÉGULIER	MIROIR DE FAILLE	RECOUVERT DE (%)	ALTÉRATION	COULEUR (XX)
DE	À				DE	À											
43,41	44,68	76	100		43,94	44,35	FRACTURE	I	70°		X		X		R,C	X	g,b
44,68	44,93	60	90														
44,93	46,43	100	100														
46,43	47,96	93	93														
47,96	49,48	95	100		48,87	49,07	FRACTURE	I	70°	X							g,b
49,48	51,00	97	100														
REMARQUES :																	
(X) : C = CALCITE R = ROUILLE (XX) : bl = BLANC DESCRIPTION QUALITATIVE DU ROC (RQD) G = GRAPHITE P = PYRITE r = ROSE I = OXYDE DE FER S = SALBANDE g = GRIS RQD % = $\frac{\text{TOTAL} > 100\text{mm}}{\text{LONGEUR DE LA COURSE}} \times 100$ K = CHLORITE A = SILT / ARGILE v = VERT E = EPIDOTE j = JAUNE B = BIOTITE b = BRUN																	
DESCRIPTION PAR : PHILIPPE BERGERON					DATE : 09/12/04			VÉRIFIÉ PAR : VINCENT FOURNIER					DATE : 09/12/17				

1504-001 \ FICHER.DWG

05.200.07F r.év. 0.0
1504-001 \RDC F-1.DWG



V.Fournier & Associés

FORAGE F-1



FORAGE F-1

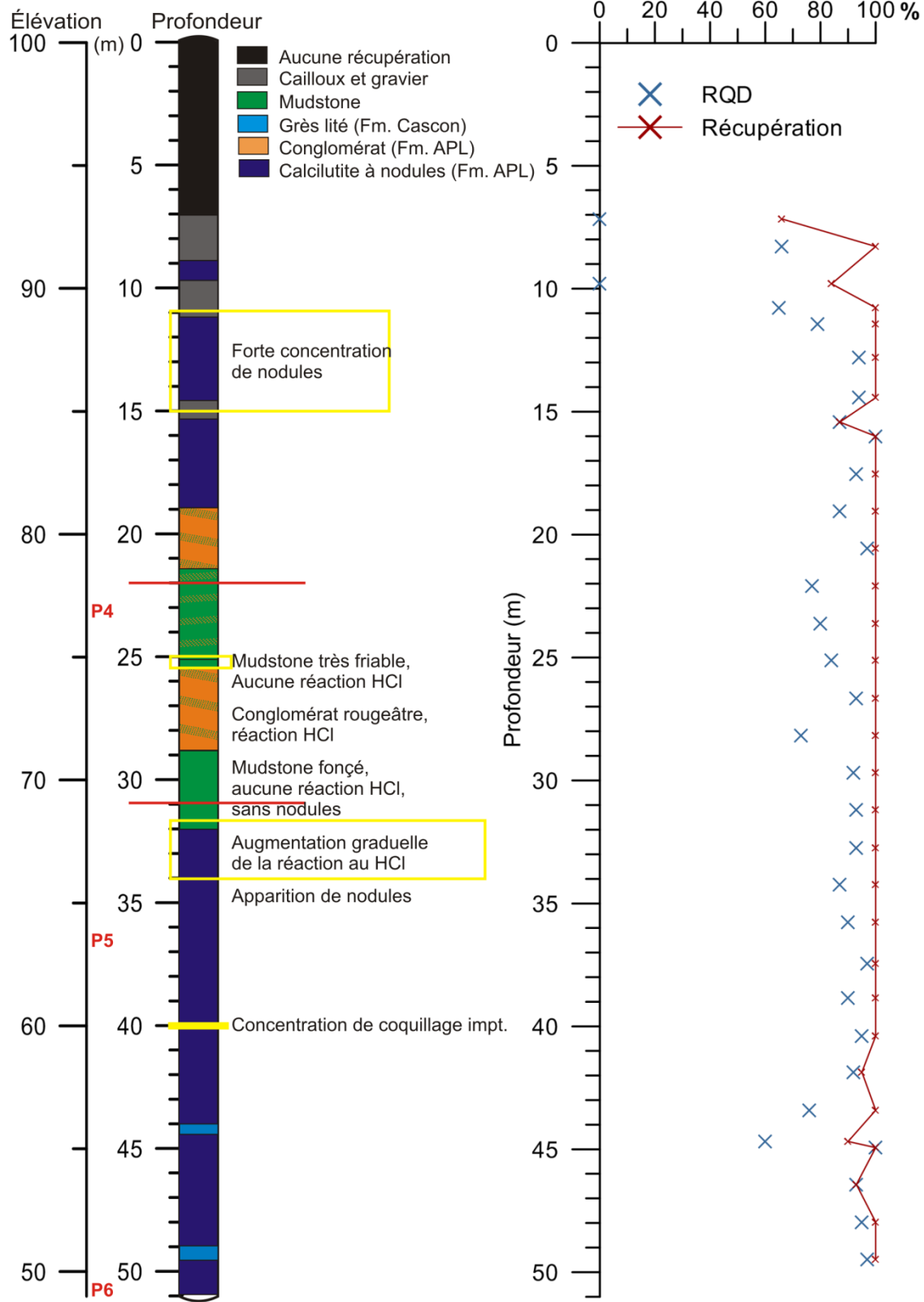
05.200.07F rév. 0.0
1504-001 \RDC F-1.DWG

39,45 m



FORAGE F-1

V.Fournier & Associés



Forage F1 réalisé au site 2. Synthèse du log de forage réalisé par Catherine Cloutier.

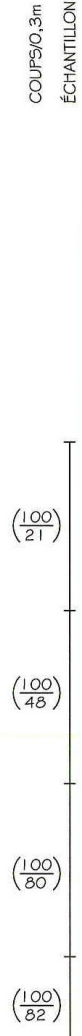
DOSSIER _____ PAR _____ DATE _____ VÉRIFIÉ PAR _____ DATE _____

FORAGE F-3

ÉLÉVATION DE LA SURFACE: 63,39 MÈTRES

PROFONDEUR EN MÈTRES	ANALYSES ET ESSAIS						
	RÉSULTATS PRÉSIDENTS AILLEURS	LIMITES D'ATTERBERG		ESSAI DE RÉSISTANCE		TENEUR EN EAU (%)	POIDS VOLUMIQUE TOTAL (KN/m ³)
		LIMITE DE LIQUIDITÉ (%)	INDICE DE PLASTICITÉ (%)	TYPE D'ESSAI	RÉSISTANCE AU CISAILEMENT		
0							
1							
2							
3							
4							
5							
6							
7							
8							

SAA



COUPS/0,3m
ÉCHANTILLON

SYMBOLE	DESCRIPTION	ÉLÉVATION EN MÈTRES
SM	SABLE SILTEUX BRUN AVEC UN PEU DE GRAVIER	63,39
	SOCLE ROCHEUX: CALCILUTE À NODULES, GRISE, AVEC MINCES LENTILLES DE CALCITE. LE PENDAGE VARIE ENTRE 20 ET 25 DEGRÉS VERS LE SUD, LES LITHOLOGIES SONT D'ÉPAISSEUR INFÉRIEURE À 0,3 MÈTRE. TRÈS MAUVAISE QUALITÉ DURETÉ INFÉRIEURE À 3	62,49
	QUALITÉ DEVIENT BONNE	55,39

RAPPORT DE FORAGE

V.Fournier & Associés

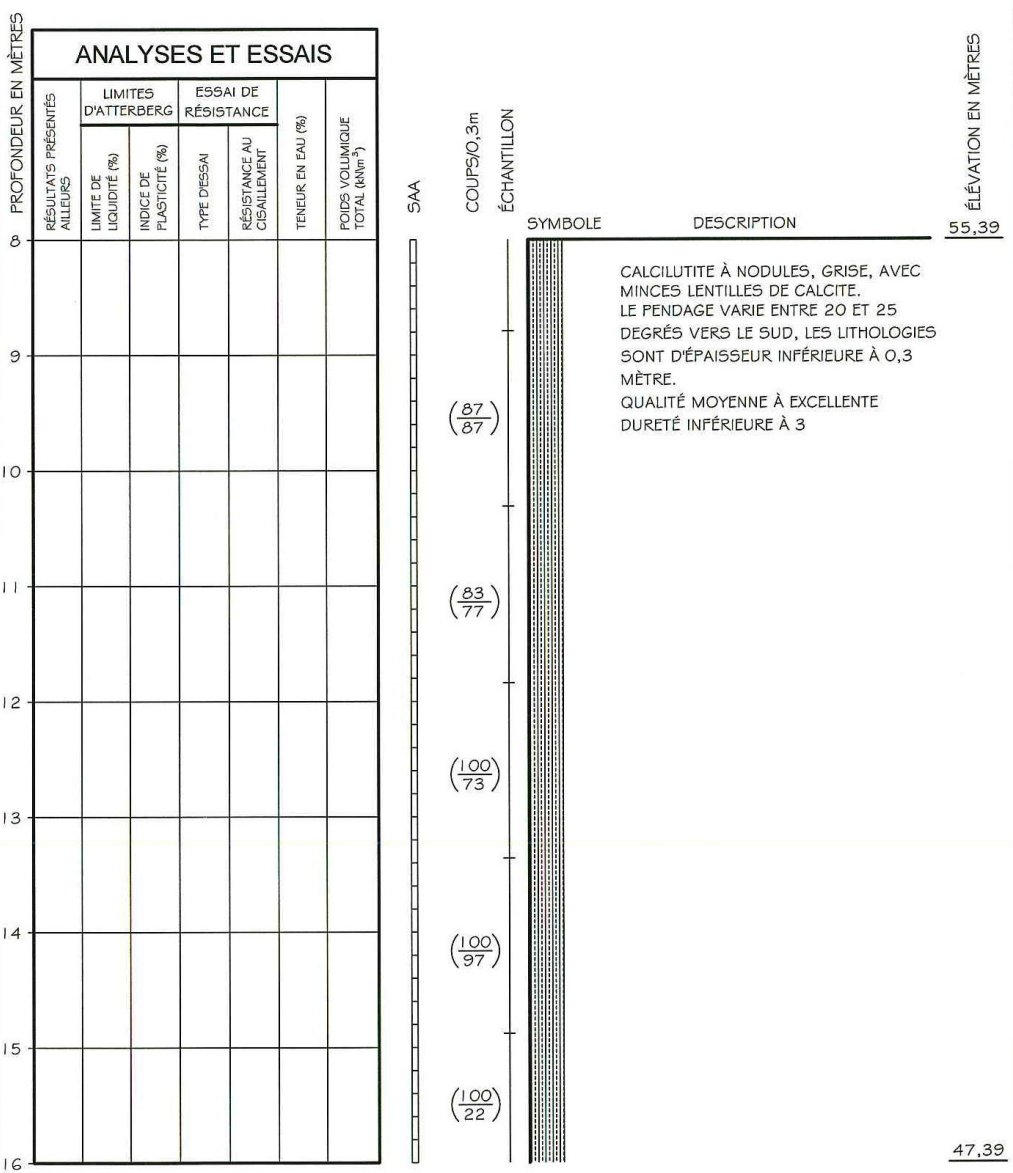
DOSSIER _____ PAR _____ DATE _____ VÉRIFIÉ PAR _____ DATE _____

05.009.07F rév. 00

1504-001 \F-1.DWG

FORAGE F-3 (SUITE)

ÉLÉVATION DE LA SURFACE: 63,39 MÈTRES



(87/87)
(83/77)
(100/73)
(100/97)
(100/22)

CALCULITE À NODULES, GRISE, AVEC MINCES LENTILLES DE CALCITE. LE PENDAGE VARIE ENTRE 20 ET 25 DEGRÉS VERS LE SUD, LES LITHOLOGIES SONT D'ÉPAISSEUR INFÉRIEURE À 0,3 MÈTRE. QUALITÉ MOYENNE À EXCELLENTE DURETÉ INFÉRIEURE À 3

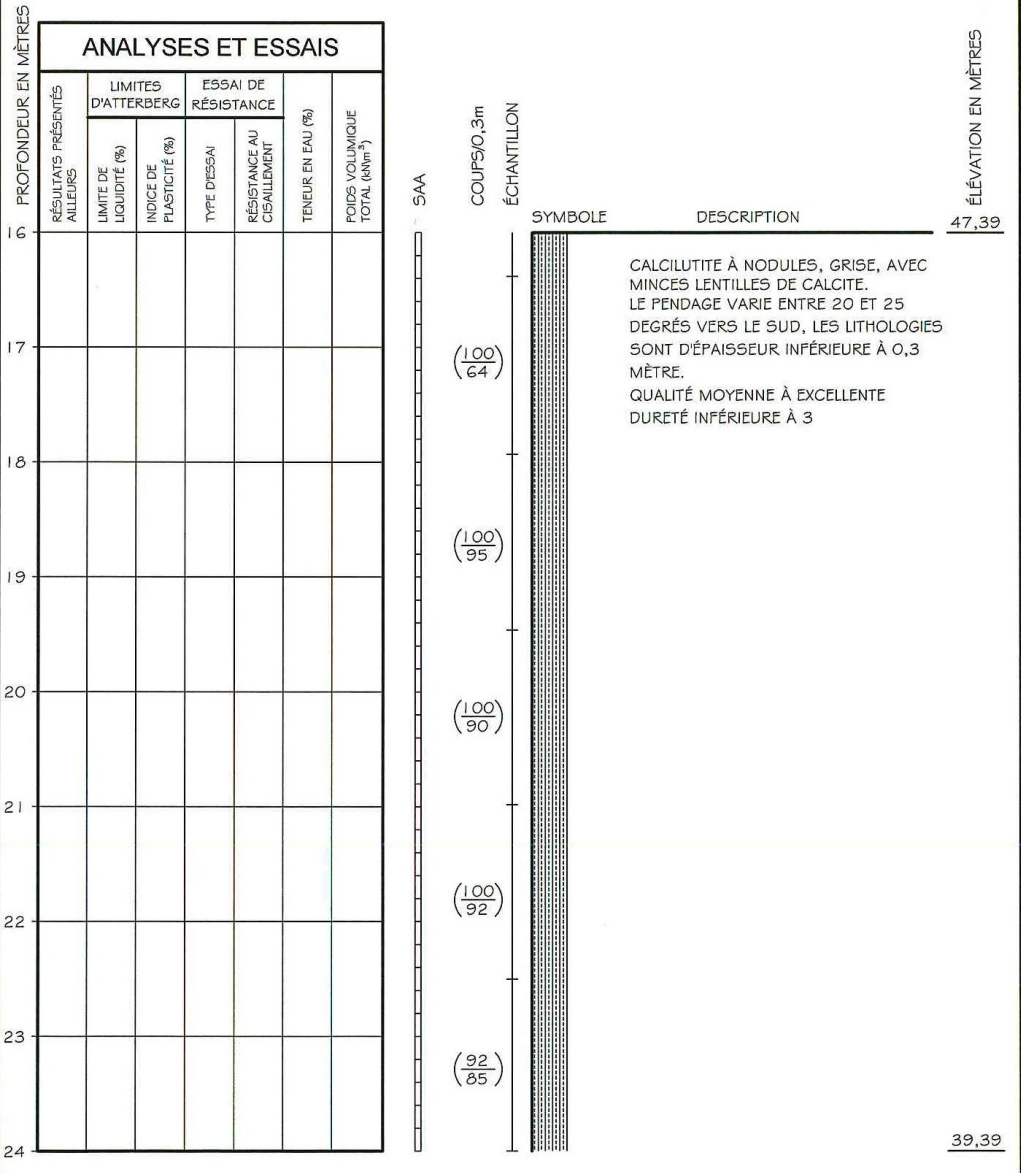
RAPPORT DE FORAGE

V.Fournier & Associés

DOSSIER _____ PAR _____ DATE _____ VÉRIFIÉ PAR _____ DATE _____

FORAGE F-3 (SUITE)

ÉLÉVATION DE LA SURFACE: 63,39 MÈTRES



RAPPORT DE FORAGE

V.Fournier & Associés

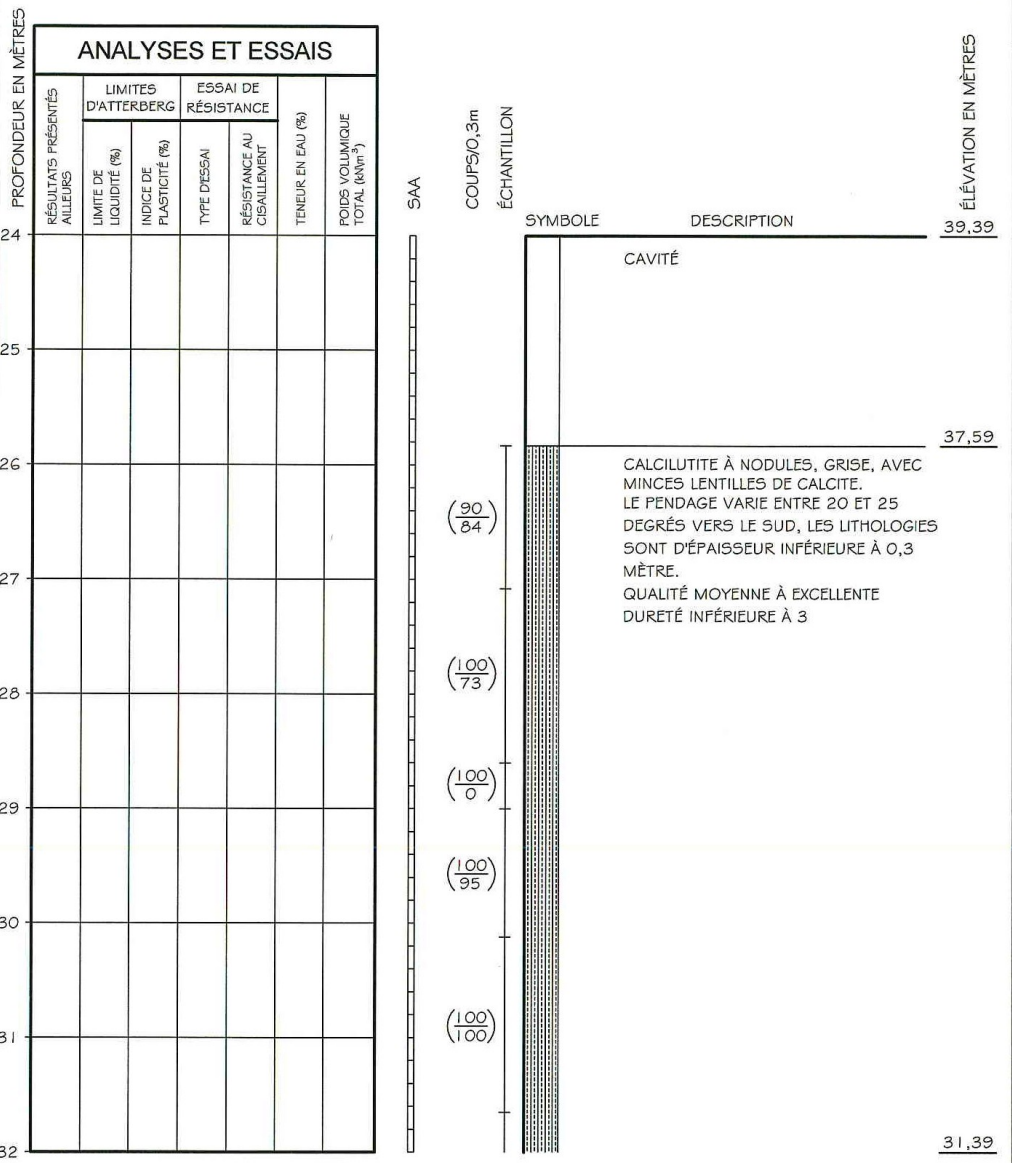
05.009.07F r-év. 0.0

DOSSIER _____ PAR _____ DATE _____ VÉRIFIÉ PAR _____ DATE _____

1504-001 \ F-1.DWG

FORAGE F-3 (SUITE)

ÉLÉVATION DE LA SURFACE: 63,39 MÈTRES



SAA

(90 / 84)

(100 / 73)

(100 / 0)

(100 / 95)

(100 / 100)

CAVITÉ

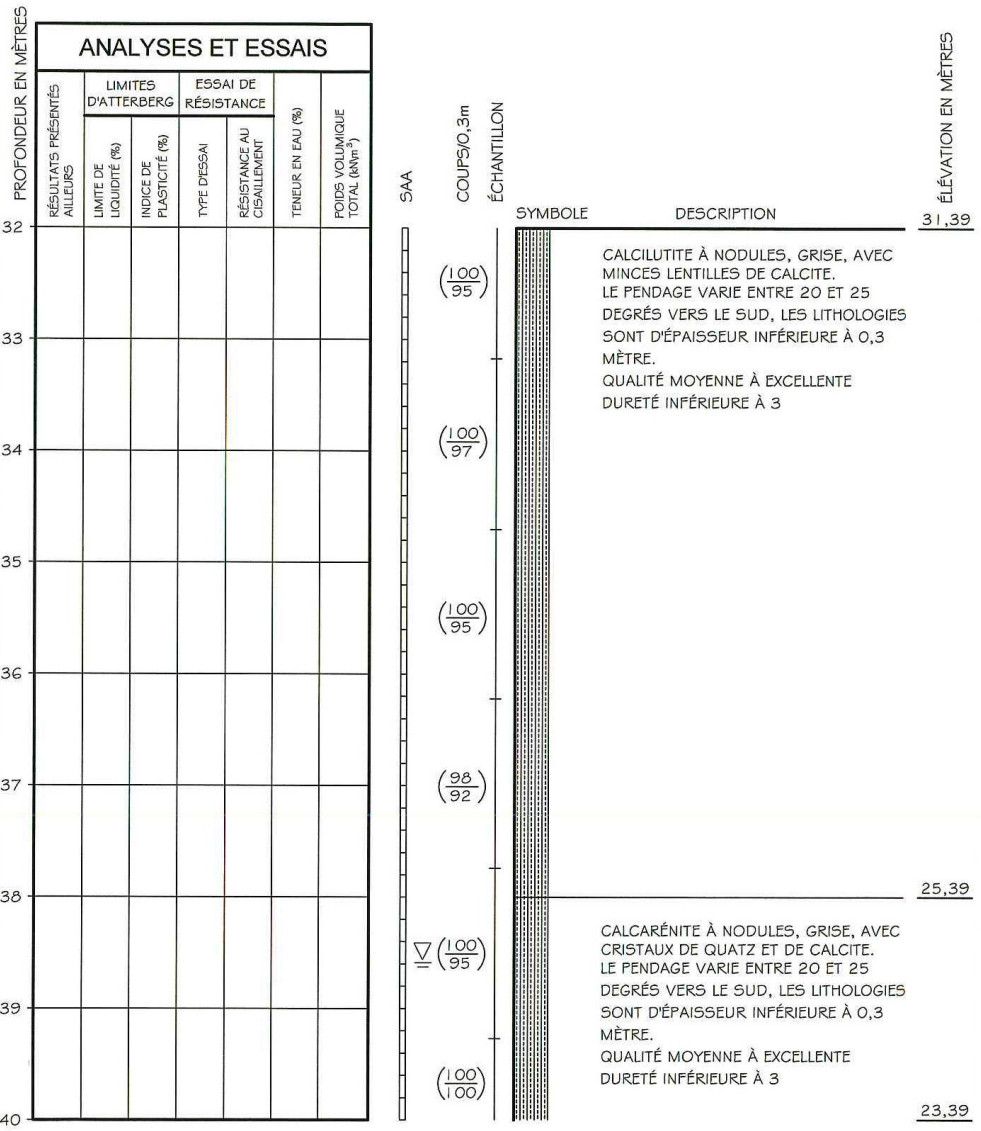
CALCILUTE À NODULES, GRISE, AVEC MINCES LENTILLES DE CALCITE. LE PENDAGE VARIE ENTRE 20 ET 25 DEGRÉS VERS LE SUD, LES LITHOLOGIES SONT D'ÉPAISSEUR INFÉRIEURE À 0,3 MÈTRE. QUALITÉ MOYENNE À EXCELLENTE DURETÉ INFÉRIEURE À 3

RAPPORT DE FORAGE

V.Fournier & Associés

FORAGE F-3 (SUITE)

ÉLÉVATION DE LA SURFACE: 63,39 MÈTRES



RAPPORT DE FORAGE

V.Fournier & Associés

DISSIER _____ PAR _____ DATE _____ VÉRIFIÉ PAR _____ DATE _____

FORAGE F-3 (SUITE)

ÉLÉVATION DE LA SURFACE: 63,39 MÈTRES

PROFONDEUR EN MÈTRES	ANALYSES ET ESSAIS							ÉLÉVATION EN MÈTRES
	RÉSULTATS PRÉSENTÉS AILLEURS	LIMITES D'ATTERBERG		ESSAI DE RÉSISTANCE		TENEUR EN EAU (%)	POIDS VOLUMIQUE TOTAL (KN/m ³)	
		LIMITE DE LIQUIDITÉ (%)	INDICE DE PLASTICITÉ (%)	TYPE D'ESSAI	RÉSISTANCE AU CISAILEMENT			
40								23,39
41								
42								
43								
44								
45								18,69
46								
47								
48								15,39

COUPS/0,3m	ÉCHANTILLON	SYMBOLE	DESCRIPTION
(100/75)			CALCARÉNITE À NODULES, GRISE, AVEC CRISTAUX DE QUARTZ ET DE CALCITE. LE PENDAGE VARIE ENTRE 20 ET 25 DEGRÉS VERS LE SUD, LES LITHOLOGIES SONT D'ÉPAISSEUR INFÉRIEURE À 0,3 MÈTRE. QUALITÉ BONNE À EXCELLENTE DURETÉ INFÉRIEURE À 3
(100/95)			
(100/87)			CALCULITE À NODULES, GRISE, AVEC MINCES LENTILLES DE CALCITE. LE PENDAGE VARIE ENTRE 20 ET 25 DEGRÉS VERS LE SUD, LES LITHOLOGIES SONT D'ÉPAISSEUR INFÉRIEURE À 0,3 MÈTRE. QUALITÉ BONNE À EXCELLENTE DURETÉ INFÉRIEURE À 3
(100/90)			
(100/92)			ZONE TRÈS FRACTURÉE ENTRE 44,7 ET 49,6 MÈTRES DE PROFONDEUR

RAPPORT DE FORAGE

V.Fournier & Associés

DOSSIER _____ PAR _____ DATE _____ VERIFIÉ PAR _____ DATE _____

FORAGE F-3

ÉLÉVATION DE LA SURFACE: 63,39 MÈTRES

PROFONDEUR EN MÈTRES

ANALYSES ET ESSAIS

PROFONDEUR EN MÈTRES	RÉSULTATS PRÉSENTÉS AILLEURS	LIMITES D'ATTERBERG		ESSAI DE RÉSISTANCE		TENEUR EN EAU (%)	POIDS VOLUMIQUE TOTAL (kNm ³)
		LIMITÉ DE LIQUIDITÉ (%)	INDICE DE PLASTICITÉ (%)	TYPE D'ESSAI	RÉSISTANCE AU CISAILEMENT		
48							
49							
50							
51							
52							
53							

SAA

COUPS/0,3m
ÉCHANTILLON

(100/62)

(100/100)

(100/100)

SYMBOLE DESCRIPTION ÉLÉVATION EN MÈTRES

15,39

ZONE TRÈS FRACTURÉE ENTRE 44,7 ET 49,6 MÈTRES DE PROFONDEUR

CALCILUTITE À NODULES, GRISE, AVEC MINCES LENTILLES DE CALCITE, LE PENDAGE VARIE ENTRE 20 ET 25 DEGRÉS VERS LE SUD, LES LITHOLOGIES SONT D'ÉPAISSEUR INFÉRIEURE À 0,3 MÈTRE. QUALITÉ MOYENNE À EXCELLENTE DURETÉ INFÉRIEURE À 3

10,39

FORAGE TERMINÉ À 52,98 MÈTRES DE PROFONDEUR LE 09/11/06

EAU SOUTERRAINE À 38,59 MÈTRES DE PROFONDEUR LE 09/11/06

RAPPORT DE FORAGE

V.Fournier & Associés

DESCRIPTION STRUCTURALE DU ROC

02.002.07F rév. 0.0

CLIENT		UNIVERSITÉ LAVAL										PROJET No		1504-001			
PROJET		FORAGES ET INSTALLATION D'INSTRUMENT, DONT DES PIÉZOMÈTRES ET UN INCLINOMÈTRE DANS LE MASSIF ROCHEUX										FORAGE No		F-3			
ENDROIT		GASCONS, GASPÉSIE										PAGE		1 DE 2			
COURSE					DESCRIPTION ET OBSERVATIONS												
PROFONDEUR (m)		ROD (%)	RÉCUPÉRATION (%)	PERTE D'EAU (%)	PROFONDEUR (m)		ÉLÉMENT DÉCRIT	NOMBRE DE RESSAINDISSEMENTS (JOINTS)	ANGLE P/R À L'HORIZONTAL	FERMÉ	OUVERT	COURBE	IRRÉGULIER	MIROIR DE FAILLE	RECOURVERT DE (X)	ALTÉRATION	COULEUR (XX)
DE	À				DE	À											
2,74	4,22	21	100		2,90	3,00	FRACTURE	1	90°		X	X	X		R	X	b
4,22	5,74	48	100		4,72	4,80	FRACTURE	1	75°		X	X	X		R	X	b
5,74	7,26	80	100		6,35	6,45	FRACTURE	1	90°		X	X	X		R	X	b
7,26	8,79	82	100														
8,79	10,31	87	87		10,06	10,21	FRACTURE	1	70°-80°		X	X	X		R	X	b
10,31	11,84	77	83														
11,84	13,36	73	100		12,09	12,17	FRACTURE	1	60°		X	X	X			X	b
13,36	14,88	97	100														
14,88	16,38	22	100		15,49	15,98	FRACTURE	1	70°-80°		X	X	X		R,C	X	b
16,38	17,93	64	100														
17,93	19,46	95	100														
19,46	20,98	90	100														
20,98	22,50	92	100		22,07	22,12	FRACTURE	1	70°		X	X	X		R	X	b
22,50	24,03	85	92		23,32	23,39	FRACTURE	1	70°		X				R	X	b,g
24,03	27,08	84	90		24,28	24,41	FRACTURE	1	75°		X	X	X				g
27,08	28,60	73	100		27,13	27,20	FRACTURE	1	70°		X		X		A	X	J
					27,66	27,76	FRACTURE	1	80°-90°		X	X	X		R	X	b
28,60	29,01	0	100														
29,01	30,12	95	100														
30,12	31,65	100	100														
31,65	33,17	95	100														
33,17	34,70	97	100														
34,70	36,22	95	100														
36,22	37,74	92	98														
37,74	39,27	95	100		37,74	37,57	FRACTURE	1	75°		X	X	X				g
39,27	40,79	100	100														
40,79	42,32	75	100		41,71	41,81	FRACTURE	1	75°		X	X	X		R,C	X	b
42,32	43,84	95	100		43,03	43,08	FRACTURE	1	60°		X	X	X		R,A	X	b
					43,54	43,64	FRACTURE	1	75°		X	X	X		R	X	b,g
REMARQUES :																	
(X) : C = CALCITE R = ROUILLE (XX) : bl = BLANC G = GRAPHITE P = PYRITE r = ROSE I = OXYDE DE FER S = SALBANDE g = GRIS K = CHLORITE A = SILT / ARGILE v = VERT E = EPIDOTE j = JAUNE B = BIOTITE b = BRUN																	
DESCRIPTION QUALITATIVE DU ROC (ROD) $ROD \% = \frac{TOTAL > 100mm}{LONGUEUR DE LA COURSE} \times 100$																	
DESCRIPTION PAR :					DATE :			VÉRIFIÉ PAR :					DATE :				
PHILIPPE BERGERON					09/12/04			VINCENT FOURNIER					09/12/17				

1504-001 \ FICHER.DWG



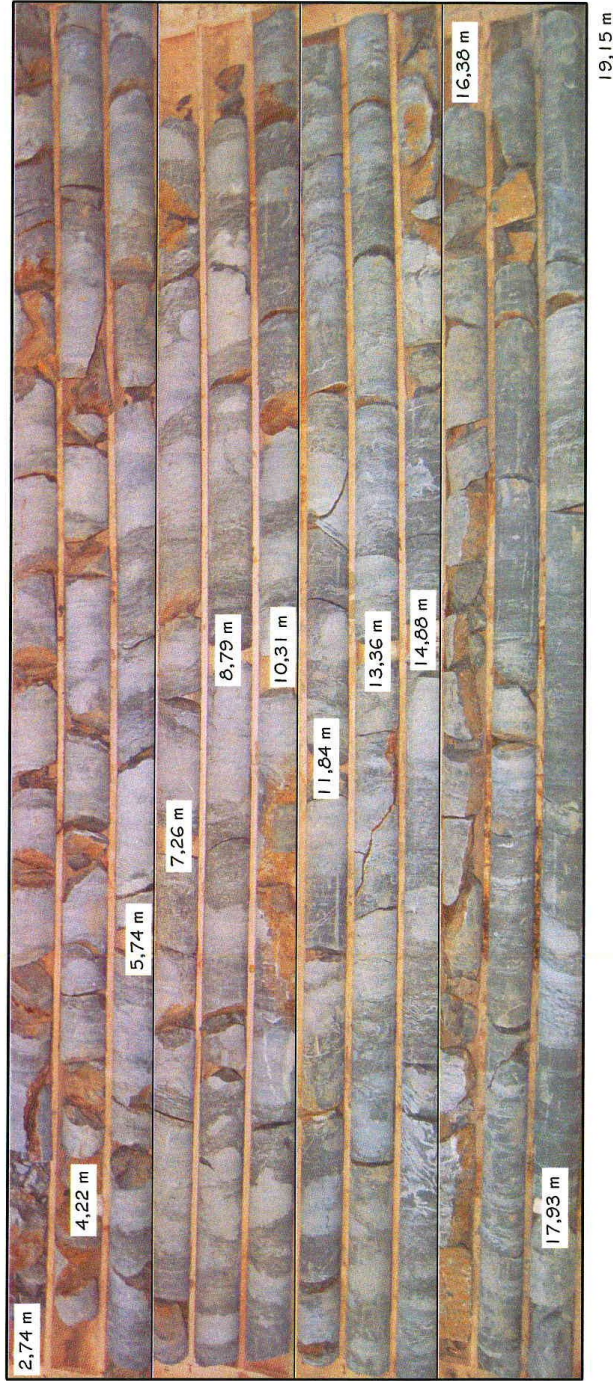
DESCRIPTION STRUCTURALE DU ROC

02.002.07F r.év. 0.0

CLIENT UNIVERSITÉ LAVAL						PROJET No 1504-001					
PROJET FORAGES ET INSTALLATION D'INSTRUMENT, DONT DES PIÉZOMÈTRES ET UN INCLINOMÈTRE DANS LE MASSIF ROCHEUX						FORAGE No F-3					
ENDROIT GASCONS, GASPÉSIE						PAGE 2 DE 2					

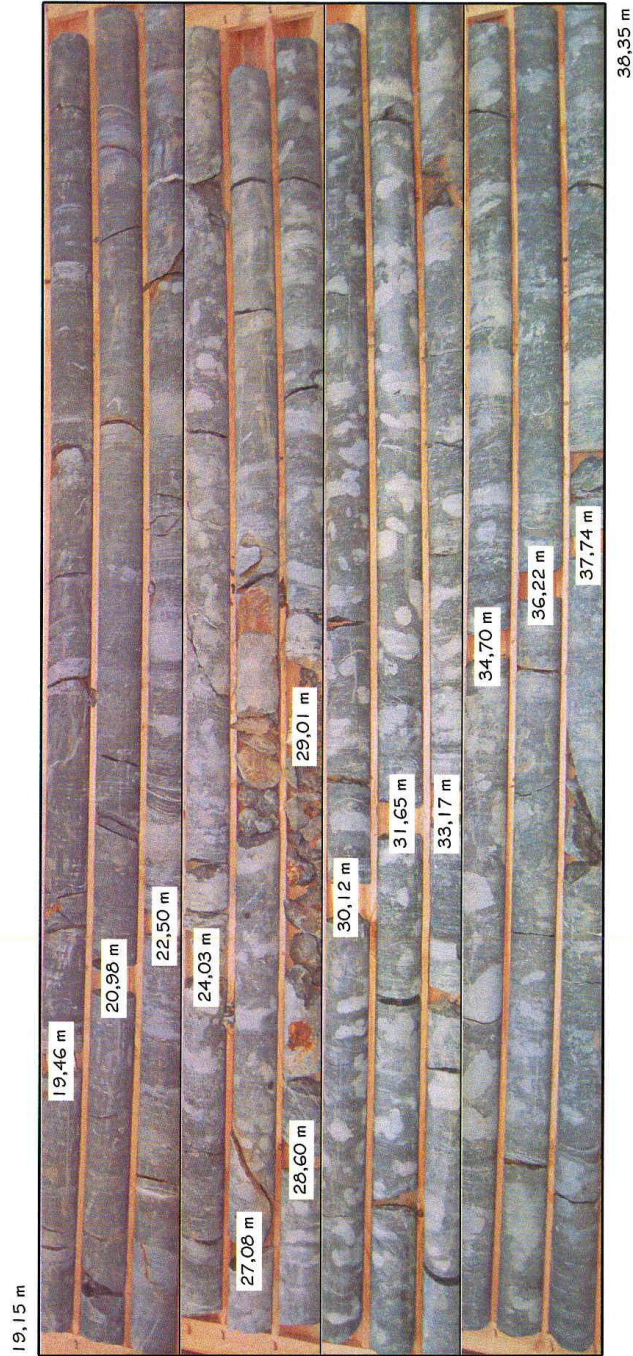
COURSE					DESCRIPTION ET OBSERVATIONS														
PROFONDEUR (m)		RGD (%)	RÉCUPÉRATION (%)	PERTE D'EAU (%)	PROFONDEUR (m)		ÉLÉMENT DÉCRIT	NOMBRE DE BRANCHES, LONGS	ANGLE FR L'HORIZONTALE	FERRÉ	OUVERT	COURBE	IRÉGULIER	MIROIR DE FAILLE	RECOURVERT DE (X)	ALTÉRATION	COULEUR (XX)		
DE	À				DE	À													
43,84	45,36	87	100																
45,36	46,89	90	100																
46,89	48,41	92	100																
48,41	49,94	62	100																
49,94	51,46	100	100		50,39	50,50	FRACTURE	1	75°±0°		X	X	X					g	
51,46	52,98	100	100																
REMARQUES :																			
<div style="display: flex; justify-content: space-between;"> <div> <p>(X) : C = CALCITE G = GRAPHITE I = OXYDE DE FER K = CHLORITE E = EPIDOTE B = BIOTITE</p> <p>R = ROUILLE P = PYRITE S = SALBANDE A = SILT / ARGILE</p> </div> <div> <p>(XX) : bl = BLANC r = ROUGE g = GRIS v = VERT j = JAUNE b = BRUN</p> <p>DESCRIPTION QUALITATIVE DU ROC (RGD) $RGD \% = \frac{TOTAL > 100mm}{LONGUEUR DE LA COURSE} \times 100$</p> </div> </div>																			
DESCRIPTION PAR : PHILIPPE BERGERON					DATE : 09/12/04				VÉRIFIÉ PAR : VINCENT FOURNIER					DATE : 09/12/17					

1504-001 \FICHER.DWG



FORAGE F-3

05.200.07F r.év. 0.0
1504-001 \RDC F-1.DWG

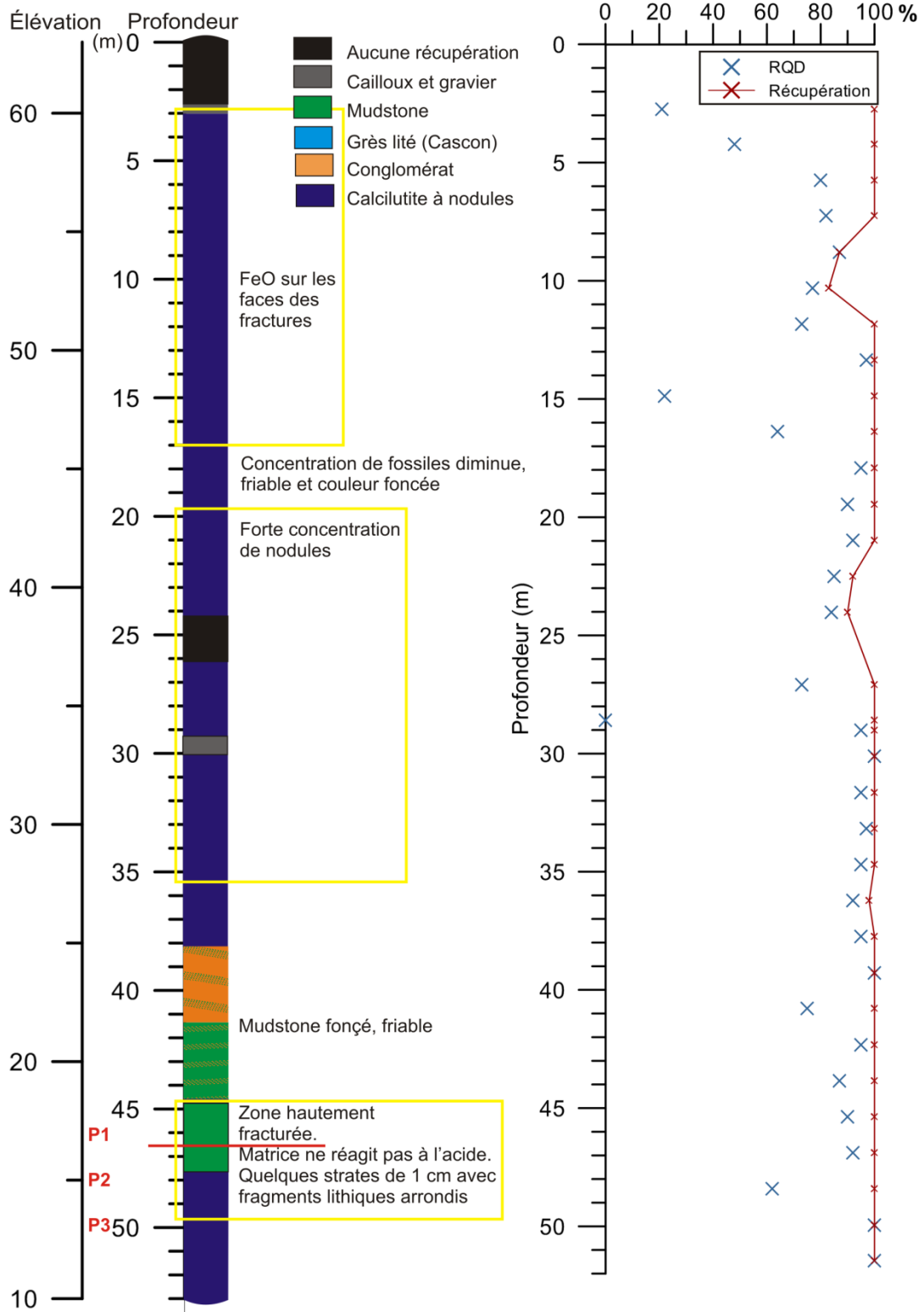


V.Fournier & Associés

FORAGE F-3



FORAGE F-3



Forage F3 réalisé au site 1. Synthèse du log de forage réalisé par Catherine Cloutier.

DOSSIER _____ PAR _____ DATE _____ VÉRIFIÉ PAR _____ DATE _____

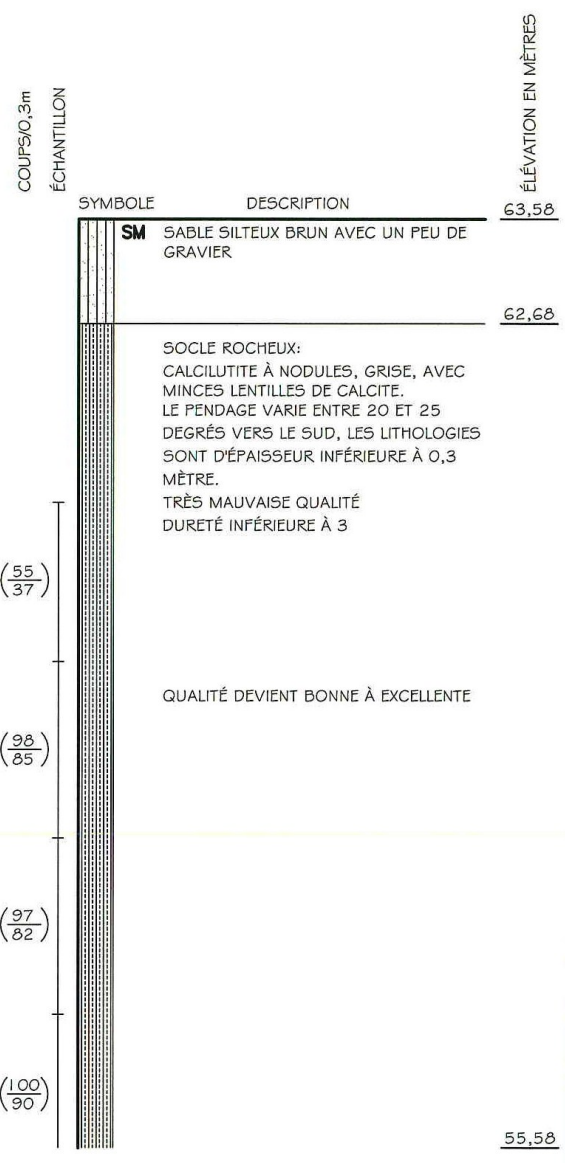
05.009.07F rév. 0.0

1504-001 \ F-1.DWG

FORAGE F-5

ÉLÉVATION DE LA SURFACE: 63,58 MÈTRES

PROFONDEUR EN MÈTRES	ANALYSES ET ESSAIS						
	RÉSULTATS PRÉSENTÉS AILLEURS	LIMITES D'ATTERBERG		ESSAI DE RÉSISTANCE		TENEUR EN EAU (%)	POIDS VOLUMIQUE TOTAL (KN/m ³)
		LIMITE DE LIQUIDITÉ (%)	INDICE DE PLASTICITÉ (%)	TYPE D'ESSAI	RÉSISTANCE AU CISAILEMENT		
0							
1							
2							
3							
4							
5							
6							
7							
8							



RAPPORT DE FORAGE

V.Fournier & Associés

05.009.07F r.év. 0.0

DOSSIER _____ PAR _____ DATE _____ VERIFIÉ PAR _____ DATE _____

1504-001 \ F-1.DWG

FORAGE F-5 (SUITE)

ÉLÉVATION DE LA SURFACE: 63,58 MÈTRES

PROFONDEUR EN MÈTRES	ANALYSES ET ESSAIS					
	RÉSULTATS PRÉSENTÉS AILLEURS	LIMITES D'ATTERBERG		ESSAI DE RÉSISTANCE		POIDS VOLUMIQUE TOTAL (kN/m ³)
		LIMITÉ DE LIQUIDITÉ (%)	INDICE DE PLASTICITÉ (%)	TYPE D'ESSAI	RÉSISTANCE AU CISAILLEMENT	
8						
9						
10						
11						
12						
13						
14						
15						
16						



SYMBOLE	DESCRIPTION	ÉLÉVATION EN MÈTRES
	CALCILITE À NODULES, GRISE, AVEC MINCES LENTILLES DE CALCITE. LE PENDAGE VARIE ENTRE 20 ET 25 DEGRÉS VERS LE SUD, LES LITHOLOGIES SONT D'ÉPAISSEUR INFÉRIEURE À 0,3 MÈTRE. QUALITÉ BONNE À EXCELLENTE DURETÉ INFÉRIEURE À 3	55,58
		47,58

RAPPORT DE FORAGE

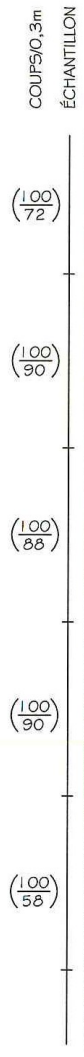
V.Fournier & Associés

DOSSIER _____ PAR _____ DATE _____ VERIFIÉ PAR _____ DATE _____

FORAGE F-5 (SUITE)

ÉLÉVATION DE LA SURFACE: 63,58 MÈTRES

PROFONDEUR EN MÈTRES	ANALYSES ET ESSAIS					
	RÉSULTATS PRÉSENTÉS AILLEURS	LIMITES D'ATTERBERG		ESSAI DE RÉSISTANCE		POIDS VOLUMIQUE TOTAL (kNm ³)
		LIMITE DE LIQUIDITÉ (%)	INDICE DE PLASTICITÉ (%)	TYPE D'ESSAI	RÉSISTANCE AU CISAILEMENT	
6						
17						
18						
19						
20						
21						
22						
23						
24						



SYMBOLE	DESCRIPTION	ÉLÉVATION EN MÈTRES
(100/72)	CALCULITE À NODULES, GRISE, AVEC MINCES LENTILLES DE CALCITE. LE PENDAGE VARIE ENTRE 20 ET 25 DEGRÉS VERS LE SUD, LES LITHOLOGIES SONT D'ÉPAISSEUR INFÉRIEURE À 0,3 MÈTRE. QUALITÉ MOYENNE À EXCELLENTE DURETÉ INFÉRIEURE À 3	47,58
(100/90)		
(100/88)	ZONE TRÈS FORTEMENT FOSSILIFÈRE CONSTITUÉ PRINCIPALEMENT D'ÉCHINODERMES ENTRE 19 ET 20 MÈTRES DE PROFONDEUR	
(100/90)		
(100/58)		
		39,58

RAPPORT DE FORAGE

V.Fournier & Associés

FORAGE F-5 (SUITE)

ÉLÉVATION DE LA SURFACE: 63,58 MÈTRES

PROFONDEUR EN MÈTRES	ANALYSES ET ESSAIS						
	RÉSULTATS PRÉSENTÉS AILLEURS	LIMITES D'ATTERBERG		ESSAI DE RÉSISTANCE		TENEUR EN EAU (%)	POIDS VOLUMIQUE TOTAL (KN/m ³)
		LIMITÉ DE LIQUIDITÉ (%)	INDICE DE PLASTICITÉ (%)	TYPE D'ESSAI	RÉSISTANCE AU CISAILEMENT		
24							
25							
26							
27							
28							
29							
30							
31							
32							

COUPS/30,3m
ÉCHANTILLON

(100 / 88)

(100 / 62)

(100 / 75)

(100 / 98)

(97 / 78)

(100 / 98)

SYMBOLE	DESCRIPTION	ÉLÉVATION EN MÈTRES
(100 / 88)	CALCULITE À NODULES, GRISE, AVEC MINCES LENTILLES DE CALCITE. LE PENDAGE VARIE ENTRE 20 ET 25 DEGRÉS VERS LE SUD, LES LITHOLOGIES SONT D'ÉPAISSEUR INFÉRIEURE À 0,3 MÈTRE. QUALITÉ MOYENNE À EXCELLENTE DURETÉ INFÉRIEURE À 3	39,58
(100 / 62)		
(100 / 75)		
(100 / 98)		
(97 / 78)		
(100 / 98)		31,58

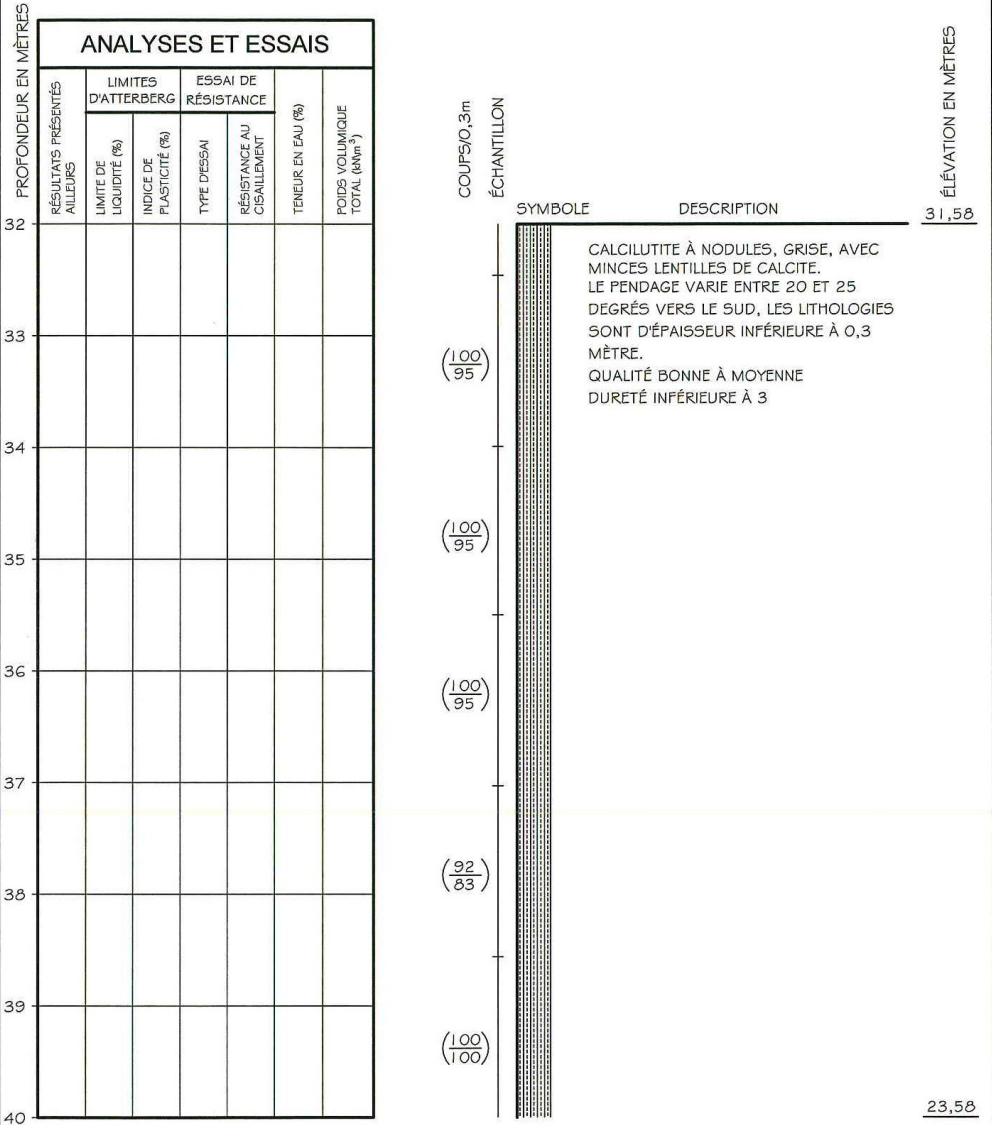
RAPPORT DE FORAGE

V.Fournier & Associés

DOSSIER _____ DATE _____ VERIFIÉ PAR _____ DATE _____ PAR _____

FORAGE F-5 (SUITE)

ÉLÉVATION DE LA SURFACE: 63,58 MÈTRES



RAPPORT DE FORAGE

V.Fournier & Associés

05.009.07F rév. 0.0

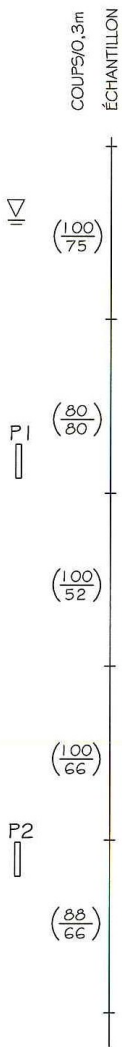
DOSSIER _____ DATE _____
 PAR _____ VÉRIFIÉ PAR _____ DATE _____

1504-001 \F-1.DWG

FORAGE F-5 (SUITE)

ÉLÉVATION DE LA SURFACE: 63,58 MÈTRES

PROFONDEUR EN MÈTRES	ANALYSES ET ESSAIS						
	RÉSULTATS PRÉSENTÉS AILLEURS	LIMITES D'ATTERBERG		ESSAI DE RÉSISTANCE		TENEUR EN EAU (%)	POIDS VOLUMIQUE TOTAL (KNm ⁻³)
		LIMITE DE LIQUIDITÉ (%)	INDICE DE PLASTICITÉ (%)	TYPE D'ESSAI	RÉSISTANCE AU CISAILEMENT		
40							
41							
42							
43							
44							
45							
46							
47							
48							



SYMBOLE	DESCRIPTION	ÉLÉVATION EN MÈTRES
	CALCARÉNITE À NODULES, GRISE, AVEC DES CRISTAUX DE QUARTZ ET DE CALCITE. LE PENDAGE VARIE ENTRE 20 ET 25 DEGRÉS VERS LE SUD, LES LITHOLOGIES SONT D'ÉPAISSEUR INFÉRIEURE À 0,3 MÈTRE. QUALITÉ MOYENNE À BONNE DURETÉ INFÉRIEURE À 3	23,58
	ZONE TRÈS FRACTURÉE ENTRE 43,7 ET 45,1 MÈTRES DE PROFONDEUR	
		15,58

P1 : PIÉZOMÈTRE SUPÉRIEUR
 P2 : PIÉZOMÈTRE MÉDIAN

RAPPORT DE FORAGE

V.Fournier & Associés

FORAGE F-5

ÉLÉVATION DE LA SURFACE: 63,58 MÈTRES

PROFONDEUR EN MÈTRES	ANALYSES ET ESSAIS						
	RÉSULTATS PRÉSENTÉS AILLEURS	LIMITES D'ATTERBERG		ESSAI DE RÉSISTANCE		TENEUR EN EAU (%)	POIDS VOLUMIQUE TOTAL (kNm ⁻³)
	LIMITES DE LIQUIDITÉ (%)	INDICE DE PLASTICITÉ (%)	TYPE D'ESSAI	RÉSISTANCE AU CISAILEMENT			
48							
49							
50							
51							

P3 : PIÉZOMÈTRE INFÉRIEUR

FORAGE TERMINÉ À 50,30 MÈTRES DE PROFONDEUR LE 09/11/12

EAU SOUTERRAINÉ À 40,73 MÈTRES DE PROFONDEUR LE 09/11/12

PIÉZOMÈTRES À CORDE VIBRANTE INSTALLÉS À 43,0, 46,5 ET 50,0 MÈTRES DE PROFONDEUR LE 19/11/12

COUPS/0,3m ÉCHANTILLON	SYMBOLE	DESCRIPTION	ÉLÉVATION EN MÈTRES
(64/38)	[Symbol]	CALCARÉNITE À NODULES, GRISE, AVEC DES CRISTAUX DE QUARTZ ET DE CALCITE. LE PENDAGE VARIE ENTRE 20 ET 25 DEGRÉS VERS LE SUD, LES LITHOLOGIES SONT D'ÉPAISSEUR INFÉRIEUR À 0,3 MÈTRE. TRÈS MAUVAISE QUALITÉ DURETÉ INFÉRIEUR À 3	15,58
(100/93)	[Symbol]		13,28

RAPPORT DE FORAGE

V.Fournier & Associés

DESCRIPTION STRUCTURALE DU ROC

02.002.07F rév. 00

CLIENT	UNIVERSITÉ LAVAL	PROJET No	1504-001
PROJET	FORAGES ET INSTALLATION D'INSTRUMENT, DONT DES PIÉZOMÈTRES ET UN INCLINOMÈTRE DANS LE MASSIF ROCHEUX	FORAGE No	F-5
ENDROIT	GASCONS, GASPÉSIE	PAGE	1 DE 2

COURSE					DESCRIPTION ET OBSERVATIONS												
PROFONDEUR (m)		RGD (%)	RÉCUPÉRATION (%)	PERTE D'EAU (%)	PROFONDEUR (m)		ÉLÉMENT DÉCRIT	NOMBRE DE (FRACTURES, JOINTS)	ANGLE PAR À L'HORIZONTAL	FERMÉ	OUVERT	COURBE	IRRÉGULIER	MIROIR DE FAILLE	RECOUVREMENT DE (X)	ALTÉRATION	COULEUR (XX)
DE	À				DE	À											
2,44	3,81	37	55		2,44	2,59	FRACTURE	1	90°		X	X	X		R	X	b
3,81	5,33	85	98														
5,33	6,86	82	97														
6,86	8,38	90	100		7,62	7,70	FRACTURE	1	60°		X	X	X		R	X	b
8,79	9,91	83	86														
9,91	11,43	80	100		10,21	10,29	FRACTURE	1	80°/90°	X			X		C		g
					10,44	10,59	FRACTURE	1	90°		X	X	X		R,C	X	b
11,43	12,95	90	90														
12,95	14,17	88	100														
14,17	15,70	97	100														
15,70	17,22	72	100														
17,22	18,75	90	100														
18,75	20,27	88	100														
20,27	21,79	90	100		21,08	21,13	FRACTURE	1	55°		X		X				g
					21,74	22,05	FRACTURE	1	80°/90°		X	X	X		R	X	b
21,79	23,32	58	100														
23,32	24,84	88	100														
24,84	26,37	62	100		25,30	25,60	FRACTURE	1	60°/90°		X	X	X		R,A	X	b,g
					25,90	26,21	FRACTURE	1	80°		X	X	X		R,C	X	b
26,37	27,89	75	100		26,52	26,77	FRACTURE	1	70°/90°		X	X	X		R,C	X	b
27,89	29,41	98	100														
29,41	30,94	78	97														
30,94	32,46	98	100														
32,46	33,99	95	100														
33,99	35,51	95	100														
35,51	37,03	95	100														
37,03	38,56	83	92														
38,56	40,08	100	100		39,19	39,32	FRACTURE	1	80°		X	X	X		C		g
40,08	41,61	75	100														

REMARQUES :

(X) : C = CALCITE R = ROUILLE (XX) : bl = BLANC
 G = GRAPHITE P = PYRITE r = ROSE
 I = OXYDE DE FER S = SALBANDE g = GRIS
 K = CHLORITE A = SILT / ARGILE v = VERT
 E = EPIDOTE j = JAUNE
 B = BIOTITE b = BRUN

DESCRIPTION QUALITATIVE DU ROC (RQD)
 $RQD \% = \frac{TOTAL > 100mm}{LONGUEUR DE LA COURSE} \times 100$

DESCRIPTION PAR :	DATE :	VÉRIFIÉ PAR :	DATE :
PHILIPPE BERGERON	09/12/04	VINCENT FOURNIER	09/12/17

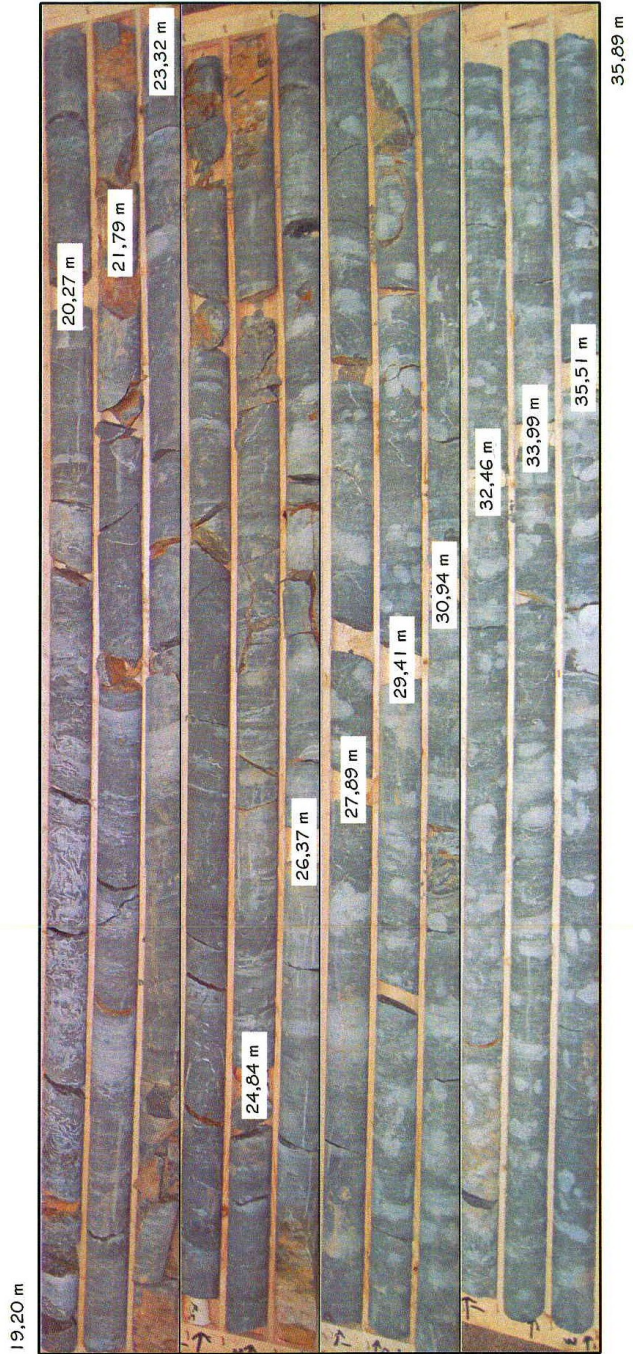
1504-001 - FICHER.DWG

05.200.07F rév. 0.0
1504-001 \RDC F-1.DWG



FORAGE F-5

V.Fournier & Associés



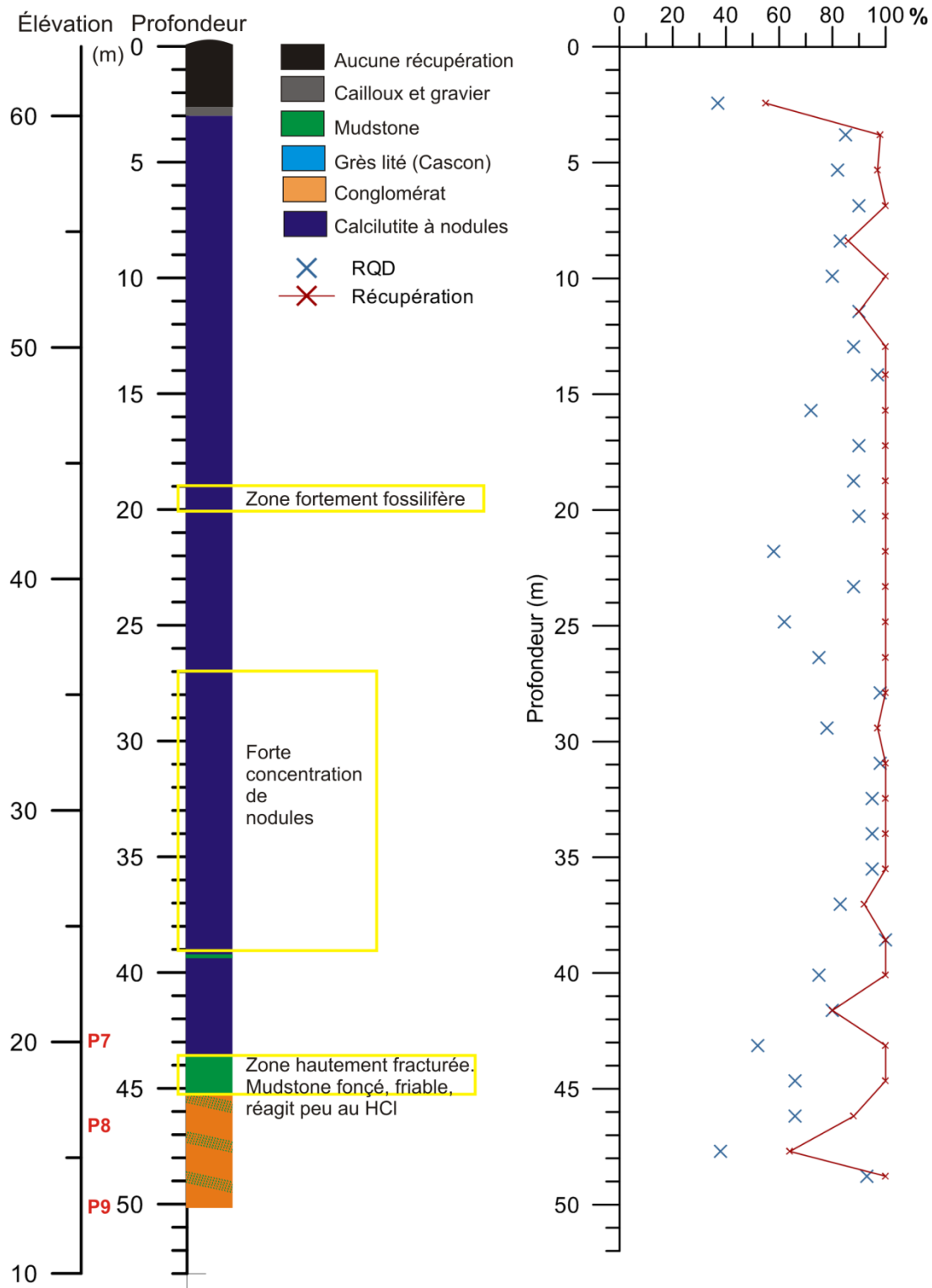
FORAGE F-5

520007F rév. 0.0
504-001 \RDC F-1.DWG



FORAGE F-5

V.Fournier & Associés



Forage F5 réalisé au site 3. Synthèse du log de forage réalisé par Catherine Cloutier.

